Concentrating solar power technology

Related titles:

Materials for energy conversion devices
(ISBN 978-1-85573-932-1)
The term electroceramic is used to describe ceramic materials that have been specially formulated with specific electrical, magnetic or optical properties. Electroceramics are of increasing importance in many key technologies, including: microelectronics, communications and energy conversion. This innovative book is the first comprehensive survey on major new developments in electroceramics for energy conversion devices. It presents current research from leading innovators in the field.

Functional materials for sustainable energy applications
(ISBN 978-0-85709-059-1)
Functional materials are a class of advanced energy conversion materials of use in photoelectric, thermoelectric, electrochemical, piezoelectric or electromagnetic applications, such as photovoltaics (PV), hydrogen production and storage, fuel cell systems, and demand-side energy management systems. Global demands for lower cost, higher efficiency, mass production and, of course, sustainably sourced materials have coupled with advances in nanotechnology to enable an increasingly important role for functional materials in the sustainable energy mix. This book presents a comprehensive review of the issues, science and development of functional materials in renewable and sustainable energy production and management applications.

Stand-alone and hybrid wind energy systems
(ISBN 978-1-84569-527-9)
Wind power generation is fast becoming one of the leading renewable energy sources worldwide, with increasing penetration of stand-alone and hybrid wind energy systems, particularly in distributed, isolated and community power networks. Advanced energy storage and grid integration systems are required to provide secure, reliable power supply to the end user. This book provides an extensive reference on the development of stand-alone and hybrid wind energy systems, as well as energy storage and building-/grid-integration systems. Chapters cover the design, construction, monitoring, control and optimisation of stand-alone and hybrid wind energy technologies, and the continuing development of these systems.

Details of these books and a complete list of titles from Woodhead Publishing can be obtained by:

- visiting our web site at www.woodheadpublishing.com
- contacting Customer Services (e-mail: sales@woodheadpublishing.com; fax: +44 (0) 1223 832819; tel.: +44 (0) 1223 499140 ext. 130; address: Woodhead Publishing Limited, 80 High Street, Sawston, Cambridge CB22 3HJ, UK)
- in North America, contacting our US office (e-mail: usmarketing@woodhead publishing.com; tel.: (215) 928 9112; address: Woodhead Publishing, 1518 Walnut Street, Suite 1100, Philadelphia, PA 19102-3406, USA)

If you would like e-versions of our content, please visit our online platform: www.woodheadpublishingonline.com. Please recommend it to your librarian so that everyone in your institution can benefit from the wealth of content on the site.

Woodhead Publishing Series in Energy: Number 21

Concentrating solar power technology

Principles, developments and applications

Edited by
Keith Lovegrove and Wes Stein

Oxford Cambridge Philadelphia New Delhi

Published by Woodhead Publishing Limited,
80 High Street, Sawston, Cambridge CB22 3HJ, UK
www.woodheadpublishing.com
www.woodheadpublishingonline.com

Woodhead Publishing, 1518 Walnut Street, Suite 1100, Philadelphia,
PA 19102-3406, USA

Woodhead Publishing India Private Limited, G-2, Vardaan House, 7/28 Ansari
Road, Daryaganj, New Delhi – 110002, India
www.woodheadpublishingindia.com

First published 2012, Woodhead Publishing Limited

British Library Cataloguing in Publication Data
A catalogue record for this book is available from the British Library.

Library of Congress Control Number: 2012948529

ISBN 978-1-84569-769-3 (print)
ISBN 978-0-85709-617-3 (online)
ISSN 2044-9364 Woodhead Publishing Series in Energy (print)
ISSN 2044-9372 Woodhead Publishing Series in Energy (online)

The publisher's policy is to use permanent paper from mills that operate a sustainable forestry policy, and which has been manufactured from pulp which is processed using acid-free and elemental chlorine-free practices. Furthermore, the publisher ensures that the text paper and cover board used have met acceptable environmental accreditation standards.

Typeset by Toppan Best-set Premedia Limited
Printed by Publishers' Graphics LLC

Contents

Contributor contact details and author biographies

(* = main contact)

Primary editor and Chapters 1* and 2*

Dr Keith Lovegrove (BSc 1984, PhD 1993) is currently Head – Solar Thermal with the UK-based renewable energy consultancy group, IT Power. He was previously Associate Professor and head of the solar thermal group at the Australian National University where he led the team that designed and built the 500 m^2 generation II big dish solar concentrator. He has served on the board of the ANZ Solar Energy Society as Chair, Vice Chair and Treasurer. For many years he was Australia's SolarPACES Task II representative.

K. Lovegrove
IT Power
PO Box 6127 O'Connor
ACT 2602
Australia
E-mail: keith.lovegrove@itpau.com.au

Editor and Chapter 1

Wes Stein is the Solar Energy Program Leader for CSIRO's Division of Energy Technology. He was responsible for establishing the National Solar Energy Centre and has since grown a team of 30 engineers and scientists and a strong portfolio of high temperature CSP research projects. He represents Australia on the IEA SolarPACES Executive Committee, and is a member of the Australian Solar Institute Research Advisory Committee.

W. Stein
CSIRO Energy Centre
Steel River Eco Industrial Park
10 Murray Dwyer Close
Mayfield West
NSW 2304
Australia
E-mail: wes.stein@csiro.au

Chapter 2

John Pye is a researcher in the Australian National University Solar Thermal Group and also lectures in the Department of Engineering.

J. Pye
Australian National University
Canberra
ACT 0200
Australia
E-mail: John.Pye@anu.edu.au

Chapter 3

Richard Meyer is co-founder and managing director of Germany-based Suntrace. From 2006 to 2009, he headed the technical analysis and energy yield teams of Epuron and SunTechnics. From 1996 to 2006, Richard worked for DLR (German Aerospace Center), where he set up the satellite-based services SOLEMI and DLR-ISIS for analyzing the potential for CSP. He co-founded the IEA Task 'Solar Resource Knowledge Management', for which he is the representative to the SolarPACES Executive Commitee. Dr Richard Meyer holds a diploma in geophysics and a PhD in physics from Munich University.

R. Meyer*, M. Schlecht and K. Chhatbar
Suntrace GmbH
Brandstwiete 46
20457 Hamburg
Germany
E-mail: richard.meyer@suntrace.de

Chapter 4

Martin Schlecht is co-founder and managing director of Germany-based Suntrace, a highly specialized expert advisory firm in large scale solar. His responsibilities include the assessment of CSP and PV project sites and their feasibility. He has a Diploma (MSc) in mechanical engineering and

more than 15 years' work experience in the power industry, covering fossil-fired, concentrating solar thermal and photovoltaic, including international hands-on project development and project implementation.

M. Schlecht* and R. Meyer
Suntrace GmbH
Brandstwiete 46
20457 Hamburg
Germany
E-mail: martin.schlecht@suntrace.de

Chapter 5

Natalia Caldés has a PhD in Agricultural and Natural Resources Economics from the Polytechnic University of Madrid and an MSc in Applied Economics (University of Wisconsin-Madison). Her most relevant professional experience is in the field of development economics as well as energy and enviromental economics. She joined the Spanish agency (CIEMAT) in 2004, where her work focuses on the socio-economic impact assessment of energy technologies, evaluation of energy policies and energy modelling.

Yolanda Lechón has a PhD in Agricultural Engineering. She joined CIEMAT in 1997. Her relevant experience involves life cycle assessment and environmental externalities assessment of energy technologies and energy modelling using techno-economic models.

N. Caldés and Y. Lechón*
Energy System Analysis Unit
Energy Department
CIEMAT – Plataforma Solar de Almería
Avda Complutense 22
28040 Madrid
Spain
E-mail: yolanda.lechon@ciemat.es

Chapter 6

David Mills has worked in non-imaging optics and solar concentrating systems from 1976. At the University of Sydney, he ran the project that created the double cermet selective absorber coating now used widely on solar evacuated tubes and developed the CLFR concept. He was Co-founder, Chairman and CSO of both SHP P/L and Ausra Inc. (later Areva Solar). He has been President of ISES (1997–99), first Chair of the International Solar Cities Initiative, and VESKI Entrepreneur in Residence for the State of Victoria (2009).

D. R. Mills
Australia
Email: davidmills1946@gmail.com

Chapter 7

Eduardo Zarza Moya is an Industrial Engineer with a PhD degree, born in 1958. At present he is the Head of the R&D Unit for Solar Concentrating Systems at the Plataforma Solar de Almería in Spain. He has 27 years' experience with solar concentrating systems, and has been the Director of national and international R&D projects related to solar energy and parabolic trough collectors. He is a member of the Scientific and Technical Committee of ESTELA (European Solar Thermal Electricity Association).

E. Zarza Moya
CIEMAT – Plataforma Solar de Almería
Carretera de Tabernas a Senés, km 5
04200 Tabernas
Almería
Spain
E-mail: eduardo.zarza@psa.es

Chapter 8

Professor Lorin Vant-Hull has been involved in Solar Energy Projects since 1972. He retired as Professor Emeritus from the physics department of the University of Houston in 2001, which he first joined in 1969. Dr Vant-Hull was a Principal Investigator on the earliest US proposal to develop the Solar Central Receiver project epitomized by the Solar One Pilot Plant (10 MWe at Barstow, California). He was program manager for eight years of a Solar Thermal Advanced Research Center. Dr Vant-Hull has been an Associate Editor for the *Journal of Solar Energy* for many years, as well as a member of the Board of Directors of ASES and of ISES.

L. L. Vant-Hull
128 N Red Bud Trail
Elgin, TX 78621
USA
E-mail: solarvanthull@uh.edu

Chapter 9

Wolfgang Schiel, Diplom Physicist, born in 1948 in Hamburg, has over 20 years' experience in solar engineering, especially in design and construction of several Dish/Stirling systems in Germany and other countries (Italy,

India, Spain, Turkey). After his degree at the University of Hamburg he worked with the German Aerospace Research Establishment in Stuttgart. In 1988 he joined schlaich bergermann und partner and became Managing Director of sbp sonne gmbh in 2009.

Thomas Keck, Mechanical Engineer, born in 1959 in Stuttgart, joined schlaich bergermann und partner in 1988 and works as project manager for Dish/Stirling projects.

W. Schiel* and T. Keck
schlaich bergermann und partner
Schwabstr. 43
70197 Stuttgart
Germany
E-mail: stuttgart@sbp.de

Chapter 10

Steve Horne is Co-Founder and Chief Technical Officer at SolFocus. He began designing the concept of SolFocus' CPV solar technology in 2005. Before co-founding SolFocus, Steve was the Director of Engineering at GuideTech, a leading semiconductor test equipment company, and had previously spent six years running a technology consulting firm Tuross Technology. He served as Vice President of Engineering at Ariel Electronics and his early career experience includes commissioning two 500 MW steam generated power plants in New South Wales, Australia.

S. Horne
SolFocus Inc.
510 Logue Avenue
Mountain View, CA 94043
USA
E-mail: steve_horne@solfocus.com

Chapter 11

Dr Wolf-Dieter Steinmann has been working at the German Aerospace Center (DLR) since 1994 and is project manager of the 'CellFlux' project aiming at the development of an innovative thermal storage concept for power plants. He was project manager of the European project DISTOR and the national project PROSPER, which both deal with latent heat storage for medium temperature applications. He completed his PhD thesis on solar steam generators and has worked on the simulation and analysis of the dynamics of thermodynamic systems.

W.-D. Steinmann
German Aerospace Center
Institute of Technical Thermodynamics
Pfaffenwaldring 38–40
70569 Stuttgart
Germany
E-mail: wolf.steinmann@dlr.de

Chapter 12

Professor Hongguang Jin works in the field of solar thermal power technology and CO_2 emission mitigation at the Institute of Engineering Thermophysics in Beijing. He established the mid-temperature solar thermochemical process for integration of solar energy and fossil fuels, and originally proposed the Chemical Looping Combustion system with CO_2 capture. He is a past winner of the best paper award of ASME IGTI – international conference. He is a subject editor for the international journals *Applied Energy* and *Energy*.

Dr Hui Hong is associate professor at the Institute of Engineering Thermophysics in Beijing. She works in the field of solar thermochemical processing.

H. G. Jin* and H. Hong
Institute of Engineering Thermophysics
Chinese Academy of Sciences
Box 2706
Beijing 100190
China
E-mail: hgjin@mail.etp.ac.cn; honghui@mail.etp.ac.cn

Chapter 13

Rosiel Millan has worked since 2009 at Solar Power Group GmbH as a Process Engineer in charge of the design of solar thermal plants. She was born in Mexico where she received her degree in Chemical Engineering. She obtained her MSc in Renewable Energies from Carl von Ossietzky Universität Oldenburg. She acquired her initial experience in thermal energy storage systems for concentrating solar power plants while working as research assistant at Fraunhofer-Institut für Solare Energiesysteme.

Count Jacques de Lalaing, founder of Solar Power Group and Managing Director, is one of the pioneers of Fresnel solar power and established the very first large-scale linear Fresnel pilot unit in the world in the 1990s. In his former capacity as Chief Technology Officer at Solarmundo, Belgium,

he raised awareness of the great potential of this new technology. In 2004, he founded Solar Power Group.

R. Millan*, J. de Lalaing, E. Bautista, M. Rojas and F. Görlich
Solar Power Group GmbH
Daniel-Goldbach-Straße 17–19
40880 Ratingen
Germany
E-mail: r.millan@solarpowergroup.com; j.lalaing@solarpowergroup.com

Chapter 14

Steven J. Smith is a Senior Staff Scientist at the Joint Global Change Research Institute, Pacific Northwest National Laboratory and University of Maryland. His research focuses on energy systems, long-term socioeconomic scenarios and the interface between socioeconomic and climate systems. Prior to joining PNNL in 1999, he worked at the National Center for Atmospheric Research. Dr Smith was a lead author for the Intergovernmental Panel on Climate Change Special Report on Emissions Scenarios. He received his PhD in physics from UCLA.

S. J. Smith
Joint Global Change Research Institute
Pacific Northwest National Laboratory and University of Maryland
5825 University Research Court, Suite 3500
College Park, MD 20740
USA
E-mail: ssmith@pnnl.gov

Chapter 15

Werner Platzer is division director ‘Solar Thermal and Optics’ at Fraunhofer ISE with more than 100 employees. Born in 1957, he graduated in 1982 in theoretical physics and acquired a PhD on solar gain and heat transport in transparent insulation at the Albert-Ludwigs-University Freiburg in 1988. He has been working in research and development of solar thermal energy, facade technology and energy efficiency. He has authored more than 150 articles and conference papers and lectures in solar thermal energy at the University of Freiburg.

W. Platzer* and C. Hildebrandt
Fraunhofer Institute for Solar Energy Systems
Heidenhofstraße 2
79110 Freiburg
Germany
E-mail: werner.platzer@ise.fraunhofer.de

Chapter 16

Gabriel Morin has been working at Novatec Solar GmbH, Karlsruhe, Germany, as a project manager in Research and Development since 2010. From 2001 to 2010, he worked at the Fraunhofer Institute for Solar Energy Systems (ISE) in the field of CSP, including as the coordinator of Solar Thermal Power Plants. Gabriel Morin wrote his PhD thesis on techno-economic design optimization of solar thermal power plants.

G. Morin
Novatec Solar
Herrenstraße 30
76133 Karlsruhe
Germany
E-mail: gabriel.morin@novatecsolar.com

Chapter 17

James B. Blackmon (Aerospace Engineer, BS, 1961, Caltech; MS, 1967 and PhD, 1972, UCLA) is currently Research Professor, Department of Mechanical and Aerospace Engineering, University of Alabama in Huntsville. He was formerly Director, Product Development, McDonnell Douglas Corporation and Boeing Technical Fellow. He was the principal Investigator for the DOE program for low cost heliostat development. His solar power system experience began with a grant to McDonnell Douglas from NSF/University of Houston for heliostat development in 1973. He has over 30 patents in space and terrestrial power, thermal management, and optical and RF systems.

J. B. Blackmon
Department of Mechanical and Aerospace Engineering
University of Alabama in Huntsville
Huntsville, AL 35899
USA
E-mail: blackmoj@uah.edu

Chapter 18

Dr Jesus Ballestrín is currently researcher at Plataforma Solar de Almería CIEMAT, Spain. He has more than 15 years' experience of research and development on solar concentrating technologies as central receivers, heliostats and solar furnaces. His research interests include: metrology of parameters related to concentrated solar radiation: high irradiances and high superficial temperature.

Greg Burgess is the manager of the Solar Thermal Research Facility at the Australian National University.

Jeff Cumpston is a PhD student in the Solar Thermal Group at the Australian National University.

J. Ballestrín*
CIEMAT – Plataforma Solar de Almería
04200 Tabernas
Almería
Spain
E-mail: jesus.ballestrin@psa.es

G. Burgess and J. Cumpston
Research School of Engineering
Building 31, North Rd
Australian National University
Canberra
ACT 0200
Australia
E-mail: greg.burgess@anu.edu.au; jeff.cumpston@anu.edu.au

Chapter 19

Dr Andreas Häberle is CEO of PSE AG, a spin-off company from the Fraunhofer Institute for Solar Energy Systems ISE. Dr Häberle studied Physics at the Technical University of Munich and then worked for seven years as scientist and project manager at the Fraunhofer ISE where he completed his PhD on concentrating solar thermal collectors before founding PSE in 1999. PSE AG specializes in solar test stands, solar consulting and solar conference management.

A. Häberle
PSE AG
Emmy-Noether-Strasse 2
79110 Freiburg
Germany
E-mail: ah@pse.de

Chapter 20

Dr Athanasios G. Konstandopoulos is Founder and Director of APTL at CPERI/CERTH (Greece) since 1996. He has served as Director of CPERI (2006–2012) and since 2011 he is the Chairman of the Board and Managing Director of CERTH. He is also Professor of New, Advanced & Clean Combustion Technologies at Aristotle University. He has a hybrid background in Mechanical (Dipl. ME, AUTH, 1985; MSc ME Michigan Tech, 1987) and Chemical Engineering (MSc, MPhil, PhD, Yale University, 1991) and received the 2006 Descartes Laureate.

Chrysa Pagkoura is a Research Engineer at Aerosol and Particle Technology Laboratory of CPERI/CERTH and member of the HYDROSOL research team.

Dr Souzana Lorentzou is an Affiliate Researcher at Aerosol and Particle Technology Laboratory of CPERI/CERTH and member of the HYDROSOL research team.

A. G. Konstandopoulos*
Aerosol and Particle Technology Laboratory
Centre for Research and Technology Hellas
6th km Harillaou-Thermi Road
57001 Thermi-Thessaloniki
Greece
E-mail: agk@cperi.certh.gr

and

Department of Chemical Engineering
Aristotle University
Thessaloniki
Greece

C. Pagkoura
Aerosol and Particle Technology Laboratory
Centre for Research and Technology Hellas
6th km Harillaou-Thermi Road
57001 Thermi-Thessaloniki
Greece
E-mail: pagoura@cperi.certh.gr

and

Department of Mechanical Engineering
University of West Macedonia
Kozani 50100
Greece

S. Lorentzou
Aerosol and Particle Technology Laboratory
Centre for Research and Technology Hellas
6th km Harillaou-Thermi Road
57001 Thermi-Thessaloniki
Greece
E-mail: souzana@cperi.certh.gr

Woodhead Publishing Series in Energy

1 **Generating power at high efficiency: Combined cycle technology for sustainable energy production**
Eric Jeffs

2 **Advanced separation techniques for nuclear fuel reprocessing and radioactive waste treatment**
Edited by Kenneth L. Nash and Gregg J. Lumetta

3 **Bioalcohol production: Biochemical conversion of lignocellulosic biomass**
Edited by K. W. Waldron

4 **Understanding and mitigating ageing in nuclear power plants: Materials and operational aspects of plant life management (PLiM)**
Edited by Philip G. Tipping

5 **Advanced power plant materials, design and technology**
Edited by Dermot Roddy

6 **Stand-alone and hybrid wind energy systems: Technology, energy storage and applications**
Edited by J. K. Kaldellis

7 **Biodiesel science and technology: From soil to oil**
Jan C. J. Bart, Natale Palmeri and Stefano Cavallaro

8 **Developments and innovation in carbon dioxide (CO_2) capture and storage technology Volume 1: Carbon dioxide (CO_2) capture, transport and industrial applications**
Edited by M. Mercedes Maroto-Valer

9 **Geological repository systems for safe disposal of spent nuclear fuels and radioactive waste**
Edited by Joonhong Ahn and Michael J. Apted

10 **Wind energy systems: Optimising design and construction for safe and reliable operation**
Edited by John D. Sørensen and Jens N. Sørensen

11 **Solid oxide fuel cell technology: Principles, performance and operations**
Kevin Huang and John Bannister Goodenough

12 **Handbook of advanced radioactive waste conditioning technologies**
Edited by Michael I. Ojovan

13 **Membranes for clean and renewable power applications**
Edited by Annarosa Gugliuzza and Angelo Basile

14 **Materials for energy efficiency and thermal comfort in buildings**
Edited by Matthew R. Hall

15 **Handbook of biofuels production: Processes and technologies**
Edited by Rafael Luque, Juan Campelo and James Clark

16 **Developments and innovation in carbon dioxide (CO_2) capture and storage technology Volume 2: Carbon dioxide (CO_2) storage and utilisation**
Edited by M. Mercedes Maroto-Valer

17 **Oxy-fuel combustion for power generation and carbon dioxide (CO_2) capture**
Edited by Ligang Zheng

18 **Small and micro combined heat and power (CHP) systems: Advanced design, performance, materials and applications**
Edited by Robert Beith

19 **Advances in clean hydrocarbon fuel processing: Science and technology**
Edited by M. Rashid Khan

20 **Modern gas turbine systems: High efficiency, low emission, fuel flexible power generation**
Edited by Peter Jansohn

21 **Concentrating solar power technology: Principles, developments and applications**
Edited by Keith Lovegrove and Wes Stein

22 **Nuclear corrosion science and engineering**
Edited by Damien Féron

23 **Power plant life management and performance improvement**
Edited by John E. Oakey

24 **Direct-drive renewable energy systems**
Edited by Markus Mueller and Henk Polinder

25 **Advanced membrane science and technology for sustainable energy and environmental applications**
Edited by Angelo Basile and Suzana Pereira Nunes

26 **Irradiation embrittlement of reactor pressure vessels (RPVs) in nuclear power plants**
Edited by Naoki Soneda

27 **High temperature superconductors (HTS) for energy applications**
Edited by Ziad Melhem

28 **Infrastructure and methodologies for the justification of nuclear power programmes**
Edited by Agustín Alonso

29 **Waste to energy (WtE) conversion technology**
Edited by Marco Castaldi

30 **Polymer electrolyte membrane and direct methanol fuel cell technology Volume 1: Fundamentals and performance of low temperature fuel cells**
Edited by Christoph Hartnig and Christina Roth

31 **Polymer electrolyte membrane and direct methanol fuel cell technology Volume 2: *In situ* characterization techniques for low temperature fuel cells**
Edited by Christoph Hartnig and Christina Roth

32 **Combined cycle systems for near-zero emission power generation**
Edited by Ashok D. Rao

33 **Modern earth buildings: Materials, engineering, construction and applications**
Edited by Matthew R. Hall, Rick Lindsay and Meror Krayenhoff

34 **Metropolitan sustainability: Understanding and improving the urban environment**
Edited by Frank Zeman

35 **Functional materials for sustainable energy applications**
Edited by John Kilner, Stephen Skinner, Stuart Irvine and Peter Edwards

36 **Nuclear decommissioning: Planning, execution and international experience**
Edited by Michele Laraia

37 **Nuclear fuel cycle science and engineering**
Edited by Ian Crossland

38 **Electricity transmission, distribution and storage systems**
Edited by Ziad Melhem

39 **Advances in biodiesel production: Processes and technologies**
Edited by Rafael Luque and Juan A. Melero

40 **Biomass combustion science, technology and engineering**
Edited by Lasse Rosendahl

41 **Ultra-supercritical coal power plant: Materials, technologies and optimisation**
Edited by Dongke Zhang

42 **Radionuclide behaviour in the natural environment: Science, implications and lessons for the nuclear industry**
Edited by Christophe Poinssot and Horst Geckeis

43 **Calcium and chemical looping technology for power generation and carbon dioxide (CO_2) capture: Solid oxygen- and CO_2-carriers**
P. Fennell and E. J. Anthony

44 **Materials' ageing and degradation in light water reactors: Mechanisms, modelling and mitigation**
Edited by K. L. Murty

45 **Structural alloys for power plants: Operational challenges and high-temperature materials**
Edited by Amir Shirzadi, Rob Wallach and Susan Jackson

46 **Biolubricants: Science and technology**
Jan C. J. Bart, Emanuele Gucciardi and Stefano Cavallaro

47 **Wind turbine blade design and materials: Improving reliability, cost and performance**
Edited by Povl Brøndsted and Rogier Nijssen

48 **Radioactive waste management and contaminated site clean-up: Processes, technologies and international experience**
Edited by William E. Lee, Michael I. Ojovan, Carol M. Jantzen

49 **Probabilistic safety assessment for optimum nuclear power plant life management (PLiM)**
Gennadij V. Arkadov, Alexander F. Getman and Andrei N. Rodionov

50 **Coal utilization in industry**
Edited by D. G. Osborne

51 **Coal power plant materials and life assessment: Developments and applications**
Edited by Ahmed Shibli

52 **The biogas handbook: Science, production and applications**
Edited by Arthur Wellinger and David Baxter

53 **Advances in biorefineries: Biomass and waste supply chain exploitation**
Edited by K. W. Waldron

54 **Geoscience of carbon dioxide (CO_2) storage**
Edited by Jon Gluyas and Simon Mathias

55 **Handbook of membrane reactors Volume 1: Fundamental materials science, design and optimisation**
Edited by Angelo Basile

56 **Handbook of membrane reactors Volume 2: Industrial applications and economics**
Edited by Angelo Basile

57 **Alternative fuels and advanced vehicle technologies: Towards zero carbon transportation**
Edited by Richard Folkson

58 **Handbook of microalgal bioprocess engineering**
Christopher Lan and Bei Wang

59 **Fluidized-bed technologies for near-zero emission combustion and gasification**
Edited by Fabrizio Scala

60 **Managing nuclear projects: A comprehensive management resource**
Edited by Jas Devgun

61 **Handbook of process integration: Energy, water, waste and emissions management in processing and power industries**
Edited by Jiří Klemeš

Foreword

During this century the human race will have to address the challenge of deeply transforming the world energy system to make it much more sustainable and environmentally friendly than the one we currently have. To achieve this, it will have to substantially increase the market penetration of all types of renewable energy technologies, and especially of solar technologies, since these technologies will be called upon to be the main pillars of the new world energy system, because of the vast quantities and the high quality of the solar energy reaching the Earth at every instant.

The shift towards a much greener world energy system requires an extraordinary mobilization of technological and economic resources. The good news is that this mobilization is starting to happen. According to the US Department of Energy, in 2011, for the first time in history, worldwide investment in renewable electricity generation capacity exceeded the worldwide investment in conventional systems.

To enable the required large-scale development and deployment of renewable energy systems worldwide, it is essential to ensure that the renewable energy industry has access to affordable finance and to the necessary renewable energy expertise and know-how.

This book represents an important contribution to disseminate the knowledge and expertise that its authors have in the field of concentrating solar power (CSP). The diversity of countries, institutions and fields of expertise represented by the contributors to this book, and the quality of their contributions also constitute an example in itself of the rapid but solid expansion that the CSP international community has undergone over recent decades.

In addition to congratulating the editors and the authors for delivering this excellent book, I would like to end this foreword by pointing out the fact that many of the contributors to this book and their institutions are active participants in the activities of SolarPACES, the Implementing Agreement of the International Energy Agency for 'Solar Power and

Chemical Energy Systems'. This is not by chance; the rapid expansion that the CSP industry is experiencing worldwide since 2003 owes much to the unfaltering work of SolarPACES over the last 30 years.

Manuel J. Blanco, PhD Dr Ing.
Chair, SolarPACES Executive Committee

1

Introduction to concentrating solar power (CSP) technology

K. LOVEGROVE, IT Power, Australia and
W. STEIN, CSIRO Energy Centre, Australia

Abstract: This introductory chapter begins by defining 'concentrating solar power' (CSP) and outlining the role of the book. It then introduces some of the historical background to the development of CSP systems and the present day context of a period of industry growth amid major changes to the world's energy systems. It describes the key approaches of parabolic trough, central receiver, linear Fresnel, Fresnel lens and paraboloidal dish concentrator systems. The prospects for continued deployment growth and parallel cost reductions are discussed. Finally the organization of the overall book is outlined.

Key words: concentrating solar power, concentrating photovoltaics, dish, trough, tower, Fresnel lens, linear Fresnel reflector, history, approaches to concentration, cost reduction, growth in deployment.

1.1 Introduction

Concentrating solar power (CSP) systems use combinations of mirrors or lenses to concentrate direct beam solar radiation to produce forms of useful energy such as heat, electricity or fuels by various downstream technologies. The term 'concentrating solar power' is often used synonymously with 'concentrating solar thermal power'. In this book the term is used in a more general sense to include both concentrating solar thermal (CST) and concentrating photovoltaic (CPV) energy conversion.

Whilst the primary commercial attention today and the emphasis in this book is on systems designed for generation of electric power, there are individual chapters that review the important market segment of process heat and also the concept of solar fuels production, which the editors suggest is likely to see a rapid rise in interest in the near future.

This book seeks to address multiple audiences, and chapters can be read selectively according to need.

- A reader with a background in science or engineering should find a resource that introduces all the key principles and the state of the art of the CSP field.
- Many of the chapters contain detailed review and presentation on various key aspects that should provide value to those experts already

working in the field and, given the pace of technological change, suggested resources for remaining up to date.
- At the same time, the book should provide value to readers without a technical background. Care has been taken to provide overviews and introductions of all key concepts in a manner targeted at the non-technical audience such as policy makers, for example.

This book seeks to provide comprehensive, complete and up-to-date coverage of the CSP field. A previous well-respected coverage of this nature was provided by Winter *et al.* (1991). There are a number of past and recent books that address broader solar energy topics and others with more technical coverage of specific issues, which are referenced in various chapters where relevant.

1.1.1 History and context

Global investments in clean energy generation are continuing to increase with global energy producers (and users) now experiencing strong signals to develop a clean energy future. Over the last three decades, the world wind industry has grown at an average rate of approximately 30% per year to reach a total installed capacity of 239 GW by the end of 2011. This represents nearly 3% of total world electricity annual generation (WWEA, 2012) and wind capacity is now being installed at a faster annual rate than nuclear.

Over a shorter period, the solar photovoltaic (PV) industry has grown with comparable or higher rates of growth but from a lower base and in 2011 had a worldwide installed capacity of approximately 69 GW (EPIA, 2012). CSP technology saw a first surge of commercial development between 1984 and 1995, but then no further commercial deployment until 2005, although in that time considerable research, development and demonstration took place. Since then, commercial CSP deployment has recommenced and gained considerable momentum. Total installed capacity is, however, an order of magnitude smaller than PV, given that commercialization of the technology is a decade or so behind.

The concept of concentrating solar energy has been a technology of interest throughout history. For example:

- Archimedes described the idea of mirrored panels to concentrate the sun in around 200 BC;
- The Greek mathematician Diocles described the optical properties of a parabolic trough in the second century BC;
- The development of heliostat designs was described by Comte de Buffon in 1746;
- Augustin Mouchot demonstrated a dish driven steam engine system at the 1878 universal exhibition in Paris.

A more contemporary historical landmark was Frank Schuman's successful parabolic trough driven pumping system built in Egypt in 1913. Experiments and prototypes were developed all through the twentieth century. The real birth of CSP as an industry came in California in the 1980s. Favourable government policy settings lead to the construction of nine separate parabolic trough based 'Solar Electric Generating Systems' (SEGS), totalling 354 MW_e of installed capacity. These were based around steam turbines for power generation, and used oil as the heat transfer fluid within the trough receivers.

These plants, with more than 2,000,000 m^2 of mirror area, continue to operate under utility ownership after more than 20 years and have established the technology as commercially proven. The tenth plant was in the early stages of construction when the effect of lower oil prices and changes in government policy led to a loss of investment and subsequent demise of the company driving the development (LUZ). However, the technology was now on the map, and over that 1984–95 period, with just 354 MW deployed, the capital cost was successfully halved.

The lead role in renewable energy development was grasped around that time by countries in north-western Europe, led by Denmark and then Germany. The emphasis was on pursuing wind power given the favourable wind and less favourable solar resources in those countries. Though wind turbines today are of the order of 3–5 MW per unit, at that time they were in the small hundreds of kW, and even though the specific capital cost was similar to or higher than CSP, the smaller modules provided a much easier investment path. Led by government incentives, PVs have moved from high cost space/satellite and small remote off-grid applications to residential applications and more recently large multi-MW installations. The renewable energy agenda has spread around the globe and overall market demand for renewable electricity continues to grow exponentially, though the 'new' renewables such as wind and PV still account for only a few percent of the world's electricity demand.

A past and continuing challenge for CSP is its dependence on the economies of scale afforded by large steam turbines, leading to large levels of risk capital per project for a relatively new technology. However, now that the size of new renewable projects has grown, there is more appetite for making the necessary investments.

Concern over human induced climate change has emerged to dominate the political agenda around energy supply. There has been a resurgence of CSP development since 2005, led partly by the recognition that it is a technology which could make large greenhouse gas emission cuts quickly, and offer the significant benefit of distributable solar power through integrated thermal storage. This growth has been led predominantly by Spain through specific and targeted feed-in tariff incentives that have

proven highly successful for the technology. Approximately 2,400 MW is approved for operation by 2014 with half of that already operating. The sun belt of the south-west USA has also been targeted for CSP through tax credits and loan guarantees with approximately 1.8 GW expected to be in operation by the end of 2013. Importantly, the majority of new installations now incorporate thermal storage, usually of the order of 6 hours or so.

Other countries with CSP projects announced or under construction include North Africa (Algeria, Morocco) and the Middle East (Egypt, Israel), China, India, Australia, South Africa, Portugal, Italy, Greece, Malta and Cyprus. In 2010, India took a major initiative with the establishment of the Jawaharlal Nehru National Solar Mission, with a target of 20 GW_e of combined PV and CSP capacity to be installed by 2022. China has a target of 1 GW of CSP by 2015. This activity has combined to give a rate of growth from 2005 to 2012 of approximately 40% per year. This is similar to the rate of growth for wind power during its first decade of modern commercial deployment, which began in approximately 1990, and faster than that for PVs when it began to accelerate commercial deployment in about 1992. Whilst the industry is still in its early stages and vulnerable to sudden policy changes in key countries, continued strong growth in global installed capacity is predicted.

Due to the 15-year hiatus in commercial CSP deployments, installed PV capacity grew to be some ten times greater than CSP, and as a result PV has seen significant cost reduction over recent years, whilst CSP is at an early stage of its cost reduction path. In 2012, PV is lower cost than CSP for non-dispatchable electricity production under most applications. Under these circumstances, greater attention is turning to CSP's potential benefits of built-in thermal energy storage and dispatchability, as well as other non-electrical applications such as fuels.

Whilst the issue of climate change is dominating the future energy agenda, the idea that demand for oil may have now passed the level of supply from conventional sources is well accepted and, despite large levels of fluctuation, the overall trend is to increasing prices. This could prove to be a very major driver for technology change both increasing demand for solar electricity and encouraging developments such as solar fuels.

1.2 Approaches to concentrating solar power (CSP)

CSP systems capture the direct beam component of solar radiation. Unlike flat plate photovoltaics (PV), they are not able to use radiation that has been diffused by clouds or dust or other factors. This makes them best suited to areas with a high percentage of clear sky days, in locations that do not have smog or dust.

The configurations that are currently used commercially in order of deployment level are:

- parabolic trough
- central receiver tower
- linear Fresnel
- Fresnel lenses (for CPV)
- paraboloidal dishes.

Each technology boasts particular advantages and in some cases particular market segments. Project and technology developers are actively pursuing all types of CSP technologies. In addition to these concepts that are applied commercially, a solar furnace arrangement is widely used as a tool for research projects. A solar furnace typically consists of a paraboloidal dish mounted in a fixed orientation in a laboratory building, with one or more external heliostats directing solar radiation to it at a fixed angle.

1.2.1 Parabolic trough

Parabolic trough-shaped mirrors produce a linear focus on a receiver tube along the parabola's focal line as illustrated in Fig. 1.1. The complete assembly of mirrors plus receiver is mounted on a frame that tracks the daily movement of the sun on one axis. Relative seasonal movements of the sun in the other axis result in lateral movements of the line focus, which remains on the receiver but can have some spill at the row ends.

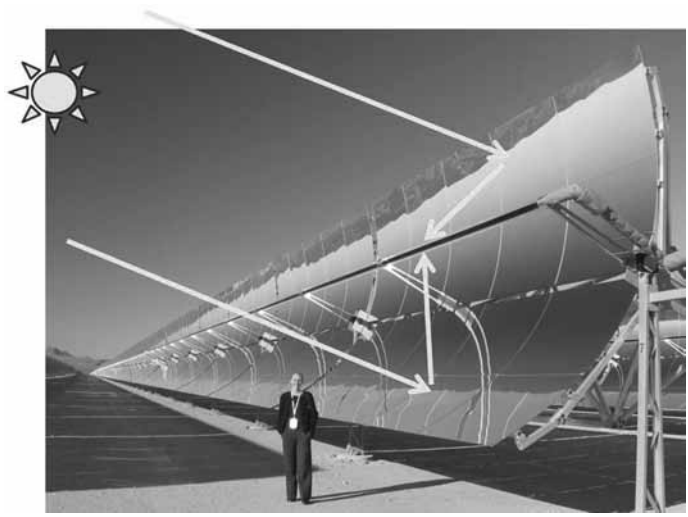

1.1 Parabolic trough collector: tracks the sun on one axis (background picture, Nevada Solar 1 plant, R. Dunn).

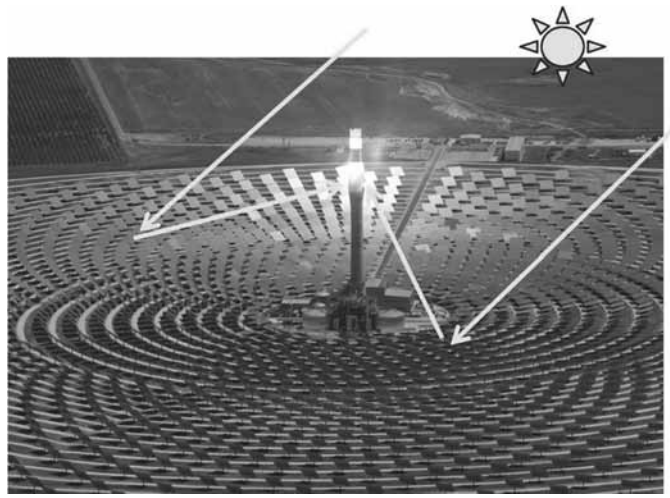

1.2 Central receiver tower plant: multiple heliostats move on two axes to focus the sun to a fixed tower mounted receiver (background picture, Gemasolar plant, owned by Torresol Energy, © Torresol Energy).

Trough systems using thermal energy collection via evacuated tube receivers are currently the most widely deployed CSP technology. In this configuration, an oil heat transfer fluid is usually used to collect the heat from the receiver tubes and transport it to a central power block. Chapter 7 examines trough systems in detail.

1.2.2 Central receiver tower

A central receiver tower system involves an array of heliostats (large mirrors with two axis tracking) that concentrate the sunlight onto a fixed receiver mounted at the top of a tower, as illustrated in Fig. 1.2. This allows sophisticated high efficiency energy conversion at a single large receiver point. Higher concentration ratios are achieved compared to linear focusing systems and this allows thermal receivers to operate at higher temperatures with reduced losses. A range of system and heliostat sizes have been demonstrated. Chapter 8 examines tower systems in detail.

1.2.3 Linear Fresnel reflectors

Linear Fresnel reflector (LFR) systems produce a linear focus on a downward facing fixed receiver mounted on a series of small towers as shown in Fig. 1.3. Long rows of flat or slightly curved mirrors move independently on one axis to reflect the sun's rays onto the stationary receiver. For thermal

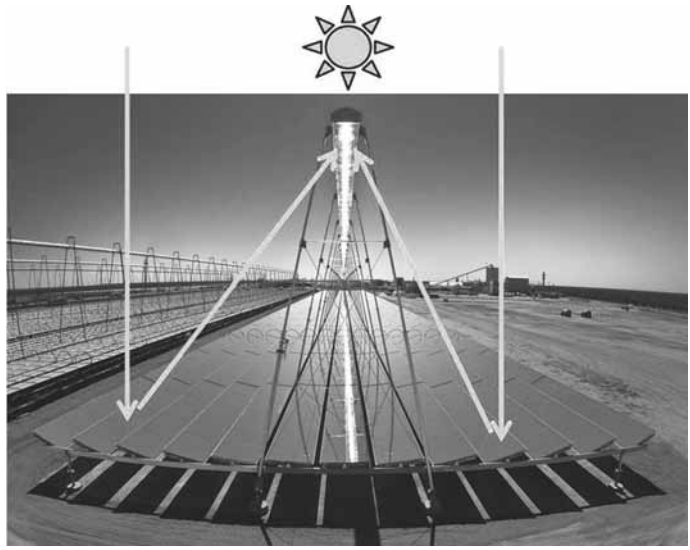

1.3 Linear Fresnel reflector: multiple mirrors move on one axis to focus the sun to a fixed linear receiver (background picture, Kimberlina LFR plant, Bakersfield California, image courtesy of AREVA Solar).

systems, the fixed receiver not only avoids the need for rotary joints for the heat transfer fluid, but can also help to reduce convection losses from a thermal receiver because it has a permanently down-facing cavity.

The proponents of the LFR approach argue that its simple design with near flat mirrors and less supporting structure, which is closer to the ground, outweighs the lower overall optical and (for CST) thermal efficiency. To increase optical and ground-use efficiency, compact linear Fresnel reflectors (CLFRs) use multiple receivers for each set of mirrors so that adjacent mirrors have different inclinations in order to target different receivers. This allows higher packing density of mirrors which increases optical efficiency and minimizes land use. Chapter 6 examines linear Fresnel systems in detail.

1.2.4 Fresnel lens

A conventional lens is expensive and impractical to manufacture on a large scale. The Fresnel lens overcomes these difficulties and has been employed extensively for CPV systems. A Fresnel lens is made as a series of concentric small steps, each having a surface shape matching that which would be found on a standard lens but with all the steps kept within a small thickness. A plastic material is usually used and arrays of multiple lens units are typically mounted on a heliostat structure as shown in Fig. 1.4. This is also a

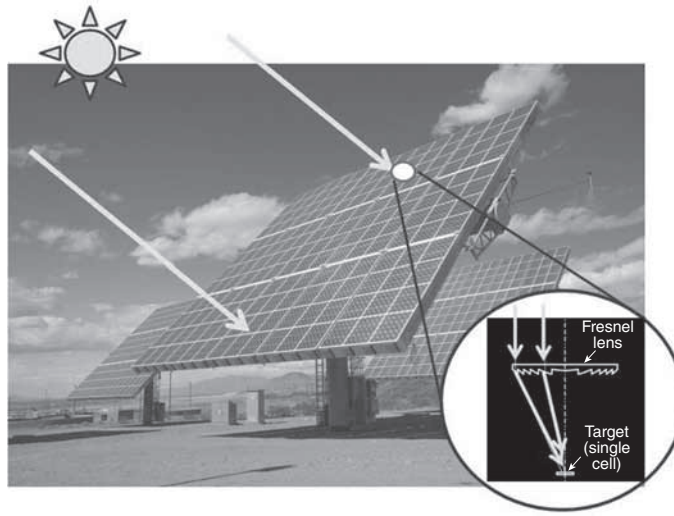

1.4 Fresnel lens-based CPV: multiple small units on a heliostat (background picture, River Mountains, USA, Amonix).

point focus approach requiring accurate sun tracking in two axes. Chapter 10 examines various CPV systems in detail.

1.2.5 Parabolic dishes

Dish systems, like troughs, exploit the geometric properties of a parabola, but as a three-dimensional paraboloid as shown in Fig. 1.5. The reflected direct beam radiation is concentrated to a point focus receiver and in CST systems can heat this to operating temperatures of over 1,000ºC, similar to tower systems.

Dish systems offer the highest potential solar conversion efficiencies of all the CSP technologies, because they always present their full aperture directly towards the sun and avoid the 'cosine loss effect' that the other approaches experience. They are, however, the least commercially mature. Dishes up to 24 m diameter have been demonstrated.

As well as thermal conversion, CPV conversion on dishes is well established, it is also applied with 'micro dishes' with diameters of just several centimetres. Chapter 9 examines dish systems in detail.

1.3 Future growth, cost and value

CSP systems produce renewable electricity that ultimately must compete with other forms of electricity generation in the marketplace. Thus the cost

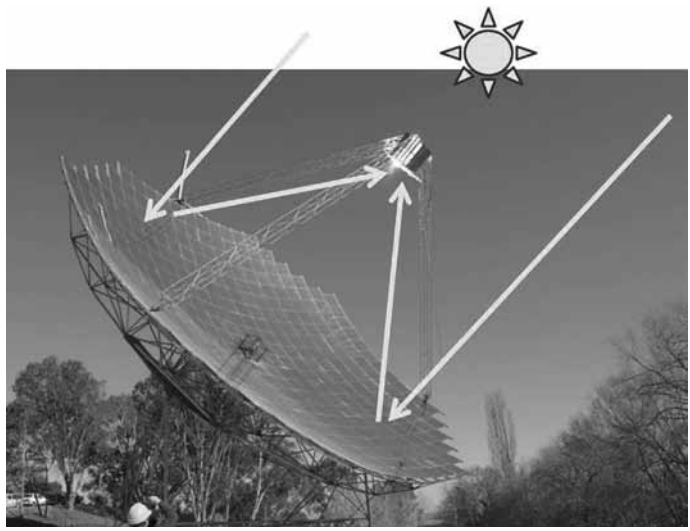

1.5 Paraboloidal dish concentrator: tracks the sun in two axes (background picture, Australian National University, 500 m^2 dish).

of CSP energy is the main preoccupation of the technology developers and research and development practitioners within the CSP community. With no fuel costs, the cost of CSP energy is dominated by the amortization of the high initial capital cost investment over the life of the plant.

CSP is a proven technology that is at an early stage of its cost reduction curve. A period of rapid growth in installed capacity, together with a rapid decay in cost of energy produced is confidently predicted by the industry. The trend of cost reduction as installed capacity increases is logically linked to:

- technical improvements, as lessons are learned from installed plants and parallel R&D efforts identify performance improvements,
- scaling to larger installed plant size, which allows for more efficient and more cost-effective large turbines and other components to be used, and
- volume production that allows fixed costs of investments in production efficiency to be spread over larger production runs.

Empirically these practical effects lead to a commonly observed trend for a new technology of a reduction in cost of an approximately fixed fraction for every doubling of deployed capacity.

An analysis of various comprehensive studies investigating feasible cost reduction paths for CSP was carried out in a study for the Global Environment Facility for the World Bank in 2006 (World Bank 2006). One comprehensive scenario predicted a pathway to install 5 GW by 2015.

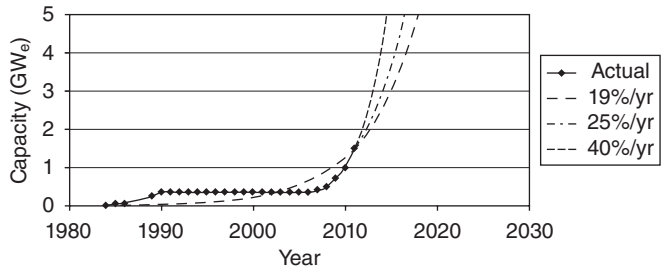

1.6 Global installed capacity of CSP plants, both actual and possible future compound growth rates.

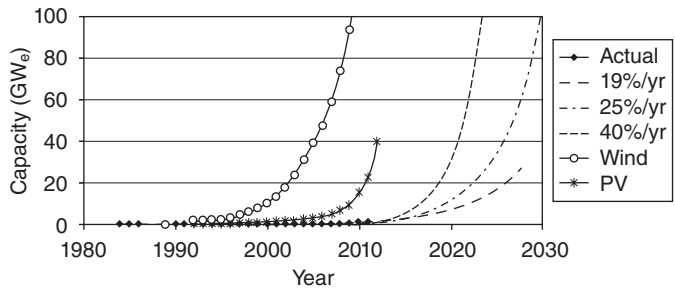

1.7 Global installed capacity of CSP plants, both actual and possible future compound growth rates together with historical data for wind and PV deployment.

A recent roadmap published by the International Energy Agency (IEA) for CSP technology presents a highly credible summary of the global situation and way forward (IEA 2010). Cost of energy reductions to around 25% of 2010 values are predicted by 2050. AT Kearney (2010) was commissioned by European and Spanish CST industry associations to produce a study of CSP energy cost reduction projections. A range of key areas for reducing cost of manufacture and increasing annual output are identified, these measures together are suggested to result in an overall reduction of cost of energy in 2025 relative to 2012 of 40–50%. Over the same time period, they suggest global installed capacity could reach between 60 and 100 GW depending on policy measures in place. Figure 1.6 illustrates the history of installed capacity to 2011 together with extrapolations based on compound growth rates of the 19% per year average since 1984 and the 40% per year average since 2005.

Figure 1.7 shows the same data on an expanded vertical axis, together with actual historical data for installed capacity of wind and PV systems. The historical high compound growth rates for these technologies can be seen together with the approximately one decade lag between PV growth

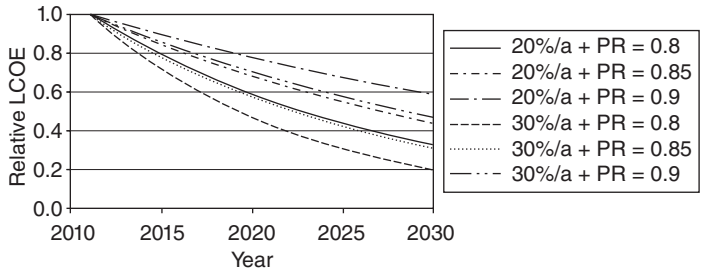

1.8 Possible relative levelized cost of energy (LCOE) reductions over time under different growth rates and progress ratios.

and that of wind. CSP is seen to be entering a similar growth phase with a further approximately one decade lag.

Other studies support the conclusions on cost reduction potential. Kutscher *et al.* (2010) identifies in detail a range of specific 'bottom-up' measures that are estimated to deliver a 40% cost of energy reduction for line focus systems by 2017. Kolb *et al.* (2010) identifies measures that will deliver 50% cost reductions for tower systems by 2020.

Available evidence points to a cost reduction of 10–15% for every doubling in global capacity (a progress ratio of 0.9–0.85). Figure 1.8 plots the progression over time of relative costs (either cost of energy or capital costs[1]) under either 20% p.a. or 30% p.a. growth rates, and for cost progress ratios of 0.8, 0.85 and 0.9.

As variable renewables like wind and PV vie for a larger proportion of energy supply, the ability to provide dispatchable power will become more important. CSP has the advantages that incorporation of thermal energy storage is cost effective, improves system performance and has very little effect on the overall cost of energy. Energy storage is examined in detail in Chapter 11. Some recent studies have begun to evaluate the extra value that can be offered by the energy storage abilities of CSP systems (e.g. Sioshansi and Denholm, 2010 and Madaeni *et al.*, 2011), and it can be 30% or more valuable than average market prices. Thus CSP can look forward to a growing recognition of the value of its energy in parallel with future cost reductions.

1.4 Organization of this book

The book is organized into three parts.

[1] Note that cost of energy is strongly dependent on capital cost, but also depends on operating and maintenance costs and financing costs. For a first approximation, cost of energy and capital cost are assumed to reduce over time according to the same progress ratio.

Part I contains fundamental introductory material of which this introductory chapter forms the first part. This is followed by Chapter 2 which overviews the fundamental principles behind CSP technologies. It is quite a technical chapter that can be skipped by those seeking to read directly about specific technology. Understanding solar resources issues, siting and feasibility studies and the techno-economic assessment of CSP systems are the subject of the other chapters in Part I.

Part II, on technology approaches and potential, contains specific chapters that review the principles, historical development and state of the art of the trough, tower, linear Fresnel and dish approaches. These are followed by further chapters on energy storage, hybridization, CPV systems and finally the economic outlook.

Part III, on optimization, improvements and applications, comprises chapters that provide in-depth coverage of a range of key issues around maximizing performance through technology and design optimization. Key applications to process heat and solar fuels are also presented as a complement to the overall emphasis on power generation. Solar fuels derived from concentrating solar systems are presented as the last chapter of the book. This reflects a belief on the part of the editors that whilst solar fuels is currently an activity still very much in the R&D sphere, it could well become the biggest future market for solar concentrating systems, given future projections of demand outstripping supply for oil.

1.5 References

AT Kearney (2010), *Solar Thermal Electricity 2025*, Report for ESTELLA by A.T. Kearney GmbH, Kaistraße 16A, 40221 Duesseldorf, Germany.

IEA (2010), *Technology Roadmap – Concentrating Solar Power*, OECD International Energy Agency, Publications Service, OECD 2, rue André-Pascal, 75775 Paris cedex 16, France.

EPIA (2012), *Global market outlook for photovoltaics until 2016*, European Photovoltaic Industry Association, Rue d'Arlon 63-67 (1040) Brussels – Belgium, www.epia.org.

Kolb G, Ho C, Mancini T and Gary J (2011), *Power Tower Technology Roadmap and Cost Reduction Plan*, SANDIA REPORT SAND2011-2419, April 2011, Prepared by Sandia National Laboratories Albuquerque, NM 87185 and Livermore, CA 94550, http://prod.sandia.gov/techlib/access-control.cgi/2011/112419.pdf.

Kutscher C, Mehos M, Turchi C, Glatzmaier G and Moss T (2010), *Line-Focus Solar Power Plant Cost Reduction Plan*, NREL/TP-5500-48175, December, http://www.nrel.gov/docs/fy11osti/48175.pdf.

Madaeni S Sioshansi R and Denholm P (2011), *Capacity Value of Concentrating Solar Power Plants*, National Renewable Energy Laboratory Technical Report NREL/TP-6A20-51253.

Sioshansi R and Denholm P (2010), *The Value of Concentrating Solar Power and Thermal Energy Storage*, Technical Report NREL-TP-6A2-45833, February.

Winter C-J, Sizmann R L and Vant-Hull L L (1991), *Solar Thermal Power Plants*, New York, Springer Verlag.

World Bank (2006), *Assessment of the World Bank/GEF Strategy for the Market Development of Concentrating Solar Thermal Power*, Report Prepared for the World Bank.

WWEA (2012), *Wind energy around the world*, World Wind Energy Association, quarterly report, Editor-in-Chief: Stefan Gsänger, Issue 1, March.

2

Fundamental principles of concentrating solar power (CSP) systems

K. LOVEGROVE, IT Power, Australia and
J. PYE, Australian National University, Australia

Abstract: This chapter provides an overview of the fundamental principles of CSP systems. It begins with the optical processes and the ultimate limits on the extent to which solar radiation can be concentrated. Practical factors that reduce achievable concentration levels further are discussed. Mechanisms of thermal energy loss from receivers are covered. Available power cycles for electricity generation are reviewed. The second law of thermodynamics is introduced to lead into a consideration of optimization of overall system efficiency via variation of operating temperature and receiver aperture size. Performance modelling of complete systems is introduced and finally the analysis of levelized cost of energy is covered, as a metric for comparing systems, and as a tool to thermo-economic optimization in design.

Key words: maximum concentrator, sun shape, circumsolar ratio, acceptance angle, efficiency, capacity factor, solar multiple, levelized cost of energy.

2.1 Introduction

A concentrating solar power (CSP) system can be presented schematically as shown in Fig. 2.1. All systems begin with a concentrator; the various standard configurations of trough, linear Fresnel, dish and tower have been introduced in Chapter 1, and are addressed in detail in later chapters. There is a clear distinction between the line-focusing systems which concentrate solar radiation by 50–100 times, and the point-focus systems that concentrate by factors of 500 to several thousand.

The concentrated radiation must be intercepted by a receiver which converts it to another form, typically thermal energy. The currently dominant trough-based CSP systems use receivers that are single steel tubes covered by a glass tube, with the annular space evacuated to reduce convection heat losses. Another commonly used option is to arrange multiple tubes to form cavity shapes (either line- or point-focus). Alternatively, 'volumetric' or direct absorption receivers aim to have the radiation absorbed by surfaces directly immersed in the working fluid. This can be

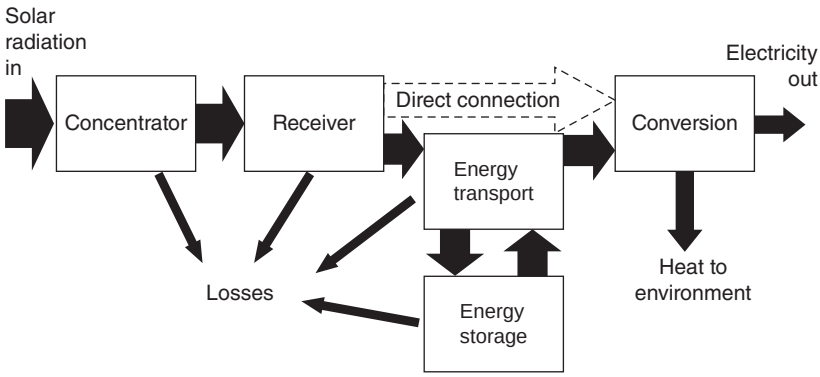

2.1 Schematic representation of the component parts of a solar thermal power system.

done by having a window in front of a cavity containing an absorbing matrix which the fluid passes over. Later chapters present details on possible receiver types for the various concentrator technologies.

After the receiver, there are two options: either the energy is further converted to the final form desired (such as electricity), or it is transported to another location for final conversion. It is possible that the power cycle is built integrally into the receiver unit (Stirling engines, for example). Solid state (semiconductor material) conversion devices such as concentrating photovoltaics and thermoelectric converters also lead to receivers built from the devices themselves.

If power conversion is carried out remote from the receivers, the collected thermal energy is carried away in a heat transfer fluid (HTF). For the trough plants built to date, this is predominantly a type of oil chosen for its transport properties as well as thermal stability. Direct steam generation has been used with all concentrator types and has the advantage that the HTF and power cycle working fluid are one and the same, eliminating the need for a heat exchanger. Molten salt as HTF was pioneered in tower systems and has also been introduced for troughs. It has the advantage that the HTF is then also a favourable energy storage medium. Use of air as a HTF has also been demonstrated, and chemical reaction systems are under development as heat transfer mechanisms.

Choice of the transport path provides the option of thermal energy storage (TES) in the intermediate thermal form before going to final conversion to electricity. The current commercially dominant approach is to use molten salt in high temperature insulated tanks. Chapter 11 covers thermal energy storage options in detail. There is also the option of designing an energy storage system after conversion to electricity; however,

electricity storage approaches are not integral to the CSP system itself but rather are independent systems that could be applied to any form of electricity generation and are not addressed in this book.

The final stage in a CSP system is electric power generation. The dominant approach here is steam turbines, with Stirling engines, organic Rankine cycles, Brayton cycles and photovoltaics also successfully proven. The efficiency of each subsystem can be defined as the ratio of energy out to energy in. The overall solar-to-electric conversion efficiency for the CSP system (η_{system}) is the product of the various subsystem efficiencies (concentrator/optical, receiver, transport, storage and conversion):

$$\eta_{system} = \eta_{optical} \times \eta_{receiver} \times \eta_{transport} \times \eta_{storage} \times \eta_{conversion} \quad [2.1]$$

These can be considered at a particular instant or averaged over a timescale such as a day or a year. Alternative naming of these efficiencies are frequently seen, and subsystems can be further grouped or subdivided according to what is being analysed.

The driving principles behind the development of CSP[1] systems are that:

- final conversion of collected thermal energy to electricity is more efficient if the energy at the conversion subsystem is available at a higher temperature;
- countering this, energy losses from receivers increase with temperature, but can be reduced by reducing the size of the receiver via concentration of the radiation;
- cost factors and material limits sometimes determine that the optimal operating conditions must be lowered.

This chapter reviews the various fundamentals that contribute to these principles and lead to the design of systems that seek to maximize overall conversion efficiencies. The chapter ends with an introduction to the key aspects of the economic analysis of CSP, since ultimately it is the cost of production of energy that matters most. Cost of energy depends strongly on the installed cost per unit of generating capacity plus also the level of solar resource and financial parameters. It is thus affected by both the efficiency of systems and their cost of construction. Ultimately the design process is one of 'thermo-economic' optimization (see, for example, Bejan *et al.*, 1996).

[1] This discussion applies most directly to CSP systems with thermal energy conversion; concentrating photovoltaic (CPV) systems are discussed briefly in Section 2.7.5 and then further in Chapter 10.

2.2 Concentrating optics

2.2.1 Solar radiation

To a good approximation, the sun is a black body[2] radiation source at its surface temperature of 5,760 K (5487°C). By the time it reaches the earth's surface, the solar spectrum has been selectively absorbed at various wavelengths by the various constituents of the atmosphere, and 5,200 K black body behaviour is a good approximation. Further details on the solar spectrum can be found in Chapter 3.

Concentrating systems only make use of the directly radiated component of solar radiation; they do not collect diffuse or scattered radiation. Direct normal irradiance (DNI) is the flux density of direct (un-scattered) light from the sun measured on a flat plane perpendicular to the sun's rays. Insolation, radiant flux, flux density and irradiance[3] are terms that are used fairly interchangeably in solar technology discussions, for the rate of solar radiation energy flow through a unit area of space, with SI units of W/m^2 (symbol G). The solar constant, which is the intensity on a plane outside the earth's atmosphere, is approximately 1,367 W/m^2 (Kopp and Lean, 2011). The maximum terrestrial DNI varies significantly with location and weather conditions, but is often taken as 1,000 W/m^2.

The heart of a CSP system is its mechanism for concentrating the solar radiation to higher intensities. An important metric is the concentration ratio. Concentration ratio can be defined in several ways, with two in common use.

- The optical concentration ratio, C_o, is the ratio of irradiance at the receiver surface G_r to the incident solar irradiance G:

$$C_o = \frac{G_r}{G} \qquad [2.2]$$

  C_o is defined at any point of an output flux distribution, with special reference being given to the point of maximum light intensity and concentration ratio which occurs at the peak of a flux distribution.
- The geometric concentration ratio C_g, is the ratio of collector aperture area A_c to receiver area[4] A_r:

[2] A black body is an ideal surface that absorbs all radiation incident on it and radiates a defined spectrum and intensity of radiation according to its own temperature. See, for example, Bergman *et al.* (2011).

[3] Intensity is also sometimes used in discussing solar irradiation; however, strictly speaking, intensity is not a radiant flux but radiant power per unit solid angle from a source.

[4] The area that is referred to here is the useful active absorbing area, often defined by an aperture.

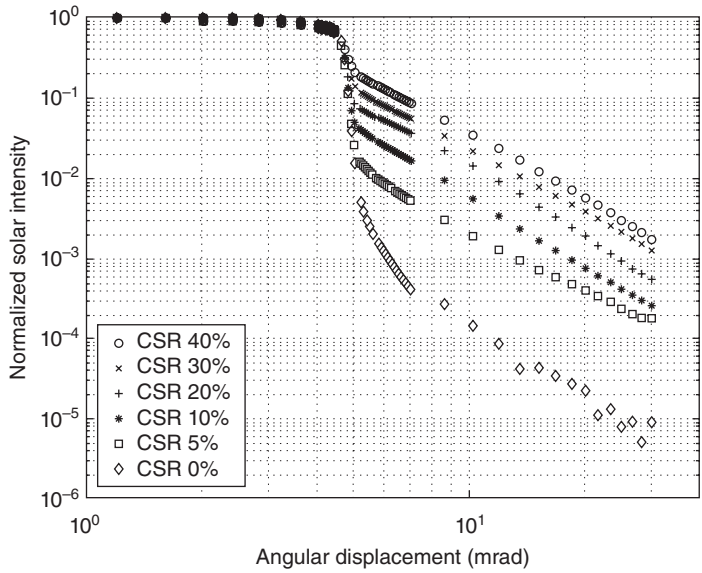

2.2 Sun shape (intensity versus angle, averaged across a large dataset) as a function of circumsolar ratio (Buie *et al.*, 2003).

$$C_g = \frac{A_c}{A_r} \qquad [2.3]$$

C_g is subject to the receiver area chosen for analysis. Receiver apertures can be chosen by design to capture as much of the focal region radiation as possible, or limited to capture only the more intense portion.

Concentration ratio values are often referred to in terms of a number of suns: a geometric concentration ratio of 1,200 would, for example, be said to be '1,200 suns'. At an assumed solar flux of 1,000 W/m^2 this would mean an average 1.2 MW/m^2 at the receiver surface.

Viewed from the earth, the sun subtends a half-angle of approximately 4.65 mrad (milliradians) (Fig. 2.3). However, the exact half-angle is complicated somewhat because the intensity distribution at the edges of the sun is not a clear step-function. Instead it falls off over a narrow angular range as shown in Fig. 2.2. This distribution of solar intensity with angular displacement is commonly referred to as the sun shape.

A key parameter is the circumsolar ratio (CSR), defined (Buie *et al.*, 2003) as:

$$\text{CSR} = \frac{G_{cs}}{G_{cs} + G_s}, \qquad [2.4]$$

where G_s is the solar intensity integrated from just the solar disc, out to its limit at 4.65 mrad, while G_{cs} is the solar intensity integrated over the annulus from 4.65 mrad to the outer extent of the solar aureole (surrounding glow), taken as 2.5° (43.6 mrad) for the sake of easy measurement using laboratory equipment.

High circumsolar ratios can significantly reduce the capture efficiency of high concentration collectors, due to a larger fraction of flux spillage. As the circumsolar ratio changes, the sun-shape distribution (intensity versus angle) also changes (Fig. 2.2). The actual sun shape is most strongly influenced by prevailing atmospheric conditions, particularly the level of particulate matter or moisture in the air.

A number of different sun-shape distributions have been proposed; a commonly used one is that by Buie *et al.* (2003) which gives:

$$I_r(\theta) = \begin{cases} \dfrac{\cos(0.326 \cdot \theta)}{\cos(0.308 \cdot \theta)}, & 0 \le \theta \le \theta_s \\ \theta^{\gamma} \exp \kappa, & \theta > \theta_s \end{cases} \qquad [2.5]$$

where

$$\gamma = 2.2 \cdot \mathrm{CSR}^{0.43} \cdot \ln(0.52 \cdot \mathrm{CSR}) - 0.1$$

$$\kappa = 0.9 \cdot \mathrm{CSR}^{-0.3} \cdot \ln(13.5 \cdot \mathrm{CSR})$$

and $I_r(\theta)$ is the relative solar intensity, relative to the intensity measured at $\theta = 0°$. Other sun-shape distributions used for modelling purposes include the Kuiper sun shape (Buie *et al.*, 2003), and that of Rabl and Bendt (1982).

The exact sun-shape distribution used for modelling purposes makes little difference except when modelling concentrators have very high optical concentration ratios (>10,000 suns), as in dish concentrators or solar furnaces, provided the optical surface is also very accurate. When dealing with lower-concentration collectors, a flat-topped intensity distribution, often called a pill-box sun shape is sufficient.

2.2.2 Calculation of sun position

A solar concentrator, whether line-focusing or point-focusing, needs to be aligned to the direction of the incident solar rays. Sun position can be very precisely predicted with a range of well-established equations as discussed in Chapter 3.

2.3 Limits on concentration

Higher levels of concentration offer the benefit of reduced thermal losses from smaller receiver apertures. However, there is a fundamental

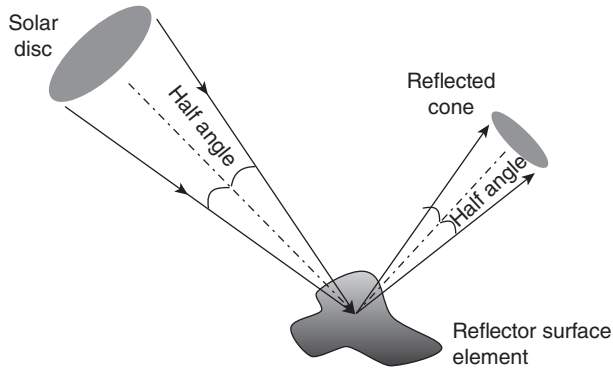

2.3 Points on a reflector surface reflect direct solar irradiation in a cone of rays.

thermodynamic limit to achievable concentration. There are further limits that result from particular concentrator geometries and then a range of practical factors that limit it further again. An authoritative presentation of the limits to concentration is given by Winston *et al.* (2005). In this section an overview of the principles and results is given.

2.3.1 A limit from the second law of thermodynamics

As a result of the finite angular width of the sun, any element of a mirror surface in a concentrator system will effectively reflect a cone of radiation with the same angular spread, as illustrated in Fig. 2.3. Energy transfer between the sun and the receiver of a solar concentrator is subject to the second law of thermodynamics. This means that the solar receiver cannot attain a higher temperature than that of the sun. Using this principle, limits on the geometric concentration ratio can be established.

Consider the sun as a black body sphere of radius r a distance R from an observer as shown in Fig. 2.4. At a distance R from the sun, all the radiation leaving the surface will be uniformly distributed across a sphere of area $4\pi R^2$. Thus, the irradiance will fall off with distance according to:

$$G = E_0\left(\frac{r^2}{R^2}\right) = E_0\left(\frac{(R\sin\theta_s)^2}{R^2}\right) = E_0\sin^2\theta_s, \qquad [2.6]$$

where

$$E_0 = \sigma T_s^4 \qquad [2.7]$$

is the black body emissive power from the sun's surface, and $\sigma = 5.670 \times 10^{-8}$ W/m^{2}K^4 is the Stefan-Boltzmann constant.

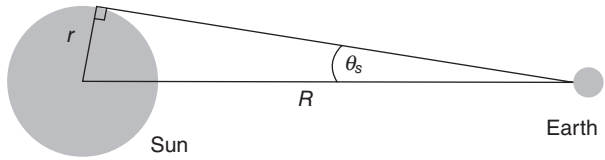

2.4 Radiation flux from a spherically symmetric black body falls off as $1/R^2$.

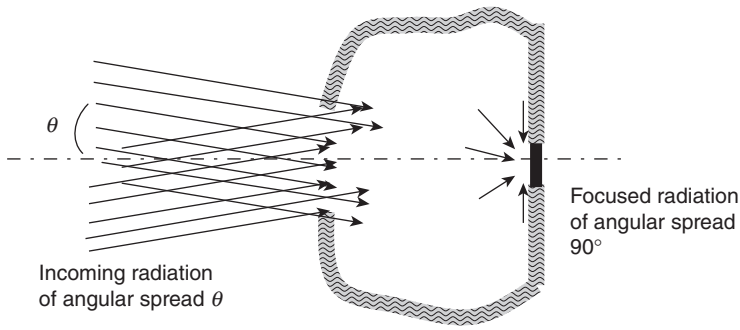

2.5 A concentrator that takes radiation with angular spread half-angle θ and concentrates it to a receiver with a final angular spread of half-angle 90°.

Now, imagine some ideal solar concentrator that takes solar radiation with angular spread[5] θ and accepts it from throughout a certain collector aperture area A_c, concentrating it onto a black-body receiver of some area A_R in a manner such that at the point of incidence, the angular spread has a half-angle of 90° (Fig. 2.5). The black-body receiver will heat up and all of its diffusely emitted radiation will follow a reverse path out of the concentrator and back to the sun. In the absence of any other heat losses, the black-body absorber will heat up until it reaches the same temperature as the source, and it will then be in equilibrium. This implies that

$$\sigma T_s^4 A_c \sin^2 \theta = \sigma T_R^4 A_R, \qquad [2.8]$$

where T_R is the absolute temperature of the receiver and T_s is the temperature of the sun's surface. Since $T_R = T_S$ at equilibrium,[6] this gives the result

[5] The angle θ is now generalized to be the acceptance angle which could be more or less than θ_s.

[6] Having established this limit under the condition of thermal equilibrium, we can then argue that it also applies away from equilibrium, since the reflections and refractions that lead to the optical concentration at the receiver are not a function of the receiver temperature. Hence this limit on concentration ratio is general.

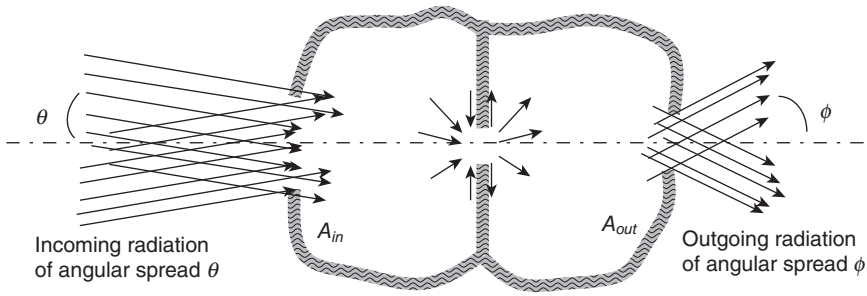

2.6 An arbitrary concentrator accepting radiation with a half-angle θ over area A_{in} and sending it out over area A_{out} with half-angle ϕ.

(the sine law of concentration) that any point-focus solar concentrator must have a concentration ratio of no more than

$$C_g = \frac{A_c}{A_R} = \frac{1}{\sin^2 \theta}. \qquad [2.9]$$

Going beyond this, imagine that the planar black-body receiver is replaced by an aperture, leading to a further optical system that transforms the radiation to a new angular spread and a third aperture area (Fig. 2.6). For the second optical subsystem, the aperture appears as a black body also and the same arguments apply leading to

$$\sigma T_R^4 A_R = \sigma T_s^4 A_{out} \sin^2 \phi. \qquad [2.10]$$

The whole device can now be viewed as an arbitrary ideal optical concentrator with

$$\sigma T_s^4 A_{in} \sin^2 \theta = \sigma T_s^4 A_{out} \sin^2 \phi \qquad [2.11]$$

and hence,

$$C_{g3D} = \frac{A_{in}}{A_{out}} = \frac{\sin^2 \phi}{\sin^2 \theta}. \qquad [2.12]$$

For a solar concentrator, θ is interpreted as the acceptance angle of the concentrator and ϕ as the angular spread of the concentrated radiation incident on the receiver.

Thus, the second law of thermodynamics leads to the conclusion that the concentration of radiation can *only* be achieved by increasing its angular spread, and this inherently limits the extent to which non-parallel radiation can in fact be concentrated.[7]

[7] This result is known in non-imaging optics as the principle of conservation of étendue. A rigorous proof is given by Chaves (2008).

A more rigorous analysis considers the possibility of materials with different refractive indices n_{in} and n_{out} at the entrance and exit respectively, and gives the result

$$C_{g3D} = \left(\frac{n_{out} \sin \phi}{n_{in} \sin \theta} \right)^2. \quad [2.13]$$

however, for most CSP purposes, concentration takes place in air, so $n_{in} = n_{out}$.

Note that the concentration depends on the acceptance angle of the concentrator, rather than the actual angular spread of the light source. A collector could be made with a very high concentration ratio by choosing to have a very narrow acceptance angle, even narrower than the angular spread of sunlight, but it would not help greatly, since it would then only collect a small fraction of the solar radiation. Conversely a wide acceptance angle could be chosen for a non-tracking concentrator at the expense of low achievable concentration ratio. Typically, the acceptance angle of a solar concentrator will be fairly close to the angular size of the sun.[8]

If the analysis is repeated for a line-focus concentrator, then the geometric limitations on acceptance apply only in one direction, and the flux density falls off as $1/R$ rather that $1/R^2$, giving the result that

$$C_{g2D} = \frac{n_{out} \sin \phi}{n_{in} \sin \theta}. \quad [2.14]$$

Using a refractive index of 1 for air, and an exit half-angle $\phi = 90°$ for maximum concentration, brings the result for a line-focus concentrator to

$$C_{g2D\max} = \frac{1}{\sin \theta}. \quad [2.15]$$

For linear concentrators, once again it is the acceptance angle that matters and this is effectively 90° in the plane of the sun and linear receiver, so concentrating light from the sun is still limited by Eq. [2.15] even though it is actually a spherical source. These final results (Eqs [2.9] and [2.15]) limit the maximum geometric concentration ratio of any solar concentrator.

Evaluating these limit equations for the actual angular size of the sun (half-angle 4.65 mrad) shows that the thermodynamic limit concentration for point-focus concentrators is 46,250 and for linear concentrators 215.

[8] An exception is the compound parabolic concentrator (CPC) used in certain non-tracking concentrators, such as for backing reflectors in solar hot water systems. CPCs also play a role in the secondary optics in certain types of systems (Meinel and Meinel, 1976).

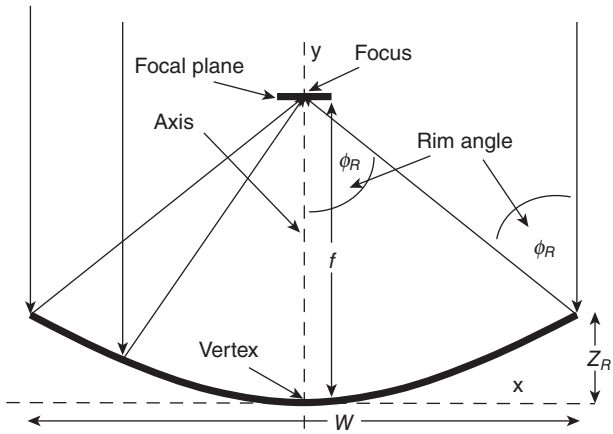

2.7 The parabola has the property that, as a reflector, all incident rays parallel to the axis will be reflected to pass through a single point at the focus.

2.3.2 Parabolas and paraboloids

The central role of the parabola in solar concentrators stems from its ability to focus parallel radiation to a point a distance f from its vertex. The parabola is a two-dimensional curve that provides the cross-sectional shape of a trough-shaped linear concentrator. Similarly, the paraboloid is a parabolic surface of revolution and is the surface shape given to dish concentrators.

The functional relationship defining a parabola with its axis aligned to the y-axis (Fig. 2.7) is

$$y = \frac{x^2}{4f}, \qquad [2.16]$$

while, for a paraboloid with its axis coinciding with the z-axis, it is

$$z = \frac{r^2}{4f} = \frac{x^2 + y^2}{4f}. \qquad [2.17]$$

The rim angle ϕ_R is the angle between the axis and a line from the focus to the physical edge of the concentrator. Together, the focal length and rim angle of a parabolic concentrator completely define its cross-sectional geometry. The rim angle of a parabola or paraboloid is given by

$$\tan\phi_R = \frac{W/2}{f - z_R} = \frac{4fW/2}{4f^2 - (W/2)^2} \qquad [2.18]$$

where W is the width and z_R is the depth of the parabola at the rim.

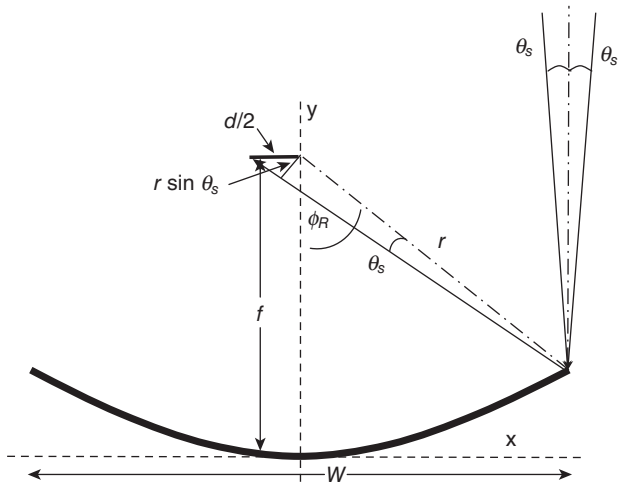

2.8 Concentrating solar radiation with a perfect parabolic mirror to a flat target.

The parabolic effect of focusing to a single point only occurs with perfectly parallel incoming radiation. As noted above, sunlight has a range of incident angle due to the physical extent of the solar source. This reduces the optical concentration achievable at the focus of parabolas and paraboloids, as discussed in the following sections.

Limits with flat receivers

Each point on a parabolic mirror will reflect a cone of rays that matches the angular distribution of the solar source (half-angle size θ_s). Consider the size of the spot formed by the cone of rays reflected from the points on the mirror, when incident on a flat target placed in the focal plane (Fig. 2.8). The rays from the rim will form the widest such spot.

The distance x of the reflection point from the axis is

$$x = 2r \sin \phi_R, \qquad [2.19]$$

and the width of the focal spot[9] on the focal plane due to reflection from this point will be

$$d = \frac{2r \sin \theta_s}{\cos \phi_R}. \qquad [2.20]$$

[9] Consideration of a precise width in this way is based on an assumed pill-box sun shape, an approximation.

The reflected cone from a single spot on the mirror will actually form an elliptical spot on the target with a major axis length of d. This applies equally for dishes and troughs.

Clearly the size of the focal-plane spot depends on the received incidence angle ϕ, so the accumulated effect of all the spots across the mirror will not be a true image of the sun formed at the focal plane. This is the reason that solar concentrator optics are referred to as non-imaging optics. If the rim angle ϕ_R is small, then r is approximately equal to f over the whole mirror, and then, to a good approximation, it will form a true image of the sun in the focal plane,[10] with the image diameter being

$$d = \frac{2f \sin\theta_s}{\cos 0} = 2f \sin\theta_s. \qquad [2.21]$$

On the other hand, for a dish or trough with a flat receiver and a rim angle of 90°, the mirror elements at the very edge will make an infinitely long spot, spreading their radiation over the entire focal plane.

If the receiver is large enough to accept reflected spots from the entire mirror surface, then the diameter of the receiver will be defined by the reflected spot size from points at the edge of the mirror with $x = W$ and $\phi = \phi_R$. The geometric concentration ratio for a parabolic trough with flat receiver will then be

$$C_g = \frac{A_C}{A_R} = \frac{LW}{Ld} = \frac{W}{d}. \qquad [2.22]$$

After substituting Eqs [2.19] and [2.20], this gives

$$C_g = \frac{\sin 2\phi_R}{2\sin\theta_s}. \qquad [2.23]$$

To find the optimal rim angle for a parabolic trough, take the derivative with respect to ϕ_R

$$\frac{dC_g}{d\phi_R} = \frac{d}{d\phi_R}\left(\frac{\sin 2\phi_R}{2\sin\theta_s}\right) = \frac{2\cos 2\phi_R}{2\sin\theta_s} = 0 \quad \text{at} \quad \phi_R = 0, 45°, 90°, \ldots \qquad [2.24]$$

The maximum concentration ratio corresponds to $\phi_R = 45°$, and gives a maximum concentration ratio[11] for a trough, with flat receiver and solar acceptance angle $\theta_s = 4.65$ mrad, of

$$C_{g,\text{trough,flat,max}} = \frac{1}{2\sin\theta_s} \approx 108. \qquad [2.25]$$

[10] This is the case with astronomical telescopes; they cannot have a large rim angle or else their imaging quality will be lost.

[11] This analysis ignores the effect of mirror shading by the receiver, and also considers only a single-sided receiver. For a fuller treatment, see Rabl (1976).

Repeating this analysis for a paraboloidal dish

$$C_g = \frac{A_c}{A_R} = \frac{\frac{\pi}{4}W^2}{\frac{\pi}{4}d^2} = \left(\frac{W}{d}\right)^2 = \left(\frac{\sin 2\phi}{2\sin\theta_s}\right)^2, \quad [2.26]$$

from which

$$\frac{dC_g}{d\phi} = \frac{d}{d\phi}\left(\frac{\sin^2 2\phi}{4\sin^2\theta_s}\right) = \frac{\sin 2\phi \cos 2\phi}{\sin^2\theta_s}$$
$$= 0 \text{ again gives maximum at } \phi = 45°. \quad [2.27]$$

Hence

$$C_{g,\text{dish,flat,max}} = \frac{1}{4\sin^2\theta_s} \approx 11{,}600. \quad [2.28]$$

These values are a half (trough) and a quarter (dish) of the thermodynamic limits of Section 2.3.1. Most dish and trough concentrators with cavity receivers (which have a flat opening) employ a rim angle close to 45°.

Limits for cylindrical and spherical receivers

Another possibility to consider is using a receiver with a circular cross-section as shown in Fig. 2.9. In this case, the diameter of the target needs to be

$$d = 2r\sin\theta_s. \quad [2.29]$$

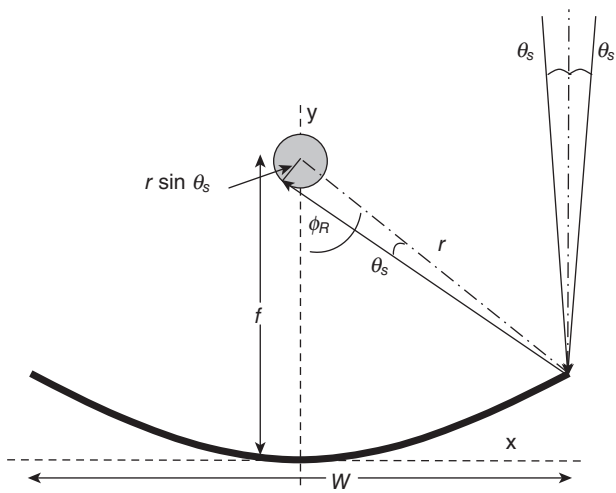

2.9 Concentrating solar radiation with a perfect parabolic mirror to a circular cross-section target.

For a trough with cylindrical receiver, then

$$C_g = \frac{A_c}{A_R} = \frac{LW}{L2\pi r \sin\theta_s} = \frac{\sin\phi}{\pi \sin\theta_s}. \quad [2.30]$$

Solving for maximum geometric concentration ratio as before, the optimal trough rim angle is $\phi = 90°$, and that at this angle, gives

$$C_{g,\text{trough,cyl,max}} = \frac{1}{\pi \sin\theta_s} \approx 68.5. \quad [2.31]$$

Trough concentrators with cylindrical evacuated-tube receivers consequently employ rim angles approaching[12] $\phi = 90°$.

For a dish with a spherical receiver, likewise,

$$C_g = \frac{A_c}{A_R} = \frac{\frac{\pi}{4}W^2}{4\pi r^2 \sin^2\theta_s} = \frac{\frac{\pi}{4}4r^2 \sin^2\phi}{4\pi r^2 \sin^2\theta_s} = \frac{\sin^2\phi}{4\sin^2\theta_s}, \quad [2.32]$$

and again the maximum geometric concentration ratio occurs at $\phi = 90°$, with

$$C_g = \frac{1}{4\sin^2\theta_s} \approx 11{,}600. \quad [2.33]$$

For troughs then, the optical analysis gives a limit that is equal to the thermodynamic limit divided by π; for dishes, the result is equal to one quarter of the thermodynamic limit.

Note that this analysis is of geometric concentration ratio, and the above derivation indicates that the local contributions to focal spot size vary as a function of reflection radius x, so the geometric concentration ratio limits are less than the optical concentration ratio limits at the centre of the focal spot.

Rabl (1976) has further results giving the mirror area per aperture area for these four different collector configurations. Optimally sized troughs and dishes with flat receivers require less mirror for a given aperture than those with cylindrical/spherical receivers, since on average the glass is reflecting at closer to a normal angle.

2.3.3 Secondary optics

The addition of a second stage of optical concentration, or secondary optics, can lead to higher concentration ratios with real results up to 80–90% of the thermodynamic limit achieved (Gordon, 2001). The single-stage concen-

[12] In practice, lower angles of the order of 80° are commonly used, because of increasing cosine losses per glass area and increasing amplification of surface errors due to the great distance from mirror to receiver.

2.10 A secondary Trombe-Meinel cusp concentrator, shown here in the Novatec linear Fresnel system, can allow concentration ratios on the absorber surface to further approach the thermodynamic limit. This receiver is also discussed in Chapter 6.

trators described above often have incident radiation at their receiver from only a relatively limited angular range (for flat absorber, a half-angle of 45°). Conservation of étendue suggests, then, that further concentration is possible; this is achieved in practice using various funnel-like mirror systems. The compound parabolic concentrator (CPC, also Winston collector), the Trombe-Meinel cusp (Fig. 2.10) and the Mouchot conical mirror are geometric configurations that can be used to gain this further degree of concentration.

2.3.4 Practical factors reducing concentration

A range of sources of errors in solar concentrators act to reduce the concentration that can be achieved. They can be categorized according to the scale of the imperfection causing the error, starting at the scale of microns, moving up to the scale of centimeters.

Specularity error

Specularity refers to the mirror-like quality of a reflector, or specifically, the degree to which reflected rays obey the law of reflection, where the reflected angle equals the incident angle. The opposite is a diffuse reflector, which scatters reflected light in a wide range of directions.[13] The specularity error

[13] A special case is the Lambertian surface, for which the apparent brightness of reflected radiation is equal in all directions. Such surfaces are useful in methods for characterizing concentrator performance, since they allow a photograph to be taken to record the irradiance in the focal plane of a dish, heliostat, etc.

σ_{sp} is defined locally on a surface as the standard deviation of the distribution of reflected ray angles at a specified incident angle; all real surfaces have some degree of specularity error, arising from the microscopic properties of surfaces.

Surface slope error

At a slightly larger scale, concentrator mirrors will have local ripples and distortions in their surfaces, and the degree of aberration is often called the surface slope error σ_{surf}, defined as the standard deviation of the angular deviations of the surface normal vectors from their ideal directions, sampled across the surface of the mirror.

The larger the surface slope error, the poorer the optical performance of the concentrator: the focal spot spread increases, and the maximum concentration ratio decreases. Values of around 0.4 mrad are found in very accurate systems, although values up to around 5 mrad can be adequate, depending on the type of concentrator and application.

Shape error

Looking at a larger scale, a concentrator is commonly constructed of facets; these facets may be oriented incorrectly, or there may be distortion of the overall structure due to thermal expansion, wind loads or the release of residual stresses. Using accurate measurement techniques such as photogrammetry, these errors can be measured and converted into an effective shape error σ_{sh}, which is the standard deviation in the surface normal angles arising from these various forms of misalignment.

Tracking error

A tracking system ideally should make the concentrator point at the sun without error. In reality, tracking systems are not perfect, and will not always point the collector exactly at the sun. This angular offset often varies with time, particularly with an 'on-off' type tracking control system. When considered over a period of time greater than the source of the error, the angular error can be characterized by the tracking error σ_{tr}, defined as the standard deviation of angular error distribution.

Combinations of errors

In a typical system, the specularity, slope, shape, and tracking errors can be combined into an overall optical error, σ_{tot}, of a concentrator. If all the sources can be modelled to reasonable accuracy as a normal distribution of

randomly distributed errors, then the overall optical error is found as a root sum of squares of the component errors. That is,

$$\sigma_{tot} = \sqrt{\sigma_{sp}^2 + \sigma_{surf}^2 + \sigma_{sh}^2 + \sigma_{tr}{}^2}. \quad [2.34]$$

Certain types of surface and shape error may not be well characterized by a normal distribution, so this equation should be used with care. Also, if modelling the sun shape as a simplified normal distribution, then an additional term σ_{sun}^2 can be added inside the square root of the above equation.

2.3.5 Cosine losses and end losses

An important source of 'loss' in solar concentrators arises from the fact that mirrors cannot always be aligned normal to the incident solar rays. When a mirror is reflecting off-axis, the apparent area of the mirror, as seen from the sun, is reduced according to the cosine of the incidence angle. Assuming that the aperture area of the concentrator to be equal to the mirror area, this reduction in apparent area then directly reduces the concentration ratio of the concentrator, hence it is referred to as a cosine loss, although strictly speaking the energy was never collected in the first place.

This cosine loss effect occurs in all forms of solar concentrators. For all concentrators except for dishes or lenses, cosine losses vary as a function of sun position. Dishes are always pointed directly at the sun, so the only cosine losses arise from the curvature of the mirrors. An attempt to minimize average cosine losses is responsible for the off-axis arrangement of most central receiver systems.

End losses are particular to trough and linear Fresnel concentrators. These refer to the radiation that is reflected from the mirrors but which, due to the sun not being directly overhead of the collector, misses the receiver, and instead is concentrated beyond the end of the receiver. Depending on the orientation (east–west or north–south), these losses might be present all year round, or else only in the mornings and evenings.

Both end losses and cosine losses are commonly incorporated as part of the calculation of $\eta_{optical}$ in Eq. [2.1].

2.4 Focal region flux distributions

Once light has been reflected or refracted on its path through a concentrator, there will be a distribution of irradiance in the focal region. Predicting and measuring the focal region flux distribution is essential for design and performance analysis of receiver systems.

2.4.1 Prediction of focal region distributions

For the prediction of the focal region distribution, a common technique is ray tracing. This computational technique involves gathering information about the collector geometry, together with the sun shape, specularity, slope, shape and tracking errors, and then creating a virtual 'scene' containing all of those elements and their associated parameters. Large numbers of simulated rays are then 'fired' into the virtual 'scene', with an angular distribution that matches the specified sun shape. Each ray is traced through the scene. At an obstacle, some of the ray's strength will be attenuated according to the surface reflectivity and the direction of the reflected ray will be assigned based on a random sample from the slope error distribution and the specularity distribution. The process of 'tracing' is repeated until the ray leaves the scene or is completely absorbed. Refractions through glass, etc., can also generally be accommodated. A grid of cells is defined on various 'virtual sensor surfaces' in the scene (usually corresponding to a receiver surface or the focal plane). Then radiation distributions can be calculated, by summing the strength of all the rays that are incident on each grid cell of the sensor surface. Accuracy is increased by calculating with larger numbers of rays and using smaller grid cells, but at the expense of increased calculation time. Several million rays are frequently required to achieve sufficient accuracy in the analysis of a solar concentrator.[14]

Leading general-purpose ray-tracing software used in the CSP field includes *ASAP*, *OptiCAD*, *OSLO*, and *ZEMAX*. A recent entrant is *Tonatiuh*, a free open-source ray-tracer specifically for solar concentrators, under active development at CENER in Spain (Blanco *et al.*, 2011). Some optical codes specifically developed for solar applications include DELSOL, MIRVAL, UHC, HFLCAL, FIAT LUX and SolTrace (Garcia *et al.*, 2008; Ho, 2008). Some of these codes make use of a convolution approach, which treats the distribution of rays as a whole, rather than calculating the path of each individual ray through the scene; the approach is reported to be within 1–2% of detailed ray-tracing, but significantly faster to calculate (Garcia *et al.*, 2008).

2.4.2 Measurement of focal region distributions

Focal region distributions can be measured directly using the various methods discussed in detail in Chapter 18. The most common of these is

[14] Note that CSP ray-tracing is quite distinct from the 'backward' ray-tracing used in CGI, animated movies, etc., which considers possible origins/luminous intensity of rays emanating from the eye of the observer in different directions.

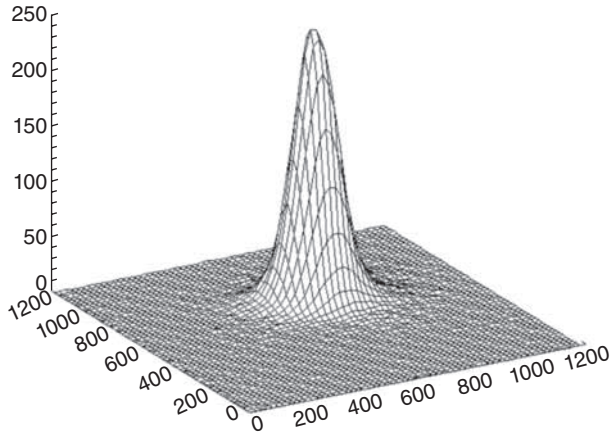

2.11 Experimentally determined irradiance distribution of the ANU 500 m^2 dish at the focal plane. Spatial units are millimetres, the vertical scale uncalibrated relative units (Lovegrove *et al.*, 2011).

the camera target method. A suitably cooled Lambertian target is placed at the focal plane of the concentrator. Then, using a camera, images of the reflected radiation from the target are captured. If the reflectivity of the surface is known and the camera is well calibrated, then the irradiance at the target can be determined.

An example of an experimentally determined distribution from the ANU 500 m^2 dish system (Lovegrove *et al.*, 2011), showing a typical Gaussian-like distribution, is shown in Fig. 2.11.

If a real receiver geometry is superimposed on a known focal region distribution, the fraction of the solar radiation initially intercepted by the concentrator aperture that is in turn intercepted by the receiver can be determined. This capture fraction or intercept factor is a major determinant of the optical efficiency of the system. Figure 2.12 illustrates the intercept fraction of a circular aperture imposed on the flux distribution of Fig. 2.11 as a function of diameter.

Optical errors lead to a spreading of the focal region distribution, and a reduction in the achievable concentration ratio. This leads to a need for larger receivers, so as to avoid flux spillage, or in other words rays that miss the receiver and are lost. On the other hand, an analysis of losses reveals that having an excessively large receiver will result in large radiative and convective losses, so, in general, some level of flux spillage will be tolerated for an optimized collector.

Knowledge of the flux density distribution allows a collector efficiency to be determined based on the actual amount of flux intercepted by the receiver aperture compared to that intercepted by the collector. This could

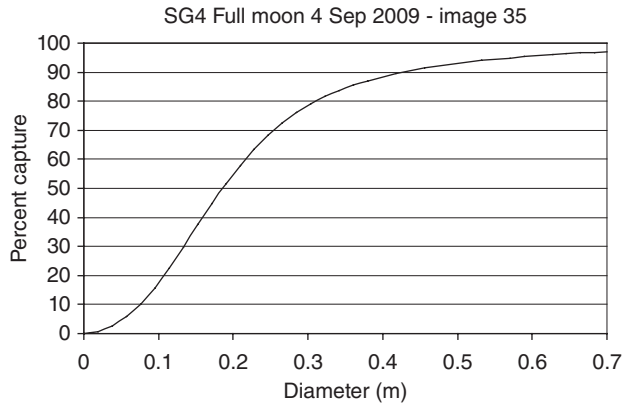

2.12 Empirical relative intensity distribution of the ANU 500 m^2 dish at the focal plane (Lovegrove *et al.*, 2011).

be evaluated at a particular instant or averaged over a time interval to capture changes in tracking or structure; for example

$$\eta_{optical} \equiv \frac{\int_{time}\int_{Aperture} G_{incident}(t)\,dA\,dt}{\int_{time} A_{collector} G_{sol}(t)\,dt} \qquad [2.35]$$

where $G_{sol}(t)$ is the time varying DNI and $G_{incident}(t)$ is the time varying concentrated irradiation at the receiver and $A_{collector}$ is the aperture area of the collector.[15] If irradiation is constant over the time interval in question, then the time integrals are no longer needed.

This definition captures several effects:

- the actual capture fraction for a perfectly aligned concentrator for a given receiver
- the loss due to non-unity mirror reflectivity
- the loss due to tracking error
- cosine losses.

2.5 Losses from receivers

At steady state, the net energy flow into a receiver from concentrated solar radiation will be balanced by energy outflows from the flow of heat transfer

[15] Note that evaluations can sometimes be presented based on aperture with or without the effect of receiver shading or total mirror area rather than aperture area, so results must be interpreted carefully.

fluid or other energy conversion process, plus a range of energy losses, due to unwanted reflection, radiative emission, convective or conductive processes, detailed in the following sections.

The total loss will be the sum of these four contributions

$$\dot{Q}_{loss} = \dot{Q}_{ref} + \dot{Q}_{rad} + \dot{Q}_{conv} + \dot{Q}_{cond} \quad [2.36]$$

The energy efficiency of a receiver is the ratio of the energy that is usefully converted to the input energy from the concentrated that is intercepted

$$\eta_{rec} = \frac{\dot{Q}_{converted}}{\dot{Q}_{input}} = \frac{\dot{Q}_{input} - \dot{Q}_{loss}}{\dot{Q}_{input}} \quad [2.37]$$

where for the receiver

$$\dot{Q}_{input} = \int_{time} \int_{Aperture} G_{incident}(t)\, dA\, dt \quad [2.38]$$

If the useful energy conversion process is 'turned off', the receiver efficiency will be zero and the receiver will heat up until the combined losses exactly balance the incident radiation. This temperature is referred to as the stagnation temperature.[16]

2.5.1 Radiative losses

Radiative loss processes include both the net emitted radiation from receivers as a consequence of their temperature and the reflection of some of the incident concentrated solar radiation. Surfaces emit and absorb radiation as essentially independent processes, with the net energy transfer taking place being the combination of the two. Each surface in a receiver will emit radiation in proportion to the fourth power of temperature, at a rate given by the black body emissive power multiplied by its emissivity.

Some fraction of the incident radiation will be reflected from any surfaces on which it is incident. The fraction of this radiation that is lost from the receiver will depend on the geometry. If glass covers are involved in the receiver construction, they will also introduce reflection losses that may be mitigated by anti-reflective coatings. For cavity receivers in particular, radiation reflected or emitted from one part of a receiver surface is quite likely to be incident on other parts, so calculating the net absorbed radiation requires a simultaneous solution of the whole process. Ray-tracing software typically does this for reflected incident radiation (but not emitted radiation).

[16] For low concentration systems, this is an experiment that can be performed, but for high concentration point focus systems, destruction of the receiver is likely before an empirical stagnation temperature could be established.

Many real surfaces can be modelled as grey bodies, meaning that they have a constant emissivity across all wavelengths of interest. An important exception is the selectively absorbing surface which, in solar thermal applications, is designed specifically to have a high absorptivity in the wavelength range of solar radiation and a low emissivity in the wavelength range associated with the (infrared) radiation emitted from hot receiver surfaces. Chapter 15 covers such surfaces in detail.

For diffusely reflecting surfaces, the methods for calculating the final distribution of incident solar radiation are the same as those required to determine how the diffuse emitted radiation from hot receiver surfaces is ultimately distributed.

The radiation leaving a surface will be partly intercepted by all the other surfaces in the field of view, in proportion to the view factor (also called radiation shape factors),

$$F_{ij} \equiv \text{the fraction of radiation leaving surface } i \text{ and reaching surface } j. \quad [2.39]$$

If these other surfaces reflect and absorb various fractions, working out the final distribution of absorbed energy becomes a complex problem. General presentations of radiation heat transfer can be found in Bergman *et al.* (2011).

The radiative energy balance of a particular (diffusely reflecting) surface element is illustrated in Fig. 2.13. In this diagram, G_i is the total irradiance

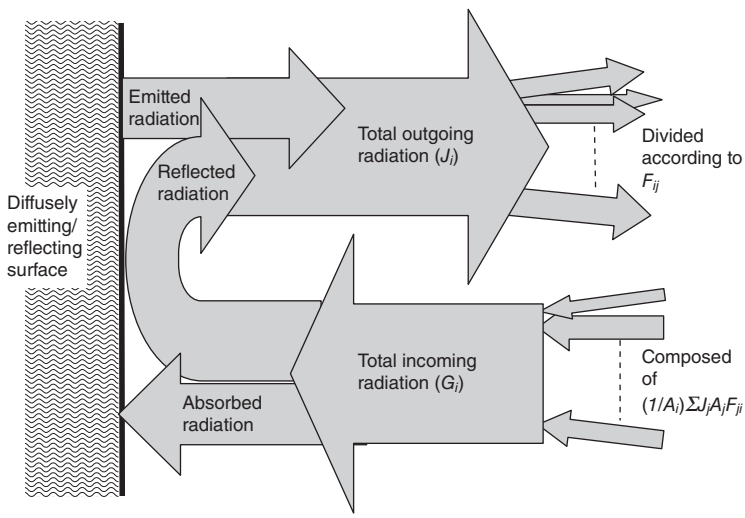

2.13 Radiation energy balance on a diffusely emitting and reflecting surface.

incident on surface i, J_i is the radiosity of surface i, defined as the total radiative flux (reflected plus emitted) leaving that surface, F_{ij} is the view factor from surface i to surface j, and A_i is the area of surface i. Each wavelength range (e.g. solar vs. thermal wavelengths) can be considered independently in this way.

For each surface in a radiation exchange network, an equation for the energy balance is written. Together, these equations form a linear system in terms of radiosity, and so they can be readily solved to evaluate the net heat transfer at each surface. Boundary conditions are required at each surface; the surface temperature can be fixed and the equation solved for net heat transfer, or else vice versa.

For a solar concentrator receiver, the radiation exchange between surfaces within it can be solved in this manner. The starting point is that the amount of concentrated solar radiation coming in through the aperture and striking each surface needs to be known from the optical properties of the concentrator. The aperture itself can be regarded as a black body surface to all radiation incident on it from other internal surfaces. Boundary conditions for external convective losses can also be introduced, relating surface temperature and the externally convected flux.

Analysis of simple grey-surface radiation exchange can be achieved with the free open-source software View3D (Walton, 2002). More sophisticated models incorporating coupled radiation and convection heat transfer are described in Section 2.5.2.

In a simplified model, if the aperture is treated as a single surface at the average receiver temperature, interacting only with the environment, then the emitted radiation loss will be given by

$$\dot{Q}_{rad} = \sigma A \varepsilon F_{RS} \left(T_{rec}^4 - T_{env}^4 \right), \qquad [2.40]$$

where F_{RS} is a simplified shape factor between receiver and surroundings. In a simplified model, reflection losses may be approximated using a single effective net absorptivity for the receiver aperture area. Thus

$$\dot{Q}_{ref} = (1-\alpha) A \dot{Q}_{sol}. \qquad [2.41]$$

2.5.2 Convection losses

Convection losses arise in solar concentrators from the movement of air over hot receiver surfaces. Efforts can be made to minimize such losses, such as by placing a glass cover over the receiver surface or using an evacuated glass tube (as with parabolic troughs). Some dish and tower systems are fitted with quartz windows able to withstand very high solar flux. In other cases, the receiver is an open cavity, and only the buoyancy of hot air

trapped inside the downward-facing receiver acts to suppress the convective loss.

Convection losses, both forced convection due to wind and natural convection due to the buoyancy effects of heated air, are difficult to measure and difficult to model. One complication is that the process of convection is coupled with the process of radiative loss, in the sense that the magnitudes of both types of loss are dependent on the surface temperature, which is in turn dependent on the external (radiation and convection) heat loss as well as the internal heat transfer (to the fluid passing through the inside of the receiver). Efforts are often made to decouple the problem, such as by assuming a uniform receiver wall temperature, or assuming uniform heat flux into the heat transfer fluid.

Convection losses are very difficult to measure directly, and usually empirical results are obtained by subtracting other known losses from the overall energy balance. Detailed convection heat transfer simulations are possible with commercial computational fluid dynamics (CFD) tools such as *FLUENT* and *Star-CCM+*. A free open-source alternative is *OpenFOAM* (OpenFOAM Foundation, 2011). For simplified analysis semi-empirical correlations for natural and forced convection heat transfer coefficients[17] can be used, but the accuracy will usually be no better than ±20%.

Once correlations have derived a value of the average convection heat transfer coefficient (h), the receiver convective loss can be calculated

$$\dot{Q}_{conv} = hA(T_{rec} - T_{amb}). \quad [2.42]$$

2.5.3 Conduction losses

There will be thermal losses through insulating covers over the back of receivers and any thermal path between hot receiver surfaces and the surrounding environment. Such losses are also linearly proportional to the temperature difference and inversely proportional to an overall 'thermal resistance' that depends on material conductivities and geometry

$$\dot{Q}_{cond} = \frac{(T_{rec} - T_{env})}{R_{th}}. \quad [2.43]$$

For a one-dimensional geometry of heat loss through a single homogeneous (insulating) layer of thickness L and thermal conductivity k, the equation is

$$\dot{Q}_{cond} = kA\frac{(T_{rec} - T_{env})}{L}. \quad [2.44]$$

[17] Usually a dimensionless heat transfer coefficient (Nusselt number) is correlated with Grashof and Prandtl number for natural convection, or Reynolds number and Prandtl number for forced convection.

2.6 Energy transport and storage

Energy transport is essentially about moving high temperature HTFs through piping networks. Chemical reaction-based energy transport is also under development. HTF networks can be extensive for distributed collector fields such as trough systems, whilst they are considerably smaller for tower systems. The basic approaches to calculating pressure drop and pumping power, plus heat loss through insulated pipes are well established in engineering practice and are not discussed further here. It is worth noting, however, that there are standard approaches for thermo-economic optimization of pipe diameter and insulation thickness that should be applied, but noting that what is cost effective in standard practice may not transpire to be so in a CSP system.

Energy storage is discussed in detail in Chapter 11. Key categories of energy storage for CSP systems include sensible storage (heating and cooling a material without change of phase), latent heat storage (melting and freezing of suitable high-temperature phase-change materials) and thermochemical storage (with reversible chemical reactions used to store and discharge energy).

Two-tank systems, molten-salt systems, incorporating sensible heat transfer with hot and 'cold' tanks of molten $NaNO_3$-KNO_3, are currently the commercially dominant approach. Most other approaches under development also involve storage of high-temperature material. Reducing direct thermal conduction losses and parasitic energy consumption are obviously important. A less obvious, but potentially more important, issue is that of the temperature decrease that is experienced in directing thermal energy to storage and then later extracting it. This temperature decrease results in a direct loss of exergy, as discussed in Section 2.8.1.

2.7 Power cycles for concentrating solar power (CSP) systems

A range of different solar to electric energy conversion systems can be applied to the various concentrator types.

2.7.1 Steam turbines

The bulk of the world's electricity is generated with steam turbines, mostly with steam produced from fossil or nuclear heat sources. One of the advantages of CSP is the ease with which a new source of heat can be applied to the dominant power generating technology. Consequently the vast majority of the CSP systems presently in operation use steam turbines. All the concentrator types have been applied to steam production for use in steam turbine energy conversion.

A plant with a Rankine cycle using a steam turbine works by:

- compressing pure feedwater to high pressure (over 10 MPa, for example);
- boiling and superheating steam in a boiler which may be in the focal point, or may be heated using a heat exchanger with another heat transfer fluid;
- expanding the steam to low pressure via a series of turbines that drive a generator; and
- at the end of the expansion process, condensing the low pressure steam with the aid of a cooling tower and then re-using it in the cycle.

The Rankine cycle has higher conversion efficiency for higher steam temperature and pressure at turbine entry (in common with all heat engine cycles). A key feature that improves efficiency is including various stages of steam bleed from the turbines that can then be used to progressively heat feedwater prior to use in boilers.

The fraction of liquid condensing within the turbine must be kept to a low value to avoid blade erosion. This can be achieved by ensuring that the vapour is sufficiently superheated prior to expansion. Increasing boiler pressure to increase efficiency can mean that the materials will not allow vapour to be superheated far enough to avoid condensation in the turbine. This problem is addressed by re-heating the vapour after partial expansion. All of these features are typically combined in a large-scale steam turbine-based power plant and the overall configuration is typically some variation of that shown in Fig. 2.14.

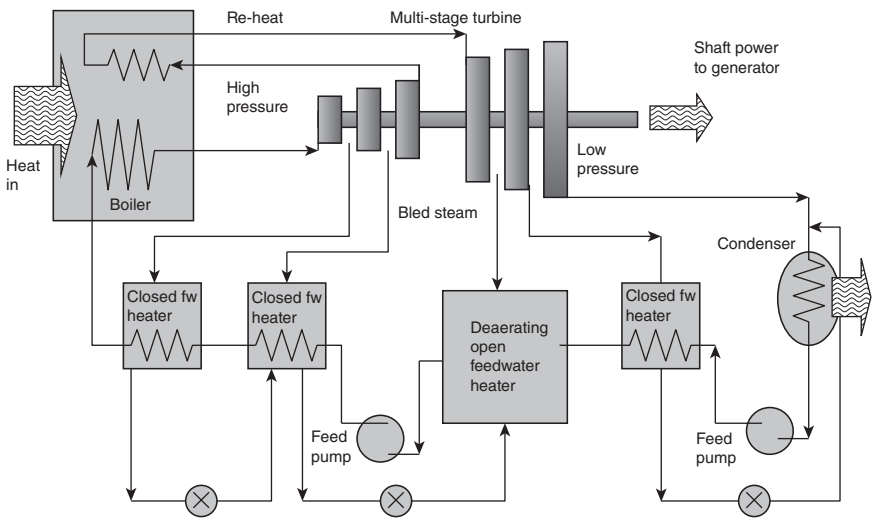

2.14 Indicative configuration for a large-scale steam turbine power plant.

At a more pragmatic level, managing the chemical composition of the cycle water is an important part of the process. A fraction of the water is periodically 'blown down' (expelled from the system) to keep the level of impurities, such as dissolved salts, within acceptable limits. An open feedwater heater involves the direct mixing of the bled steam and feedwater. It is operated at atmospheric pressure and the heating also has the effect of driving off dissolved air prior to sending feedwater to the boiler.

Systems are more efficient if they are built as larger units and run at full load. Most, but not all, of the size efficiency advantage is achieved at the 50 to 100 MW_e scale. Larger systems are less costly per unit of capacity. Large-scale power-generating turbines used in coal power stations are typically around 500 MW_e. For a CSP application, a larger turbine requires a large field, which results in extended thermal line losses, and so there is a trade-off against turbine size, with a 250 MW_e unit being suggested by many observers as offering the lowest cost of energy. As of early 2012, no CSP systems have been built to this size, although there are several in planning stages.

The most efficient state-of-the-art steam turbines work at up to 700°C steam inlet temperature. Trough and linear Fresnel concentrators are, however, limited to around 400°C if thermal oil heat transfer fluid is used, and up to 500°C if an alternative HTF such as direct steam generation (DSG) is used. Tower and dish systems are able to reach the temperatures needed for the highest possible steam turbine inlet temperatures and pressures; the limitation in that case becomes survival of materials either in the turbine or in the solar receiver.

State-of-the-art steam turbines are now produced that work at supercritical conditions, for maximum conversion efficiency. Supercritical steam is steam at pressures and temperatures above the critical point (22 MPa, 374°C); at these conditions, the phase-change occurs continuously rather than via nucleate boiling, at higher temperatures. Viable only at very large scales, these turbines have not yet been applied to CSP plants.

A major area of difference between solar and fossil operation of steam turbines is the intermittent and changing nature of solar input. This has two potential impacts:

- the wish to vary turbine speeds up and down more frequently and more rapidly than in steady-state fossil-fuelled operations, and
- the wish to run at part-load more frequently.

Whilst inclusion of energy storage can mitigate these effects to some extent, directly transferring technologies and practices from conventional generation does not necessarily give optimal results. Turbine manufacturers are now producing steam turbines customized for CSP application, with these issues in mind. Such steam turbines are able to reach full power within 30

minutes from a cold start and less for a warm start. Typical steam turbine heat to AC electricity conversion efficiencies for existing CST plants are around 40% gross at full load.

Reciprocating steam engines are more efficient than turbines at very small scales. They are still produced commercially but remain relatively unpopular due to complexity and maintenance issues.

2.7.2 Organic Rankine cycles

An organic Rankine cycle (ORC), is fundamentally the same as a steam Rankine cycle; however, it uses a lower boiling point organic fluid to better match its operation to lower temperature heat sources. ORC systems can achieve better efficiencies than steam turbines for smaller systems (less than a few MW_e). However, the capital and operating and maintenance (O&M) costs are higher per installed MW than for a water/steam system. ORC technology is being actively pursued for geothermal power applications because of its better match to lower temperature sources. ORC systems have been applied to a few modest sized linear concentrator CSP systems.

Another potential application for ORC systems in CSP is as a 'bottoming cycle', whereby a high temperature cycle (see discussion of Brayton cycle below), produces exhaust heat (that would otherwise be wasted) which is at sufficiently high temperature to drive an ORC system for additional power generation.

2.7.3 Stirling engines

A Stirling engine is an externally heated engine with reciprocating pistons that operate on a fixed, enclosed amount of gaseous working fluid, usually hydrogen or helium or possibly air. The ideal cycle is made up of a mix of constant temperature and adiabatic (zero heat transfer) processes. In the ideal limit, it is capable of the highest thermodynamically possible conversion efficiencies between two constant temperature limits.

The Stirling engines contemplated for CST applications to date have all been small (in the tens of kW_e range), although large, fossil-fuelled systems for marine propulsion do exist. Dish-mounted Stirling engines incorporate receiver, engine and generator in a single package at the focus (see Chapter 9).

Stirling engines have long been applied to dish concentrators. This long history and predominance leads many in the CSP field to refer to dish systems in general as 'dish-Stirling', even though dishes have been applied to direct steam generation, photovoltaics and other approaches. Stirling engines have not so far been applied in any serious way to other collector types.

There are two types of Stirling engines: piston-crankshaft types built in a similar manner to internal combustion engines and free-piston engines which involve an oscillating piston attached to a linear generator, but with no physical restraining linkage. Both types have been used in practice.

Dish-Stirling systems continue to hold the record for the highest solar to electric conversion efficiency of any technology, with total solar to AC electric efficiencies of around 30% at design point DNI, reliably reproduced. Stirling systems can be used for much smaller systems than Rankine cycles, but in the dish-Stirling configuration, thermal storage is yet to be developed.

2.7.4 Brayton cycles

The Brayton cycle is the basis of jet engines and the turbo generators used in gas turbine power stations. It is a common misconception that 'gas turbines' are so named because they burn gas; however, the name actually refers to the fact that a gas (usually air) is the working fluid. In fuel-fired mode, any hydrocarbon fuel, such as aviation fuel, diesel, LPG, propane or bio gas, could be burnt to achieve the required heating. Alternatively solar heat could be used to raise the temperature of the compressed air before expansion. With temperatures before expansion of around 1,000°C needed for efficient operation, this is only likely to be achieved with tower systems or dishes. Demonstration CSP systems using solar heating of a Brayton cycle have been operated.

In fossil-driven applications, a combined cycle power plant uses a gas turbine with its high temperature exhaust gases then directed to a 'heat recovery steam generator' that provides steam for a steam turbine cycle. Potentially the combined conversion efficiency is in excess of 50% and represents the highest thermal to electric conversion efficiency solution currently available commercially. A major attraction with applying the Brayton cycle to CSP applications is to also implement combined cycle operation with either steam or ORC bottoming cycles in a similar high efficiency manner.

For dish applications, the Brayton cycle offers the potential of reduced O&M costs compared to Stirling engine systems. An area of current solar thermal energy research interest is in supercritical carbon dioxide Brayton cycles (s-CO_2 cycles). The different thermodynamic properties of CO_2 compared to air allow higher overall cycle efficiencies to be achieved.

2.7.5 Concentrating photovoltaics

Concentrating photovoltaic (CPV) systems are discussed in detail in Chapter 10. They typically use expensive, high efficiency cells to gain

maximum advantage from the investment in concentrator systems. High-quality, single-crystal silicon cells with efficiencies of around 20% have been utilized. Going beyond this, cells, such as the multi-junction cells developed for space applications, have had a rapid efficiency increase over the last decade (from 30% efficient to 43% efficient).

With a CPV system, there are parasitic losses relating to tracking system operation, controls, wiring losses, inverter efficiencies and operation of the cooling system. These parasitic losses reduce the useful AC output of the entire system.

A key issue with any high concentration PV system is the heat that results from the photons that are not converted directly to electricity. At 500 suns, a triple-junction cell would be destroyed within a few seconds without a highly efficient cooling system to extract the heat.

2.7.6 Others

There are other ways of converting solar radiation to electricity that may eventually be competitive, for example:

- The Kalina cycle is a modified Rankine cycle involving mixtures of ammonia and water of varying concentration, that offers higher performance for temperatures between 200 and 300°C. It is being pursued commercially and also targeted at geothermal power applications.
- Thermoelectric converters produce electricity directly from heat. Semiconductor-based systems work in an analogous way to photovoltaic cells, except that excitation of electrons into the conduction band is via thermal excitation rather than individual photon absorption.
- Thermionic converters also produce electricity directly from heat; they excite electrons from an active surface across an evacuated region to a collector.
- Thermo-photovoltaics use PV cells tailored to thermal radiation wavelengths to convert the radiation re-emitted from heated surfaces.
- Magneto-hydrodynamic converters use the expansion of heated ionized gas through a magnetic field to generate a potential difference.

Whilst this book is primarily directed at electric power generation, final conversion can also be to drive a chemical process such as discussed in Chapter 20 or for process heat as discussed in Chapter 19.

2.8 Maximizing system efficiency

Previous sections have discussed optical errors, concentration ratio, and the sources of thermal losses from a receiver. Performance of these

subsystems are combined, into an overall system efficiency (Eq. [2.1], repeated here):

$$\eta_{system} = \eta_{optical} \times \eta_{receiver} \times \eta_{transport} \times \eta_{storage} \times \eta_{conversion}.$$

A common convention is for the concentrator/optical efficiency $\eta_{optical}$ to include all reflectivity and flux spillage losses up to the point where radiation enters the receiver. The receiver efficiency $\eta_{receiver}$ includes both reflective losses from the receiver as well as radiative, convective and conductive losses. Transport efficiency $\eta_{transport}$ includes thermal losses from pipework conveying the heat transfer fluid to either the storage or the power cycle (or the chemical or industrial heating process), as well as losses in heat exchangers between the HTF and the power cycle working fluid. Storage efficiency $\eta_{storage}$, as an energy efficiency, accounts for thermal losses from the storage vessel as well as possible losses in pressure or chemical potential, depending on the type of storage; it may also include losses in heat exchangers between the HTF and the storage medium, and between the storage medium and the power cycle working fluid. Finally, the power cycle efficiency $\eta_{conversion}$ (or conversion efficiency) accounts for the thermal, friction, and electrical losses in the power cycle, noting that this is limited by the second law of thermodynamics as discussed below.

It must be noted that the overall system efficiency is not maximized by individually maximizing each of the component efficiencies; the maximum is found only by examining all effects together.

2.8.1 The second law of thermodynamics and exergy analysis

Maximizing overall system efficiency in energy terms is an appropriate goal. However, consideration of the issues in purely energy terms does not provide all the information needed for optimization.

The second law of thermodynamics addresses the inherent of irreversibility of processes and leads to the ultimate limiting conversion efficiency of a heat engine between isothermal reservoirs, given by the well-known Carnot limit on the efficiency, η

$$\eta \equiv \frac{W}{Q_{\mathrm{H}}} = \frac{Q_H - Q_L}{Q_{\mathrm{H}}} = 1 - \frac{Q_L}{Q_{\mathrm{H}}} = 1 - \frac{T_L}{T_{\mathrm{H}}}. \qquad [2.45]$$

In this equation, temperatures are absolute temperatures, expressed in SI units of kelvin, with 0 K = –273.15°C. Clearly operating at low temperatures to achieve high receiver efficiencies does not result in efficient power generation.

An ideal Stirling engine is the only power cycle that has a conversion efficiency as indicated by the Carnot expression. In a receiver-mounted application at steady state, a Stirling engine operates between a fixed high temperature receiver and a fixed low temperature environment. However, for systems where a HTF is employed between receiver and power cycle, the power cycle is no longer operating between effective isothermal reservoirs. The Carnot efficiency quantifies the special case of the maximum amount of work that can be extracted between two isothermal reservoirs. It can be used further to develop a very useful thermodynamic concept called 'exergy'.[18] Textbooks such as Çengel and Boles (2010) or Moran and Shapiro (2011) give essential background theory for this area.

The exergy Φ of a system is defined as the maximum amount of work that could usefully be done whilst bringing the (thermodynamic) system to equilibrium with its surroundings. In this context, a system could simply be a particular unit mass of a substance such as a heat transfer fluid. Following on from this definition, every energy flow can be associated in a quantitative sense with a corresponding exergy flow, being the ideal amount of work that could be extracted from the energy flow. Exergy analysis is a powerful tool in understanding and improving CSP systems which are designed to produce power as their ultimate output.

Each subsystem efficiency in Eq. [2.1] can have a corresponding exergetic efficiency defined. Since Eq. [2.1] as it stands includes a final output form of electricity (pure exergy), maximization of either overall energy or exergy efficiency will occur for the same design and operating parameter values.

Table 2.1 illustrates the temperature dependence of the Carnot efficiency together with the exergy-to-energy ratio of some potential HTFs at the same temperature. It can be seen that operating thermal systems at realistically achievable temperatures represents a major step down in the potential to extract work compared to the sun's surface temperature. It can also be seen that transfer of heat from an isothermal source to a real HTF heated to the same temperature also reduces the potential to extract work. That is, it is an irreversible process that destroys exergy.

It can be seen that, for a given temperature, the Carnot efficiency for operation from an infinite isothermal source is higher than the exergy-to-energy ratio of the alternative working fluids. Energy in a finite amount of a substance at a particular temperature can be thought of as being available over the range from its temperature down to ambient temperature

[18] Exergy is also sometimes referred to as availability. This should not be confused with availability as a term used in the power industry for the fraction of time that a piece of equipment is available to function on demand.

Table 2.1 Thermodynamic efficiency metrics relative to an environment of 298 K, 1 bar

Temperature (°C)	Temperature (K)	Carnot efficiency (%)	Exergy-energy ratio of a constant specific heat HTF (%)	Exergy-energy ratio of steam at 15 MPa (%)	Exergy-energy ratio of steam at 5 MPa (%)	Typical real steam cycle net efficiency (%)
5,527	5,800	94.9	84.1			n.a.
1,000	1,273	77.0	56.1			n.a.
700	973	69.9	48.3	48.0	44.6	40–45
400	673	56.5	35.9	43.4	40.2	35–40
300	573	48.9	29.8	31.5	39.0	25–30
200	473	38.0	22.0			

according to the amount needed for each increment of temperature rise. Steam has a profile that is strongly affected by the phase change from water to steam. Depending on how close this is to the actual steam temperature, its exergy-to-energy ratio is either increased or decreased relative to a constant specific heat fluid.

The concept of regenerative feedwater heating in a steam cycle using bled steam is best understood from an exergy point of view. Partially expanded steam has already given up some of its exergy to power generation, so using it to pre-heat feedwater destroys less exergy than allowing the highest temperature heat source to heat the feedwater from ambient temperature. Applying this to a CSP system, then, we can say that sending the HTF to the receivers at a higher temperature increases the potential to generate work from the energy that is absorbed in the receivers. Doing so, however, means receiver average temperature and associated losses are increased and higher HTF flow rates must be maintained.

2.8.2 Heat exchange between fluids

A major cause of exergy loss in CSP systems is any place in a system where heat transfer from one fluid to another occurs, usually in a heat exchanger. Major areas of heat exchange in CSP systems can include:

- from HTF to storage medium
- from HTF to power cycle working fluid
- from storage medium to power cycle working fluid
- from power cycle working fluid to ambient air (condenser or cooling tower).

Well-designed heat exchangers create a large interface area between two fluid streams, such that heat transfer can be achieved with a lower temperature drop, even if the overall heat transfer coefficient is not high. To build such a heat exchanger can be extremely expensive however, so a cost-benefit optimization is usually required.

Systems that avoid unnecessary heat exchange steps are receiving increased attention, including in areas of direct steam generation, and molten-salt parabolic trough fields.

Irrespective of the overall heat transfer coefficient achieved in a heat exchanger, the fluids involved may not have the same profiles of enthalpy increase to temperature increase. This is particularly true if one has a phase change (water to steam). This can be a major source of exergy loss.

In complex processes with multiple heating and cooling requirements, the technique of pinch analysis, attempts to combine all heat transfer temperature profiles in an optimal manner.

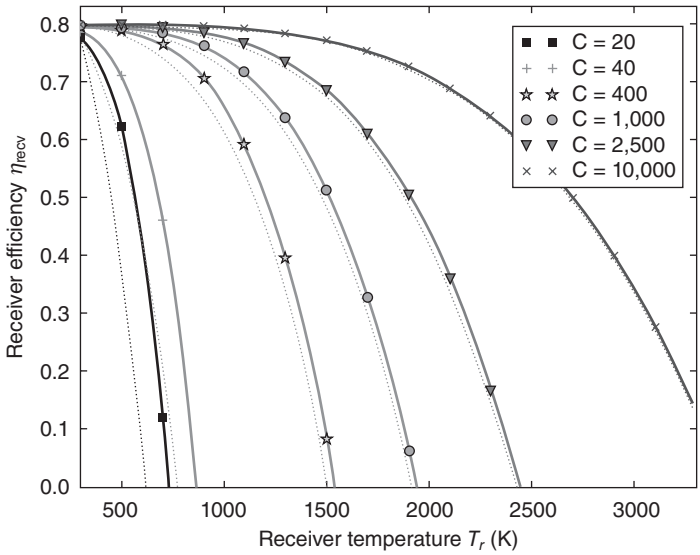

2.15 Efficiency of a simplified solar collector with 100% optical efficiency, average absorptivity of 0.8 (assumed equal to emissivity) plotted both with no external convective loss (solid lines) and with 20 W/m^{2}K external convective loss (dotted lines). DNI is 800 W/m^2, ambient temperature 300 K, and sky temperature 270 K.

2.8.3 Optimization of operating temperature

A simplified analysis of the performance of a solar thermal energy system is useful in demonstrating the competing design demands. From the theory of reversible heat engines, we know that power cycles running from high-temperature thermal reservoirs are most efficient, but we also know that thermal losses increase as receiver temperatures increase.

Using the simplified expressions for the various loss mechanisms, and some typical parameter values, gives the results for receiver efficiency as a function of concentration ratio and temperature shown in Fig. 2.15. It can be seen that at low temperatures, all efficiencies reduce to the average absorptivity value. As temperature is increased,[19] efficiencies drop with higher concentration systems having higher receiver efficiencies at any given temperature. The various curves intersect the x-axis at the corresponding stagnation temperature.

[19] In a real system, operating temperature can be controlled through variation of HTF flow rate, for example.

To simulate an idealized operating regime for maximizing power production, the receiver efficiency must be multiplied by a power cycle conversion efficiency to yield an overall ideal system efficiency.[20] To a large extent, power cycle efficiency dependence on operating conditions is complex and must be established from empirical performance curves. The difference in exergy value of the HTF before and after transfer of heat to the working fluid at input to the power cycle provides a good indicator, with real power cycles extracting something over 70% of the available exergy as work. The Carnot expression provides a good qualitative illustration of the principles, however.

If the receiver efficiency results of Fig. 2.15 are multiplied by the Carnot efficiency pertaining to the receiver temperature at each point to give a semi-ideal system efficiency, the results are as shown in Fig. 2.16. It can be seen that there is now a clear peak efficiency at a particular temperature for each concentration ratio. Higher concentration ratios have higher peak efficiencies and these occur at higher receiver temperatures.

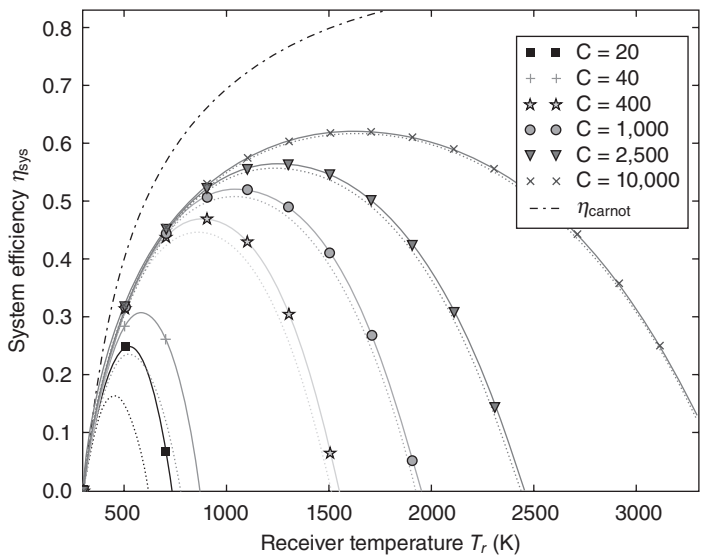

2.16 Ideal system efficiency as a function of receiver temperature. Carnot efficiency is also shown as a dashed line as a function of receiver temperature. The dotted lines include the effect of convective heat loss, for a fixed convection coefficient as described in Fig. 2.15.

[20] This is equivalent to treating optical efficiency and energy transport and/or storage efficiency as 100%.

2.8.4 Optimization of aperture size

Receiver aperture size is an important parameter to optimize. Radiative and convective losses are essentially proportional to aperture area, for receiver temperature held constant, suggesting that this area should be minimized. On the other hand, a larger aperture will intercept more of the incident radiation so increasing the optical efficiency. For a given focal-region flux distribution and operating temperature, there will be an aperture size beyond which any further increases will increase thermal losses by more than the collected energy is increased.

This choice of optimum aperture and operating temperature will be different for every concentrator and application. To illustrate the idea, the following results are taken from Steinfeld and Schubnell (1993). They analysed the optimum choices based on an actual flux distribution measured with a small solar furnace. Figure 2.17 shows the actual focal plane flux map as a contour plot. Steinfeld and Schubnell assumed only radiation losses from a hypothetical receiver and treated it as a uniform temperature blackbody disc. On this basis they defined an absorption efficiency equal to the product of concentrator and receiver efficiency. They determined this for a

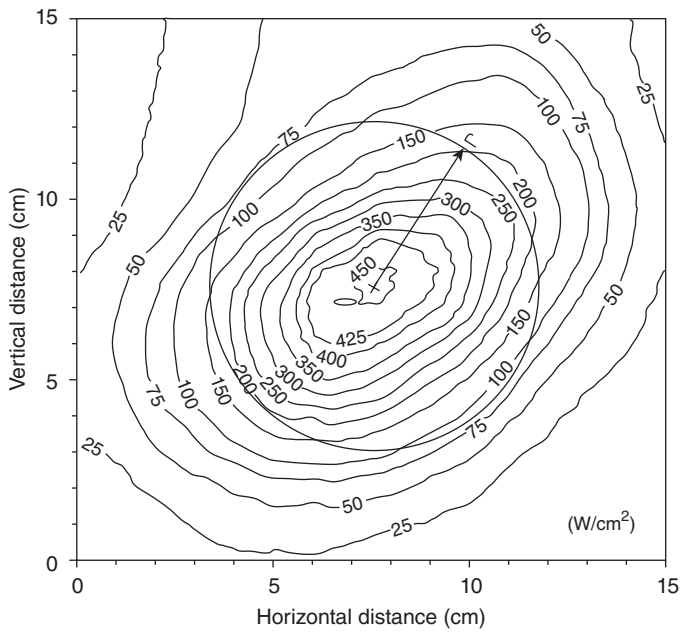

2.17 Solar flux distribution measured at the focus of the Paul Scherer Institute solar furnace in October 1990. The power intercepted by the aperture can be found by integrating solar flux through the circled area (reproduced from Steinfeld and Schubnell, 1993).

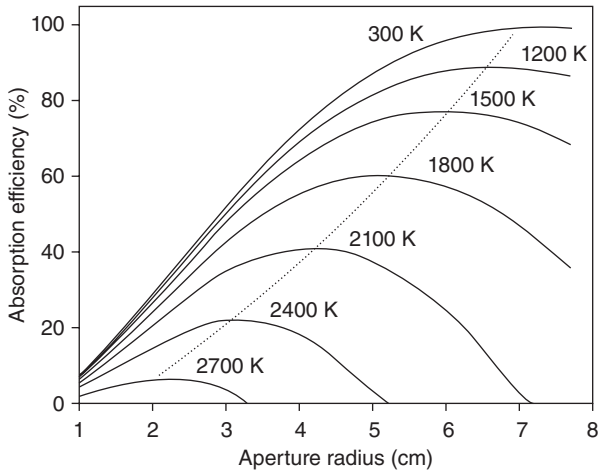

2.18 Energy absorption efficiency as a function of aperture radius for various receiver temperatures. The dotted line is the locus of maximum efficiency, for which optimum aperture radii are determined (reproduced from Steinfeld and Schubnell, 1993).

range of receiver temperatures and radii and produced the results shown in Fig. 2.18. For each operating temperature, the absorption efficiency first increases as aperture size is increased and more radiation is intercepted, but it then reaches a peak and decreases once the increased radiation loss from area increase outweighs the extra incident radiation intercepted. For any particular operating temperature, there is an optimum aperture radius. Higher temperatures with associated higher levels of re-radiation dictate smaller aperture size. Choice of higher operating temperature also limits the maximum absorption efficiency that can be achieved.

Taking this further to a semi-ideal overall system efficiency by multiplying the absorption efficiency by the Carnot efficiency at the receiver temperature yielded the results in Fig. 2.19 and shows that an ideal Carnot cycle driven by a black-body receiver on this collector would have a peak overall efficiency when operated at 1,200 K with a 7 cm radius aperture.

2.8.5 Solar multiple and capacity factor

It is the overall average system efficiency which is most important, rather than the design point steady state efficiency. The concepts of capacity factor and solar multiple are important in this respect. The capacity factor, CF, of a piece of equipment is its fractional utilization calculated over a long time period. In the case of a CSP system, full utilization corresponds to the power

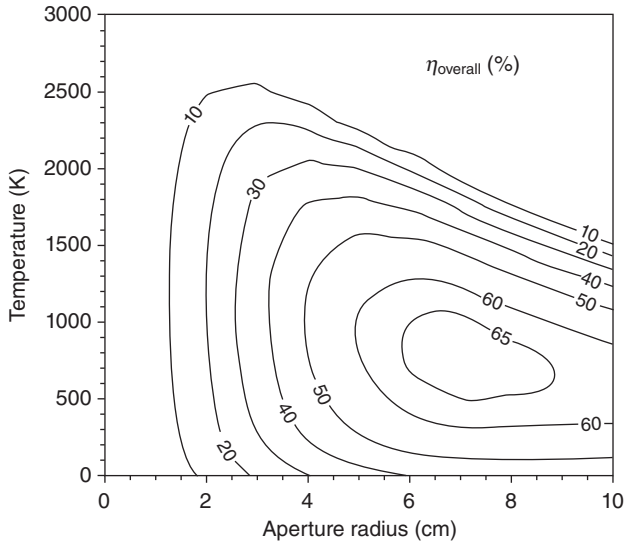

2.19 Overall system efficiency as a function of the aperture radius and temperature, using the solar flux distribution of Fig. 2.17 (reproduced from Steinfeld and Schubnell, 1993).

block running at its nominal (rated) design point or 'nameplate' electrical output power $\dot{W}_{des,pb}$. A capacity factor of 100% means that the plant is running at full rate all of the time; 25% capacity factor means that the long-term average of the power block electrical output $\dot{W}_{avg,pb}$ is 25% of the design point output

$$CF = \frac{\dot{W}_{avg}}{\dot{W}_{des,pb}}. \qquad [2.46]$$

For CSP systems without energy storage or backup boilers, the turbine will not be operating at night, nor during periods of cloudy weather; for systems such as this, the capacity factor will be approximately 20%, purely due to sun position and weather effects. With the addition of energy storage, the capacity factor can be increased greatly, up to as much as 75% or more, allowing round-the-clock operation for much of the sunnier part of the year.

The capacity factor for the power block of a CSP system can also be increased by oversizing the solar field (more heliostats or troughs per steam turbine, for example). This leads to the definition of the solar multiple, SM, which is the ratio of the solar field design point thermal power output $\dot{Q}_{des,field}$ (normally calculated at solar noon on a clear midsummer day) to

the thermal power demand of the power block when running at its nominal capacity $\dot{Q}_{\text{des,pb}}$.

$$\text{SM} = \frac{\dot{Q}_{\text{des,field}}}{\dot{Q}_{\text{des,pb}}}. \quad [2.47]$$

When a thorough economic analysis (Section 2.10) is performed on a CSP plant, it will typically be found that an optimal solar multiple for a system without storage will be in the range 1.15 to 1.30, while for systems with storage, the optimal solar multiple will be 2 or higher, depending on how much storage is installed. This is because there are efficiency and capital cost penalties associated with a power block that frequently runs at part-load; it is better to waste a little of the collected heat during the maximal solar periods in exchange for running the power block at its design point capacity, at consequently higher efficiency, for more of the year.

2.9 Predicting overall system performance

Predicting the output of a CSP system with reasonable accuracy is a complex process. Thermal systems include multiple subsystem components with thermal capacity whose behaviour at any point in time depends not only on the instantaneous conditions the whole system experiences, but also the recent history of its operation. Power cycles have efficiencies that change with load and can take significant time to start up and shut down.

There is a range of approaches to modelling CSP systems and it is an ongoing area of R&D. One can distinguish between those that model on half to one hour time steps and treat most thermal components as being in 'pseudo steady-state' and more fundamental approaches that attempt to track short duration cloud and thermo-fluid transients.

A recent review of CSP system simulation work, together with an overview of background theory for simulation of a complete plant including storage is given by Llorente García *et al.* (2011). Standardization and benchmarking of CSP simulation tools is currently in progress by the SolarPACES organization (Eck *et al.*, 2011). Commercial software for energy system modelling which has been used in solar thermal applications includes *IPSEpro*, *Ebsilon*, *EcoSimPro*, *TRNSYS*, *GateCycle*, *Dymola*, *Mathematica* and *Aspen*. The System Advisor Model (*SAM*) from NREL (NREL, 2012) is an easy-to-use, free, but closed-source package that uses the well-known *TRNSYS* simulation engine internally. Possibly the only complete free open-source system model is *SOLERGY* (Stoddard *et al.*, 1987). Key outputs from such analyses include annual power output, capacity factor. To obtain optimal sizing and operational strategies, the analysis must be coupled with an economic analysis (Section 2.10).

2.9.1 Case study using the system advisor model (SAM)

As an example of a system modelling analysis, results for a trough system modelled with the System Advisor Model (SAM) are presented here. SAM can predict hourly, monthly and annual output of CST, CPV, flat PV and also a range of other renewable energy systems. There has been an extensive body of work around its application to CSP systems in particular.

The key inputs for system performance forecasting are the direct normal irradiation (DNI) time series data, together with the associated ambient temperature, humidity and wind speeds. SAM accepts weather files in a range of 'typical meteorological year' (TMY) formats, meaning an artificial year assembled from real months from real years that yield a match with overall long-term averages, as well as containing a representative range of unusual/extreme days. Generally the expectation is that the TMY file will provide hourly data.

There is a range of available templates and files of predetermined case studies for use with SAM. One of these is a verified model of the actual *Nevada Solar 1* 64 MW_e trough system that is located near Las Vegas. The key parameters of the plant are:

- 64 MW_e nominal electrical power output
- no storage
- solar multiple of 1.264 (i.e. solar field is oversized relative to power block system capacity at design conditions)
- total trough aperture (collector) area of 357,428 m^2.

Figure 2.20 shows the daily profiles of DNI and net generation levels for a clear day and two days that show partial cloud events in the afternoon. Several key effects can be seen:

- Prior to start-up each day, there is a period of negative generation (net energy consumption) as the system is prepared for operation.
- During the morning start-up phase, generation levels lag behind the rising DNI levels, reflecting the inertia of the system.
- During periods of continuous high DNI levels, system output can vary, presumably reflecting the variation in factors like ambient temperature affecting overall performance.
- For DNI levels below a threshold level, no generation is produced.

Figure 2.21 shows the results for predicted monthly output for this system at its Las Vegas, USA, site and three alternative sites in Australia. Key parameters and outputs for these cases are listed in Table 2.2.

The northern hemisphere site has output peaking in mid-year whereas the southern hemisphere Australian sites have output peaking at the beginning/end of the calendar year. The three Australian sites span from northern

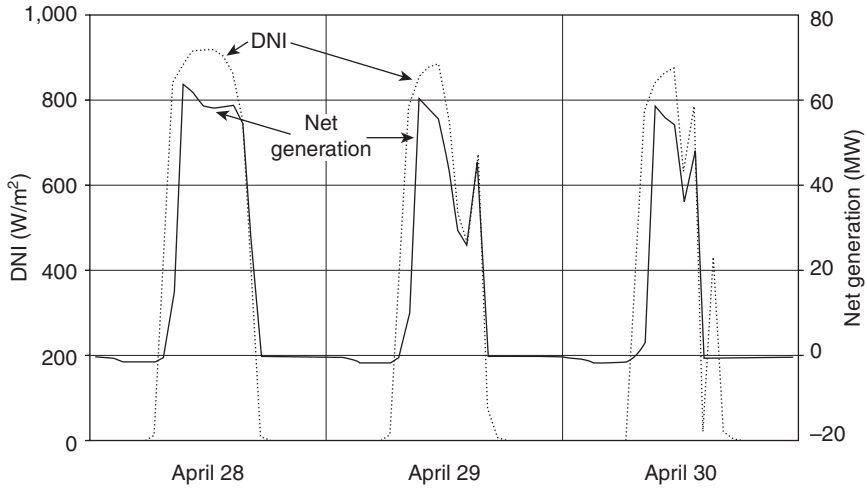

2.20 Three days of modelled output of a 64 MW_e parabolic trough system using Longreach, Australia, weather data points.

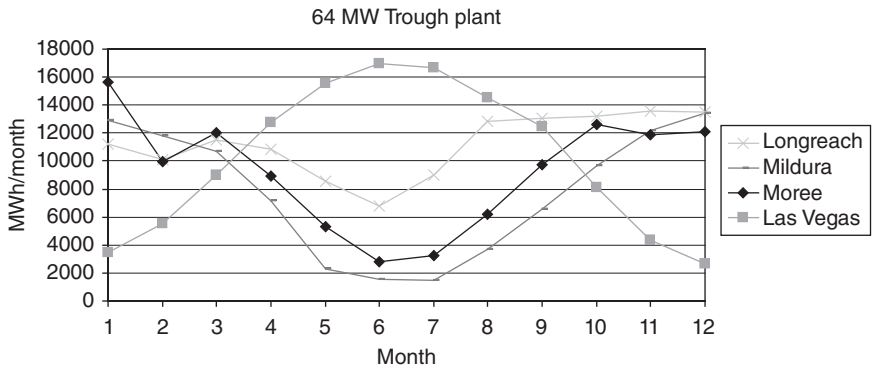

2.21 Modelled output of a 64 MW_e parabolic trough system sited at Las Vegas (USA) and Longreach, Moree and Mildura (Australia).

to southern latitudes. It is apparent that the Longreach site, which is closest to the equator,[21] shows the most uniform output through the year.

Overall annual generation correlates with annual DNI, but in a non-linear manner. Referring to Table 2.2, it can be seen that Longreach outperforms the Las Vegas site, even though it has slightly lower DNI. Conversely, Mildura, with around 20% lower DNI than the best sites, shows output reduced by around 40%. High ambient temperatures and high

[21] Whilst being closer to the equator improves the performance in inland Australia, note that equatorial regions generally offer poor performance due to tropical cloud and humidity.

Table 2.2 Modelled outputs of a 64 MW_e parabolic trough system in Las Vegas and at various sites in Australia

Location	Net annual generation (MWh_e)	Annual conversion efficiency	Capacity factor	DNI ($kWh/m^2/yr$)	Latitude	Longitude	Average ambient temp. (°C)	Average wind speed (m/s)
Las Vegas (Nevada, USA)	117,147	12.57%	20.90%	2,606.6	36.08	−115.167	19.5	4.1
Longreach (North Queensland, Australia)	128,794	14.05%	22.90%	2,564.4	−23.43	144.28	23.9	2.4
Moree (NSW, Australia)	106,165	13.17%	18.90%	2,254.6	−29.48	149.83	18.7	2.3
Mildura (North Victoria, Australia)	89,714	11.81%	16.00%	2,124.6	−34.23	142.08	16.9	3.4

average wind speeds would work to reduce the system output; however, the variation in these parameters does not appear significant between the sites. Another differentiator is the extent to which low DNI days are made up of short intervals of broken cloud or whole days of no sun. Broken cloud works against output for CST systems, since the time taken for the system to reach operating temperatures makes operation extremely inefficient in such circumstances.

2.10 Economic analysis

The discussions above have suggested that CSP system design must consider cost trade-off issues as well as simply maximizing efficiencies. This section introduces the relevant aspects to complete the picture. A definitive description of methodologies for the financial analysis of energy systems is given by Short *et al.* (1995).

CSP systems have high capital costs and no fuel costs. Initial investments must be amortized over the working life of systems. Thus the key issue is the net present value (NPV) over the lifetime. The basic formula for evaluating NPV is

$$\mathrm{NPV} = \sum_{i=1}^{N} \frac{C_i}{(1+DR)^i} \qquad [2.48]$$

where the cash flows C_i are those occurring in time interval (year) i, DR is the discount rate and N is the total number of compounding periods.[22]

Cash flows can be measured in either nominal or real currency units. A real cash flow is adjusted for inflation and expressed in a currency value of a specific year irrespective of the year it takes place and thus has a constant effective value. The discount rate can be either nominal or real. NPVs can be calculated using real currency cash flow measurements together with real discount rates, or nominal currency cash flow measurements with nominal discount rates; the same NPV will be obtained in either case.

For a CSP system, the key cash flows are the initial capital investments (negative), ongoing O&M costs (negative), the costs of ongoing inputs such as fuel for hybrid operation or water for cooling (negative), revenue from direct energy sales (positive) and possible provision of ancillary services (positive). Key parameters are the discount rate and the assumed lifetime of plants, both of which have a significant impact on overall NPV results. A longer assumed plant life and a lower discount rate both work to increase

[22] This is the most commonly recognized form of NPV on the assumption of annual compounding. Compounding can actually be done on any time scale including continuously. Also, in a strict mathematical sense, DR is a fraction per unit time and is multiplied by the compounding time interval (in this case 1 year).

NPVs for renewable generation. If the 'marketplace' assesses that a project or technology is 'high risk' this leads to the use of shorter lifetimes for amortization and application of higher discount rates.

The levelized cost of energy (LCOE, also known as levelized energy cost, LEC) is the most frequently used economic performance metric for power generation plant. It is a standard metric used not just for CSP or other renewable energy systems but for any form of generation technology. It is defined as the constant per unit cost of energy which over the system's lifetime will result in a total NPV of zero. In other words it is the 'break even' constant sale price of energy. Thus

$$\mathrm{NPV} = \sum_1^N \left(\left(\mathrm{LCOE} \times E_{annual} \times (1-T) \right) \Big/ (1+DR)^j \right) - \mathrm{NPV}_{LCC} = 0, \qquad [2.49]$$

where T is the tax rate and NPV_{LCC} is the net present value of all lifecycle costs and E_{annual} the annual generated electrical energy. This gives

$$\mathrm{LCOE} = \frac{\mathrm{NPV}_{LCC}}{\sum_1^N \left(\left(E_{annual} \times (1-T) \right) \Big/ (1+DR)^j \right)}. \qquad [2.50]$$

From a purely societal perspective, tax would be omitted from the calculation; however, from a plant owner/business perspective, it is assumed that tax would be applied to energy sales, whilst various tax deductions would work to reduce costs.

For fossil fuel power systems, a major part of the lifecycle costs will be the fuel that is consumed on an ongoing basis in inverse proportion to the conversion efficiency. For CSP and other renewable systems, the dominant lifecycle cost is the initial capital investment, with ongoing operations and maintenance costs as a small but significant contributor.

LCOEs can be in real (inflation independent) or nominal terms, which can be confusing because they are expressed in year 0 dollar values in either case. A nominal LCOE represents a hypothetical income that declines in real value year by year, whereas a real LCOE has a constant 'value'. Since the total NPV using either method must be the same by definition, the nominal LCOE will be the higher of the two. Real LCOEs are typically used for future long-term technology projections, whereas nominal ones are often used for short-term actual projects.

From a pure societal perspective, it can be argued that tax issues can be left out of the LCOE. However, from the perspective of a commercial entity owning a system, the prevailing assumption is that, in order to break even, it must be assumed that energy produced is taxed at the standard corporate tax rate. Against this, interest, depreciation and operating costs are tax deductible.

Detailed, project-specific LCOE evaluations are based on complex calculations summing every discounted cash flow over the system lifetime, which are then solved iteratively to establish the real dollar value of energy which gives the total NPV of zero. Issues that are typically encountered include:

- debt financing (loans) may be paid off over a different timescale to equity investments
- tax benefits may apply in different jurisdictions
- tax deductible depreciation may apply over a shorter timescale than the project
- construction is staged over several years and subject to higher interest rates for finance
- system output may take some time to stabilize as commissioning processes proceed after first start-up
- system output may be subject to other predictable variations over time (such as a component with known degradation rate)
- major plant upgrade expenditures may be predicted at certain times in addition to overall continuous O&M
- various inputs may be subject to different escalation rates.

All these issues are project-specific, depending on technology type, developer status and site location.

Studies that report the LCOE for CSP systems and other generation types are often poor at documenting all of their input parameter assumptions and describing the methods used in a comprehensive way. In many cases, the methodology is actually intentionally withheld as it is embodied in proprietary financial models.

A methodology that is somewhat simplified but has sufficient complexity to allow issues of tax, cost of equity and cost of debt to be examined, is based on a life cycle costs NPV calculation embodied in the following formula

$$\mathrm{NPV}_{LCC} = EQ - \sum_1^{ND} \frac{DEP \times T}{(1+DR)^j} + \sum_1^{NL} \frac{LP}{(1+DR)^j} - \sum_1^{NL} \frac{INT \times T}{(1+DR)^j} + \sum_1^{N} \frac{AO \times (1-T)}{(1+DR)^j} - \frac{SV}{(1+DR)^N}, \quad [2.51]$$

where EQ is the initial equity contribution from the project developer, DR is the nominal discount rate, ND the period (number of years) over which the system can be depreciated for tax purposes, DEP is the amount of depreciation in a year, T is the taxation rate applying to assumed income from energy sales, LP is the annual loan payment, INT is the reducing amount of interest paid each year as the loan is paid off, NL is the term (number of years) of the loan, AO is the annual operations cost which could

be calculated from fixed and variable maintenance contributions and any fuel costs as needed, N is the project lifetime[23] and SV is the end of project life salvage value.

The simplifying assumptions used are as follows:

- The analysis begins from the time of plant commissioning.
- Annual energy production is assumed constant over project life.
- The equity contribution is assessed at the beginning of year 1 and so is assumed to have all costs of construction finance rolled into it.
- Depreciation is linear in nominal dollars.
- Loan payments are constant for each year of the loan and are in nominal dollars based on amortization of a debt across a loan term.
- Annual O&M costs are constant per year in nominal dollar terms across project life. (This is possibly the most significant, since it does not reflect the lumpy expenditure likely on component overhaul).

To aid in understanding, LCOE can be simplified further if tax is not considered and the cost of capital (both debt and equity) can be rolled into a single discount rate and the debt and equity investments rolled into a single capital cost. If fixed and variable operation costs are separated out, the result is

$$\mathrm{LCOE} = \frac{(F_R + \mathrm{O\&M}_{fixed})C_0}{PF_c} + \frac{C_{fuel}}{\eta_{conversion}} + \mathrm{O\&M}_{variable} \qquad [2.52]$$

where P is the nominal design point electrical power capacity of the system, F_c is the capacity factor (the annual average fraction of nominal capacity achievable), O&M are operation and maintenance costs that are split between those that are in proportion to generation (variable, expressed in the same units as the LCOE) and those that are fixed annual costs (expressed as a fraction of capital cost per year), C_o is the total initial capital cost, C_{fuel} is the per unit energy cost of any fuel used in a hybrid system, $\eta_{conversion}$ is the conversion efficiency of fuel to electricity and

$$F_R \equiv \left(\frac{DR(1+DR)^n}{(1+DR)^n - 1} \right)$$

is the capital recovery factor.

The capital recovery factor (sometimes called annualization factor) is dimensionally the same as the discount rate and represents a rate of repayment that covers return on investment (at the assumed discount rate) plus paying off the capital in the system's lifetime. The dependence of capital recovery factor on discount rate and system life is illustrated in Table 2.3.

[23] In a literal sense, a plant may be decommissioned at the end of its useful life. However, if a conservative assumption has been made, it may prove to be the case that the plant's life actually exceeds the value assumed.

Table 2.3 The dependence of capital recovery factor on discount rate for system lifetimes of 20, 25 and 30 years

Discount rate (%/year)	Capital recovery factor for 20-year life (%/year)	Capital recovery factor for 25-year life (%/year)	Capital recovery factor for 30-year life (%/year)
3.00	6.72	5.74	5.10
4.00	7.36	6.40	5.78
5.00	8.02	7.10	6.51
6.00	8.72	7.82	7.26
7.00	9.44	8.58	8.06
8.00	10.19	9.37	8.88
9.00	10.95	10.18	9.73
10.00	11.75	11.02	10.61
11.00	12.56	11.87	11.50
12.00	13.39	12.75	12.41

The correspondence between installed capital cost, discount rate and LCOE is shown in Table 2.4 for a 25-year life and O&M costs expressed purely as a fixed cost of 1% of capital cost per year.

CSP research and development efforts are all essentially directed at reducing construction costs, improving efficiencies and increasing capacity factors, these being the technical options for reducing the LCOE.

2.10.1 Stochastic modelling of CSP systems

As a CSP project approaches the point of being financed and constructed, investors will require analysis of increasing detail and accuracy. In other words, the confidence interval for the LCOE needs to be known. If done rigorously, this requires an analysis of the propagation of errors from all measurement and data sources (including estimated values). These include errors in weather data, fluid properties including specific heat capacity of storage media and HTF, power cycle performance and collector and pipework heat transfer coefficients. Recently the SAM simulation tool has incorporated the ability to perform analysis such as this, and similar capability is offered by some other simulation tools (Ho, 2008).

2.11 Conclusion

This chapter has presented the fundamental principles of CSP systems by tracing the flow of solar energy from initial collection, through to final conversion to electricity, and has considered the limitations that arise in each of the subsystems of concentrator, receiver, transport, storage and conversion.

Table 2.4 The dependence of LCOE on discount rate and capital cost for a 25-year life, 20% capacity factor and fixed O&M costs at 1% of capital cost per year. The currency units can be interpreted as US or Australian dollars, or euros, providing that the currency of the LCOE is the same as the currency of capital cost used

Specific capital cost for 20% capacity factor ($/kW$_e$)	1,000	2,000	3,000	4,000	5,000	6,000
Discount rate (%/year)	LCOE (c$/kWh)					
3.00	4.6	7.7	11.5	15.4	19.2	23.1
4.00	5.7	8.4	12.7	16.9	21.1	25.3
5.00	6.8	9.2	13.9	18.5	23.1	27.7
6.00	8.0	10.1	15.1	20.1	25.2	30.2
7.00	9.1	10.9	16.4	21.9	27.3	32.8
8.00	10.3	11.8	17.8	23.7	29.6	35.5
9.00	11.4	12.8	19.1	25.5	31.9	38.3
10.00	12.6	13.7	20.6	27.4	34.3	41.2
11.00	13.7	14.7	22.0	29.4	36.7	44.1
12.00	14.8	15.7	23.5	31.4	39.2	47.1

The basic physical principles are derived from the principles of optics, heat transfer and thermodynamics. Exergy analysis provides a valuable source of insight and a tool to further optimize performance during design.

Finally, use of discounted cash flow analysis to derive levelized cost of energy (LCOE) has been introduced. Ultimately, it is the cost of energy relative to the income that can be earned that is paramount for CSP systems. Thus system optimization is a problem that is thermo-economic in nature. In addition to this, and not covered by this chapter, CSP systems are informed by a range of other engineering disciplines. Mechanical design, materials, wind loads, control systems, etc., are all encountered. CSP systems are a classic example of interdisciplinary systems engineering.

2.12 Sources of further information and advice

In addition to references that have already been cited and which are listed below in Section 2.13, a number of excellent books have been written in the fields of solar energy in general, solar thermal energy and also concentrating systems specifically, all of which can offer extra insights. Some of them are now unfortunately out of print. They include:

Becker M, B Gupta, W Meinecke and M Bohn (1995) *Solar Energy Concentrating Systems, Applications and Technologies*, C.F. Mueller Verlag, Heidelberg.

Casal F G (1987) *Solar Thermal Power Plants*, Springer Verlag, New York.
Duffie J A and W A Beckman (2006 [1980]) *Solar Engineering of Thermal Processes*, Wiley, New York.
Goswami Y, F Kreith and J Kreider (2000) *Principles of Solar Engineering*, CRC Press, Boca Raton, FL.
Kalogirou S (2009) *Solar Energy Engineering: Processes and Systems*, Academic Press, New York.
Larson R and West R (1996) *Implementation of Solar Thermal Technology (Solar Heat Technologies)*, MIT Press, Cambridge, MA.
Sayigh A (1978) *Solar Energy Engineering*, Academic Press, New York.
Winter C J, R L Sizmann and L L Vant-Hull (eds) (1991) *Solar Power Plants, Fundamentals, Technology, Systems, Economics*, Springer Verlag, New York.

2.13 References

Bejan A, G Tsatsaronis and M Moran (1996) *Thermal design and optimization*, Wiley, New York.
Bergman T L, A S Lavine, F P Incropera and D P DeWitt (2011) *Fundamentals of Heat and Mass Transfer*, 7th edn., Wiley, New York.
Blanco M, A Mutuberria, A Monreal and R Albert (2011) *Results of the empirical validation of Tonatiuh at Mini-Pegase CNRS-PROMES*, Proceedings of SolarPACES 2011, Granada, Spain. See also http://code.google.com/p/tonatiuh/.
Buie D, A G Monger and C J Dey (2003) Sunshape distributions for terrestrial solar simulations, *Solar Energy,* **74**, 113–122.
Çengel Y and M Boles (2010) *Thermodynamics: An engineering approach*, McGraw-Hill, New York.
Chaves J, (2008) *Introduction to Nonimaging Optics*, CRC Press, Boca Raton, FL.
Eck M, H Barroso, M Blanco, J-I Burgaleta, J Dersch, J-F Feldhoff, J Garcia-Barberena, L Gonzalez, T Hirsch, C Ho, G Kolb, T Neises, J A Serrano, D Tenz, M Wagner and G Zhu (2011) *guiSmo: guidelines for CSP performance modelling – present status of the SolarPACES Task-1 project*, Proceedings of SolarPACES 2011, Granada, Spain.
Garcia P, A Ferriere and J Bezian (2008) Codes for solar flux calculation dedicated to central receiver system applications: A comparative review, *Solar Energy*, **82**(3), 189–197.
Gordon J (ed.) (2001) *Solar Energy – The State of the Art*, International Solar Energy Society, James and James, London.
Ho C K (2008) *Software and Codes for Analysis of Concentrating Solar Power Technologies*, Sandia report SAND2008-8053, Sandia National Laboratories, Albuquerque.
Kopp G and J L Lean (2011) A new, lower value of total solar irradiance: Evidence and climate significance, *Geophysical Research Letters* **38**, L01706, doi: 10.1029/2010GL045777.
Llorente García I, J L Álvarez and D Blanco (2011) Performance model for parabolic trough solar thermal power plants with thermal storage: Comparison to operating plant data, *Solar Energy*, **85**, 2443–2460.

Lovegrove K, G Burgess and J Pye (2011) A new 500 m^2 paraboloidal dish solar concentrator, *Solar Energy*, **85**, 620–626.

Meinel A B and M P Meinel (1976) *Applied Solar Energy*, *An Introduction*, Addison-Wesley, Reading, MA.

Moran M J and H N Shapiro (2011) *Fundamentals of Engineering Thermodynamics*, John Wiley and Sons, New York.

NREL (2012) *System Advisor Model (SAM)*. https://sam.nrel.gov/, accessed 29 February 2012.

OpenFOAM Foundation (2011) *OpenFOAM User Guide*, http://www.openfoam.org/docs/user/, version 2.1.0, accessed 29 February 2011.

Rabl A (1976) Comparison of solar concentrators, *Solar Energy,* **18**, 93–111.

Rabl A and P Bendt (1982) Effect of circumsolar radiation on performance of focusing collectors, *Journal of Solar Energy Engineering*, **104**(3), 237.

Short W, D J Packey and T Holt (1995) *A Manual for the Economic Evaluation of Energy Efficiency and Renewable Energy Technologies*, NREL/TP-462-5173, National Renewable Energy Laboratory, Colorado.

Steinfeld A and M Schubnell (1993) Optimum aperture size and operating temperature of a solar cavity receiver, *Solar Energy,* **50**, 1925.

Stoddard M C, S E Faas, C J Chiang and A J Dirks (1987) *SOLERGY – A Computer Code for Calculating the Annual Energy from Central Receiver Power Plants*, SAND86-8060, Sandia National Laboratories, California.

Walton G N (2002) *Calculation of obstructed view factors by adaptive integration*, Technical Report NISTIR–6925, National Institute of Standards and Technology, Gaithersburg, MD. See also http://view3d.sf.net/.

Winston R, W T Welford, J C Miñano and P Benítez (2005) *Nonimaging Optics*, Elsevier Academic Press, Maryland Heights, MO.

3

Solar resources for concentrating solar power (CSP) systems

R. MEYER, M. SCHLECHT and
K. CHHATBAR, Suntrace GmbH, Germany

Abstract: Direct sunlight or beam irradiance is the key resource for any concentrating solar system. Beam irradiance has a significantly higher variability in space and time in comparison to global irradiance, and its measurement requires higher accuracy and attention. Therefore uncertainty of beam irradiance is higher and solar resources must be measured with great care. In order to get realistic long-term values, satellite-derived values are taken into account in addition to ground measurements to mitigate the high inter-annual variability. The short-term variability of beam irradiance in terms of fluctuations should be properly represented as CSP systems are sensitive to transient conditions.

Key words: solar radiation, direct normal irradiance (DNI), irradiation, pyrheliometer, rotating shadowband irradiometer (RSI), satellite-derived irradiance, radiation measurement.

3.1 Introduction

A concentrating solar thermal power plant converts solar irradiance into thermal energy, and ultimately into electrical power. This is done by means of high temperatures and efficient heat-to-electricity conversion systems, such as steam turbines. Conventional fossil-fuelled power plants actively control the rate of heat generation, and thus can adapt energy production to match demand. Usually they can be classified into peak-load, mid-load and base-load categories, each having different flexibilities in start-up, load change and shut down characteristics. These processes are manageable and established in practice.

In solar thermal power systems, the controllable conventional fuel is replaced with solar irradiance, a variable source of energy, which is not in the control of the plant operator. Solar irradiance incident at ground level depends mainly on the sun elevation angle, which defines its path length through the atmosphere and on the constituents of the atmosphere. Clouds, aerosols and water vapour play a dominant role that affects the amount of solar radiation reaching the ground. The amount and fluctuation of these atmospheric constituents obviously are beyond the direct control of the

plant. To maximize the yields of a solar thermal plant, available solar irradiation must be used to the largest possible extent.

Acquiring information about typical solar irradiation available at potential plant sites is of high importance for planning of new solar plants. The climatological average annual solar irradiance is most important in the planning process, but the characteristic frequency distribution also plays an important role. Both phenomena are summarized under the notion 'solar resources', which is the subject of this chapter. The term 'solar resources' here does not include 'solar irradiation forecasting', which more precisely is the process of predicting solar radiation conditions for certain time steps in the future.

This chapter gives an overview of those solar radiation characteristics, which are relevant for concentrating solar power (CSP) plants. It defines and describes the most important terms and units. The use of satellites to derive solar radiation data is discussed. Best practices to reach reliable estimates of solar irradiance conditions for a specific CSP plant location are explained.

As solar thermal power plants are very large installations and often exposed to harsh desert environments, other meteorological parameters also need to be analysed for specific project locations. In the worst case, wind gusts might harm the large sail-like mirror structures. Ambient air temperature and humidity affect cooling conditions and thus influence the efficiency of the power cycle. These parameters are also required for site-specific engineering and are summarized in Section 3.6 on auxiliary meteorological parameters. Section 3.7 gives practical recommendations for a step-by-step approach along the process of project development.

3.2 Solar radiation characteristics and assessment of solar resources

Solar resource assessments should describe characteristic solar radiation conditions based on historic data for the assessed plant location, assuming similar intensities and patterns for future time periods. Maps of solar resources are of highest importance for site selection (see Chapter 4). Solar resource characteristics in the form of time-series in high time-resolution are an important requirement for site-specific engineering and optimization of plant layout towards high yields with moderate technical effort. Well-proven site-specific solar resource assessment is usually an essential factor during due diligence assessment of CSP projects. Actual solar forecasting then is eventually needed on-line with CSP plant operation. Similar techniques to those used for assessing solar resource in the early project stages are applied, but focus of this chapter is the assessment of solar resources.

All CSP technologies need to concentrate sunlight. As optical concentration cannot be achieved based on diffuse light coming from various directions, only the direct beam irradiance component is relevant for CSP. Direct beam irradiance is usually specified in reference to a tracking area oriented normal towards the sun and hence is called direct normal irradiance (DNI). In contrast global horizontal irradiance (GHI) includes both the direct irradiance and the diffuse irradiance (related to the horizontal plane). As non-concentrating photovoltaic (PV) can also utilize a substantial amount of diffuse irradiance, GHI is closely related to the assessment of PV energy yields, while DNI is applied for estimation of energy yields from CSP and CPV (concentrating PV) plants.

The distribution of DNI across the globe is much less homogeneous than GHI (see Plate I between pages 322 and 323). While GHI reaches relatively good values in latitudes higher than 45° and is also quite high around the equator in tropical climates, DNI is usually highest in the subtropics around 23°N or 23°S. These latitudes ±10° or around 1000 km from the equator are the regions of the world where the highest DNI values are reached. Therefore these bands on both sides of the equator are also called the 'sunbelts'.

Site-specific DNI data are difficult to obtain and often include a high uncertainty. Therefore special care should be addressed to solar resource assessment during project development. The long-term average of solar irradiation and its variability need to be analysed for a reliable projection of their availability in the future. This must carefully take into consideration the uncertainties related to the derivation of solar irradiance data. When evaluating the conversion of solar irradiance into thermal energy and then into electricity, the fluctuation patterns of solar irradiation have transient effects on plant performance and thus influence energy production. The impact of these effects depends on system inertia, technical configuration of the plant and operational and control strategies. To allow the detailed assessment of these effects with sophisticated energy yield modelling tools, the DNI data should be available in small time steps with high accuracy and realistic frequency distribution.

The typical lifetime of a solar thermal power plant is expected to be 25 to 40 years. The financing of plants usually assumes a loan period within 15 to 25 years. Compared to global irradiance, the direct beam component shows much more variability in space and time. DNI values obtained from a data source vary from year to year and inter-annual variability can be very extreme. This variability in annual averages of DNI is reflected in the estimation of energy yield of CSP plants.

A general assumption in climatology is that when considering meteorological data spanning 30 years, weather conditions at the site are averaged out and hence they can be used to calculate the long-term average of the

meteorological conditions. Under the best possible condition, ground-measured meteorological data covering the above-mentioned period should be available. But in reality 30 years of measured data are available only for few scientifically monitored locations, but not for potential locations of commercial CSP plants. Lohmann *et al.* (2006) shows that for most sites in the sunbelt, if data from at least 10 years are taken into account the maximum deviation of DNI-averages falls below ±5% from the long-term average.

Thus, for site qualification and yield evaluation of potential construction sites for solar thermal power plants it is highly desirable to have reliable historical data of direct irradiation, ideally for at least 10 years. However for most potential plant locations only satellite data are available for such period.

3.2.1 Important solar radiation terms

The term irradiance is used to describe the solar power (instantaneous energy flux) falling on a unit area per unit time, i.e. in W/m^2. The term irradiation is used to consider the amount of solar energy falling on a unit area over a stated time interval such as a day or a year. In climatology, solar irradiation typically is given in J/m^2 summed over the period of a day, whereas solar engineering solar irradiation is often reported in units of kWh/m^2.

According to the standard EN ISO 9488 (ISO, 1999), the symbol for the irradiance is G and for the irradiation is H. However, often the same symbols are used for irradiance and irradiation. Then they have to be differentiated by context or by the attached units.

When the term 'irradiation' is used, it is necessary to indicate the period over which the irradiance is integrated, as it cannot be seen in the units. Therefore it is better to avoid the term irradiation and use only irradiance. Instead of the annual sum, the yearly average of irradiance can be indicated in units of $kWh/(m^2a)$; instead of daily irradiation, the daily average irradiance may be indicated by $kWh/(m^2d)$. In the CSP industry, the most commonly used units for solar irradiation are $kWh/(m^2a)$ or $kWh/(m^2d)$ or W/m^2. The conversion of solar irradiance from one unit to another is shown in Table 3.1. This assumes years of 365 days, neglecting the effect of leap years. Following this, for example, a DNI of 2000 $kWh/(m^2a) \approx 5.48$ $kWh/(m^2d) \approx 228$ W/m^2 is equivalent to a daily mean of 19.7 MJ/m^2.

In meteorology, average solar irradiance values usually consider full days with 24 hours including nighttime. However, in engineering, sometimes only the period when the sun is above the horizon is relevant for design purposes. The latter has the advantage that average irradiance is closer to actual intensity observed during the day. Irradiance averages only referring to

Table 3.1 Conversion table for solar irradiance values related to 24 hour days

Unit	W/m^2	$kWh/(m^2d)$	$kWh/(m^2a)$	$MJ/(m^2d)$
Value	1	0.024	8.76	11.574

sunshine duration and not to intensity are more complicated to calculate and less correlated to actual daily irradiation. Ambiguities can also occur if sunrise and sunset times are not calculated astronomically assuming a flat horizon, but from the actual period covering first and last visibility of the sun, which depends on local topography. To avoid these problems and to easily convert from average values to daily or annual values, it is recommended to refer to 24-hour average irradiance values.

The extraterrestrial solar irradiance is the solar radiation received at the top of the Earth's atmosphere. The extraterrestrial solar irradiance varies slightly due to variations in energy emitted by the sun and variable distance of the Earth from the sun in the course of the year. The solar constant I_0 is defined as the solar irradiance at the top of the earth's atmosphere on a plane normal to the direction of this radiation, when the Earth is at its mean distance from the sun (149,597,871 km). Its measured average value in the current period is 1366 $W/m^2 \pm 0.6$ W/m^2 (ISO, 2007).

As illustrated in Fig. 3.1, the extraterrestrial irradiance is attenuated on its way through the atmosphere. The unattenuated extraterrestrial irradiance, which is not absorbed or scattered by the atmosphere and reaching the surface directly, is the direct irradiance G_b, which is related to the horizontal plane. According to ISO 9448 (1999) DNI is defined as the direct irradiance on a plane normal to its angle of incidence. Direct beam irradiance strictly refers to non-scattered solar radiation. This comes from the solar 'disk'only, which covers a solid angle of around 0.5°. Due to measurement reasons ISO 9448 (1999) allows an acceptance angle of up to 6° around the centre of the sun's disk for measurement of DNI. On the other hand, most radiative transfer algorithms define beam irradiance as only that particular part of solar radiation which does not experience any scattering – even forward-scattering within the 0.5°-cone of the sun is not considered in this definition. Therefore, simulated direct irradiance is slightly lower than the beam irradiance DNI. As most CSP technologies have a wider acceptance angle than 0.5°, the DNI-definition related to the typically measured 5° cone is considered here.

The diffuse irradiance G_d (see Fig. 3.1) is the scattered irradiance that reaches the ground. Scattering might occur by various processes in the atmosphere, like Rayleigh scattering by air molecules or Mie scattering by

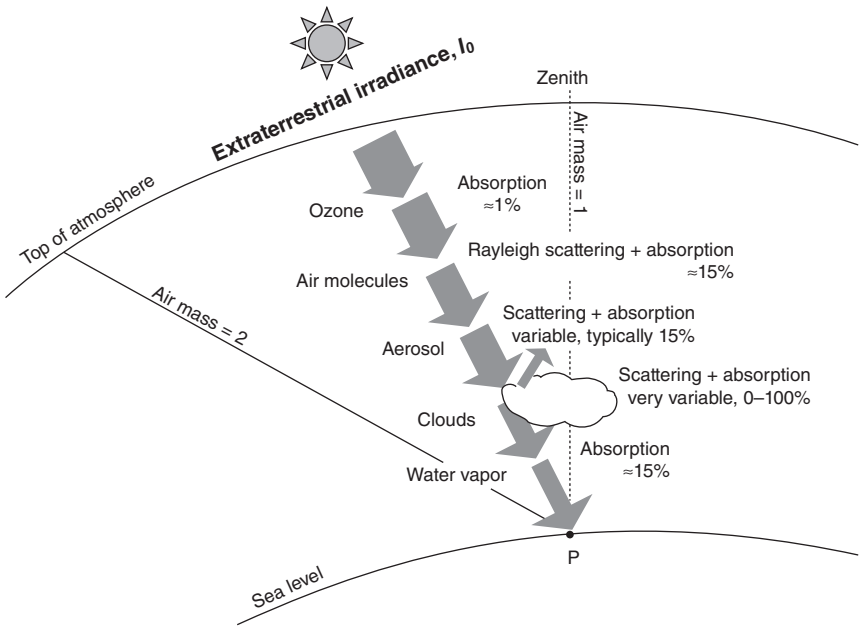

3.1 The main processes influencing solar radiation in the atmosphere and split into the major three components (global, direct, diffuse).

aerosol or cloud particles. Solar radiation reaching the surface, where it partly gets reflected and backscattered, e.g. by clouds, also contributes to diffuse irradiance. If albedo is high, e.g. in regions with snow or white sand cover, the latter process can play a significant role.

Direct horizontal irradiance is related to DNI via the cosine of the solar zenith angle. The sum of direct horizontal irradiance and the diffuse horizontal irradiance (DHI) results in the total irradiance or global horizontal irradiance:

$$G = G_d + G_b = \mathrm{DHI} + \mathrm{DNI}/\cos(\theta_z) \qquad [3.1]$$

where θ_z is the solar zenith angle (see Fig. 3.2).

3.2.2 Seasonal variation of global and beam irradiance

Knowledge of geometrical parameters of the solar trajectory is very important in solar energy applications. Every 365.25 days the Earth revolves around the sun in an elliptical orbit with a mean Earth–sun distance of 149,597,871 km, defined as one astronomical unit. The plane of this orbit is called the ecliptic plane. In this century, the maximum distance of Earth from the sun of 152,101,100 km, which also is called aphelion, is reached by

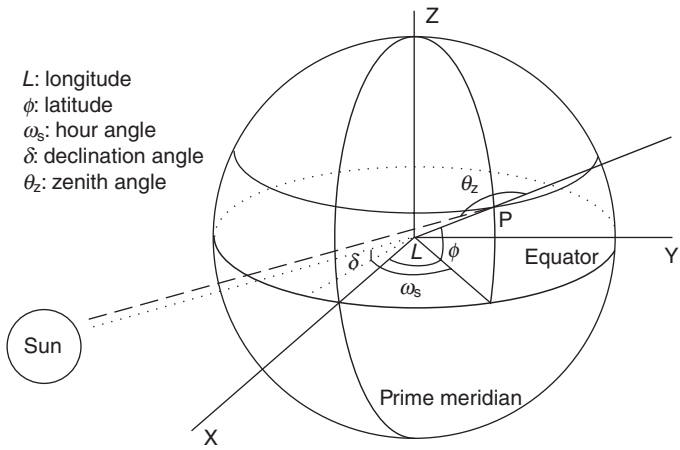

3.2 Solar position in the terrestrial coordinate system for point P at a location of approximately 15 degrees E 45 degrees N at approximately 13:00 UTC.

the Earth's orbit on about 3 July. The perihelion, which is the minimum Earth-sun distance, occurs on about 2 January, when the Earth is 147,101,100 km from the sun.

The Earth rotates about its own polar axis inclined to the ecliptic plane by 23.45°, in approximately 24-hour cycles which produces day and night. The tilt of this axis relative to the ecliptic plane produces the seasons as the Earth revolves around the sun. To predict the direction of sun rays relative to a point on the Earth, the solar time is used, which is dependent on local longitude and is generally different from local clock time. Consequently, at 12:00 solar time, the sun is at its highest point in the sky and exactly due south in the northern hemisphere, or north in the southern hemisphere. The regional clock time is instead defined by politically defined time zones. Accurate knowledge of the difference between solar time and the local clock time is required for energy demand correlations, system performance correlations, determination of true south, and tracking algorithms.

As seen in Fig. 3.2, the Earth's rotation around its polar axis is described by the solar hour angle ω_s, which is the angular distance between the meridian of the observer, and the meridian, whose plane contains the sun. The solar hour angle is zero at solar noon, since the meridian plane of the observer contains the sun at this time, the sun is said to be 'due south' for an observer in the northern hemisphere or 'due north' in the southern hemisphere. The solar hour angle increases by 15° every hour and is calculated by:

$$\text{Solar hour angle} \quad \omega = 15° \cdot \Delta t \qquad [3.2]$$

Any location on the surface of the Earth can be defined by the combination of a longitude angle L and a latitude angle ϕ. The angular distance between the projections of meridian of the local point and the prime meridian on the equatorial plane is defined as the longitude. The angle between the line from a point on the Earth's surface to the centre of the Earth and the Earth's equatorial plane is the latitude. The equator at 0° latitude designates the intersection of the equatorial plane with the surface of the Earth. The Earth's surface at 90° latitude (north pole) and –90° latitude (south pole) is intersected by the earth's axis of rotation.

Figure 3.2 also shows the declination δ, the angle between the Earth's equatorial plane, which is the plane that includes the Earth's equator, and the line of the centre of the Earth and the sun. On 21/22 June at noontime the sun is at its highest point in the sky in the northern hemisphere, and its lowest in the southern hemisphere, with a declination of +23.45°, because at this time of the year the Earth's equatorial plane is inclined 23.45° to the Earth–sun line. This condition marks the beginning of summer in the northern hemisphere and is called summer solstice.

About three months later, i.e. on 22/23 September, a line from the Earth to the sun lies on the equatorial plane and the declination is zero; this condition is called an equinox. At this time the sun at the equator is directly overhead at noontime. Anywhere on the Earth during an equinox, the time during which the sun is visible (daytime) is exactly 12 hours. There are two such conditions during a year. There are the autumnal equinox around 22/23 September, marking the start of autumn and the vernal equinox around 20/21 March, marking the beginning of spring.

On about 21/22 December the winter solstice occurs and marks the point where the equatorial plane is tilted relative to the Earth-sun line such that the northern hemisphere is facing away from the sun. Consequently, at noontime the sun is at its lowest point in the sky, meaning that the declination is at its most negative value. Northern winter declination angles are negative by convention.

For CSP systems it is essential to track the sun exactly during the day and also from one day to another. For this purpose the sun is observed from a position on the Earth's surface. It is of interest to define the sun's position relative to a local coordinate system (see Fig. 3.3). A zenith line (straight up) and a horizontal plane containing a north–south line and an east–west line are the conventional Earth-surface based coordinates.

The actual position of the sun from a point can be defined by two angles: solar azimuth γ_s and solar elevation or solar height h_s. The solar height (or solar elevation) is defined as the angle between the centre of the sun and a horizontal plane containing the observer. Solar height alternatively can be indicated in terms of the solar zenith angle θ_z, which is simply the complement of the solar elevation angle.

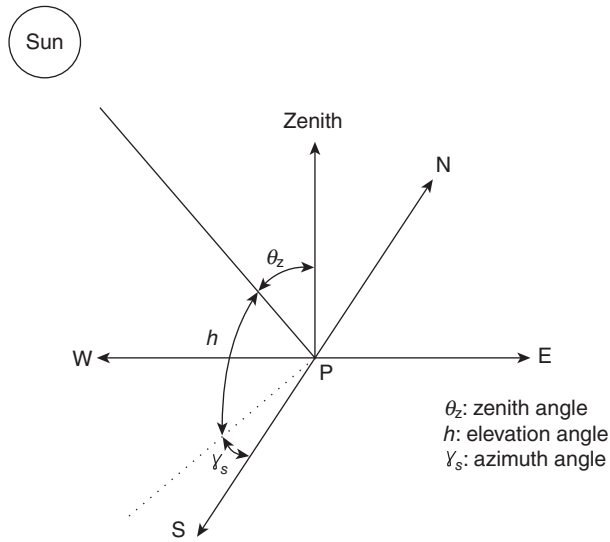

3.3 Solar position viewed from a point P on the Earth's surface in a local coordinate system.

$$\theta_Z = 90° - h_s \qquad [3.3]$$

The disadvantage of the term sun height is that it requires a clear definition of the unobstructed flat horizon. It is more difficult to fix this plane compared to the direction of the zenith, which is defined by the vertical line, which aligns at most places better than 0.1° with the plumb line.

The solar azimuth is the second angle used to define the exact position of the sun. Solar azimuth angle is defined as the angle between the projection of sun's centre onto the horizontal plane and due south direction. According to ISO 9488 (1999) it is defined as 0° at solar noon and increases thereafter, when the sun position goes toward west. Before noon towards east it is negative reaching 0° at solar noon as the day progresses. Alternatively, it is often indicated clockwise from geographic north to the projection of the sun's centre onto the horizontal plane.

For solar energy system design and operation, it is important to be able to calculate both solar angles at any time for any location on the Earth. For this task many different algorithms have been proposed (e.g. Spencer (1971); Michalsky (1988); Blanco *et al.*, (2001); Reda and Andreas (2004)). Simple algorithms only consider the geometrical position of the sun. Others also take into account the angular deviation due to refraction in the atmosphere. According to the review paper of Lee *et al.* (2009) it is recommended to use, for easy and fast applications, Grena (2008) or for applications requiring higher accuracy, the computational more expensive algorithm of Reda and Andreas (2004).

3.2.3 Influence of atmospheric constituents on direct beam irradiance

Gases, liquid and solid particles and clouds attenuate the intensity of extra-terrestrial solar radiation traversing through the Earth's atmosphere. Three groups of atmospheric constituents determine the interaction of solar radiation with the Earth's atmosphere:

- gases (air molecules like ozone O_3, carbon dioxide CO_2, oxygen O_2 and water vapour H_2O),
- solid and liquid particles (aerosols),
- clouds (condensed water in the form of droplets or ice particles).

The available solar radiation at the Earth' surface is primarily linked to the length of the optical path through the atmosphere. This is based on solar position above the horizon as described above. The topography of the location defines the elevation of a point, as well as shadowing by neighbouring terrain features. These geometrical factors can be modelled to a high level of accuracy. The attenuation by gas constituents is mainly caused by absorption and by Rayleigh scattering. The attenuation by aerosols is dominated by Mie scattering and also some absorption. A summary of all non-cloud effects can be described by the Linke turbidity *TL*. It indicates the optical density of a hazy cloud-free atmosphere in relation to a clean and dry atmosphere. *TL* is the number of clean dry air masses that would result in the same attenuation of radiation as the actual hazy and humid air. Because of the dynamic nature of turbidity, its calculation and subsequent averaging leads to some generalization. There are seasonal changes of turbidity, in which the lowest values in many regions appear in winter and springtime and higher values in summer. The values of turbidity differ from place to place in a similar degree of magnitude. Differences are related to the terrain elevation, the intensity of industrialization and urbanization.

However, the strongest attenuation of solar radiation at the ground level is from clouds. For determining the influence of clouds on solar radiation, detailed information regarding geometrical thickness, position and number of layers of clouds, as well as their optical properties are required. Therefore, in solar energy the attenuation by clouds is often estimated by simple empirical techniques.

3.2.4 Spectral characteristics of solar radiation

Solar radiation is electromagnetic radiation emitted by the sun, in which approximately 99% of the solar radiation incident on the Earth's surface is encompassed within the wavelength range from 0.3 μm to 3.0 μm. This wavelength range is called the solar range. Figure 3.4 shows its spectral distribution outside the atmosphere and at sea-level after molecular

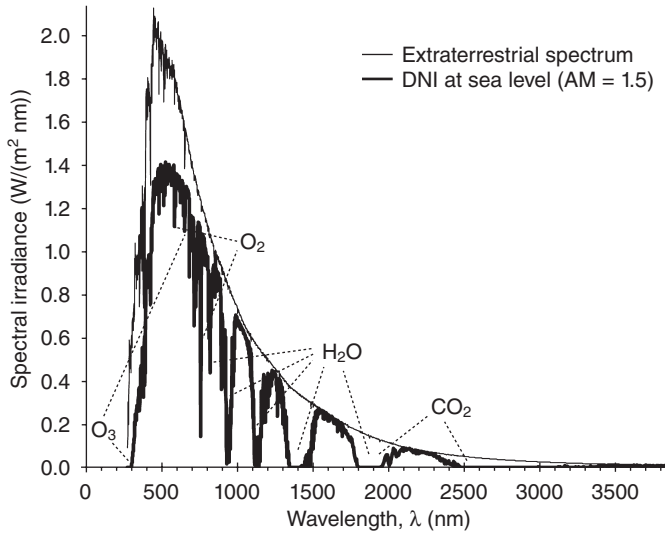

3.4 Spectral distribution of sunlight and molecular absorption at sea level with standard atmosphere.

absorption. The sun's spectrum is dominated by the emission of the sun's outer spheres. It can be approximated by a black body with a surface temperature of approximately 5,778°K or around 6,000°C. Ozone is the main absorption factor in the ultraviolet spectral range (100 nm to 400 nm, according to ISO 21348 (2007)) and, with less impact at 612 nm. Water vapour is another absorption factor with impact at wavelengths above 500 nm, but with increased impact above 1000 nm. At this wavelength, carbon dioxide is also a strong absorption factor, at a similar wavelength to water vapour.

3.3 Measuring solar irradiance

Measuring the sun's energy incident on the Earth's surface is one of the most difficult field measurement exercises. The measurement technology applied today is based on an energy conversion process whereby electromagnetic radiant energy is converted into another form of energy, which can be detected by measurements. Conversion into an electric signal is preferred.

Solar instruments with a hemispherical (180°) field of view are called pyranometers. In contrast are pyrheliometers, instruments using only a narrow field of view (typically 5°). These are designed to measure the radiation coming from the solar disc and the adjacent region around the sun (circumsolar). Consequently, a pyrheliometer must be accurately tracking the sun to keep it properly oriented.

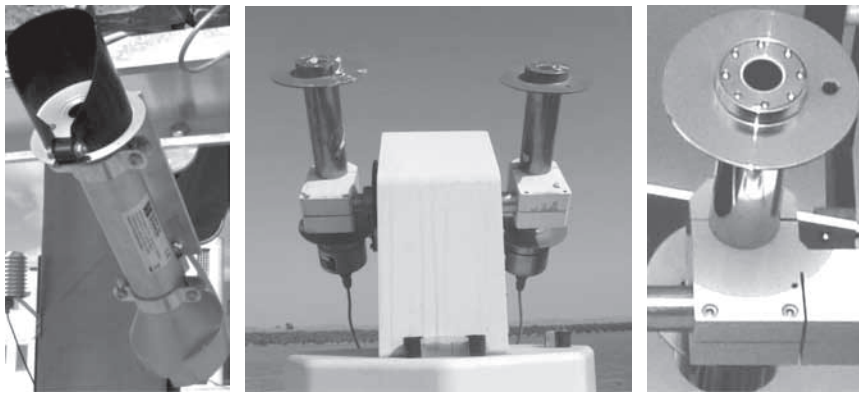

(a) (b) (c)

3.5 Thermopile pyrheliometer instruments (a) Kipp & Zonen CHP1 (b) Eppley solar tracker with two arms for pyrheliometers and (c) Eppley NIP.

The sensor principles employed today either follow the thermoelectric or the photoelectric effect. Both have specific advantages and shortcomings.

3.3.1 Thermal sensors

With thermal solar radiation sensors, the radiant energy is initially converted into thermal energy by means of a black absorbing surface, and then into an electrical signal by a thermopile. This electrical output can be measured with a voltmeter.

As an example, various thermal pyrheliometers which are designed to measure DNI directly are shown in Fig. 3.5. Alternatively, if measured by pyranometers, DNI can be derived indirectly by simultaneous measurement of global horizontal irradiance and diffuse irradiance, with arithmetic deduction of values via equation [3.1]. Figure 3.6 shows examples of thermopile pyranometers designed to measure hemispherical irradiance.

Ideally, the black surface of thermopile instruments should absorb like a perfect black body, which is a body fully absorbing and also emitting radiation of all wavelengths. Such a photon trap converts all radiation into heat, allowing the conversion of solar radiation intensity into a temperature signal, which then can be measured for example through a thermopile element.

Such a thermopile element consists of a large number of thermocouple junction pairs electrically connected in series. A thermocouple consists of two dissimilar metals connected together. The absorption of thermal

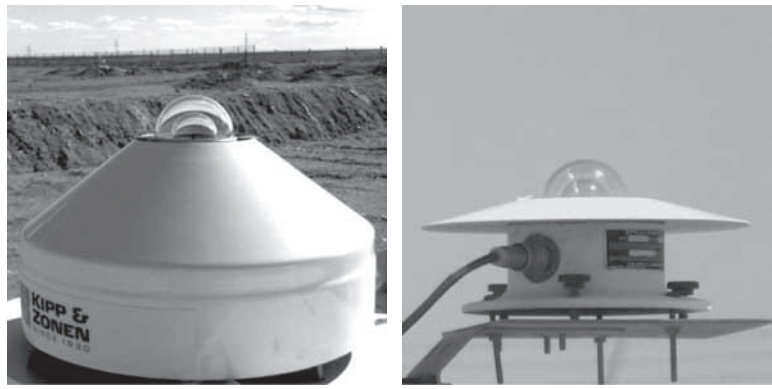

(a) (b)

3.6 Examples of thermopile pyranometers (a) Kipp & Zonen CHP21 and (b) Eppley PSP.

radiation by the active (or 'hot') thermocouple junctions increases its temperature to T_1 and the reference (or 'cold') junction is kept at a fixed temperature T_2. The differential temperature between the active junction and a reference ('cold') junction produces an electromotive force directly proportional to the differential temperature created. This effect is called the thermoelectric effect. The magnitude and direction of the electromotive force is affected by the type of metal and the temperature difference between the hot and cold ends. The relationship between the temperature difference and the output voltage of a thermocouple is nonlinear and is approximated by a polynomial interpolation.

Due to the functional principle of thermopile radiometers, they are sensitive in a wide spectral range. Around 97–98% of the total irradiance energy is absorbed by the thermal detector (Fig. 3.7). A disadvantage of thermopile pyranometers in comparison to photoelectric pyranometers is a higher price and frequent soiling of the glass dome (Pape *et al.*, 2009).

3.3.2 Photoelectric sensors

Photoelectric instruments convert the radiant energy directly into electrical energy by a photodiode. A photodiode is usually a silicon semiconductor with p-i-n structure or p-n junction. Photodiodes can be used under either reverse bias (photoconductive mode) or zero bias (photovoltaic mode).

In zero bias, solar radiation incident on the diode causes a current across the device, leading to forward bias, which in turn induces 'dark current' in the opposite direction to the photocurrent. This is called the photovoltaic

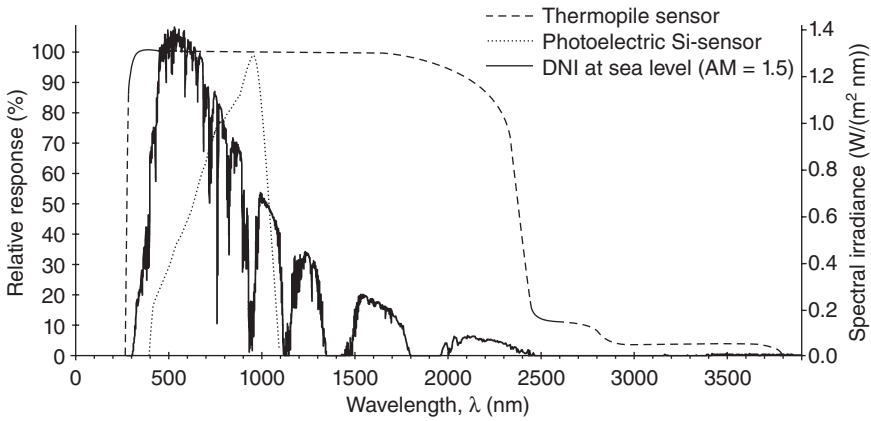

3.7 Solar irradiance spectrum at the Earth's surface and typical pyranometer response functions (dashed line = thermopile instrument; dotted line = silicon photodiode).

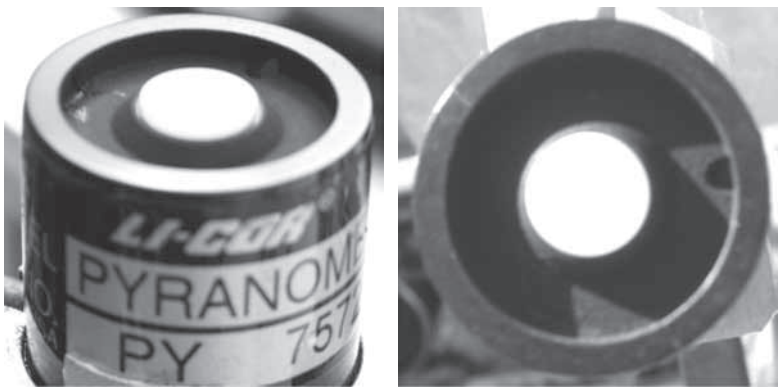

(a) (b)

3.8 Photoelectric pyranometer LI-COR LI-200SZ (a) front view and (b) top view.

effect, which is the basis for solar cells. Figure 3.8 shows the photoelectric pyranometer LI-200SZ by LI-COR (2005).

The response of pyranometers, which measure the irradiance with a photodiode, have a much narrower spectral sensitivity compared to that measured by thermopiles (Fig. 3.7). Its spectral response typically is in the range between 0.4 and 1.2 μm and it is not uniform. Therefore, narrow-to-broadband corrections need to be applied to derive the full solar range. Ideally, these consider the spectral effect of lower air masses and also that of various contents of atmospheric trace gases and aerosols. DNI can be

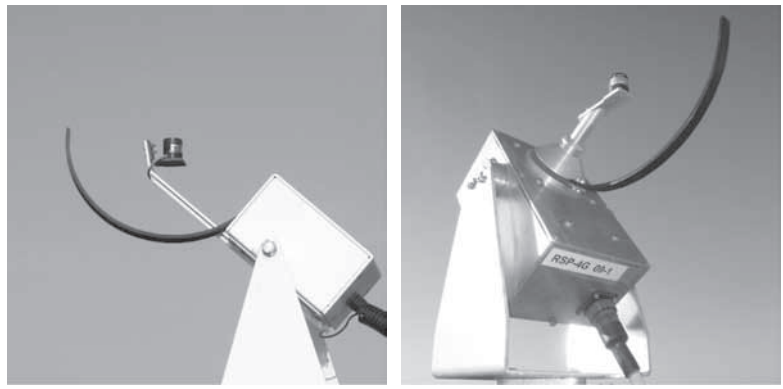

(a) (b)

3.9 RSI instruments (a) RSR2 of Irradiance Inc and (b) RSP4G of Reichert GmbH.

determined from a single photoelectric pyranometer, if it is assembled in an arrangement that periodically blocks the direct beam radiation and causes it to measure global irradiance and diffuse irradiance alternately.

Rotating shadowband irradiometers (RSIs) usually employ a photoelectric radiometer (Fig. 3.8) to measure incident solar radiation. As shown in Fig. 3.9 the pyranometer is mounted on a 'head unit' apparatus, which permits unobstructed measurement of global horizontal irradiance (GHI) and to measure horizontal diffuse irradiance (DHI) by means of a motor-driven shadowband which periodically blocks the direct beam component.

RSI operation is realized by a program code, which drives a motor control module. The code is usually run by a datalogger, which processes and collects the measured values. Typically once every 30 seconds the shadowband rotates over the photodiode, taking approximately one second for this motion. During this period the photoelectric pyranometer signal is sampled about 1,000 times and when the sensor is completely shaded from the sun by the shadowband the lowest pyranometer readings occur. During this short moment, the photoelectric pyranometer measures only the diffuse irradiance. The software detects the DHI from all values, finding the average of minimum values. Finally, DNI is calculated from measurements of GHI and DHI, and the sun's zenith angle using relation mentioned in equation [3.1].

DNI measurements derived by RSIs are not reaching the exact same accuracy compared to pyrheliometer measurements, as long as the pyrheliometer tracking is accurate and the measurement device is maintained and properly cleaned. Soiling of measurement devices is often an issue with pyrheliometers, as these are easily affected by dust and dirt accumulation

and need daily and careful cleaning. In practice, often the cleaning of pyrheliometers is not practical as this is difficult to carry out in remote desert locations – the typically preferred areas for CSP application. RSI type instruments on the opposite are less susceptible to soiling and thus require very little attendance and maintenance. They are also less expensive compared to a pyrheliometer station with a solar tracker. For maximum data reliability, solar monitoring stations with both sorts of instruments are typically configured with redundant sensors, which also allows comparison of both sensors regarding parallel measurement of the same DNI intensity.

3.4 Deriving solar resources from satellite data

In cases where ground-based measurements are not available, satellite-derived solar radiation values are used. Satellites measure reflected radiation from the Earth's surface in several wavelength bands. Known albedo values by location and complex models and algorithms can be used to determine global, diffuse and direct beam irradiance components. Raw data are available from various satellite operators and these in turn are processed by several different organizations providing solar resource satellite data services. In some cases these are commercial services and in other cases, research or government. One of the best known data set is provided by NASA (http://eosweb.larc.nasa.gov/sse/).

The NASA website offers DNI data to the public without charge for any location across the globe. The data are in the form of monthly averages and were derived from 22 consecutive years of satellite data with a basic resolution of approximately 30 km, which has been processed to a $1° \times 1°$ geographical grid.

All satellite data providers have different temporal and spatial coverage, different temporal and spatial resolution, use different algorithms and different inputs. As a result, solar radiation values derived for a given place from different satellite providers can differ significantly.

There are many advantages associated with satellite-derived values:

- satellites have high spatial resolution covering most of the sites of interest
- the temporal coverage of meteorological satellites is quite long; some data date back to the late 1970s, and more or less continuous coverage in some regions can be reached since the 1980s. Since satellites cover such long terms of data, the historic data basis can be applied to estimate future irradiation, and thus can serve as basis for planning and sizing of solar systems
- satellite-derived solar radiation values (real-time data) can be utilized for monitoring and managing dispersed solar power in the grid.

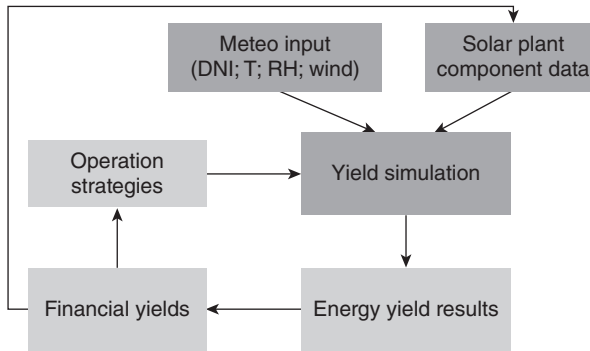

3.10 Flow chart showing the energy yield evaluation process.

The derivation of solar irradiation values from satellite data is realized by radiative transfer calculations. Irradiation is calculated from infrared and visible channels of satellites with a nominal spatial resolution of 3 km × 3 km at ground level and 5 km × 5 km at ground level for the second and first generation of Meteosat, respectively. The annual sums of satellite-derived data can coincide with ground-measured data within a range of +/– 5%. However, in some cases deviations of around 20% have been observed (Gueymard, 2010). For shorter time periods like single months, days or hours the deviation of satellite-derived and measured solar irradiance values can increase significantly (Zelenka *et al.* 1999).

Due to insufficient accuracy of satellite data, precise ground-measured data are essential for validation and calibration of long-term satellite-derived data. The minimum measurement period should cover a duration of one year, so that at least one complete seasonal cycle can be evaluated.

Figure 3.10 shows the simplified structure of the power plant energy yield evaluation process, with obtaining and processing of the solar irradiance measurement being integrated.

3.5 Annual cycle of direct normal irradiance (DNI)

Whilst annual average DNI levels are a good indicator of potential annual generation levels, there is often large variation of solar radiation values observed in different seasons. It is important that this be taken into account during project feasibility studies, as the varying level of average output with seasons through the year can affect plant economics and off-take agreements. Plate II (between pages 322 and 323) illustrates the global distribution of DNI at different times of the year. Obviously the strongest effect is the underlying variation in DNI when a hemisphere is further from

the sun during winter or closer to the sun during summer. This variation increases with growing distance to the equator. However, in addition to this, there are (seasonal) variations in cloud cover, which are very location-specific. For example, in tropical regions near the equator, monsoon-type weather cycles dominate the pattern.

3.6 Auxiliary meteorological parameters

Solar radiation and particularly DNI is the major meteorological parameter that influences energy yields of CSP plants. The influence of other meteorological parameters like ambient temperature, wind speed, relative humidity, etc., is minor as long as the variations are not too extreme. Therefore, such parameters are termed auxiliary. The auxiliary meteorological parameters that affect the performance of CSP plants include ambient temperature and relative humidity. These parameters, for example, have influence on the operating conditions and, thus, the efficiency of the steam turbine cooling system. Ambient temperatures also have an effect on thermal losses from receivers.

If wind speed regularly exceeds design limits, it may lead to higher frequency of solar field safety shutdowns (moving to the stow position), reduce performance due to increased thermal and optical losses (shattering of mirrors), potential damage of system components due to higher forces on structures and motors, reducing plant availability and increasing operational expenditures (OPEX) (Chhatbar and Meyer, 2011).

3.6.1 Air temperature

The ambient temperature has two contrasting effects: one on the efficiency of the solar field and other on the efficiency of power block. The efficiency of the solar field depends on the convective losses of the heat transfer fluid (HTF) and the collectors to the ambient air. These losses are dependent on ambient temperature. The lower the ambient temperature, the higher the losses and vice versa. In addition, the efficiency of the power block is indirectly a function of the ambient temperature. The overall efficiency of power block is dependent on the condenser efficiency. For wet cooling, the efficiency of the condensers increases with decreasing wet bulb temperature, which is a function of ambient temperature and relative humidity, and vice versa.

3.6.2 Humidity

The efficiency of the wet cooling system decreases with increasing relative humidity, which in turn results in reduced efficiency of the power block. As

a result the overall energy yield of CSP plants is affected by changing relative humidity conditions.

3.6.3 Wind speed

At higher wind speeds, optical losses in the solar field increase because of distortion of the geometry of collectors and this reduces efficiency. Moreover, convective heat losses in the solar field also increase with increasing wind speed, which further reduce the efficiency. Too high wind speed conditions might also lead to plant shutdown in order to protect the mirrors from being damaged, further reducing performance. Thus, in general it is assumed that the energy yield decreases with increasing wind speed. As a result, it is necessary to take these parameters into consideration while assessing the solar resources at the site of interest for a CSP project. Moreover, once a meteorological station is set up to measure solar radiation, additional equipment should also be used to measure the corresponding parameters.

3.7 Recommendations for solar resource assessment for concentrating solar power (CSP) plants

At present there is no standard procedure for processing solar radiation data or a set of procedures to be followed for solar resource assessments. As a result, and due to pressing deadlines for projects, project developers do not always follow a strict approach for solar resource assessments. The majority of the decisions for site selection of CSP plants are still based on the usually rough initial site assessments. In such cases, the solar radiation conditions such as annual cycle of DNI, frequency distribution of DNI, inter-annual variability and the uncertainty have not been assessed in detail, and as a result the current knowledge of solar resources available at the site stays limited.

Based on practical experience and analysis of various data products and methods, best practices to achieve high quality assessments with reasonable effort are proposed. Following Meyer (2010) the recommended procedure is as follows:

- In the first place, when no detailed assessment of a project location has been made, multiple satellite-based sources based on average values, and if available, ground measurements, should be taken into consideration. At this point, long-term average values of DNI from these sources may suffice.
- Calculate a quality-weighted best average (Meyer *et al.*, 2008) and determine the resulting uncertainty by Gaussian error propagation.

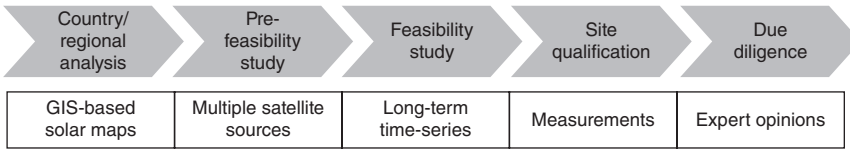

3.11 Recommended steps for solar resource assessment in CSP plants.

- Once a project site has been confirmed for further development of the CSP project, a suitable measurement station should be installed at the site in order to reach the 1 year of measurement data in parallel with the project approval process.
- Determine the long-term best estimate for the specific project site (in 1 km × 1 km resolution) and based on as many years of satellite data as available. For DNI, a minimum of 10 consecutive years should be considered, because inter-annual variability is high.
- Multiple site-specific data sets from satellites and ground-based measurements, with overlapping time periods can provide independent information and increase accuracy when combined. Only reliable data sets shall be considered. The uncertainty of the data is determined individually for each data set.

Site specific satellite data time series are required to reflect the long-term history of irradiation and must be adapted based on overlapping time periods between different satellite and measurement data sets. To be site-specific, at least a 10 km × 10 km spatial resolution is required, preferably it should be 1 km × 1 km resolution.

The accuracy and reliability of the satellite data provider is important as random and systematic errors can result in data of poor quality. Satellite providers often have a regional focus, so that one provider is not always recommended for all global regions. The current state of satellite-derived methods leaves room for improvement. Also ground-based measurements can be of poor quality depending on the individual maintenance of the measurement station over the complete measurement period. Therefore, when a location is seriously considered during the site qualification phase the satellite-derived time series should be overlapped with, and adapted to the ground-measured data, e.g., using the procedure of Schumann *et al.* (2011). From the long-term satellite data, which are corrected with the measurement data, the average DNI can be derived, representing the P50 value. P50 means, that the value should be exceeded in 50% of all years. From the corrected satellite data the climatological average of DNI can also be derived.

For the creation of most reliable CSP-specific typical meteorological years (TMY), site-specific measurements are of great value. According to Hoyer *et al.* (2009) data selection for TMY-building should be done in a way that for each month data are selected, which are closer than 5% to the climatological average. The annual average in the TMY should be within 1% of the climatological average.

Finally, for bankable expert opinions on meteorological conditions for CSP, usually data with a lower probability of underperformance are required to satisfy conservative approaches from banks and lenders. So that in addition to the P50 TMY additional TMYs based on a more conservative approach are required to assess the risk of lower irradiance values. For this purpose typically either, e.g., P70 or P90 data sets are derived. These represent the data of a typical year, which values would be exceeded in 70% or 90% of all years respectively.

Alternatively, a risk assessment using performance simulation results based on several good and bad years could give sufficient comfort to the banks. These time series can be derived from satellites but should also be adapted to site-specific characteristics based on ground-measured data. This approach would allow a more detailed assessment of the influence of variable DNI conditions.

Also from processing of at least 10 years of data, P70 or P90 values could be derived, which usually are used as basis to calculate the financial base case for a project. Compared to the simpler approach of only using P70 or P90 years, the advantage of using multiple years is that on one side the effects of meteorological variability and uncertainty, and on the other hand the effect of uncertainties resulting from technical parameters (describing the plant or the uncertainty of the performance simulation models) can be assessed in more detail.

3.8 Summary and future trends

Solar resource data are currently available from different data providers whose values differ from one another for the same geographic location. At present there is no standard procedure for processing solar radiation data or a set of procedures to be followed for solar resource assessments. Good inter-comparable benchmarking of satellite-derived DNI products for sites in CSP regions is an important missing link. Further improvement of measurements seems feasible and a clearer definition of processes will lead the way to standardization of the overall task. Currently, often pyrheliometer stations are applied, but are often not properly maintained and thus data quality is reduced against the ISO standardized accuracy. On the other hand, rotating shadowband pyranometers are also applied to derive DNI for CSP project qualification and deliver more reliable data from remote

and unattended locations, but are not yet ISO standard. Standardizing of calibration and application of such instruments would be of benefit to the industry. However, efforts are being made towards standardization and integration of procedures for data bankability under the Task 46 of Solar Heating and Cooling programme of the International Energy Agency. This subtask mainly focuses on improving the procedures for measurement of solar radiation for improving the accuracy. Optimization and standardizing of procedures for combining satellite-derived long-term data sets with ground-measured data is foreseen for sound planning and risk analysis of large-scale solar energy projects. Moreover, efforts are also being made towards benchmarking of satellite-derived data (Meyer *et al.*, 2011).

The realm of resource forecasting is becoming more important for plant dispatch as higher penetration of solar power is reaching the electric grid systems. An accurate forecast could increase grid stability and solar plant operator profits by optimizing energy dispatch into the time periods of greatest value. The accuracy of the available information can be improved by:

- additional meteorological measurement stations optimized for DNI in the areas of interest for CSP and their proper operation and maintenance
- improvement of the temporal resolution
- better availability of atmospheric data and higher accuracy for input into satellite models
- improvement of satellite algorithms
- standardization of the procedures for measurements with RSI type instruments and their calibration, input files and methodology for certification of solar resource assessment.

All measures described in this chapter mainly aim to derive as good as possible the solar resources at CSP sites. An important prerequisite for all introduced methods is that climate change will not significantly affect the availability of DNI. In the course of the 21st century, however, it is expected that there will be strong changes of regional climate, which then would also affect the average DNI conditions. For the long-term operation of CSP this might have some influence over its typical lifetime of more than 25 years. Even though Lohmann *et al.* (2006) shows that during the 21 years from 1984 to 2004 no significant changes of DNI have occurred, it is likely that the rate of climate change is increasing. Thus, additional research towards this is recommended.

3.9 References

Benedikt, P., Batlles, J., Geuder, N., Piñero, R.Z., Adan, F., Pulvermueller, B. (2009) Soiling impact and correction formulas in solar measurements for CSP projects. In *Proceedings of SolarPACES 2009 Symposium*, Berlin, Germany.

Blanco-Muriel, M., Alarcón-Padilla, D.C., López-Moratalla, T., Lara-Coira, M. (2001) Computing the solar vector. *Solar Energy* 70, 431–441.

Chhatbar, K., Meyer, R. (2011) The influence of meteorological parameters on the energy yield of solar thermal plants. In *Proceedings of the SolarPACES Symposium*, Granada, Spain, 20–24 September.

Grena, R. (2008) An algorithm for the computation of the solar position. *Solar Energy* 82, 462–470.

Gueymard, C. (2010) Variability in direct irradiance around the Sahara: are the modeled datasets of bankable quality? SolarPACES Conference, Perpignan, France.

Hoyer, C., Hustig, F., Schwandt, M., Meyer, R. (2009) Characteristic meteorological years from ground and satellite data. In *Proceedings of SolarPACES 2009 Symposium*, Berlin, Germany.

ISO (1999) EN ISO 9488, Solar energy – Vocabulary, International Organization for Standardization.

ISO (2007) EN ISO 21348-2007, Space environment (natural and artificial) – Process for determining solar irradiances, International Organization for Standardization.

Lee, C.Y., Chou, P.-C., Chiang, C.-M., Lin, C.-F. (2009) Sun tracking systems: a review. *Sensors* 9, 3875–3890; doi:10.3390/s90503875.

Lohmann, S., Mayer, B, Meyer, R. (2006) Long-term variability of global and direct solar irradiance for solar energy applications. *Solar Energy* 80, 1390–1401.

Meyer, R. (2010) Recommendations for bankable meteorological site assessments for solar thermal power plants. In *Proceedings of the SolarPACES Symposium*, Perpignan, France, September.

Meyer, R., Butron, J.T., Marquardt, G., Schwandt, M., Geuder, N. Hoyer-Klick, C., Lorenz, E., Hammer, A. Beyer, H.G. (2008) Combining solar irradiance measurements and various satellite-derived products to a site-specific best estimate. In *Proceedings of the SolarPACES Symposium*, Las Vegas, USA, 4–7 March.

Meyer, R., Gueymard, C., Ineichen, P. (2011) Standardizing and benchmarking of model-derived DNI data products. In *Proceedings of the SolarPACES Symposium*, Granada, Spain, 20–24 September.

Michalsky, J. (1988) The astronomical almanac's algorithm for approximate solar position (1950–2050). *Solar Energy* 40, 227–235.

Pape, B., Batlles, J., Geuder, N., Zurita Piñero, R., Adan, F., Pulvermueller, B. (2009) Soiling impact and correction formulas in solar measurements for CSP project. *Proceedings of SolarPACES 2009 Symposium*, Berlin, Germany.

Reda I., Andreas, A. (2004) Solar position algorithm for solar radiation applications. *Solar Energy* 76, 577–589.

Schumann, K., Beyer, H. G., Chhatbar, K., Meyer, R. (2011) Improving satellite-derived solar resource analysis with parallel ground-based measurements. In *Proceedings of the ISES Solar World Congress*, 29 August–1 September, Kassel, Germany.

Spencer, J.W. (1971) Fourier series representation of the position of the sun. *Search* 2, 172–173.

WMO (2006) Secretariat of the World Meteorological Organization, *CIMO Guide to Meteorological Instruments and Methods of Observation*, Preliminary 7th edn, WMO-No.8, Geneva, Switzerland.

Zelenka, A., Perez, R., Seals, R., Renné, D. (1999) Effective accuracy of satellite-derived hourly irradiances. *Theoretical and Applied Climatology* 62, 199–207.

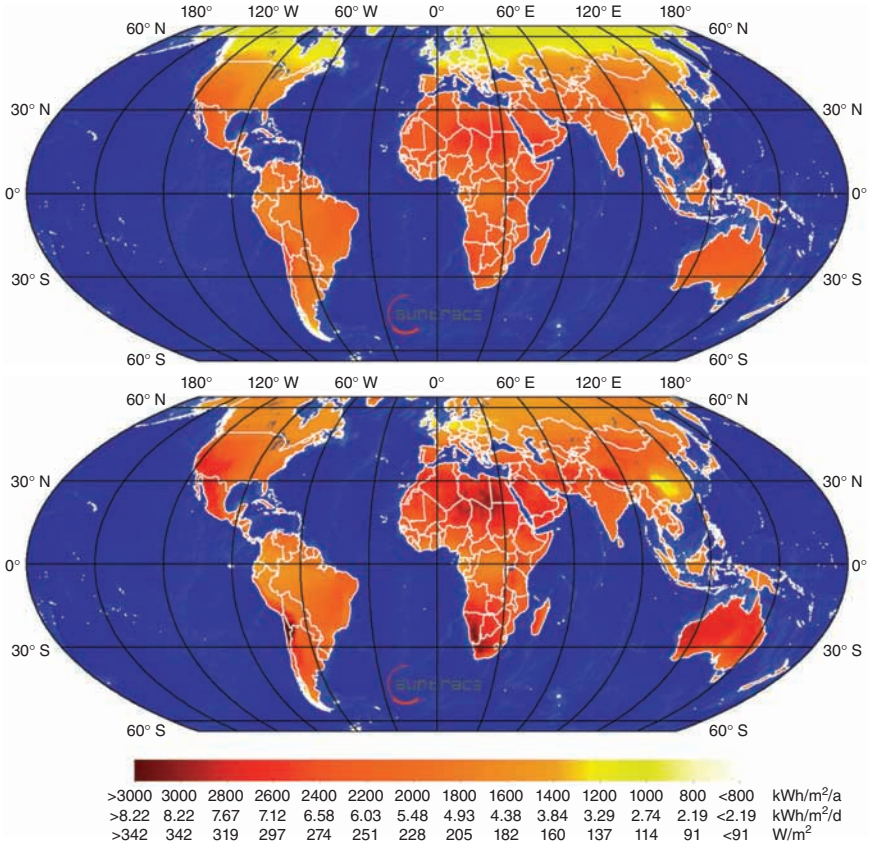

Plate I World map of long-term global horizontal (GHI, top) and direct normal (DNI, bottom) irradiance derived by Suntrace from DLR-ISIS (Lohmann, 2006), NASA-SSE version 6.1 and adaption to elevation and local measurements.

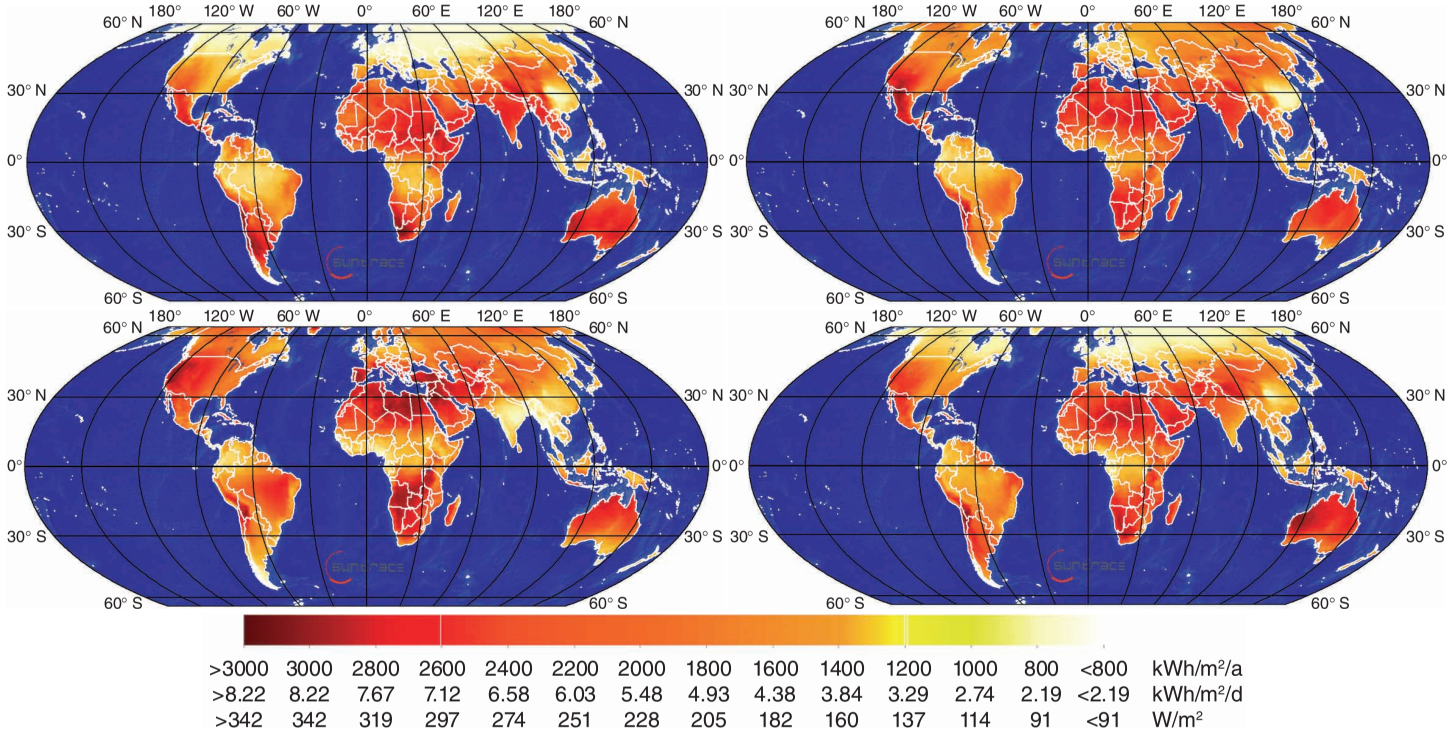

Plate II World map of long-term seasonal averages of DNI: Northern hemisphere winter months (December to February in upper left), spring (upper right), summer (lower left) and autumn (lower right). Maps derived by Suntrace from DLR-ISIS (Lohmann, 2006), NASA-SSE version 6.1 and adaption to elevation and local measurements.

4

Site selection and feasibility analysis for concentrating solar power (CSP) systems

M. SCHLECHT and R. MEYER, Suntrace GmbH, Germany

Abstract: This chapter aims to provide an overview of the processes of site selection and feasibility analysis for concentrating solar power (CSP) projects and the challenges involved. It describes the aspects considered in an iterative pre-feasibility analysis and a fully-fledged feasibility study. These include: solar irradiance, site characteristics and infrastructure connections, cost of installation and market and political environment. All information gathered is considered as part of the overall project development process. Specific conclusions are drawn for each project depending on its boundary conditions and strategic goals.

Key words: concentrating solar power (CSP), site assessment, site selection criteria, feasibility analysis, project development, project viability, risk mitigation.

4.1 Introduction

Site selection and feasibility analysis are in principal two successional, independent tasks. The site selection process for concentrating solar power (CSP) technology should lead to the identification of a potential site, then a decision needs to be made as to the most suitable technical concept for the project. When choosing the technical concept, one has to consider the project economics, which depend on the cost of the technology, the financing conditions and, in particular, the revenue generated from energy sales. National or regional government guidelines and rules may restrict size of plants and technical configurations for permission or allocation. In an iterative manner, different aspects come into play such as: solar irradiance, site characteristics and infrastructure connection, technology selection and technical concept, and market and political environment. Every aspect has a bearing on the feasibility of the whole solar thermal project.

A typical project development approach for CSP does not differ much in principle from other types of development projects, such as projects to build conventional fossil power plants, photovoltaic (PV), wind or hydro power plants or real estate projects. In an ideal world, a pre-feasibility analysis would be executed for a preselected site and available information would be gathered. Investing in specialist studies and expensive details

would only be conducted in a limited way, usually with the aim of obtaining mandatory and essential information.

After a positive outcome of pre-feasibility analysis, a fully-fledged feasibility study would be conducted, supplanting the pre-feasibility initial assumptions and procuring and elaborating on details. The site qualification process is then initiated and accomplishes the whole permitting and engineering work, eventually culminating in the signing of the main project contracts (equipment, O&M (operations and maintenance), environmental) and in financing of the project so that construction can begin.

Through such a careful and step-by-step approach, the main project development risks will be mitigated properly, fatal flaws can be identified at an early stage, and substantial amounts of development work is carried out only on the most promising projects.

CSP, however, has specific features which require a unique approach based on sufficient knowledge of certain specifics:

- A project site has to match certain criteria regarding direct normal irradiance (DNI), land area, topography or slope, water, and interconnection options to grid, road and qualified staff.
- The technical concept and the expected plant performance must provide sufficient energy to allow an economically feasible plant. Specific care has to be applied when estimating the plant's yield, as transient effects during conversion from fluctuating solar radiation to heat and/or electricity cannot easily be calculated with conventional power software tools.
- High cost of technology and the resulting high cost of generated power do not yet supply energy generation at market rates. Incentive mechanisms are required as support which, in turn, set their own guidelines and create a dependency on political mechanisms and stability.
- High capital costs and the implications of financing costs (interest rates on debt and return on equity) are the most significant operational expense during the debt repayment period (typically 15–20 years). Political risk insurance and reliability of energy off-take agreements are important factors for financing.

The blend of factors that determine the feasibility of a project differs among projects. Depending on the strategic goals of the promoter or owner, the applicable weight of selection criteria for each site will be different.

The recommended approach is to start on a general basis, collecting together all available information to obtain an initial overview of the project covering all aspects. As the assessment and qualification of the site progresses, the required information will be procured in greater detail, which will improve the accuracy of the feasibility analysis. This is an iterative process, where most parts influence each other.

It is beneficial to work from rough draft to detailed analysis as each detail involves a certain cost, be it the procurement of a DNI measurement station and measurement data, the optimization of the technical concept or a time-consuming permissions process, etc. It is important to carry out a fatal flaw analysis at the beginning of a project to get a clear view of the risks involved and chances of success.

This chapter aims to give an overview of the process and the challenges involved. It cannot provide a detailed step-by-step recipe for site assessment, as projects in all locations have strong specific aspects and comparison in most cases is not easy. However, it does aim to provide a guide for CSP site selection and feasibility analysis.

4.2 Overview of the process of site selection and feasibility analysis

When it comes to identifying the main criteria for siting or locating a concentrating solar power, or solar thermal energy system, it is preferable to have a comprehensive checklist and a straightforward approach that perfectly blends into the general project strategy and time schedule.

Site selection and feasibility analysis for a CSP plant is not as simple as it may appear at first glance. Unlike photovoltaics or wind, where multiples of identical single units can be installed in parallel and connected on the electrical side, solar thermal energy does not have a simple system design. Instead solar thermal energy systems are tailor-made and complete systems, where the thermal process interconnects the solar field with power generation. In some cases, they provide electricity and combined heat and power, with the heat used for industrial and/or desalination processes. The application of thermal energy storage and hybrid fuel solutions, be they regenerative or fossil fuels, can also significantly enhance the availability and dispatchability of solar thermal plants to the point of base load energy generation.

CSP in 2012 still largely depends on the incentive mechanism provided at the targeted project location. Examples of this are: grants, government guarantees, feed-in tariffs, competitive bidding or tendering processes with government backed power purchase agreements (PPA). The motivations of governments can change over time, and it can be observed that regulations for renewable energy projects have been adjusted frequently. Reliability of regulations and political stability in the long term is an important aspect when selecting a target market for a project location. Localization of manufacturing and supply of materials is an important aspect for most governments when introducing incentive mechanisms. However, with political risk insurances for imported items through export credit agencies (ECA) and loans from developed countries favouring supplies from abroad, this creates

a general conflict regarding sourcing of materials. An additional aspect that needs mentioning is that international sourcing is a typical practice in order to obtain the lowest cost items.

When looking at the timeline for development and implementation of a 'typical' project, it usually takes at least 2–3 years from the initiation of project development until start of construction, with an additional 2–3 years for construction, plus the expected lifetime of 30+ years for the plant and a loan period of 15–20 years.

A typical site identification process, if started from scratch for a completely unknown market, is illustrated in Fig. 4.1. The sequence and aspects of this process are described in the following sections.

4.2.1 Market analysis

The selection of a specific market should be accompanied by an assessment of the overall market facts and perspectives for CSP. The function of market analysis is to verify whether the existing basis and outlook of the market are, in principle, suitable and provide sufficient prospects for feasible CSP projects. This assessment would typically take into account and analyse the energy market, off-take options and energy price ranges, and government support with its political and legal frameworks.

4.2.2 Regional or national study and site identification

When targeting a preselected CSP region or country for siting of a solar thermal power plant, it is desirable to obtain a comprehensive overview of the entire area. Instead of the substantial effort of travelling the whole region to look for prospective sites, a geographic information system (GIS) can be used to identify preferred regions. 'A geographic information system is an information system that is designed to work with data referenced by spatial or geographic coordinates. In other words, a GIS is both a data base system with specific capacities for spatially-referenced data, as well as a set of operations for working with the data' (Star and Estes, 1990). Therefore a GIS-based analysis makes use of many different remotely sensed information layers and information obtained from ground-based surveys or a combination of both. The GIS requires an input of the most reliable data sets which include direct normal irradiance (DNI), topography, road system, electric grid, surface water and hydrological maps, etc. The GIS, then, based on pre-defined criteria and a selection algorithm, highlights the best matching regions for a CSP site. The preselected regions are then assessed in more detail. An example of a software-based selection process with integrated GIS, covering multiple aspects is described for North Africa in Broesamle (1999) and Broesamle *et al.* (2001).

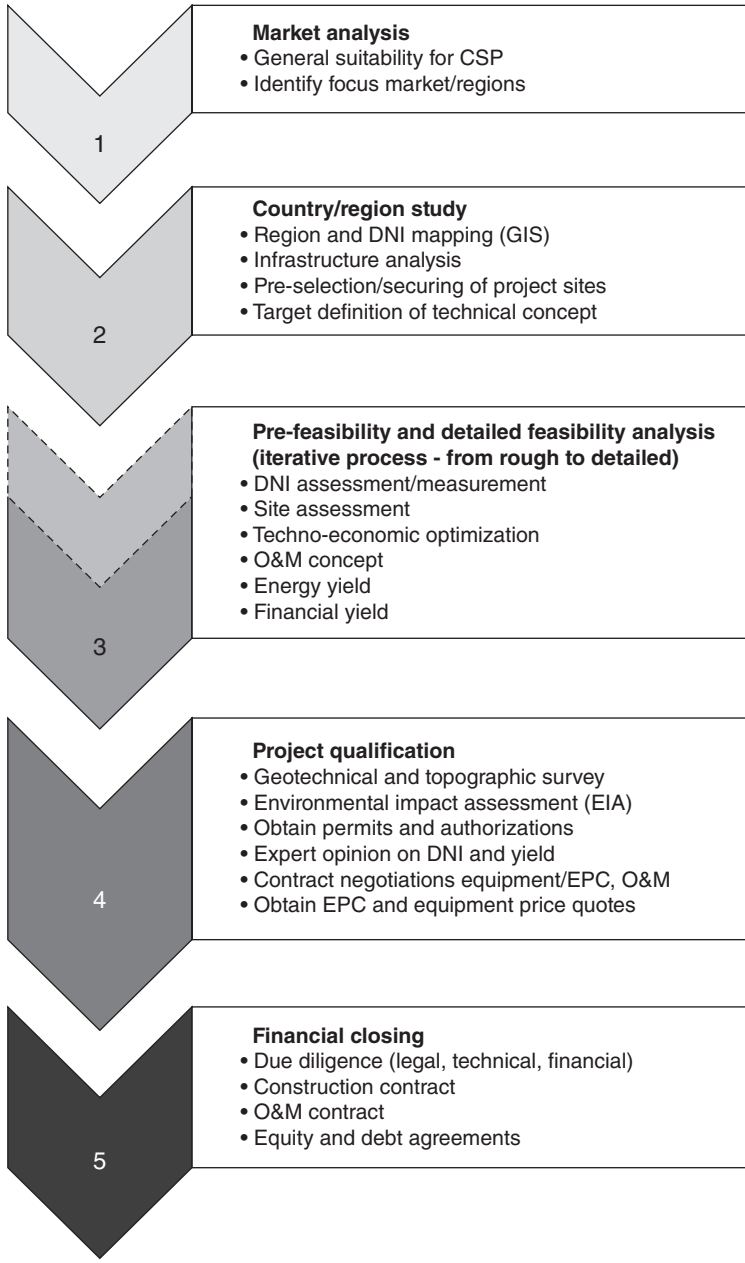

4.1 CSP site selection and qualification process (© Martin Schlecht, Suntrace, 2012).

Eventually, travel to the region of interest is necessary to verify the GIS findings at the location (ground truth), and with the use of accurate GIS system data and thorough analysis, these visits can be much more efficient and less time consuming. Personal visits also allow gathering more information regarding the neighbourhood, availability of land, contact with local authorities and persons, and so on. Following these site visits, a ranking of sites should be made based on individually defined criteria. As an outcome, the selected location(s) can then be subject to a site-specific pre-feasibility.

Some regional studies have been conducted through public funds and by research institutes and government agencies. An example is the analysis of renewable energy potential for North Africa, as initiated by Broesamle (1999), which was continued in much more detail and covering broader aspects. The results are presented in several studies: Med-CSP (Trieb *et al.*, 2005), Trans-CSP (Trieb *et al.*, 2006) and Aqua-CSP (Trieb *et al.*, 2007).

Another example of country-wide assessments of CSP resources using GIS is presented by Mehos and Perez (2005). Their analysis of DNI data, 'combined with geographical information system (GIS) data, has quantified the solar resource potential for large-scale power generation using CSP technologies. . . . Prime locations for future solar power plants can also be identified by factoring in information on constraints on electricity transmission and access to load centers, which are the regions where electricity is consumed.'

Stoddard *et al.* (2006) has also applied a GIS-based approach for a study on CSP potential and benefits in California.

4.2.3 Pre-feasibility analysis

The aim of a pre-feasibility study is to assess at an early stage and on an indicative but comprehensive basis the general feasibility of a pre-selected project site. Starting the pre-feasibility analysis is not straightforward as all aspects influence each other significantly. Pre-feasibility would typically include a fatal flaw analysis of the project site, a first assessment of site parameters to decide on potential technology configurations and a complete overview of project economics. The whole approach is cyclical, and adjustments of a single parameter may impact the overall result requiring an iterative procedure as shown in Fig. 4.2. This would include assessment of project site, infrastructure and solar resource. Initial technical concepts would be developed and modelling of energy yields and financial yields will give first results.

Initial numbers and figures can usually be based on qualified assumptions and publicly available data, so that the expenses involved with gaining precision and detail can be deferred to a later stage when a positive

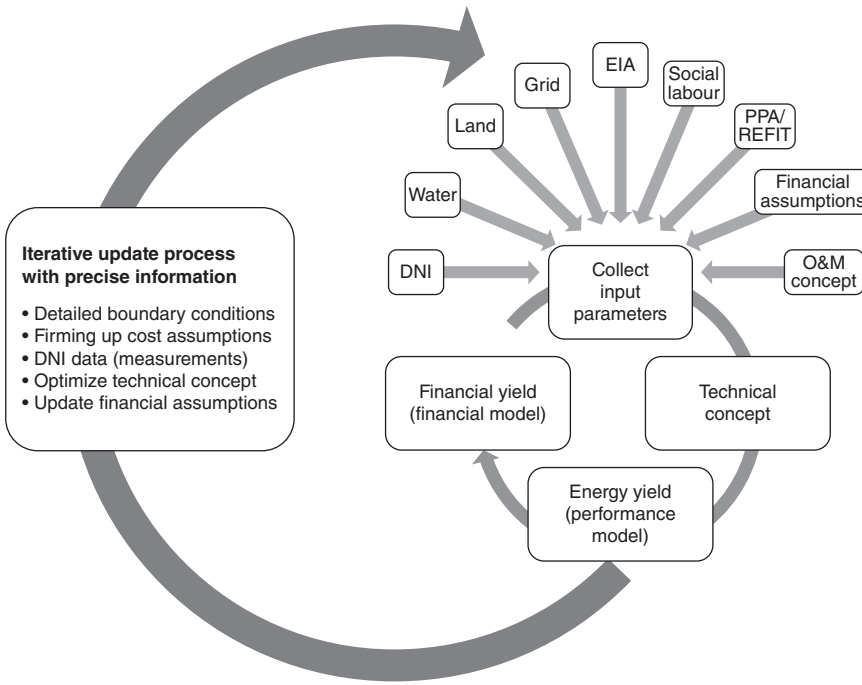

4.2 Process from pre-feasibility to a bankable project through iteration with continuously more detailed and realistic data (© Martin Schlecht, Suntrace, 2011).

conclusion for the project site has already been made. Therefore, the degree of detail and the accuracy of information may be kept brief on a case-by-case decision.

Sensitivities of main project parameters, such as the range of expected DNI, equipment prices and off-take prices can give perspectives of worst case and optimistic scenarios. In case of multiple sites under consideration, a parallel pre-feasibility analysis can exploit synergies which allows a ranking of the sites. Such multiple site assessment within a pre-feasibility analysis is given by Stoddard *et al.* (2005) as an example regarding selection of two options for locations with the US state of New Mexico. Since most projects are pursued by private entities and are not usually accessible in the public domain, the number of published examples is limited.

4.2.4 Feasibility analysis

The feasibility analysis continues seamlessly from where the pre-feasibility analysis concludes. The aim of the feasibility analysis is to obtain more

detailed information on a project that has a high chance of realization, and by doing so clarify most of its aspects and address most of the concerns associated with it. An abundance of data, which may have been taken as qualified assumptions or on the basis of educated guesses will need to be verified and made more detailed during the course of this analysis. For the feasibility analysis, specialist studies will be required: a DNI measurement campaign and solar resource assessment, the use of these measurements in combination with long-term satellite time-series, geotechnical and topographical site assessment, engineering for technical concept and energy yield modelling, permit engineering, environmental and socio-economic assessments, financial modelling, legal guidance on administrative processes.

Just like during the pre-feasibility stage, the process is not straightforward. The results in one area could influence conclusions drawn from results in another area to a certain extent. The whole approach remains circular. Through several rounds of iteration, the conclusions will be refined as shown in Fig. 4.2. As mentioned above, most projects are conducted by private entities, and feasibility reports are usually not in the public domain, and therefore there is a scarcity of published examples.

4.2.5 Project qualification phase

During the project qualification phase, the required work will be performed to develop the project until it is ready for financing and the start of construction. This includes the process to apply and obtain all required permits and authorizations, conclude all required project contracts, prepare for equity and debt funding, and secure the technology. The results from the feasibility analysis will be used as the starting point for this phase.

The main layout of the plant has to be finalized, as significant parameter values will be required as input for permit applications (water consumption, water discharge limits, plant footprint, land area covered and owners affected, route for transmission line, technical plant and operation patterns, etc.). At an advanced permitting stage, time management is vital, every adjustment to the system design will require additional work, involved cost and additional time to reach approval and receive the required permits.

As the project progresses, the adjustment of figures and details may require a frequent review and update of the project feasibility. It is expected that assumptions and results will be further refined, reducing uncertainty of the overall project economics to a level considered reliable for financing the project. Towards the end of the project qualification phase, several independent expert opinions need to be obtained to support the most relevant figures, such as detailed assessment of solar resources and energy yield. In the project qualification phase, at least one year of measurements

should be completed and, together with updated site-specific satellite-derived data, these form the base for site-specific meteorological data sets, which should be as precise as possible to minimize uncertainty of the potential power output.

4.2.6 Finalization of contracts and start of construction

At this stage, permissions and authorizations, off-take agreements, land contracts and many other items are completed, and the last project feasibility update has proven the assumptions correct. At this point, a risk assessment and due diligence assessment of the whole project must be carried out. All the project details will be required for this, and thorough preparation will assist and ease the process. Unresolved issues may appear and may need resolving under increasing pressure and time constraints. During this period, all main project contracts are finalized, such as the construction contract, off-take agreement (PPA), grid interconnection agreement, land contract, rights of way for transmission line, piping and roads and O&M contract. Equity and debt agreements shall be arranged and the final version of the financial model established.

4.3 Main aspects considered during the pre-feasibility and feasibility phases

The goals and requirements for the solar thermal project need to be clearly determined in the first instance, taking into account all criteria. Locating a site for a CSP system usually requires an individual approach, depending on a blend of fulfilment of prerequisites, the requirements of the system and existing boundary conditions. Important aspects and criteria for a site have a specific impact on the technical and economic feasibility of the project. Each criterion also influences the others, creating a circumferential relationship. An iterative analysis process is therefore required (see Fig. 4.2).

4.3.1 Economic assumptions

The cost of the project, achievable off-take prices and the terms and conditions for the financing of the project are significant factors in terms of project feasibility, and should be reviewed initially and on a more general market approach basis, before investing too much time (and money) on site studies. A prerequisite for a feasible project is a viable off-take agreement for the plants' products (electricity, heat, water, pressurized air and other elements that are applicable).

4.3.2 Solar irradiation

There should be an appropriate amount of solar irradiance for the project to be feasible, but the minimum threshold has to be determined for each project on an individual basis. DNI converts to energy, which converts into money and has to provide the expected returns for the project. If the DNI data is very accurate, this will reduce the uncertainty of the project economics directly, and will influence the base case for the project economics. Details of solar resource assessment have been discussed in Chapter 3. With projected reduction in total project costs in the future, lower DNI regions will become more economically attractive at the same energy off-take prices.

4.3.3 Land, topography and soil

Siting has to reflect land plot borders related to ownership. The next step is to collect requirements for slope and soil, which are different for the various CSP technologies and need to be considered. Levelling and terracing works can be done but both incur extra costs. Soil replacement, earth movement or extensive foundation works are also determinants of cost. How much the project can afford has to be determined on an individual basis. A GIS system with an detailed topographic map included can help to identify areas with acceptable slope and topography as described in Broesamle (1999).

4.3.4 Water

Water availability can enable the possible use of wet cooling systems for the power block, which have a significant economic advantage over dry cooling systems as they are more efficient and involve a smaller financial investment. Dry cooling, however, is a feasible option from a technical point of view, and the project economics may have to support the use of this technology.

4.3.5 Infrastructure

Grid access

The main issue concerning infrastructure is the connection point to the electric grid for power evacuation. The distance to the electrical grid is associated with a cost per km and the upgrade of facilities at the grid tie-in point.

Interconnection with other plants and processes

If the plant will be supplying products other than electricity, the interconnections with the customers for those other products need to be considered. For example, if the plant will produce heat, the consumers need to be situated adjacent to the CSP plant.

Roads and highways

The accessibility of the plant is important. During construction, heavy hauling of the main equipment items and all deliveries of materials and construction machinery and vehicles must be possible. During operation, delivery trucks and maintenance must also have access. Therefore costs of access roads and potential upgrades of bridges for heavy hauling may have some impact on the cost of the project.

4.3.6 Environmental impact assessment (EIA)

An EIA study is usually required. It has to reflect the applicable local standards and will most likely conclude with certain restrictions on the technical concept and the plant layout and may define mitigating measures for the project. Animal and plant habitats and nature conservation and protected areas must be respected to avoid significant problems and delays during permitting.

4.3.7 Population and labour

A site in the vicinity of larger villages and/or cities can ensure the availability of qualified local staff both during construction and O&M phases. If qualified personnel have to be brought in from distant locations, or even from foreign countries, this also increases the cost.

4.3.8 Socio-economic impact assessment

The various facets of the social impact of the project on the prescribed region often need assessment, but the depth of assessment can vary significantly. The socio-economic impact assessment usually assesses the sustainability of a project in the host country/region. Involvement of municipalities in the development process with respect to their role as authorities but also as a stakeholder is critical. In this case the host country or region will expect to gain certain benefits in terms of economic development from the project, such as tax revenues, improvement of infrastructure, qualification and employment of local persons, etc. The benefits may also include the

economic development of local businesses such as for manufacturing, maintenance works, etc.

In countries like South Africa, the socio-economic development aspect is almost institutionalized (with respect to the involvement of historically disadvantaged groups), while in other markets, this topic may be covered in a much more general sense and may not require specific action.

4.4 Boundary conditions for a concentrating solar power (CSP) project

The market and the available incentive mechanisms define the route to follow for CSP projects. The general type of application, technology selection and technical concept define the overall approach to a project site in terms of size, infrastructure requirements and meteorological parameters. The following gives a summary of criteria, which influence other criteria and the decision to initiate a project, even before commencing the processes of site selection and feasibility analysis.

4.4.1 Off-take and market

The energy off-take agreements are the central contracts for any energy project. The reliability of the agreement and the off-taking party are key criteria, specifically when the financing of the project relies on a non-recourse or limited recourse scheme, where the lending bank's assessment and criteria define the financing of a project. As off-take agreements are usually part of the incentive mechanisms, an appraisal of these is equally important. In the case of government-regulated feed-in tariffs, these are generally reliable, with the political risk remaining the largest obstacle in the formula. However, the off-take body introduced by the government should be a reliable and bankable stand-alone player or at least sufficiently supported by the government.

4.4.2 Incentives and support schemes

In most markets, CSP will need financial support through incentives in the next few years for the project economics to be feasible, as cost reduction measures will not lead to grid parity at wholesale level in the near future. IEA (2010) states 'In the sunniest countries, CSP can be expected to become a competitive source of bulk power in peak and intermediate loads by 2020, and of base-load power by 2025 to 2030'. One possible incentive mechanism is feed-in-tariff (FIT) schemes. In the cases of other incentive mechanisms such as capital grants, the reliability of these should be considered with equal importance. As CSP projects are capital intense, a long-term

investment horizon of 15–18 years is usually required. In cases where process heat will be provided simultaneously, or used via co-generation to produce desalinated water, for example, and a blend of revenue streams provides the economic basis for the project, the matter becomes progressively more complex, as most incentive schemes currently do not provide for the remuneration of solar generated heat or other products. The assessment of a project should also examine the possibility of failure to qualify for an off-take agreement such as a PPA or FIT, if for example, competitive bidding or tendering is required. It can be of value to have a long-term perspective of the market, which is not solely dependent on a single attempt.

4.4.3 Specification of energy products

The general aim of a project has a major influence on the selection of a site and technical concept. CSP plants can be used to generate electricity and/or process steam, and/or they may have other uses such as production of hot water and pressurized air or heating, cooling, desalination, etc. If solar generated process heat will be produced, the plant must be located in the vicinity of the customer. Also the load and capacity requirement from the heat off-taker might determine and define the technical concept of the CSP plant. If the CSP plant is to be combined with other, possibly fossil fuel-fired steam heat and power generating systems, the concept has to be evaluated comprehensively and most criteria for sizing the solar plant will be defined by the overall concept. In the case of solar electricity generation, the vicinity and accessibility to the electric grid plays a key role, while giving a broader range of possible locations for such projects. In this case, apart from grid and DNI, also water, roads and other infrastructure criteria will become part of the evaluation. However, usually there is no 'standard technical concept', as most projects will require tailoring of technology to the project-specific boundary conditions.

4.4.4 Dispatch mode: storage and hybridization

The energy production of a CSP plant that is 'solar only' will follow the availability of sunshine hours with sufficient DNI, starting up on a daily basis after sunrise, with peak production at sun peak, fluctuating according to weather patterns and shutting down with sunset. A CSP system can be enhanced with thermal energy storage and be hybridized with fuel firing systems (fossil or renewable fuels) increasing the full-load operating hours. These features will also lead to an increased dispatchability of the plant, which supports the management and stability of the electricity grid. These plants could even provide base-load energy or shift energy generation to

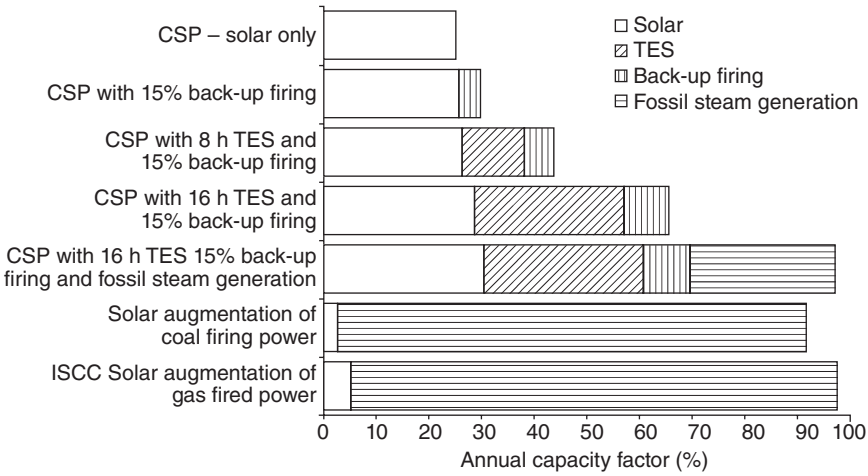

4.3 Achievable capacity factors for different CSP storage and hybrid concepts (© Martin Schlecht, Suntrace, 2011).

specific times of the day when it is most needed (peak load). Figure 4.3 provides an overview regarding technical concepts and their potential capacity factors (Schlecht, 2011).

Enhancements with fuel firing can be on an incremental basis from 0% fuel firing up to almost 100% fuel firing. Booster firing to increase steam temperatures to in excess of 500°C can increase the thermodynamic efficiency, while supplemental heat transfer fluid (HTF) heaters can mitigate cloud periods and keep the HTF warm during the winter season and shutdown periods. Implementation of parallel steam generators can also add to the solar plant's ability to provide base-load energy. Conventional steam generating units can be combined with a solar boiler as back-up and also extend operating hours up to base-load. These plants can be designed to match load curves of the grid as required by the operator. At the other end of the spectrum, a plant in which a solar field is attached to a large conventional power plant (coal- or gas-fired) generates only a very small percentage of its energy from solar resources.

4.4.5 Regulatory restrictions or technical plant concepts

Any incentive scheme typically brings a set of rules, which are imposed on a project in order to qualify for the incentive. This often affects the technical concept, as certain technical features may be excluded, required or restricted. Current global feed-in schemes focus on solar generated electricity only, and no general incentive scheme currently features solar process heat or combined heat and power (CHP) applications. The implementation of

thermal energy storage (TES) is also not explicitly supported by current incentive schemes. For example, there are no schemes that remunerate the higher value of dispatchable electricity. Examples of policy restrictions and effects on technical concepts include:

- Spain only permits co-firing by fossil fuel up to 12–15% related to the annual energy production. If this is not the case the plant cannot qualify for the feed-in tariff. Additionally, plant capacity is capped at 50 MWe by law for renewable energy plants. This restriction, however, does allow the application of TES, which enables CSP plants to generate solar electricity also during night time on the same remuneration basis. The Andasol 1 project, which has been operational since 2008, includes a molten salt-based two-tank thermal energy storage. A total of 28 out of 61 pre-allocated CSP projects in Spain will implement thermal energy storage with more than six equivalent full-load hours capacity according to Protermosolar (2011).
- The Solar Nevada One project in Nevada, USA, is only allowed to use a 2% energy contribution from gas for freeze-protection measures. This project reached an individual agreement for its PPA and governmental support.
- Solar-fossil hybrid CSP plants only comprise a few complete systems presently, and each of them is based on individual regulations for the energy off-take. The integrated solar combined cycle (ISCC) projects in Morocco, Algeria and Egypt have been set up under a specific incentive funding scheme from the World Bank's Global Environmental Facility (GEF).
- The United Arab Emirates/Abu Dhabi located Shams 1 project from Masdar has fossil-fired booster-firing to superheat live steam to 540°C. The technical concept was determined by a public tender process, which was focused on lowest electricity price.

It is apparent that each market and incentive scheme requires an individual approach to integrate the specific regulatory boundary conditions into the feasibility.

4.4.6 Overall project viability

A general assessment of the solar resources of a target region should be made as a first step in order to map the distribution of solar irradiation. DNI directly converts into energy produced and is a major influence on the income stream from energy sales.

A general conclusion is that DNI values below 2,000 kWh/m^2/a may not yield a viable project, but the levelized cost of energy of a specific project must show parity with the energy off-take price achievable in the market.

This price is specific for each market or for a single project in the same market. Both figures define the investment the project can carry. Eventually the cost of the project must match the prices of technology and financing. Every project promoter must assess their individual threshold for DNI in the specific market or project depending on the desired technology, and then decide on the detailed project location. As equipment prices are poised for reduction over the next years, new markets will open up when levelized cost match off-take prices achievable.

4.4.7 Long-term perspective: political stability

Considering the capital intense investment into a solar thermal plant, a long-term perspective for the project is essential. This should factor in the following aspects:

- reliability regarding level and duration of off-take agreements
- off-taking party/company stability and commitment
- political security regarding the long-term financial security of the project, e.g. no uncompensated expropriation, fulfilment of incentive schemes, and no retroactive changes to FIT or PPA prices.

Protection against some of these aspects may be possible with commercial insurance companies or government agencies, such as export credit agencies like the German Hermes. In the end, this aspect is part of the risk assessment and can usually be mitigated to a large extent. However, as this mitigation is part of the financing strategy of the project, fatal flaws should be identified in the initial approach to the project.

4.5 Detailed analysis of a qualifying project location

4.5.1 Site-specific solar resources and meteorological patterns

Direct normal irradiation

The Direct normal irradiance (DNI) is one of the most crucial aspects when assessing and optimizing the technical concept for a CSP plant. Much emphasis should be placed on the thorough determination of the relevant DNI for a particular project and its specific location. Every reduction in uncertainty in terms of the solar resource will directly result in a better predictability of the energy production capabilities of a particular concept (which can be determined through performance modelling).

Microclimate can have a significant influence on the DNI at a specific location. There is a high chance of introducing an error if analysis results from a larger area are used instead of assessing the specific DNI of each

potential location. On-site DNI measurement for at least a full year, in order to cover a complete seasonal cycle, is usually required for a project at the stage of financing. This data, when properly applied, can be correlated with overlapping satellite data. This, together with historical satellite data (stretching back a minimum of 10 years) can be used to project the specific solar potential of a project site for the lifetime of the plant (Meyer *et al.*, 2008). Without on-site readings, the uncertainty in terms of the DNI could be as high as ±30% in some regions such as India or northern Africa.

Wind

Strong wind speeds can have a direct impact on power generation, as they can affect the focusing of sunbeams by creating vibrations and bending mirrors. The various technologies and makes have individual requirements in this regard, so cut-off wind criteria should be requested from applicable manufacturers. Countermeasures such as wind-breaking barriers and fences can mitigate this effect. When looking at the annual average, the influences of wind are in most cases fairly small, and it will not have a critical influence on the overall economics, as long as it is factored into the calculations.

Ambient conditions

Other meteorological parameters such as ambient pressure, temperatures and humidity have some influence on the overall plant performance, thus they must be assessed together with DNI and wind. Wet and dry bulb temperatures define the achievable cold-end temperature of the power plant, and thus have an influence on the steam turbine design and efficiency. This is of relevance for both wet and dry cooling systems.

Weather patterns

Clouds, rain and other weather patterns are included in the DNI assessment, as these factors have direct influence on DNI. A long-term assessment based on satellite data will provide the best estimate for the plant operational lifetime. If weather patterns indicate strong rain, stormwater run-off and flooding concepts should be assessed individually taking into account the topography of the site and surrounding area.

4.5.2 Land and surroundings

Orientation and slope

Generally a north–south orientation of the land plot is important. As all technologies can cope with some degree of slope, the gradient should

preferably face towards the equator. Parabolic trough technology accepts less than 2% slope while linear Fresnel reflector systems can accommodate up to 5% slope. Solar tower systems can accommodate a steeper slope, as long as access for construction and maintenance is sufficient and the slope supports the arrangement of the heliostat field. The feasibility of building on steeper slopes also depends on the tower technology concept, which varies considerably between different designs. Dish systems can be installed as distributed arrays; so the only relevant factor to consider would be units shading others, so long as access was acceptable.

For parabolic trough systems, the solar field is usually divided into several subfields, which could allow a terracing approach with different elevations for each subfield. Again, this would mean that a site with an initial slope steeper than 2% could be used; however, such terracing works are usually quite cost intensive, so this cost must be considered in the overall economic evaluation.

Topography and soil

Should the slope not be perfect and continuous over the requirements for area, earth and levelling works must be assessed. This should also include an analysis of the soil conditions, as these are a most crucial input for sizing and dimensioning of foundations and civil works design. Substantial subsoil structures might be required on sites with soft soil, while sandy topsoil might need to be replaced or removed. In turn a rocky surface might need severe treatment when it comes to levelling works. Soil patterns might vary across a typically large project site of several square kilometres, so a thorough soil analysis over the whole area should be part of the assessment procedure.

Free horizon

No obstacles in the vicinity should shade the mirrors, preferable down to a minimum angle (e.g. 3°) above the horizon. Given the anticipated 20–40 year lifetime of a plant, it should be checked that no future developments in the vicinity are likely to create such obstacles. This assessment should also take into account the fact that dust and aerosols (e.g. vapour from cooling towers, smoke-stacks, etc.) can reduce the DNI partially.

Footprint and scaling

The footprint of a solar thermal energy plant is scalable with the installed capacity. However, some restrictions have to be considered from the technical side:

- Parabolic trough (PT) and linear Fresnel systems typically apply certain modular length patterns to one particular loop, which then would be applied in serial/parallel arrangements. Most PT plants today require about 40 × 300 m for one single loop, with 100+ loops for a simple 50 MWe plant in Spain, while a linear Fresnel loop could require a straight 25 × 1000 m for one loop, with 22+ loops for a simple 50 MWe plant in Spain. New developments on PT aim at larger aperture width.
- Solar tower plants are preferably built on circular or semi-circular shaped footprints, but also rectangular fields are feasible.
- Additional space for service roads surrounding the solar field, fencing, possible wind-breaking measures (earth banks, walls or vegetation) should be considered at the boundary of the plant.
- Depending on the outcome of the environmental impact assessments, specific requirements could be imposed on a plant, which require additional efforts.

With these patterns, one can see how a plant layout could fit into a given land plot and its usually non-technical provided borders. However, with a preselected technology the requirements for a solar project site can be more specifically defined.

Ownership structures

The legal situation of the required property is also a crucial selection criterion. When approaching the legal side of ownership structures the following questions should be considered: Is the land public or private? Will it be a direct purchase or a purchase option or a lease option? How secure is the land for the project throughout a possibly lengthy development process? Also depending on the type of financing, the required legal certainty on the complete property becomes a crucial matter, as agreements with all owners have to be completed and the surface rights for the installation of the CSP system should be recorded in the title of the land.

4.5.3 Infrastructure interconnections

In addition to a suitable land area with sufficient solar resource, the standard of the surrounding infrastructure is of significant importance.

Electricity grid

The generated power must be evacuated from the plant; therefore it needs to tie into a high voltage (HV) electricity line with sufficient voltage level. Projects of more than 20 MW capacity usually have to look for lines of 60–400 kV, depending on the applicable grid code and network voltage levels.

Determination of a feasible tie-in point always requires the cooperation of the grid operator, who needs to analyse the capacity of the proposed tie-in location in relation to the capacity planning of the whole network. Tie-in into a HV line by building a new substation may be an option for larger plants, but most likely one has to tie in at an existing substation, which also needs to have the available capacity. The procedures for getting a capacity reservation for a project are different in each country, so one has to adjust to the local codes and requirements.

Distance to the grid should be kept minimal, as each km of transmission line requires additional investment. Larger projects usually can afford longer transmission lines, as the specific cost for the transmission line can be utilized by a larger amount of energy.

The routing of the transmission line has to be approached carefully, as usually permits and rights of way related to the properties along the projected route need to be secured upfront, and reaching consent with the respective authorities and landowners can involve a time-consuming effort. Also environmental concerns must be considered, as a specific environmental impact assessment for the transmission line is required in most countries.

Road network

The connection to the road network serves two purposes. During construction of the plant, all materials have to be transported to the project site by trucks. As this includes heavy equipment, the route for heavy hauling (e.g. the capacity of road bridges from ports of landing for overseas shipments) has to be considered. Some improvements required specifically for construction transport can be on a temporary basis.

For operation of the plant, access roads should be erected as permanent structures. They should suffice for all regular trucking of materials and during maintenance periods. It should be considered that, during the 20–40 year operation period, major overhauls of steam turbines and generators would be made, in addition to possible future improvements to the installation. It will be a strategic decision between actual needs and benefits for further requirements. The cost and authorization effort for this road will also depend on the distance to the existing public road network.

Fuel availability

For most CSP plants, some small degree of supplemental fossil fuel firing is considered. Fuel availability and specific cost for transporting it to the project should be considered. For larger fossil fuel shares, such as an ISCC (integrated solar combined cycle) system, the fuel sourcing becomes a much more significant aspect for the feasibility of the project. It may mandate, as

additional location criteria, the vicinity of a pipeline, or a train connection for liquid or solid fuels.

4.5.4 Hybridization with other fuels

A hybrid concept with a reduced solar share may lead to a complete shift in perspective compared to a fully stand-alone solar electric generating facility. The availability of fuel to the plant becomes more important with the higher degree of fuel compared to solar resource input. The vicinity to fuel infrastructure (pipelines, ports, railways) may become a primary criterion for site selection. If a solar field is being added to an existing conventional energy plant (coal, gas, industry application), the siting of the plant has to be in the vicinity of the existing plant. The process boils down to the general applicability of CSP, the technical concept and the commercial feasibility when overcoming whatever compromise might be required with given boundary conditions.

4.5.5 Water: sources, uses and related requirements

When it comes to the water consumption during operation, the discussion focuses very much on the cooling system for the steam turbine condenser. As the highest DNI usually appears in desert areas, typically regions with very little water resource (aside from salt water at sea shoreline), the usage of large volumes of water may be restricted or it may simply not be available.

Water qualifying for cooling purposes could be any surface water – salt and fresh water both can be applied – or subsurface water (from wells). If wet cooling is an option, hydrology and groundwater availability and accessibility should be examined in detail. The biggest obstacle will most likely be the authorization for water use, so the permitting and legal processes for this should be part of the feasibility analysis for a project.

Dry vs wet cooling technologies

From an economic perspective, wet cooling (usually with wet cooling towers) will always be the preferred method, as long as water is available and affordable. Dry cooling is technically feasible for all CSP technologies, and is not a technology risk, as the technology has been implemented in conventional power plants over the globe for a long time. The issue with dry cooling is its negative impact on project economics:

- Air as a cooling medium has a lower heat transfer coefficient than water. If air is used, advantage also cannot be taken of the chilling effect produced by evaporation when wet cooling towers are used. Therefore the exhaust temperature of the steam from the turbine is several degrees higher. This results in reduced efficiency of the water-steam cycle.

- Air-cooled condensers require a larger mass flow of air for cooling, so the fan power required by a dry cooling tower is higher than that required by a wet cooling tower. This results in increased electricity consumption within the power plant (parasitic consumption) and reduces the revenue through power sales.
- The investment cost and required land area for air-cooled condensers are usually higher, so the total investment cost of the project will be increased.

In comparison to these disadvantages, the benefit of a reduction in water consumption with dry cooling is in the range of 85–90%. In conclusion, dry cooling imposes some economic burdens on solar thermal power plants compared to wet cooling, but significantly reduces the amount of water required for plant operation and is not difficult to implement from a technical point of view. However, the possibility of lower electricity prices often gives wet-cooled projects an advantage when competing with dry-cooled projects during a tender process.

Water requirements

A solar plant requires a certain volume of water. The uses can be divided into:

- 85–90%: Wet cooling tower (evaporation replacement and blow-down/make-up)
- 15–10%: Process, service, demineralized and mirror washing water.

With dry cooling, even a truck-based supply of water might be feasible.

Water-steam cycle

Demineralized water is required for the water-steam cycle due to the nature of steam production. Steam generation for subsequent power generation dominates in all large-scale CSP technologies. Small-scale technologies, though, such as Stirling dishes or small solar tower concepts use air/gas as the HTF. Demineralized water should be processed on-site from raw water in a specific water treatment plant. The volume of water required for this purpose is not very large. It has very specific purity requirements, though, which are defined by steam turbine makers. Consumption is usually defined by blow-down and leakage replacement, except for some specific uses for shutdown and start-up of the plant.

Process and service water

A power plant usually requires process water for various purposes: cooling of rotating equipment bearings (pumps, motors, etc.), washing and cleaning of the plant, etc.

Mirror cleaning

Mirrors need frequent cleaning to maintain proper reflectivity. The cleaning frequency is specific for each project. It depends on the dust load at the specific site, and on the economic feasibility of cleaning: cost of water and labour for cleaning versus increased energy sales through higher reflectivity of mirrors. For cleaning of mirrors, it is recommended to use demineralized water to avoid staining the mirrors.

Condenser cooling system

Depending on the type of cooling systems, different volumes of water are required.

- Dry cooled condensers will not require almost any additional water apart from a potentially increased condenser hotwell volume, which does not increase consumption.
- Hybrid cooling towers are a mixture of dry cooling and wet cooling, as some water is sprayed on the exterior of the condenser tubes which will evaporate and lower the achievable condensate temperature. Water consumption will still be significantly lower compared to a wet cooling system.
- Wet cooling tower systems will utilize with roughly 10 times the volume of water (when compared to dry cooled condensers) during operation as a consequence of the evaporative cooling in the cooling tower. In addition, as a consequence of the evaporation process, the constituents such as minerals and other solids and dissolved solids in the cooling water will remain and their concentration will increase. The concentration is usually limited (by technical and/or regulatory requirements). Therefore a fraction of the water needs to be blown down and replaced with fresh water on a regular basis.
- Once-through water cooling could be an option if plants are installed in the vicinity of water bodies, however this cooling method is not expected to be a serious option since regions for CSP projects are typically characterized through water scarcity. This cooling method requires by far the largest amount of water, even though water is only heated by a couple of degrees Celsius and then routed back to the water body.

Water quality and volume requirements

The quality of the available water is important for the determination of required water volumes and for the design of water treatment facilities. This is of significant importance at an early project development stage, as usually

authorizations are required for both water extraction and water discharge. Environmental regulations will limit volume in supply and discharge, and will control concentration limits of certain constituents in wastewater discharge.

The water volume required for the plant operation is based on several factors:

- Projected operating hours and the related heat to be discharged from the condenser via the cooling system:
  - a higher power block efficiency requires a lower specific cooling water volume
  - annual variability of sunshine hours must also be considered, as during years of more sunshine, operating hours could be up to 10% higher than assumed during the typical meteorological year (TMY); this will need to be defined through performance calculations for the plant.
- The environmental permit defining concentration limits for some constituents in the water discharge from the cooling system.
- The quality of the raw water to the plant determines the possible number of cycles in the cooling system, and defines the blow-down rate required for water discharge and the make-up water volume. Surface water quality has seasonal cycles, as sediments and concentrations in the water can be washed into the water from rain or melt water, or also from industrial/sewage discharges into rivers or lakes upstream of the water extraction point. A thorough analysis with frequent sampling and laboratory analysis will provide the basis for the design.

In conclusion, the quality of water from available raw water sources is a significant factor in determining the water volume required for a solar thermal power plant, in particular when wet cooling is to be applied. The assessment of water quality and the permissions for water uses and discharge needs special attention, as permits with too stringent requirements can restrict the operation of the plant after certain volumes are consumed or if limits are exceeded frequently during regular operation.

4.5.6 Natural hazards risks and mitigation

The risk of natural hazards for the selected area should be assessed, based on historical events and regional specifics. This assessment should include the risk of occurrence of earthquakes, tsunamis, bush-fires, flooding from nearby rivers, severe storm events (e.g. hurricanes, typhoons, hail- and thunderstorms) and volcanic eruptions, as applicable. Mitigation measures should be developed based on the risk assessment for all risks classified as relevant.

Part of the risk mitigation should be through technical measures in design and construction of the plant, while the remaining risk could be covered by insurance. If a specific natural hazard risk for the selected region dominates, the insurability against such incident should be confirmed. Otherwise the financial risk will remain completely with the owner and the financing banks and, if such risk cannot be accepted, the project location may be considered unfeasible.

4.5.7 Labour

An important aspect for a project is the availability of qualified staff during construction and operation of a plant. Construction of a solar thermal power plant is expected to take between 18 and 36 months depending on the size of the installation and the experience of the contractor. In this period several hundred workers will be required for the construction, and at peak times a multiple of this (up to 2,000 or more workers at a time). All these workers need at least basic skills, as the quality of the installation should be appropriate for the expected lifetime of the plant. Higher degrees of expertise are required for supervisors and construction engineers.

Sourcing of this labour from the vicinity of the construction is advantageous for the owner. Local labour will increase the acceptance of the project in the municipality and with the population. Training in particular skills and education of workers for the construction project benefit many households in the long term, regardless of whether the plant offers equivalent employment in the medium and long term. To bring in all workers from far away, or from abroad, will be expensive and imposes a logistical challenge for the contractor.

From the developers' and owners' perspective, a fair collaboration with the surrounding municipalities will be beneficial to the project in the short and long term. However, balancing the relationship with local politicians can be a permanent challenge, even during operation of the plant.

Solar thermal power plants require permanent staffing, often on a 24-hour shift basis. The staff will include experienced engineers, technically skilled persons and supporting staff (security, housekeeping, mirror-washing, gardening, etc.). A motivated and skilled operations team is a key element for a successful plant. Preventive maintenance and pro-active optimization of operations will be of great importance in meeting or exceeding energy production projections. This is already the case for conventional power plants, but with the fluctuating solar resource, optimized operation is essential to capture as much of the limited solar resource as possible and convert it into energy as efficiently as possible.

In remote locations, staff salary packages for qualified staff will be more expensive. Offers will also need to remain attractive in order to avoid a high rate of turnover in key positions. The plant commissioning process is a

unique and important period for the key staff members in terms of their training to operate the plant, as the strong and weak aspects of the plant can be observed. 'Hands-on' experience will then help to increase their understanding of the operational behaviour of the plant.

4.5.8 Permissions

Another essential part of a successful project is to obtain all required permits and authorizations. The regulations to be considered concern every aspect of the project. The main types of permits can be classified into:

- land: register surface rights or full ownership in title of land
- tariff/PPA/off-take agreement
- grid access and capacity reservation, transmission line rights of way
- permits to construct and operate
- environmental approval
- water extraction and discharge permit, rights of way for pipe routes
- road access, rights of way for access road
- use of land for industrial purpose (rezoning)
- municipal construction permits (civil related)
- social and economic impact assessment/economic development criteria
- archaeological clearance
- other.

It should be expected that obtaining these permits is a requirement in most countries. They will be classified differently across the world, though, and will not always be the responsibility of the same office holders. In some cases, the allocation of a project is the first step, and following this, obtaining most other permits is a time-consuming formality. In other cases, each single permit has to be secured before the project is qualified to receive a feed-in tariff.

Tender schemes are becoming more popular and are posing a middle way option, as in most cases project sites and preliminary clearances are prerequisites for successful allocation. It is to be expected that the market and the incentive schemes will continue to evolve in the future.

4.6 Summary and future trends

4.6.1 Summary

Site selection and feasibility analysis of projects are always integrated into an overall project development strategy, regardless of whether the project originated in the public or private sector. A sound and successful site

selection process, in which the guiding criteria and rules are identified in the beginning, and their impacts on possible technical concepts in a target region and the resulting cost of energy are analysed, is an integral part of the development process. The selection of a project site is then the outcome of the first complete iterative cycle of the feasibility analysis. The term 'feasibility analysis' should not be adhered to too strictly, as from the authors' point of view, feasibility analysis is an ongoing, iterative process in which conclusions for a particular project are refined along the development process, eventually concluding in the financial viability of a project at financial close. If pursued consistently and in a structured way, risks can be identified and mitigated at an early stage, and sunk costs in the project development phase can be avoided to a greater extent.

4.6.2 Future trends

The development of sites for CSP projects is of strategic importance in the context of efforts to increase global implementation of CSP. Apart from technology solutions (industry) and incentive mechanisms (governments), the availability of qualifying project sites is a prerequisite for project implementation and the site qualification process usually takes a couple of years. In markets with clear guidelines, such as Spain from 2006 to 2009, many project sites have been developed. In other markets where incentive schemes are not attractive, though, the development of project sites depends purely on the initiative of the project developer and requires an appetite for fairly high risks.

In terms of overall global politics and aspirations, it can be observed that due to climate change and with growing mass production and large-scale implementation of renewable energy technologies (mainly wind and photovoltaic), the acceptance of renewable energy as a contributor to national energy supply has substantially improved. Today, even countries like China, India and South Africa, which still oppose concrete commitments to act against climate change, are commencing large programmes for installation of renewable energy capacity.

Given the volatility of the resource (such as wind or sun), renewable energy brings power fluctuation to the grid system, which will be a growing challenge for grid operating companies with increasing share of renewable energy. NREL has assessed this for the US market and came to the conclusion that, as a key difference from PV, CSP when using high-efficiency thermal energy storage (TES) can be considered a partially dispatchable resource (Denholm and Mehos, 2011). Due to the storage capabilities, solar energy can be shifted to peak demand periods, providing firm power, creating additional value and reducing grid integration challenges. The NREL study concluded that a major benefit of the inclusion of CSP in the energy

mix is its ability to enable greater penetration of PV (and e.g. wind) than would be possible without CSP integration. Under such a view, PV and CSP are partially complementary.

Based on this assessment and a general view of other markets apart from the US, it is expected that CSP will be a significant contributor to renewable energy generation, and a mandatory part of the renewable energy mix, in locations that are at least within reach of solar-rich regions. Even Europe is considering the import of solar energy from Middle East and northern Africa (MENA) regions on a large scale.

As renewable energy has to be harvested at source (be it coastal/offshore areas or deserts) and thus has to be transported to the load centres, the establishment of feasible CSP project locations is part of the global challenge to add renewable energy to the electric distribution system. Both central and distributed renewable energy generation will add to the picture, requiring new grid systems, which are able to shift energy around the continents with high flexibility. Business models for a coordinated trans-national grid upgrade seem to be lacking to some extent. In particular government owned monopoly-style utilities tend to resist the refurbishment of the system instead of moving forward.

With regard to CSP project locations, areas favourable in terms of DNI will need to be linked to the electricity system. Energy and infrastructure planning at government level is required to enable these system upgrades. For example, when looking at Europe and the northern Africa region, a political effort between the European and African countries is required to provide the framework for economic agreements and investments into such infrastructure. Both on a government and industry level, organizations have been formed to pursue this task, but outcomes are not yet conclusive.

Solar park concepts are coming into fashion. Under such schemes a government initiated solar park authority provides infrastructure such as grid access, land, water, centralized maintenance, so that multiple solar power plants can settle in the park area and share these facilities. The success of such models is still to be observed, but if governments are willing to back these parks – with regard to off-take of energy, simplified authorization, clear economic and technical conditions – then this could become an interesting solution.

4.7 References

Broesamle, H. (1999), 'Solar thermal stations, localization and assessment of the potential with the planning tool STEPS', University of Vechta, Doctoral Thesis, in German.

Broesamle, H., Mannstein, H., Schillings, C. and Trieb, F. (2001), 'Assessment of solar electricity potentials in north Africa based on satellite data and a geographic information system', *Solar Energy*, 70 (1), 1–12.

Denholm, P. and Mehos, M. (2011), 'Enabling greater penetration of solar power via the use of CSP with thermal energy storage', NREL, Golden, CO.

IEA (International Energy Agency) (2010), 'Technology roadmap concentrating solar power', OECD/IEA, Paris.

Mehos, M. and Perez, R. (2005), 'Mining for solar resources, US Southwest provides vast potential', *Imaging Notes*, 20 (3), 12–15.

Meyer, R., Torres-Butrón, J., Marquardt, G., Schwandt, M., Geuder, N., Hoyer-Klick, C., Lorenz, E., Hammer, A. and Beyer, H.G. (2008), 'Combining solar irradiance measurements and various satellite derived products to a site-specific best estimate', *SolarPACES Symp.*, Las Vegas, NV, March.

Protermosolar (2011), The Spanish Solar Thermal Industry Association (http://www.protermosolar.com/mapa.html), map with status of projects in Spain (frequently updated), at December 2011, in Spanish.

Schlecht, M. (2011), 'Storage and hybridization options', Presentation at CSP Summit Seville, Spain, November.

Star, J. and Estes, J. (1990), *Geographic Information Systems – An Introduction*, Prentice-Hall, Englewood Cliffs, NJ.

Stoddard, L., Owens, B., Morse, F. and Kearney, D. (2005), 'New Mexico concentrating solar plant feasibility study', Final Report to the New Mexico Department of Energy, Minerals, and Natural Resources, February.

Stoddard, L., Abiecunas, J. and O'Connell, R. (Black & Veatch) (2006), 'Economic, energy, and environmental benefits of concentrating solar power in California', Subcontract Report NREL/SR-550-39291, April.

Trieb, F., Schillings, C., Kronshage, S., Viebahn, P., May, N., Paul, C., Klann, U., Kabariti, M., Bennouna, A., Nokraschy, H., Hassan, S., Georgy Yussef, L., Hasni, T., Bassam, N. and Satoguina, H. (2005), 'Concentrating solar power for the Mediterranean region', German Aerospace Center (DLR), Final Report of the MED-CSP Study for the German Ministry of Environment, Nature Conervation and Nuclear Safety, April.

Trieb, F., Schillings, C., Kronshage, S., Viebahn, P., May, N., Paul, C., Klann, U., Kabariti, M., Bennouna, A., Nokraschy, H., Hassan, S., Georgy Yussef, L., Hasni, T., Bassam, N. and Satoguina, H. (2006), 'Trans-Mediterranean interconnection for concentrating solar power', German Aerospace Center (DLR), Final report of the TRANS-CSP Study for the German Ministry of Environment, Nature Conservation and Nuclear Safety, June.

Trieb, F., Gehrung, J., Viebahn, P., Schillings, C., Hoyer, C., Kabariti, M., Altowaie, H., Sufian,T, Alnaser, W., Bennouna, A., El-Bassam, N., Kern, J., Nokraschy, H., Knies, G., Möller, U., Aliewi, A. Shaheen, H., Elhasair, I. and Glade, H. (2007), 'Concentrating solar power for seawater desalination', German Aerospace Center (DLR), Final Report of the AQUA-CSP Study for the German Ministry of Environment, Nature Conservation and Nuclear Safety.

5

Socio-economic and environmental assessment of concentrating solar power (CSP) systems

N. CALDÉS and Y. LECHÓN, CIEMAT – Plataforma Solar de Almería, Spain

Abstract: A general introduction to the main environmental and socio-economic aspects associated with concentrating solar power (CSP) systems is presented. The chapter then analyses the state of the art in the methods available to quantify the main environmental impacts of CSP systems. The results of life cycle assessments (LCA) and environmental externalities assessments of CSP systems are provided. The chapter then describes the main socio-economic impacts that can arise from the implementation of a CSP system and provides results obtained using the input–output method that show increased demand for goods and services and employment.

Key words: life cycle assessment, externalities assessment, input–output analysis.

5.1 Introduction

Various environmental and socio-economic drivers are likely to accelerate the deployment of concentrated solar power (CSP) technologies in the near future. Consequently the careful assessment of the environmental and socio-economic impacts of current and future CSP technologies will play a key role in determining their development pathway. Besides differing in production costs, the various energy technologies have different collateral effects on society and the environment. When such effects are not incorporated in the market price of the energy products they generate, they are named externalities. One of the consequences of the presence of externalities in the energy market is that the resulting energy mix is inefficient from a social welfare point of view.

Energy market externalities are of various types and magnitudes. However, compared with fossil fuel technologies, most environmental and socio-economic externalities associated with renewable energy technologies are positive, resulting in a better social welfare. For example, most renewable energy technologies contribute to a reduction in emissions of greenhouse gases (GHG) as well as other pollutants, help diversify and guarantee the energy supply and are good instruments for the generation

Table 5.1 Energy policy objectives to which CSP systems can contribute

Energy policy objectives	CSP contribution in meeting such objectives
Guaranteeing economically viable electricity prices	Strong pushing driver
Guaranteeing security of supply	Strong pushing driver
Climate protection	Strong pushing driver
Very high potential worldwide	Strong pushing driver
Aiming at conflict neutral technologies	Pushing driver
Increasing demand for local added value and labour	Pushing driver
Potential for technology exports	Pushing driver
Preferring non-intermittent electricity suppliers	Strong pushing driver

Source: adapted from Viebahn *et al.* (2008).

of wealth and employment in rural areas, thus contributing to socio-economic development. Consequently, though most renewable energy technologies are not yet price competitive in the energy market, their competitiveness is substantially improved when, besides the private electricity production costs, their associated externalities are taken into account. In order to do so, and in order to guarantee a sustainable energy mix which maximizes social welfare, it is important that public decision makers use economic instruments to incorporate externalities into market prices; in other words, that they conduct careful assessments to quantify the externalities and assign them a monetary value.

Besides the need to internalize the environmental and socio-economic externalities, there are other arguments that justify conducting a socio-economic and environmental assessment of these promising technologies.

According to various experts, there exist various energy policy objectives which are likely to be the guidelines for the development of the energy system over the next five decades and, as shown in Table 5.1, CSP technologies can contribute to meeting some of these objectives (Viebahn *et al.*, 2008). Discussing each of these in turn:

- *Guaranteeing future economically viable prices*: In the context of ongoing increases in fossil fuel prices, the extensive exploitation of renewable energy sources such as solar energy is key to achieving a long-term decoupling from the fossil energy prices.
- *Guaranteeing security of supply*: By replacing fossil fuel technologies with renewable technologies, such as CSP systems, it is possible to (i) increase the reliability of the electricity supply by diversifying the energy mix and (ii) decrease dependency on fossil fuels.

- *Contribute to climate protection*: The installation of CSP may reduce global warming emissions if generating power from CSP plants offsets generation from fossil-fuelled plants.
- *Take advantage of energy potentials worldwide:* CSP technologies take advantage of an inexhaustible resource which is very abundant in various developing countries around the world, where the domestic technical potentials exceed possible demands by orders of magnitude. Consequently, there is an argument for the expansion of CSP plants on the global scale.
- *Aim towards conflict neutral technologies*: Most fossil fuel reserves are located in geopolitically unstable countries which exacerbates military conflicts around the world. Another world security threat arises from the proliferation of nuclear weapons. In this sense, CSP is a more conflict-resistant technology since it does not involve conflict-relevant materials. Most importantly, though, the solar resource is abundant and inexhaustible and thus will not incite conflicts over rights of use.
- *Increasing demand for local added value and local labour*: CSP technology investment decisions have the potential to have a large impact in terms of local added value as well as employment generation and accumulation of local expertise. Compared to other energy technologies, CSP technology investments do not require very 'high-tech' components, while they do require large amounts of steel, concrete, mirrors and labour.
- *Potential for technology exports from countries that are leaders in technology development*: The CSP technology industry in countries that are leaders in technology development (which includes small- and medium-sized component suppliers, engineering consultants and large power companies) has the opportunity to expand its global export volumes.
- *Preference for non-intermittent electricity suppliers*: Compared to other alternative renewable energy technologies, by incorporating thermal storage and co-firing options, CSP technologies are able to offer fully dispatchable energy at a competitive price level.

5.2 Environmental assessment of concentrating solar power (CSP) systems

A key benefit of the use of CSP plants is the potential to reduce conventional and greenhouse gas emissions caused by electricity generation. The installation of CSP may reduce atmospheric emissions if generating power from CSP plants offsets generation from fossil-fuelled plants. In order to estimate these benefits several methodologies can be used. In this section results will be provided for CSP systems from two well-recognized meth-

odologies and compared with results for other energy generation technologies. The two methodologies in question are:

- life cycle assessment
- environmental externalities assessment.

Apart from the beneficial effects described above, the deployment of CSP can cause some unintended environmental impacts. The main impacts are impacts on amenities and relate to the large area required for the technology. The main impacts identified are the following (IEA, 1998):

- visual impacts
- noise
- ecological impacts due to land use
- water resources impacts.

Most of these impacts are local and are therefore highly affected by the siting of the technology; some of them can be minimized by a sensitive siting choice. CSP plants using conventional steam turbines to generate electricity have a requirement for condenser cooling which has until now been satisfied using evaporative cooling towers consuming fresh water. Because solar abundance and fresh water constraints often coincide geographically, the cumulative impacts of installing numerous CSP plants in a region raise policy concerns. The trend is towards more freshwater-efficient cooling technologies (Carter and Campbell, 2009).

5.2.1 Life cycle assessment of CSP systems

Life cycle assessment (LCA) is a method for systematic analysis of environmental performance from a cradle to grave perspective. This analytic tool systematically describes and assesses all flows that enter into the studied systems from nature and all those flows that go out from the systems to nature, all over the life cycle.

The interest in LCA started in the 1990s and since then a strong development has occurred. The practice of LCA is regulated by the international standards ISO 14040 and 14044 (ISO, 2006a,b), and there are several introductions (Guinée *et al.*, 2002; JRC IES, 2010) and databases (Ecoinvent, 2007) available. LCA is a robust and mature methodology, although some aspects are still under development. A thorough review of the recent advances of the methodology can be found in Finnveden *et al.* (2009).

A complete LCA study consists of four steps:

1. Definition of the goal and scope of the study.
2. Life cycle inventory (LCI phase) where the collection of all the environmental inflows and outflows takes place.

3. Life cycle impact assessment (LCIA) phase.
4. Interpretation of the results.

However, it is quite typical that some LCAs only perform the inventory analysis, delivering a list of emissions, or only evaluate some of the impacts (like global warming impacts).

There exist several environmental assessments of solar thermal technologies in the scientific literature. Lenzen (1999) evaluated the GHG emissions of different configurations of CSP plants hypothetically located in Australia. Weinrebe *et al.* (1998) performed a life cycle assessment of two plants, an 80 MW SEGS (solar energy generating systems) plant and a 30 MW Phoebus power tower. Viebahn, within the SOKRATES (Viebahn, 2003) and INDITEP (Viebahn, 2004) projects, also conducted LCAs of different configurations of solar thermal plants, a direct steam generation (DSG) plant, a SEGS plant, and a FRESNEL-type plant. Pehnt (2006) conducted a dynamic LCA showing the evolution of the impacts of several renewable technologies including CSP. Lechón *et al.* (2008) performed an LCA of two CSP plants in Spain. Within the EU project NEEDS (www.needs-project.org) an LCA of current and future configurations of CSP plants was performed showing also the evolution of the environmental performance of this technology with time.

All of these studies show important benefits in terms of reduced environmental impacts for solar thermal power plants compared to other competing electricity generation technologies, especially in terms of emissions of greenhouse gases. Burkhardt *et al.* (2010) performed an LCA of a reference design of a parabolic trough CSP facility in California and evaluated the effects on LCA results and freshwater requirements of different power plant designs. GHG results of these studies are summarized in Table 5.2.

Values of global warming emissions in solar only operation reported in the literature range from 11 g/kWh to 60 g/kWh and from 12 g/kWh to 90 g/kWh for central tower and parabolic troughs, respectively. These emissions are well below the emissions produced by conventional electricity generation sources (see Fig. 5.1). Discrepancies among studies can be due to several factors including methodological issues such as the GHG emission intensity of the different materials, technological differences in the plant configuration, as well as some issues related to the location, life time, capacity factors and other operational characteristics of the plants considered.

The values calculated by Vant-Hull (1992) are the lowest of the reviewed studies probably due to the low emission factors associated to some materials and due to the fact that emissions associated to the operation and maintenance activities are not included as discussed by Lenzen (1999). The values calculated by Kreith *et al.* (1990) only include CO_2 and do not include

Table 5.2 Greenhouse gas (GHG) emissions of CSP plants

GHG emissions (g CO_2 equiv/kWh)	Central receiver	Parabolic trough
Solar only operation		
Kreith *et al.* 1990 (Solar Two type) (I-O LCA)	43	
Vant-Hull 1992 (Solar Two type) (Process LCA)	11	
Norton and Lawson 1996 (Process LCA)	21–48	30–80
Röder 1997 (Phoebus type CR and SEGS type PT) (Process LCA)	39–46	26
Weinrebe *et al.* 1998 (Phoebus type CR and SEGS type PT) (Process LCA)	23–25	17
Lenzen 1999 (Solar Two type CR and ANU type PT) (Process LCA)	33–39	16
Lenzen 1999 Including operation and maintenance (Solar Two type CR and ANU type PT) (I-O LCA)	60	90
Viebahn 2003 (SEGS type PT) (Process LCA)		12
Viehban *et al.* 2008 (Solar Tres type for CR and ANDASOL type for PT) (Process LCA)	22	33
Pehn 2006 (Process LCA)		14
Burkhardt *et al.* 2010 (Hybrid EIO LCA)		26 (24–39)
Hybrid operation		
Weinrebe *et al.* 1998 (Process LCA)	345	234
Lenzen 1999 (Natural gas back-up capacity factor 50%) (I-O LCA)		300
Lechón *et al.* 2008 (natural gas back-up capacity factor 71% CR and 44% PT) (Process LCA)	203	185
de la Rúa 2009 (Solar Tres type) (Process LCA)	186	
de la Rúa 2009 (Solar Tres type) (I-O LCA)	188	
Viebahn *et al.* 2008 (Solar Tres type for CR and ANDASOL type for PT) (Process LCA)	128	160

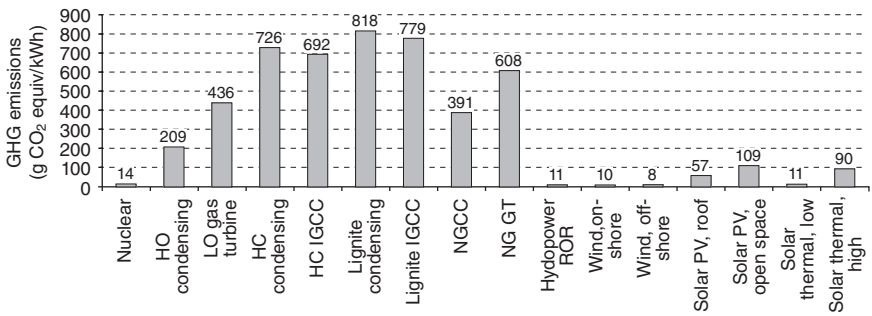

5.1 Greenhouse gas emissions of different electricity generating technologies (source: CASES project www.feem-project.net/cases). HO: heavy oil; LO: light oil; HC: hard coal; IGCC: integrated gasification combined cycle; NGCC: natural gas combined cycle; NG: natural gas; GT: gas turbine; ROR: run of river; PV: photovoltaic.

the effect of other greenhouse gases, nor the emissions associated to the operation and maintenance (O&M) activities. Values reported by Weinrebe *et al.* (1998) are also quite low probably due to differences in GHG emission intensities of materials.

The values reported by Lenzen (1999) are the highest in the range of reported values. One of the reasons behind this, also acknowledged by the author, could be the methodological approach followed by this author. In fact, Lenzen's values are calculated using an input–output methodology which is able to capture the indirect requirements neglected by the standard process LCA (for an introduction to I–O analysis applied to LCA, see Finnveden *et al.*, 2009 and de la Rúa, 2009). These indirect requirements are especially relevant when dealing with O&M activities. A standard LCA process of a solar plant only cannot capture the emissions associated to these activities since these emissions are indirect emissions produced in the relevant sectors of the economy such as technical services, mechanical repairs, business services, marketing and business management, insurance, etc.

Emissions are higher in hybrid operation for the obvious reason of fossil fuel consumption. These emissions increase with the degree of hybridization.

The work of Lenzen (1999) showed how the GHG emissions depend on whether the plant's capacity factor is increased using a fossil fuel back-up (650 g CO_2 equiv/kWh at 60% capacity factor) or heat storage system (60 g/kWh for the same 60% capacity factor). Lenzen also demonstrated that additional capacity factor in the form of heat storage and oversized solar field can be installed at lower marginal GHG cost than the base solar capacity itself, and that there are clear economies of scale in the GHG emissions of both parabolic troughs and central receiver plants.

In general, the reviewed studies show that the main constituents of the sum of the GHG emissions in solar only operation are the steel used in the solar field, the concrete used in the solar field and in the tower and the salts used in the storage systems.

Electricity and other fuels are consumed in the manufacturing of the materials used to build the CSP plants. The impacts imported into the CSP systems through these energy vectors are an example of what Pehnt (2006) called 'imported impacts' which are impacts brought into the system due to the 'background system' and which are not inherent to the renewable technology. These impacts can change with time as the mix of technologies used to produce those energy vectors changes.

The relative contribution to GHG emissions of the different aspects of the operational stage of one of the CSP plants studied by Lechón *et al.* (2008) is shown in Fig. 5.2. It is worth noting the relevant contribution to the global warming emissions of the electricity consumption of the plants in this study. Electricity consumption in the plants is taken from the grid

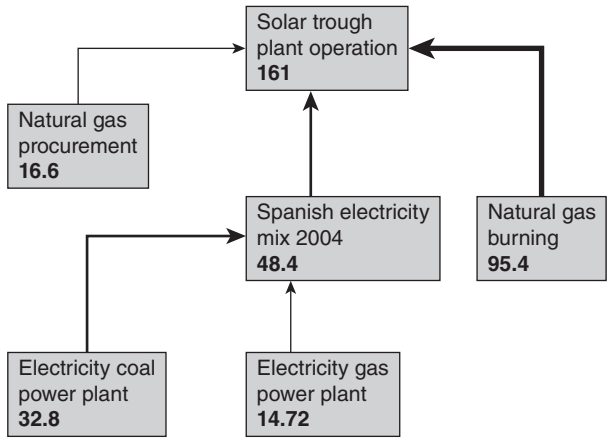

5.2 Relative contribution to GHG emissions (g/kWh) of the different aspects of the operational stage of a parabolic trough CSP plant (source: Lechón *et al.,* 2008).

instead of from the self-produced electricity. The contribution of electricity consumption to the GHG emissions is mainly due to the fact that an important part of the electricity generation in Spain is produced in coal power plants with very high associated greenhouse gas emissions.

Recent work by Burkhardt *et al.* (2010) shows the effect of different thermal energy storage systems, cooling systems and different origin of the salts in LCA results. According to these authors, the use of thermocline thermal energy storage instead of a two-tank configuration allows the reduction of 2 g CO_2 equiv/kWh due to the significantly lower material requirements. The use of a dry cooling system instead of a wet cooling system increases GHG emissions by 2 g CO_2 equiv/kWh due to the reduction in the efficiency of the steam cycle. The use of synthetic salts instead of mined salts, considered in their base assumption, increased GHG emissions by 13 g CO_2 equiv/kWh. Finally, according to their results, if both synthetic salts and a thermocline configuration are used, the negative effects of synthetic salts are compensated by the reduced salt requirements of the thermocline system and the GHG emissions are increased by only 2 g CO_2 equiv/kWh.

Other impacts usually assessed in LCA are acidification and eutrophization. The term acidification refers to the processes that increase the acidity of water and soil systems through the deposition of negatively charged ions that are then removed by leaching or biochemical processes leaving excess H^+ concentration in the system. Acidification of soils causes losses in forest and plant health and also ecotoxicological impacts due to the mobilization of aluminium. Acidification of water leads to loss of aquatic

Table 5.3 Acidification impacts of CSP plants

Acidification (mg SO_2 equiv/kWh)	Central tower	Parabolic trough
Solar only operation		
Viehban 2004 (SEGS type PT)		69.28
Pehnt 2006		98
Hybrid operation		
Lechón *et al.* 2008	612	590
Weinrebe *et al.* 1998	370	510

Table 5.4 Eutrophization impacts of CSP plants

Eutrophization (mg PO_4 equiv/kWh)	Central tower	Parabolic trough
Solar only operation		
Viehban 2004 (SEGS type PT)		5.69
Pehnt 2006		10
Hybrid operation		
Lechón *et al.* 2008	49.6	49.7
Weinrebe *et al.* 1998	40	56

life (Udo de Haes *et al.*, 2002). Eutrophization refers to the nutrient enrichment of aquatic or terrestrial environments. Aquatic eutrophization leads to a shift of the biological structure of the aquatic environment with adverse effects on the fauna and flora through a complex chain of ecological effects. Terrestrial eutrophization refers to the adverse effects of excess nutrients on plant functioning and on species composition in natural ecosystems.

With regard to acidification and eutrophization impacts, CSP systems also show clear benefits. If electricity produced by CSP plants offsets electricity produced by, for example, the Spanish electricity mix with an acidification potential of around 5,000 mg SO_2equiv/kWh and an eutrophization potential of around 250 mg PO_4/kWh (Ecoinvent, 2007), significant impacts are avoided.

Acidification and eutrophization impacts reported in the literature are shown in Tables 5.3 and 5.4. In the case of CSP plants operating in solar only mode, acidification values reported by Viebahn (2004) are 69.28 mg SO_2 equiv/kWh for a parabolic trough plant and Pehnt (2006) reported values of 98 mg SO_2 equiv/kWh. In the case of hybrid operation, the values reported in the literature are considerably higher: 590–612 SO_2 equiv/kWh reported by Lechón *et al.* (2008) and 370–510 reported by Weinrebe *et al.*

Table 5.5 GHG emission factors and acidification and eutrophization potentials of different materials

	GHG emission factor (kg CO_2 equiv/kg)	Acidification potential (g SO_2 eq/kg)	Eutrophization potential (g NOx eq/kg)
Aluminium (production mix)	2.9	14.5	6.8
Cast iron	3.1	10.4	8.9
Chromium steel	5.3	27.1	15.7
Reinforcing steel	1.5	5.2	3.8
Concrete	262.6	437.0	603.7
Copper	2.2	14.9	5.7
Glass coated	0.7	9.4	6.2
Glass uncoated	0.6	8.5	5.5
Glass tube	2.5	10.9	14.7
KNO_3 as N	16.1	42.4	81.4
$Ca(NO_3)_2$ as N	4.0	12.7	7.1

Source: Ecoinvent (2007).

(1998). However, it is important to acknowledge that most of the impacts are produced in the operation of the power plant due to the consumption of natural gas and external electricity. In the case of eutrophization the values found in the literature range from 6 to 10 mg PO_4/kWh in the CSP plants operation in solar only mode and around 50 PO_4/kWh when operating in hybrid mode.

The impacts associated with the solar field are also of great importance in some impact categories such as human toxicity and freshwater aquatic eco-toxicity. When tracing back the origin of these impacts, it was found that they were due to the use of steel in the metallic structure of the collectors (Lechón *et al.*, 2008).

GHG emission factors and acidification and eutrophization potentials of different materials used in the construction of a CSP plant are shown in Table 5.5. As shown in Table 5.5, aluminium has lower associated environmental impacts than chromium steel, which is the material usually employed in the construction of the metallic structure of the collectors of parabolic trough CSP plants. The use of aluminium instead of steel in the frames as in the case of the Acciona Solar Power SGX2 (Fernández-García *et al.*, 2010) space frame could reduce these impacts accordingly.

Regarding freshwater consumption of CSP plants, the work of Burkhardt *et al.* (2010) provides very interesting results of a dry cooling system design. According to these authors, the CSP plant using a wet cooling system would consume 4.7 l of fresh water per kWh of electricity produced, while a dry cooling system would achieve a 77% reduction in this water consumption.

5.2.2 Environmental externalities assessment of CSP systems

As explained in the introductory section of this chapter, all power generation technologies are accompanied by externalities, costs imposed on individuals or the community that are not paid for by the producer or consumer of electricity.

The most important project on determining the externalities of energy is the European ExternE project (www.externe.info). It was launched in 1991 by the European Commission and the US Department of Energy, and the European Commission has been supporting the research until now through several projects. The last one of these projects is the NEEDS Project (New Energy Externalities Development for Sustainability, www.needs-project.org/).

The ExternE methodology is widely accepted by the scientific community and is considered as the world reference in the field. The quantification of the external costs is based on the 'impact pathway' methodology, which was developed in the series of ExternE projects, and has been further improved in the NEEDS projects and other related projects like the EU CASES project (www.feem-project.net/cases). The impact pathway methodology aims at modelling the causal relationships from the emission of a pollutant to the impacts produced on various receptors through the transport and chemical conversion of this pollutant in the atmosphere. The main receptors of the impacts are human health, crops, ecosystems and materials. Welfare losses produced by these impacts are assessed using economic valuation methods. Impact categories, pollutants and effects considered in the ExternE methodology are summarized in Table 5.6.

Global warming impacts assessment is subject to a high degree of uncertainty. Within NEEDS, the model FUND 3.0 was used to estimate the marginal external costs of GHG emissions (Anthoff, 2007). Results differ greatly depending on the assumptions regarding some very influential parameters such as discounting and equity weighting. Two sets of external costs factors were used in NEEDS, trying to reflect these uncertainties (Preiss and Friedrich, 2009).

The results of the external costs assessment of CSP plants from the NEEDS project are shown in Fig. 5.3. External costs other than global warming costs decrease with time as the technology matures and the inventories of pollutant emissions decrease. However, marginal external costs for GHG emissions increase with time, and therefore the total external costs of CSP systems increase. External costs calculated for CSP technology are quite low compared with other competing electricity generation technologies as shown in Fig. 5.4. Fossil fuel technologies have external costs above 1.4 eurocent/kWh. These costs are dominated by global warming impacts in the case of coal, lignite and natural gas and by health effects in the case

Table 5.6 Impacts, pollutants and effects covered by the ExternE methodology

Impact category	Pollutant	Effects
Human health – mortality	PM_{10}, SO_2, NO_x, O_3	Reduction in life expectancy
	As, Cd, Cr, Ni	Cancer
	Accident risk	Fatality risk from traffic and workplace accidents
Human health – morbidity	PM_{10}, O_3, SO_2	Respiratory hospital admissions
	PM_{10}, O_3	Restricted activity days
	PM_{10}, CO	Congestive heart failure
	PM_{10}	Cerebro-vascular hospital admissions
		Cases of chronic bronchitis
		Cases of chronic cough in children
		Cough in asthmatics
		Lower respiratory symptoms
	Pb	Neurotoxicity
	O_3	Asthma attacks
		Symptom days
	Benzene	Cancer risk (non-fatal)
	Benzo-[a]-pyrene	
	1,3-butadiene	
	Diesel particles	
	Noise	Myocardial infarction
		Angina pectoris
		Hypertension
		Sleep disturbance
	Accident risk	Risk of injuries from traffic and workplace accidents
Building materials	SO_2	Ageing of galvanized steel, limestone, mortar, sandstone, paint, rendering, and zinc for utilitarian soiling of buildings
	Acid deposition	
	Combustion particles	
Crops	NO_x, SO_2	Yield change for wheat, barley, rye, oats, potato, sugar beet
	O_3	Yield change for wheat, barley, rye, oats, potato, rice, tobacco, sunflower seed
	Acid deposition	Increased need for liming
Global warming	CO_2, CH_4, N_2O, N, S	World-wide effects on mortality, morbidity, coastal impacts, agriculture, energy demand, and economic impacts due to temperature change and sea level rise
Ecosystems	Acid deposition	Acidity and eutrophication (avoidance costs for reducing areas where critical loads are exceeded)
	Nitrogen deposition	

Source: EC (2005).

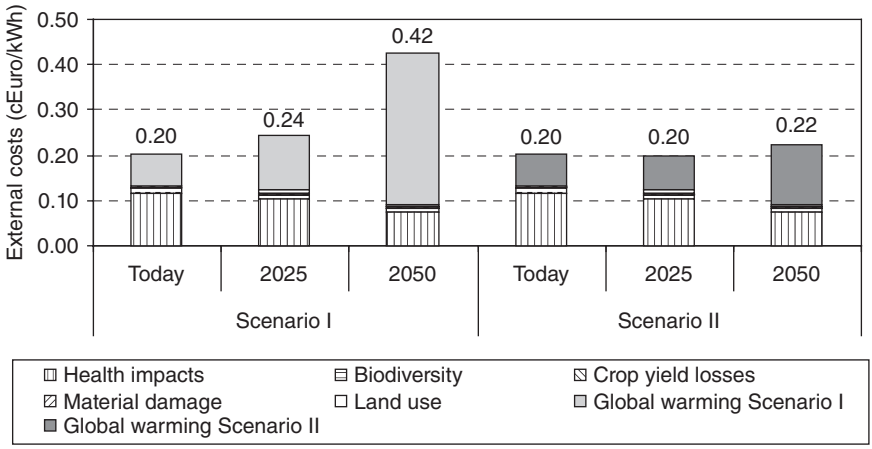

5.3 External cost evolution of CSP systems (source: authors' elaboration using data from NEEDS project).

of heavy and light oil. Among fossil technologies, the ones with higher efficiencies have correspondingly less external costs per kWh. Nuclear energy external costs are very low in these calculations, but do not take into account the effects of a possible nuclear accident or the effects on the future environment and society of the possible accidental release of the nuclear waste that has been disposed of (Lecointe *et al.*, 2007). Solar PV technologies have sensibly higher external costs than CSP and these costs are dominated by the health effects arising from the emissions originated by the energy requirements of the upstream processes related to the production of silicon and PV wafers (Frankl *et al.*, 2006). Improvements in energy consumption and also the better efficiencies that are foreseen for this technology would reduce the external costs accordingly.

5.3 Socio-economic impacts of concentrating solar power (CSP) systems

The benefits associated with solar thermal electricity deployment are various in nature and should be taken into consideration in order to design support policies aimed at compensating its higher electricity production costs compared to fossil fuel alternative technologies. As described in detail in the previous section, among other environmental impacts associated with the gradual substitution of fossil fuel technologies by CSP technologies, CO_2 emissions as well as energy consumption reductions are some of the most notable benefits (Lechón *et al.*, 2008). However, other socio-economic impacts should equally be taken into consideration.

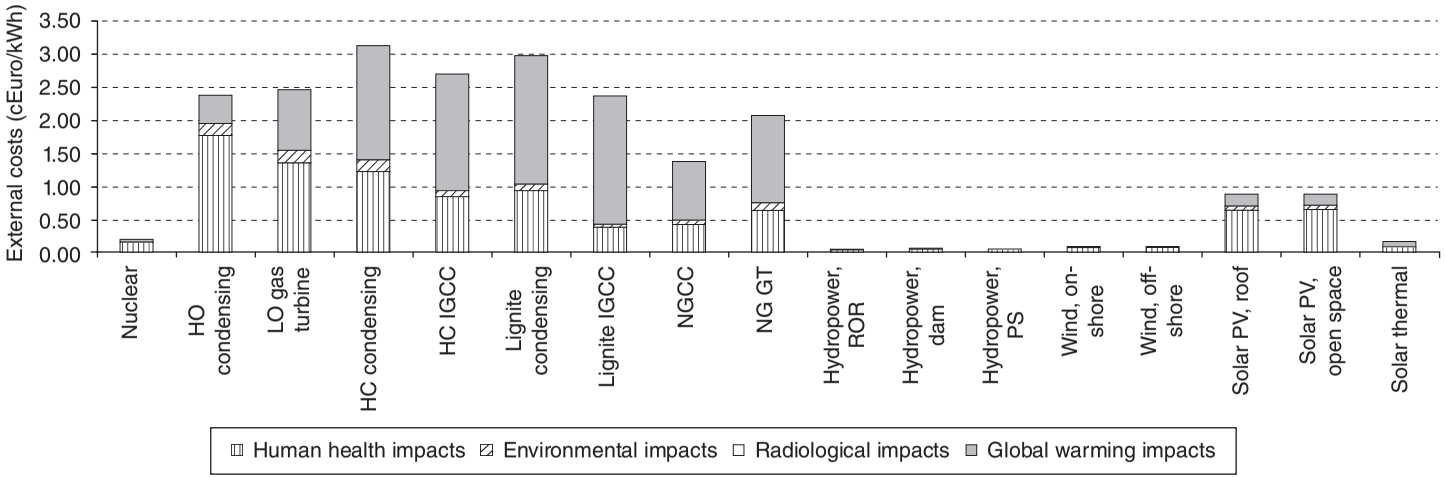

5.4 External costs of different electricity generating technologies (source: authors' elaboration using CASES project data, www.feem-project.net/cases).

As previously mentioned, compared to fossil and other renewable energy technologies, one of the most relevant of CSP's associated socio-economic impacts is its capacity to stimulate the economy and create new jobs at the local level. One of the main reasons for this is that CSP's 'high-tech' component requirements are low and its main components include steel, concrete, mirrors and labour. Such local effects may be realized through an increase in the demand for goods and services as well as through the creation of new jobs. These impacts may take the form of:

- direct effects – accrued due to the increase in the demand for those industries that directly provide goods and services required to construct, operate, maintain and dismantle a plant,
- indirect effects – originated due to the effect that such new investment has on new flows of purchases and/or sales among other productive sectors in the economy, and
- induced effects – related to the expansion of private expenditure in goods and services (food transportation, health, services, etc.) from the workers employed – in a direct or indirect way – by the project.

In that sense, Kulstic *et al.* (2007) highlight the fact that many assessments currently underestimate the total socio-economic effects since they only take into account the direct effects and disregard induced and most important indirect effects that take place during the construction, operation, maintenance and dismantling of any power plant. In order to fully account for the impacts on the demand for goods and services as well as on employment, one of the soundest analytical tools is the input–output methodology, which will be presented below. After describing the methodology as well as highlighting its main advantages and limitations, the following section will present an example of its application used to estimate the socio-economic impacts associated with the solar thermal energy deployment in Spain.

5.3.1 Input–output methodology

The input–output (I-O) methodology, which was first developed by Wassily Leontief in the late 1930s, has been widely used to trace out a portrait of the whole national economic structure (Leontief, 1966, 1986). The input–output symmetric table is an economic analysis tool that reflects the value of the different goods and services that are exchanged in an economy. The structure of the I-O table is such that, along the different rows and columns of the matrix, one can find the different sectors within the economy set in a symmetrical way. The different elements displayed along each row describe the different uses of each sector's production. In a similar manner, for each sector in the economy, the elements along the columns of the symmetric input–output table account for the resources that have been consumed from

Table 5.7 Input–output table structure

Resources (columns)	Uses (rows)
1. Intermediate resources	1. Intermediate products
2. Value added	2. Final consumption
3. Effective production (1 + 2)	3. Gross capital formation
4. Imports	4. Exports
	5. Final uses (2 + 3 + 4)
5. Total resources (3 + 4)	6. Total uses (1 + 5)

Table 5.8 I-O symmetric table scheme

	Sectors' consumption				Final demand Y	Total production X
Sectors' production	1	2	3	n		
1	X11	X12	X13	X1n	Y1	X1
2	X21	X22	X23	X2n	Y2	X2
3	X31	X32	X33	X3n	Y3	X3
n	Xn1	Xn2	Xn3	Xnn	Yn	Xn
Intermediate consumption I	I1	I2	I3	In		
Added value V	V1	V2	V3	Vn	GDP	
Total production X	X1	X2	X3	Xn		

Source: Hendrickson *et al.* (2006).

other sectors in order to obtain a certain production in each sector. In a schematic and simplistic way, an I-O table can be depicted as in Table 5.7.

Based on the input–output symmetric table shown in Table 5.8, the matrix of coefficients summarizes the interdependencies between production sectors (Ten Raa, 2005) and is used to analyse the economic activity and employment impacts induced by an increase in the demand of any particular economic sector.

Increase in the demand for goods and services

According to the I-O methodology, the relationship between the expenditure generated by a certain project and its impact on the demand for goods and services is depicted by the following relation:

$$\Delta Q_y = (I - A)^{-1} \Delta D_y \qquad [5.1]$$

where: ΔQ_y = increase in the total demand for goods and services (direct and indirect), I = matrix unit, A = technical coefficients matrix, and ΔD_y =

increase in direct demand for goods and services generated by the development of a certain project *y*.

The different elements included in matrix A $(n \times n)$ are named technical coefficients (a_{ij}) which reflect the percentage of goods or services from sector '*i*' that are required to produce one good or service unit from sector '*j*'. Put another way, the technical coefficients indicate the amount that sector '*j*' requires from sector '*i*' in order to produce one unit of product or service *j* (both quantities should be expressed in their monetary value at constant prices).

$$A = \{a_{ij}\}, \quad \text{being} \quad a_{ij} = \frac{x_{ij}}{x_j} \qquad [5.2]$$

where x_{ij} = goods or services that sector *j* requires from sector *i* (in monetary terms), and x_j = total production from sector *j*.

In most countries, an official institution regularly publishes the technical coefficient matrix A (as well as the symmetric input–output table, upon which the technical coefficient matrix is built). In the case of Spain, every five years the National Statistics Institute (INE) publishes the National Input–Output tables based on the National Accounts records. Once the so-called Leontief inverse matrix $(I\text{-}A)^{-1}$ has been constructed, it is then possible to estimate the impact derived from a certain project by multiplying $(I\text{-}A)^{-1}$ by the investment as well as operation and maintenance costs vector ΔD associated to the project. The result from this operation is a column vector $\Delta Q(n * 1)$ the sum of whose elements is the total impact of the investment, which includes both direct and indirect impacts.

Employment creation

Besides increasing the demand for certain goods and services, the development of any project generates impacts on the employment in a direct and indirect way. In order to estimate such effect, a column vector L_s must be constructed based on the number of employed people across each sector in the economy (expressed as number of employed people for every million euros produced in each sector). Secondly, L_s must be multiplied by ΔQ (which represents the previously obtained vector that accounts for the total economic impact). The result from this multiplication is the total number of employments that have been created in each sector due to this project. Each element of the resulting vector shows the total number of new jobs in each sector created both in a direct or indirect way.

$$L_s \Delta Q_y = L_y \qquad [5.3]$$

where L_s = vector of employees per sector, and L_y = direct and indirect impact of employment due to the project. Based on this estimation, the

number of direct and indirect employments could be estimated using the following expressions:

$$\text{Direct employment} = L_s \Delta D_y;$$

$$\text{indirect employment} = L_s (\Delta Q_y - \Delta D_y)$$

Finally, and based on the previous results, it is then possible to compute the multiplying effect of a certain project. A multiplier is a number that indicates by how much a certain economy is going to grow due to a certain project development (taking into account both direct and indirect effects). The general formula to compute the multiplying effect (M) is:

$$\text{Multiplier } (M) = \frac{\text{Total effects}}{\text{Direct effects}} = \frac{\Delta Q}{\Delta D} \quad [5.4]$$

Compared to other alternative analytical methods, the most relevant advantages of the input–output methodology are its simplicity, intuitive understanding, basic software requirements as well as its acceptability within the scientific community. However, among its limitations, it is worth mentioning that its constant technical coefficients do not always take into account technological improvements, import substitution, change in consumption patterns or relative price variations that take place from one year to another (Holland and Cooke, 1992). Moreover, homogeneity among sectors as well as lack of production capacity limitations is assumed.

Despite the above mentioned limitations, the input–output methodology has been widely applied to study the socio-economic impacts of various energy projects (Tegen, 2006; Lantz and Tegen, 2009; Linares *et al.*, 1996; Caldés *et al.*, 2009; de la Rúa, 2009; Lanier *et al.*, 1998). In that sense, in a recent study by the National Renewable Energy Laboratory (Lantz and Tegen, 2009), the input–output methodology is presented as one of the most consolidated methods recognized by the scientific community.

5.3.2 Application of an input–output analysis: estimation of the socio-economic impacts of CSP energy deployment in Spain

Over the last few years, Spain's solar thermal electricity deployment has been remarkable, mainly due to its regulatory environment as well as favourable climatic conditions. This favourable context has brought forth an upsurge in solar projects – mainly using either a central receiver or parabolic trough technologies – and it is expected that, in the near future, the potential CSP capacity in Spain will exceed 500 MW; the Spanish Renewable Energy Plan (PER) goal for solar thermal installed capacity by 2010.

In this context, the goal of the work by Caldés *et al.* (2009) that will be presented here was to estimate the socio-economic impacts of increasing the installed solar thermal energy power capacity in Spain by using an input–output analysis. For more detailed information, see Caldés *et al.* (2009).

In order to estimate such effects, two scenarios were considered:

1. The first scenario considered the individual impacts derived from the construction and operation of two solar thermal power plants with the following specifications:
   - A 50 MW power plant consisting of 624 parabolic trough collectors. This plant uses synthetic oil as the heat transfer fluid and molten salts to provide seven hours' storage at peak output. Following the current regulatory framework, 15% of total output is generated by natural gas.
   - A 17 MW central solar tower power plant consisting of 2,750 heliostats. This plant uses molten salts both as a heat transfer fluid and storage system. This power plant occupies 150 ha and, as in the previous case, the power plant generates 15% of electricity from natural gas.
2. The second scenario replicates the PER installed capacity goal for solar thermal power by 2010 which would lead to 500 MW installed capacity. According to this hypothetical scenario, it was assumed that 80% of such capacity would be met by parabolic trough plants, while 20% would be met by solar tower power plants.

Solar thermal plant costs

Based on actual cost data of CSP projects currently in operation in Spain, this section presents a summary of the main data and assumptions used to construct the plant as well as O&M cost vectors associated to each of the power plants analysed. It must be noted that, due to the lack of precise data on employment and salary figures, induced effects were not estimated. In the same way, due to the lack of data, the end-of-life dismantling phase of the project was not taken into account.

Parabolic trough power plant (50 MW)

Of the total investment costs (265,837 k€), the solar field accounts for 46% of the total investment cost, power block 21%, storage 13%, construction 10% and the remaining 10% is accounted for by engineering costs and contingencies. With respect to the annual operation and maintenance costs (12,300 k€), an operational lifetime of 25 years with an annual discount rate of 8% was considered. Within total operation and maintenance costs (240,380 k€ over the life of the plant), it was assumed that the payment of employees' wages account for 80% of such costs (representing 1,033.6 k€/

year), while the rest is accounted for by administration services, insurance, etc. Consequently, and given that the average salary of a Spanish employee working in the electricity generation and distribution sector amounts to 46.3 k€/year (INE, 2006), the estimated number of people annually working in the operation of this plant would amount to 22 people. Finally, expenses associated with natural gas and electricity consumption were also accounted for and the estimation of the financing expenses has been computed assuming a 12-year repayment loan with a 7% interest rate.

Solar tower power plant (17 MW)

Out of the total investment cost of the plant (147,016 k€), it was assumed that the solar field accounts for 43% of the investment, power block 20%, tower and receptor 16%, storage system 6%, construction 7% and the remaining 8% is accounted for by engineering and contingencies costs. With regard to its annual operation and maintenance costs (7,154 k€/year), it was assumed that the operational period lasted 25 years with a 2% annual discount rate. As in the previous plant, within the total fixed operation and maintenance costs (139,811 k€ over the life of the plant), it was assumed that 80% of such costs accrued to employees' wages and the rest was accounted for by administrative services, insurances, etc. As in the previous case, the estimated number of people annually employed in the plant amounted to 22 people. Both gas and electricity costs required to operate the solar plant were taken into account and investment costs were financed with a loan to be repaid over 12 years with an annual interest rate of 7%.

National economic data

At the time when this study was conducted, the most up-to-date official Spanish input–output table was used. This 2000 I-O table was published by the National Statistics Institute in 2007 and reflected all transactions that had taken place across economic sectors in the form of increased demands as well as intermediate and final production across 73 national economic sectors. Based on this original I-O table, a reduced table consisting of the 22 most relevant economic sectors for this analysis was constructed. Finally, total costs associated with the studied plants had to be broken down later and associated with the different sectors in the reduced I-O table.

Results: parabolic trough plant

As shown in Table 5.9, the total effect associated with this plant amounts to 930 M€ (equivalent to 18.6 M€/MW), of which total indirect effect generated during the construction and operational phase accounts for 445 M€.

Table 5.9 Total effect on the demand for goods and services as well as employment per MW of installed capacity for 50 MW parabolic trough power plants (PTP)

	Effect on demand for goods and services	
	Demand ratio (M€/MW)	Total effect (M€)
Direct demand (Const + Operation)	9.7	485
Indirect demand (Const + Operation)	8.9	445
Total increase in demand (Const + Operation)	18.6	930
	Effect on employment creation	
	Employment ratio (person years/MW)	Total employment (person years)
Direct employment (Const + Operation)	111	5,553.5
Indirect employment (Const + Operation)	81	4,030.2
Total employment	192	9,583.7

The associated multiplier effect is 1.92 which means that for every euro invested during the construction and operation phase of the plant, an aggregate demand of 1.92 euros is generated.

With respect to its effect on employment creation, the above mentioned increased demand for goods and services would generate 9,583.7 additional person years of employment (of which 5,553.5 and 4,030.2 are directly and indirectly created, respectively). This figure implies that for every 19.8 thousand € directly invested, one person year of employment is created.

Results: solar tower plant

With respect to the socio-economic impacts associated to the solar tower plant (Table 5.10), the total effect on the demand for goods and services amounts to 521.9 M€ which is equivalent to 30.7 M€/MW. Of this total effect, the indirect effect generated during the construction and operation phase accounts for 256 M€ and the total multiplier effect is 1.96.

With respect to the employment effect, during the construction and operation of the plant, 5,491 person years of employment would be created

Table 5.10 Total effect on the demand for goods and services as well as employment per MW of installed capacity for 17 MW solar tower power plant (TP)

	Effect on demand for goods and services	
	Demand ratio (M€/MW)	Total effect (M€)
Direct demand (Const + Operation)	15.7	266
Indirect demand (Const + Operation)	15	256
Total increase in demand (Const + Operation)	30.7	522
	Effect on employment creation	
	Employment ratio (person years/MW)	Total employment (person years)
Direct employment (Constr + Operation)	189	3,213
Indirect employment (Constr + Operation)	133	2,278
Total employment	322	5,491

(3,213 directly and 2,278 indirectly) implying that one new person year of employment is created for every 20.6 thousand euros directly invested.

Compliance with the PER objectives

Based on these individual plant results, the socio-economic impacts associated to the compliance with the Spanish Renewable Plan 2005–2010 (PER) were estimated. It was assumed that in order to meet the 2010 PER solar thermal installed capacity goal (500 MW installed capacity), 400 MW of parabolic trough plants (80% of the total power) would be installed, while the rest (20%) would be met with 100 MW of solar thermal tower plants. Furthermore, it was assumed that during the period under consideration, operation and investment costs would remain constant, an assumption supported by the literature (DLR, 2005; DLR *et al.*, 2005).

Results show that the total increase in the demand for goods and services generated as a result of compliance with the PER solar thermal goal would amount to 10,538 M€ (equivalent to an average of 21 M€/MW) (Table 5.11).

Table 5.11 Total effect on the demand for goods and services as well as employment per MW of installed capacity for 500 MW PER 2005–2010 solar thermal goal

	Effect on demand for goods and services	
	Demand ratio (M€/MW)	Total effect (M€)
Total increase in demand (Const + Operation)	21	10,538
	Effect on employment creation	
	Employment ratio (person years/MW)	Total employment (person years)
Total employment (Const + Operation)	218	108,992

Source: Ragwitz *et al.* (2009).

Total employment would amount to 108,992 person years of employment (63,485 direct jobs and 45,508 indirect jobs). Results show that the total effect on the demand for goods and services would amount to 10,538 MW which is equivalent to an average of 21.1 M€ for every MW installed. With respect to the effect on the job creation, total direct employment generated would be 63,485 person years while the indirect employment generated would reach 45,508.

Although results should be interpreted with caution due to the methodological limitations of the input–output methodology, it can be concluded that the socio-economic benefits derived from the accomplishment of the PER's solar thermal installed capacity in Spain would be remarkable, both in terms of increased demand for goods and services as well as employment creation.

While few studies have specifically analysed the impact of CSP technologies on employment (Caldés *et al.*, 2009; de la Rúa, 2009), there exist other reports that simultaneously estimate the employment impact derived from the deployment of various renewable energy technologies at the national level (GFME, 2006; Hillebrand *et al.*, 2006; APPA/Deloitte Consulting, 2009). At the European level, it is worth mentioning the work by Whitely *et al.* (2004) and Ragwitz *et al.* (2009). The latter is one of the most comprehensive studies in this area since it estimates the gross and net effect

Table 5.12 EU economic and employment impact of RES deployment in 2005

		Direct impact	Indirect impact	Total impact
Gross value added	bin. €2,000	31.9	26.4	58.3
Employment	min. employees	0.8	0.6	1.4
Employment in SME	min. employees	0.5	0.4	0.9
Employment in agriculture/ forestry	min. employees			0.2
Relative impacts:				
Gross value added compared to total GDP		0.32%		0.58%
Employment compared to total employment		0.36%		0.64%

Source: Ragwitz *et al.* (2009).

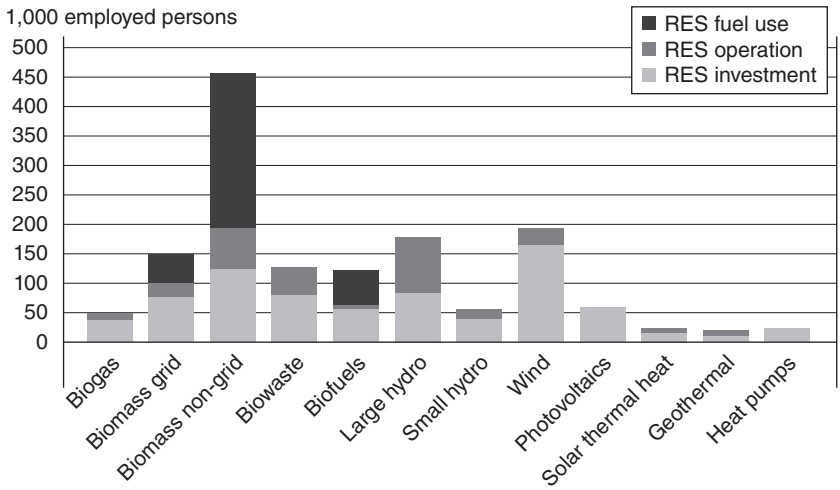

5.5 EU economic and employment impact of RES deployment in 2005 (source: Ragwitz *et al.*, 2009).

that the different renewable energy (RE) technologies have on both employment generation as well as on the economy at the EU-27 level in 2005 and under two different future RE deployment scenarios (see Table 5.12 and Fig. 5.5).

5.4 Future trends

The role of solar technologies in a future energy supply system remains uncertain but, according to various experts, due to the expected future

technology innovation and developments, it indeed looks promising (Nuño, 2008). With regard to CSP, and according to various experts, over the next 50 years, constructions, functional surfaces, mirrors, heat transfer media and systems design will be greatly optimized in regard to costs, efficiency and environmental impact. It is expected that part of the cost reduction potential and efficiency increase should be realized by R&D, scale effects and volume effects (Viebahn *et al.*, 2008).

5.4.1 Projections of environmental impacts

The evolution of the GHG and other emissions over time is evaluated in the work performed in the NEEDS project. When assessing the emissions of future configurations of CSP power plants, a clear reduction is observed showing an 'environmental learning' of the technology (see Fig. 5.6). The three development scenarios, very optimistic, optimistic-realistic and pessimistic, refer to different assumptions on the anticipated penetration of the technology into the energy market, reaching an installed capacity in 2050 of 1,000 GW, 405 GW and 120 GW, respectively. In these scenarios the prevailing CSP technology differs. Greenhouse gas emissions show a large reduction throughout the scenario development. The reason is the reduction of salt used in the different storage systems. Concrete storage or PCM storage-based power plants perform better than the current molten salt-based ones. The results show a continuous optimization from the 'pessimistic' to the 'very optimistic' scenario as well as over time.

5.4.2 Projections of socio-economic impacts

As explained previously, some of the most relevant CSP socio-economic impacts include their potential to stimulate the local or national economy by increasing the demand for goods and services as well as to generate new jobs. The magnitude of such effects will greatly depend on the future evolution and characterization of CSP's costs as well as on the location and labour intensity of such investments.

With regard to the 2050 CSP cost development target, several studies and models expect to reach 4–5 ct/KWh for base load, 5–8 ct/KWh for mid-load and more than 10 ct/KWh for pure peak load. Various factors affect future evolution of the resulting levelized cost of energy (LCOE), which is the most important determinant of the assumed development of the specific investment costs for new plants. This value comprises the assumptions about cost reduction due to technical learning, scale-up and volume effects (Viebahn *et al.*, 2008). Nevertheless, according to the European Solar Thermal Electricity Association (ESTELA), only a moderate reduction of LCOE can be expected due to high increase of raw materials such as steel and concrete.

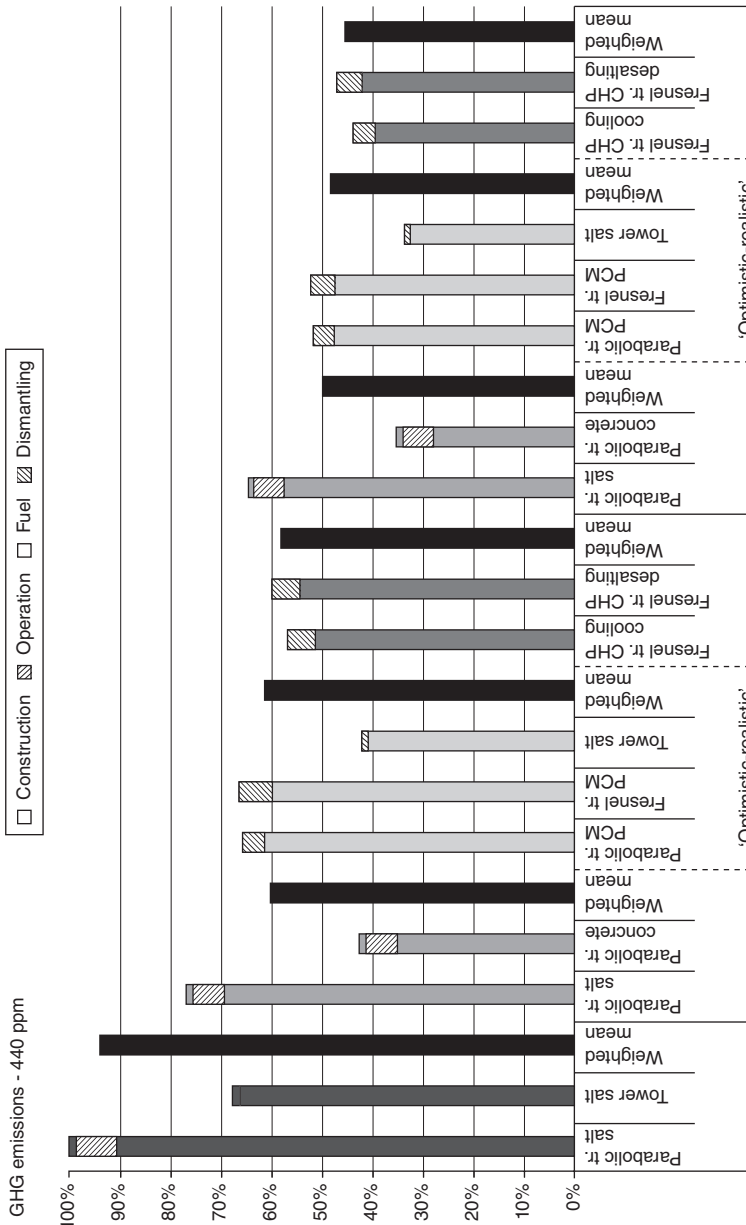

5.6 Evolution of the GHG emissions of CSP technologies (source: Viebahn *et al.*, 2008).

Table 5.13 CSP investment cost projections

	'Today'	2020	2025	2030	2040	2050
NEEDS (Viebahn *et al.*, 2008)						
Global cumulated capacity (GW)	0.4		63			405
Investment costs in € 2005/kW	5,300		3,720			2,770
Energy Technology Perspectives (Blue scenario) (International Energy Agency, 2008)						
Global cumulated capacity (GW)				250		630
Investment costs in € 2005/kW	3,620					
Energy Revolution (Greenpeace International/European Renewable Energy Council, 2008)						
Global cumulated capacity (GW)						
Investment costs in € 2005/kW	6,000	4,170		3,530	3,480	3,440
Leitstudie (BMU, 2008)						
Investment costs in € 2005/kW		3,600		3,300	3,200	3,100

Source: German Federal Environmental Agency (2009).

With regard to CSP investment cost projections, a recent study by the German Federal Environmental Agency (2009) made a comparison of four cost projections derived from various energy scenarios (see Table 5.13). Despite the future LCOE, cost decline will be responsible for lower socio-economic impacts by MW, the overall contribution to the economy and employment will grow due to the expected installed capacity increase.

According to the four studied future energy scenarios, the investment cost evolution is promising. However, as highlighted by the German Federal Environmental Agency, a number of aspects should be take into account. In the first place, thermal storage system is a key aspect which greatly affects investment costs, not only due to the direct costs for the thermal storage itself, but also because of the effects on the overall power plant configuration (i.e. larger collector field). However, one must take into account that while storage increases cost per installed kW, the capacity factor goes up and the associated LCOE could be lower. Secondly, it is important to highlight the fact that given the limited number of CSP commercial power plants currently in operation, the analysed studies present learning curves which are not based on historical data but rather apply the concept of learning curves and an assumed learning curve (German Federal Environmental Agency, 2009).

5.4.3 Location of future CSP plants

As previously stated, one of the advantages of CSP technologies is that they take advantage of an inexhaustible resource which is widely abundant in

various developed and developing countries around the world (Viebahn *et al.*, 2008). Given their high solar radiation, various countries are expected to invest in new CSP capacity in the future. The most promising regions include: Southeast of the United States, Central and South America, Africa, Middle East, European countries along the Mediterranean, Iran, Pakistan and the desert areas of India, as well as the former USSR, China and Australia (Aringhoff *et al.*, 2005).

Consequently, materializing the deployment of CSP technologies in these countries, and in particular in least developed countries, could represent a unique opportunity to promote their development by creating new employment opportunities as well as by stimulating the national economy.

5.5 Summary and conclusions

While there exists a vast literature regarding current and future CSP technological aspects, literature that focuses on CSP's environmental and socio-economic assessments is relatively scarce. It is expected that in the near future this knowledge gap will be reduced since both socio-economic and environmental factors are going to play a key role in determining future energy scenarios and therefore in promoting CSP deployment at the global level. In order to improve the competitiveness of renewable energy technologies in the energy market, it is required that support policies take into account both their environmental and socio-economic benefits.

This chapter has reviewed the existing LCA and external costs studies on CSP technologies. Values of global warming emissions in solar only operation reported in the literature range from 11 g/kWh to 60 g/kWh and from 12 g/kWh to 90 g/kWh for central tower and parabolic troughs, respectively. These emissions are well below the emissions produced by conventional electricity generation sources. With regard to acidification and eutrophization impacts, CSP systems also show clear benefits. Results of the external costs assessment of CSP plants are around 0.2 cEuro/kWh, well below those of other competing electricity generation technologies.

The current and future estimated socio-economic impacts of CSP technologies are not negligible. Compared to conventional fossil fuel technologies, the impact of the deployment of CSP technologies on the national and local economy as well as on employment can be remarkable. This is particularly the case for countries such as Spain where its favourable climatic conditions and support policies have generated an upsurge in CSP projects. By conducting an input–output analysis, the work presented in this chapter has attempted to first estimate the direct and indirect socio-economic impacts associated with the construction as well as O&M phases of two individual solar thermal power plants – a 50 MW parabolic trough plant and a 17 MW tower plant. Based on the former results, the Spanish Plan

de Energías Renovables (PER 2005–2010), the associated socio-economic impacts (which states that by 2010 solar thermal installed capacity should reach 500 MW) have been estimated. Results show that the total effect on the demand for goods and services would amount to 10,538 M€ which is equivalent to €21.1 million for every installed MW. With respect to its effect on employment, 108,992 new jobs would be created.

5.6 References

Anthoff, D. (2007) *Report on marginal external costs inventory of greenhouse gas emissions*. NEEDS Deliverable D5.2, RS1b.

APPA/Deloitte Consulting (2009) *Impacto macroeconómico de las energías renovables en España.*

Aringhoff, R., G. Brakmann, M. Geyer and S. Teske (2005) *Concentrated Solar Thermal Power Now*. ESTELA/IEA SolarPACES/Greenpeace.

BMU (2008) *Leitstudie 2008: Weiterentwicklung der 'Ausbaustrategie Erneuerbare Energien' vor dem Hintergrund der aktuellen Klimaschutzziele Deutschlands und Europas.* Federal Ministry for the Environment, Nature Conservation and Nuclear Safety, Berlin.

Burkhardt, J., G. Heath and C. Turchi (2010) Life Cycle Assessment of a Parabolic Trough Concentrating Solar Power Plant. NREL. Available at: http://www.lcacenter.org/LCAX/presentations-final/121.pdf

Caldés, N., M. Santamaría, M. Varela and R. Sáez (2009) Economic impact of solar thermal electricity deployment in Spain. *Energy Policy* 37, 1628–1636.

Carter, N. and R. Campbell (2009) *Water Issues of Concentrating Solar Power (CSP) Electricity in the U.S. South West*. Congressional Research Service.

DLR (2005) MED-CSP Concentrating Solar Power for the Mediterranean Region–Executive Summary. Available at: www.dlr.de/tt/med-csp (accessed March 2010).

DLR *et al.* (2005) *ECOSTAR European Concentrated Solar Thermal Road Mapping.* SES6-C6-2003-502578. Edited by R. Pitz-Paal, J. Dersch and B. Milow.

de la Rúa, C. (2009) *Desarrollo de la herramienta integrada 'Análisis de ciclo de vida-input output' para España y aplicación a tecnologías energéticas avanzadas*, PhD Thesis, Universidad Politécnica de Madrid.

EC (2005) ExternE, Externalities of Energy. Methodology 2005 Update. EUR 21951.

Ecoinvent (2007) Swiss Centre for Life Cycle Inventories (Ecoinvent Centre). Ecoinvent Database. Ecoinvent Centre, Dübendorf, 2004 and 2007. Available at: http://www. ecoinvent.org (accessed March 2010).

Fernández-García, A., E. Zarza, L. Valenzuela and M. Pérez (2010) Parabolic-trough solar collectors and their applications. *Renewable and Sustainable Energy Reviews* 14, 1695–1721.

Finnveden, G., M. Z. Hauschild, T. Ekvall, J. Guinée, R. Heijungs, S. Hellweg, A. Koehler, D. Pennington and S. Suh (2009) Recent developments in life cycle assessment. *Journal of Environmental Management* 91, 1–21.

Frankl, P., E. Menichetti and M. Raugei with contributions by S. Lombardelli and G. Prennushi (2006) NEEDS. New Energy Externalities Developments for Sustainability Deliverable 11.2 – RS 1a 'Final report on technical data, costs and life cycle inventories of PV applications'.

German Federal Environmental Agency (2009) *Role and Potential of Renewable Energy and Energy Efficiency for Global Energy Supply*.

GFME (German Federal Ministry for the Environment) (2006) Nature conservation and nuclear safety. Renewable energy: employment effects. Impact of the Expansion of Renewable Energy on the German Labour Market. Summary.

Greenpeace International/European Renewable Energy Council (2008) *Energy Revolution. A Sustainable Global Energy Outlook.*

Guinée, J. B., M. Gorrée, R. Heijungs, G. Huppes, R. Kleijn, A. de Koning, L. van Oers, A. Wegener Sleeswijk, S. Suh, H.A. Udo de Haes, H. de Bruijn, R. van Duin and M.A.J. Huijbregts (2002) *Handbook on Life cycle Assessment – Operational guide to the ISO standards. I: LCA in perspective. IIa: Guide. IIb: Operational annex. III: Scientific background*. Kluwer Academic Publishers, Dordrecht.

Hendrickson, C. T., L. B. Lave, *et al.* (2006) *Environmental Life-Cycle Assessment of Goods and Services: An input-output approach*. Resources for the Future, Washington, DC.

Hillebrand, H., G. Buttermann, J.M. Behringera and M. Bleuel (2006) The expansion of renewable energies and employment effects in Germany. *Energy Policy* 34, 3484–3494.

Holland D. and S. Cooke (1992) Sources of structural change in the Washington economy: an input–output perspective. *Annals of Regional Science* 26, 155–170.

INE (Instituto Nacional de Estadísticas) (2006) Available at www.ine.es. (accessed March, 2010).

International Energy Agency (1998) *Benign Energy? The Environmental Implications of Renewables.* IEA, Paris.

International Energy Agency (2008) *Energy Technology Perspectives 2008 – Scenarios and Strategies to 2050.* IEA, Paris.

ISO (2006a) ISO 14040:2006. *Environmental management: Life cycle assessment – principles and framework*.

ISO (2006b) ISO 14044:2006. *Environmental management: Life cycle assessment – requirements and guidelines.*

JRC IES (2010) *ILCD Handbook, General Guide for Life Cycle Assessment – Detailed Guide*. Luxembourg: Publications Office of the European Union.

Kreith, F., P. Norton and D. Brown (1990) A comparison of CO_2 emissions from fossil and solar power plants in the United States. *Energy* 15, 1181–1198.

Kulstic, B., R. Loizou and V. Segon (2007) Impact of biodiesel production on Croatian economy. *Energy Policy* 35(12), 6036–6045.

Lanier, J., S. Bernow and J. Decicco (1998) Employment and other macroeconomic benefits of an innovation-led climate strategy for the United States, *Energy Policy* 25(5), 425–433.

Lantz, E. and S. Tegen (2009) *NREL response to the report 'Study on the effects on employment of public aid to Renewable Energy Sources' from King Juan Carlos University (Spain)*, White Paper, NREL/TP 6A2-46261.

Lecointe, C., D. Lecarpentier, V. Maupu, D. Le Boulch and R. Richard (2007) NEEDS. New Energy Externalities Developments for Sustainability. D 14.2 – RS 1a 'Final report on technical data, costs and life cycle inventories of nuclear power plants'.

Lechón, Y., C. de la Rúa and R.M. Sáez (2008) Life cycle environmental impacts of electricity production by solar thermal power plants in Spain. *Journal of Solar Energy Engineering* 130, 021012-1–021012-7.

Lenzen, M. (1999) Greenhouse gas analysis of solar-thermal electricity generation. *Solar Energy* 65(6), 353–368.

Leontief, W. (1966) *Input–Output Economics.* New York: Oxford University Press.

Leontief, W. (1986) *Input–Output Economics*, 2nd edn. New York: Oxford University Press.

Linares P., J. Leal and R. Sáez (1996) *Evaluación de las externalidades de la biomasa para producción eléctrica.* Documentos CIEMAT.

Norton, B. and W. R. Lawson (1996) *Full Energy Chain Analysis of Greenhouse Gas Emissions for Solar Thermal Electric Power Generation Systems*, Vienna: IAEA.

Nuño, F. (2008) Bulk Solar Power Generation: CSP and CPV technologies. Cooper Institute. Available at: www.leonardo-energy.org (accessed March 2010).

Pehnt, M. (2006) Dynamic life cycle assessment (LCA) of renewable energy technologies. *Renewable Energy* 31, 55–71.

Preiss, P. and R. Friedrich (2009) *NEEDS Technical paper 2° 7.2 – RS 1b 'Report on the application of the tools for innovative energy technologies*'.

Ragwitz, M., W. Schade, B. Breitschopft, R. Walz and N. Helfrich (2009) *EmployRES: The impact of renewable energy policy on economic growth and employment in the EU.* Karlsruhe: Fraunfofer ISI.

Röder A. (1997) Vergleich regenerativer Energiesysteme bez-u¨glich Kosten, Treibhausgasemissionen, Ressourcenver-Press, Cambridge. brauch. Report No. TM-51-97-04, Paul-Scherrer-Institut, as cited in Lenzen (1999).

Tegen S. (2006) *Comparing Statewide Economic Impacts of New Generation from Wind, Coal and Natural Gas in Arizona, Colorado and Michigan*, NREL/tp-200-37720.

Ten Raa T. (2005) *The Economics of Input–output Analysis*. Cambridge: Cambridge University Press.

Udo de Haes, H.A., G. Finnveden, M. Goekoop, M. Hauschild, E.G. Hertwich, P. Hofstetter, O. Jolliet, W. Klopffer, W. Krewitt, E. Lindeijer, R. Müller-Wenk, S.I. Olsen, D.W. Pennington, J. Potting and B. Steen (2002) *Life Cycle Impact Assessment: Striving towards best practice*. SETAC.

Vant-Hull, L.L. (1992) Solar thermal electricity: an environmental benign and viable alternative. *Perspectives in Energy* 2, 157–166.

Viebahn, P. (2003) *SOKRATES – Projekt, Solarthermische Kraftwerkestechnologies für den Schutz des Erdkimas, A. P.2.2.*

Viebahn, P. (2004) *INDITEP, Integration of DSG Technology for Electricity Production, WP 4.3, Impact Assessment, Life Cycle Assessment of Construction Materials, Energy Demand and Emissions of DSG*, Final Report.

Viebahn, P., S. Kronshage, F. Trieb and Y. Lechón (2008) *NEEDS Project 'Final report on technical data, costs, and life cycle inventories of solar thermal power plants' Deliverable 12.2 – RS 1a.*

Weinrebe, G., M. Böhnke and F. Trieb (1998) Life cycle assessment of an 80 MW SEGs plant and a 30 MW Phoebus power tower. *Proc. Int. Solar Energy Cont.*, ASME.

Whitely, M., A. Zervos, M. Timmer and F. Butera (2004) *Meeting the targets and putting renewables to work. Overview Report for MITRE Project, ALTENER Programme*. Directorate General for Energy and Transport.

6

Linear Fresnel reflector (LFR) technology

D. R. MILLS, formerly Ausra Inc., Australia

Abstract: A single-axis linear Fresnel reflector (LFR) system is composed of many long row reflectors that together focus sunlight images that overlap on an elevated linear tower receiver running parallel to the reflector rotational tracking axis. This allows a large size array to be constructed inexpensively using very similar or identical long focal length (and therefore almost flat) glass mirror elements. The chapter reviews the historical and recent technical development of LFR technology. Thermal performance trade-offs and future trends are also examined.

Key words: Linear Fresnel reflector (LFR), linear Fresnel, concentrating solar thermal (CST), concentrating solar power (CSP), solar thermal electricity (STE), solar concentrators.

6.1 Introduction

Historically, most solar thermal electricity systems have used large continuous curvature parabolic troughs. Geometrically, the ideal reflectors to use with single receivers of solar energy are continuous reflectors of parabolic or paraboloidal shape. However, at large scale, these become unwieldy and may require extensive structures to withstand wind loadings. Operations and maintenance (O&M) for large mirrors can also become a problem, since such structures can be much taller than maintenance staff, who then may require tall vehicles or cranes to perform routine cleaning and maintenance.

Large reflectors can be simulated by small reflector elements distributed over some suitable (ground or roof) surface. This allows large concentrator systems to be built up from small elements, avoiding the large structures and cleaning accessibility problems associated with very large reflectors. Linear Fresnel reflector (LFR) solar mirrors are analogues of the parabolic trough mirror, just as central receiver heliostats are analogues of parabolic dish collectors (Fig. 6.1).

Today's usual single-axis tracking LFR differs from a parabolic trough in that the reflector is composed of many long row segments which focus collectively on an elevated long linear tower receiver running parallel to the reflector rotational axis (Figs 6.1 and 6.2). Unlike parabolic troughs, the LFR receiver is fixed in space, and the reflectors rotate to maintain focus

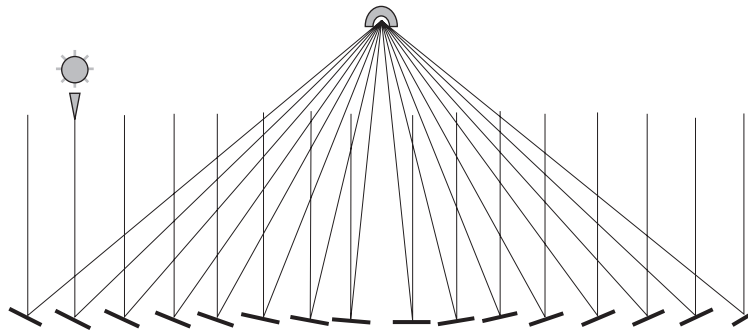

6.1 Basic linear Fresnel reflector configuration seen from one end. The individual reflectors each track the sun by turning about a horizontal axis normal to the page.

on the fixed receiver. The reflector rows all track through the same number of degrees during the day as the sun moves but are inclined at different angles at any one time because they have different positions relative to the tower target. This allows a very large basic unit made up of identical relatively small reflectors of long focal length, which in turn leads to the ability to use almost flat, lower cost glass mirror elements.

The LFR approach to concentrating solar power (CSP) is less commercially mature than trough systems. The field is best examined by looking at the specific activities of the current major commercial initiatives: Areva Solar, Novatec Solar, Solar Power Group and the smaller process heat Industrial Solar company. This chapter reviews the historical development of LFR technology and then examines the business and technical development history of these players. Thermal performance issues and future trends are also presented.

6.2 Historical background

Linear Fresnel reflector solar collector systems are called 'Fresnel' reflectors after the great French optical physicist Augustin-Jean Fresnel, who in about 1818 discovered that the effect of large lenses can be duplicated using many small lens components. However, he was long preceded by the famous polymath Georges-Louis Leclerc, Comte de Buffon. Buffon had previously performed experiments in 1746 with the first solar heliostat-like reflectors (Buffon, 1830), which were manually tracked heliostats similar to those in modern solar central receiver towers (Fig. 6.2), fashioned out of many pieces of flat glass installed at slight angles to form a distant focus. Buffon demonstrated on many occasions that such reflectors would ignite wood and melt metal. Given the precedence of Buffon and the solar ancestry,

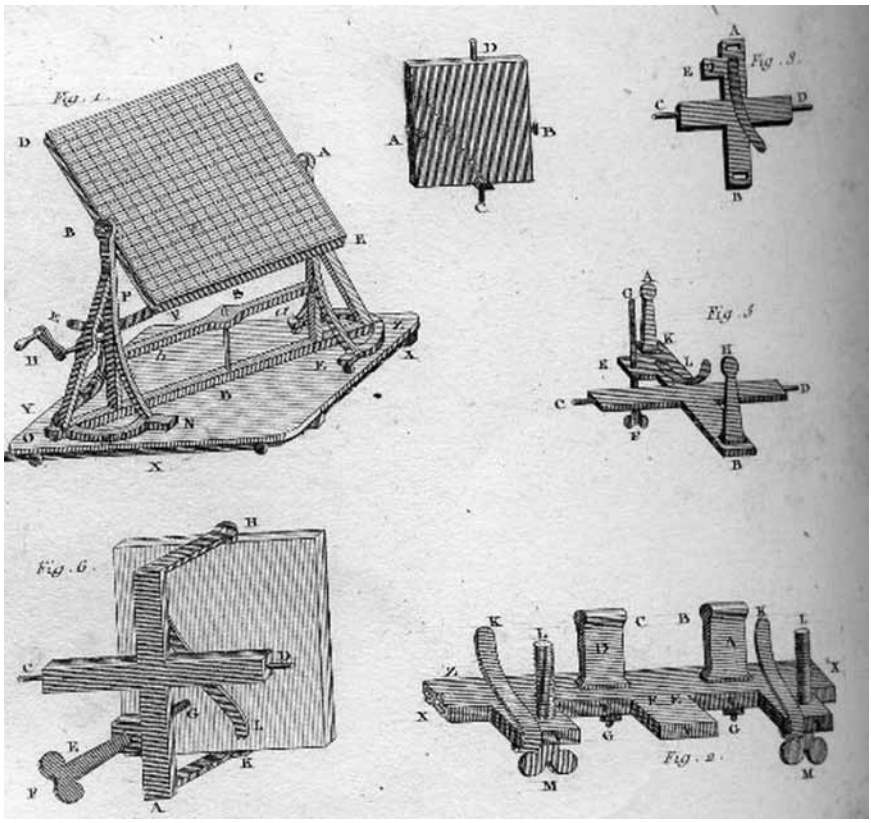

6.2 View of an early heliostat used for experiments by Buffon, who used many small flat glass mirrors to form a single image in 1746.

Fresnel solar reflector systems might more justly have been called 'Linear Buffon' reflector systems, but the Fresnel name is now too established. Buffon's heliostats, however, were not single-axis tracking systems, but two-axis.

The first person in modern times to apply this principle in a reasonably large system for solar collection was the Italian solar pioneer Giovanni Francia (Francia, 1968) who developed both linear and two-axis tracking Fresnel reflector systems, and was thus the father of both LFR and central tower systems. Figure 6.3 shows his first prototype array from 1961, built in Marseille. His papers provided little in terms of theory or detailed efficiency results, but showed that elevated temperatures could be reached using such systems.

In the 1970s Francia worked in the United States primarily on central receiver power tower systems, but continued to maintain an interest in

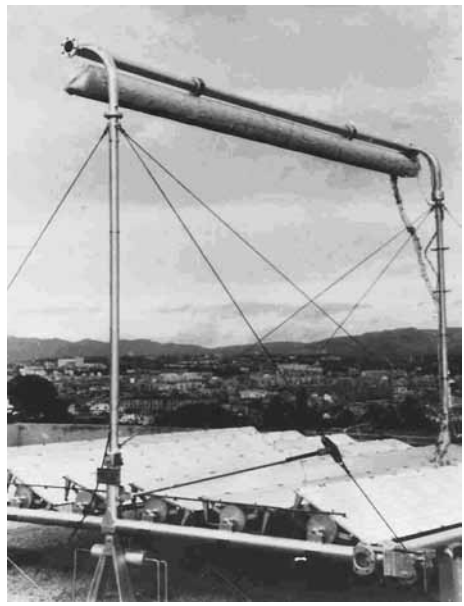

6.3 The first LFR prototype set up in Marseille by Francia in 1961 (Francia, 1968) (reproduced with permission from Elsevier).

linear systems and Fig. 6.4 shows a drawing from an Ansaldo/Cesen brochure from about the time of his death in 1980 with his impressions of a future LFR plant, which show a remarkable similarity to the initial three-line, ten reflector per tower Kimberlina plant built by Ausra Inc. (now Areva Solar) in California in 2008.

At least three other LFR systems were under development in the 1970s after the oil shock in 1973. The first was designed by Suntech (no relation to the current PV manufacturer) and consisted of ten long slightly curved reflector mirrors 6.1×0.3 m, yielding a concentration factor of 40 times. In a 1970s report, it is mentioned that Sheldahl received a government contract to develop the concept (USOTA, 1978), but nothing further is known about the project.

A second design, called 'Itek', is shown in Fig. 6.5. This used seven reflectors and a cylindrical glass receiver containing a restricted aperture, an absorber pipe and insulation. This was evaluated in 1979 by Shaner and Duff (1979), who decided that trough collectors had superior performance.

A third and major effort was described by Di Canio *et al.* (1979) of the FMC Corporation, who produced a detailed project design study in 1979 for a linear plant of between 10 MW(e) and 100 MW(e), with a mirror field on one side of a 1.68 km linear cavity absorber mounted on 61 m high

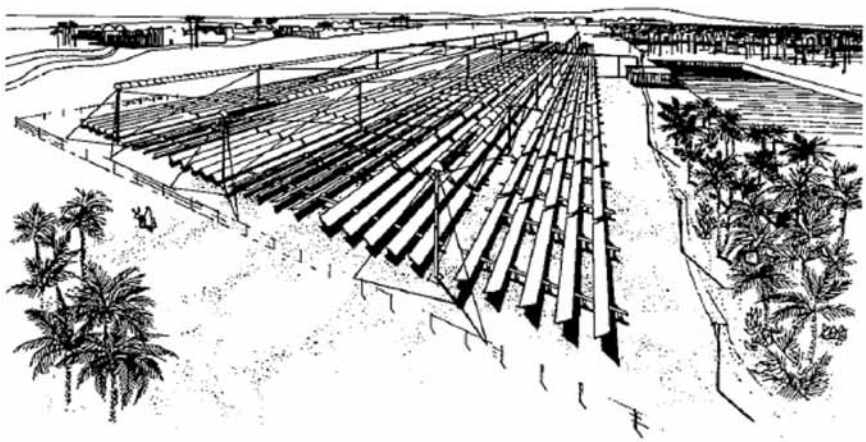

6.4 Sketch of a LFR solar plant in a desert environment (courtesy of Cesare Silvi, Italian Group for the History of Solar Energy (GSES) and the Italian Committee 'The History of Solar Energy' (CONASES)).

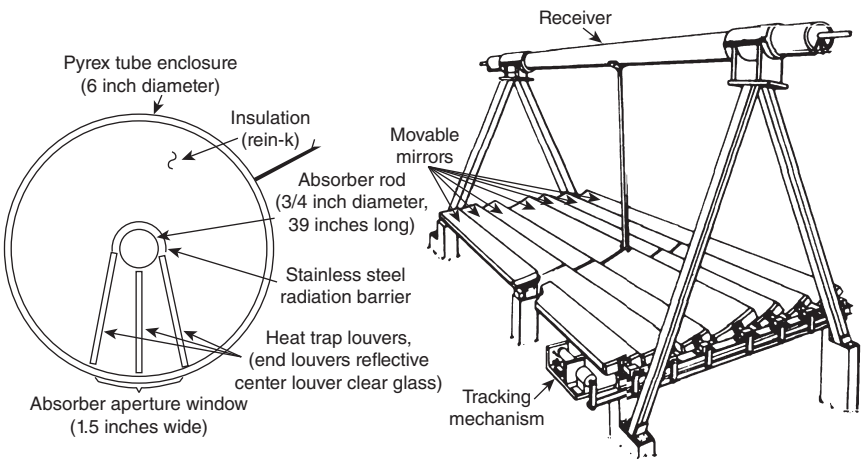

6.5 The Itek LFR concept from the 1970s (USOTA, 1978).

towers adapted from transmission towers. Funding was cancelled just as initial absorber testing was underway. Unusually, the FMC design was an east-west axis plant and had an aperture cover that could open and close to retain heat when the sun was not available.

During the developmental flurry of the 1970s, substantial advances were made in the areas of spectrally selective absorbers and secondary concentrators, both of which act to alleviate thermal losses from these linear designs. These were probably the major area where these early LFR systems

suffered most in the 1970s when compared with higher cost central receivers or trough systems. There is no doubt that there is a link back to the early experiments of Francia, the founder of this technical area. Experiments were begun in the USA in the 1970s during Francia's time spent there, but after the election of the Reagan Administration, LFR fortunes, along with CSP generally, fell and interest in LFR technology moved elsewhere.

A new effort to produce a tracking linear Fresnel reflector was made by the Israeli company Paz which began design work in 1986 and was later assisted by the Jacob Blaustein Institute at Sede Boqer (Feuermann and Gordon, 1991; Feuermann, 1993) in southern Israel. Jeff Gordon had worked with Ari Rabl and Roland Winston, who had published an early paper on secondary concentrators (Winston and Rabl, 1976) to increase radiation concentration on a receiver illuminated by a primary mirror. Intended for 150°C operation, the Paz technology used a secondary concentrator somewhat related to the compound parabolic concentrators first proposed by Winston and Rabl together with an evacuated tube receiver. Rows of mirrors were linked together for tracking, and the problems with linkages, non-parallel mirrors and eccentric mirror mountings led to a beam uncertainty of more than 2°. Unfortunately, the array exhibited aberration difficulties caused by the movement of reflectors around an axis parallel to, but displaced from, the reflector optical axis. Performance was less than 50% of that predicted, but the researchers' report provided valuable practical lessons for later workers. It was the first to use non-imaging optical theory to design a secondary reflector near the receiver to increase concentration, and the first LFR to use an evacuated tube. No photos were available of the installation but the author of this chapter recalls seeing it in the mid 1990s. Figure 6.6 is created from drawings in Feuermann and Gordon (1991).

Before 1993, the LFR concept had each field of reflectors directed to a single tower. However, if one assumes that the size of the field will be large, as it must be in technology supplying electricity in the multi-megawatt class, it is reasonable to assume that there will be many towers in the system. If they are close enough, then some of the field reflectors will have the option of directing reflected solar radiation to at least two towers rather than just one. Development began on an Australian design at the University of Sydney in 1993, in which a single field of reflectors could use multiple linear receivers by allowing reflectors to change their focal point from one receiver to another during the day in order to minimize shading in the dense reflector field. This additional variable in reflector orientation provides the means for much more densely packed arrays, because patterns of alternating reflector orientation can be set up such that closely packed reflectors can be positioned without shading and blocking. The interleaving of mirrors between two receiving towers is shown in Fig. 6.7. The arrangement mini-

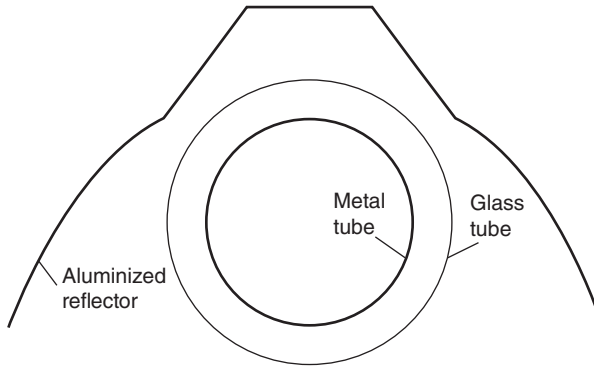

6.6 Drawing of the Paz LFR reflector and tube adapted from Feuermann and Gordon (1991), reproduced with permission.

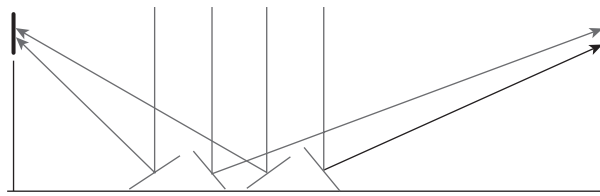

6.7 Early 1990s diagram by the author of a CLFR showing interleaving of mirrors minimizing shading between mirrors.

mizes beam blocking by adjacent reflectors and allows high reflector densities and low absorber tower heights to be used.

The proposed systems were called compact linear Fresnel reflector (CLFR) systems and their mirrors occupy an area approximately 70% of the ground area spanned, compared with about 33% for trough fields. The original CLFR concept was developed with the use of vertically mounted evacuated tube receivers in mind (Mills, 1995a), later also described in a paper in 1999 (Mills and Morrison, 1999), but both these and inverted cavity receivers were anticipated in the original patent (Mills, 1995b).

The CLFR was first developed in ignorance of previous LFR work. It was conceived of as a multiple line technology from the start, emerging from a study of minimum reflector area for light capture. However, the previous work of Francia soon came to light. Later, the Israeli LFR work came to the attention of David Mills, leader of the University of Sydney effort, in 1994 and Feuermann kindly supplied Mills with a detailed laboratory report. Although not a CLFR project, the Paz project work provided the University of Sydney with useful heliostat design information, especially approaches that did not work well, and this helped define the direction of field design of the later projects.

Although a specialist in both non-imaging optics and evacuated tubes, Mills felt that the hurdles of secondary reflector degradation under high solar flux, loss of optical efficiency in the secondary reflector (>10% in the reflectors available at the time) and the high cost of parabolic trough-type evacuated tubes were serious practical issues. It was decided not to use a secondary reflector, and instead use a receiver composed either of an array of proven small low-cost evacuated tubes as developed by the University of Sydney, or a simple non-evacuated absorber composed of steel tubes with selective paint. This was an important decision which ultimately led to Areva/Ausra technology differing from other designs 10–15 years later.

However, the university would not protect the technology, so ownership of the intellectual property (IP) was re-sold to Mills, and further IP filings and modelling development were undertaken through Solsearch Pty Ltd, a company created by Mills and Graham Morrison of the University of New South Wales. A second CLFR patent covering fully ganged reflector systems was filed in 1997, but the main research effort was directed at systems without linked rows because of mechanical issues with linkages. Solar industry partner Solahart also assisted by designing a four-mirror heliostat (Fig. 6.8). After the Kyoto climate meeting, interest increased in CLFR within the Australian utility industry. Austa Energy in Queensland (not to be confused with the later Ausra LFR company) agreed to develop a 4 MW(e) CLFR plant with Solsearch under a grant from the Australian Greenhouse Renewable Energy Showcase scheme in 1999. The project sought to supply an existing coal-fired plant called Stanwell with extra energy. Mills and Chris Dey presented a conceptual work on supplementation of coal-fired plants with LFR technology (Mills and Dey, 1999); nowadays these are called 'solar booster plants' and have become an emerging solar market sector.

6.8 LFR test rig built by Solahart for the University of Sydney test programme comparing evacuated and non-evacuated absorbers (supplied by the author).

6.9 Ray trace illustration of a CLFR array with multiple cavity receivers in late 1990s (with thanks to University of Sydney School of Architecture).

By 1999, the Austa/Solsearch project group were actively developing a cavity receiver design after concluding Solsearch funded experiments at the University of Sydney, comparing evacuated tubes against side-by-side blackened steel boiler tubes in a cavity receiver. Single vacuum absorber tubes were too small to be used as an entire absorber, and multiple small vacuum tubes exhibited large optical losses in the gaps between the cover glass and absorber that brought performance down below the cavity (Dey *et al.*, 2000). New collector designs based on using downward-facing cavity receivers were researched (Fig. 6.9) and visualized, and flow modelling was undertaken (Reynolds *et al.*, 2001). The receiver was envisaged as an inverted, trapezoidal, linear cavity receiver with a window at the base of the cavity that was larger than the receiver. The insulated cavity was trapezoidal to allow concentrated light from the reflector field to strike the absorber directly without incurring an optical loss in a secondary reflector. The 'window' had a transmissivity of 0.95 at solar wavelengths. The absorber was envisaged as either a flat plate attached to tubes or tubes bonded together. In addition, an initial heliostat prototype was developed by the industrial collaborator, Solahart (Fig. 6.10). This had a 'backbone and rib' structure.

In 1993, Belgian investors bought the bankrupted Luz technology assets for trough collectors and evacuated tubes. They created two companies, Solel Israel and Solel Europe, based in Belgium. In 1994, these investors entered into a commercial in-confidence agreement with the University of Sydney regarding the early CLFR technology. Concepts such as nylon gears running flat mirrors with torque tubes, long single one-ended steam receiver pipes with internal water feed tubes, and non-imaging CPC-type secondary reflectors without vacuum receivers were all discussed in confidence at the

6.10 Prototype backbone and rib heliostat produced by Solahart in Perth in 1999 for the project (courtesy of Solahart Pty Ltd).

time, but the joint venture was discontinued by the university when Solel Europe became insolvent in 1995. A detailed 'recipe' for the revolutionary evacuated tube double cermet solar selective absorber coatings (Zhang and Mills, 1992) by the University of Sydney was passed in confidence to Solel Israel about two years ahead of the announcement of the UVAC2 receiver in 1997. Israeli staff stated to the author they had been close to patenting a similar surface when the Sydney University patent was filed in 1991. The university selective surface coating is now used on a very large scale in China for evacuated tube hot water heaters.

In 1998, one of the former owners of Solel Europe co-founded the Solarmundo company using private funds from Spain (Manuel Sureda) and Belgium (Count de Lalaing). By 2001 Solarmundo had built a 2,400 m^2 prototype collector field of the LFR type at Liège in Belgium (see Fig. 6.18). Delays in the Australian project due to the breakup of the Queensland state utility, Austa Energy, ensured that the Solarmundo array became the first project of any size to be demonstrated since the work of Paz a decade earlier, and it was the largest LFR array ever built up to that time. While the prototype used some concepts discussed in Sydney in 1994/5, 'mirror flipping' was not used, so it was not a CLFR.

The following sections follow the four major commercial initiatives currently offering LFR systems. Names of all participants have changed, so the current company name is used to head the sections with the previous names in parentheses. It is important to note that the assessment of any particular system is based on the published data available. Comparisons are sometimes difficult to make without access to what continues to be proprietary commercial information. Where it has been necessary to make any assumptions in assessing a particular system, these have been clearly stated so that readers can reach their own conclusions. Where there is insufficient published data available on a system to make an assessment, it has not been discussed in this chapter.

6.11 First sketch of the SHP design from early 2002 (courtesy of P. Le Lièvre).

6.3 Areva Solar (formerly Ausra, Solar Heat and Power)

In late 2001, Mills, Morrison and Peter Le Lièvre formed a new company in Sydney called Solar Heat and Power (SHP). Previous IP from Solsearch and the University of Sydney efforts was taken over by the new company. Le Lièvre designed a support structure for the reflectors based upon a space frame concept that is still used by Areva Solar today.[1] He also worked with the other company founders to develop the remainder of the design, which was built upon Solsearch know-how and IP. Figure 6.11 shows a sketch of the first small array that was planned at the time.

In keeping with the Solsearch design philosophy, secondary reflectors were not used, partly to avoid losses in optical efficiency in mirror absorption, and partly to avoid rapid degradation of the reflector surfaces under high heat loading. A new tracking design using low-cost drive hoops was chosen to turn the reflectors. The previous Solsearch/University of Sydney work had proposed trapezoidal receivers with welded or thermally connected steel tubes, but the new SHP design separated the tubes in the receiver, allowing differential thermal expansion between tubes at slightly different temperatures. This was analysed for thermal convective and radiation losses in a paper by Pye *et al.* (2003). Figure 6.12 shows a schematic diagram from the paper representing a trapezoidal receiver.

In 2003, an agreement with Macquarie Generation in New South Wales was concluded to develop the technology at Liddell Power Plant as a coal plant booster. By 2004, SHP had built a 61 m long 1,340 m^2 prototype LFR on the grounds of the Liddell coal-fired power plant near Singleton in New

[1] Dr David Mills has not worked with AREVA Solar since June 2010 and has no direct knowledge of Areva Solar's present-day technology.

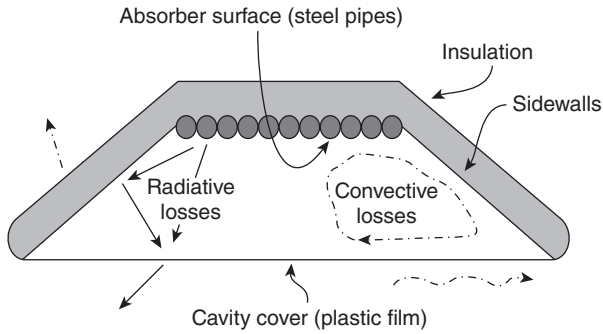

6.12 Schematic of a trapezoidal inverted cavity receiver with a plastic transparent cover. Ultimately, a glass cover proved to be more durable (courtesy of G. Morrison).

6.13 Stage 1 of the Liddell array in 2004 soon after initial operation (copyright Areva Solar, used with permission).

South Wales that was smaller than the 2,400 m^2 array erected in 2001 by Solamundo. This was a 1 MW prototype (Fig. 6.13) not connected to the power block and intended only to demonstrate operation at the temperatures and pressures required by a power plant preheater (280°C and 80 bar). The SHP prototype achieved its design goals quickly, and later was operated briefly to demonstrate 'once through' production of superheated steam. Figure 6.14 shows the flow schematic of the prototype. A journal paper was published on the initial prototype and future plans in 2006 (Mills *et al.*, 2006). The absorber in the first SHP prototype consisted of 16 parallel DN 25 pipes, each 60 m long, made of 304 stainless steel, and mounted

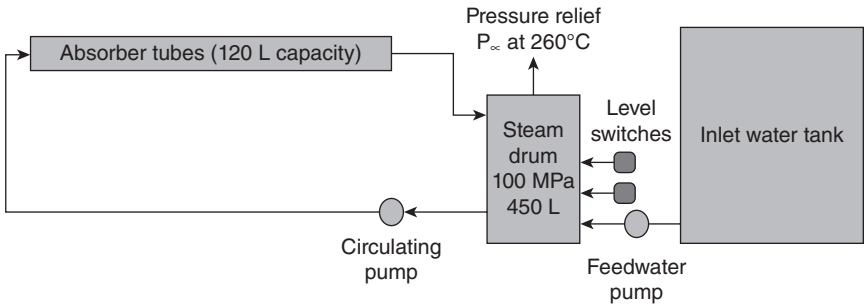

6.14 Schematic of prototype system at Liddell, which was not connected to the coal-fired station (courtesy of G. Morrison).

side-by-side with very little spacing, for a total absorber width of 575 mm. Absorber pipes in the prototype were connected via a set of manifolds into a four-pass configuration, so that the total length of a flow path was approximately 240 m, emulating a much longer collector. Water was introduced into the outer tubes in a preheating arrangement and returned via the centre tube, where it turned into saturated or superheated steam. The system thus had connections at one end and the other end was free to move to accommodate thermal expansion. The tubes were suspended by rollers positioned periodically down their length. Anti-reflection layers were introduced on the inverted cavity glazing. The tubes were coated with black non-selective coating, awaiting commercial deployment of an in-house developed selective coating.

In 2004 Mills delivered papers suggesting that very large plants using LFR technology around 300°C could use low pressure nuclear type turbines as a low-cost generation possibility (Mills *et al.*, 2004a, 2004b). At the same conference, a study in Germany (Häberle *et al.*, 2004) was presented suggesting that LFRs were potentially viable as a competitor to troughs. At this time there were no high temperature air stable selective coatings, so operation at high efficiency would be limited to that of air stable coatings like Black Chrome, which is stable up to about 300°C. This temperature was only slightly above the preheating temperatures that would be required for coal plant booster arrays discussed by Mills and Dey in 1999, including the next stages of the Liddell project.

In 2006 the Liddell project began Stage 2, a 20,000 m^2, 5 MWe stage that was connected to the main station power block to supply thermal energy to the final feedwater heater. Stage 2 used an improved commercial model of the collector (Fig. 6.15) with several changes from the first prototype. The mirror reflectivity was increased from 84% to 92.5%, the reflector width increased from 1.82 m to 2.25 m, the length increased from 12.2 to 12.9 m

6.15 Stage 2 of the Liddell array in 2006 (copyright Areva Solar, used with permission).

and the number of reflectors per absorber line reduced to ten from the original twelve. The tower and absorber dimensions were unchanged.

In late 2006, SHP was invited to start up a US operation funded by Silicon Valley venture capitalist companies, named Ausra Inc. ('Ausra' is one version of the ancient Indo-European word for the Goddess of the Dawn), ultimately obtaining US$130 million in international venture capital. Ausra subsequently bought all SHP assets including all IP, and the centre of technical operations shifted to California. SHP became Ausra Pty Ltd in Australia.

In 2008, the company built a redesigned pre-commercial unit of three 384 m lines located at Kimberlina in Bakersfield, California (Fig. 6.16). This employed a redesigned A-frame tower (similar to the 1970s Itek tower and the contemporary Industrial Solar design) to increase earthquake resistance and simplify receiver installation and maintenance. The unit was connected to a dedicated turbine, a 5 MW former biomass steam turbine that was already installed on the site for a previous project. The plant was the first LFR built for electricity production in North America and was opened in October 2008 by Arnold Schwarzenegger, the Governor of California, who noted it was the first solar thermal electricity plant of any kind to enter operation in California in nearly 20 years. Unfortunately, serious technical problems arose with the second-hand turbine that were unrelated to the collector system, and these were not repaired until the spring of 2009, when the installation was finally connected to the California grid.

The field length at Kimberlina is given by NREL as 385 m (Ausra, 2007). In the first three lines built there were 25,988 m^2 in 30 reflector rows each

6.16 The three-line Kimberlina array in Bakersfield, California, in late 2008 of LFR technology (copyright Areva Solar, used with permission).

having 24 modules per line. Thus, each mirror module has close to 36.1 m^2 of reflector in five reflector panels 2.25 m wide, for a module length of 16.0 m. The mirror modules used at Kimberlina were manufactured at Ausra's automated solar thermal power factory in Las Vegas, Nevada, which is designed to produce one reflector module every 8 minutes, or 4 m^2 per minute, or 3,360 m^2 over two 7-hour shifts per day. The 2008 array was designed for 300°C saturated steam, but was also used as a test unit for superheated operation throughout 2009. Kimberlina has since been used intensively to verify the array performance for prospective customers and investors.

However, for large projects the company needed significant backing. By 2010, competitors like Solel, Solargenix, Solar Reserve and SES had already been purchased or backed by much larger companies. In early 2010, Ausra was bought outright by the French nuclear giant Areva and was renamed Areva Solar. Areva is experienced in mounting large projects, so the company is now effectively in the business of selling both steam technology and power projects. In early 2010, a $105 million 18 line 44 MWp(e) steam booster project was secured with the utility CS in Queensland to go online in 2013. The system will operate at 330°C. Its technology has been selected for a 250 MWp(e) flagship solar project in Queensland (Solar Dawn, 2011), but this was shelved in July 2012 due to lack of a buyer for the power. However, a similar 250 MW plant announced for India in 2012 is under construction by AREVA at the time of writing. In 2011 Areva Solar also announced a memorandum of understanding to commence engineering studies for a 150 MW CLFR free-standing plant (PEM, 2011) to be installed near Fresno, California.

6.17 The fourth line at Kimberlina in operation. It differs from the first three lines in using 13 reflectors instead of ten, and in operating as a superheating line at 400°C (copyright Areva Solar, used with permission).

Areva Solar has more recently tested a fourth, newer technology line called SSG4 (Conlon, 2011) at Kimberlina in 2010, pressurized to 92 bar (Fig. 6.17) that uses a 13 mirror line configuration with a superheated steam receiver, unlike the previous ten mirror line saturated steam units. In the fourth line there are 11,261 m^2 in 13 reflector rows each having 24 modules per line. We previously learned each module is 16.0 m long and the reflectors 2.25 m wide, yielding 29.25 m^2 of reflector per lineal metre of receiver. Areva states the heating surface area to be 210.0 m^2 for a line, so the heating surface must be 210/385 = 0.545 m wide. The peak ratio of primary reflector to heating surface area for the smaller 545 mm wide receiver is thus about 29.35/.545 = 53.7. The performance tests below 400°C were overseen by the consultant engineers Black and Veitch and 100% availability was achieved during the June–October testing period in 2010. Performance is said by the company to have met or exceeded modelling predictions (Conlon, 2011). Interestingly, Conlon says that in a 'lights out' test, the array line had enough thermal inertia to deliver 18 minutes of superheated steam.

Areva has stated that it is developing a 482°C version available for 2011 with 165 bar operation (Areva, 2012) , which may be the 13 reflector line version described by Conlon (2011), who cites a design operational temperature of 450°C and pressure of 165 bar with a maximum pipe wall temperature of 482°C. Areva has also suggested a version 2.0 to be under development, so it is possible that the next version could be designed for maximum steam temperature of more than 500°C, but that is not clear at the time of writing.

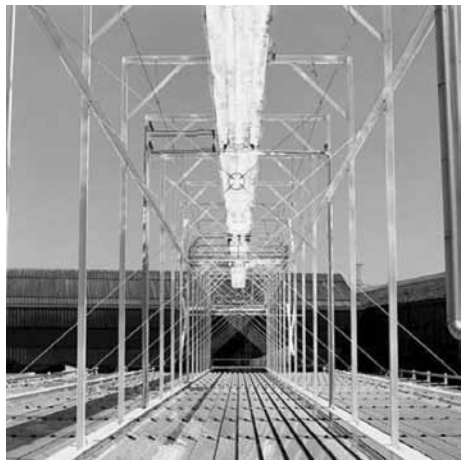

6.18 The Solarmundo prototype at Liège (copyright Solarmundo 2001).

6.4 Solar Power Group (formerly Solarmundo, Solel Europe)

As stated in Section 6.2, the founder of Solel Europe joined forces with Belgian investors to found Solarmundo in the late 1990s. The design was an LFR using a non-imaging receiver secondary reflector for use with a custom-built non-evacuated absorber tube, a similar concept to the earlier Paz receiver design.

The Liège prototype (Fig. 6.18) built by Solarmundo was operated as a test bed until 2004 when the company was closed down. The Count de Lalaing then founded Solar Power Group (SPG) to continue his work on the LFR. This prototype marked the establishment of German interest in the technology; before the move to Germany, Solarmundo used the resources of German research institute PSE to attack the issues of optical reflector design, selective coating durability at higher temperatures, and secondary mirror stability. In 2005, SPG entered a cooperative agreement with Ferrostaal, a subsidiary of the industrial group MAN. In 2007, Ferrostaal acquired 25% of SPG, and later in 2009, increased its ownership to 43%.

Because of generous German government assistance, the majority of publicly available research on LFR work has for a long period been associated with the SPG technology, so that general conclusions about LFR viability have tended to use the SPG technology as a quasi-standard, rather than the more secretive but commercially active Areva and Novatec Solar technologies. A great deal of early research has emerged into the public

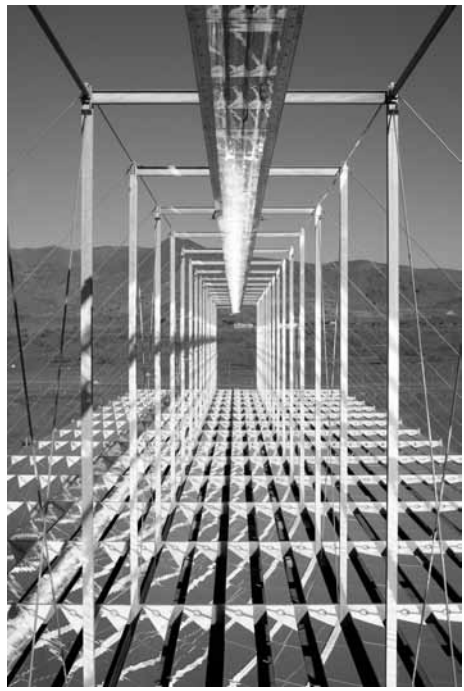

6.19 The FRESDEMO SPG prototype at PSA. The tower has been made narrower in the newer version and bracing is less optically intrusive than the earlier prototype (copyright MAN Ferrostaal and Solar Power Group GmbH 2007).

sphere because of the SPG project (Bernhard *et al.*, 2008; Morin *et al.*, 2006; Mertins *et al.*, 2004; Eck *et al.*, 2007).

In 2007, the company undertook construction and operation of their FRESDEMO pilot collector in the Plataforma Solar de Almería (PSA) in Spain (Figs 6.19 and 6.20). Land for its construction was provided by CIEMAT at the PSA. The DLR's Institute of Technical Thermodynamics analysed the thermal characteristics and thermal losses of the linear Fresnel collector in order to determine the thermal collector efficiency at different receiver temperatures. Fraunhofer ISE was assigned by MAN to validate the collector models of the optical efficiency and thermal losses with the measurements.

The FRESDEMO re-optimized design had a length of 100 m and a total width of 21 m including 15 m of cumulative mirror surface width. The absorber tube dimensions consist of a 14 cm outer diameter with an approximate 12.5 cm inner diameter. There are 15 m^2 of reflector per linear metre of absorber tube, so the geometrical concentration (the ratio of aperture area to receiver emitting surface area) is 34, about 20% higher than

6.20 Public showing of the FRESDEMO prototype at the PSA in Spain (copyright MAN Ferrostaal and Solar Power Group GmbH 2007).

parabolic troughs. The steel structure of the prototype supports a fixed central absorber tube located in the centre of a secondary reflector and 25 rows of slightly curved primary mirrors.

The FRESDEMO collector can be operated in three different operational modes that can be pre-selected:

- preheating (absorber fed with cold or preheated water)
- evaporation (absorber fed with preheated water and saturated steam)
- superheating (absorber fed with saturated or superheated steam only).

Inside the cavity is a single absorber tube with an inner diameter of 18 cm and coated with a non-selective absorber coating. The optical efficiency measured at PSA (Bernhard *et al.*, 2009) first suggested 63%, and this efficiency reduced to about 53% over some months. However, periodic calibrations of the primary mirrors, as recommended by PSE AG, were not performed for various reasons. After recalibration and a complete cleaning, the original efficiency of over 60% was achieved again in 2009. Also the soiling of the glass plate below the cavity could account for about 2% efficiency decrease per month and measurements of glass plate soiling did not commence until June 2008, nearly 30 days after initial cleaning, so a peak optical efficiency of 64% is likely to have been the initial state. A raytrace calculation suggested a peak optical efficiency of 65.2%, close to the 64% estimated from measurements.

The FRESDEMO design lost about 850 W of thermal energy per metre of receiver length at 300°C according to Bernhard *et al.*, and has 15 m^2 of reflector per lineal metre of receiver length, so the thermal loss was about 57 W/m^2 of field reflector, higher than Novatec Solar and Industrial Solar

contemporary secondary reflector designs as calculated later in this chapter (see Fig. 6.29). This is likely to be because the Novatec design has significantly higher optical concentration on its receiver, while the Industrial Solar design uses a low loss evacuated tube receiver. However, that information was published relatively recently. Before that, early low temperature testing <300°C by all LFR manufacturers had fostered a general assumption in the solar industry that LFRs were low temperature devices by nature, an opinion only now being abandoned as most new model LFRs are now being designed and tested at or above 450°C, higher than most current PTCs (parabolic trough collectors). FRESDEMO finally broke the myth in September 2008, operating at up to 450°C an in-line superheater for a trough direct steam generator (SPG, 2008), the highest LFR temperature so far achieved at the time.

Cooperation with German technology groups has led to significant progress in the reflector optical design and sputtered selective coating area. Selective absorber surfaces have been developed that may be reliable at 450–500°C, though the cost of these somewhat complicated layered sputtered surfaces is not known. There has been relatively little available description of this surface work in the open literature, but the SPG Managing Director Count Jacques de Lalaing described the effort as follows in a radio interview (de Lalaing, 2009):

> [O]ne of the main differences that we have with our competitors is that we've developed a coating that is holding at a higher temperature and it allows us to reach 450 degrees . . . we can produce steam at 450 degrees in a very stable condition, super-heated steam, and of course that gives us an edge over the competitors because the higher the temperature of your steam, the higher the efficiency of the turbine that you hook up behind it.

The high temperature mirror stability issue has been more difficult, and progress was slower, but the problem has been taken up by glass reflector manufacturers who are expected to offer products soon that will allow high reflectance secondary reflectors suitable for high temperature cavity receivers.

Within the extensive paper by Bernhard *et al.* (2008), researched by SPG together with the Fraunhofer Institut für Solare Energiesysteme (ISE) and the German Aerospace Center (DLR), the technical aims of SPG are clearly stated:

> SPG is planning a future collector design in which the primary mirror accuracy is increased significantly. A new substructure for the primary panels is being developed together with an automated gluing process and an integrated optical measurement system to supervise the manufacturing process. This will guarantee long lasting and stable primary mirrors with higher accuracy, manufactured in a mass production process. Quality management systems will be integrated

> also in the assembly process into the steel structure. By using a more accurate sun tracking algorithm and drives with a higher accuracy as well as inclination angle encoders with an acute sampling rate, higher precision resulting in a considerably higher optical efficiency will be achieved. The revised receiver design will omit openings to the atmosphere preventing efficiency losses due to rain water and dust ingress.

It is interesting to note that SPG does not, in the above, mention the use of evacuated tubes. It may be that they are undecided as to whether there is a value proposition in their use, or have decided not to use them, or are not disclosing an evacuated tube programme. Their design would require a single evacuated tube receiver larger than current evacuated tubes. Morin *et al.* (2009) have suggested that this substitution of a 70 mm evacuated tube would substantially reduce heat loss and improve overall efficiency, even though annual optical efficiency would drop by 10% because the 70 mm receiver is half the original absorber size. The collector and the Schott receiver have not been designed for each other, and a situation where the collector is optimized for the receiver would be more optimal. In spite of this, Morin *et al.* came to the conclusion that even with too small an evacuated tube, the advanced model LFR with the smaller tube had a break-even cost of 80% of the PTC cost, while the current model breaks even at 53% of the PTC cost. This appears, at first glance, to be a strong argument for changing to evacuated tubes in an extensively redesigned collector if the financial assumptions are correct. SPG's competitor Novatec is doing just that. Also, higher optical concentration is not mentioned, although this would be preferable. The ratios of primary reflector area to hot surface area achieved by Novatec Solar and Areva Solar are above 50, but for SPG only 34. It would be surprising if this were not increased in SPG's next model.

In terms of project development, SPG has had a long-standing interest in the Middle East and North Africa (MENA) market, and signed a memorandum of understanding (MOU) with Libya in 2006. This is explained on their website, which states 'Of special interest to SPG and MAN Ferrostaal is the MENA region, that not just offers optimal climatic conditions but also is the home of IPIC (International Investment Petroleum Company), which has recently acquired a 70% participation in MAN Ferrostaal'.

In 2010, SPG signed an agreement with GDF Suez for the construction a 5 MW(th) add-on onto a coal-fired power plant in Mejillones. The construction of the plant should start in 2011 and will use the new design developed by SPG over the last two years. In early 2011 SPG also signed a licence agreement with JFEE, a large Japanese EPC company, that will use SPG technology in plants to be built in southeast Asia and Oceania. It states (SPG, 2011) that it is 'developing projects in parallel in Southern Europe, Northern Africa, South America, and Australia, varying in scale'.

6.5 Industrial Solar (formerly Mirroxx, PSE)

PSE AG is a solar energy technology and service company that was a spin-off of Fraunhofer ISE, the noted solar research institute in Freiburg. PSE, under the leadership of Andreas Häberle, assisted Solarmundo from 2000 onwards in the area of optical design, collector performance modelling and selective surface development, and much of the research that assisted SPG also came from this source. However, PSE developed a small LFR of its own for rooftop mounting using a single 70 mm diameter Schott evacuated tube receiver by 2005. Intended for the process heat market, it employs an A-frame support similar to the previous Itek collector from the 1970s and the later Areva system. The system, called the FL-11, uses a water circuit pressurized at 16 bar to transfer process heat with temperatures up to 200°C. This falls within the pressure restrictions of the evacuated tubes used, which were designed for the pressures used in oil heat transfer systems.

The basic reflector system has modules that are 4 m long × 8 m wide with 11 primary mirror rows. Like other companies, it uses flat white glass mirrors, possibly slightly curved elastically, and a polished aluminium secondary reflector. Each of the individually driven mirror rows features an electric drive motor.

A second prototype with an aperture area of 132 m^2 and output 66 kWp(th) was installed in Bergamo, Italy to power an ammonia-water absorption chiller. It was operated and monitored from August 2006. In late 2007, a third Fresnel process heat collector with a 352 m^2 aperture area attaining a peak of 176 kW(th) was installed on the roof of the Escuela Técnica Superior de Ingenieros (ESI), a School of Engineering building in Seville, Spain (Fig. 6.21). The collector total length is given as 64 m (16 × 4 m long modules) and otherwise similar in design to the ones in Freiburg and Bergamo. Each module thus has 5.5 m^2 of reflector per lineal metre of receiver, and 0.5 m per reflector per lineal metre of receiver. As each reflector including spacing is 4.06 m, a 4 m reflector length is likely and the reflector width is about 2 m^2 in area. The collector powers a double effect H_2O/LiBr absorption chiller with a maximum cooling capacity of 174 kWth for air-conditioning the building. At this site, the wet cooling tower for heat rejection, which is usually necessary for H_2O/LiBr absorption chillers, was substituted by a water heat exchanger fed by water from a local river. The double-effect absorption chiller offers a coefficient of performance (COP) of up to 1.3. A fourth project was a solar cooling system with a NH_3/H_2O chiller at a winery in Tunisia.

The Mirroxx company was launched as a PSE spin-off in December 2008, taking over PSE's LFR commercialization activities. With Mirroxx GmbH, a basis for industrial series production and strategic marketing of the Fresnel collector technology had been formed. In November 2010, Mirroxx

6.21 The third Industrial Solar project, built in 2007 in Seville, Spain, with an aperture area of 352 m^2, length 65 m, pressurized water circuit at 16 bar, and operating temperature 180°C. The application was solar cooling with a double-effect absorption chiller (175 kW) (courtesy Industrial Solar GmbH, reproduced with permission).

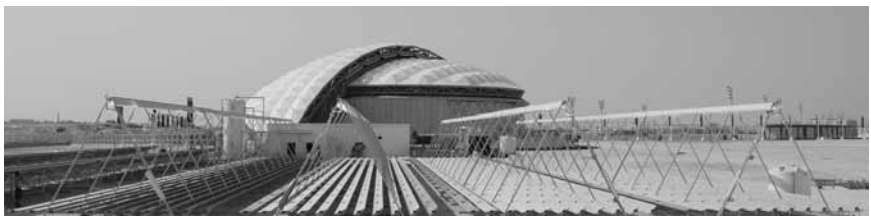

6.22 Industrial Solar Fresnel collector field in Doha (Qatar) (built in 2010, aperture area 1,408 m^2, length 65 m, pressurized water circuit at 16 bar, operating temperature 180°C, application: solar cooling with double-effect absorption chiller (750 kW)) (courtesy Industrial Solar GmbH, reproduced with permission).

commissioned its largest collector field so far in Doha (Qatar) (Fig. 6.22). The heat generated by the collector field is used to power an absorption chiller, which provides air-conditioning for a 500-seat showcase football stadium constructed by ES-Group/London and designed by Arup Associates. The system was described in the December 2010 issue of *Renewable Energy World* (Appleyard, 2010). The solar thermal field, supplied by German engineering and manufacturing group Mirroxx GmbH, features single-axis tracking flat-plate mirrors which focus solar energy onto a Schott PTR® evacuated tube receiver using water as the heat transfer fluid, pressurized to 16 bar at 200°C. Collector aperture area is 1,400 m^2, peak thermal output 700 kW, and it was stated that Mirroxx claimed a maximum optical

efficiency for direct normal irradiation (DNI) of 62%, slightly lower than the more recent figure below.

In April 2011, Mirroxx changed its name to Industrial Solar 'to reflect the company's focus on industrial applications' (Industrial Solar, 2011a). The target market consists of industries in sunny countries which require process heat up to 400°C. In essence, the company has been steadily improving the original Israeli Paz system secondary reflector concept also favoured by SPG and Novatec Solar to the point where it has the basic requirements for not only an industrial system, but a high temperature superheated LFR steam generation system, including a selectively coated evacuated tube, and a secondary high efficiency reflector. At 400°C, Industrial Solar is delivering thermal energy in the same temperature range as the electricity LFR companies, and could therefore conceivably be a player in the high temperature electricity generation sector in the future, although the company has not announced any such ambitions. In the downloadable 2011 Industrial Solar brochure, it is stated that 'it is also possible to directly generate or even superheat steam.' In addition, it was stated that although 40 bar was now standard, pressures up to 120 bar were offered, greater than the Novatec Solar Supernova steam pressure of 90 bar (Paul *et al.*, 2011), even though Novatec central generation LFR uses evacuated tubes as well. The Industrial Solar brochure also provides useful technical data (Industrial Solar, 2011b) for the FL-11 collector and reference conditions as follows:

- Thermal loss at 400°C ($\mu = 0.00043$ W/(m^{2}K^2))
- Reference temperature conditions: 30°C ambient; 160°C inflow; 180°C outflow
- Angle-independent optical efficiency (with 100% clean primary and secondary reflectors and receiver glass tube)
- Optical efficiency $\eta_0 = 0.635$ (for sun in zenith)
- $\eta_{max} = 0.663$ for sun at 5° transversal zenith angle
- Mirror reflectivity 95%
- Schott PTR®70 Receiver thermal emittance @ 380°C: 9%
- Solar absorptance direct: 95%

6.6 Novatec Solar (formerly Novatec-Biosol, Turmburg Anlagenbau)

In 2005, a new LFR company was formed, called Turmburg. Its technology founder, Max Mertins, had previously done modelling work for Fraunhofer ISE where he worked extensively on the Solarmundo collector. Mertins had also participated in a joint German government LFR workshop (Morin *et al.*, 2006) attended by both SHP's European division and SPG and was thus familiar with both designs. 'VDemo-Fresnel' was funded by the German

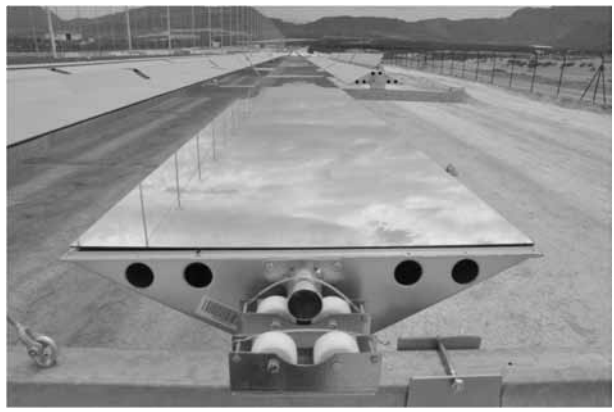

6.23 End view of a Novatec reflector showing polymer support bearings. It is of monocoque construction (courtesy Novatec Solar GmbH).

Ministry of Environment, Nature Conservation and Nuclear Safety (BMU). The new company produced a design using a CPC cavity receiver somewhat resembling the SPG design, but using a 70 mm receiver size like the PSE design, with a supporting design tower similar to the small 'V' support used in the V1.1 SHP CLFR.

A primary design difference between the Turmburg and other designs was in reflector construction. The new design was a monocoque one, where much of the strength is derived from the metal skin (Fig. 6.23). The reflectors are lightweight and can be lifted without the need for machines. They are amenable to mass production and an automated production unit was designed and built based on automobile component production methods.

In late 2006, the company received investment and commissioned a prototype plant in Spain as a basic module suitable for 270°C operation (Fig. 6.24). The name of Novatec-Biosol was adopted for the company. In this section, the company will be referred to as Novatec Solar, the most recent name at the time of publication, or 'Novatec'.

The basic solar boiler module (NOVA-1, 2011a) was called Nova-1 and has a receiver height of 7.4 m measured from a mirror hub height 1.2 m above the ground. It uses 128 reflectors in 16 reflector lines, 8 to a line, with a cumulative width of 12 m (0.75 m individual reflector width) and a total module reflector area of 513.6 m^2. This can be calculated by dividing the quite precisely provided 18,489.60 m^2 in the previous reference for the array PE-1 by 36, the nearest whole number of modules. This calculates to an individual reflector area of 4.01 m, and an individual reflector length of 5.35 m. The module length is 44.8 m. Each module thus has 513.6/44.8 = 11.5 m^2 of field reflector per lineal metre of receiver. The total

6.24 The 2005 Novatec demonstration module in the south of Spain (courtesy Novatec Solar GmbH).

6.25 Illustration of Novatec dry cleaning robots moving down a reflector line (courtesy Novatec Solar GmbH).

circumference of the receiver is 0.22 m, so the ratio of reflector to hot receiver surface is about 52. A cleaning robot has been developed to keep the reflectors at high efficiency (Fig. 6.25). This moves down the line automatically and does not use wet cleaning.

The automated production line started to produce primary mirrors in May 2008, and the first 4,600 manufactured primary mirrors were installed in the demonstration plant PE-1, located in Calasparra (Spain), with a nominal capacity of 1.4 MWe. The two parallel collector rows of PE-1 (see Fig. 6.26) with a length of 806.4 m produce a steam–water mixture at up to 55 bar (270°C). This is separated into steam and water phases in a steam

6.26 PE-1 1.4 MW powerplant (courtesy Novatec Solar GmbH).

drum with the saturated steam directly feeding the turbine while the water phase is mixed with the feedwater and recirculated to the inlet of the solar field (Fig. 6.27).

Alluding to its location Puerto Errado in Spain, PE-1 was connected to the Spanish electrical grid in 2009, slightly in advance of the Ausra Kimberlina project. A company online brochure (NOVA-1, 2011a) claims an optical efficiency of 67%, and an operating temperature of 270°C. One year later it was followed by the start of construction of 30 MW PE-2 with 302,000 m^2 of collector area (NOVA-1, 2011a). The latter plant is expected to be completed in March 2012.

Data released thus far (NOVA-1, 2011b) on the Nova-1 technology are:

- Convective thermal loss at coefficient $\mu_0 = 0.056$ W/(m^2K)
- Radiative thermal loss at coefficient $\mu_1 = 0.000213$ W/(m^2K^2)
- Power lost $P_{\text{loss}} = \mu_0 \Delta T + \mu_1 \Delta T^2$
- Reference temperature conditions: 40°C ambient; 100°C inflow; 270°C outflow
- Angle-independent optical efficiency $\eta_0 = 0.67$ (for sun in zenith) (with 100% clean primary and secondary reflectors and receiver glass tube)
- No wind assumption stated
- 246.2 kW per module
- 541 W/m^2 collected per area of primary reflectors (502.3 W/m^2 PE-1)
- 900 W/m^2 direct normal radiation (DNI) at azimuth angle 0°, zenith angle 30°.

In the Nova-1 projects, Novatec Solar uses the low temperature saturated steam approach earlier used by SHP, but like Areva Solar and SPG, they

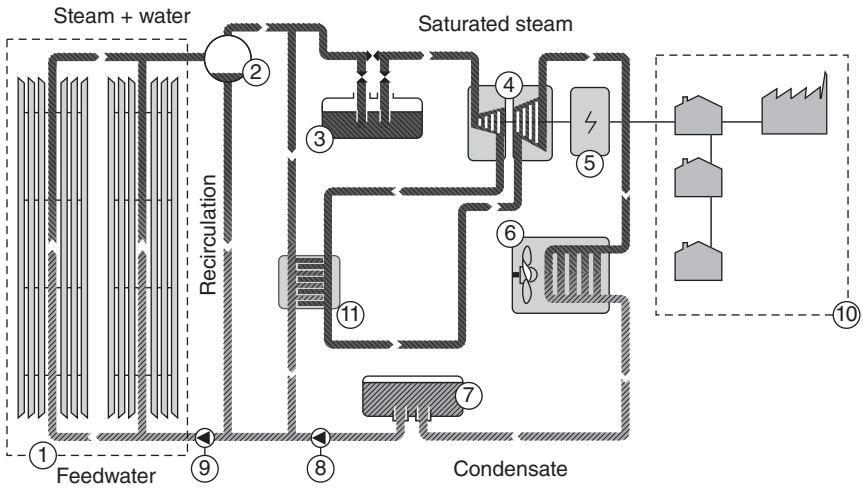

1. Solar field
2. Steam separator
3. Steam storage
4. Turbine
5. Generator
6. Air-cooled condenser
7. Deaerator/feedwater tank
8. Feedwater pump
9. Recirculation pump
10. Public electricity grid
11. Moisture separator and reheater

6.27 PE-1 1.4 MWe powerplant schematic. The system uses a saturated steam turbine. From Novatec PE-1 brochure (courtesy Novatec Solar GmbH).

are developing superheated systems. In 2010 Novatec announced the development using Schott evacuated tubes instead of the current non-evacuated tubes (SuperNOVA, 2011). The new collector model was called SuperNOVA and was used at the PE-1 site prior to September 2011. Novatec state that heat loss is reduced by 50% compared to the Nova technology, but not at which temperature this takes place. Although the company announcement brochure announces 500°C, Paul *et al.* (2011) of Novatec Solar used a steam temperature of 450°C at 90 bar in their calculations for a 50 MW(e) Supernova, so this might be the normal output temperature like Novatec's competitors, even though higher temperatures are possible. (450°C is also specified in the Areva Solar SSG4 array with a peak wall temperature of 482°C at a stamped pressure of 92 bar, and by SPG in superheating tests of the FRESDEMO.) The increase in electrical output for a 100% solar plant was calculated by Paul *et al.*, and the annual electric yield is 0.322 MWh(e)/m^2 for a SuperNOVA operating at 450°C and 90 bar, compared to a NOVA-1 value of 0.298 MWh(e)/m^2 operating at 285°C and 70 bar, an 8% improvement. Paul *et al.* also point out that power block costs are lower at 450°C than 285°C, and that 'a further improvement including

a reheat stage in a SuperNOVA power plant – as has been done for NOVA-1 – will allow further efficiency improvement'.

Novatec has won a contract to add to the existing solar facility built by SHP at Liddell power station in New South Wales, Australia, using Nova-1 technology. The new array will deliver a peak of 9 MW(th) and has a planned array area of 18,490 m^2. It was stated to be expected to commence in early 2011 and be completed in 2012.

On 16 March 2011, Novatec announced that the large energy technology company ABB had signed an agreement to buy a 35% shareholding in Novatec Solar, including an option to acquire 100% of Novatec Solar and an agreement to cooperate on future solar power plant projects.

6.7 LFR receivers and thermal performance

Thermal efficiency and heat losses are critical to design viability. One might think that there would be only one optimal design, but the Areva Solar multiple tube cavity receiver is now becoming significantly divergent from the SPG, Novatec Solar and Industrial Solar secondary reflector designs.

Historically, the original decision by SHP to avoid hot mirrors and secondary reflector absorption losses led to a very optically efficient receiver design based on low-cost multiple tubes of small diameter arranged horizontally to maximize the effectiveness of the cavity receiver. While it uses inexpensive reflectors to the side of the cavity to capture some stray light, these reflectors stay out of the main beam; the receiver does not use secondary reflectors as a primary method of light capture. However, this system requires the development of steam control systems for very long multiple tube arrays, a technical problem at the leading edge of steam engineering practice. The company has been also developing a low-cost selective surface for sustained operation above 300°C so that the thermal emittance losses would remain acceptable. However, releases of information have been difficult to interpret and compare as each company presents its information differently.

The Novatec, Industrial Solar and SPG technologies all use an improved version of the secondary reflector configuration first attempted by Paz, and similar to that shown in Fig. 6.28. These three companies have recently provided in the literature clearer information on heat loss and the efficiency of conversion. In Bernhard *et al.*, the heat loss from the SPG FRESDEMO collector is given as the simple equation developed by the Fraunhofer ISE in Freiburg; this was used by the author. A second closely matching curve fit was also developed by the DLR but was not used here. The ISE version is

$$q' = 0.011635 \cdot \Delta T^2$$

6.28 Cross-sectional sketch of the Novatec receiver and secondary reflector (courtesy Novatec Solar GmbH).

where q' is the thermal energy lost in W/m^2 of hot receiver surface, ΔT is the difference in tenperature in °K between the output fluid temperature and the ambient temperature near the collector. The ambient temperature is not stated, but likely to be around 293–303°K. Bernhard *et al.* (2009) present a graph (Fig. 3) of this heat loss compared to some actual data points and also to a test of the Schott PTR-70 evacuated receiver. In the graph, the evacuated receiver heat loss appears lower by a factor of 5 at 300°C above ambient. The same paper describes a measured optical efficiency of 0.62 but explains that the cover was not clean and makes a case that a new cover would result in an optical efficiency of 65%, which is accepted here as the SPG value.

Novatec give their heat loss as

$$P_{\text{loss}} = \mu_0 \Delta T + \mu_1 \Delta T^2 \qquad [6.1]$$

where P_{loss} is the heat loss in Watts per m^2 of primary reflector, $\mu_0 = 0.056$ W/(m^{2}K) and $\mu_1 = 0.000213$ W/(m^{2}K^2). The ambient temperature is 313 K. ΔT is the difference between ambient temperature and the output temperature (normally 270°C). The optical efficiency is stated to be 67%.

Industrial Solar give their loss as simply the thermal loss per m^2 of primary reflector,

$$P_{\text{loss}} = 0.00043 \text{ W/(m}^2\text{K}^2\text{)} \qquad [6.2]$$

where the ambient temperature is taken as 303 K. The best optical efficiency is 66.3% at a sun angle 5° from the zenith – the central reflector is shaded with the sun at zenith and the figure is consequently slightly lower at solar noon. Industrial Solar has stated that the new design of SPG has much lower losses but, as yet, there is no published data to verify this.

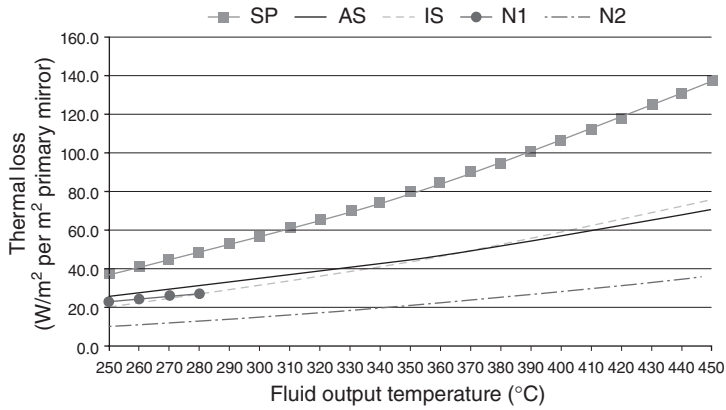

6.29 Comparison of estimated heat losses using information obtained from several LFR manufacturers, present and future as described in the text. The optical concentrations used were 54 for AS, 34 for SP, 25 for IS, and 52 for N1 and N2.

Figure 6.29 presents this heat loss data in a single graph with the ambient temperature of 303 K used in each case. There are two Novatec-like cases; the N1 using the published NOVA-1 heat loss and concentration data, and the N2, using the same concentration but, like the SuperNOVA, a receiver similar to a Schott-manufactured evacuated tube (Burkholder and Kutscher, 2009) with thick enough metal walls for the production of high pressure superheated steam. The IS case heat loss is modelled on the published thermal loss per m^2 of the Industrial Solar system, which also uses a Schott evacuated tube receiver, but uses about half the optical concentration of the N2. Thus, the N2 heat loss modelled uses the Industrial Solar loss rate multipled by 25/52 as a prediction of thermal loss, since the Industrial Solar and Supernova systems have optical concentrations of 25 and approximately 52, respectively. The resulting N2 heat loss is about half the N1 case. Therefore, the heat loss per m^2 of reflector area of the IS system should be quite similar to that of the N1 system, as is borne out in Fig. 6.29 up to 280°C. The published heat loss and relatively lower optical concentration from SPG FRESDEMO are used in the SP case and heat loss is comparatively higher than N1 or IS, and much higher than N2.

Concerning Areva collection efficiency, Conlon (2011) describes the peak thermal input from SSG4 to the heat transfer fluid as 7.86 MW at summer solstice; the DNI assumed by Conlon is not stated but should lie in the range of about ±5% of 950 W/m^2. This would yield an optical efficiency of 7.86 MW/(950 W/m^2 × 11,261 m^2/1,000,000) = 0.734 ± 0.0374. After thermal losses, the mid-range efficiency is 7.30/10.7 = 0.682 ± 0.341. At 370°C and 104 bar pressure, the thermal loss is 0.56 MW, 49.7 W/m^2 of reflector, and 5.2% of

950 W/m^2 DNI. Areva have not released the thermal loss per m^2 of their system over a range of temperatures, but an approximate heat loss curve was constructed by the author that uses the (non-evacuated tube) N1 data for convective thermal loss (adjusted for concentration ratio) and a radiative component from Industrial Solar that is adjusted for concentration ratio togather with a higher assumed Areva emissivity that would produce the known 49.7 W/m^2 loss at an exit temperature of 370°C. The emissivity adjustment factor that was necessary to produce this was 1.418, suggesting a substantially higher emissivity for the Areva receiver than for the surface in the Schott tubes, about 0.113 using this approximate method.

The AS loss curve in Fig. 6.29 shows this case, and suggests that the Areva Solar heat loss might lie close to the Industrial Solar case, the increased Areva concentration compensating for a higher surface emissivity and convective loss. The N2 heat loss, however, is about half that of AS, suggesting that SuperNOVA heat loss might be significantly lower than for the Areva SSG4. Emissivity largely dominates both heat loss systems at higher temperature, and the Novatec and Areva systems have similar optical concentration. The heat loss estimated for the Areva system seems plausible but could be slightly higher or lower at other temperatures than 370°C according to actual selective surface coating performance and convection performance.

Does this heat loss advantage extend to efficiency? The Novatec efficiency is published but the Areva figures are less clear. Two graphs (Figs 6.30 and 6.31) have been shown in a recent Areva presentation as adjoining slides (Venetos, 2010), with the latter also shown in Conlon (2011).[2] Figure 6.31 was dated is September 2010, but both are almost certainly taken the same day since a dropout in DNI occurs at 11.40 a.m. in both cases and at no other time. From Fig. 6.30, the Areva line delivers a peak of around

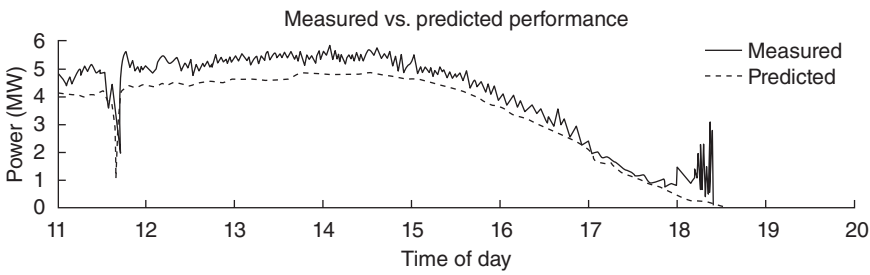

6.30 Measured thermal output from SSG4. This appears to be the same day as indicated for the temperature and DNI in Fig. 6.31 (copyright AREVA Solar, used with permission).

[2] Dr David Mills has not worked with AREVA Solar since June 2010 and has no direct knowledge of Areva solar's present-day technology.

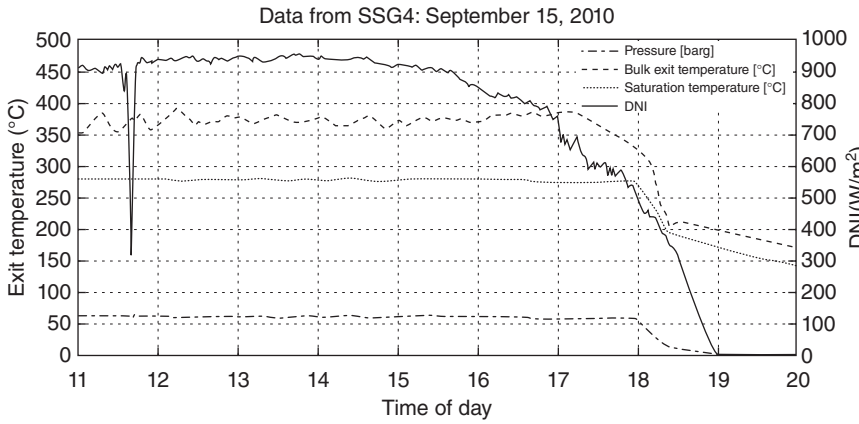

6.31 Measured DNI and temperature from SSG4. This appears to be the same day as indicated for the peak output in Fig. 6.30 because of the 11.40 a.m. cloud event (copyright AREVA Solar, used with permission).

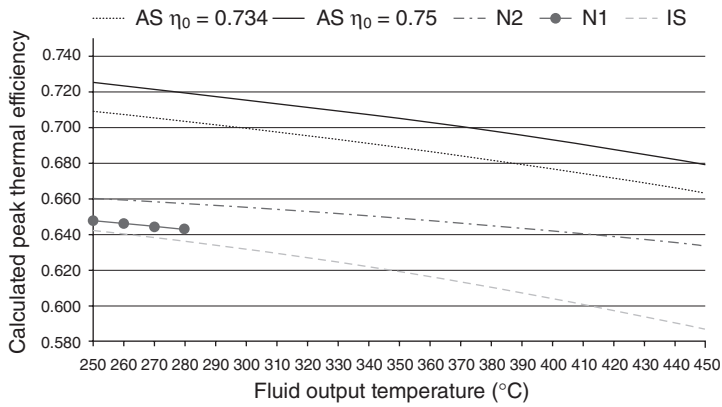

6.32 Presentation of estimated peak thermal efficiency of AS-type collectors with optical efficiency $\eta_0 = 0.75$ and 0.734 (solid and dotted lines), N2-type using $\eta_0 = 0.67$ (large dashes and dots), IS-type collectors with secondary reflectors with $\eta_0 = 0.663$ (short dashes), and N1-type with $\eta_0 = 0.67$ (large dots). These curves are based on heat losses as per Fig. 6.29.

5.5 MW(th) for about 90 minutes from a mirror area of 11,261 m^2 at just after 1.15 p.m., and in Fig. 6.32, the DNI averaged 950 W/m^2 in the second graph for about 90 minutes after 1 p.m.. There is a sizable time lag in such long systems to allow fluid flow in such a long collector, hence the difference in timings. The latitude of Bakersfield, the location of the Kimberlina array, is 35.37°N, and using the US Naval Observatory website, the average cosine

factor for the zenith angles averaged for the 90 minutes starting at 1p.m. on 15 September near Bakersfield was found to be about 0.7365 (USN, 2011). Thus, the 'averaged peak' DNI of 950 W the incidant radiation around that time was about $950 \times 0.7365 = 700$ W/m^2 of collector area. For a 11,261 m^2 array this amounts to 7.88 MW(th). The peak thermal efficiency of the unit in September was thus calculated as 5.5/7.88 = 70% which should be expected to be lower than the summer solstice figure already calculated, but is in fact higher than the mid-range 68.2% solstice estimation based on 950 W/m^2 of DNI. This suggests a higher optical efficiency, at least 5.5/7.88 + 0.052 of heat loss = 0.750 and possibly higher. A higher figure than 0.75 is possible if the peak performance at solstice is based, for example, on 900 W/m^2 DNI instead of 950.

Figure 6.32 shows peak performance modelling of systems with the thermal loss data from Fig. 6.29 for the temperature range 250–450°C. In the graph, two AS case curves are shown assuming optical efficiencies of 0.75 and the earlier estimation of 0.734. The results suggest that, in spite of dramatically lower losses, there are some important downsides to evacuated tube and secondary reflector use. In 2008, NREL tested the heat loss from two PTR-70 tubes (Burkholder and Kutscher, 2009), which have a lower heat loss than UVAC tubes (Burkholder and Kutscher, 2008). According to Appendix IV of the NREL report (Burkholder and Kutscher, 2009), the current 4 m PTR-70 evacuated tubes lose cumulatively 3.4% of optical input due to light striking the end bellows. If we assume that the much longer butt-welded non-evacuated tubes currently used in some designs like Areva have a 0.4% connector optical loss (it could be even lower), then the net optical deficit associated with evacuated tube use is assumed to be about 3%. This at first suggests a peak optical efficiency for N2 of close to 64% instead of the N1 0.67. However, Industrial Solar already achieve $\eta_0 = 66.3\%$ using a similar Schott evacuated tube, so the author adjusted the assumption of optical efficiency of the calculated N2 system to 67% in Fig. 6.32 after discussion with a reviewer; the assumption is that compensating improvements have been made, but the effect still limits optical efficiency compared to an inverted AS1 or AS2 receiver. A second smaller disadvantage is that reflection losses may be greater for the cylindrical evacuated tube cover tubes than for a flat cover; Morin *et al.* (2011) state that 'rays which are reflected at the secondary concentrator may pass several times through the evacuated glass tube'. No SP case was calculated in Fig. 6.32 but if evacuated tube optical obstructions limit maximum optical efficiency, then one might expect any revised future non-vacuum SP-type prototype to do better by at least 3%, achieving about 70% optical efficiency. In support, Morin *et al.* (2009; 2011) suggest that $\eta_0 = 0.705$ is possible for SPG type collectors with upgrading.

The calculations are subject to several uncertainties, including the likely optical cleanliness of the field, the relative blocking and shading of the reflectors in different systems, and the relative absorptances of the tubes used. Something favouring Areva in the calculation is that this is a peak calculation with the sun essentially overhead; the Areva reflectors are larger relative to the aperture with potentially greater off-angle astigmatism, but this would not affect the zenith angle figure used. If it were a big problem, then small Novatec style mirrors could be used, but Areva have not done this. On the other hand, a scale drawing (fig. 2 in Conlon, 2011) shows a widening gap between reflectors with greater distance from the receiver, which would reduce shading and blocking at normal incidence and allow a closer-packed field. It is obvious when seeing such a figure that keeping the mirror field close to the receiver reduces image size and possible spillage; Novatec and Industrial Solar use a constant gap that is larger between reflectors closer to the receiver line, shifting the reflector field outward and increasing average image size. This benefit for Areva may or may not persist for off-angle of incidence solar radiation, but without comparative raytraces and detailed measurements of reflector separations and tower heights, it cannot be easily estimated in this review chapter.

Low concentration non-imaging LFR secondaries typically have an average of about 0.5 reflections before reaching the receiver. For a clean high-quality secondary reflector surface of 90–95% specular reflectance, one might expect about between 5 and 2.5% loss respectively due to absorption or surface scattering in a reflector such as polished aluminium at 90% or thin high temperature glass at 95%. However, primary reflector inaccuracy increases the number of reflections in the secondary, and we have seen that evacuated tubes can cause a 3% extra optical loss due to obstruction, and there may be a small extra loss due to low angle incidence reflections from tubes. The results thus seem to suggest, but do not yet prove, that the secondary losses in the reflector are a main source of the apparent optical performance deficit, and obstructions by the evacuated tube have a comparable negative effect. Note that all of the peak optical efficiencies will drop for off-axis ray incidence, and that average daily optical efficiency will be lower than the peak near noon on all days.

How do these estimates compare with trough collectors? In some respects, a typical parabolic trough is a lot like an Industrial Solar system using similar tubes and similar reflector area. A typical trough has an optical efficiency of 0.75 according to NREL. Using Burkholder and Kutscher (2009), the Schott PTR-70 evacuated receiver loses about 230 W/m length at 400°C, a lower figure than its Solel UVAC3 tube competitor. Again according to NREL, in a typical trough using the PT-70, there are 5.75 m^2 of aperture per linear metre, so the loss is 40 W per m^2 of primary field at

400°C, 30% less than the A2 non-evacuated system but 40% higher than the SuperNOVA. At 400°C, the peak trough thermal efficiency would be around 0.71, slightly ahead of the author's calculation of approximately 70% for the Areva LFR. Thus, in terms of peak thermal performance, the parabolic trough and LFR are converging.

However, this is not the whole story. The conventional parabolic trough arrangement is north-south tracking with plenty of room between the reflectors to maintain the peak efficiency over much of the solar day. This yields a higher capacity factor and annual output for the trough than is possible for closely packed Fresnel designs, but also uses much more land. The 'capacity factor deficit' is a big issue facing all LFR collectors and will be discussed in the last section. On the other hand, LFR system cost is lower.

6.8 Future trends

The companies who are currently the primary competitors in the LFR market have a closely linked history, but have developed different priorities and have chosen different technical development paths for their products. There are a number of different issues to consider.

The original SHP (now Areva Solar) technology was initially developed under the premises that

1. large high temperature evacuated tubes were expensive
2. small evacuated tubes were cheap but unsuitable for larger scale power production for several reasons, including optical losses from groups of receivers and coating limitations
3. hot cavity mirrors were unstable, air stable selective coatings were unstable above 300°C but good performing surfaces near 300°C were available
4. secondary reflectors can lose significant output in absorption
5. low temperature reheat turbines might be able to be used.

These days, highly efficient small reheat turbines have not come to the market, hot mirror stability is improving, and secondary reflector performance and stability have been increased. However, the important efficiency loss in LFR secondary reflectors remains and a peakier daily output than troughs is a market problem. Evacuated tubes have the lowest loss rate, they reduce heat stress on the secondary reflectors and also eliminate the cost of a cover, but evacuated tubes are less optically efficient and may be more prone to breakage than the simple cover solution. Another justification might be that evacuated tubes might be cheaper. That seems unlikely, but Areva and SPG have not released details of their absorber coating process or tube cost.

But there is perhaps a broader question to ask. Do we need such high temperature solutions everywhere in an LFR field? What is sometimes overlooked is that in a solar collector system in which water is preheated, boiled and superheated, the majority of the receiver system – perhaps 80% – comprises the preheater and boiler, and here the peak temperatures for these collector operations will lie in the temperature range below 370°C, which may be accessible to low-cost selective absorber coating systems. In other words, different receiver tube materials and coatings may be employed for different parts of the solar array or even deployed together on one line. If this comes to pass, then the low cost and high optical efficiency of present day non-evacuated receivers may be applicable to most of the array, and only a relatively small high temperature superheater section might need to have specialist high temperature Schott-type evacuated tube solutions, if they need them at all. SPG has announced that in large-scale implementation, their new high temperature glass reflector and absorber that will be used in Mejillones should not be more expensive than the current mid-temperature ones.

Both Areva and Novatec-Biosol have demonstrated automated mirror production in the arrays commissioned in 2009 (Fig. 6.22). This presumably is becoming standard. Installation is another matter. SHP/Ausra/Areva have chosen a large reflector unit size, able to be installed by two staff using a telehandler. In contrast, SPG and Novatec have chosen a small reflector design able to be handled and installed by two or more staff. Each Ausra/Areva reflector is about 36 m^2 in area, about nine times that of Novatec Solar and SPG reflectors. It is difficult to guess whether the 36 m^2 mirror approach of Areva Solar installed by telehandlers will win over the Novatec/SPG approach of using many smaller mirrors. There are no doubt differences in the cost of shipping of different designs to the site, but this information is not available.

In terms of field configuration, the Areva arrays appear to be still growing in size with each improvement, while the others have not changed significantly. This may be becasue the secondary reflector approach with evacuated tubes allows only one tube per receiver, restricting receiver size and elevation. SPG has a much shorter line length (100 m) than Areva (384 m) and Novatec (up to 986 m). This allows smaller scale arrays, but can lead to increased optical end-effect losses. Longer arrays, however, increase thermal expansion variations in the absorber tubes.

The notion of high temperature LFR operation becomes even more powerful if one thinks about the combined impact of even higher LFR optical concentration combined with better selective coatings. However, there has been much confusion in the marketplace about concentration ratios. Some trough manufacturers quote optical concentration as the ratio between the mirror aperture and the absorber tube diameter, but this has

no optical collection or thermal loss relevance, because no real or imaginary surface along the diameter of the tube accepts or emits radiation. What emits re-radiation is part, or all, of the absorber tube perimeter, depending on the design. When viewed from the point of view of the standard definition of geometrical concentration, which might be defined as the ratio of the collector aperture divided by the smallest surface area that can be drawn around the re-radiation emitting portion of the receiver, today's LFRs at 50X+ are already substantially higher in concentration than the 25–30X typical of troughs.

Some studies have suggested that LFRs may not be efficient enough to compete with troughs. However, these studies have been based around the more public SPG system, not higher optical efficiency lower thermal loss configurations like the Areva and Novatec systems. The origin of the LFR performance deficiency relative to troughs is not so much in peak performance; for example, Areva collectors are close to trough peak performance at high temperature. It is rather the flatter output characteristic of north-south axis troughs during the day that increases their plant capacity factor (CF). But in compensation, there seems to be acceptance that LFRs are considerably cheaper to build than PTCs. Two future changes can profoundly affect this cost debate; field design and thermal storage.

The current tendency to crowd the LFR reflectors together means that each individual reflector does well at midday but less well at other times of day when blocking occurs by adjacent reflectors. The recent paper by Chavez and Collares-Periera (2010) suggests that optical concentration close to 100 times is possible in ideal CLFR systems, and both Collares-Periera and the author believe that practical systems of 75 times optical concentration can be expected in the foreseeable future. For this, we need wider systems. A wider spacing can yield an output per m^2 which may be superior if the receiver is designed to accept light from distant reflectors without spillage. Current receivers are not designed to efficiently collect from distant reflectors, but Chavez and Collares-Periera have discussed such a system and the author has shown a design for a single tube (Mills, 1995c). Mirror-flipping, the defining characteristic of CLFRs discussed early in this chapter, is also more effective if the receiver can collect more efficiently from distant field reflectors. The penalty of any spread-out system will be some compromise of the ground area efficiency because the low angles of radiation reflected to the tower demand wider spacing, but the benefits of lower area cost and better distant mirror performance will likely outweigh this. While the 'spread-out' system would incur some added secondary reflector absorption penalty for a higher concentration system, the author believes this can be held to between 1 and 2% for future designs. The lower relative receiver cost and better thermal performance of high

concentration systems become very important at the higher operating temperatures of ~550°C.

The other way to attack the capacity factor problem is to use storage. Dersch *et al.* (2009) describe annual dumping fractions, the greatest of which is caused in peak periods by a mismatch to turbine size. The peakier LFR characteristic and higher dumping necessary when there is no storage decrease the LFR plant capacity factor and total energy output per m^2 relative to a trough. The price that north-south tracking axis troughs pay for this advantage is a much larger land footprint, because the trough reflectors need much more ground area than an LFR in order not to block and shade one another as they track the sun's elevation. Given the low price of arid land, this is acceptable. However, the LFR capacity factor deficit suddenly disappears with the advent of sufficient thermal storage, which removes dumping and smooths output.

If we look briefly beyond LFRs, we see that Enel has recently built a salt circulation trough plant using a new evacuated tube from the Archimede company in Italy and Siemens (Archimede, 2011) to operate at 550°C, so perhaps the worries of engineers can be resolved with respect to salt freezing in the field at night and overnight heat loss. If Archimede can produce a successful salt storage receiver for trough plants, there is absolutely nothing to stop an LFR using the same receiver technology, and possibly a non-vacuum version can be designed also. Indeed, an LFR seems a superior configuration to a linear salt plant, with fixed piping easily heated by reflectors and excellent drain-down possible. At temperatures of 550°C, heat loss is important, and the higher concentration of LFRs would reduce that liability relative to a trough. If concentration can be extended to 75X in the future as the author believes, then the LFR would require half the number of receivers as a trough of the same annual output and have accordingly lower heat loss. A company called Skyfuel (2011) currently is investigating a molten salt LFR concept under a US DOE grant.

Molten nitrate salt is the current pre-eminent storage medium. It has been demonstrated in troughs at lower temperatures and towers at 550°C (Gould, 2011). At the higher temperatures, the amount of salt required to store heat is substantially reduced through a larger temperature difference (perhaps by a factor of 3) so that the CF difficulties previously alluded to now largely disappear because the plant can follow the load precisely by storing any excess energy in the molten salt tank. However, molten salt is not the only high temperature circulation medium. The demonstrated ability of LFR manufacturers to produce direct steam generation more easily than trough collectors gives a powerful momentum for the development of 500–550°C superheated steam systems using the higher optical concentration possible in an LFR system. If a storage system can be developed to store the output from a superheated steam LFR, then this may be

the lowest cost system, and easier to manage than salt-filled linear collectors. The DLR is already working on such systems.

If significant thermal storage becomes standard, then it would seem that the collector design that collects the most energy for the least cost will be the commercial winner, regardless of the collector thermal output profile. Current LFRs are strong on the low-cost aspect but weaker on the annual energy per collector area side. However, in a short time they have begun to approach trough performance and if capacity factor issues are reduced through storage or field design, they may prevail.

6.9 Conclusions

The LFR market is already highly competitive, and all of the major LFR manufacturers are now progressing with versions that surpass most current trough output temperatures (about 400°C), and later will approach current tower technology temperatures. The recent superheating results above 450°C by SPG, Areva and Novatec herald this future. In this chapter, comparisons have sometimes been difficult to make without access to what continues to be proprietary commercial information, but it is clear that development of both major collector types is rapid and each can use any storage technology developed for troughs. No decision on the correct design for an LFR can yet be made, although peak performance is approaching that of troughs in the case of the non-secondary reflector LFR. What can perhaps be said with greater confidence is that LFR energy production cost is dropping rapidly compared to trough technology.

Towers on their own promise high temperature through very high optical concentration, but low field and O&M costs seem to be elusive. In the recent competitive shortlisting for the Australia flagship project, LFRs and troughs proceeded to the short list but no tower did. Troughs offer high field efficiency, proven technology, and a flat daily output pattern, but downsides are low concentration and high field costs. With LFRs and CLFRs, the advantages of high temperature, fixed pipes for high pressure operation, low losses using selective coatings and medium concentration, low field cost, and relatively compact land usage are potentially available in one package.

Francia's inspiration 50 years ago was a profound one. Yet many significant improvements are still possible in what is a young, exciting technology. This coming decade will see many new LFR developments take their place in the market.

6.10 References

Appleyard D (2010), 'Chilling in the heat of the Doha sun', *Renewable Energy World*, December.

Archimede (2011), Solar Receiver Tubes for Thermodynamic Power Plants, Archimede Solar website, http://www.archimedesolarenergy.com/en_home.asp (accessed 15 January 2012).

Areva (2012), CLFR performance and specifications, at http://www.areva.com/EN/operations-3641/compact-linear-fresnel-reflector-technology.html (accessed 6 January 2012).

Ausra (2007), CLFR Coal saver plants. Statement by Ausra, the predecessor of Areva Solar, at http://www.solarpaces.org/Tasks/Task1/clfr_coal_saver.htm (accesssed 15 January 2012).

Bernhard R, Laabs HJ, de Lalaing J, Eck M, Eickhoff M, Pottler K, Morin G, Heimsath A, Georg A, Häberle A (2008), 'Linear Fresnel collector demonstration on the PSA, Part I – Design, construction and quality control', *Proc. 14th International Symposium on Concentrated Solar Power and Chemical Energy Technologies*, 3–7 March, Las Vegas.

Bernhard R, Lalaing J, Kistner R, Eck M, Eickhoff M, Feldhoff JF, Heimsath A, Hülsey H, Morin G (2009), 'Linear Fresnel collector demonstration at the PSA – Operation and investigation', *Proc. 15th International Symposium on Concentrated Solar Power and Chemical Energy Technologies*, 14–18 Sept., Berlin.

Buffon G-L (1830), 'Burning instruments', in *The Edinburgh Encyclopaedia*, D. Brewster (ed.). 135–137.

Burkholder F and Kutscher C (2008), Heat Loss Testing of Solel's UVAC3 Parabolic Trough Receiver. National Renewable Energy Laboratory Report NREL/TP-550-42394, January.

Burkholder F and Kutscher C (2009), Heat Loss Testing of Schott's 2008 PTR70 Parabolic Trough Receiver. National Renewable Energy Laboratory Report NREL/TP-550-45633, May.

Chavez J and Collares-Periera M (2010), 'Etendue-matched two-stage concentrators with multiple receivers', *Solar Energy*, 84 (2), 196–207.

Conlon W (2011), 'Superheated steam from CLFR solar steam generators', *Proc. 16th International Symposium on Concentrated Solar Power and Chemical Energy Technologies, 21–24 Sept., Perpignan, France.*

de Lalaing J. (2009), Interview with Jaques de lalaing by Beyond Zero Emissions, August. Available at http://w.w.w.beyondzeroemission.org/media/radio/count-jaques-de-lalaing-solar-power-groups-linear-fresnel-solar-thermal-090817.

Dersch J, Morin G, Eck M, Häberle A (2009), 'Comparison of linear Fresnel and parabolic trough collector systems – system analysis to determine break even costs of linear fresnel collectors', *Proc. 15th International Symposium on Concentrated Solar Power and Chemical Energy Technologies*, 14–18 Sept., Berlin.

Dey CJ, Mills DR, Morrison GL (2000), 'Operation of a CLFR research apparatus', *Proc. New Zealand Solar Energy Society Annual Conference – From Fossils to Photons*, Brisbane.

Di Canio DG, Tretyl WG, Jur FJ, Watson CD (1979), 'Line-focus solar thermal central receiver research study', Final Report 1977–79 DOE/ET/20426-1, OSTI ID: 5535434, FMC Corporation, Santa Clara, CA.

Eck M, Uhlig R, Mertins M, Häberle A, Lerchenmüller H (2007), 'Thermal load of direct steam-generating absorber tubes with large diameter in horizontal linear Fresnel collectors', *Heat Transfer Engineering*, 28 (1), 42–48.

Feuermann D (1993), 'Analysis and evaluation of the solar thermal system at the Ben-Gurion Sede Boqer Test Center for solar electricity generating technologies',

Final Report, Contract No. 88169101, Israel Ministry of Energy and Infrastructure, Jerusalem, July.
Feuermann D and Gordon JM (1991), 'Analysis of a two-stage linear Fresnel reflector solar concentrator', *Transactions of the ASME*, 113, 272–279.
Francia G (1968), 'Pilot plants of solar steam generation systems', *J. Solar Energy*, 12, 51–64.
Gould W (2011), 'Solar Reserve's 565 MWt molten salt power towers', *Proc. 16th International Symposium on Concentrated Solar Power and Chemical Energy Technologies*, 21–24 Sept., Perpignan, France.
Häberle A, Mertins M, Lerchenmüller H, Heinzel V (2004), 'Geometry optimization of Fresnel collectors with economic assessment', *Proc. 14th International Sonnenforum – Proceedings 1, EuroSun2004*, 1-918–1-925.
Industrial Solar (2011a), 'Mirroxx is now Industrial Solar'. Pressbox Industrial Solar GmbH, 4 May, at Hhttp://www.pressebox.com/pressreleases/industrial-solar-gmbh/boxid/416345 (accessed 31 May 2011).
Industrial Solar (2011b), 'Technical Data; Industrial Solar linear Fresnel collector LF-11', 30 March, at http://www.industrial-solar.de/cms/uploads/media/IS_technical_data_300311.pdf (accessed 31 May 2011).
Mertins M, Lerchenmüller H, Häberle A (2004), 'Geometry optimization of Fresnel collectors with economic assessment', *Proc. 14th International Sonnenforum, EuroSun2004*, 20–24 June, Freiburg, Germany.
Mills DR (1995a), 'Proposed solar cogeneration powerplant for 2000 Olympics', *Proc. Solar '95 Renewable Energy: the Future is Now*, 33rd Annual Meeting, 465–473, International Solar Energy Society Congress (also presented at the Harare ISES meeting, but no proceedings were forthcoming).
Mills DR (1995b), Australian patent #694335, plus filings in USA, Europe, China.
Mills DR (1995c), 'Two-stage collectors approaching maximal concentration', *Solar Energy*, 54 (1), 41–47.
Mills DR and Dey CJ (1999), 'Transition strategies for solar thermal power generation', *Proc. International Solar Energy Society Congress*, Jerusalem, 5–9 July.
Mills DR and Morrison GL (1999), 'Compact linear Fresnel reflector solar thermal powerplants', *Solar Energy*, 68 (3), 263–283.
Mills DR, Morrison G, Le Lièvre P (2004a), 'Design of a 240 MWe solar thermal power plant', *Proc. 14th International Sonnenforum, EuroSun2004*, 20–24 June, Freiburg, Germany.
Mills DR, Morrison G, Le Lièvre P (2004b), 'Lower temperature approach for very large solar power plants', *Proc. 12th SolarPACES International Symposium*, Oaxaca, Mexico, October.
Mills DR, Morrison G, Pye JD, Le Lièvre P (2006), 'Multi-tower line focus Fresnel array', *Journal of Solar Energy Engineering*, 128 (1), 118–120.
Morin G, Platzer W, Eck M, Uhlig R, Häberle A, Berger M, Zarza E (2006), 'Road map towards the demonstration of a linear Fresnel collector using a single tube receiver', *Proc. of SolarPACES 13th International Symposium on Concentrated Solar Power and Chemical Energy Technologies*, 20–23 June, Seville, Spain.
Morin G, Dersch J, Eck M, Häberle A, Platzer W (2009), 'Comparison of linear Fresnel and parabolic trough collector systems – influence of linear Fresnel collector design variations on break even cost', *Proc. 15th International Symposium on Concentrated Solar Power and Chemical Energy Technologies*, 14–18 Sept., Berlin.

Morin G, Dersch J, Häberle A, Platzer W, Eck M (2011), 'Comparison of linear fresnel and parabolic trough power plants', *Solar Energy*, doi:10.1016/j.solener.2011.06.020, in press.

NOVA-1 (2011a), 'The future. Today. PE 1 – World's first Fresnel Solar Power Plant in commercial operation', at http://www.novatecsolar.com/files/mne0911_PE1_broschure_english.pdf (accessed 15 January 2012).

NOVA-1 (2011b), Technical data sheet, at http://www.novatecsolar.com/files/mntd1102_technical_data_sheet.pdf http://www.novatecsolar.com/files/mn1102_nova1_brochure_eng_web.pdf (accessed 15 January 2012).

Paul C, Bachelier C, Teichrew O, Weckert C (2011), 'Power plant concepts between CSP solar-only developments and integrated solar combined cycles based on the latest commercially available Fresnel collectors', *Proc. 16th International Symposium on Concentrated Solar Power and Chemical Energy Technologies*, 21–24 Sept., Perpignan, France.

PEM (2011), FNEG Solar, *Power Engineering Magazine*, 30 March, at http://www.power-eng.com/articles/2011/03/areva-fneg-solar.html (accessed 15 January 2012).

Pye JD, Morrison GL, Behnia M, Mills DR (2003), 'Modelling of the cavity heat transfer for the compact linear Fresnel reflector', *Proc. Australia and New Zealand Solar Energy Society Conference*, Adelaide.

Reynolds D, Jance M, Behnia M, Morrison GL (2001) 'An experimental and computational study of the heat loss characteristics of a trapezoidal cavity absorber', *Proc. of International Solar Energy Society Solar World Congress*, Adelaide.

Shaner WW and Duff WS (1979), 'Solar thermal electric power systems: comparison of three line focus collectors', *Solar Energy*, 22 (1), 49–61.

Skyfuel (2011), High temperature linear Fresnel, at http://www.skyfuel.com/index_main.html#/OUR%20TECHNOLOGY/HIGH%20TEMPERATURE%20LINEAR%20FRESNELR/ (accessed 15 January 2012).

Solar Dawn (2011), Website regarding the 250 MW flagship solar project in Queensland, at http://solardawn.com.au/ (accessed 15 January 2012).

SPG (2008), Continuous steam production at 450°C, 15 September, at http://www.solarpowergroup.com/169.0.html (accessed 15 January 2012).

SPG (2011), Continuous steam production at 450°C. Solar Power Group web address http://www.solarpowergroup.com/113.0.html (accessed 15 January 2012).

SuperNOVA (2011), 'Fresnel specialist Novatec Biosol turns to superheated steam to boost efficiency by 50%', *Renewable Energy Magazine*, 4 June, at http://www.energias-renovables.com/energias/renovables/index/pag/solar_thermal_electric/botid/73/colright/solar_thermal_electric/tip/articulo/pagid/12273/title/Fresnel%20specialist%20Novatec%20Biosol%20turns%20to%20superheated%20steam%20to%20boost%20efficiency%20by%2050porciento/len/en (accessed 15 January 2012).

USN (2011), Sun or Moon Altitude/Azimuth Table, US Naval Oceanography Portal, at http://aa.usno.navy.mil/data/docs/AltAz.php (accessed 1 June 2011).

USOTA (1978), Application of solar technology to today's energy needs, Chapter VIII, Collectors, 270. Report by the Congress of the United States Office of Technology Assessment (USOTA). Available for free download at http://www.princeton.edu/~ota/disk3/1978/7802/780212.pdf.

Venetos M (2010), 'Compact Linear Fresnel Reflector Technology for Power Augmentation', *Proc. Solar Power International*, Los Angeles.

Winston R and Rabl A (1976), 'Ideal concentrators for finite sources and restricted exit angles', *Applied Optics*, 15 (11), 2889–2883.

Zhang Q-C and Mills DR (1992), 'New cermet film structures with much improved selectivity for solar thermal applications', *Appl. Phys. Lett.*, 60 (5), 545–547.

7

Parabolic-trough concentrating solar power (CSP) systems

E. ZARZA MOYA, CIEMAT – Plataforma Solar de Almería, Spain

Abstract: This chapter gives an overview of the parabolic-trough collector (PTC) technology, the technology most widely used in solar thermal power plants today. It includes a brief history of the earliest parabolic-troughs and a description of the first commercial projects implemented in the 1980s, the main parameters and basic equations of a typical PTC, design criteria, operation and maintenance issues and expected technology improvements in working fluids and solar collectors that could be implemented in the short to medium term.

Key words: solar energy, parabolic-trough collectors, solar concentration, linear solar collectors, solar thermal power plants.

7.1 Introduction

A parabolic-trough collector (PTC) is a linear-focus solar collector, basically composed of a parabolic-trough-shaped concentrator that reflects direct solar radiation onto a receiver or absorber tube located in the focal line of the parabola (see Fig. 7.1). The larger collector aperture area concentrates reflected direct solar radiation onto the smaller outer surface of the receiver tube, heating the fluid that circulates through it. The solar radiation is thus transformed into thermal energy in the form of sensible or latent heat of the fluid. This thermal energy can then be used to feed either industrial processes demanding thermal energy (e.g., food industry, petro-chemical industry, etc.) or Rankine cycles to produce electricity with a steam turbine in a 'solar thermal' power plant.

With today's technology, parabolic troughs can deliver useful thermal energy up to 398°C. The main limitation on the maximum temperature is imposed by the thermal oil currently used as the working fluid, because it quickly degrades above 398°C. However, research in new fluids promises higher temperatures close to 500°C in the mid term.

7.1.1 Historical development

The first document describing the optical properties of a parabolic-trough collector was written by the Greek mathematician Diocles in the second

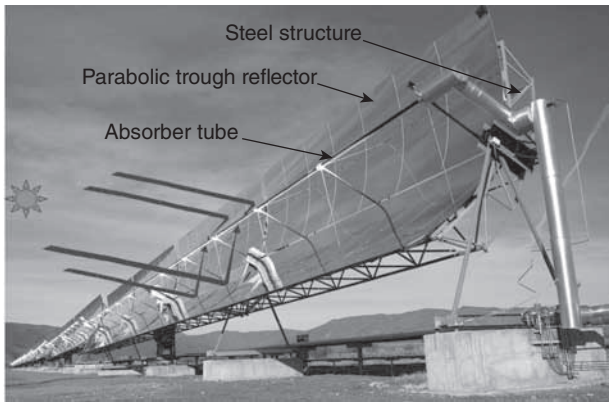

7.1 A typical parabolic trough collector.

century BC. Diocles explained that a parabolic mirror reflects the solar rays towards a common point located at a specific place (i.e., the focal point of the parabola). However, more than 20 centuries had to pass before the first solar system using parabolic-trough collectors was actually erected. The first graphically documented parabolic-trough solar collector was designed and built by Swedish engineer, John Ericsson, at the end of the nineteenth century. This collector had a solar radiation collecting surface of 3.25 m^2 and produced saturated steam for a small 373 W steam engine. In 1883, the original design using reflectors made of polished sheet metal was improved by Ericsson with the installation of flat strips of silvered-glass reflectors in a frame providing the parabolic shape with a 3.35×4.9 m aperture. It produced saturated steam at 0.24 MPa to drive a 120 rpm steam engine with a single 0.153 m diameter 0.2 m stroke piston. Any possibility of commercial development died with Ericsson in 1889 because he always kept the technical details secret.

Later, in 1913, the American engineer, Frank Shuman, designed and built a parabolic-trough collector solar plant in Egypt that produced 0.1 MPa saturated steam to drive a steam engine for pumping irrigation water for a farming community in Meadi, near Cairo. Shuman had the financial support of British investors, and with the valuable technical advice of British professor, C.V. Boys, improved the overall plant design. Figure 7.2 shows one of the five collectors installed at Meadi in 1913. Every collector was 62.17 m long with a 4.1 m wide parabola, for a total solar field collecting surface of 1274.5 m^2, and 40% collector efficiency. Water was pumped at a flow rate of 380 l/s with the energy supplied by the solar field. The reflectors and receiver tubes were supported by a metal structure on a concrete foundation. The photograph in Fig. 7.2 was taken from the book by Hans Gunther (1922). Although the quality is not very good due to the age of the original

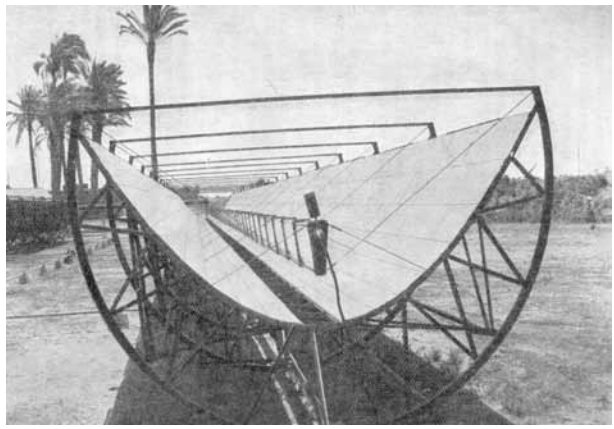

7.2 One of the five parabolic-trough collectors installed by Frank Shuman at Meadi (Egypt) in 1913.

photograph and the digitalization required for reprinting here, the similarity between the parabolic-trough collectors designed by Shuman in 1912 and the collectors installed in solar thermal power plants today is clear. However, the First World War and the entry of oil into the energy market resulted in no more such plants being built at that time.

Twenty years later, in 1935, C.G. Abbot converted solar energy into mechanical power using a parabolic-trough collector (PTC) and a 0.37 kW steam engine (Pytlinski, 1978). After that, there was no further outstanding PTC development in the twentieth century until a renewed interest in solar energy following the 1973 oil price crisis when three PTC prototypes were developed and tested in the USA by Sandia National Laboratories, Honeywell International Inc. and Westinghouse, and a detailed cost study was carried out in 1979 (Shaner and Duff, 1979). A short time later, in the 1980s, several other companies developed new PTC designs and entered the market with small industrial process heat applications and small solar thermal power plants. Table 7.1 gives the details of four small demonstration solar thermal power plants built in the USA, Japan, Spain and Australia at that time.

Among others, the Acurex Solar Corp. (PTC models Acurex 3001 and Acurex 3011), Suntec Systems Corp./Excel Corp. (PTC models IV and 360), Solar Kinetics Corp. (PTC models T-700 and T-800), General Electric, Honeywell Inc. and Jacobs Del. Corp., manufactured and marketed a number of PTCs during the early 1980s (Fernandez-García *et al.*, 2010). Simultaneously, the only two-axis PTC that has ever been marketed, the Helioman 3/32, was developed by the German company Maschinenfabrik Augsburg-Nürnberg (MAN).

Table 7.1 Details of demonstration trough-based solar thermal power plants built during the early 1980s

	Coolidge (USA)	Sunshine (Japan)	IEA-DCS (Spain)	STEP-100 (Australia)
Net electric power	0.15 MW_e	1 MW_e	0.5 MW_e	0.1 MW_e
Total aperture area	2,140 m^2	12,856 m^2	7,622 m^2	920 m^2
Heat transfer fluid	Synthetic oil	Water/steam	Synthetic oil	Synthetic oil
Effective storage capacity	5 MW_{th}	3 MW_e	0.8 MW_e	117 MW_{th}
Duration of service	1980–1982	1981–1984	1981–1987	1982–1985

Although other companies, among them the American company Industrial Solar Technologies (IST), entered the market with successful PTC designs later on, they were mainly for industrial process heat applications. The most outstanding event related to PTC technology in the twentieth century was the design and implementation of the nine SEGS (Solar Electricity Generating System) plants in the Mohave Desert (California, USA) by LUZ International Limited from 1984 (SEGS-I) to 1990 (SEGS-IX). Table 7.2 gives the specifications for the nine SEGS plants, while Fig. 7.3 shows one of the SEGS plants and Fig. 7.4 illustrates the operating principle schematically. A synthetic heat transfer oil is pumped through the trough array and heated by concentrated solar radiation as it circulates through the receiver pipes. This oil is then used to produce steam in heat exchangers before being circulated back to the solar field. The steam is used in a conventional steam turbine-based electricity generating plant. Although some hot oil-based energy storage was provided in the first plant, the SEGS systems overall rely on natural gas firing to provide continuous operation when the sun is not available.

With a total electrical output of 354 MW and more than two million square meters of parabolic-trough collectors, the SEGS plants have been an invaluable aid in the improvement and commercial deployment that parabolic-trough collectors are now experiencing at the beginning of the twenty-first century (Harats and Kearney, 1989). The fact that these plants are still in daily operation after so many years provides a high level of technical credibility and confidence for both investors and promoters. But the SEGS plants have not only contributed to the commercial take-off of parabolic-troughs by acting as a 'technology showcase' for new projects promoted in the twenty-first century, they have also made possible the existence of an industrial capability to at least partly satisfy the initial demand for essential components, such as receiver tubes and reflectors.

Table 7.2 Specifications for the nine SEGS plants built by the company LUZ International

	SEGS 1	SEGS 2	SEGS 3	SEGS 4	SEGS 5	SEGS 6	SEGS 7	SEGS 8	SEGS 9
Duration of service	1984–present	1985–present	1986–present	1986–present	1987–present	1988–present	1988–present	1989–present	1990–present
Net electric power	13.8 MW_e	30 MW_e	30 MW_e	30 MW_e	30 MW_e	30 MW_e	30 MW_e	80 MW_e	80 MW_e
Efficiency in solar mode (%)	28.5	29.40	30.60	30.60	30.60	37.70	37.50	37.60	37.60
PTC model	LS1	LS1/LS2	LS2	LS2	LS2	LS2	LS3	LS3	LS3
Total aperture area (m^2)	83,000	188,990	230,300	230,300	233,120	188,000	194,280	464,340	483,960
Solar field inlet/outlet temperatures (°C)	241/307	248/320	248/349	248/349	248/349	293/393	293/393	293/390	293/390
Synthetic oil (HTF)	ESSO-500	M-VP1	M-VP1	M-VP1	M-VP1	M-VP1	M-VP1	M-VP1	M-VP1

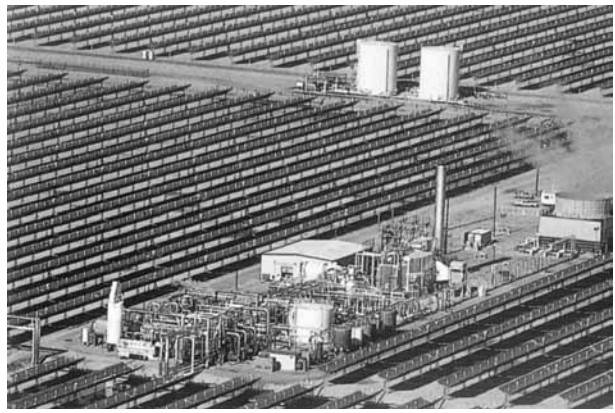

7.3 View of one of the SEGS plants.

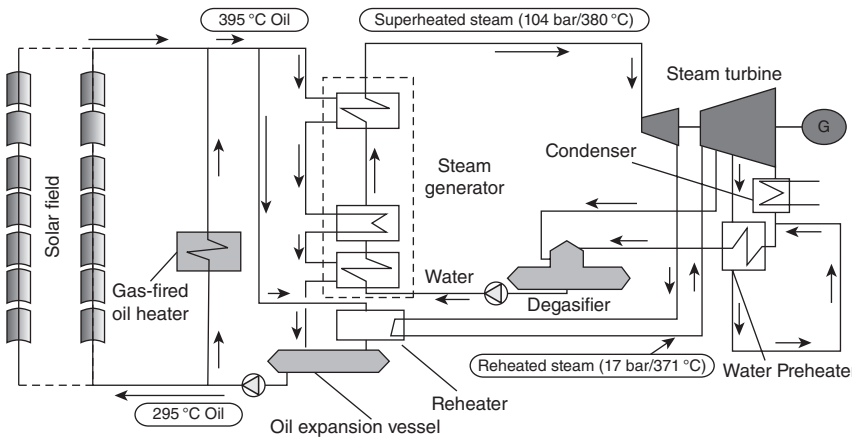

7.4 Schematic configuration of a typical SEGS plant.

The SEGS plants were developed because of the favorable conditions defined by the legal framework implemented in the United States as a consequence of the steep rise in oil prices in the 1970s. However, these government incentives for renewable systems were cut and became insufficient when the oil price fell again in the 1980s, thus making installation of more SEGS plants unfeasible (Lotker, 1991).

Since early in this century, government incentives have again been set up in some countries (e.g., tax credits in the USA, a favorable feed-in tariff in Spain and Algeria, etc.), promoting a multitude of solar thermal power plant projects. Most of these new projects are based on parabolic-trough collectors, because long-term successful track records of the SEGS plants establish them as the 'least risk' and most readily financeable solution. This

surge of new solar power plants has led to a significant investment in R&D, and the development of many new parabolic-trough collector designs and new factories for key components (e.g., reflectors and receiver tubes) in the USA and Spain.

7.2 Commercially available parabolic-trough collectors (PTCs)

7.2.1 Large PTCs

One of the achievements of LUZ International was the development of three reliable, durable PTC designs, called the LS1, LS2 and LS3, which were successfully implemented and operated in the SEGS plants. Although the LS1 installed by LUZ at the SEGS-I plant in 1984 had a unit length of 50.2 m and a parabola width of 2.5 m, which was similar in size to other designs developed during the early 1980s, it soon became evident that bigger PTCs would have to be developed for larger CSP plants. This was the reason why LUZ developed the LS2 and LS3 designs, with aperture areas of 235 and 545 m^2 per collector, respectively. After the demise of LUZ, one of the barriers to the installation of large solar fields with parabolic troughs was lack of a suitable PTC. In view of this, a European consortium composed of industry, engineering firms and R&D centers was formed in 1998 to develop a new PTC suitable for large CSP plants. The result was the Eurotrough-100 (ET-100) and EuroTrough-150 (ET-150) designs, which were then improved, leading to their successor, the SKAL-ET, the collector installed at the ANDASOL-I plant in Spain in 2007. Figure 7.5 shows the

7.5 Steel structure of the Eurotrough-100 collector design.

Table 7.3 Parameters of the Eurotrough-150 collector design

Parabola width (m)	5.76
Overall length of a single collector (m)	147.5
Length of every module (m)	12.27
Number of parabolic trough modules	12
Outer diameter of the steel receiver pipe (m)	0.07
Inner diameter of the steel receiver pipe (m)	0.065
Collector aperture area (m^2)	822.5
Mirrors reflectivity	0.93
Steel receiver pipe absorptance	0.95
Intercept factor	0.90
Receiver pipe glass cover transmittance	0.95
Peak optical efficiency	0.75

steel structure of the ET-100 design, and Table 7.3 gives the parameters of the ET-150 collector design.

Highly precise assembly of the steel structural profiles is required to achieve perfect parabolic shape of the concentrator and overall structural rigidity, while at the same time keeping assembly cost low. Thus, although not all PTC designs require assembly jigs, most of the modern designs do require them to meet the design tolerances, which are usually around ±1 mm. Figure 7.6 shows the final check of an assembly jig for the EuroTrough collector design.

The collector design shown in Fig. 7.5 has a central space frame, called *torque box*, which provides good rigidity and prevents torsion, which is very important to ensure good PTC optical and geometrical performance under moderate wind speeds (below 35 km/h). Figure 7.6 also shows how a Eurotrough parabolic-trough module looks when all its components have been mounted in the assembly jig. In large parabolic-trough solar fields, two or three assembly lines are used in parallel to shorten the construction time. Another PTC design approach is the replacement of the torque box by a central steel tube (called the *torque tube*). However, assembly of the steel mirror support frames on this central tube must also be highly accurate. Figure 7.7 (bottom) shows a detail of the collector developed by the Spanish company, Albiasa Solar (www.albiasasolar.com), using the torque tube concept. The collectors developed by the Spanish companies, SENER (www.sener.es) and URSSA (www.urssa.es), in 2006–2010 also have a torque tube instead of a torque box.

The main advantage of PTC torque box designs is their usually better performance and rigidity under wind loads, while their main disadvantage is their higher assembly cost due to the number of steel profiles which require high-precision assembly. Torque tube designs, on the other hand, are usually somewhat cheaper, but are subject to more deformation from

7.6 Check out of the assembly jig for EuroTrough collectors (top) and a parabolic-trough module assembled in the jig (bottom).

gravity (bending) and wind loads (torsion) than those using a torque box. In any case, rigidity in wind loads of both PTC designs is good enough to keep deformation within reasonable limits.

There are also commercial PTC designs which provide a good stiff structure without a torque box or a torque tube, which are replaced by a metallic space frame, such as the one with a 430.8 m^2 collector aperture area used by Solargenix and Acciona in the Nevada Solar One Plant, or the American Skyfuel company's SkyTrough collector, which has a collector aperture area of 690 m^2 (www.skyfuel.com). The design used by Solargenix and Acciona is also notable in that it is one of the few PTC designs that does not use an accurate jig for assembly, but instead relies on the accuracy of the preformed parts and fasteners to generate an accurate shape. Figure 7.7 (top) shows the space frame developed by the company Gossamer Space Frames for Solargenix and successfully used in the CSP plant Nevada Solar One, and which provides good torsional rigidity and performance in wind loads.

7.7 PTC designs using a space frame (top) and torque tube (bottom) to provide good torsional rigidity.

Other means of providing a stiff structure in order to reduce costs and simultaneously maintain good rigidity and assembly accuracy are under study. However, these innovative designs were only in the prototype stage at the end of 2010.

Since the size and number of components in the structure of large PTC collectors used in solar thermal power plants make correction of errors almost impossible after the structures have been installed in the solar field, an effective quality control procedure during the whole assembly process is extremely important to ensure that design tolerances and performance are met. In addition to a highly accurate assembly of the steel structures, the alignment of the parallel rows of collectors in the solar field must also be accurate to avoid solar tracking errors, especially when open-loop tracking systems based on mathematical calculation of sun coordinates are used.

Any misalignment would introduce a tracking error and a corresponding reduction in the concentrated solar radiation finally reaching the receiver pipes.

Although the main type of reflector used in commercial PTC designs is the curved back-silvered low-iron thick-glass mirror, it can also be made of polished sheet metal, or silver or aluminum-coated films that can be laminated onto a rigid parabola-shaped substrate. There are several suppliers of this type of polymer film reflector. Vikuiti™ marketed by 3M (http://www.solutions.3m.com) and ReflecTech® marketed by Reflectech Inc. (http://www.reflectechsolar.com) are two examples of polymer film reflectors for solar applications. However, experimental data about their outdoor performance and durability are still limited and not as plentiful as for glass mirrors.

7.2.2 Small PTCs

Although most of the R&D effort in the late twentieth century and early in the twenty-first century has been devoted to big parabolic-trough collectors for large solar thermal power plants, new smaller troughs have also been developed for process heat applications with temperatures below 300°C. These collectors can provide process heat to a wide range of applications replacing natural gas, such as crop drying and food preparation. Industrial processes such as biofuel production, water purification, desalination and absorption-chiller air conditioning for commercial and industrial buildings are within the capability of these small parabolic-trough collectors.

IST was very active in developing several collectors and installing a number of commercial plants in the USA. In 2007 IST was purchased by the Spanish industrial group, Abengoa, and their IST-PT1 and IST-RMT collectors were then marketed by Abengoa Solar IST (www.abengoasolar.com). Both collectors have non-evacuated receiver pipes with a black-chrome coating and glass envelope, and maximum working temperatures of 288°C and 204°C, respectively.

Another small PTC for process heat applications is the PTC-1800 collector developed by the German-Turkish company, SOLITEM (www.solitem.de). The maximum working temperature of this collector is 200°C and the collector aperture area is 36.65 m^2.

The Australian company, NEP Solar Pty Ltd (www.nep-solar.com), also developed a small PTC, the PolyTrough-1200, suitable for temperatures up to 230°C. The 24 m long, 1.2 m wide PolyTrough-1200 collector consists of composite reflector panels with aluminum sheets which can be mounted either on roofs or at ground level.

SOPOGY (www.sopogy.com), with head offices in Honolulu (Hawaii), has developed a 3.7 m long, 1.35 m wide parabolic-trough collector module marketed as Soponova 4.0, which is suitable for both process heat

7.8 The Soponova 4.0 parabolic-trough concentrator developed by SOPOGY.

applications and electricity generation. Figure 7.8 shows a Soponova 4.0 collector module. In 2010, eight solar power plants had been built around the world by SOPOGY. The most recent was in Keahole (Hawaii), inaugurated in December 2009, with a 2 MW_e rated power output. SOPOGY developed a small solar thermal power plant concept scalable from 250 kW_e to over 20 MW_e based on Soponova 4.0 trough-collector arrays. This concept of a scalable solar thermal power plant was patented by SOPOGY under the trade name MicroCSP™.

Table 7.4 gives the technical parameters of the small parabolic-trough collectors marketed by Abengoa Solar IST, SOLITEM and SOPOGY.

7.2.3 Receivers

The typical PTC receiver tube is in fact composed of two concentric pipes, an inner steel pipe containing the working fluid and an outer glass tube surrounding the steel pipe. The glass tube is made of low-iron borosilicate glass to increase its transmittance for solar radiation. The outer surface of the steel pipe has an optically selective surface with a high solar absorptance and low emittance for thermally generated infra-red radiation. The principles of such surfaces are discussed in detail in Chapter 15. The glass tube is usually provided with an anti-reflective coating to achieve a higher solar transmittance and better annual performance.

Receivers for parabolic-trough collectors can be classified as either evacuated or non-evacuated. Evacuated receivers are commonly used for temperatures above 300°C because they have a high vacuum (i.e., 10^{-5} mbar) between the steel pipe and the glass cover, thus reducing thermal losses and

Table 7.4 Technical parameters of Abengoa IST, SOLITEM and SOPOGY parabolic troughs

	IST-RMT	IST-PT1	PCT-1800	Soponova 4.0
Structure	Steel/ aluminium	Steel/ aluminium	Aluminium	Steel/ aluminium
Reflectors	Polished aluminium	Aluminium acrylic	Al-coating 0.5 mm	Aluminium
Trough module size	3.66 × 1.13 m	6.1 × 2.9 m	5.09 × 1.8 m	3.66 × 1.52 m
Receiver tube	Non-evacuated, with black-chrome coating	Non-evacuated, with black-chrome coating	Non-evacuated, with selective coating	Non-evacuated, with selective coating
Maximum temperature	204°C	288°C	~200°C	260°C

increasing the overall efficiency of the PTC, especially at higher operating temperatures. Figure 7.9 shows a typical evacuated receiver. The glass cover of these receivers is connected to the steel pipe by means of stainless steel expansion bellows which not only compensate for the different thermal expansion of glass and steel when the receiver tube is working at nominal temperature, but also provide a tight annular gap between both tubes to make the vacuum. One end of these expansion bellows is directly welded to the outer surface of the steel pipe, while the other end is connected to the end of the glass cover by means of a glass-to-metal welding. Shown in Fig. 7.9 are chemical 'getters' placed in the gap between the steel receiver pipe and the glass cover to absorb gas molecules passing from the fluid to the annulus through the steel pipe wall. Since the evacuated receivers are expensive (about 850 €/unit in 2010) due to their technical complexity, they are used only for higher temperatures, when good thermal efficiency is required and the high cost is compensated by a higher thermal output.

At the end of 2010, there were only three manufacturers of evacuated PTC receivers: Schott, Siemens and ASE. Most of the parabolic-trough solar thermal power plants implemented around the world until 2009 had receivers manufactured by either the Israeli company, Solel (purchased in 2009 by Siemens, www.energy.siemens.com), or the German company, Schott (www.schottsolar.com). In 2009, a third manufacturer, the Italian company, Archimede Solar Energy (ASE, www.archimedesolaenergy.com), announced that they were launching a new receiver tube called HEMS08,

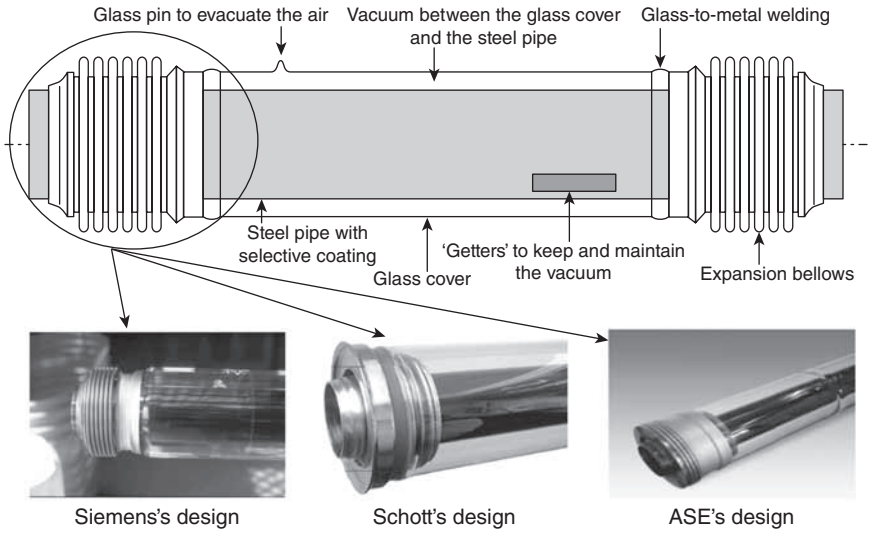

7.9 A typical evacuated receiver for parabolic-trough collectors.

suitable for fluids up to 550°C. The first plant using HEMS08 receivers was the Archimede Plant, located in Syracuse (Italy) and ready to operate in 2010 using molten salt (a mixture of sodium and potassium nitrate) as the receiver working fluid.

Figure 7.9 shows how these three manufacturers join the glass cover and the inner steel pipe by means of flexible bellows. The glass-to-metal welding used to connect the glass cover to the flexible bellows is a weak point in the receiver tube and has to be protected from the concentrated solar radiation to avoid high thermal and mechanical stress that could cause the welding to crack. An aluminum shield is therefore usually placed over the flexible bellows to protect the welding. Table 7.5 shows the technical parameters of the receivers manufactured by the Schott, Siemens and ASE companies.

Non-evacuated receivers are suitable for applications with a working temperature below 300°C, because thermal losses are not so critical at these temperatures. Although non-evacuated receivers are also composed of an inner steel pipe and a glass cover, they have neither vacuum between the steel pipe and its glass cover nor glass-to-metal welds. Selective coatings used for non-evacuated receivers are simpler than those used for evacuated receivers. Black-chrome or black nickel coatings are commonly used because they are cheap and easy to produce.

Due to manufacturing constraints, maximum receiver tube length is usually less than 5 m, so they are connected in series up to the total length of the PTC. Evacuated receivers are usually welded, while non-evacuated receivers are usually connected by special threaded joints.

Table 7.5 Technical parameters of the receivers commercialized by Schott, Siemens and ASE

	Schott PTR-70	Siemens UVAC-2010	ASE HEMS08
Solar absorptance	≥0.95	≥0.96	≥0.95
Solar transmittance	≥ 0.96	≥ 0.96	n.a.
Thermal emittance	≤0.1 at 400°C	≤0.09 at 400°C	≤0.1 at 400°C ≤0.14 at 580°C
Steel pipe inner/ outer diameters	70/65 mm stainless steel	70/65 mm stainless steel	70/65 mm stainless steel
Thermal losses	250 W/m at 400°C	n.a.	230 W/m at 400°C
Glass cover	Borosilicate	Borosilicate	Borosilicate
Active length ratio at 350°C	>96%	96.4%	n.a.
Maximum fluid temperature	400°C	400°C	550°C

7.3 Existing parabolic-trough collector (PTC) solar thermal power plants

Figure 7.10 shows the configuration of a typical parabolic-trough solar thermal power plant with thermal oil (the HTF[1], or heat transfer fluid technology). Such plants, which were the industry standard at the end of 2010, can be divided into three subsystems:

1. The solar field. This is where the direct solar radiation is collected and converted into thermal energy in the form of the sensible heat of the working fluid between the solar field and the power block or thermal storage system. The solar field is composed of parallel rows of solar collectors.
2. The thermal energy storage system. Shown at the centre of Fig. 7.10, this subsystem is not essential to plant operation. However, a thermal storage system provides clear benefits to plant operation, because it not only increases annual hours of operation, and thereby, the amount of electricity produced, but also improves plant dispatchability and enhances plant operation during cloud transients by sending the entire thermal energy produced by the solar field to the storage system instead of to the power block. This operating strategy avoids damage to the steam turbine from unstable steam parameters by acting as a thermal buffer between the

[1] The term heat transfer fluid is used because the fluid transfers heat from the solar field to the point of use and typically (for power generation) is different from the power cycle working fluid.

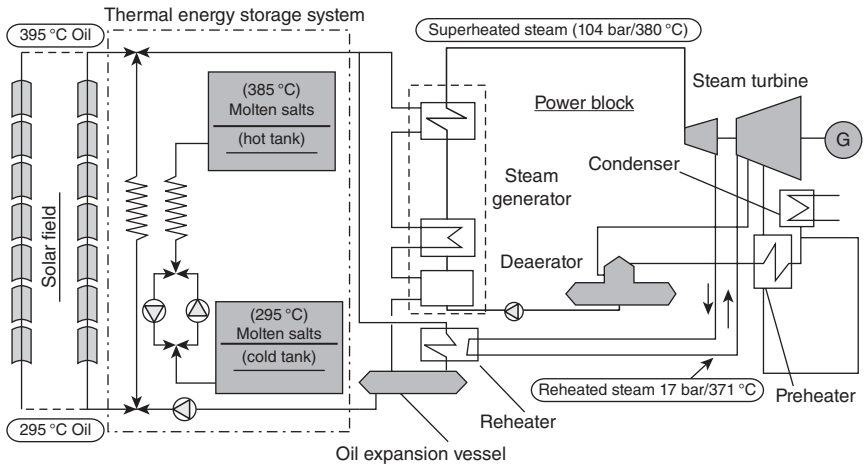

7.10 Configuration of a typical solar thermal power plant with parabolic-trough collectors.

solar field and the power block, and its thermal inertia filters any temperature-related instability in the solar field outlet. However, even without thermal storage, the significant thermal inertia provided by the solar field piping and the steam generator of a large solar thermal power plant can provide enough thermal energy to run the power block at steady output for a few minutes after a cloud affects the solar field. The thermal storage system shown in Figure 7.10 is a two-tank (cold and hot) molten-salt system and its operation is explained in Section 7.6.

3. The power block. This is where the thermal energy delivered by either the solar field or the storage system is converted into electricity by means of a steam Rankine cycle. Since the power block for a parabolic-trough system is similar to conventional power plants (e.g., water pumps, wet cooling systems, steam turbine, electricity generator, de-aerator and water/steam heat exchangers), the required maintenance work is also the same or very similar.

Although not shown in Fig. 7.10, these solar power plants may use an auxiliary gas-fired oil heater to allow plant operation when solar radiation is not available and there is no thermal energy available in the storage system. This heater is usually installed in parallel to the solar field because the experience gained with the SEGS plants showed that plant operation is more difficult if the gas-fired heater is installed in the power block and produces the superheated steam for the steam turbine directly. Although overall plant efficiency would be higher with this configuration because it avoids thermal losses in the oil circuit, the change from solar to fossil plant operating mode would be much more complicated.

On a typical clear day, the solar field tracking is started when direct solar radiation is in the 100–300 W/m^2 range. During the first few minutes, the thermal oil is recirculated through the solar field until it reaches the nominal outlet temperature, and then sent to either the thermal storage system or to the steam generator to start the power block. During daylight hours in summer, the solar field of plants with a thermal storage system delivers enough energy to keep the power block running at full load and at the same time charge the storage system. Since the solar collectors are usually installed with their rotation axis oriented north-south, the thermal output of the solar field on clear winter days is much less than in summer, and thermal storage is not used often because the thermal output of the solar field on clear winter days is only enough to feed the power block. This is the reason why the use of the thermal storage system in winter is usually limited to partly cloudy days.

The profitability achieved in a few countries due to public incentives in the form of feed-in tariffs or tax credits implemented during the first decade of the twenty-first century promoted a multitude of solar thermal power plant projects, most of them with parabolic-trough collectors, because the successful track record of the SEGS plants established it as the most financeable, 'least-risk' technology. Although the world financial crisis of 2008 was a serious barrier to developing all the projects that were initially proposed at that time, many of them became a reality and a significant number of CSP plants with parabolic troughs were in operation at the end of 2010. Table 7.6 gives the list of CSP plants in operation with parabolic troughs at the end of 2010, producing a total electrical output of 876 MW$_e$. Since, due to the strong industrial competition, most of the owners of these plants are rather reluctant to publish annual performance data, such information could not be included in Table 7.6.

7.4 Design of parabolic-trough concentrating solar power (CSP) systems

This section explains the most important parameters of a typical parabolic-trough collector (PTC) and makes recommendations to achieve a good performance. It also describes the PTC energy balance and solar field design criteria.

7.4.1 Basic PTC parameters

Commercial PTC designs for solar thermal power plants are 100 m to 150 m long, and have a parabola width of about 6 m, which provides an aperture area of 550 m^2 to 825 m^2 (approx.). Larger PTC designs are under development and could become commercially available in the mid term.

Table 7.6 List of CSP plants with parabolic troughs in operation at the end of 2010

Plant name	Nominal Power (MWe)	Location	Owner	Remarks
Solar Energy Generating Systems (SEGS-I, IX)	354	California, USA	Sunray Energy, (SEGS I + II) FPL Energy (SEGS III–IX)	Collection of nine units ranging from 14 to 80 MWe and operating since the 1980s
Solnova-I, III and IV	150 (3 × 50)	Seville, Spain	Abengoa	Solnova I (May 2010) Solnova III (May 2010) Solnova IV (August 2010)
Andasol I and II	100 (2 × 50)	Granada, Spain	ACS	Andasol I (2008) Andasol II (2009)
Nevada Solar One	64	Nevada, USA	Acciona Solar Power	Completed in June 2007
Ibersol Puertollano	50	Puertollano, Spain	Iberdrola	Completed in May 2009
Alvarado I	50	Badajoz, Spain	Acciona Solar Power	Completed July 2009
Extresol 1	50	Badajoz, Spain	ACS	Completed in February 2010
La Florida	50	Badajoz, Spain	SAMCA	Completed in July 2010
Archimede solar power plant	5	Siracusa, Sicily, Italy	ENEA	ISCC with molten-salt heat storage Completed in July 2010
Saguaro Solar Power Station	1	Arizona, USA	Arizona Public Services	2006
Keahole Solar Power Plant	2	Hawaii, USA	Keahole Solar Power	Inaugurated in December 2009
La Risca	50	Badajoz, Spain	ACCIONA	Completed in July 2009
Planta Termoel. de Majadas	50	Caceres, Spain	ACCIONA	Completed in November 2010
La Dehesa	50	Badajoz, Spain	SAMCA	Completed in July 2010
Hassi'R Mel-1	20	Laghoutat, Algeria	ABENER + NEAL	150 MW_e ISCCS plant with 20 MW_e solar. Completed in Summer 2010
Kuraymat	40	Kuraymat, Egypt	NREA	470 MW_e ISCCS plant with 40 MW_e solar. Completed in December 2010

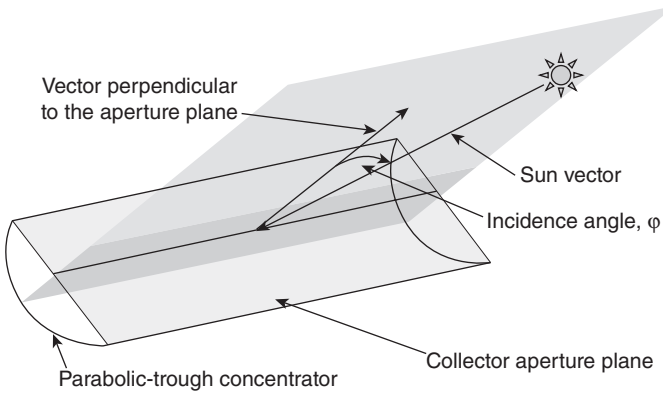

7.11 Correct positioning of a parabolic-trough concentrator.

As solar concentrating devices, parabolic-trough collectors require solar tracking systems to modify their position with the changing apparent sun position in the sky from sunrise to sunset. Movement of this type of solar collector has only one degree of freedom, on-axis rotation. The concentrator must always reflect and concentrate the beam solar radiation onto the receiver tube, and a proper concentration is not possible if the rotation angle is not right. Figure 7.11 shows how direct solar radiation has to reach the collector aperture plane in order to be properly reflected onto the receiver tube. The position of the PTC must be such that the sun vector, the collector focal line and the vector perpendicular to the collector aperture plane are on the same plane. The angle defined by the two vectors shown in Fig. 7.11 is called the incidence angle. It strongly affects the amount of incident solar flux available on the PTC aperture plane, as the smaller the incidence angle, the more incident solar flux can be reflected and converted into useful thermal energy in the receiver pipe. Since diffuse solar radiation falling on the Earth's surface has no specific direction, this component of the solar radiation is useless to a PTC, because it cannot be reflected onto the receiver tube by the concentrator. The fundamentals of CSP systems have been described in general terms in Chapter 2, so some of this material is repeated here with additional specific details for PTC systems.[2]

The most important PTC parameters are the geometric concentration ratio, acceptance angle, rim angle and peak optical efficiency. These parameters are explained in the following paragraphs.

The *geometric concentration ratio*, C_g, is the ratio between the collector aperture area and the total absorber tube area (see Fig. 7.12). This concentration ratio is usually about 25, although theoretically, the maximum is on

[2] Note that the symbols used for variables are similar but not identical to those in Chapter 2.

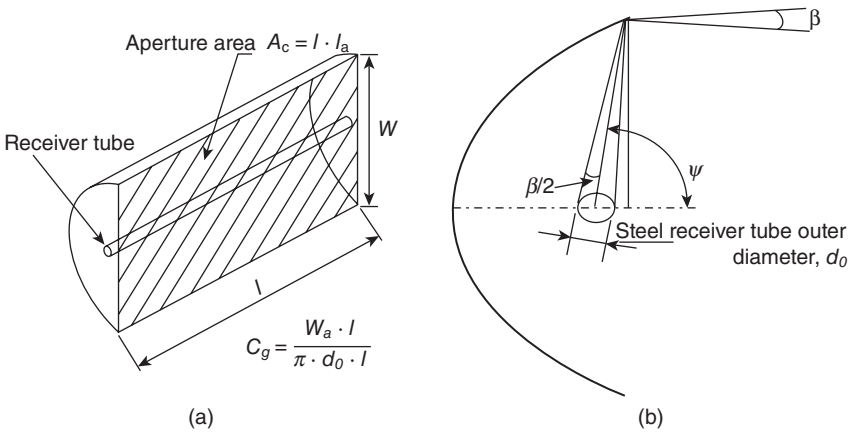

7.12 (a) Geometric concentration ratio, C_g and (b) acceptance angle, β and aperture angle, ψ of a parabolic-trough collector.

the order of 70. High concentration ratios are associated with higher working temperatures. The Geometric concentration ratio, C_g, is given by Eq. [7.1]:

$$C_g = \frac{W \cdot l}{\pi \cdot d_o \cdot l} = \frac{W}{\pi \cdot d_o} \qquad [7.1]$$

where d_o is the outer diameter of the receiver steel pipe, l is collector length, and W is the parabola width.

The acceptance angle, β, is the maximum angle that can be formed by two rays on a plane transversal to the collector aperture in such a way that, when they are reflected by the parabolic mirrors, they intercept the absorber pipe. The wider the collector acceptance angle is, the less accurate the sun tracking system has to be, as the collector will not need to update its position as frequently. Small acceptance angles are associated with high concentration ratios, which require the installation of very accurate solar-tracking systems and, consequently, higher costs. The minimum acceptance angle is 32′ (0.53°), which is the average solid angle with which the solar disk is seen from the Earth. Therefore, any PTC with an acceptance angle smaller than 32′ would always lose a fraction of the direct solar radiation. In fact, recommended acceptance angles for commercial PTCs are in the range 1–2°. Smaller angles would demand very accurate and more expensive solar-tracking systems, while wider angles would lead to small concentration ratios and, therefore, lower working temperatures. So most commercial PTC designs have acceptance angles within the range 1–2°, with geometric concentration ratios of 20 to 30.

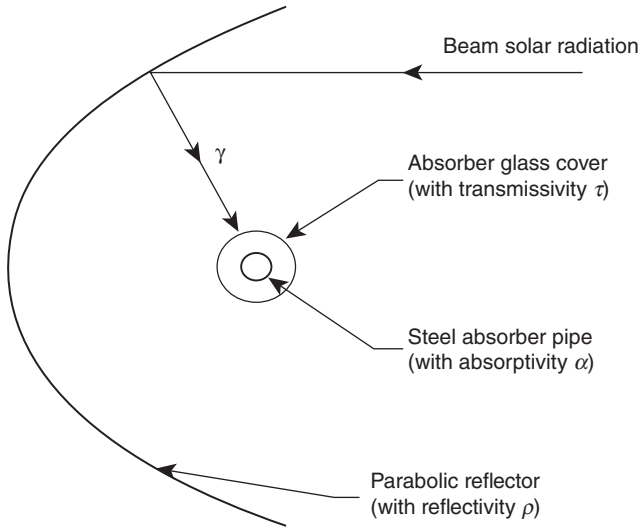

7.13 Optical losses in a parabolic-trough collector.

The *rim angle*, ψ, which is directly related to the concentrator arc length, can be calculated from Eq. [7.2] as a function of the parabola focal distance, *f*, and aperture width, *W*:

$$\frac{8 \cdot f \cdot W}{W^2 - 16 \cdot f^2} = \tan \psi \qquad [7.2]$$

Usual rim angles are in the range 70–110°. Smaller rim angles are not advisable because they reduce the aperture surface. Rim angles over 110° are not cost-effective because they require the whole reflecting surface to be enlarged without significantly increasing the area of the aperture plane.

Optical losses are very important in parabolic-trough collectors because they are about 25% of the total solar flux incident on the PTC aperture plane. Optical losses are associated with the following four parameters (see Fig. 7.13):

- *Reflectivity, ρ, of the collector reflective surface*. Since the reflectivity of the parabolic-trough concentrator is less than 1, only a fraction of the incident solar flux is reflected towards the receiver tube. Typical reflectivity values of clean silvered glass mirrors are around 0.93.
- *Intercept factor, Υ*. A fraction of the direct solar radiation reflected by the mirrors does not reach the active surface of the receiver pipe due to either microscopic imperfections of the reflectors, macroscopic errors in the parabolic-trough concentrator shape (e.g., inaccuracies during assembly), mechanical deformation of the PTC, flexible bellows, or

shadowing by the receiver tube supports. If microscopic imperfections are neglected, the intercept factor with a 0° incidence angle of the beam solar radiation can be considered the result of three parameters: geometrical errors in the parabolic-trough concentrator shape, γ_1, shadowing by the flexible bellows, γ_2, and mechanical deformation (i.e., bending + torsion) of the support structure, γ_3. All of the above parameters cause either some rays to be reflected at the wrong angle or block some of the reflected rays, preventing them from intercepting the steel absorber tube. All these losses are globally quantified by the intercept factor, γ. This optical parameter is typically within the 0.91–0.93 range for high-quality PTCs because $\gamma_1 \cong 0.97$, $\gamma_2 \cong 0.96$ and $\gamma_3 \cong 0.99$.

- *Transmissivity of the glass cover, τ.* The steel receiver tube is inserted in a glass cover to reduce thermal losses. A fraction of the direct solar radiation reflected by the mirrors onto the glass cover of the receiver pipe is unable to penetrate it. The ratio of the radiation passing through the glass cover to the total incident radiation on it, is the transmissivity, τ. of the glass. It is typically $\tau = 0.93$, and can be increased up to 0.96 by anti-reflective coatings applied on both sides of the glass cover.
- *Absorptivity of the receiver selective coating, α.* This parameter quantifies the amount of energy absorbed by the steel receiver pipe over the total radiation reaching its outer wall. This parameter is typically 0.95 for receiver pipes with a cermet selective coating, and slightly lower for pipes coated with black nickel or chrome.

Multiplication of these four parameters (reflectivity, intercept factor, glass transmissivity, and absorptivity of the steel pipe) when the incidence angle of the solar flux onto the PTC aperture plane is 0° gives the *peak optical efficiency* of the PTC, $\eta_{opt,0^\circ}$:

$$\eta_{opt,0^\circ} = \rho \times \gamma \times \tau \times \alpha|_{\varphi=0^\circ} \qquad [7.3]$$

$\eta_{opt,0^\circ}$ is usually in the range 0.74–0.79 for clean, good-quality parabolic-trough collectors.

Taking the four optical parameters included in the peak optical efficiency into consideration, it clearly represents the percentage of the beam solar radiation reaching the PTC aperture plane finally absorbed by the receiver pipe when the incidence angle is 0°.

The incidence angle of the beam solar radiation, φ, affects the four optical parameters mentioned above and the useful aperture area of the collector. This effect is quantified by the *incidence angle modifier*, $K(\varphi)$, which includes all optical and geometric losses in a PTC due to an incidence angle greater than 0°. So the percentage of the beam solar radiation reaching the PTC aperture plane with the incidence angle φ that is finally absorbed by the receiver pipe is the result of multiplying the peak optical efficiency, $\eta_{opt,0^\circ}$, by the incidence angle modifier, $K(\varphi)$.

$$\eta_{\text{opt},\varphi\neq 0^\circ} = \eta_{\text{opt},0^\circ} K(\varphi) \quad [7.4]$$

The incidence angle modifier depends directly on the incidence angle and is usually given by a polynomial equation such that it is equal to 0 for high φ (≥85°), and to 1 for $\varphi = 0°$. Thus the incidence angle modifier for an LS-3 PTC, for instance, is given by:

$$\begin{aligned} K(\varphi) &= 1 - 2.23073\text{E-}4 \times \varphi - 1.1\text{E-}4 \times \varphi^2 \\ &\quad + 3.18596\text{E-}6 \times \varphi^3 - 4.85509\text{E-}8 \times \varphi^4 \qquad (0^\circ < \varphi < 80^\circ) \\ K(\varphi) &= 0 \qquad (85^\circ < \varphi < 90^\circ) \end{aligned} \quad [7.5]$$

Thermal losses are also very important in parabolic-trough collectors because they significantly affect the overall collector efficiency. Total thermal losses in a PTC, $\dot{Q}_{collector\_ambient}$, are due to radiative heat losses from the steel receiver tube, $\dot{Q}_{absorber\_ambient}$, and convective and conductive heat losses from it to its glass cover, $\dot{Q}_{absorber\_glass}$. Though these heat losses are governed by the well-known mechanisms of radiation, conduction and convection, they are experimentally calculated for every PTC and receiver pipe design by operating the collector under real solar conditions at several temperatures. These experimental results are then processed to find the thermal loss equation as a function of the steel receiver tube temperature and the ambient air temperature. Sometimes, thermal losses are calculated as a function of the working fluid temperature, the ambient air temperature and the solar flux incident onto the aperture plane. In any case, the result is a mathematical equation delivered by the PTC manufacturer to the solar field designer for calculating overall thermal losses in the PTC, $\dot{Q}_{collector\_ambient}$.

Today's high temperature PTCs are provided with evacuated receiver pipes, thus avoiding convection losses between the steel pipe and its glass cover.

7.4.2 Energy balance in a PTC

Figure 7.14 illustrates the energy balance in a typical PTC. The solar energy flux incident on the aperture plane of the PTC, $\dot{Q}_{sun\_collector}$, is shown on the left, and the useful thermal energy delivered by the PTC, $\dot{Q}_{collector\_fluid}$, is on the right. The three sources of energy loss in the PTC explained in Section 7.4.1 and shown at the bottom of Fig. 7.14 are:

- optical losses due to mirror reflectivity, intercept factor, glass transmissivity and solar absorptance of the receiver tube when the solar radiation incidence angle is equal to 0°, $\eta_{\text{opt},0^\circ}$
- additional optical and geometrical losses due to an incidence angle greater than 0°, $K(\varphi)$; these additional losses do not exist when the incident angle is equal to 0° because $K(\varphi = 0^\circ) = 1$
- thermal losses from the receiver pipe to the ambient, $\dot{Q}_{collector\_ambient}$.

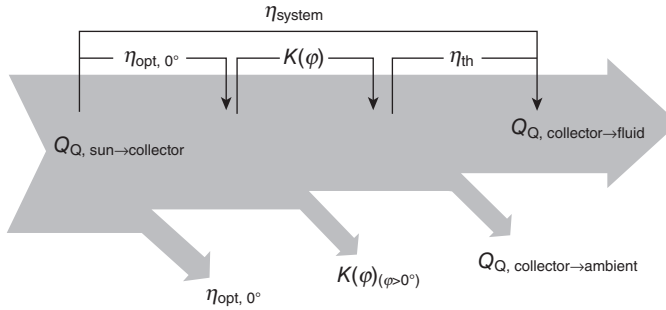

7.14 Energy balance in a parabolic-trough collector.

Taking into consideration the energy balance illustrated in Fig. 7.14, overall PTC efficiency, η_{system}, is calculated as the ratio of the net thermal output power delivered by the collector, $\dot{Q}_{collector\_fluid}$, to the solar energy flux incident on the collector aperture plane, $\dot{Q}_{sun\_collector}$, according to Eqs [7.6], [7.7] and [7.8]:

$$\eta_{system} = \frac{Q_{Q,collector \rightarrow fluid}}{Q_{Q,sun \rightarrow collector}} \quad [7.6]$$

$$\dot{Q}_{sun\_collector} = A_c \cdot E_d \cdot \cos(\varphi) \quad [7.7]$$

$$\dot{Q}_{collector\_fluid} = \dot{m} \cdot (h_{out} - h_{in}) \quad [7.8]$$

where A_c is the collector aperture surface, E_d is the direct solar irradiance, φ is the incidence angle, $\dot{m}$ is the fluid mass flow through the collector receiver tube, h_{in} is the fluid specific mass enthalpy at the collector inlet, and h_{out} is the fluid specific mass enthalpy at the collector outlet.

Equation [7.8] is used when the PTC is in operation and mass flow and temperatures are known. Since the fluid mass flow and the inlet and outlet temperatures are not known during the solar field design phase, the expected net thermal output has to be theoretically calculated from the energy balance shown in Fig. 7.14, and direct solar irradiance, ambient air temperature, incidence angle and PTC optical, thermal and geometrical parameters using Eq. [7.9]:

$$\dot{Q}_{collector\_fluid} = A_c \cdot E_d \cdot \cos(\varphi) \cdot \eta_{opt,0^\circ} \cdot K(\varphi) \cdot F_e - \dot{Q}_{collector\_ambient} \quad [7.9]$$

All the parameters used in Eq. [7.9] were explained above, except for the soiling factor, F_e, which is calculated as the ratio between average PTC mirror reflectivity during real operation and the nominal reflectivity when the PTC is completely clean. So, for instance, if the nominal mirror reflectivity of a PTC is 0.93 and the PTC is washed when reflectivity falls to 0.89, the average mirror reflectivity is (0.93 + 0.89)/2 = 0.91 and F_e =

0.91/0.93 = 0.978. F_e for commercial PTC solar fields is usually in the $0.95 < F_e < 1$ range.

The collector aperture area, optical peak efficiency, incident angle modifier, and thermal losses versus the PTC working conditions and ambient air temperature in Eq. [7.9] are supplied by the PTC manufacturer, while the beam solar irradiance, soiling factor and incident angle are defined by the solar field designer taking local weather conditions, site latitude and longitude and the solar field mirror washing procedure to be used by the plant owner into consideration.

The optical and thermal quality of modern parabolic-trough collectors used in solar thermal power plants is very high. Evacuated receiver pipes significantly reduce thermal loss to less than 35 kW for an average fluid temperature of 375°C in a complete 150 m long and 828 m^2 aperture collector. The useful thermal output (Eq. [7.9]) for a beam solar radiation of 925 W/m^2 and an incidence angle of 15° is about 450 kW at an ambient temperature of 25°C.

The high optical quality of reflectors used in high-temperature PTCs, along with the high accuracy ensured by the assembly procedure, lead to an excellent peak optical efficiency, $\eta_{opt,0°}$, in the 0.74–0.79 range. This high optical efficiency and the low thermal loss ensured by the evacuated receivers achieve a high overall efficiency (Eq. [7.6]) of about 70% for working temperatures of 375°C. Since most of the high-temperature PTCs in solar thermal power plants employ similar solar reflectors and evacuated receivers and have similar assembly tolerances, their performance is also very similar. Smaller PTC designs for industrial process heat applications are less efficient, because they do not have evacuated receivers and the optical quality of the solar reflectors commonly used (polished-aluminum metallic reflectors) leads to lower overall efficiencies, usually in the 0.5–0.65 range at a working temperature of 250°C. However, performance can vary a lot from one collector model to another.

7.4.3 Design of parabolic-trough solar fields for CSP plants

A typical parabolic-trough collector field (Fig. 7.15) is composed of parallel rows of collectors. Each row, in turn, is composed of several collectors connected in series so that the working fluid circulating through the receiver pipe is heated as it passes from the inlet to the outlet of each row.

There are three stages in parabolic-trough collector solar field design:

- Stage 1: Define the design point, which is the set of assumed design values.
- Stage 2: Calculate the number of parabolic-trough collectors to be connected in series in each parallel row.

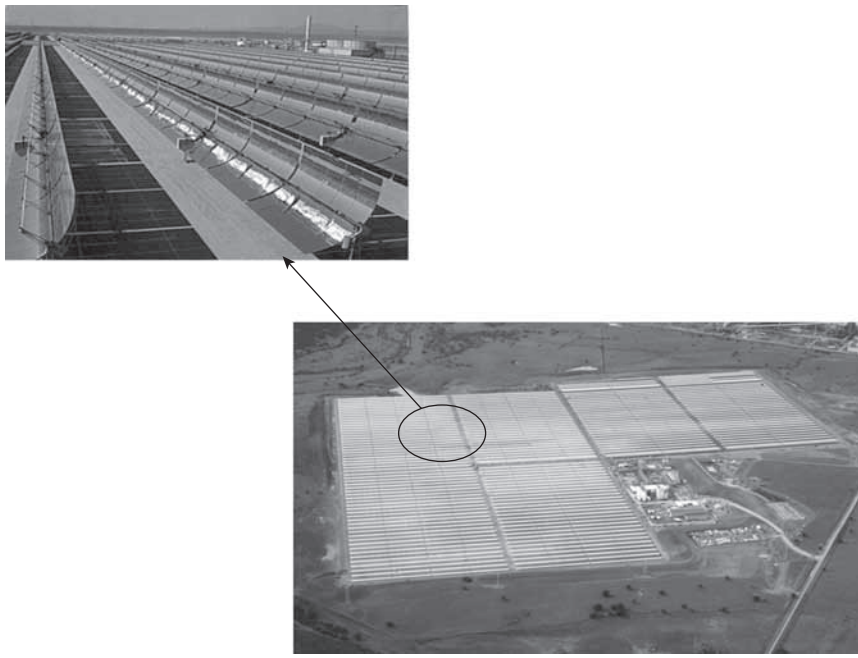

7.15 Parallel rows in a solar field with parabolic-trough collectors.

- Stage 3: Calculate the number of parallel rows to be installed in the solar field.

For Stage 1 (definition of the design point) the solar field designer must consider not only local weather conditions, but also the parameters of the PTC design chosen for the plant and any customer specifications. Since solar radiation is a non-constant energy source, it is evident that the thermal output delivered by a solar field will not be constant either. This means that the thermal power delivered by the solar field will sometimes be higher and sometimes lower than the design one. The solar field produces the nominal thermal output when working conditions and parameters are the same as assumed for the design point. Parameters and working conditions to be defined for the design point are:

- collector orientation
- design point date (month and day) and time
- site location (latitude and longitude)
- direct solar irradiance and ambient air temperature for the selected date and time
- total thermal output power to be delivered by the solar field
- soiling factor of the solar field

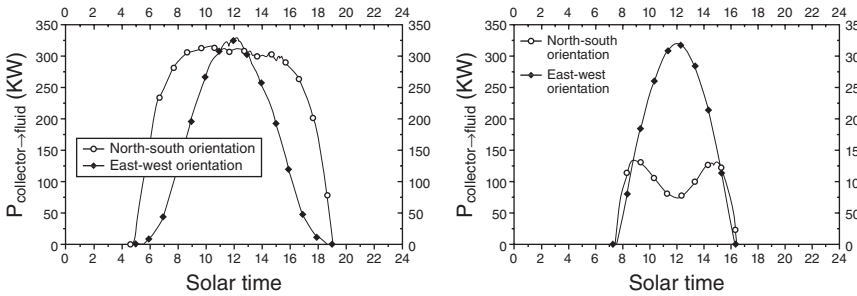

7.16 Daily thermal output of a EuroTrough-100 parabolic-trough collector located in Southern Spain, on a Summer (a) and Winter (b) clear day, and with two different orientations of its axis (north-south and east-west).

- solar field inlet/outlet temperatures
- solar collector working fluid
- nominal fluid flow rate.

The collector orientation is vey important because the seasonal performance of a PTC depends strongly on this parameter. Figure 7.16 shows the daily thermal output of a typical PTC located in Southern Spain, on a clear day in summer (Fig. 7.16 (a)) and winter (Fig. 7.16 (b)), and with two different axis orientations (north-south and east-west). The PTC design assumed in the figure is a Eurotrough-100. It may be clearly observed that with a north-south orientation there are significant seasonal variations between summer and winter, so the peak thermal output in winter is less than 50% of the peak thermal output in summer, while a PTC with east-west orientation has similar peak thermal output in winter and summer. Figure 7.16 also shows that the thermal energy delivered by the north-south collector in winter is about 50% of the thermal energy delivered by the east-west collector, while the opposite is true in summer. However, since there are more clear days and hours of daylight in summer, the north-south orientation has a higher yearly thermal output. Although the seasonal differences in collectors oriented North-South decrease as the site nears the Equator, Fig. 7.16 is valid for most countries where solar thermal power plants are being installed, because they are in latitudes within the range 20–40°N.

Taking into consideration the seasonal performance associated with different orientations, the solar field designer must select the best orientation for the solar plant, depending on the thermal output demand and the site's geographic coordinates. Since current solar thermal power plants need to maximize their yearly electricity production, they all use north-south

oriented collectors, because this allows the CSP plant to provide more electricity at peak hours in the summer months, when the electricity demand increases due to air-conditioners, and electricity is more expensive, thus increasing revenues from electricity sales. However, in principle, any intermediate angle between north-south and east-west is also possible.

The design point date and time usually chosen is a summer day at noon (for instance 21 June in the northern hemisphere) because the thermal output of north-south oriented collectors is maximum at that date and time. If the solar field were designed for a winter's day, a huge thermal storage system would be necessary to avoid dumping thermal energy in summer when the solar field delivers more than 200% of the mid-winter power.

Once the design point date and time has been chosen by the designer, and the geographic location has been defined by the client, the designer must assume design point weather conditions (e.g., direct solar radiation and ambient air temperature) usual at that site, date and time. Weather stations located nearby or a synthetic meteorological year obtained from satellite data can be used for this purpose.

The rated thermal output power to be delivered by the solar field and its inlet/outlet temperatures are imposed by the thermal industrial process or power block to be fed. For solar thermal power plants, the nominal inlet/outlet temperatures are 293°C/393°C (approx.) because thermal oils currently used as the working fluid rapidly degrade above 398°C, and overall plant efficiency is maximized with a temperature step of about 100°C in the solar field. For industrial process heat applications, the solar field outlet temperature needs to be at least 15°C higher than the steam temperature demanded by the process to be fed. So if the industrial process requires steam at 300°C, the oil temperature at the solar field outlet must be about 315°C. This difference is necessary to compensate thermal losses between the solar field outlet and the steam generator inlet, and provides a temperature differential and compensates the boiler pinch point, which is on the order of 5–10°C.

The selection of the working heat transfer fluid (HTF) for a PTC solar field is also important in the design phase. A single-phase liquid provides the best heat transfer coefficients and stable operation. Thermal oil is commonly used in parabolic-trough collectors for temperatures above 200°C. Water maintained as a liquid by pressurizing beyond the saturation pressure requires high pressure inside the receiver tubes and piping at these operating temperatures, requiring stronger joints and piping, and thus raising the price of the collectors and solar field. For temperatures below 200°C, either a mixture of water/ethylene glycol or pressurized liquid water can be used as the working fluid because only a moderate pressure is required to keep the fluid in liquid phase. Direct conversion of liquid water into high-pressure saturated or superheated steam in the receiver pipes of the solar

collectors, the so-called direct steam generation process, has been studied thoroughly at the Plataforma Solar de Almería (PSA) since 1998 and its technical feasibility has been proven, so its marketing will soon be a reality (Zarza *et al.*, 2004).

Several thermal oils are suitable for use as HTFs for parabolic-trough collectors. One of the key parameters to be considered when choosing the appropriate type of oil is the maximum bulk temperature at which the manufacturer guarantees oil stability. The oil most widely used in parabolic-trough collectors for temperatures up to 395°C is a eutectic mixture of 73.5% diphenyl oxide/26.5% diphenyl (Dawtherm A or VP-1 thermal oil). The main problem with this type of oil is its high crystallization temperature (12°C), which requires installation of an auxiliary heating system if oil piping temperature could drop below this temperature limit. Since the boiling temperature at 1013 mbar is 257°C, the oil circuit must be pressurized with nitrogen, argon or another inert gas when oil is heated above this temperature. Blanketing of complete oil circuit with an oxygen-free gas is necessary when working at high temperatures, because high pressure mists could form an explosive mixture with the oxygen present in the air. Though there are other thermal oils suitable for slightly higher working temperatures and lower solidification temperatures (e.g. Syltherm 800), they are too expensive for large solar plants.

The nominal mass flow per row is calculated to achieve a good heat transfer coefficient between the steel receiver tube and the fluid circulating inside it, while the pressure drop in the row is kept reasonable. Since the solar field parasitic electricity consumption depends directly on the pressure drop and the pressure drop in turn depends on the mass flow, the nominal mass flow per row of PTCs in a solar field is designed as a compromise between a good heat transfer coefficient inside the absorber tubes and a reasonable pressure drop between the row inlet and outlet. Reynolds numbers above 10^5 give a good heat transfer coefficient; additionally, if they are kept below10^6 the pressure drop will not be excessive. The number of PTCs connected in series in each parallel row depends on the nominal mass flow per row because the higher the flow the more collectors must be connected in series to achieve the nominal temperature difference between the row outlet and inlet. The reason why several collectors are connected in series in each row is that a single collector is not able to provide a high enough temperature difference if the working fluid mass flow is high enough to guarantee a good heat transfer coefficient. The higher the mass flow the smaller the temperature difference that can be provided by a single parabolic-trough collector at design point. So the number of collectors to be connected in series in each row is found by dividing two parameters, the temperature difference between the solar field inlet and outlet and the temperature difference that can be provided by a single collector at design

point. The temperature difference in a single collector at design point is calculated using the energy balance explained in Section 7.4.2, with the PTC optical, geometrical and thermal design parameters.

Most of the parabolic-trough collector designs in recent solar thermal power plants have technical characteristics similar to the EuroTrough-150, as listed in Table 7.3. Rows that are 600 m long (four 150 m collectors or six 100 m collectors in series) are becoming common in PTC solar power plants, because the mass flow of the thermal oil required to achieve a temperature increase of 100°C in the row meets the heat transfer coefficient and pressure drop recommendations, with a reasonable piping cost. This configuration requires a design point fluid mass flow per row of about 5 kg/s and a temperature step of 25°C in every PTC. The shape of the plot of land where the solar field has to be implemented also needs to be taken into consideration when determining the number of collectors in series per row.

Once the number of collectors to be connected in series in a row has been calculated, the next step is to determine the number of rows to be connected in parallel. This number depends on the thermal power demanded by the industrial process to be fed. The number of rows is determined by a very simple procedure: the ratio of the thermal power demanded by the industrial process to be supplied by the solar field to the thermal power delivered by a single row of collectors at design point. It should be explained here that the solar fields of solar thermal power plants with the same rated (nominal) power may be very different sizes, depending on whether they have a thermal storage system or not. So for instance, a 50 MW_e solar power plant in Spain with a 1 GWh thermal storage system requires a 155-row solar field with four PTCs in each for a total collecting surface of 510,000 m^2, while a solar plant with the same rated power (50 MW_e) and no thermal storage requires 88 rows with four collectors in each row, with a total solar field collecting surface of 288,000 m^2. The reason for this difference is that in a solar plant with a thermal storage system, the solar field must not only supply thermal energy to the power block but also to the thermal storage system to keep the power block running at full load for seven-and-a-half hours after sunset. Although both plants have the same rated power, they have solar fields with very different sizes and their yearly hours of operation are therefore very different too.

Two parameters are essential for calculation of solar field size and rated plant power: the solar multiple and the capacity factor. The solar multiple is the ratio between the solar field thermal output at design point (the design point is usually set at noon on a summer day in the northern hemisphere) and the thermal power required to feed the power block at nominal (rated) power. Therefore, the bigger the solar field, the higher the solar multiple for the same rated power plant. So, in Spain, Morocco and other

countries at a similar geographic latitude, solar multiples for 50 MW_e plants without a thermal storage system are in the range 1.15–1.30, while for plants with a 1 GWh thermal storage system, the solar multiple is close to 2.

The capacity factor of the solar plant is the ratio between the number of equivalent full-load solar-only operating hours a year and the maximum number of hours of plant operation if it were operated around the clock ($365 \times 24 = 8{,}760$ hours). Since a thermal storage system increases the number of hours of operation, the capacity factor for plants with thermal storage is higher than plants with none. For instance, in southern Spain, the capacity factor of a 50 MW_e solar plant with a 1 GWh thermal storage system is about 0.4, while the capacity factor with no thermal storage is about 0.22.

Since a large commercial parabolic-trough system may have more than 80 km of collectors distributed in many parallel rows, the way in which the rows are connected and the solar field piping layout are very important to keep pressure losses, and thus parasitic electricity consumption, reasonably low. The three basic layouts used in parabolic-trough collector solar fields are called direct return, reverse return, and center feed, as shown schematically in Fig. 7.17. In every option, the hot outlet piping is shorter than the cold inlet in order to minimize thermal losses. There are advantages and

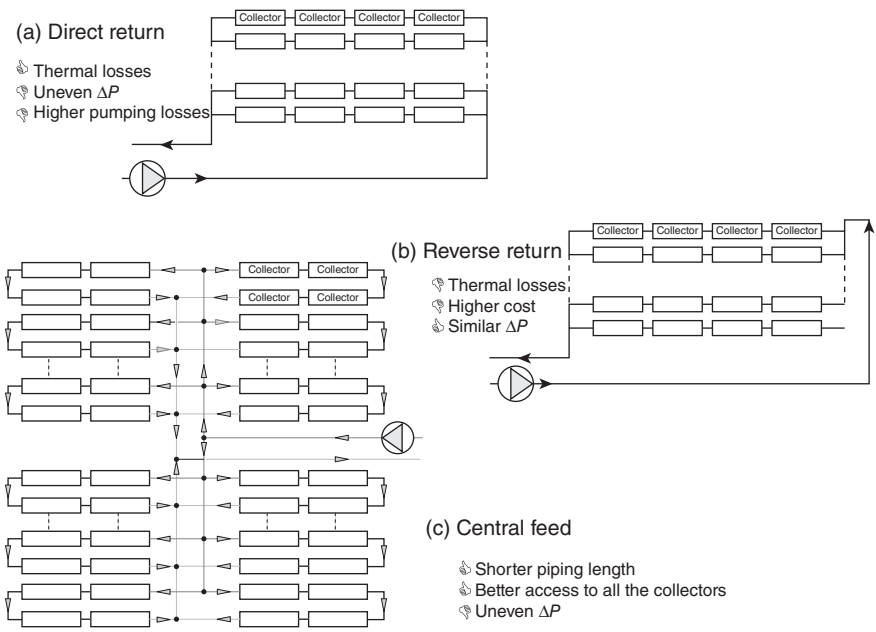

7.17 Different piping layouts for solar fields with parabolic-trough collectors.

disadvantages in each of these three configurations, which are briefly explained in following paragraphs.

The direct-return piping configuration is the simplest and probably most extensively used in small solar fields. Its main disadvantage is that there is a much greater pressure difference between the parallel row inlets, so manual valves must be installed in them to keep a constant flow through each row. These valves cause an additional pressure drop in the solar field, and their contribution to the total pressure loss in the system can be significant. The result is higher parasitic energy consumption than for the reverse-return layout, where the fluid enters the collector array at the opposite end and the rows with a longer inlet piping have a shorter outlet piping, thus better balancing the pressure drop associated with each row. However, the total length of the piping in the reverse-return layout is longer than for the direct-return configuration, thus increasing thermal losses, although this strongly depends on the solar field inlet temperature. If this temperature is low, additional heat loss is negligible. Adding length to the pipes, however, results in higher piping, insulation, and fluid inventory costs. In a reverse-return piping arrangement, to ensure a completely uniform flow distribution among all the parallel rows without valves, the header pipes must step down in size on the inlet and step up in size on the outlet to achieve constant fluid velocity through the headers.

The center-feed configuration is the most widely used layout for large solar fields. Like the direct-return design, pressure loss in the solar field is higher if balancing valves are installed at the row inlet. This layout minimizes piping because there is no pipe running the length of the collector row. Also, direct access to each collector row is possible without any need for underground piping. This is a significant advantage of the center-feed layout, because access to the solar field is often required for collector washing. Since manual valves have to be installed at the inlet and outlet of every row for maintenance, these valves can be used to balance the pressure drop in the parallel rows at no extra cost. The center-feed layout has therefore become the preferred option for large PTC solar fields.

It is also very important for solar field piping to be well insulated, because overall efficiency decreases with inadequate thermal insulation. The length of the piping is significant and excessive thermal losses would reduce the amount of useful thermal energy delivered to the power block. Thermal bridges in piping supports and other components (e.g., oil tanks, pumps, etc.) must also be avoided for the same reason.

Drain and venting valves in the piping are also important items in the construction of parabolic-trough collector fields. Venting valves must ensure that no air bubbles remain inside piping after filling with the thermal oil working fluid, while the drain valves are essential for maintenance to drain pipe segments for repair. Since thermal oil pollutes and is flammable at high

temperatures, no welds or repairs may be done before the pipe segment involved is fully drained and inertized with oxygen-free gas.

7.5 Operation and maintenance (O&M) of parabolic-trough systems

The fraction due to operation and maintenance (O&M) of the total cost of electricity produced by large solar thermal power plants is within the 0.02–0.035 €/kWh range (approximately 8% of the total cost of the electricity produced by the solar plant). Since the fuel (i.e., solar radiation) is free of charge, most of this is manpower for plant operation and system maintenance.

The most frequent activities related to solar field O&M are periodic measurement of mirror reflectivity and their washing. Mirror reflectivity directly affects the amount of useful thermal energy delivered by the solar collectors, because a 10% higher reflectivity means a 10% increase in useful thermal energy generated. Dust carried by ambient air is progressively deposited on the surface of the mirrors gradually reducing their reflectivity after each mirror washing. Reflectivity of a recently-washed back-silvered glass mirror is typically 0.93%. Mirror soiling is very site-specific. Experience in Spain is that in summer, reflectivity rapidly decreases at a rate of about 0.0025% per day during the first two weeks after washing. So in ten days after washing, reflectivity is only about 0.90, and the mirrors must be washed again to recover the solar field's nominal reflectivity and optical efficiency. Reflectivity decreases more slowly in winter and mirrors need not be washed as often as in summer. Specially designed mirror washers are used for this purpose. Demineralized water is carried through the solar field on a tank truck that pumps it at 200 bar to remove the dust deposited on the front surfaces of the mirrors. Figure 7.18 (a) shows one of the mirror washers, called Twister, used at the SEGS plants in California. When mirrors are not very dirty, simple demineralized water curtains can be used to wash the mirrors (see Fig. 7.18 (b)). In either case, the consumption of demineralized water required to wash the mirrors is about 0.7 l/m^2. Although the photographs shown in Fig. 7.18 were taken in the morning, mirrors are typically washed at night so the entire solar field remains in operation during daylight hours for maximum collection and conversion of solar radiation.

Breakage of mirror glass does not occur very frequently in parabolic-trough systems (much less than 0.1% per year) and durability of back-silvered glass mirrors is excellent provided that they do not have to withstand wind speeds over 110 km/h. When the mirror glass breaks, the side effects can be more important than the breakage itself, because the pieces of falling glass could hit and break the glass receiver pipe cover, which costs about 800€/unit to replace (plus manpower).

(a)

(b)

7.18 Typical devices for mirror washing in a parabolic-trough solar field.

Another solar field maintenance task is checking collector alignment and solar tracking systems. Small displacements in the concrete foundations or malfunction of the solar tracking system can lead to incorrect positioning of the receiver pipes and significant reduction of the intercept factor.

Periodic maintenance of the ball-joints installed between adjacent collectors to allow thermal expansion of the receiver pipes and independent collector movement is also required. Their graphite packing must be refilled every 4–5 years of operation to prevent leaks. Portable chemical detectors are used to check for the small amounts of oil vapor that always precede a visible oil leak through the ball-joint packing.

Last but not least, thermal oil parameters and condition must be analyzed every year. A sample is taken by the plant owner and sent to the oil supplier, who is responsible for the analysis. Although the durability of thermal oils currently used as heat transfer fluids in parabolic-trough systems is excellent, the maximum bulk temperature recommended by the supplier must not be exceeded in order to avoid rapid degradation that would significantly increase the amount of oil that must be replaced yearly. With proper O&M, less than 3% of the thermal oil has to be replaced every year, although this percentage could increase up to 20% or higher if the recommended maximum bulk temperature is exceeded often.

7.6 Thermal storage systems

Energy storage is discussed in detail in Chapter 11. Here the specific aspects as applied to PTC systems are reviewed.

Practical experience with thermal storage systems is more limited than experience with solar collectors because only the first SEGS plant was provided with a thermal storage system, which used ESSO 500 thermal oil in two tanks with a thermal capacity of 140 MWh. This system, which was put into operation in 1984, was destroyed by a fire in 1999. The operation of this thermal storage system had been reliable and efficient until that date. A 5 MWh thermal energy system using 115 m^3 of Therminol 55 thermal oil in a thermocline tank has been in operation at the Plataforma Solar de Almería (PSA) since 1982, and has proven to be highly reliable with a 0.92 charge/discharge efficiency.

Due to the high environmental risk of large tanks filled with hot thermal oil, recent large PTC solar thermal power plants have two-tank molten-salt thermal storage systems with the configuration shown in Fig. 7.10. This configuration was used in several plants built in Spain during the first decade of this century. The salt used is a mixture of 60% $NaNO_3$ and 40% KNO_3, with a melting point in the range 225–238°C. With a nominal electrical output of 50 MW_e, these plants have a solar field aperture area of

510,000 m^2 and a thermal storage system with a capacity of 1 GWh, which is able to keep the power block running at full load for seven-and-a-half hours after sunset. The solar field is big enough to feed the plant power block and charge the thermal storage system during daylight hours on clear summer days. The storage system is charged when molten salt pumped from the cold tank to the hot tank is heated by the oil delivered by the solar field at 395°C. The system is discharged when the molten salt stored in the hot tank at 385°C is pumped to the cold tank and its thermal energy is transferred to the thermal oil, which is then sent to the power block steam generator. Since the first of these 1 GWh thermal storage systems with molten salt was put into operation in 2008, practical experience is still very limited, and a longer time period is needed to assess their durability and reliability. However, the results are so far very encouraging and positive.

The predecessor of the 1 GWh molten-salt thermal storage systems now in use was the molten-salt system tested in the American Solar Two Project at the end of the last century (James, 2002; Reilly and Kolb, 2001). Since the size of the storage system tested in Solar Two was only 7% of current 1 GWh systems, the significant difference in size demanded careful analysis and engineering to solve some technical constraints associated with the size of the components and melting of 30,000 MT of salt.

The first years of operation with the large 1 GWh molten-salt storage systems installed in Spain at the end of the first decade of this century have provided encouraging results. However, the cost of these systems has increased significantly due to an increase in the cost of salt. The various other approaches to energy storage that are under investigation are reviewed in Chapter 11.

7.7 Future trends

Although solar thermal power plants with parabolic-trough collectors are now profitable in a few countries due to public incentives in the form of feed-in tariffs or tax credits, it is clear that ways to improve efficiency and reduce costs must be found, because the current public incentives will be progressively reduced in the future. The main goal of current incentives is to make the first commercial projects financially feasible for investors, thereby stimulating the implementation of first plants. Pushed by the need to improve the technology and reduce the cost of the electricity generated, many private and public entities worldwide are carrying out a significant number of R&D projects to improve components, operation and maintenance procedures, and solar system-to-power block connection.

These R&D activities are also motivated by the growing demand for parabolic-trough collectors and their components due to public incentives

implemented in the USA, Spain and other countries at the beginning of the twenty-first century for electricity produced by solar thermal power plants. Since these incentives made this type of solar power plant profitable, many companies undertook development of new PTC designs and components to meet the growing demand and to lower costs.

Due to the logical limitation of space in this section, it describes only future trends in working fluids for parabolic-trough collectors and new PTC designs.

7.7.1 New working fluids

The thermal oils currently used as heat transfer fluids have two clear limitations, their degradation at temperatures above 400°C and the environmental and fire hazards due to possible leakages. The thermal limit imposed by these oils is a serious barrier to increasing power block efficiency, because the temperature of the steam delivered to the power block cannot be higher than 390°C, thereby limiting steam turbine efficiency. However, since higher working temperatures in the solar field also increase thermal losses, the overall solar plant efficiency does not increase at the same rate as the power block. Another advantage of operating the solar field at higher temperatures is the fact that it decreases the size, and hence the cost, of the thermal storage system needed to achieve the required storage capacity.

New fluids are under study for replacing thermal oil: molten salt, pressurized gases and water/steam. All three of these fluids have advantages and disadvantages when compared to thermal oil, as listed in Table 7.7. The use of the same molten salt in the solar field and in the thermal storage system has clear advantages, because the molten salt currently used has good thermal stability up to 575°C (175°C higher than the oil) and the overall plant configuration would be simpler, because the oil/molten-salt heat exchanger now needed in current plants would no longer be needed. However, the crystallization point of molten salt (>125°C) is significantly higher than oil (>12°C), and a very efficient, and expensive, heat tracing system is required in the solar field to avoid solidification of the molten salt in cold weather.

The use of water/steam for direct steam generation (DSG) would also avoid the problem associated with thermal oil, but the two-phase flow (i.e., liquid water + steam) in the evaporating section of every row of collectors in the solar field introduces some technical constraints demanding a more complex solar field control to keep the steam temperature and pressure stable at the solar field outlet during solar radiation transients. The main advantage of this option is that plant configuration is so simple, because the steam demanded by the power block is produced directly in the solar field.

Table 7.7 Advantages and disadvantages of new working fluids compared to thermal oil for parabolic-trough collectors

Fluid	Advantages over thermal oil	Disadvantages compared to thermal oil
Molten salt	• More efficient heat storage • Higher working temperature • No pollution or fire hazards	• Higher thermal losses overnight • More complex solar field design • Higher electricity consumption
Water/steam	• Simple plant design • Higher working temperature • No pollution or fire hazards	• Lack of suitable storage system • More complex solar field control • Solar field higher pressure
Gas	• Higher steam temperature • Thermal storage enhancement • No pollution or fire hazards	• Poor heat transfer in the receiver tubes • More complex solar field control • Solar field higher pressure

On the other hand, the main barrier at present is the lack of a suitable thermal storage system for this option, because current storage systems based on sensible heat are not suitable for DSG solar fields, which delivers steam that must be condensed to release its thermal energy. Since steam condensation takes place at a constant temperature, special thermal storage systems based on latent heat are needed. Such systems must use a storage medium that melts during charging by steam condensation. The melted storage medium must crystallize during discharge to produce the steam required for the power block. Although development of latent-heat storage systems is already under way, much R&D is still needed before commercial units become available.

Research in the use of a compressed gas (e.g., CO_2, air or N_2) inside the receiver pipes to convert the solar radiation into thermal energy in the form of the sensible heat of the gas is also under way, because this option would overcome the barriers associated with the thermal stability and fire hazards of thermal oil. The possibility of working with gas at temperatures over 500°C is also of great interest because thermal storage would be enhanced by the greater difference between the hot and cold temperatures, and less storage medium would be required to store the same amount of energy. The main constraint on the use of compressed gas is the pressure drop in the

solar field piping, which would demand more pumping power, and therefore, also more internal consumption of electricity.

Although the technical feasibility of these three new fluids has been already proven at CIEMAT's small test facilities in Spain (Zarza *et al.*, 2004; Rodríguez *et al.*, 2009) and ENEA's in Italy (Maccari, 2006), the three options have to be evaluated and tested in pilot plants large enough to ensure that results can be extrapolated to large commercial plants. A 5 MW_e pilot plant promoted by ENEA with molten salt in the solar field is expected to enter into operation in 2011, while a 3 MW_e plant with direct steam generation is expected to enter into operation in Spain in 2012 (Zarza *et al.*, 2008).

7.7.2 New PTC designs

A significant number of new PTC designs were developed in the USA and Spain in the period 2005–2010, clearly indicating the great commercial interest in this technology. The new designs were specially aimed at reducing the manufacturing and assembly costs because these items are a significant fraction of the total solar field cost. The use of components made of stamped sheet steel and the design of special torque tubes with enhanced resistance to bending are good examples of innovations introduced in recent PTC designs. A number of these new designs have already been deployed commercially (e.g., SenerTrough, Skal-ET), while at the end of 2010, others were still awaiting their first implementation in a large commercial plant (e.g., AlbiasaTrough, URSSATrough, etc.).

Future trends in new PTC designs concern two main topics:

- innovative means of providing a stiff structure, other than the torque box, torque tube or space frame concepts, with a low manufacturing and assembly cost, while maintaining good mechanical rigidity in wind loads
- Larger collector aperture area and parabola width.

The innovative collector design proposed by the Alcoa Company is a good example of the first topic, as explained in http://www.alcoa.com/global/en/innovation/info_page/home.asp. The Alcoa design uses a monolithic structure that enables simple 'drop-in-place' collector assembly, and glass reflectors are replaced by highly reflective aluminum mirrors. A first prototype was installed at NREL's test facilities in Golden, Colorado (USA) early in 2010 for outdoor testing.

Although most of the new PTC designs retain the general EuroTrough dimensions (Luepfert *et al.*, 2003), the technical and commercial feasibility of a parabola width over 5.76 m is currently under evaluation in several

countries and the first prototypes will be tested in the 2010s. These larger designs require larger receiver tubes, and sometimes larger parabolic mirror segments. The main benefit expected from these larger designs is a cost reduction, especially due to a reduction in the number of drive units and ball-joints. On the other hand, their main technical constraint is the higher wind load they have to withstand and the heavier structure required to support all the components. An example of this trend in parabolic-trough collectors is the HelioTrough design developed by Solar Millennium, Flagsol GmbH and Schlaich Bergermann und Partner (SBP) (Germany) with a parabola width of 6.77 m and a steel receiver pipe diameter of 89 mm. A first HelioTrough collector loop was under testing at the SEGS V plant in Kramer Junction (California, USA) in 2010.

Experimental results from outdoor testing with the first prototypes using new and larger sizes will demonstrate whether these approaches are a good choice or not. The significant R&D effort undertaken by industry in collaboration with public centers to develop improved collector designs and components leads us to believe that cost reduction is likely to be rapid.

7.8 Conclusions

Public incentives in the form of feed-in tariffs or tax credits implemented in the USA, Spain and other countries during the first decade of the twenty-first century have promoted a multitude of solar thermal power plant projects, most of them with parabolic-trough collectors, because the successful track record of the SEGS plants established them as the 'least risk' and most financeable technology. Although the world financial crisis of 2008 was a serious barrier to development, many of the projects that were initially proposed at that time have been successful and 19 parabolic-trough CSP plants with 876 MW_e total power output were in operation at the end of 2010.

However, it was clear from the beginning of this new construction phase that ways to lower costs and increase efficiency had to be found to make the continuation of commercial deployment compatible with the expected and logical reduction in public incentives. This was the driving force behind a significant effort in R&D by industry, engineering firms and public centers to develop new collectors, components (receivers, solar reflectors) and fluids (molten salt, direct steam generation and compressed gas) during the first decade of this century.

Although most of the financial and R&D effort was focused on large-area parabolic troughs for CSP plants, industrial process heat applications are also a potential market where smaller parabolic-trough collectors can find a profitable niche.

7.9 Sources of further information and advice

Since the commercial deployment of large-scale parabolic-trough systems is very recent, the generally available literature is not abundant. However, some documents for further information about various aspects of this technology are given below.

For detailed information about PTC designs developed in the USA in the 1970s and 1980s see:

Dudley V.E., Workhoven R.M. (1981) 'Performance testing of the Acurex Solar Collector Model 3001-03'. Tech. Rep. No. SAND80-0872. Albuquerque: SANDIA.

Kesselring P., Selvage C.S. (1986) *The IEA/SSPS Solar Thermal Power Plants. Vol. 2: Distributed Collector System* (*DCS*), 1st edn, Berlin: Springer-Verlag.

Dudley V.E., Workhoven R.M. (1982) 'Performance testing of the Solar Kinetics T-700A Solar Collecto'. Tech. Rep. No. SAND81–0984. Albuquerque: SANDIA.

Cameron C.P., Dudley V.E. (1986) 'Solar kinetics incorporated modular industrial solar retrofit qualification test result'. Tech. Rep. No. SAND85–2320. Albuquerque: SANDIA.

Cameron C.P., Dudley V.E., Lewandowski A.A. (1986) 'Foster Wheeler solar development corporation modular industrial solar retrofit qualification test results'. Tech. Rep. No. SAND85–2319. Albuquerque: SANDIA.

Concerning basic principles of optics and geometry, two books with useful information are:

Rabl A. (1985) *Active Solar Collectors and their Applications*. Oxford: Oxford University Press.

Duffie J.A., Beckman W.A. (1991) *Solar Engineering of Thermal Processes*. New York: John Wiley & Sons.

A document published by Sandia National Laboratories in 1999 on the experience gained at the SEGS plants is very valuable for operation and maintenance of parabolic-trough systems:

Cohen G.E., Kearney D.W., Kolb G.J. (1999) 'Final report on the operation and maintenance improvement program for concentrating solar power plants'. Tech. Rep. No. SAND99-1290. Albuquerque, SANDIA.

In 2010 the International Energy Agency published the book entitled, *Technology Roadmap for Concentrating Solar Power*, available at hhtp://www.iea.org. This document gives a complete overview of the commercial situation of solar thermal power plants, the expected cost reduction, and boundary conditions required for large commercial deployment in Sunbelt countries.

For further technical information related to R&D activities as well as commercial and financial information, the Proceedings of the SolarPACES conferences held in Berlin (Germany), Perpignan (France) and Granada (Spain) in 2009, 2010 and 2012, respectively, contain very interesting papers. The plenary sessions of these conferences are especially interesting for subjects related to strategy and market.

For specific information on R&D activities, the web pages of public research centers usually have yearly reports available in PDF format. For example, the annual reports of the Plataforma Solar de Almería (Spain) are available free of charge at: http://www.psa.es.

7.10 References and further reading

Fernandez-García A., Zarza E., Valenzuela L. and Pérez M. (2010) 'Parabolic-trough solar collectors and their applications'. *Journal of Renewable and Sustainable Energy Reviews*, 4(7), 1695–1721.

Gunther H. (1922) *Technische Traeume (Technical Dreams)*, Rascher und Cie. Verlag, Switzerland.

Harats Y. and Kearney D. (1989) 'Advances in Parabolic-Trough Technology at the SEGS Plants'. Proceedings of the 1989 ASME International Solar Energy Conference, San Diego, April, 471–476.

James E.P. (2002) 'Final Test and Evaluation Results from the Solar TWO Project'. Report SAND2001-0120, Sandia National Laboratories, Albuquerque.

Lotker M. (1991) 'Barriers to Commercialization of Large Scale Solar Electricity. The LUZ Experience'. Tech. Rep. No. SAND91-7014, Sandia National Laboratories, Albuquerque.

Luepfert E., Zarza E., Schiel W., Osuna, R., Esteban A., Geyer M., Nava P., Langenkamp J. and Mandelberg E. (2003) 'Eurotrough collector qualification complete – Performance test results from PSA'. Proceedings of the ISES 2003 Solar World Congress, June 16–19, Göteborg (Sweden).

Maccari A. (2006) 'Innovative heat transfer concepts in concentrating solar fields'. Available at: http://ec.europa.eu/energy/res/events/doc/maccari_enea.pdf.

Price H., Lüpfert E., Kearney D., Zarza, E., Cohen Gee R. and Mahoney R. (2002) 'Advances in parabolic-trough solar power technology'. *Journal of Solar Energy Engineering*, 124, 109–125.

Pytlinski J.T. (1978) 'Solar energy installations for pumping irrigation water'. *Solar Energy*, 21, 255–258.

Reilly H.E. and Kolb G.J. (2001) 'An Evaluation of Molten-salt Power Towers Including Results of the Solar Two Project'. Report SAND2001-3674, Sandia National Laboratories, Albuquerque.

Rodríguez M.M., Marquez J.M., Biencinto M., Adler J.P. and Díez L.E. (2009) 'First experimental results of a solar PTC facility using pressurized gas as the heat transfer fluid'. Proceedings of the SolarPACES-2009 Congress, Berlin, September 15–18.

Shaner W.W. and Duff W.S. (1979) 'Solar thermal electric power systems: comparison of line-focus collectors'. *Solar Energy*, 22, 13–49.

Zarza E., Valenzuela L., León J., Hennecke K., Eck M., and Weyers H.-D. (2004) 'Direct steam generation in parabolic troughs: Final results and conclusions of the DISS project'. *Energy – The International Journal*, 29(5–6), 635–644.

Zarza E., López C., Cámara A., Burgaleta J.I., Martín J.C. and Fresneda A. (2008) 'Almería GDV – The First Solar Power Plant with Direct Steam Generation'. Proceedings of the 14th SolarPACES International Symposium, Las Vegas, March 4–7.

8

Central tower concentrating solar power (CSP) systems

L. L. VANT-HULL, formerly University of Houston, USA

Abstract: In this chapter we first address the conception, design and construction of central receiver tower systems, including a summary of commercial plants operating or in construction. We then discuss a variety of issues affecting the design and performance of central receiver systems. These include initial considerations, elements of cost and performance, characteristics of the heliostat, characteristics of the receiver, and any external constraints on the design such as flux density limitations or land constraints. Finally, several variants on the simple configuration are critically discussed.

Key words: solar central receiver, solar power tower, concentration optics, optimization, heliostat field, beam errors, spillage, constrained optima, off-axis aberrations, secondary reflectors, beam down, receiver flux density, field layout, net energy.

8.1 Introduction

A central receiver system consists of an array of tracking mirrors, or heliostats, which are spaced in a field to avoid mechanical or optical interference with one another as they pivot to reflect incident direct-beam sunlight onto an elevated receiver or secondary reflector (Hildebrand and Vant-Hull, 1977). The receiver is designed to effectively intercept the concentrated incoming sunlight (solar energy) and (usually) absorb it as heat at an elevated temperature. This energy is collected by a working fluid and stored as thermal energy, used to drive an electrical generator, or used as process heat. Many of the additional issues which must be addressed in designing, building, and operating a complete solar thermal power station are discussed in more detail in a recent Sandia report (Kolb, 2011). Alternatively, photovoltaic panels could replace the thermal receiver, or the light (photons) can be used directly to drive a chemical reaction or even a laser. The optical design and optimization of central receiver (CR) systems (also known as solar power towers) are somewhat complicated by the multitude of variables one must consider and the continuous variation in configuration and performance of each of the heliostats as they track the sun and interact with one another. However, the efficient collection, high concentration and high temperature of the heat collected are of interest for many applications.

Central receivers have the advantage that all the solar energy conversion takes place at a single fixed region, i.e., the receiver. This allows the receiver to be fixed, largely avoiding the need for energy transport networks, and allows more cost-effective investment designed to improve the efficiency and sophistication of the energy conversion process. They have been built most often as single large systems to power a steam cycle; however, smaller systems or modular systems employing multiple towers have attractions in some applications. A universal disadvantage is that the fixed position of the receiver means that heliostats do not generally point directly at the sun, so that the amount of collected solar radiation per unit area of mirror is reduced compared to a dish concentrator (the cosine effect). Of course, much of the reflector in parabolic dishes or troughs is also tilted with respect to the sun so the reflector area is, again, larger than its aperture area. However, in these collectors, little or none of the incoming light is bypassed to the ground, as is characteristic in Fresnel systems such as the solar tower or linear Fresnel systems. In such systems, facets of the parabolic surface are projected to the ground where the tracking mirrors redirect the sun to the receiver. Consequently, it is necessary to forego collection of some of the incoming energy by spacing the mirrors in order to avoid serious shading of adjacent mirrors as the sun moves, or blocking of some of the reflected light on its way to the receiver. These issues result in a trade-off among the competing events in order to collect light onto the receiver most cost effectively. This chapter addresses the conception, design and construction of central receiver tower systems and a variety of issues affecting the design and performance. Further consideration of heliostats and their size/cost optimization can be found in Chapter 17.

8.1.1 Basic configurations

The CR concept can be realized in several configurations, defined essentially by the receiver, as indicated in Fig. 8.1. If the receiver consists of an external cylinder, the absorbing surface can be seen from all directions, resulting in a surrounding field of heliostats defined primarily by their relative efficiency in directing sunlight onto the receiver (Fig. 8.1(a)). For a given power level, this results in a shorter and lower cost tower and vertical piping. The associated disadvantage is that the heated surface is exposed to the elements and all thermal re-radiation and convection is lost.

The principal alternative is a cavity receiver in which the heated surface is contained in an insulated enclosure containing a large aperture to admit the sunlight (Fig. 8.1(b) and (c)). This has the effect that light can only be effectively collected from heliostats within a cone defined by the normal to the aperture, as heliostats far off-normal will see an aperture foreshortened by the cosine of the cone angle (50% at 60°). Usually the aperture is directed

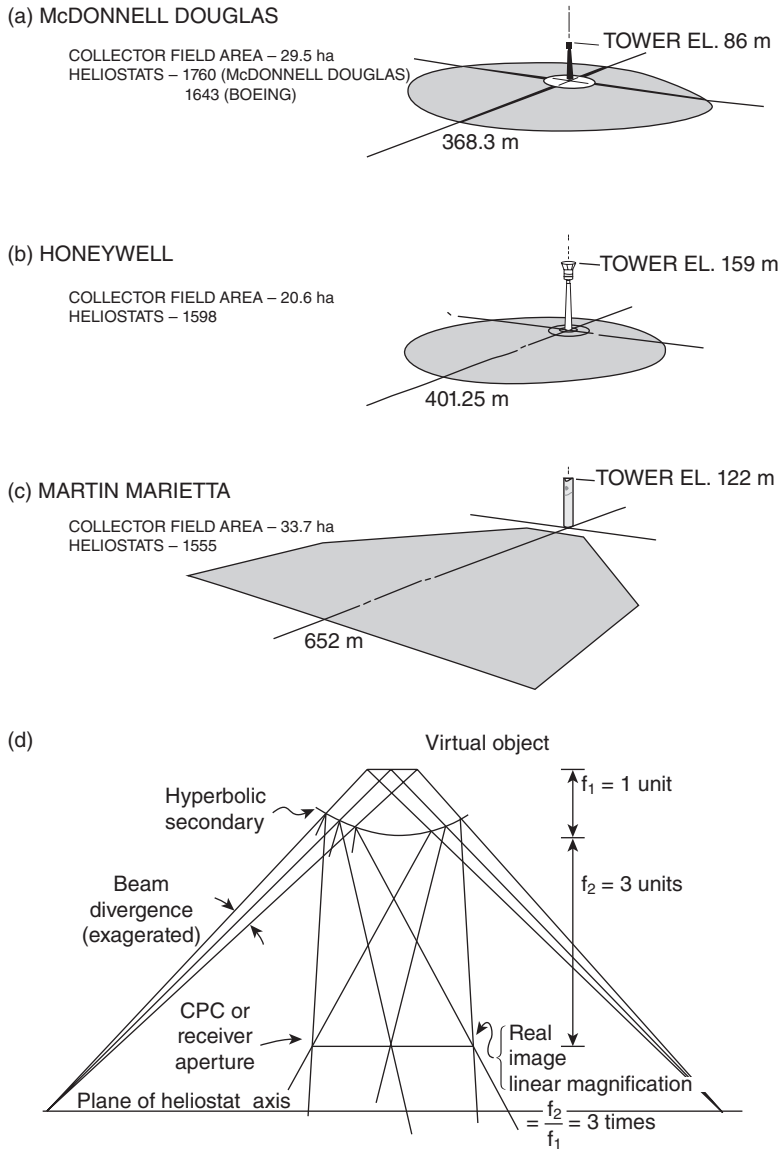

8.1 (a), (b) and (c) To-scale sketches of CR configurations proposed for the Solar One facility: external receiver with surround field, down-looking cavity receiver with surround field, cavity receiver with north field (modified from Sandia sketches); (d) also a representative beam-down surround field with secondary hyperbola (sketch by author).

somewhat downward and toward the pole to face an array of heliostats positioned to most effectively illuminate the aperture as in Fig. 8.1(c). This means the heliostats will tend to be primarily on the polar side of the aperture (north field in the northern hemisphere, south field in the southern hemisphere), where the angle of incidence on the heliostats at a noon time design point is best. The resulting field will be more optically efficient than a surround field around noon, but less efficient in the morning and afternoon when the cosine effect on the heliostats plays a large role. With a noon time design point, but for the same heliostat area, the *annual* energy collected will be lower compared to the surround field. This is because the west field performs very well in the morning and the east field does well in the afternoon when the polar field performance suffers large cosine losses.

Cavity receivers are most likely to play a role where the required output temperature is very high (of the order of >1,000 K), or the allowable flux density on the receiver surface is very low (as for a gas cooled tubular receiver). Although it is commonly thought the cavity receiver will have significantly less losses than an external receiver, as we discuss in Section 8.6.2 this is not always the case. Because the cavity can only view a limited section of the surrounding terrain, its tower will be taller to collect the same amount of energy. Alternatively, several separate cavities viewing different fields (e.g., NE and NW, or E, N, W) can be mounted on a single tower, or the aperture can be horizontal as in Fig. 8.1(b). Partial (or shallow) cavities are also used.

A third alternative is the beam-down concept. Here all the heliostats direct their beams at a point (the virtual focus) but a (generally) hyperbolic secondary mirror intercepts the light and redirects it toward the ground (Fig. 8.1(d)). Here, at the lower focus of the secondary, the redirected sunlight is captured by an upward-looking receiver often supplemented by a compound parabolic concentrator (CPC) to recover some of the concentration. This is important because the secondary magnifies the image which would have been formed at the initial focal point by the ratio of the distance from the vertex of the secondary to each of the two focal points (the linear magnification, LM). If one wishes to make the secondary small, it must be placed near the virtual focal point to intercept all the light from the heliostat field. However, this results in a large LM of the final image and reduces the concentration by the square of the LM. To achieve a small LM requires a large secondary which is more costly and will create additional shading of the field.

8.2 History of central receivers

8.2.1 Early evolution

Delivery of solar energy as thermodynamically useful heat for power cycles requires temperatures significantly above the 100°C or so available from

flat plate collectors, so tracking concentrating collectors are required. To deliver significant commercial quantities of solar energy, either as electricity or process heat, total collector areas might typically be of the order of a square kilometer, which clearly cannot track the sun as a monolithic structure. One solution is to combine a multitude of point focus (dish) collectors, or line focus (trough) collectors to achieve the required power level. This involves a multitude of distributed receivers and an energy collection and transfer network to assemble the collected energy for use.

An alternate solution, reported by the Russian, Victor Baum (Baum *et al.*, 1957), is to conceptually break the reflector into facets and project them outward from the receiver to the ground. These ground-based segments (heliostats) can be individually tracked to maintain the reflected direct-beam sunlight on a receiver. As heliostats on the polar side of the receiver have an average incidence angle closer to zero than those on the equatorial side, they are more effective. Consequently, Professor Baum proposed to mount multiple heliostats on trains of rail cars, which would move on a set of circular rails to predominantly stay on the polar side of the receiver, in order to maintain a constant geometry vs. the sun's azimuthal motion during each day. The elevated cavity or flat-plate receiver at the center of the circles would rotate in synchronism to face the array, from west to north (in Russia) to east in order to capture the reflected rays. He received permission to build the device at his university, but no funding was provided (private communication).

In Italy (San Ilario), Professor Giovanni Francia (1968) reported on a 'receiver oriented' drive mechanism, which automatically redirected a solar beam to the receiver when activated by a simple clockwork drive. Periodic (≈weekly) declination adjustments were also required. The ~130 kW_t system of 135 m^2 of ≈1 m diameter focused mirrors, built in 1968, was actuated by a pendulum clock driven by weights, and worked quite well for over a decade, producing very high temperature steam with little supervision.

In the 1950s Professor Felix Trombe at Odellio, France, built several solar furnaces using a single large tracked mirror to fill a fixed horizontally oriented parabola with paraxial sunlight. The largest of these was a 1 MW_t solar furnace (Trombe, 1957). He installed the ≈2,000 m^2 faceted parabola as the north side of an eight-story laboratory, with a focal building about 30 m in front of it. He then broke the required 2,835 m^2 primary mirror required to 'fill' this parabola into 63 flat heliostats, each of 45 m^2, which he distributed carefully on the steep side of an adjacent mountain to provide parallel horizontal beams of sunlight to fill the parabola for several hours each day, as shown in Fig. 8.2. The highly flat and precisely tracked heliostats and the ~9,000 precisely adjusted curved facets of the parabola produced excellent results, with a peak flux density of ~13,500 suns. These were the

8.2 The French 1 MW solar furnace at Odellio employing a field of 63 heliostats each 45 m^2 in area. The working area is in the focal building just in front of the large parabolic mirror.

first 'commercial' heliostats and they remain representative of the current generation.

In 1972, Hildebrand *et al.* published a 'reinvention' of the central receiver as a hemispherical or cylindrical receiver atop a tall tower surrounded by a field of carefully positioned heliostats. Thinking big, they evaluated a conceptual 450 m tower producing 565 MW_{th} at 1,000–2,000 K (to power a steam turbine or a magneto hydrodynamic generator). No technical impediments were envisaged with the tower or heliostat field. (The proposed tower was about twice as high as current analysis shows, is actually required to deliver 565 MW_{th}.)

8.2.2 International test facilities and pilot plants

Between 1980 and 1990, a number of international test facilities and pilot plants were built and operated as shown in Table 8.1. Because of their small scale, all of these facilities (other than Solar One and Two) employed 'north field' designs (for northern hemisphere) using a flat panel or small cavity receiver. Only in the range above about 10 MW_e do a surround field and a cylindrical receiver begin to become economically advantageous due to the reduced tower and piping costs and to the complications implicit with a single large cavity receiver.

These facilities provided experience with various types of heliostats and various working fluids, including oil, water steam, molten salt, and sodium. Most of them also employed small storage units and were equipped to generate electricity, although not as a commercial entity. Many lessons were

Table 8.1 Summary of central receiver demonstration electric power plants

	Eurelios (Italy)	Sunshine (Japan)	IEA-CRS (Spain)	Solar One (USA)	Solar Two (USA)	CESA 1 (Spain)	Themis (France)	MSEE (USA)	SES 5 (CIS-USSR)	Weizmann (Israel)
Net turbine rating	1 MW_e	1 MW_e	0.5 MW_e	10 MW_e	10 MW_e	1.2 MW_e	2.5 MW_e	0.75 MW_e	~	0.5 MW_e
Thermal power (MW_t)		5.95 MW_t	7.7 MW_t	43.4 MW_t	56 MW_t	7.7 MW_t	8.9 MW_t	5.5 MW_t	5 MW_t	
Irradiance (W/m^2)	850	750	7,920	950	950	700	1,040	~1,000	800	
Reflector area	6,260 m^2	12,912 m^2	3,655 m^2	71,095 m^2	81,344 m^2	11,880 m^2	10,740 m^2	7,845 m^2	40,584 m^2	3,500 m^2
Field area	3.5 ha	~2 ha	~2 ha	29.1 ha	35 ha	7.7 ha	~2 ha			
Target height	55 m	69 m	43 m	80 m	80 m	60 m	106 m	61 m	80 m	80 m
Receiver	Cavity	Cone/ Cavity	Cavity	External cylinder	External cylinder	Cavity	Cavity	Cavity	External	CPC + cavity 'porcupine'
Heat transfer fluid	Water/ steam	Water/ steam	Sodium	Water/ steam	Molten salt	Water/ steam	Molten salt	Molten salt	Water/ steam	Beam down air
Storage capacity (MWh_{th}) or heat to provide ...	0.036 MWh_{th}	3 MWh_e	1.0 MWh_e	28 MWh_e	107 MWh_{th}	3.5 MWh_e	12.5 MWh_e	2.5 MWh_e	1.5 MWh_e	n.a.
Period of service	1980–81	1981–84	1981–85	1982–88	1996–99	1983–84	1983–86	1984–85	1985–	2001–

Adapted from Lovegrove and Luzzi (2002).

learned from these facilities concerning control systems, heliostats, pumps, valves, receivers and working fluids. One of the most important was that great care must be exercised in selecting 'off the shelf' commercially produced items. Often they are designed for a few hundred or thousand thermal stress cycles during their projected lifetime, but solar plants cycle once or several times a day, and the 'life' can be used up in a year or two, resulting in failure.

8.2.3 Solar one and solar two

The central receiver system built in the Mojave desert in 1981–2 deserves special consideration. This system represented a major milestone as the first system in the world configured as a mature pre-commercial pilot plant. It started life as 'Solar One' and was later re-configured and re-launched as 'Solar Two', shown in Fig. 8.3. Lessons from this system are central to, and are still being utilized by, the present commercial activity with tower systems.

In 1973, Vant-Hull and Hildebrand at the University of Houston received funding from the National Science Foundation (under the Research Applied to National Needs program) to study the feasibility of 'Solar Thermal Power

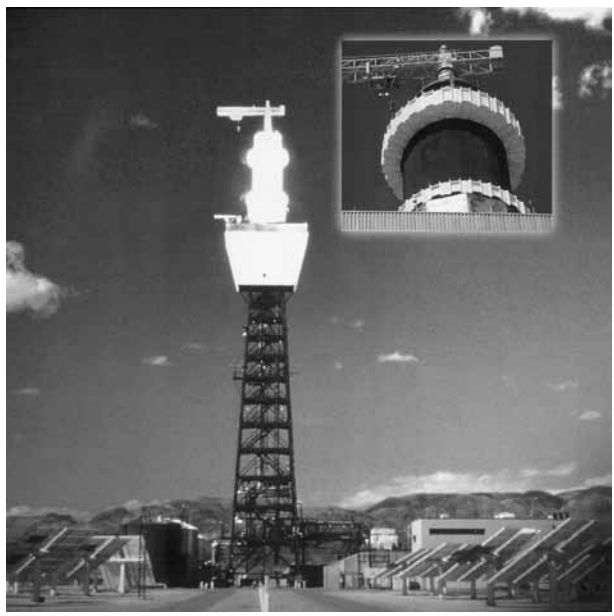

8.3 Solar Two, the molten-salt system with 28 MW_{he} of two tank (warm and hot) salt storage: using the tower and heliostat field of 1,818 heliostats each of 39 m^2 of Solar One and 10,000 m^2 of additional larger heliostats (Boeing).

Systems Based on Optical Transmission'. This study led directly to the construction of Solar One, a 10 MW_e 'pilot plant' tied to the Southern California Edison grid. This facility was a scaled down prototype of an optimized 100 MW_e central receiver system using steam as a working fluid and designed for commercial operation. Three teams with significantly different design concepts (shown in Fig. 8.1) competed in a US Department of Energy funded design study for the pilot plant: McDonnell Douglas (using pedestal heliostats surrounding a central cylindrical receiver), Honeywell (using heliostats consisting of four elevation-tracked mirrors mounted on a rotating frame to illuminate a down-facing cavity receiver), and Martin Marietta (using U-frame type pedestal heliostats placed on the polar side of a pole-facing cavity receiver). In the event (DoE, 1977), Solar One used a 45 MW_t cylindrical receiver (McDonnell Douglas, provided by Rocketdyne) at the focal point (76 m) of a surround field of 1,818 pedestal mounted glass/metal heliostats (McDonnell Douglas design, provided by Martin Marietta). These nearly square heliostats had an area of 39 m^2 consisting of 12 facets, each nominally focused and canted to superimpose the solar images from all facets of the more distant heliostats at the receiver.

The optical design process for the heliostat field, tower and receiver sought to minimize the capital cost plus present value of operations and maintenance divided by the annual thermal energy delivered to the ground. It closely followed the methods and considerations discussed in Section 8.4.

An optimal field layout was established to achieve the minimal value for the levelized cost of heat delivered to the ground for a hypothetical commercial 100 MW_e system. In an iterative process, the focal height, receiver dimensions, and heliostat field were varied (subject to flux density limitations on the receiver which were ameliorated by an automated aiming strategy). For Solar One, these results were not re-optimized, but were scaled to 10 MW_e so the pilot plant would better emulate the issues that would arise in a commercial facility.

Solar One utilized a 'once through to superheated steam' receiver, so the conservative allowable flux on the receiver of this pilot plant was only about 300 kW/m^2, consequently the receiver was rather large (13.7 m high and 7 m diameter to handle 45 MW_t maximum absorbed energy). In the event, budget constraints led to a decision to remove some of the heliostats which were least efficient at the equinox noon design point (on the south side of the field, poor cosine, etc.); consequently, the south part of the receiver could not generate 510°C steam and the south quadrant was relegated to a water preheat function.

In Solar One, storage was provided in the form of a single rocks- sand- and oil- thermo-cline tank which was sized to allow 4 hours of turbine operation at 7 MW_e, i.e. 145 MWh_t. At ground level, the 440°C superheated steam was split between the turbine inlet and a steam/oil heat exchanger.

Caloria HT-43 from the heat exchanger was delivered to the top of the storage unit at 304°C to charge the unit, and upon demand, extracted from the top at 302°C to a steam generator delivering steam to the turbine at 276°C. While the storage unit operated satisfactorily, it was primarily used for testing purposes and to deliver auxiliary steam for start-up and during cloud events. As operation under storage steam was only about 70% as efficient as normal due to the lower steam temperature (277°C vs. 500°C), and operating the storage system was cumbersome, it was not normally used to drive the turbine in this test facility.

Overall, Solar One met most of its test objectives in the initial two-year test period (1982–84), and operated for an additional three years (1984–87) in a power production mode until support funding for the pilot plant ran out. During these five years, many useful lessons were learned for future plants (Kelly, 2000). Generation of steam in the receiver at over 500°C and high pressure required the use of very heavy wall tubing, which was subject to large heat fluxes. The thermal gradients, and resulting stresses significantly limited the allowable flux density. In addition, rapid changes in receiver power resulting from cloud passage, etc., made control difficult, and subjected the turbine to rapid changes. This was alleviated somewhat by the stratified-bed storage system, but that was also difficult to use, and direct storage of steam at high temperature and pressure is costly at other than small scale. Such considerations led to a search for a single phase medium for use in the receiver which could also be used directly for storage.

Due to its high specific heat and boiling point and its good heat transfer properties, non-toxicity, and modest cost, it was determined that (Na60%, K40%)NO_3 salt would provide a superior receiver working fluid, heat transfer fluid, and storage fluid, even compared to pure liquid sodium, which has better heat transfer properties, but is more difficult to handle and more expensive (Utility Study, 1988). These conclusions were supported by the results from several of the small-scale test pilot plants operated in the 1980s. Consequently, the heliostat field, tower, and turbine of Solar One were reconfigured as Solar Two. The receiver was replaced with a molten salt receiver (with approximately three times the allowable flux density and around one-third the active area), the receiver feedwater pumps and piping were replaced to allow salt transport, and the storage unit was replaced with warm and hot salt tanks and a salt-to-steam generator. The room of 10-year-old computers was also replaced with a pair of briefcase-sized DEC Alphas, and 10,000 m^2 of new 95 m^2 heliostats were added, primarily on the south side to overcome the problems of uneven receiver illumination noted at Solar One.

In the design of Solar Two, the early decision to direct all hot salt from the receiver to the hot salt tank and to only operate the turbine from steam generated using salt from storage (Fig. 8.4) made the collection and the

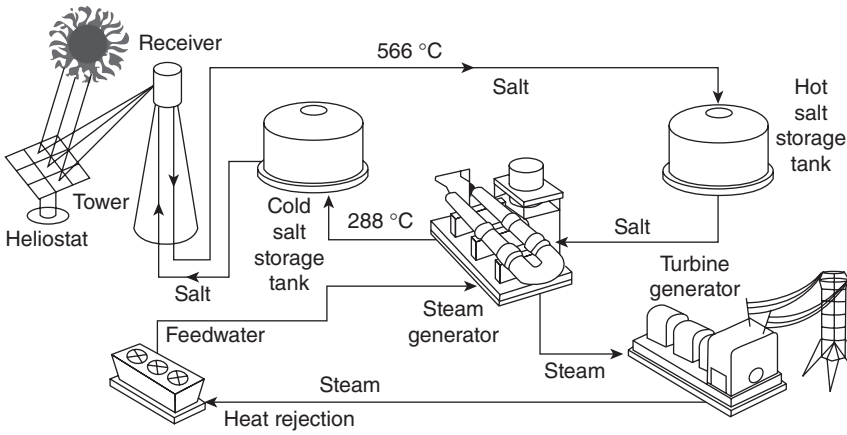

8.4 Schematic of Solar Two operation showing two tank (warm and hot) molten-salt storage of the receiver heat transfer fluid (Bechtel Group International, with permission).

dispatch of energy completely independent of each other. If there was hot salt and demand, the turbine could be operated; if there was warm salt and sunlight, the receiver could be operated, making the collected energy fully dispatchable.

The low pressure of the salt compared to steam allowed much thinner walled receiver tubes to be used at Solar Two compared to Solar One. This reduced thermal stress, and along with the much better heat transfer characteristics of the salt, allowed a much higher receiver allowable flux density, up to 1 MW/m^2 (and in future designs up to 1.5 MW/m^2). Combined with a multilevel vertical aim strategy, this allows use of a much smaller receiver than used in Solar One.

Because the receiver is drained every night to avoid freezing of the salt (freezing point 220°C), it must be preheated each morning prior to filling, to avoid tube blockages – the heliostat field is used for this purpose. Only about 10% of the heliostats were used to avoid overheating of the empty tubes, and these heliostats must be selected primarily from the sunrise side of the field (where the cosine efficiency is very low) to provide a uniform heating. A special processor, which sequentially identifies the heliostat contributing most to any computed hot spot and removes it from track, was found to be quite satisfactory for this purpose (Vant-Hull *et al.*, 1996). Due to the high velocity of salt flow required to achieve the high heat transfer, the salt flow is multi-pass. Salt enters on the (high flux density) polar side, flows in serpentine fashion to the east and west, crosses over to balance the diurnal difference between the power delivered by the east and west fields, and exits from the equatorial-side panels. Here, the lower flux density

accommodates the lower heat transfer coefficient of the hot salt and its propensity, at the 565°C outlet temperature, to initiate corrosion in contact with the hot tube (Bradshaw, 1987; Smith, 1992). In fact, it was found to be cost effective to move some heliostats from the high-performance north field to the lower-performance south field. This reduced the total power on the limiting northern panels, and the resulting lower power level and flux density there allowed use of a shorter and lower cost receiver while remaining within the flux density limitation. The 565°C salt in the downcomer was depressurized by flow restrictors and deposited in the hot salt tank at atmospheric pressure. Upon demand, hot salt was pumped through a preheater-boiler-superheater heat exchanger train, and the resulting superheated steam was directed into the same 10 MW_e turbine used for Solar One.

Several easily-preventable failures reduced the operating time for Solar Two. The prefabricated heat trace tape at the top end of the salt riser was found by the installers to be too long (due to use of too large a pitch while winding), so was double wound at the top to use the whole length and avoid field installation of new connectors. Consequently, the top of the riser pipe became overheated and began to oxidize to the extent that, after a time, rust particles broke off and eventually caused a number of receiver tube failures due to blockage. In addition, a portion of the riser pipe had to be replaced. Better quality control during construction or an appropriate filter would have prevented this costly exercise.

After a time, the steam generator failed. It turned out that it was designed using a common utility steam generator code. Inadequate salt circulation in a localized area resulted in excessive stress during each thermal cycle, and failure resulted after 500 cycles or so. It should be noted that 500 thermal cycles would actually represent a very long life for a utility steam generator under normal operating conditions, highlighting the challenges of using existing commercial solutions in CSP systems. It had to be removed, redesigned, and rebuilt.

After two years of test and three years of grid tied operation, the receiver panels developed considerable warpage. This was initially due to inadequate allowance for thermal expansion in the original design, which assumed normal operating conditions for the panels. During off-design conditions, the entire length of the panels could be at the maximum temperature and so experience constraint and warpage. Once this constraint was remedied, residual flux gradients caused significant additional warpage by the time operation was terminated.

Several 'peripheral' problems such as this depleted the operating budget to the extent that, shortly after the pre-designated test plan had been completed, Solar Two was shut down (in 1999) prior to significant commercial operation. Thus, much of the operating experience so useful in establishing

the 'bankability' of the molten salt central receiver concept did not eventuate.

8.2.4 Period of transition

The period from 1990 to 2005 was a difficult time for solar energy in general, and due to the large capital investment required and the restricted years of operation of demonstration plants, for central receiver plants in particular. During this period, substantial progress was made in heliostat design leading to lower costs and higher performance. In addition, receiver coatings were improved, and work was initiated to develop specialized molten salts with lower freezing points and higher working temperatures. Studies using fluids other than steam or molten salt in the receiver were undertaken. In particular, supercritical steam or supercritical carbon dioxide offer significant advantages in turbine generator efficiency. However, the very high temperatures and pressures involved result in very high costs for the receiver, and even for the risers and downcomers. The containment costs of supercritical fluids at very high temperatures and pressures make storage of the working fluid itself expensive (Kelly, 2010).

An alternative receiver concept is a volumetric receiver in which ambient air is drawn through a 'thick' porous mesh or grid, which is simultaneously irradiated at high flux density. Volumetric receivers can be operated at either atmospheric or elevated pressure. If the latter, then a transparent window is required to maintain the pressure while allowing radiation onto the absorber surface. A window also allows the use of an alternative working fluid. Extensive experimental and development work was carried out on the volumetric approach by researchers in Europe and Israel. The incident flux is absorbed within the volume of the mesh, heating it. Meanwhile, the airflow effectively cools the outer surface of the mesh, thereby reducing its temperature and re-radiation. The air is further heated within the hot mesh and by the ambient solar and infrared radiation. In this way, sufficiently high temperatures (>900°C) can be achieved to run an efficient Brayton cycle engine, with storage possible by passing the air through a ceramic bed.

In the years since 1970, there was increasing awareness of the issues of global warming, peak oil and the limitations of fossil fuel reserves, and the general issue of the uncosted effects of pollution from fossil fuels. Consequently, starting about 2000, several organizations renewed efforts to implement central receiver power plants. Many studies were undertaken for specific applications and sites, but for a long time economic conditions were not appropriate to allow successful financing of the first plant, even with substantial governmental incentives or tax breaks. For example, Bechtel (Nexant) carried out a preliminary design for a plant in Spain (Solar Tres, 2000) in response to the Royal Decree promising significant feed-in tariffs,

and in South Africa (Eskom, 2002) in response to a request from the state utility, Eskom, but in neither case was it possible to close the financial deal. Certainly, other organizations had similar experiences.

Several companies and organizations developed experimental/test facilities at this time to better position themselves and their new concepts for the commercial boom that was expected as economic, political, and energy requirements developed.

8.3 Activities since 2005

8.3.1 Research, development and demonstration

As with CSP in general, 2005 marked a change in activity for central receivers and the beginning of the contemporary period of industry expansion.

- The test facilities at Sandia and at Plataforma Solar were upgraded, providing facilities for the testing and verification of small-scale projects.
- The Themis site has been designated to test 4 MW_t volumetric gas receivers in an open cavity.
- Abengoa Solar New Technologies have been operating a 5 MW research tower in between its PS10 and PS20 towers. A fourth small tower is under construction at the same facility for development of air receivers.
- CSIRO in Australia built two small high flux towers (600 kW_{th} and 1.2 MW_{th}) for development of high temperature concepts in steam, storage, solar fuels, and both air and supercritical CO_2 Brayton cycles. They operate regularly at >1,000 K and up to 1,600 K. The larger of the two towers uses 450 small (4.5 m^2) low-cost, high precision heliostats (Stein, 2011).
- At Jülich, Germany, a north field solar tower facility was designed to test open volumetric air receivers at the 1.5 MW_e level. It has been operating up to 650°C since March 2009.
- Mitaka Kohki of Japan has built a small experimental scale beam-down system with an elliptical secondary at 10 m elevation illuminating a cavity equipped with a CPC to recover some of the concentration. Seventy highly precise heliostats carrying four each 1/4 m^2 facets power the system.
- The Chinese Academy of Sciences has built a 7.5 MW_{th} experimental/demonstration plant 75 km north of Beijing. This plant uses 100 m^2 heliostats to illuminate a cavity receiver producing steam and includes a storage unit (Fig. 8.5).
- Korean Institute of Energy Research have built a 200 kW_e tower in Daegu, Korea.

8.5 Photo of the 7.5 MW_{th} experimental/pilot plant of the Chinese Academy of Science near Beijing, China. The illuminated initial cavity receiver/tower stands behind the new tower which has several test apertures (Zhifeng Wang, with permission).

Several companies were interested in larger scale commercial facilities. Test platforms were built by companies including Abengoa Solar, LuzII (BrightSource) and a number of smaller companies to qualify their proprietary heliostats, control systems, and receivers.

In Israel, a number of the engineering and management personnel who designed and built the LUZ parabolic trough plants in the 1980s (345 MW_e still operational in 2012) reconstituted themselves as LUZII and initiated the design of a central receiver system. Their first effort was to produce a 20 MW_{th} heliostat field, control system, and receiver test facility in the Negev desert in Israel. The BrightSource (LuzII) test facility in Israel really approximates a sector of their first plant and consists of 1,600 heliostats of 14 m^2 in two facets, illuminating a flat panel receiver atop a 60 m tower. The system can generate saturated or superheated steam. It has been operating since 2009 to validate the heliostat operation, control system, and receiver designs.

In 2009 BrightSource continued with the construction of a 29 MW_{th} enhanced oil recovery facility at Coalinga, between San Francisco and Los Angeles. It uses 3,822 of the same two-facet mirrors to illuminate a flat panel steam receiver atop a ~100 m tower.

In 2009 eSolar brought two demonstration modules of their proposed 10–14 unit commercial plant into operation in California. One utilized a north and a south facing pair of cavity receivers producing superheated steam, the other a receiver that consisted of four flat-panel units facing NE,

NW, and SE, SW, with steam superheating taking place near the north and south corners. The field uses small 1.14 m^2 heliostats factory mounted on truss structures to minimize field installation. In their test/demonstration facility, they used 24,000 such heliostats, 6,000 each in a north and a south field for each receiver. They generated superheated steam at over 400°C in each receiver module, with each such module rated at ~10 MW_{th}. The objective of these developmental facilities was to test and demonstrate the heliostat concept, control system, and receiver capability. In addition, the two receiver outputs were ducted to a 5 MW_e turbine to demonstrate stability of the entire system, with the electricity sold to a local utility company (Meduri *et al.*, 2010). As of 2011, a second-generation demonstration module of a proposed ten-module 100 MW_e molten salt plant is undergoing commissioning in Rajasthan, India.

8.3.2 Commercial power plants

By 2010 there were five or more companies actively engaged in developing large-scale commercial central receiver projects: Abengoa Solar in Spain (and a 50 MW_e project recently announced in South Africa), eSolar in the US and in India, Sener-Torresol Energy in Spain, BrightSource (Luz II) in the US (and Israel), and Solar Reserve in the US. Each had a different approach to commercialization, involving various heliostat concepts, receiver designs, working fluids, storage methodology, field configurations, and plant sizes. Each of these currently has a commercial tower plant in operation or under construction.

Abengoa Solar, a large Spanish company with numerous trough plants in operation, was first to proceed to commercial construction and operation in 2006 with PS10 near Seville, Spain. PS10 is a 10 MW_e North (polar) facing hemi-cylindrical 'cavity' receiver at 100 m elevation, generating saturated steam at 240°C, using 624 canted and focused 120 m^2 heliostats. In addition to powering the turbine, the saturated steam provides 20 MWh of thermal storage. This was followed by the 20 MW_e plant, PS20 (Fig. 8.6), which uses essentially the same configuration with some improvements in receiver efficiency, and a one hour storage system. It began commercial operation in 2009.

eSolar has taken a considerably different approach, using a close-packed array of co-mounted 1.14 m^2 heliostats to irradiate a receiver atop a 'low' tower (Fig. 8.7). The commercial concept is for modules to produce 50 MW_t each (10–14 units would produce a total of 500–700 MW_{th}, providing steam to a 100 MW_e turbine with a 50–75% capacity factor respectively, using molten salt storage). A preliminary design of such a system using molten salt as the receiver working fluid and for storage at the centrally located power block is currently (2011) under development for a plant in Rajasthan,

8.6 The two commercial Abengoa (Spain) saturated steam systems, PS10 and PS20 (in back), with 120 m^2 heliostats in foreground.

8.7 Two 10 MW_{th} modules of the eSolar (USA) Sierra Sun Tower facility. The receiver in the foreground utilizes four flat panels in an external square configuration, while the background tower carries a north-facing and a south-facing cavity receiver. A total of 24,000 heliostats, each 1.14 m^2, are factory mounted on support structures (eSolar, with permission).

8.8 Torresol's Gemasolar 19.9 MW_e commercial molten-salt facility with heliostats and a local BCS station in the foreground and tower/receiver in back, probably in preheat configuration. The active receiver is the central 20% of the white area with the bottom 40% comprising the BCS target (K. Younglove, with permission).

India, where a second generation demonstration field module is undergoing commissioning (Pacheco *et al.*, 2011).

Torresol Energy has built a commercial molten salt facility (Gemasolar) with 15 hours of molten salt storage (Lata *et al.*, 2010), which began commercial production in the second half of 2011 (Fig. 8.8). The plant employs 2,650 heliostats of 115 m^2, resulting in an external-cylindrical-receiver rating of 154 MW_{th} (delivered to storage), but uses only a 19.9 MW_e turbine (to stay within the limitations of the Spanish tariff regulations). In fact, this plant has been operated continuously for several days, proving baseload capability for a CSP plant. As the local peak-load period is largely after dark (between the hours 12:00 and 22:00), the storage is utilized every day to match the peak, making the plant much more valuable to the utility.

The US company, BrightSource, is making good progress (construction started in October 2010) to satisfy a power purchase agreement for 392 MW_e, comprising three units, at Ivanpah in the California desert near Las Vegas, taking advantage of a federal loan guarantee. They use 14 m^2 heliostats mounted on posts driven into the ground (to reduce both costs and habitat degradation) to produce a total of 300–400 MW_{th} per plant on four nominally flat panels facing the cardinal directions. The superheated steam will drive a conventional turbine or will be directed to heat exchangers to produce high temperature salt for storage in a two-tank system. The first component is scheduled for operation in early 2013. 22 months after ground breaking, in August of 2012, the received was installed on the tower and over 90% of the heliostats installed on the first unit (Fig. 8.9). The receiver is being installed on the second unit, as is the heliostat field, at 500 heliostats

8.9 Phase 1 of 3: BrightSource Ivanpah facility near Las Vegas, January 2012. 121 m steel tower is ready for receiver installation. Over 20% of the 40,000 heliostat pedestals are installed for this 110 MW_e plant and heliostat installation proceeds at 100+ per day (Michel Izygon, with permission).

per day. The tower of the third plant is up and field work is underway. In total, BrightSource has 1.3 GW_e of PPAs in place with Southern California Edison and 1.3 GW_e with PG&E. Some of the these plants will incorporate molten salt storage (BrightSource press release, November 28, 2011 and August 12, 2012).

SolarReserve in the US licensed the proprietary design information that Rocketdyne (now Pratt & Whitney Rocketdyne, a subsidiary of United Technologies Corporation) had developed in the construction of the molten salt receiver, pumps, thermal storage units, and steam generators of Solar Two. They are currently (mid 2012) in the initial construction phase (all permits received and a federal loan guarantee in hand and the central tower completed, awaiting a receiver) for the first of three 110 MW_e (565 MW_{th}) molten salt plants with an approximately 50% capacity factor to be installed near Tonopah, Nevada (Fig. 8.10).

Table 8.2 shows a summary of central receiver commercial power plants.

8.10 SolarReserve demonstration heliostat on Crescent Dunes site, November 17, 2011, 170 m concrete tower completed February 9, 2012, awaiting addition of cylindrical receiver (SolarReserve, with permission).

8.4 Design and optimization of central receiver systems

8.4.1 Determination of system configuration

Before one can initiate the serious design of a CR system, it is essential that the application be selected, thus determining the power level and the receiver operating temperature and conditions. For example, a 1 MW_{th} solar furnace producing a peak flux density of 10 MW/m^2, a 10 MW_e peaking plant, a 200 MW_e 'baseload' plant powering a supercritical turbine, or a plant to provide 10 MW of process heat at 300°C to a food processing plant or at 1,000°C to a metal refinery. The details of the application will define the operating temperature, the receiver working fluid, the load, and the solar multiple required to satisfy the load by storing energy during available sun hours. The receiver working fluid may be used directly by the load, used to charge storage, or used in a heat exchanger, etc. Once these details are worked out and the design-point power level, output temperature, and maximum allowable flux density of the receiver defined, serious design of the CR system can be initiated. Site elevation and latitude are also essential in order to define the nature of the insolation and the longitude (site) to define the insolation profile. Of course, an experienced solar engineer should be involved in all these decisions, or unrealizable conditions may (will) be defined.

Table 8.2 Summary of Central Receiver commercial power plants (2012)

Responsible organization	Abengoa SA		eSolar	Torresol	BrightSource Industry		SolarReserve	eSolar
Plant designation (plant country)	PS10 (Spain)	PS20 (Spain)	Sierra Sun Tower (USA)	Gemasolar (Spain)	Chevron (USA)	Ivanpah (USA)	Crescent Dunes (USA)	Bikaner (India)
Net electric power	10 MW_e	20 MW_e	5 MW_e pilot plant	19.9 MW_e	Process heat	3 × 130 MW_e	110 MW_e 500 GW_{he}/yr	100 MW_e prelim. des
Thermal power	55 MW_t	*110 MW_t	2 × 10 MW_t	*220 MW_t	29 MW_t	3 × 3,000 MW_t	565	10 × 50 MW_t
Irradiance W/m²	*~800	*~800	~900	*~800	~	~	950	
Reflector area	75,216 m^2	*~150,000 m^2	2 × 13,600 m^2	304,750 m^2	53,500 m^2	3 × 900,000 m^2	1,081,000 m^2	*10 × 68,000 m^2
Field area ha				185 ha			540 ha	
Target height	100 m	140 m	65 m	130 m	100 m	130 m	180 m	*~100 m
Receiver	Hemi-cylindrical Cavity (4-panel)	Hemi-cylindrical cavity	Dual cavity external 4-panel	External cylinder	Flat panel	External 4-panels N, S, E, W	External cylinder	External 4-panels
Heat transfer fluid	Saturated steam, 250°C @ 40 bar	Saturated steam	Superheated steam	Molten salt	Saturated steam	Superheated and reheated steam	Molten salt	Molten salt
Storage capacity	50 min @ 50%	~1 hour	None	278 MW_{he}	None	None	3,000 MW_{ht}	3,500 MW_{ht}
First operation	2006	2009	2010	2011	2010	2013	2013 (projected)	2012+

Based on data from developers' presentations, websites and data sheets.
* Supplemented by estimates by the author: January 2012.

Commercialization of CR systems has to some extent been delayed by the significant capital cost of the very large capacity systems that many commercial proponents believe to be more cost effective than small or modular systems. Recognition of this issue has recently led to the design and construction of smaller systems designed to benefit from a lower capital cost requirement, as well as smaller and hence easier to handle components, more rapid progress down the learning/experience curve, easier access to capital, shorter construction time, and possible use of available off-the-shelf components (eSolar, 2011). It remains to be seen if these benefits can outweigh the economies of scale of larger systems. Recently, successful operation of a one MW_e unmanned trough-thermal-electric system showed promise for small CSP systems in general (Arizona Power Systems, 2006). Unmanned operation is an important capability in allowing smaller systems to be economical. Such small systems can be clustered to meet larger applications and also to achieve lower operating and maintenance (O&M) costs. However, energy transport costs to the central site must be considered carefully as fewer larger units may be more economical once the energy transport is accounted for.

8.4.2 The objective function for optimization

The designer of a CR plant must have in mind some criteria, which will drive the design. In most cases this will result in a system trade-off or optimization process. Because the collectors are expensive, one might select maximum plant efficiency, achieved via high output temperature to allow better Carnot efficiency, but this is likely to call for more accurate (possibly more expensive) heliostats and is sure to result in higher receiver thermal losses and optical spillage and more expensive receiver materials, and generally a more expensive power block, though higher efficiency can reduce costs of auxiliaries such as cooling. Nonetheless, some cycles such as the supercritical CO_2 Brayton turbine promise very high efficiency at quite achievable temperatures.

Aiming for lowest capital cost, on the other hand, may result in the choice of less accurate heliostats, thus a larger receiver to overcome spillage, higher thermal losses or a lower operating temperature, and a poor system performance, perhaps resulting in a higher levelized electricity cost (Pitman and Vant-Hull, 1986). One could also choose to design the plant for a particular day or time, resulting in relatively poor performance at other times and on an annual basis.

For a commercial CR plant, we assume the customer for the thermal energy produced is a power plant or a process heat application. The exact application will then define the specific required power and capacity factor, and a likely temperature range. The solar plant is then designed to meet

this *annual* demand at the lowest cost per unit of energy. The appropriate objective function is then a cost benefit ratio: total capital cost of the installed plant plus present value of operations and maintenance over the projected life of the plant all divided by the net output of the plant over its design lifetime: i.e., the lifetime cost per MWhr of the thermal energy delivered (Lipps and Vant-Hull, 1978). It is important to note that multi-year average diurnal insolation should be used in the optimization. A single selected year is unlikely to be representative and, while a 'typical year' may be constructed, an insolation model based on long-term atmospheric properties is easier to construct and understand.

An alternative objective function that is frequently used (Dellin and Fish, 1979) is levelized cost of electricity (LCOE) (discussed in detail in Chapter 2), defined as the unit cost at which the product must be sold to provide a defined rate of return over the life of the plant. This is a more complex analysis and one must define the financial details completely and into the future (and they strongly affect the result). Further, the cost and performance details of the non-solar balance of the plant are required. Hardly any of these issues are solar related, and while LCOE is a quantity easily recognized by utilities and banks, financial quantities vary markedly over time, and the performance details of the subsystems may be difficult to obtain and implement in a meaningful manner. Nonetheless, the emergence of dispatchability as a primary advantage of CSP means a financial analysis method that can model the benefits of time of day dispatch (whereby a kWh of electricity may be worth more in the afternoon/evening than in the middle of the day, for example) will be of most value for investors.

SANDIA has developed codes such as Solergy (Stoddard *et al.*, 1987) to accept the diurnal efficiency curves for the optimized fields produced by programs such as RCELL or DELSOL, and do a detailed calculation of the energy or electricity produced during a representative or average year. Solergy has incorporated the thermodynamic quantities and the financial parameters required to develop an LCOE. A good summary of software and codes for analysis of concentrating solar power plants is provided in Ho (2008), though even more models have emerged since then.

The effects of inflation must be accommodated. As various subsystems or components may be costed at different times, it is reasonable to multiply each cost by an appropriate inflation factor. The familiar consumer price index offers a generic method for accommodating inflation; however, at the component level a more appropriate method may be to use an engineering source such as the Chemical Engineering Plant Cost Index (CEPCI, published monthly by the American Society of Chemical Engineers). Costs generated at various times can be compared and/or used coherently in a study if each cost is divided by the index value appropriate for the date it is generated, and multiplied by the current index value. This allows 'legacy'

costs from earlier work to be used alongside current costs. Many countries have such resources. A more complex consideration can be the incorporation of international currency exchange rates.

8.4.3 Items to include in the cost function

The numerator in the objective function is money invested over the life of the plant. This may be considered in three categories: preliminaries and fixed, purchase and construction, and finally, operations and maintenance (O&M).

Fixed costs such as permitting, design, and access

These should include most general costs such as plant design; environmental and political permitting; central facilities such as control room, fire and safety facilities, maintenance shop; and access roads and transmission lines to the site – which may be substantial if the site is isolated. As each of these quantities can cost over a million dollars, they must be considered carefully and should be prorated to the various subsystems of the facility. In fact, they are a primary reason energy from small, stand-alone plants tends to be more expensive. This issue may be somewhat mitigated if a number of small plants are integrated or co-located with one another or with the energy user.

Capital costs

The major solar-related capital costs of a CR plant are the heliostats, the receiver, the tower, the thermal transport system, and the thermal storage system if included. It is important that each of these be not just the purchase price of the item, but include the installation cost (transportation, foundations/support structures, construction or installation, connection to power and control system, quality control, and testing). The cost of a heliostat on the factory floor may be little more than half of its final cost as an installed, wired, aligned, tested, calibrated, and operational heliostat at a distant site. Similarly, the vertical piping cost must include transportation to the site, hangers, an allowance for expansion bends, on-site welding and inspection, insulation, heat trace if needed, temperature sensors, valves, etc. It is often a surprising but important fact that the actual cost of the constructed active receiver (tubes and headers, etc.) is only a small part of the cost of the receiver. The majority of the cost is in the strong backs and hangers the panels are mounted on, the support structure, insulation, temperature sensors, valves and controls, header shields and ovens (if needed), and the transition from the tower to the support structure. These costs are even

higher for a cavity receiver, which must also maintain the receiver tubes and headers in a high temperature enclosure.

To allow for optimization of the CR plant, the cost of each subsystem must be provided at the outset in terms of the appropriate design variables in simple relations valid over the range of practical values. For example, towers of a few heights based on designs appropriate for the local earthquake regime and assumed top loading due to expected receiver size, weight, and wind speeds can be developed. Then the tower cost for any height within an appropriate range can be approximated with a power law or exponential fit, after any obvious fixed or linear costs are accounted for (soil testing, safety lighting, elevators, etc.). Of course, the final design will provide a more detailed and precise tower design and cost.

Land

A good solar site will likely be relatively isolated, have a peak direct-beam insolation of the order of 1 kW/m^2, and an annual beam insolation (DNI – direct normal insolation) preferably >2,000 kWh/m^2/yr, be of suitable size (including buffer), moderately level (less of a requirement for central receivers than troughs) and suitable for construction. It must also have easily resolved environmental constraints, good and guaranteed access to nearby transmission lines able to accept the power and to roads adequate to handle construction equipment, and a willing seller. Such ideal land may sell in the USA for \$1–2/m^2 (or \$4,000–8,000/acre). While much cheaper land may be available, satisfying or coping with all the conditions above can be very expensive, and time consuming, while permitting may be impossible. Gently rolling land can be accommodated, but will significantly complicate the layout of heliostats. Sloping land, up to perhaps 10°, can be accommodated in the system design of a central receiver plant with varying effects such as: later sunrises/earlier sunsets due to virtual horizons, shifting the centroid of the field downhill, or moving the diurnal energy output curve toward morning hours if the slope is up to the west or to better meet an afternoon peak load if up to the east.

Heliostats

Heliostats must be accurate enough to not degrade the solar image excessively (beam error less than ~2–3 mrad) and rigid enough to sustain gravity and wind loads while maintaining this accuracy. Such heliostats are presently estimated to cost ~\$200/m^2 in 2010 US dollars (Kolb *et al.*, 2007; Kolb, 2011) and most cost targets are between \$100 and \$130/m^2 once volume production and learning curve effects begin to take effect (Mancini *et al.*, 2011). The long-term DOE SunShot goal is \$75/m^2, which will be difficult to achieve.

The optimum heliostat area is hard to define as it involves a trade-off between many effects such as reflector support deflections under gravity and wind load, spillage (beam size at the receiver), and number of control systems, etc., to be built and maintained. Current 'commercial' heliostats range from 1 m^2 to 150 m^2; however, designs up to 200 m^2 have been developed, and some companies have considered ganged or autonomous heliostats much smaller than 1 m^2. See Chapter 17 for a more detailed analysis.

To be cost effective, a heliostat must make a net positive contribution to the economic performance of the plant. For example, if the land cost associated with a heliostat near the center of the plant is 2% of the heliostat cost, near the field boundary where the heliostat density is typically one-third that at the center of the field, the effective land cost will be 6%. Atmospheric attenuation between the heliostats and the receiver has a similar effect as does spillage losses. The cost of conventional wiring and control systems also has a negative impact due to the larger radial spacing far from the receiver. Thus the position of the outer boundary and heliostat losses and associated costs need to be traded off to optimize the objective function.

Present value of subsystem operations and maintenance (O&M) costs

Annual operations and maintenance (O&M) costs may amount to a quarter of the annual charges for the capital costs. As a result, it is important to include such costs in the optimization. However, it is inappropriate to simply multiply the overall plant cost by 125%, as O&M cost comprises both fixed and variable components and varies widely from subsystem to subsystem. For example, the Utility Study of the 1980s (Utility Study, 1988) used the consensus estimates for the annual O&M relative to each subsystem capital cost for that molten salt system: tower 0.2%; receiver 2%; vertical piping 1%; feed pump 5%; heliostats 1%. For the 39 m^2 heliostat considered at that time the costs were split equally between the reflectors (area) and the tracking system (number). Experience since then will allow more operational values to be developed for each subsystem, but the argument is unchanged. Note that for comparison to capital costs, these percentages must be multiplied by a present value factor which may range from 10 to 20 times the annual costs depending upon the real rate of return assumed (see Chapter 2).

8.4.4 Choice of performance criterion

Design point or annual

The objective function for optimum design of a CSP plant has costs in the numerator and performance in the denominator. There are a number of options for definition of the performance, and some are much better than

others. Choosing performance at the design point will lead to a lower cost system with excellent performance at that time, but relatively poor performance at other times throughout the year, and consequently a lower annual energy output. While this may be suitable for a solar furnace with short seasonal operating times, it is inappropriate for a power plant. Here the requirement is lowest LCOE, so the denominator must be delivered annual energy.

Incident, absorbed, or delivered energy

The energy incident at the receiver is reduced by the receiver interception and reflectivity (1 – absorptivity); radiation and convection losses (although conduction losses are negligible); piping thermal losses; and the parasitic losses of the feed pumps, valve and heliostat actuators, etc., required for operation of the solar complex (converted from electrical to thermal by multiplying by the heat rate of the turbine or charged directly as purchased electricity). The result is the net delivered thermal energy available to the turbine or to charge the thermal storage unit.

Inclusion/effect of time-of-day pricing, sloped fields

If time-of-day pricing is in effect, it can be used by the plant designers to improve the annual revenue of the plant by configuring the field layout so it is more effective during the period of peak electrical price. This can be used with or without storage. A more effective approach is to value the sunlight proportionately to the time-of-day price prior to optimizing the field. Thus, high value sunlight will play an enhanced role in establishing the heliostat spacings everywhere, and in defining the boundary of the plant. With an afternoon peak price, this will lead to an east-biased field both in heliostat density and field boundary. A field that slopes up to the east will have a similar effect and is favoured in case of afternoon peak pricing. An upslope to the north (or south in the southern hemisphere) will produce a somewhat more effective field, but the cost of installing heliostats on a sloped field must be accounted for and a more polar bias of the field must be accommodated.

8.4.5 Effect of constraints on optimization

Any constraint on the system design will have a negative impact on the resulting optimized field/system, and an even greater impact if the constraint is imposed after the optimization. The unconstrained optimization process strives for the lowest LCOE. Consequently, for a specific tower height and receiver aperture, it defines the heliostat spacing and number (field boundary) and evaluates the design point power and annual output

power. One can achieve a lower design point power and perhaps higher efficiency by trimming heliostats from the boundary of the field, but the LCOE will be increased as cost-effective heliostats are removed. Alternatively, one could constrain the design point power at the onset and the optimization process will lead to a lower tower, smaller receiver, and intermediate area field – at an intermediate LCOE. Clearly, the least constrained system will be most cost effective, and the best time to introduce any constraint is prior to the optimization. Definition of a polar-facing aperture is clearly a severe constraint, but the use of two or three cavities to enhance the azimuthal acceptance angle can ameliorate the constraint somewhat.

8.5 Heliostat factors

8.5.1 Beam errors

An ideally focused optical mirror operating on-axis can form an image of the sun on the receiver at a distance of one focal length. As the sun is a distant object with an angular diameter of 9.306 mrad, the image will not be a point, but have a diameter of 0.0093 times the focal length. At 1,000 m, this amounts to a 9.3 m diameter, and would display the limb darkening of the sun (due to scattering in the solar atmosphere) and the solar aureole (light appearing outside the limb of the sun due to scattering in the Earth's atmosphere). For the purposes of CSP systems involving concentrator optics, we are interested, not in forming an image, but in collecting most of the energy cost effectively. Thus, the sun may be conveniently represented by a Gaussian function which is a least square fit to the limb-darkened solar image, resulting in a second moment (sigma) of 2.770 mrad, but will overestimate the peak flux density by about 16%. The resulting Gaussian 'spot' at 1,000 m will have a diameter of 5.54 m at the one-sigma radius (relative intensity = 0.607) and a diameter of 11.08 m at the two-sigma radius (relative intensity =0.135). The energy beyond this diameter (i.e., the spillage for a circular target) would be mathematically equal to the relative intensity at the defined radius, assuming the Gaussian is a reasonable approximation to the solar aureole. A better fit to the true sunshape can be accomplished by adding to the second moment (sigma^2) higher moment terms such as fourth moment (a measure of kurtosis), sixth moment, etc., in a Hermitian series (Walzel *et al.*, 1977), but if beam errors are comparable to the second moment of the sunshape the improvement is marginal and the complication significant. For detailed flux analysis, it is useful to include terms in the Hermite series to sixth order.

Beam errors encompass all imperfections in the heliostat system and are expressed in terms of the divergence half angle of the beam leaving the heliostat if illuminated by a true point source. It is assumed that all systematic errors are identified and corrected by normal O&M procedures so the

remaining errors are essentially random, at least if averaged over an array of heliostats. Residual mechanical errors, which may affect the orientation of the mirror, are doubled upon reflection. Such errors include tracking errors, effects of wind or gravity on the heliostat, etc. It is very convenient to handle all of these random errors by summing them in quadrature (after doubling mechanical errors) to obtain the 'total beam error', and then adding them in quadrature to the second moment of the limb-darkened sun (2.770 mrad) to form a 'degraded sun'. This avoids all the issues of convolving a multitude of errors on a multitude of heliostats. This also provides a useful reference for judging the importance of beam errors, if the total beam error is equal to that of the sun (2.770 mrad) it will produce a degraded sun with a sigma of 1.41*2.770 = 3.92 mrad, if the beam error is much less, it will be relatively unimportant, if much larger it will be dominant. The idea of a degraded sun gains validity from the fact that we usually have thousands of heliostats, so individual instantaneous displacements of individual beams or facets can be treated as random variables. It does give up the ability to predict realistic images from a single heliostat. Higher order moments of the sun and of the errors can also be incorporated via the Hermite method mentioned above.

8.5.2 Heliostat size

The discussion of sun-shape and beam errors provides the optical rational for considering heliostat size. An optically flat heliostat will simply project an image of the sun from each point, forming an image of the mirror with the effects of umbra and penumbra representative of the solar beam. So long as the angular size of the mirror as seen from the receiver is small compared to the angular size of the sun, the intensity of the image will not be reduced significantly compared to a focused mirror. If the mirror is comparable to or larger than the projected solar image, there will be a serious decrease in intensity from a flat mirror compared to a focused mirror, accompanied by a corresponding increase in the spot size as discussed in Section 8.5.3.

8.5.3 Focusing and facet canting

The spot degradation caused by large, flat mirrors can be largely recovered by cutting the mirror into facets (which also makes them easier to handle) and canting each one to superimpose their images at the receiver (which carries some cost in hardware and labor). Alternatively, the mirror, or the individual facets, can be curved to focus their beam near the receiver surface (often termed as 'to slant range') in order to reduce the effect of the facet diameter on the solar spot. As it is much easier to bend glass into a cylinder than a sphere (due to Poisson ratio effects), frequently mirrors

are focused only on the long axis. Whatever the optical geometry (figure), the image (from a point sun) of the error-free mirror can be projected to the receiver via ray-trace and the second moment (and higher moments) of this 'spot' can be calculated and added in quadrature to that of the degraded sun (Walzel *et al.*, 1977), or the image may be generated by detailed ray tracing.

8.5.4 Off-axis aberration

Either canting or focusing results in an effect known as off-axis aberration (Rabl, 1985, p. 177). Effectively the focal point is modified by the angle of incidence (ι) of the sunlight on the mirror, so in the transverse direction the focal length (f) is reduced by cos ι and in the sagittal direction increased by 1/cos ι, forming two line foci with a circle of least confusion between them near f. For a mirror of diameter w and incident angle i, the diameter of this circle is $w(1 - \cos i)$. At an off-axis ι of 60°, this leads to a heliostat image from a 'perfectly focused on axis to slant range' parabolic (or small spherical) mirror of one-half the mirror dimension (to be added in quadrature to the sun image and the effects of beam errors discussed above). The situation becomes more complicated as one departs from the nominal focal length.

8.5.5 Effects of tracking mode

There are a number of possible mounting systems to accomplish the tracking of the heliostat image onto the receiver. Most common is the elevation–azimuth (el-az) system, in which the assembly is rotated in azimuth, and above that is mounted the orthogonal elevation axis carrying the mirror. While simple and economical to build, this scheme has several disadvantages. One is that the reflector rotates in azimuth but does not retain its orientation with respect to the sun-mirror-receiver plane. Consequently, the angle-of-incidence effects mentioned above cannot be resolved, so the (nearly flat) mirror is generally given the optical figure of a sphere as the best option. Alternatively, the mirror can be given a third axis of rotation (about its center) and rotated continuously to retain the correct orientation with respect to the sun-mirror-receiver plane (Zaibel *et al.*, 1995; Chen *et al.*, 2001). A tracker with the first axis pointing toward the receiver, or spinning-elevation tracking system accomplishes this also (Zaibel *et al.*, 1995). The mirror can then be given an appropriate off-axis parabolic optical figure, obviating the cos ι effect.

In any case, to avoid collisions with its neighbours in case tracking control fails, el-az mirrors require a 'clear-out circle' with diameter equal to the maximum dimension of the horizontal mirror (D for a circle, 1.41 S for a

square, $(L^2 + W^2)^{0.5}$ for a rectangle, etc.). Typically 30 cm or so (for a large heliostat) is added as a safety factor, or more if the axis of rotation does not pass through the center of the horizontal mirror. This 'mechanical limit' may increase the required separation of heliostats, a problem particularly in the most effective portion of the field where heliostats tend to be most crowded. Conceptually, collisions of more closely spaced heliostats can be avoided by computer algorithm, but failures will be costly.

An elevation/polar-axis mounting system carries a mirror which does not rotate in azimuth. This allows close packing of the mirrors giving twice the maximum mirror density for square mirrors compared to the el-az mount. It also tracks at a constant rate about the polar axis. The orthogonal axis requires only slow corrections for seasonal changes in solar declination.

A mounting system with the first axis pointing toward the receiver can rotate at a constant rate, so a second axis is always perpendicular to the sun vector (Francia, 1968). The mirror in this case will always retain the correct orientation with respect to the sun-mirror-receiver plane. Thus, if given the optical figure of an appropriate off-axis parabola, there will be no cos ι effect.

It is important to consider the added cost compared to the advantages of these, and other, exotic mounting systems before selecting them.

8.5.6 Effects of heliostat size on heliostat cost and other factors

All of these effects must be taken into account when selecting the heliostat size. Clearly, heliostat dimensions affect the concentration and spillage. In addition, larger heliostats benefit from economy of scale (to a point) while smaller heliostats will require a greater number of pedestals, controls, actuators, etc., and so benefit more from learning/experience curve effects. Heliostats from 1 to 200 m^2 have been developed, with no consensus as yet (see Chapter 17). Clearly small systems will benefit from smaller heliostats, but O&M costs must also be considered.

8.5.7 Reflectivity and cleanliness

Of course, all heliostat mirrors suffer losses due to imperfect reflectivity. This can vary from 3% for a well protected front surface silvered mirror to 4–5% for a second-surface mirror employing water-white glass, to 10–15% for thicker, high-iron glass. This pristine reflectivity will remain quite stable in time for any acceptable mirror, but may well be degraded by 1% or so by surface dents or scratches, etc., by the time it is installed in the field. Any decrease in reflectivity degrades the performance of the heliostat, so the added cost/m^2 of better reflectivity should be compared, not to the cost/m^2 of the mirror, but to the cost/m^2 of the heliostat field (typically five times larger).

Once installed, the reflectivity of corrosion free mirror declines by perhaps 2% per month, partially due to easily removed dust and partially due to a harder to remove surface film (depending on the site and atmospheric conditions). Cleaning equipment is costly and somewhat labor intensive, so one must trade the washing frequency (cost) against the cost of lost reflectivity, as zero loss implies infinite cost. Rinsing to remove the dust can be done with a boom truck and is quite fast, while scrubbing to remove the surface film requires a more costly brushing rig and is slower. If the mirrors are scrubbed at the optimum rate, the loss in average reflectivity may be limited to about 6%, while if a lower-cost rinse cycle is added to simply remove the dust between scrubbings, the loss in average reflectivity with optimum cleaning may fall to 3.5% (depending on the environment, rig costs, and labor costs). By trading decreased washing costs against the cost of the added heliostats required for the dirty field to provide the same energy, an optimum average reflective loss can be determined. The optimized average reflectivity should be used in determining the required size of the heliostat field, or production goals will not be met (Kattky and Vant-Hull, 2012).

8.6 Receiver considerations

8.6.1 Cavity vs flat vs cylindrical receivers

Field constraint

A typical design constraint is to define a restricted receiver aperture, e.g., a billboard or a cavity receiver rather than a cylindrical receiver. While a cylinder has a field of view of 360°, a billboard is restricted to 180°, and often much less, although inclining the aperture forward can put a larger ground area within the field of view. A polar-facing billboard with a 120° field of heliostats will perform very well near noon, when most of the heliostats experience near 0° angle of incidence of the sunlight and so have a 'cosine effect' near unity (a combination of the foreshortening of the heliostat by cos ι and off-axis aberrations). However, as the solar azimuth changes (at other times of the day) the performance falls rapidly. In contrast, a system utilizing a cylindrical receiver will have moderate performance near noon (due to the reduced cosine experienced by heliostats on the equatorial side of the receiver). However, as the azimuth of the sun moves away from its noontime value (by more than 100° in the summer), the nearly circular nature of the surround field tends to maintain the average value of the cosine over the field, so the annual performance for the surround field exceeds that for the polar field of the billboard or cavity. For small systems, a billboard may be significantly cheaper than a cylindrical receiver, and for high temperature working fluids with low heat transfer coefficients (gases), a cavity may be required to reduce thermal losses, but

the effects of the resulting constraint on the field performance must be taken into account.

Reflective, radiative, and thermal loss of the cavity

It is not true that the aperture of a cavity is a 'black hole'. In fact, a positive feature of cavities is that the sunlight entering the aperture may be distributed over the absorbing surface to reduce the issues of excessive flux density. This process is usually accomplished by having much of the sunlight reflected or scattered from adiabatic surfaces. This results in a significant amount of diffuse solar light bouncing around in the cavity, some of which finds the aperture and is lost, effectively reflected. A secondary effect is that much of the interior of the cavity absorbs and reradiates light at a temperature above that of the heat transfer surface, and a significant portion of this infrared energy is also emitted from the aperture. Finally, the entire interior of the cavity is in contact with the enclosed air, heating it to a very high temperature and instigating turbulent convective circulation rolls. Depending on the orientation of the cavity, such circulation can carry heat to the aperture and out, strongly encouraged by ambient wind. The result is that a poorly designed cavity receiver can experience greater losses than a billboard or cylindrical external receiver. For small receivers a window can help, but this has difficulty with scaling up for commercial scale systems.

Cost and weight

Cavity receivers have specific application for very high temperature systems where there is benefit in having a small ratio of aperture to absorber area and where high fluxes can be absorbed. However, a cavity must both support and enclose the heat-collecting surface, it will clearly be larger than the support structure required for an external receiver where total absorbed flux is the same. In addition, it must be well insulated to reduce conductive losses through its large surface area. The result is a larger, heavier, and more expensive housing for the actual receiver. Cavity receivers are usually designed for smaller capacity systems, because the limited cone angle demands a higher tower. It is routinely found that the receiver tubing, headers, valves, etc., represent only a small fraction of the cost of the entire assembly, even for an external receiver.

8.6.2 Effect of allowable flux density on design

It is quite easy to design a heliostat field which produces a peak concentration of several thousand suns (several MW/m^2). However, most commercial system receiver designs can only tolerate a flux density in the order of

1.0 MW/m^2 (e.g. for molten salt) due to the heat transfer characteristics of the fluid. Thus, a larger receiver must be used than the size of the minimum achievable focal spot. The aspect ratio of an external receiver (height/diameter) should be greater than one to allow close-in heliostats, which see a severely foreshortened receiver, to be effective. In addition, it is typical that the receiver designer requires a significant tube length to achieve design temperature at the high heat-transfer-media flow rates required to enhance the allowable flux density. The final receiver aspect ratio will typically be between one and two. The allowable flux is then achieved by defining several (2–5) aim levels to each of which specific fractions of the heliostats are assigned. A smart strategy that estimates the beam radius, and moves the image associated with heliostats assigned to the outer aim levels so their beam just remains on the receiver, will introduce very little spillage while reducing the peak flux by 1.5–4.0 times.

A second requirement may be that the ratio of north to south side flux be constrained to maintain some balance on the receiver panels, and to reduce transverse gradients on each panel. This can be accomplished by enhancing the field boundary on the 'weak' side at the expense of the other. A more sophisticated approach (Vant-Hull and Pitman, 1990) involves modifying the objective function of the optimizer with a function (for example, cosine) of the azimuth angle to 'inform' the field of the new constraint. At some cost, this penalizes the polar heliostats and benefits the equatorial heliostats so the density and extent of the fields are modified, retaining the concept of an optimized field but relieving the receiver, saving money. The flux density gradient across each panel may also be a concern, but this is largely defined by the ratio of anti-sun to sun-side flux which can be modified as above. Transverse shifts of smaller images can reduce the local transverse gradient somewhat.

8.6.3 Emissivity vs absorptivity vs temperature

At the reduced temperatures and concentrations typical of linear systems, reduced emissivity absorbers (solar selective surfaces) can be used effectively to limit the radiative losses. However, it is difficult to design selective absorbers that will survive when exposed to the atmosphere while operating at temperatures over 500°C. As $\alpha = \varepsilon$ at each wavelength, and both the sun and a hot receiver emit significant energy in the near infrared range, reducing the emissivity here will also reduce the absorptivity. A sharp change from $\alpha \approx 1$ to $\alpha = \varepsilon << 1$ between wavelengths of 1.5–2 microns is required. It is most important to keep in mind that the objective is to improve the net energy captured in the receiver, and at a solar flux density of 1 MW/m^2, a reduction in α of 0.01 (or 0.02) loses 10 (or 20) kW/m^2 requiring, at a surface temperature of 527°C (800 K), a reduction in ε from 1.0 to 0.56 (or

0.12) to achieve $(1 - \varepsilon)\sigma T^4 > 10$ (or 20) kW/m^2 just to break even. As higher temperature receivers are anticipated (e.g. to drive a supercritical turbine) and the surface temperature significantly exceeds the working fluid temperature, thermal losses will increase, but so will the overlap of the solar and IR spectra, making the task even more challenging.

8.7 Variants on the basic central receiver system

8.7.1 Polar vs surround fields

A billboard or cavity receiver naturally results in a polar field (generally termed a north field in the northern hemisphere), i.e., one with heliostats on the polar side of the anti-polar facing receiver, due to much smaller incidence angles on the antisun side of the receiver. Such a field will have very good performance at noon but will fall off rapidly at larger solar azimuths due to the increased values of incidence angle (decreased cosine) on nearly all the heliostats. In contrast, a cylindrical receiver will be best matched by a surround field, usually biased toward the pole to take advantage of the better cosine effect, having a pole/equator energy ratio between 1.5 and 2. This system will exhibit a lower average performance at midday compared to the polar field, but at large solar azimuth, the east or west fields will contribute strongly to the energy collection, as will the weaker equatorial field. The net result is that, for a given design point power, annual energy collected is substantially higher for the surround field with a cylindrical receiver, and thus it is superior on a cost-per-unit-of-energy basis.

8.7.2 Beam-down systems

In a beam-down CRS (Fig. 8.1(d)), a secondary mirror is inserted between the heliostat field and its elevated focal point to redirect the collected sunlight to the ground. In order to produce a focused spot near the ground, the mirror must be a hyperbola (or if above the primary focal point an ellipse), and must be large enough to intercept the entire cone of light from the field. Such a system is used effectively in astronomy and is known as a Cassegranian system.

The first response to a tower or even a dish system is often: 'If you have the receiver supported on a tall tower and the engine down on the ground, why not use a Cassegranian system with a small elevated mirror and the receiver down near the ground where it is easy to connect to the engine and to service? It works in astronomical telescopes, why not here? And it would save much of the heat transfer piping.' The answer is that astronomical telescopes universally have a small *f* number (ratio of aperture diameter to focal length), while solar collectors often (usually) have an aperture diameter several times the focal length. This is because stars really are unresolvable

point objects so magnification of the image is really a virtue, not a problem. In contrast, the sun has a diameter of 9.3 mrad, and we are trying to form a concentrated 'image'. In a Cassegranian system, the elevated 'hyperbolic' mirror forms an image of the virtual object (the image which *would* be formed by the converging light from all the heliostats at the focal point of the array). The real image formed (perhaps near the ground) from this virtual object is magnified by the ratio of the distance from the secondary mirror to this real image divided by the smaller distance from the virtual object to the secondary mirror. The convex-downward hyperbolic Cassegranian mirror must be large enough to intercept the entire cone of rays directed toward the focal point, so in order to have a small secondary mirror (relative to the area of the collector field), the secondary mirror must be near the (virtual) focal point of the array and far from the ground (actually, the receiver aperture which may be elevated somewhat). However, the ratio of the distance from the virtual focal point to the vertex of the secondary and the distance from the secondary to the receiver aperture (which may have a small elevation) is what defines the linear magnification of the assembly, which would be 10 to produce a secondary mirror area 1% of the field area (3 or 4% of the collector area due to heliostat spacing). The resulting area magnification of the virtual object $10 \times 10 = 100$ reduces the flux concentration by 100 (from a few thousand to a few tens), and is generally disastrous to the objective of obtaining a high temperature with low loss. Moving the secondary mirror downward improves the final concentration, but requires an impractically large mirror and three or four support towers. Moving it to the halfway point recovers the full concentration at the ground (i.e., the required flat mirror images the virtual image exactly). However, then the secondary must be half the diameter of the field, or have an area essentially equal to the area of the mirrors (assuming an average ground coverage of 25%). It will also produce a large shadow on the field. Supporting the receiver above the ground level reduces the magnification, and so should be considered if the beam-down configuration is required.

8.7.3 Use of compound parabolic concentrators

Some of the concentration lost by the beam-down configuration can be regained by use of compound parabolic concentrators (CPCs) at the receiver aperture (Rabl, 1985, p. 191). The acceptance angle of the CPC must be set to accept the entire beam reflected by the secondary, i.e., at the cone half angle given by secondary radius/secondary distance (from the CPC aperture). This angle, ϕ, also defines the concentration of the 2D (conical) CPC as $(1/\sin \phi)^2$. If the final image from the secondary is large, a 'flies eye' array of 7 or 19 CPCs may be required, but each should view the entire secondary to avoid excessive rejection of light outside the view angle. While workable designs can be developed, the added two reflections, the

extra expense and complication of the CPC array, and the cost of the secondary and of supporting it on multiple (although smaller) towers nearly always result in a non-competitive design (Vant-Hull, 1991).

The use of a CPC with a normal central receiver system is questionable due to the large angular extent of the field (as seen from the tower-mounted receiver.). However, at the Sandia 5 MW_{th} test facility, several linear CPCs, each viewing a different sector of the north field (NE, N, and NW), were stacked to enhance the flux on a long, narrow panel receiver under test. This imaginative solution worked very well, but it was also quite expensive.

An important characteristic of a CPC is that the concentrated light at the exit aperture is diffuse light; that is, it expands into the full 2Pi steradians. This can be ameliorated somewhat by truncating the exit aperture, which also reduces the concentration.

8.7.4 Optical beam splitting

It is sometimes suggested that a beam splitter be used to divide the energy at the receiver into two or three wavelength bands, so that each beam could be used most effectively, especially where the energy conversion device performance is sensitive to wavelength. A possible motivation for doing this would be to apply selected wavelengths to a concentrating photovoltaic conversion process and to use the remainder for thermal conversion. There are numerous research projects, but thus far no commercial implementation. The simplest application would be to mount transparent solar cells in front of the receiver, with all light not used by the PV cells transmitted on to the receiver. While difficult to implement in large systems, this could be used effectiviely in dish systems. A thermal receiver is generally a wide band absorber, and would absorb the entire solar beam quite effectively – nothing is really going to waste. Where a concentrating photovoltaic device produces electricity more cost effectively than a thermal device, then it would be up to the thermal device to make use of the remaining spectrum, if sufficient energy remains to warrant the cost. In addition, there is little energy in the UV rays to start with, and most of this is absorbed in the initial reflection (due to impurities in the glass, though not an issue with front surface reflection) so very little reaches the receiver. Perhaps it would be possible to separate the IR from the visible beam at the receiver, but it is hard to imagine a better use for this IR than to contribute to the energy absorbed by a thermal receiver.

8.8 Field layout and land use

Any straightforward land constraint simply reduces the energy available at the receiver and increases the cost/benefit ratio of the design. If allowed,

the system will add heliostats at the boundary of the field, increase the density of heliostats everywhere in the field, and increase the height of the tower to compensate, but the LCOE will increase.

It is interesting that a well-defined, optimized, unconstrained field (with a cylindrical receiver), characterized by the annual output/m^2 of glass, is nearly circular, but offset from the tower toward the pole by 10–20%, depending on latitude. However, if land use is at an absolute premium, a field boundary that is defined by the output/m^2 of ground ends up being very nearly a circle centered on the tower.

8.8.1 Field layout for optimized systems

It has been found empirically (Lipps and Vant-Hull, 1978) that a circular radial-stagger (RS) heliostat layout is the best compromise. Far from the receiver, blocking from those aligned neighbors nearer the tower predominantly controls the radial heliostat spacing. The RS configuration overcomes this issue by moving the nearest radial neighbor two circles away. The annual shading footprint is more nearly circular, tending toward the pole. This leads to a requirement that nearest heliostats be at least two diameters apart in azimuth nearly everywhere. This also allows the distant heliostats to avoid blocking by 'peaking through' between the neighbors in the first inner circle. Near the tower the heliostats tend to operate close to horizontally to illuminate the receiver. Consequently, there is essentially no blocking and little shading, and they can be much more closely spaced. Here the issue of mechanical limits must be imposed to prevent errant heliostats from hitting one another. In this region, round heliostats have an advantage, as do polar mounting systems, which never allow the mirror to move outside its initial footprint. Near the tower, the RS layout becomes inefficient because of the rapid variation of azimuthal separation imposed by the expanding circles. One alternative is to use a hexagonal close-packed configuration near the tower, converting to the RS configuration at a radius of one or two tower heights and merging the interface smoothly (Walzel, 1978). A second alternative is to simply pack the heliostats closely on circles surrounding the tower and space the circles as closely as possible to allow servicing and obey mechanical limits, as was done at Gemasolar. At some radius, blocking will become significant and the RS configuration can be implemented. The 'peaking through' advantage does not occur so much in a close-packed field with polar/elevation tracking.

Clearly, 'more optically efficient' layouts can be generated for energy production at some defined design point; however, these may not be the most cost effective, and often do not consider receiver constraints.

Ease of access for maintenance

It is important to maintain ready access to each heliostat to allow regular washing and occasional repairs. The RS configuration allows this, as does the east-west, while some proposed layout schemes are exceedingly close packed or essentially random (each heliostat is installed at the 'best position' based on area left by previous heliostats). Pragmatic consideration needs to be given by field designers to installation and ongoing O&M requirements, and some minimum constraints are needed prior to optical optimization.

8.9 Future trends

R&D in research institutions and in industry will lead to better, longer-lived reflectors and absorbers, which will reduce the size and cost of systems delivering a specific power proportionately. Mass production and learning will reduce the manufacturing cost and materials requirements and likely follow a typical 85% learning curve (cost drops by 15% for every doubling of installed plant) until irreducible materials costs dominate. Well-designed small systems can compete with larger systems if they are clustered to achieve economy of scale, co-located with an industrial partner, or designed for unattended operation. Otherwise, operator costs will exceed the income.

The ability to operate efficiently with large, low-cost storage is a big advantage of CSP. For central receivers, storage efficiency is higher than in lower temperature systems (storage systems are covered in detail in Chapter 11). Of the numerous thermal storage options under development, two-tank molten salt at this time appears to be the most attractive within its temperature constraints. Thermocline storage is more complicated to operate and maintain and less efficient, while phase-change storage shows promise though a deal of work is required for temperature ranges of interest to central receivers. Both do have the potential cost advantage of requiring only one tank. Solar multiples of 2–4 will be common, with most of the energy being sent to storage to provide dispatchability and satisfy peaking loads or in the far term, perhaps base loads. Molten salt was used successfully in Solar Two, and is in current use at Gemasolar, and improved salts are being developed to increase the outlet temperature well above 565°C and to simultaneously reduce the freezing temperature to well below 200°C. This would allow higher efficiency supercritical turbines to be used, and heat tracing needs will be reduced.

High temperature volumetric receivers using air or a gas as a working fluid are under development, and can be used with Brayton cycle engines at high efficiency. Combined with a ceramic bed storage unit, these show promise. The combination of a large fixed focal zone and of high achievable temperatures also makes the CR system particularly suitable for

solar driven chemical processes such as sustainable fuels production (see Chapter 20).

Overall, central receiver systems are on the brink of a major growth phase. Many hundreds of 100+ MW_e plants, many with capacity factors well over 50%, are likely to be built worldwide in the next 50 years providing a significant proportion of world electricity demand, and possibly fuels. Most will be dry-cooled. Such a typical plant will produce over 400 GWhr of electricity per year, with essentially zero on site pollution.

As central receiver plants demonstrate they are basically benign and less risky than the alternatives that deface land and pollute water, emit pollutants or leave a legacy of nuclear waste, the desert and arid areas of the world will bloom with central receiver plants and there will be plentiful, clean, inexhaustible, and inexpensive energy for many generations to come.

8.10 Sources of further information and advice

Rabl A (1985), *Active solar collectors and their applications*, New York and Oxford: Oxford University Press

An excellent general reference and detailed textbook for all solar things thermal, from equipment, solar geometry and insolation, to flat plate and concentrating collectors, heat transfer, modelling, economics, and optimization.

Boer K W (ed.) (vol. 1–12), Goswami Y, Boer K W (eds) (vol. 13–14), Goswami Y (ed.)(vol. 15–17), *Advances in Solar Energy*, Boulder, CO: American Solar Energy Society

Goswami Y, ed. (vol. 18-) *Advances in Solar Energy*, Freiburg, Germany: International Solar Energy Society

This excellent series contains chapters by experts in the general field of solar energy. Vol. 10 contains a chapter by S. Awerbuch on valuing the economics of solar collectors. Vol. 13 contains several chapters on climate change, carbon limitation, and prospects for solar to mitigate the effects. Vol. 15 has a chapter on the design, operation and performance of the SEGS parabolic trough plants and a chapter providing a 'recipe' for the design and optimization of central receiver plants. Vol. 16 contains a chapter on recent advances in solar trough technology. Vol. 17 discusses solar heat for industrial processes and issues related to solar energy in the Middle East and North Africa.

C.-J. Winter, R. L. Sizmann and L. L. Vant-Hull (eds) (1991) *Solar power plants*, Berlin and New York: Springer Verlag

The editors gathered a group of authors who were all currently active workers in the field to collect vital information on a common basis for the design, operation, costing, and performance of both concentrating solar

thermal plants and photovoltaic plants. The book features an extensive tabulation of solar thermal and of photovoltaic power plants and test facilities around the world (as of 1991).

Journal of Solar Energy Engineering, American Society of Mechanical Engineers
ASME Solar Energy Proceedings
Solar Energy, International Solar Energy Society, Elsevier
ISES bi-annual conference proceedings
Each of these publications contain significant archival articles on the state of the art in many aspects of solar, including CSP.

Vant-Hull L L (1985), 'Solar thermal power generation', *Natural Resources Journal*, 25, 1099–1117
Vant-Hull L L(1992), 'Solar thermal electricity: an environmentally benign and viable alternative', *Perspectives in Energy*, 2, 157–166
Burkhardt, J J III, G Heath and E Cohen (2012), 'Life cycle greenhouse gas emissions of trough and tower concentrating solar power electricity generation: systematic review and harmonization', *Journal of Industrial Ecology*, 16 (S1), S93–S109, www.wileyonlinelibrary.com/journal/jie
The above three papers present energy input vs energy output results presented as life cycle analysis (LCA); important as a measure of CO_2 mitigation. The first two present a detailed evaluation for the commercial designs on which Solar One and Solar Two were based. The third is a meta-analysis in which many trough and central receiver LCAs are 'harmonized' to put them on an equal footing regarding assumed insolation, etc., and a 'best value' is defined for each (nearly the same).

SolarPACES Proceedings
In 1982, a group of designers and operators of concentrating solar thermal power plants was assembled in Claremont, CA, from around the world by the US DOE to discuss the state of the art. Conferences have been held every two years since then (annually since 2006), and the proceedings constitute a significant history and research direction for the field. In about 1998 the title 'Solar Power and Chemical Engineering Systems' (SolarPACES) was adopted by the organization. SolarPACES is now an IEA-sponsored organization with a series of tasks assigned to various country task leaders to organize. Each country is responsible for funding in-house research on projects it accepts.

L L Vant-Hull, *Heliostat Field Analysis*, May 1978 ORO 5178-78-2: UC 62
A contractor's report on a sensitivity analysis of the 100 MW_e Solar One baseline plant vs heliostat cost, land cost, land slope, receiver size, tower height, etc. Note: at 10 MW_e, Solar One was a scaled prototype of this 100 MW_e design.

F W Lipps and L L Vant-Hull, Parametric study of optimized central receiver systems, *Proceedings of the 1978 Annual Meeting, Vol. 2.1*, American Section of the International Solar Energy Society, Inc. pp. 793–798.
F K Falcone, *A Handbook for Solar Central Receiver Design*, SAND80-8000.
L G Radosevich, Final report on the power production phase of the 10-MW_e solar thermal central receiver pilot plant (Solar One), SAND87-8022.
B Kelly, Lessons Learned, Project History and Operating Experience of the Solar Two Project, SAND2000-2598.
A B Zavoico, Solar Power Plant Design Basis Document, SAND2001-2100.
J E Pacheco (ed.) Final Test and Evaluation Results from the Solar Two Project, SAND2002-0120.
G J Kolb, An Evaluation of Possible Next-Generation High-Temperature Molten-Salt Power Towers, SAND2011-9320.
The above documents from Sandia staff and contractors represent a definitive report on the information gained during the design, construction, operation, and evaluation of the 10 MW_e emulation of a 100 MW_e salt cooled power plant with molten salt storage.

8.11 Acknowledgements

The author would like to thank the editors for extra help with some sections of this chapter.

8.12 References

Arizona Power Systems (2006), 'APS completes first solar trough power plant in Arizona'. Available from: http://www.aps.com/main/news/releases/release_315.html (accessed 10 February, 2012).
Baum V A, R R Aparase, and B A Garf (1957), 'High-power solar installations', *Solar Energy*, 1(1), 6–12.
Bradshaw R W (1987), 'Oxidation and chromium depletion of alloy 800 and 316 SS by molten $NaNo_3$-KNO_3 at temperatures above 600 deg C,' Technical Report SAND86-9009, SANDIA National Laboratories, Livermore, CA.
Chen Y T, K K Chong, T P Bligh, L C Chen, J Yunus, K S Kannan, B H Lim, C S Lim, M A Alias, N Bidin, O Aliman, S Salehan, S A H Shk Abd Rezan, C M Tam, and K K Tan (2001), 'Non-imaging focusing heliostat', *Solar Energy*, 71(3), 155–164.
Dellin T A and M J Fish (1979), 'Heliost at design cost/performance trade offs', SAND-79-8248.
DoE (1977), 'Recommendations for the conceptual design of the Barstow, California, Solar Central Receiver Pilot Plant, Executive Summary', SANDIA

Albuquerque and Livermore, for the United States Energy Research and Development Agency, October, Contract AT (29-1) 789, SAND77-8035.
Eskom (2002), A study for a 100 MW_e central receiver in SA carried out by the Bechtel – affiliated company, NEXANT under funding from the South African utility, Eskom. No external documents have been published.
eSolar (2011), 'Our solution' Available from: http://www.esolar.com/our_solution/ (accessed December, 2011).
Francia G (1968), 'Pilot plants of solar steam generating systems', *Solar Energy*, 12, 51–55.
Hildebrand A F and L L Vant-Hull (1977), 'Power with heliostats', *Science*, 198, 1139–1146.
Hildebrand A F, G M Haas, W R Jenkins, and J P Colaco (1972), 'Large-scale concentration and conversion of solar energy', *EOS*, 53, 684–692.
Ho C K (2008), 'Software and codes for analysis of concentrating solar power technologies', SAND 2008-8053.
Kattky K and L Vant-Hull (2012), 'Optimum target reflectivity for heliostat washing', paper submitted to SolarPACES 2012 Symposium.
Kelly B D (2000), 'Lessons learned, project history and operating experience of the Solar Two project', SAND2000-2598. Sandia National Laboratories, Albuquerque, NM.
Kelly B D (2010), '*Advanced Thermal Storage for Central Receivers with Supercritical Coolants*', DOE Grant DE-FG36-08GO18149, Abengoa Solar Inc., Lakewood, CO, June 15.
Kisler B L (1986), *A users' manual for DELSOL3: a computer code for calculating the optical performance and optimal system design for solar thermal central receiver plants*, SAND 86-8018, SANDIA National Laboratories, Livermore, CA.
Kolb G J (2011), 'An Evaluation of Possible Next-Generation High-Temperature Molten-Salt Power Towers', SAND2011-9320. Sandia National Laboratories, Albuquerque, NM.
Kolb G J, S A Jones, M W Donnelly, D Gorman, R Thomas, R Davenport, and R Lumia (2007), 'Heliostat Cost Reduction Study', SAND2007-3293. Sandia National Laboratories, Albuquerque, NM, June.
Lata J, S Alcalde, D Fernández, and X Lekube (2010), 'First Surrounding Field of Heliostats in the World for Commercial Solar Power Plants – Gemasolar'. SolarPACES 2010 Symposium, Perpignan, France.
Lipps F W and L L Vant-Hull (1978), 'A cellwise method for the optimization of large central receiver systems', *Solar Energy*, 20, 505–516.
Lovegrove K and A Luzzi (2002), 'Solar thermal power systems', *Encyclopedia of Physical Science and Technology*, 3rd edn, Volume 15, Academic Press, San Diego, CA, pp. 223–235.
Mancini, T R, J A Gary, G J Kolb, and C K Ho (2011), 'Power tower technology roadmap and cost reduction plans', SAND 2011-2419.
Meduri P, C Hannsmann, and J Pacheco (2010), 'Performance characterization and operation of eSolars's Sierra suntower power tower plant', SolarPACES 2010 Symposium, Perpignan, France.
Pacheco J, M C Moursund, D Rogers, and D Wasyluk (2011), 'Conceptual design of a 100 MW_e modular molten salt power tower plant', SolarPACES 2011 Symposium, Granada, Spain.

Pitman C L and L L Vant-Hull (1986), 'Performance of optimized solar central receiver systems as a function of receiver thermal loss per unit area', *Solar Energy*, 37(6), 457–468.

Rabl A (1985), *Active solar collectors and their applications*, New York, Oxford, Oxford University Press.

Smith D (1992), 'Design and optimization of tube type receiver panels for molten salt applications', Solar Engineering – Proceedings of the 1992 ASME International Solar Energy Conference, Vol. 2, pp. 1029–1036.

Solar Tres (2000), Task 1, 'Application of solar two lessons learned to a commercial plant', Cooperative Agreement DE-FC04-01AL67310, prepared by Nexant for the United States Department of Energy Albuquerque Operations Office and Sandia National Laboratories, Albuquerque, New Mexico.

Stein W (2011), Private communication, CSIRO, Australia.

Stoddard M C, S E Faas, C J Chiang, and J A Dirks (1987) 'Solergy – A computer code for calculating the annual energy from central receiver power plants', SAND86-8o68. Sandia National Laboratories, Albuquerque, NM.

Trombe F (1957), 'Solar furnaces and their applications', *Solar Energy*, 1(2–3), 9–15.

Utility Study (1988), Arizona Public Service, 'Utility Solar Central Receiver Study, Vols. 1 & 2, Arizona Public Service (APS), Black & Veatch Engineers-Architects (BV), Babcock & Wilcox (B&W), Pitt-Des Moines, Inc. (PDM), Solar Power Engineering Co. (SPECO), and University of Houston (UH)', November, DOE Reports No. DOE/AL/38741-1 and 38741-2 (NTIS).

Vant-Hull L L (1991), 'Concentrator optics', in C Winter -J, R L Sizmann and L L Vant-Hull, *Solar Thermal Power Plants*, New York, Berlin, Heidelberg: Springer Verlag.

Vant-Hull L L and Pitman C L (1990), 'Static and Dynamic Response of a Heliostat field to Flux Density Limitations on a Central Receiver', Proceedings of 1990 ASME Intern. Solar Engineering Conference, Miami FL.

Vant-Hull L L, M E Izygon, and C L Pitman, (1996), 'Real Time Computation and Control of Solar Flux Density on a Central Receiver (Solar Two – Preheat)', Solar Engineering 1996, presented at 1996 ASME International Solar Energy Conference, San Antonio, TX.

Walzel M D (1978), 'An investigation of optimum heliostat spacings for the subtower region of a solar power plant', Proceedings of the 1978 annual meeting, Vol. 2.1, American section of the International Solar Energy Society, Inc.

Walzel M D, F W Lipps, and L L Vant-Hull (1977), 'A solar flux density calculation for a solar tower concentrator using a two-dimensional Hermite function Expansion', *Solar Energy*, 19(3), 239–253.

Zaibel R, E Dagan, J Karni, and H Ries (1995), 'An astigmatic corrected target-aligned heliostat for high concentration', *Sol. Energy Mater. Sol. Cells*, 37, 191–202.

9

Parabolic dish concentrating solar power (CSP) systems

W. SCHIEL and T. KECK,
schlaich bergermann und partner, Germany

Abstract: The main parts and working principle of dish engine (dish Stirling) systems are explained. An overview of the historical development and present systems is given. The energy conversion processes are explicated as well as performance and operational characteristics. Manufacturing aspects of components are discussed and future development trends are shown.

Key words: dish concentrator, parabolic concentrator, dish/Stirling.

9.1 Introduction

Dish concentrating solar power (CSP) systems use paraboloidal mirrors which track the sun and focus solar energy into a receiver where it is absorbed and transferred to a heat engine/generator or else into a heat transfer fluid that is transported to a ground-based plant. Dish concentrators have the highest optical efficiencies, the highest concentration ratios and the highest overall conversion efficiencies of all the CSP technologies. The bulk of commercial CSP activity with dish concentrators involves the use of receiver integrated Stirling engines for direct production of electricity. However, dish concentrators can be used to drive the whole range of energy conversion processes that are open to CSP technologies in general.

The field of possible applications covers, on the one hand, the support of smaller or large grid connected systems, and on the other hand, stand-alone systems that can power, for example, water pumps or desalination plants. If dish Stirling systems are installed in clusters, applications up to 10 MW can be realized. Above this range, other solar thermal systems may be economical or more efficient.

Dish Stirling systems have demonstrated the highest efficiency of any solar power generation system by converting nearly 30% of direct normal incident (DNI) solar radiation into electricity after accounting for parasitic power losses (EPRI Report, 1986). These high-performance solar power systems have been in development for more than two decades, with the primary focus in recent years on reducing the capital and operating costs

of systems. Dish Stirling systems currently cost about US$10,000 per kW installed; major cost reduction will occur with mass production and further development of the systems. Substantial progress has been made to improve reliability, thereby reducing the operating and maintenance (O&M) costs of the systems.

As capital costs drop to about US$3,000 per kW, promising market opportunities appear to be developing in green power and distributed generation markets in the south-western United States, India, the Mediterranean region as well as in southern Europe and Africa.

With the worldwide restructuring of utility markets, the emergence of green power markets, and the increased worldwide demand for distributed generation, the opportunities for small power systems ranging in size from a few kW to several MW are increasing at a rapid rate. This increasing demand is largely being met today by existing internal combustion and gas turbine power generators, but it is also the motivation for new technology development such as micro turbines, fuel cells, and other alternative power generators. Large-scale grid connected systems based on dish systems with either Stirling engines, Brayton cycles or steam generation for ground-based turbines are also proposed. In this regard, dish systems are the least commercially developed CSP technology today. However, the high conversion efficiencies achievable motivate the continued efforts.

9.2 Basic principles and historical development

9.2.1 Basic principles

A dish system consists of: (a) a parabolic shaped concentrator, (b) tracking system, (c) solar heat exchanger (receiver), (d) an (optional) engine with generator and (e) a system control unit (Fig. 9.1). The concentrator tracks the sun bi-axially in such a way that the optical axis of the concentrator always points to the sun. The solar radiation is focused by the parabolic concentrator onto the solar receiver which is situated close to the focal point of the parabola. The receiver captures the high temperature thermal energy into a fluid that is either the working fluid for a receiver-mounted engine cycle, or is used to transport the energy to ground-based processes. In the case of a receiver-mounted engine, a directly coupled generator finally converts mechanical energy into electricity.

A reflective surface on the paraboloidal concentrator, either metallized glass or plastic, reflects incident sunlight to a small region called the focus. The ideal shape of the reflecting surface of a solar concentrator is a paraboloid. The size of the focus depends on the precision of the shape of the concentrator, surface reflectivity and condition as well as focal distance. Common dish concentrators achieve geometric concentration ratios

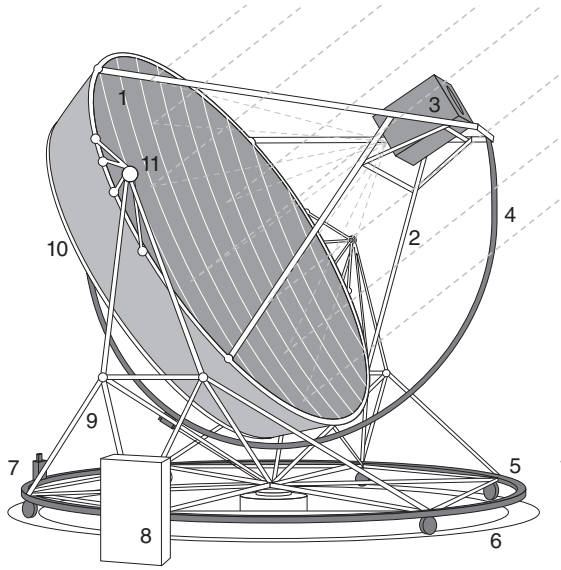

9.1 Schematic representation of an example of a dish system.

between 1,500 and 4,000. Dish concentrator diameters range from 1–2 m up to 25 m.

In order to track the sun, concentrators must be capable of moving about two axes. Generally, there are two ways of implementing this, both having advantages:

- Azimuth-elevation tracking (illustrated in Fig. 9.2a), in which the dish rotates in a plane parallel to the earth surface (azimuth) and around an axis perpendicular to it (elevation), gives the collector up/down and left/right rotations. Rotational rates about both axes vary throughout the day but are predictable.
- Alternatively with the polar-equatorial tracking method (illustrated in Fig. 9.2b), the collector rotates about an axis parallel to the Earth's axis of rotation. The collector rotates at a constant rate of 15°/hr, the same rotation rate as the Earth's. The other axis of rotation, the declination axis, is perpendicular to the polar axis. Movement about this axis occurs slowly and varies by ±23½° over a year (a maximum rate of 0.016°/hr).

The biaxial tracking system is normally driven by electric motors working through gearbox units, although hydraulic systems have also been developed. The tracking position is found with sun or reflected beam sensors and/or with a tracking algorithm that calculates the actual position of the sun from the date and time of day for the known location of the system. For

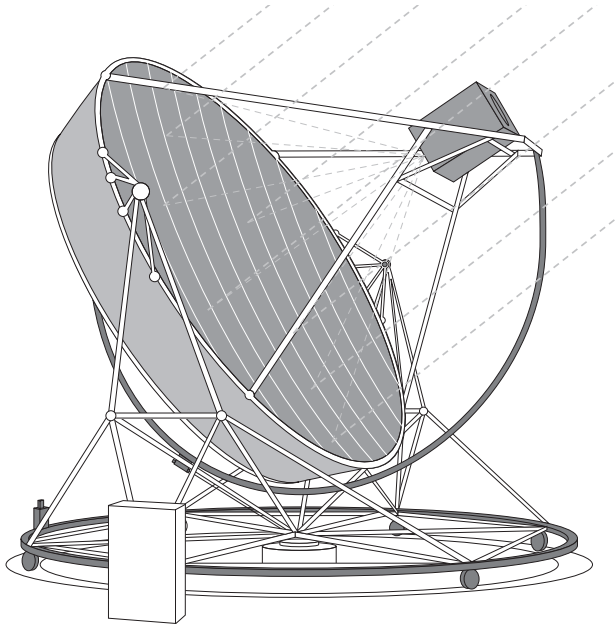

(a)

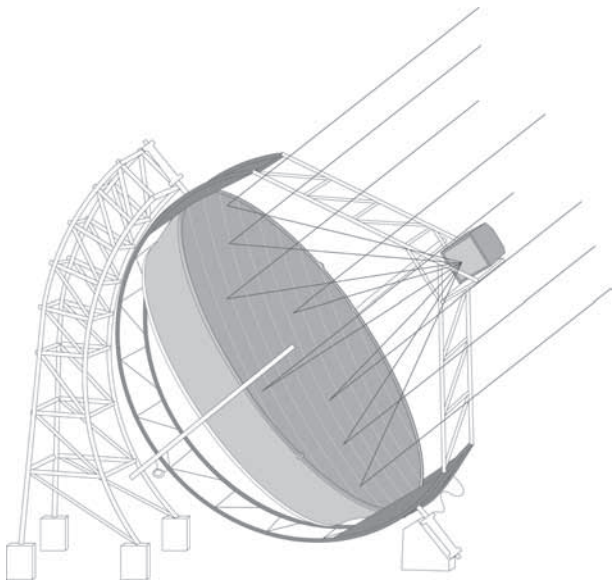

(b)

9.2 Principle of (a) azimuth-elevation and (b) polar-equatorial mounted systems.

control of these drives and for the whole system including the Stirling engine, micro controllers or PCs are used. The operation is therefore fully automatic and remote control via the Internet is possible.

The receiver has two functions: (1) to absorb as much of the solar radiation reflected by the concentrator as possible and (2) to transfer this energy as heat to the working fluid.

Although a perfectly reflecting paraboloid reflects parallel rays to a point, the sun's rays are not quite parallel because the sun is not a point source. Also, any real concentrator is not perfectly shaped. Therefore, concentrated radiation at the focus is distributed over a small region, with the highest concentration of flux in the centre, decreasing towards the edge.

Efficient receivers for dish systems are cavity receivers with a small opening (aperture) through which concentrated sunlight enters. The absorber is placed behind the aperture to reduce the intensity of concentrated solar flux. The insulated cavity between the aperture and absorber reduces the amount of heat lost. The receiver aperture is optimized to be just large enough to admit most of the concentrated sunlight but small enough to limit radiation and convection loss (Stine and Harrigan, 1985).

9.2.2 Historical development

As with the other approaches to concentrator design, the concept of using mirrored dishes to focus the sun has been around since 200 BC. One of the earliest actual implementations of a dish system was by the Frenchman Augustin Mouchot, who built a series of dish-driven engine systems as early as 1864, and displayed a dish concentrator at the Universal Exhibition in 1878 in Paris (Gordon, 2001).

The dish technology of today began evolution with the sudden increase in activity in all aspects of CSP in the early 1980s following the oil price shock in the 1970s. Much of the early activity was centred in the USA. Innumerable dish prototypes were designed and built by researchers, large and small commercial organizations and even private individuals. Stine and Diver (1994) have edited a comprehensive overview of systems as well as components. A representative selection of key examples is reviewed here.

The first of the commercially prototyped systems using a Stirling engine, the 25 kW Vanguard system built by ADVANCO in Southern California, achieved a reported world record net solar-to-electric conversion efficiency of 29.4% (EPRI Report, 1986). The Vanguard dish Stirling system utilized a glass-faceted dish 10.5 m in diameter, a direct insolation receiver (DIR), and a United Stirling 4-95 Mark II double-acting kinematic Stirling engine (Fig. 9.3).

In 1984, two 50 kW dish Stirling systems were built, installed and operated in Riyadh, Saudi Arabia, by schlaich bergermann und partner (sbp) of

9.3 Vanguard 1 concentrator.

9.4 17 m metal membrane concentrator built by sbp.

Stuttgart, Germany (Koshaim, 1986). A similar unit was also installed at the German Aerospace Centre (DLR) facility in Lampoldhausen, Germany. The dishes were 17 m diameter stretched-membrane concentrators, by drawing a vacuum in the plenum space formed by the dish rim and front and back thin steel membranes. The optical surface of the dish was made by bonding thin glass tiles to the front membrane. The receivers for the sbp dishes were direct illuminated tube receivers and the engines were United Stirling 4-275 kinematic Stirling engines (Fig. 9.4).

A dish Stirling system was built by McDonnell Douglas Aerospace Corporation (MDAC) in the mid-1980s and, when MDAC discontinued development of the technology, the rights to the system were acquired by Southern California Edison (SCE) (Lopez and Stone, 1992, 1993). The parts

9.5 McDonell Douglas Corporation concentrator (copyright: DOE/NREL).

for eight systems were manufactured, and three systems were tested in the early 1980s. The MDAC/SCE dish was the first dish Stirling system designed to be a commercial product (Fig. 9.5). It was built on the design of the Vanguard dish Stirling system, using the same DIR and the USAB 4-95 Mark II engine. SCE operated the system from 1985 to 1988. Stirling Energy Systems (SES) of Phoenix, Arizona, acquired the technology rights and system hardware in 1996 and have continued development of the system.

In 1989, schlaich bergermann und partner built the first of their smaller 7.5 and 8.5 m stretched-membrane concentrators equipped with a 10 kW SOLO V160 Stirling engine. First, in polar tracking configuration and later in an azimuth-elevation tracking configuration, six of the systems have together operated for more than 30,000 hr in sun at the Plataforma Solar de Almería in Southern Spain (Fig. 9.6).

In 1991, Cummins Power Generation, working under cost share agreements with the US Department of Energy and Sandia National Laboratories, started the development of two dish Stirling systems – a 7 kW system for remote applications and a 25 kW system for grid-connected power generation (Fig. 9.7) (Gallup and Mancini, 1994; Bean and Diver, 1995). Cummins was innovative in its dish Stirling systems, incorporating advanced technologies into the designs, such as a solar concentrator with a polar-axis

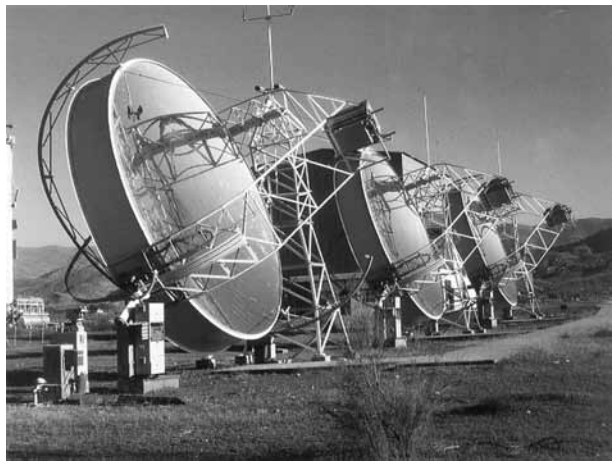

9.6 7.5 m Generation I, polar tracking metal membrane dish systems built by sbp operating at PSA, Spain (Copyright: schlaich bergermann und partner).

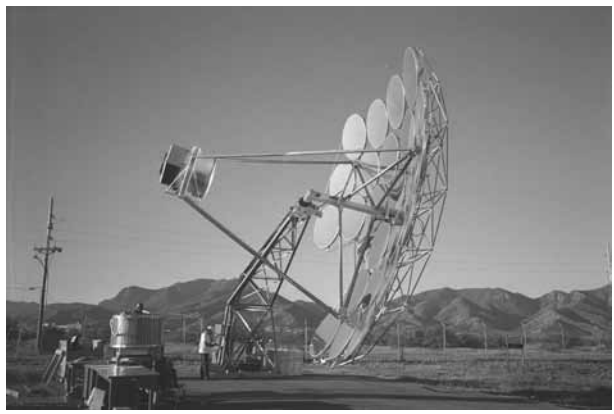

9.7 Cummins Power Generation CPG-460 concentrator.

drive and polymer, stretched-membrane facets, heat-pipe receivers, and free-piston Stirling engines. The heat-pipe receiver transfers the absorbed solar heat to the engine by evaporating sodium and condensing it on the tubes of the engine heater head. The receiver serves as a thermal buffer between the concentrator and the engine, and because it transfers heat to the engine by condensation, it allows the engine to operate at a high and uniform average temperature and efficiency (Andraka *et al.*, 1993). The two Cummins programmes made progress, but were terminated in 1996 when

Cummins' parent company, Cummins Engine Company, realigned business along its core area of diesel engine development. The assets of the Cummins solar operations were sold to Kombassan, a holding company in Alanya, Turkey (Mancini *et al.*, 2003).

In these early projects, dish Stirling systems have demonstrated their capability of producing electricity for the grid and for remote power applications at high solar to electric efficiencies. All systems so far were built in single piece production and therefore have a high investment cost level. Additionally, Stirling motors still require regular maintenance. Thus the aims for further developments are an increase in system reliability and further cost reduction. Therefore current efforts are focused on establishing reliability and, through break-and-repair approaches, identifying the components that require improvement, redesign and replacement. In a parallel approach, advanced components, such as system controls and improved optical surfaces, that promise higher efficiencies and reliabilities at lower cost, are being developed and tested. In addition, industrial series component production is being implemented.

Along with the approach of using Stirling engines with receivers mounted in the dish focal point, the use of dishes to provide heat to a central generating plant has also been pursued. Many receiver development experiments of various kinds have been reported in the research literature.

A notable example of an attempt to demonstrate commercial scale operation was the La Jet 'Solarplant1' 4.9 MW_{el} system built in California in 1984. As shown in Fig. 9.8, it consisted of 700 La Jet dishes (essentially the same as the Cummins technology) with stretched-membrane mirror elements. The total collecting area was 30,590 m^2. Six hundred of the dishes produced saturated steam at approximately 6 MPa and the remaining 100 dishes were used to further superheat it to 460°C. The plant was operated

9.8 La Jet plant with 700 units in California.

9.9 ANU dish installation in White Cliffs, Australia (Copyright: ANU Solar Thermal Group).

until 1990. Whilst this plant successfully demonstrated centralized steam-based generation with dishes, the main negative issues were a lack of durability with the mirror membrane reflective polymer film and a large startup time due to excessive thermal inertia in the receivers.

In Australia, the early work of the group at the Australian National University (ANU) leads to the construction of a 14 dish system in the remote town of White Cliffs in New South Wales (Australia) (Fig 9.9). Each dish has an aperture area of 20 m^2 and has small flat mirror tiles bonded to a single fibreglass paraboloid. Superheated steam was generated directly in monotube 'semi cavity' receivers and networked to a central power block, using a 25 kW_{el} reciprocating steam engine/generator (Kaneff, 1991).

In 1999 and 2000, WG Associates designed the WGA-500 dish concentrators MOD1 and MOD2 with 8.8 m diameter and 41 m^2. The dish was pylon mounted, the reflector made from sandwich panels with thin glass mirrors. Two prototypes were built and operated with the 10 kW SOLO 161 Stirling engine.

9.3 Current initiatives

In this section a short description of the ongoing major dish initiatives is given.

9.3.1 Stirling Energy Systems (SES)

In 1996, Stirling Energy Systems, Inc. (SES) was formed and acquired all design and engineering patents on the solar Stirling dish engine technology

9.10 Stirling Energy Systems new 25 kW concentrator (SunCatcher) (Copyright: Sandia National Laboratories/Randy Montoya).

that had been developed over nearly three decades by MDAC/SCE. SES launched two strategic, collaborative public–private partnerships with Sandia National Laboratory, Albuquerque, New Mexico and the United States Department of Energy (DOE) in order to commercialize this technology. Over this period, SES has re-engineered the licensed technology, improved its design, performance and cost, while achieving high solar-to-electricity conversion efficiency. Today, SES technology is a dish Stirling unit called SunCatcher using a double-acting 25 kW kinematic Stirling engine based on the developments by United Stirling in Sweden (Fig. 9.10). A plant with 60 dishes, 1.5 MW_{el} system using the SunCatchers has been constructed by SES in Pheonix, USA. SES together with the sister company, Tessera Solar North America, has signed several power purchase agreements (PPA) for two large plants with 709 and 850 MW with utilities in the US. Both the system and the project development for the commercial plants had been far advanced, but SES went into bankruptcy after failing to receive a governmental loan guarantee.

9.3.2 schlaich bergermann und partner (sbp)

In 1998 sbp started together with European partners the development of the EuroDish (Fig. 9.11). In a first step, two 8.5 m diameter dish concentrators, equipped with an improved Stirling engine, were erected and tested at the Plataforma Solar de Almería (PSA). The EuroDish incorporates a newly developed concentrator, made up of a sandwich shell from fibre glass reinforced plastic and the well proven and further improved single-acting

9.11 10 kW EuroDish by sbp.

SOLO Stirling 161 with 10 kW_{el} capacity. The tracking and control system was also revised and simplified, and remote control capability has been implemented. Two EuroDish prototypes were built in Spain for testing and continuous operation.

After intensive testing several so-called 'country reference units' were erected in Spain, Germany, France, Italy and India to demonstrate the technology to the market and gain substantial operation experience at various sites in the world under different climatic conditions.

9.3.3 Infinia Corporation

Infinia Corporation, based in Ogden, Utah, USA is a privately owned technology company that has been developing free piston Stirling engines since 1967. In 2006 Infinia started the development of the 4.7 m diameter PowerDish equipped with a self-developed, low-cost, long-life and maintenance-free 3.2 kW free piston Stirling engine. The dish was designed together with schlaich bergermann und partner. It is an automatic, self-contained system and Infinia claims no maintenance of the hermetically sealed engine is required over the whole life span of 25 years.

A first prototype was erected in 2007. Pre-production and test units are currently operating at ten different sites around the world; Infinia commissioned their first commercial installation of 30 units in Yuma, Arizona in August 2010 (Fig. 9.12). Infinia has partnered with large Tier 1 automotive component manufacturers and suppliers and has utility-scale projects in the US, Europe and India following soon after the project in Yuma with full production launch in 2012.

9.12 PowerDish installation in Yuma, Arizona 2010 by Infinia Corp. (Copyright: Infinia Corp.).

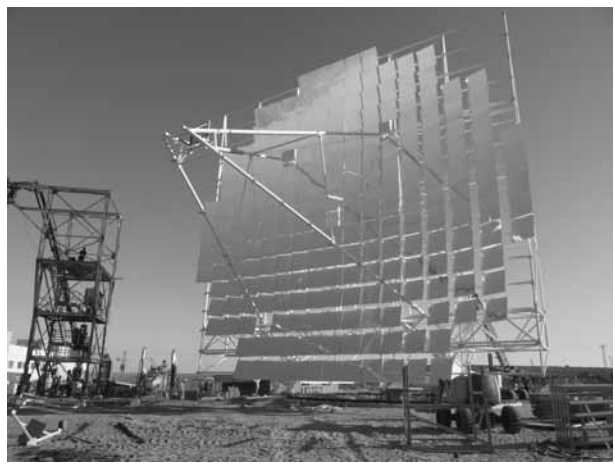

9.13 HelioFocus 500 m^2 dish.

9.3.4 HelioFocus

HelioFocus Ltd of Ness Ziona, Israel, was founded in 2007. They completed a low cost, large scale dish development (500 m^2) together with schlaich bergermann und partner (Fig. 9.13). The first prototype was erected in mid 2011 as part of a solar boosting experiment with the Israeli utility company. The dish is made of a flat support structure with mirrors arranged in a Fresnel-like array and tracks the sun using a hydraulic drive system. The first application is generating high temperature air as heat transfer fluid

(HTF), using a pressurized volumetric receiver. Steam is produced via a heat exchanger and fed into a fossil-fuelled power plant (boosting). In the medium term, HelioFocus intend to develop a system with a micro turbine.

9.3.5 Solar Cat/SouthWest Solar

SouthWest Solar Technologies of Phoenix, Arizona, USA, have also developed a large dish concentrator, measuring 23 m in diameter (320 m^2). The prototype was commissioned in 2011. It is suspended on a pylon and feeds a 80 kW_{el} micro turbine from Brayton Energy LLC. Hybrid operation and compressed air storage is intended (SouthWest Solar, 2011).

9.3.6 Solar Systems

The Australian-based company Solar Systems Pty. Ltd, now owned by Silex Systems Ltd, has been working in CPV with dish concentrators since the late 1990s. Their CS500 130 m^2 dish generates 35 kW and is pylon mounted (Fig. 9.14). Several projects with a total of 40 units have been realized. Today, the system is called 'Dense Array Converter', with a similar dish design measuring 140 m^2 and a PV generator with 40% efficiency. According to Silex information, a 60 unit/2 MW plant shall be commissioned in early 2013 in Mildura, and another 102 MW (40 kW per dish) will follow.

9.3.7 Australian National University (ANU)

Following on from the 14-dish system at White Cliffs, in 1994, the 400 m^2 dish SG3 was designed and built by the Australian National University

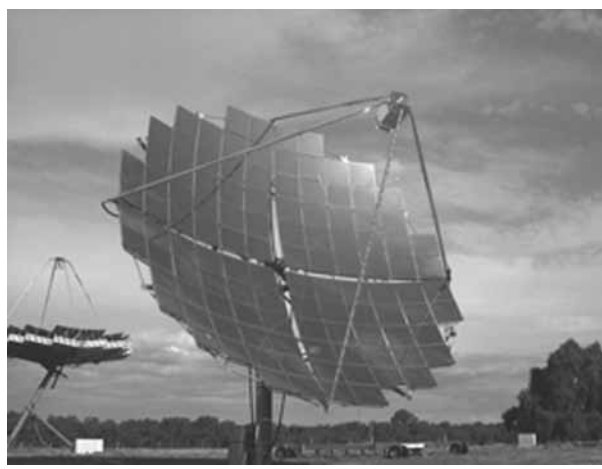

9.14 Solar Systems CS500 Dense Array CPV dish system.

9.15 ANU 400 m^2 dish SG3 (Copyright: ANU Solar Thermal Group).

(ANU) (Fig. 9.15). It is made up of 54 triangular mirror facets on a space frame. The concentrator is mounted on a turntable and rotates in azimuth on a base frame with six wheel assemblies on a concrete ring. A monotube boiler receiver was used to generate superheated steam. The size was motivated by an analysis that concluded that larger dishes are more cost effective per unit area than small ones. Large-scale grid connected systems using ground steam turbine-based generation were targeted, so the availability of suitable engines to be mounted at focal did not constrain the design.

In 2009, a dish design with 500 m^2 aperture area was designed and built by ANU in collaboration with Wizard Power Pty Ltd, a startup company established to commercialize the technology. The new dish was optimized for mass production for large-scale plants. It features 380 interchangeable square mirror panels which are also designed to provide a structural contribution for the dish (Fig. 9.16). The panels are again supported by a space frame and mounted on a turntable running on wheels on a steel track (Lovegrove *et al.*, 2011).

9.3.8 Others

A considerable number of small and early stage initiatives both in research centres and the commercial arena are developing dish and dish/engine systems, too numerous to be mentioned here. They cover a large variety of designs and size.

9.4 Energy conversion, power cycles and equipment

Although a Brayton engine has been tested on a dish (Jaffe, 1988) and some companies are currently adapting micro-turbine technology to dish engine

9.16 ANU/Wizard Power 500 m^2 dish (Copyright: ANU Solar Thermal Group).

systems, kinematic and free piston Stirling engines are currently being used in the majority of dish systems offered commercially today. Stirling engines are preferred for these systems because of their high efficiencies (thermal-to-mechanical efficiencies in excess of 40% have been reported), high power density (40–70 kW/litre for solar engines), and potential for long-term, low-maintenance operation. Dish Stirling systems are modular, i.e., each system is a self-contained power generator, allowing their assembly into plants ranging in size from a few kilowatts to tens of megawatts.

9.4.1 Stirling engines

Thermal energy provided by concentrated solar radiation can be converted into electrical energy using a Stirling engine with coupled generator. Stirling engines belong to the group of hot-gas machines and use a closed thermodynamic process; i.e. always the same working gas is used within the working cycle. In contrast to Otto or Diesel engines, energy is provided by external heat supply, so that Stirling motors are also suitable for solar operation.

The basic principle of a Stirling engine is based on the cyclic compression and expansion of gas at different temperature levels to produce a net conversion of heat energy to mechanical work. The ideal process is based on a combination of isothermal compression of the cold and isothermal expansion of the hot medium plus constant volume (isochoric) heating and cooling processes (Fig. 9.17(c)). Periodic temperature change – and thus continuous operation – can be ensured by moving the working gas between two chambers of constantly high and constantly low temperature.

For the technical realization using crankshaft-linked pistons (a kinematic engine), a compression piston is moved to the closed side, so that the cold

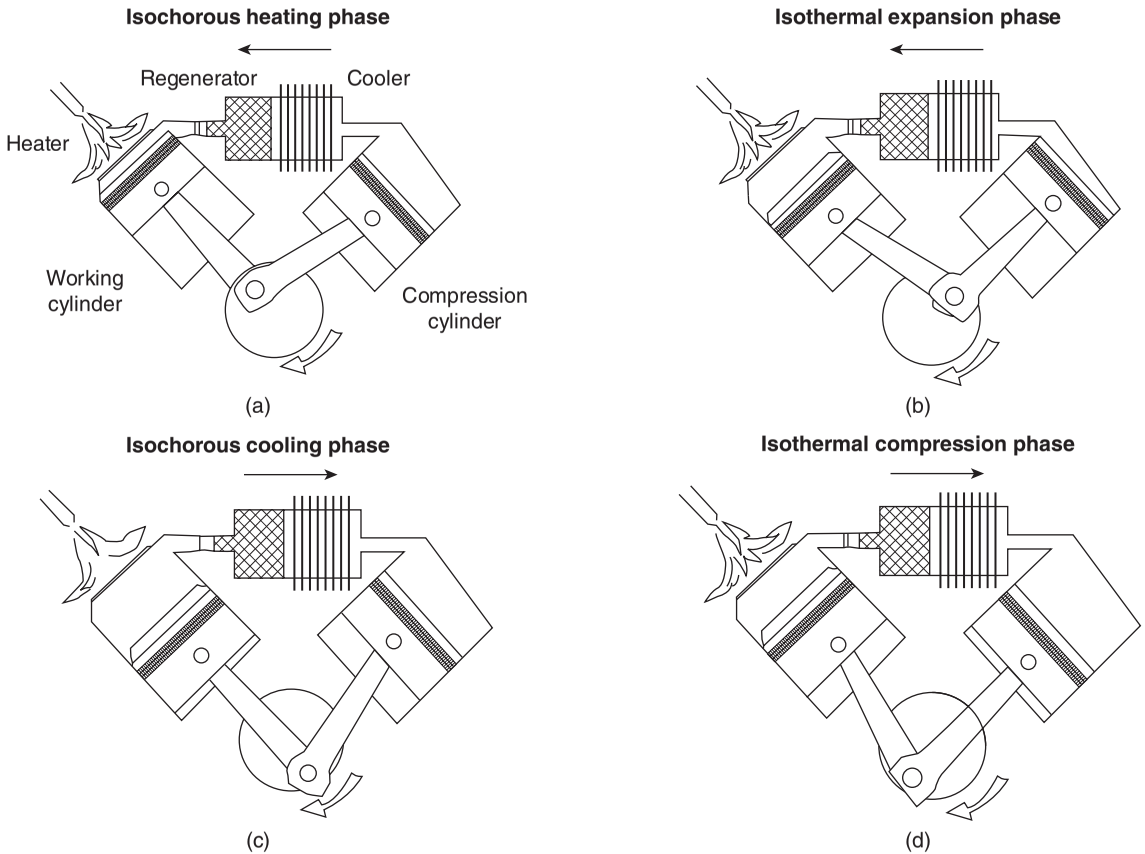

9.17 Working principle of a Stirling engine.

working gas flows to the warm space, passing through a regenerator. The regenerator transmits the previously absorbed heat to the working gas (isochoric heating phase; Fig. 9.17(a)). The gas is warmed up to the temperature of the hot space while the regenerator cools down to the temperature of the cold space. Subsequently, the working gas inside the hot space expands isothermally and absorbs the heat from the hot space (isothermal expansion phase; Fig. 9.17(b)).

The expanding working gas moves the working piston out of the cylinder and so performs work. When the working piston passes below dead centre and begins to close, the hot working gas is forced to pass the regenerator and to move into the cold space. Heat is transferred isochorically from the working gas to the regenerator (isochoric cooling phase; Fig. 9.17(c)). The gas is cooled down to the temperature of the cold space while the regenerator is warmed up to the temperature of the hot space. The working gas is subsequently compressed isothermally and transmits exhaust heat to the cold space (isothermal compression phase Fig. 9.17(d)).

The basic system components thus include the heated working cylinder, the cooled compression cylinder and a regenerator for intermediate energy storage. In most cases, the regenerator is a highly porous body of a high heat capacity; this porous body has a considerably larger thermal mass than the gas mass flowing through the body. The more complete the alternating heat transmission is performed inside the regenerator, the higher the mean temperature difference between working and compression cylinder and thus the efficiency of the Stirling engine. If the displacing piston is coupled to the working piston at the appropriate phase angle via a driving mechanism or a vibratory system, the whole system can serve as thermal engine.

In terms of mechanical design, single- and double-acting machines are sometimes employed. In single-acting machines, only one side of the compression or expansion piston undergoes pressure fluctuations inside the working space, while the pressure of the working gas is effective on both sides of the piston of double-acting machines; in the latter case, they simultaneously work as compression and expansion piston.

Stirling engines can be categorized into kinematic and free piston Stirling engines. Kinematic Stirling engines perform power transmission via a crankshaft mechanism. A generator can be coupled to this shaft. Free piston Stirling engines lack mechanical inter-linkage between the working piston, the displacement device and the environment. Both pistons move freely. The converted energy can be transferred to the exterior by an axial generator, for instance. Mechanical inter-linkage is replaced by an interior spring damping system; this is why only two movable parts are required. The machine can be hermetically sealed, so that tightening issues are avoided. Free piston Stirling machines present the theoretical benefits of a simple

structure and high reliability, but still lag somewhat behind in terms of development when compared to kinematic machines.

The engines applied for dish Stirling systems use helium or hydrogen at working gas temperatures between 600 and 800°C. Power output of the Stirling motor is controlled by varying the working gas mean pressure or piston stroke.

9.4.2 Brayton cycle

The Brayton engine is usually seen in the jet engine, combustion turbine or gas turbine, as an internal combustion engine which produces power by the controlled burning of fuel. In the Brayton engine, like in Otto and Diesel cycle engines, air is compressed, fuel is added, and the mixture is burned. The engine consists of a compressor turbine followed by a constant pressure heat addition (usually combustion) and by an expansion turbine coupled to an alternator. In a dish/Brayton system, solar heat is used to replace (or supplement) the heat input from fuel. The resulting hot gas expands rapidly and is used to produce power. As in the Stirling engine, recuperation of waste heat is key to achieving high efficiency. Therefore, waste heat exhausted from the turbine is used to preheat air from the compressor. The recuperated gas turbine engines that are candidates for solarization have pressure ratios of approximately 2.5, and turbine inlet temperatures of about 850°C (1,562°F). Predicted thermal-to-electric efficiencies of Brayton engines for dish/Brayton applications are over 30% (Koshaim, 1986; Lopez and Stone, 1993).

9.4.3 Other cycles

As discussed previously, dish systems can also be used to provide steam for ground-based steam turbine systems. Such systems are potentially the same as those employed for tower, trough or Fresnel-based power generation as discussed in Chapters 8, 7 and 6 respectively. Dishes can also be used for PV concentrator systems as discussed in Chapter 10 and also for driving thermochemical processes as discussed in Chapter 20.

9.4.4 Equipment

Alternator

The mechanical-to-electrical conversion device used in dish/engine systems depends on the engine and application. Induction generators are used on kinematic Stirling engines connected to an electric utility grid. Induction generators synchronize with the grid and can provide single- or three-phase

power of either 230 or 400 volts. Induction generators are off-the-shelf items and convert mechanical power to electricity with an efficiency of about 94% in the relevant power capacity range.

Alternators, in which the output is conditioned by rectification (conversion to DC) and then inverted to produce AC power, are sometimes employed to handle mismatches in speed between the engine output and the constant electrical grid frequency. The high-speed output of a gas turbine, for example, is converted to very high frequency AC in a high-speed alternator, converted to DC by a rectifier, and then converted to 50 or 60 Hz single, or three-phase power by an inverter. This approach can also have performance advantages for operation of the engine.

Cooling system

Heat engines need to transfer waste heat to the environment. Stirling engines use a radiator to exchange waste heat from the engine to the atmosphere. In open-cycle Brayton engines, most of the waste heat is rejected in the exhaust. Parasitic power required for operation of a Stirling cooling system for fan and pump, concentrator drives and controls is typically about 0.5–1 kW_{el} for a 10 kW_{el} system.

Receivers

In a receiver for a Stirling engine, two methods are used to transfer absorbed solar radiation to the working gas (Fig. 9.18). In the first type of receiver, the directly illuminated tube receiver (DIR), small tubes through which the engine's working gas flows, are placed directly in the concentrated solar flux region of the concentrator. The tubes form the absorber surface (Fig. 9.19). The other type of receiver uses a liquid metal intermediate heat transfer fluid. The liquid metal is vaporized on the absorber surface and condenses on tubes carrying the engine's working gas. This second type of receiver is called a heat pipe receiver because the vapour condenses and flows back to be heated again (Fig. 9.20).

For receiver designs in which liquid metal is used as an intermediate heat transfer fluid, two methods of supplying liquid metal to the absorber are under development: pool boilers and heat pipes. With the first method, a pool of liquid metal is always in contact with the absorbing surface. The second method involves a wick attached to the back of the absorber. The capillary forces in the wick draw liquid metal over the surface of the absorber where it vaporizes.

For steam generation, monotube receivers have been developed. They consist of a long tube that forms the absorber surface (see Fig. 9.21). The water evaporates while flowing along the tube.

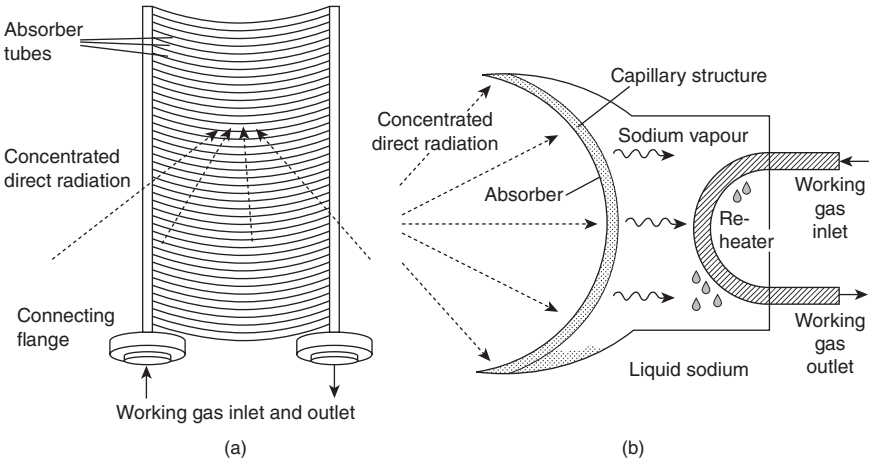

9.18 Receiver design principle: (a) direct illuminated tube receiver; (b) heat pipe receiver.

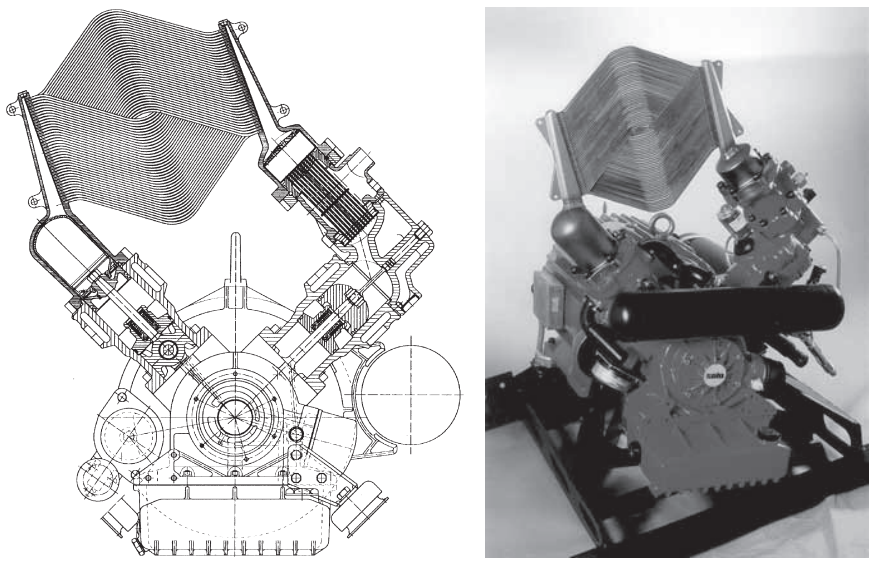

9.19 Example of a DIR for the 10 kW SOLO Stirling engine, section (a) and overview (b) (SOLO).

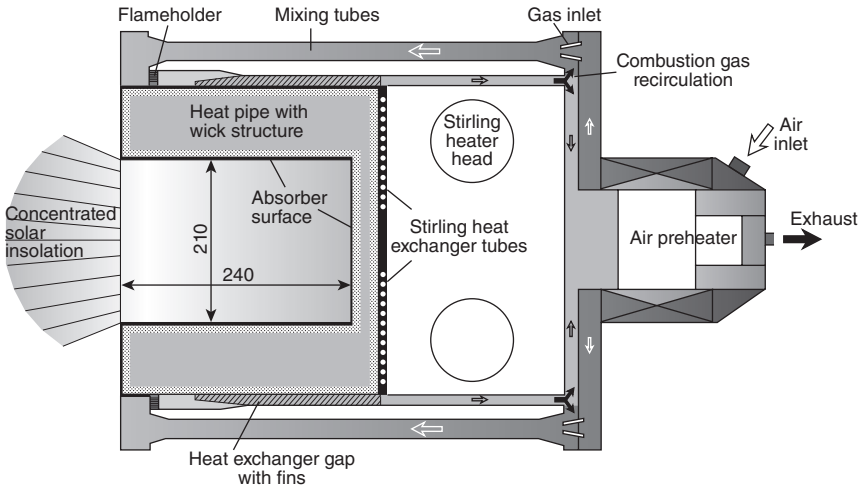

9.20 Schematic (a) and prototype (b) of a Stirling hybrid heat pipe receiver for 10 kW engine (DLR) (Copyright: DLR).

Volumetric receivers have been designed for generation of hot air for Brayton cycles or for thermochemical reactions (Fig. 9.22). The concentrated sunlight is absorbed in the volume of a porous high temperature material. The heat is transferred to the air flowing through the absorber. Usually the air is pressurized up to 10 bar which requires an airtight and pressure-proof construction as well as a transparent window (quartz) (Buck *et al.*, 1996).

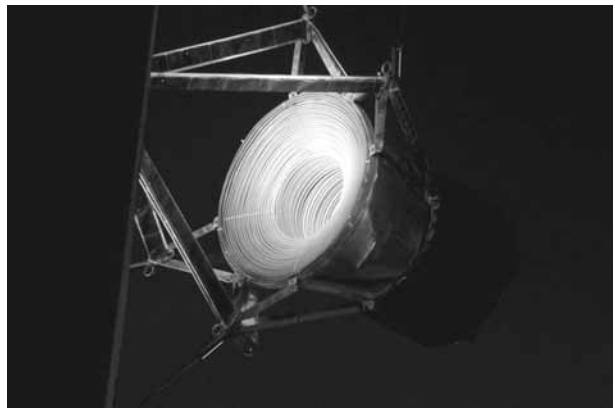

9.21 Example of a monotube open receiver (ANU) (Copyright: ANU Solar Thermal).

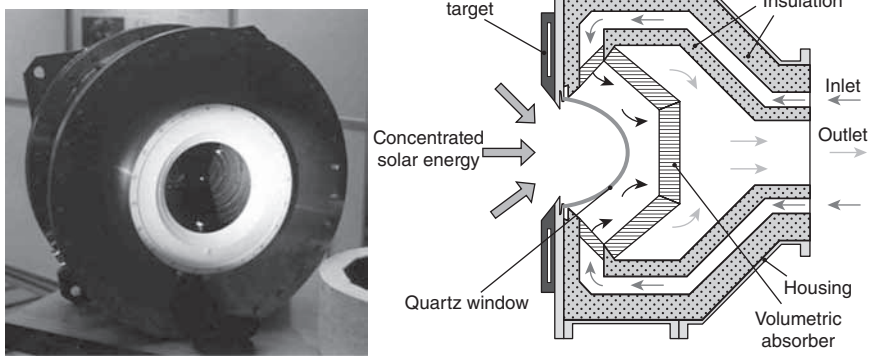

9.22 'Example of a volumetric pressurized receiver: (a) overview and (b) section (Copyright: DLR).

9.5 System performance

In general, overall system performance depends on system design parameters, i.e. engine efficiency and especially part load behaviour of the engine as well as the optical performance of the concentrator (reflectivity of the mirrors, contour accuracy of the reflector, stiffness of the support structure, etc.) and available solar insolation (DNI). Ambient temperature acts as the lower temperature of the thermodynamic cycle, which impacts the efficiency. This section discusses the operation and output characteristics of typical dish Stirling systems. Other thermal power generation systems behave in qualitatively similar ways.

Typical design and operation criteria are:

Operation wind speeds:	up to 15–20 m/s
Survival wind speed:	up to 45 m/s in a wind stow position
Ambient temperature:	–10 to 50°C
Humidity:	up to 100%
Maximum power output:	at 800–1,000 W/m^2 DNI
Engine pressure:	0–15 MPa
Working gas upper temperature:	500–700°C
Grid connection:	single systems are connected to 230/400 V line

Due to the low thermal inertia, a dish Stirling System reacts very quickly on changes in solar thermal input. Thus steady state operation is achieved within a few minutes after system start.

A typical daily pattern of net electric energy production over a day is given in Fig. 9.23 and a measured input–output diagram of a dish Stirling system is shown in Fig. 9.24. From these diagrams it can be seen that a dish Stirling system already starts net electric energy production when direct beam insolation (DNI) reaches values around 200–300 W/m^2 (DNI) in the morning, depending on mechanical and thermal losses of the engine as well as the optical performance of the concentrator. Maximum power output is normally reached at 1,000 W/m^2 of DNI. If the concentrator is over sized, maximum power output is already achieved at a lower insolation level, e.g., at 800 W/m^2. The negative power dip on startup of the engine is due to warming up of the engine's hot parts. Daily power output of a grid-connected dish Stirling system with unfavourable irradiation conditions is shown in Fig. 9.25.

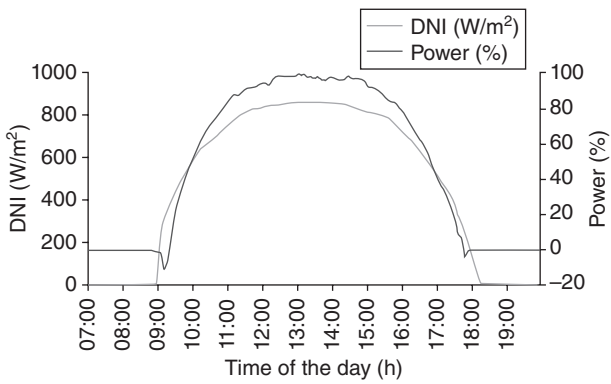

9.23 Daily power output of a grid-connected dish Stirling system with favourable irradiation.

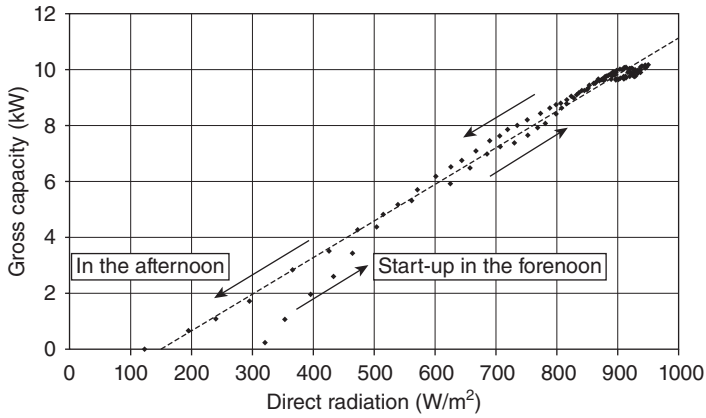

9.24 Typical input–output diagram of a dish Stirling system.

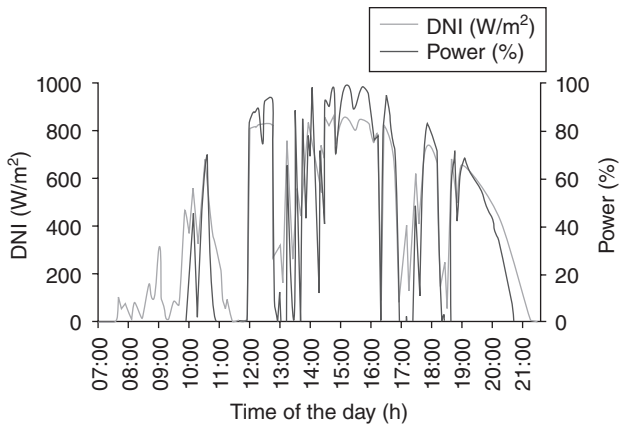

9.25 Daily power output of a grid-connected Dish Stirling system with unfavourable irradiation.

With the help of the available weather data (DNI, wind data, ambient temperature etc.), the plant's daily and annual net energy can be simulated for specific locations. Using typical meteorological year (TMY2s) data, histograms of yearly electric energy production can be developed. Modern dish Stirling simulation codes take care of all system loss mechanisms, i.e. engine, generator and receiver losses as well as the optical losses of the concentrator.

Figures 9.26(a)–(c) present the results of a system simulation for a dish Stirling power plant with 200 units each with 10 kW. All single system coefficients were considered, including dirt on the mirrors as well as clouding

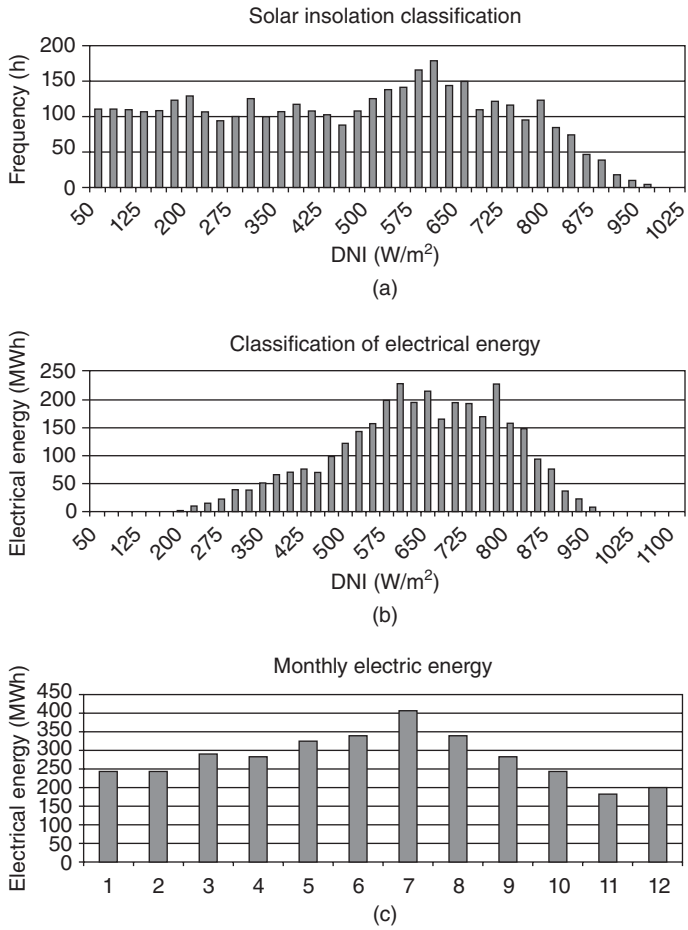

9.26 Simulation of 2 MW dish/Stirling plant with 200 units of 10 kW, showing (a) annual distribution of insolation levels, (b) electrical energy vs. insolation level, and (c) monthly electrical energy.

(3% in the morning and evening). Availability was considered at 98%. Table 9.1 gives parameters for the expected annual energy production of the dish/Stirling plant.

9.5.1 Hybrid operation

If power output is required independent of the existing meteorological conditions, in the evening or at night as is required in many applications, the dish Stirling system can, besides the use of batteries, be configured as hybrid system. 'Hybrid system' means that additional fossil energy sources

Table 9.1 Parameters for the expected annual energy production of a dish/Stirling plant

Available radiation energy of direct radiation:	approx. 2,200 kWh/m^2/a
Available radiation energy of direct radiation: (aperture of a single system)	approx. 124.9 MWh/a
Available radiation energy of direct radiation: (aperture of power plant)	approx. 25.0 GWh/a
Net annual energy production of the plant:	approx. 4.5 GWh/a
Net annual efficiency of the plant:	approx. 18%

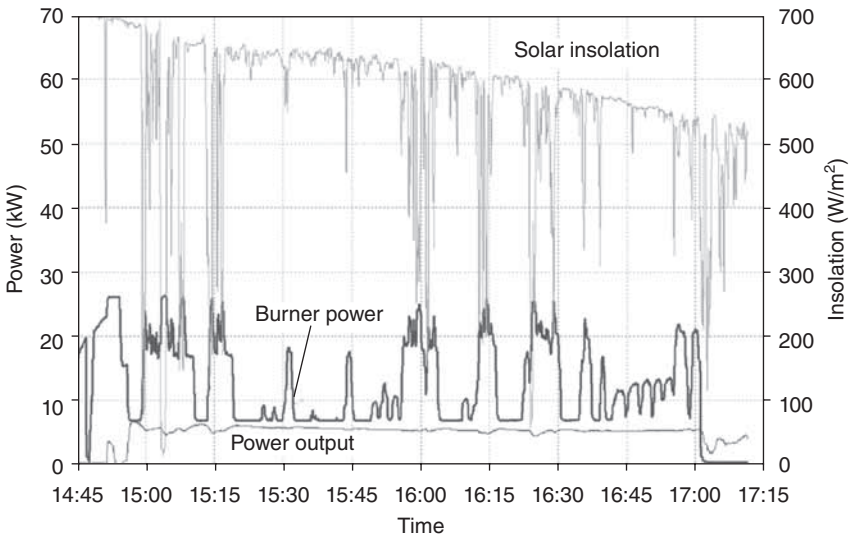

9.27 Hybrid operation.

(e.g. biogas) can be used to add thermal energy to the Stirling engine to stabilize power output over the day and during cloud passages and for prolongation of system operation into night hours. The first hybrid systems have already been developed and the first prototypes successfully tested (Laing and Reusch, 1998; Moreno *et al.*, 1999).

A system operating in hybrid mode is shown in Fig. 9.27. In hybrid mode, the required engine pressure and consequently output power have to be pre-set. The burner is then turned on automatically once the engine pressure falls below this level. It can be seen from the figure that the combustion system can follow the passage of cloud very well and net electric power output is kept fairly constant at approx. 5 kW.

9.5.2 Stand-alone operation

One of the possible markets for a dish Stirling system is to drive a water pump off grid in a remote location. Standard water pump equipment is typically driven by 480/440 V, three-phase induction motors at a constant 50 or 60 Hz. The amount of water pumped is fairly constant and is dependent on the pump and motor characteristics and the depth of the well. When the source of the power is solar energy, the amount of water pumped should ideally vary with the amount of sunlight available. Sandia National Labs developed a stand-alone water pumping dish Stirling system in 2000 (Diver *et al*., 2003). The following explains the approach adopted in this project.

Several options were considered to pump water independent of the utility grid. These included coupling the induction generator with another power source capable of providing three-phase 480 V power. The other generator could be a battery bank with three-phase inverter or a fossil-fired generator set. The speed of the other generator would be regulated according to a fixed schedule proportional to DNI. The dish Stirling with induction generator would then follow the other generator and together they would provide power to the water pump. The use of a DC generator and DC water pump motor, or a DC generator with three-phase inverter was also considered. Photovoltaic field experience indicates that there are significant reliability concerns with DC water pumps and pump controllers.

The power management selected for the Sandia stand-alone dish Stirling system utilizes a three-phase synchronous generator to directly drive a 10-HP, three-phase, 480 V induction submersible water pump motor. This approach was the simplest, lowest cost, and highest efficiency option considered, but also had technical risk. The synchronous generator is self-excited and incorporates a microprocessor-controlled field to produce voltage that is proportional to speed, and speed is proportional to power. This approach has the advantage of utilizing standard water-pumping hardware and opens up possibilities for driving other single-motor applications that can accommodate a variable rotational speed.

Fig. 9.28 shows a plot of key operational parameters during a typical startup of a remote dish Stirling system. During startup, engine speed is regulated by the engine control system at about 800 rpm. At this speed the generator does not generate power and the instantaneous loads associated with starting the induction motor are avoided. After the engine warms up and is capable of producing power without stalling, the power conversion unit controls allow the engine speed to gradually increase and the load of the motor to be gradually introduced. The engine then operates, for example, at a speed proportional to insolation level, typically between about 1400 and 1,850 rpm. Note the idle mode at around 800 rpm, where no power is generated. When the engine is released from idle, the generator begins to

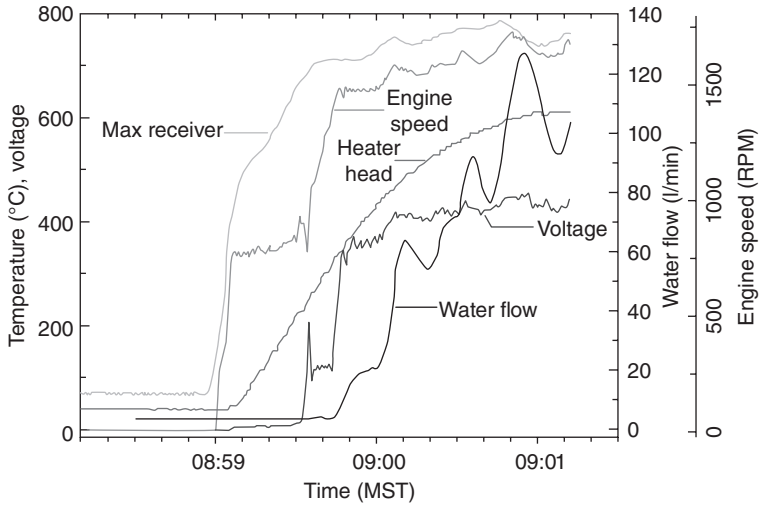

9.28 Typical startup of a dish Stirling off-grid system.

generate power. The heater head temperature is indicative of the warm-up of key engine components, which occurs much more slowly than the low-thermal-mass receiver tubes.

9.6 Optimization of manufacture

9.6.1 Reflector fabrication

Facetted paraboloids (i.e., consisting of individual spherical or parabolically shaped segments) and full-surface paraboloids are encountered in different design approaches. For facetted concentrators, several mirror segments are mounted on a supporting structure. The segments are attached and oriented individually. Such mirror segments may either consist of glass mirrors or substrates covered with reflecting foil or thin-glass mirrors.

For full-surface concentrators, the entire concentrator surface is shaped parabolically by a forming process. For instance, the spb membrane dishes use a pre-stressed metallic membrane attached on both sides to a stable ring (stretched membrane technology). Subsequently, it is transformed into the desired shape via a forming process (e.g., by water load) and stabilized via a controlled vacuum. Such low weight metal membrane designs provide full-surface concentrators with high rigidity and high optical quality. Alternatively, the surface may be made from sandwich elements made of fibre glass reinforced epoxy resin with thin glass mirrors glued onto them (e.g., the EuroDish). For the small dishes employed by Infinia, injection moulded plastic elements are used.

With many dish concentrators, the reflector is made up of facets mounted on a supporting structure. There is a considerable variety of facet designs that have been realized:

- Sandwich substrates from reinforced plastic or metal (e.g., WG Associates/Cummins WG-500 dish) with bonded thin glass mirrors (typically 0.8–1.2 mm)
- stamped steel (e.g., SES Suncatcher) or composite plastic substrates (e.g., Infinia Power dish) with thin glass mirrors
- above substrates can also be equipped with metallized plastic foils or anodized aluminium sheets
- self-carrying slumped glass mirrors are the standard solution for parabolic trough concentrators but have not been applied for dishes except single prototypes.

With the quantities of dish concentrators likely to increase, facet manufacturing technologies for large-scale production like stamping have become more important. They require major investments in tooling but can achieve low cost and high precision. An important field of optimization and cost reduction for thin glass mirrors is bonding onto the substrate. The initially flat thin mirror tiles are limited in size to withstand the biaxial bending and handling issues, thus a considerable number of tiles may be required for every facet. Robotic application with adhesive foils or sprayed fluid glue can be used, but is nevertheless a significant cost factor. Metallized plastic foils and anodized aluminium could achieve a cost reduction in this process. However, verification of their long-term stability in outdoor applications is still ongoing, therefore they have not yet been used in major projects.

The support structures are frameworks or truss/girder systems from steel sections in most cases. Typically, subassemblies are welded and corrosion protected in the factory and bolted together on the erection site. Parabolic trough collectors have proven that this concept can be cost effective even in large quantities. Alternatively, smaller dishes have also been made up from stamped parts, and this has the potential for further cost reduction as stamped parts have low specific cost. Since the maximum size of stamped parts is limited by the availability of large presses, this procedure has not been applied for bigger concentrators.

9.6.2 Drives

Many pylon-based dish designs use slewing drives for azimuth and linear drives for elevation movement. Both azimuth and elevation drives can profit from the large market for tracking PV and heliostats where similar solutions are used, and suppliers are already manufacturing large volumes. One difference from PV applications is that high stiffness and low backlash

are a necessity. However, slewing drives in particular are a considerable cost factor which calls for new and advanced solutions.

Turntable-based dish mounting and tracking (e.g., EuroDish) is characterized by small and cost-effective gears but needs many structural parts to be assembled and large foundations, for big systems to be equipped with rails. Their application is mainly for large dishes (e.g., ANU dishes) where the cost for pylon-based drives is too high and their stiffness is too low.

9.6.3 Trade-off between concentrator accuracy and cost

The optical quality of the concentrator is the major factor for concentrator performance. If power conversion units with high operating temperatures like Stirling engines are to achieve reasonable efficiency, they need a compact absorber or, in the case of a cavity receiver, a small aperture to reduce infrared radiation and convection losses. For this, a dish with high optical quality and a high concentration factor is required, which is directly coupled to the need for high accuracy of the reflective surface. Besides the desire for a highly specular reflection, a characteristic of solar concentrator optics is that slope deviations from nominal are the most relevant factor. For high performance dish concentrators, the average slope errors typically range between 0.5 and 3 mrad (0.03 to 0.17°). High precision is required to achieve numbers towards the lower end, which is highly cost related and therefore an important factor for the economic analysis.

Depending on the design and shape of the absorber, the alignment of facets may have to be tailored to achieve a flux distribution adapted to the needs of the power conversion unit.

The optical quality impact on concentrator performance and the allowable cost for reflectors with different surface slope errors were studied in Andraka (2008). The outcome was that high precision reflectors pay out in the end even at relatively high cost.

Other factors for concentrator performance are stiffness of the structure under dead weight and wind load, facet alignment in the case of multifacet concentrators, alignment of the absorber along and across the optical axis and tracking accuracy when following the sun.

Figures 9.29–9.35 show how the above-mentioned errors and deformations affect the reflector contour and the flux distribution on the absorber of a Stirling engine. A dish consisting of six gore-shaped facets was used for this example.

A comprehensive system optimization has to consider all the above factors. Since the optimum is always cost driven, achieving an economic concentrator design needs detailed knowledge of the cost of different manufacturing and assembly methods.

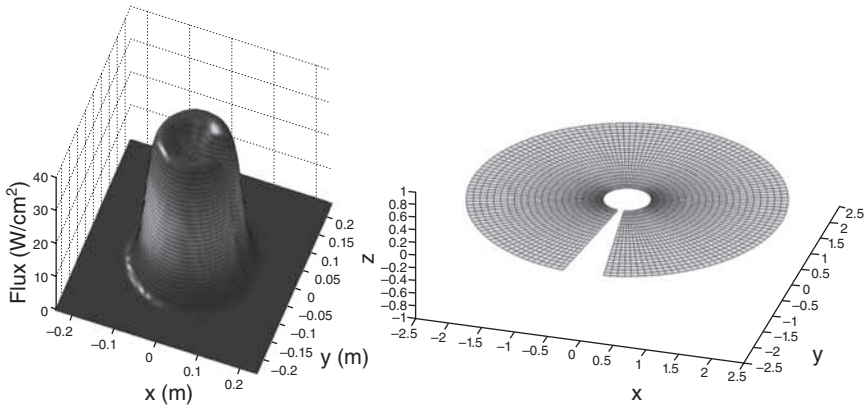

9.29 Ideal undeformed structure.

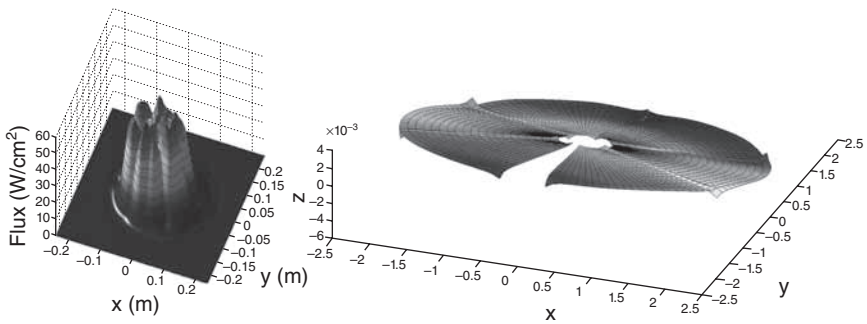

9.30 Structure under dead weight and wind.

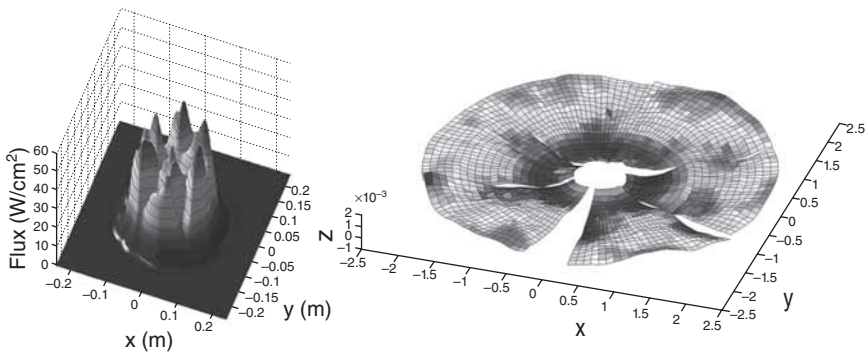

9.31 Isolated effect of reflector element waviness.

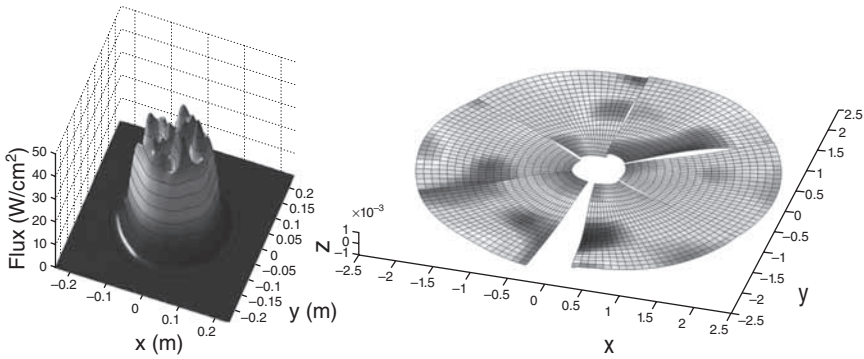

9.32 Isolated effect of reflector element support point deviations.

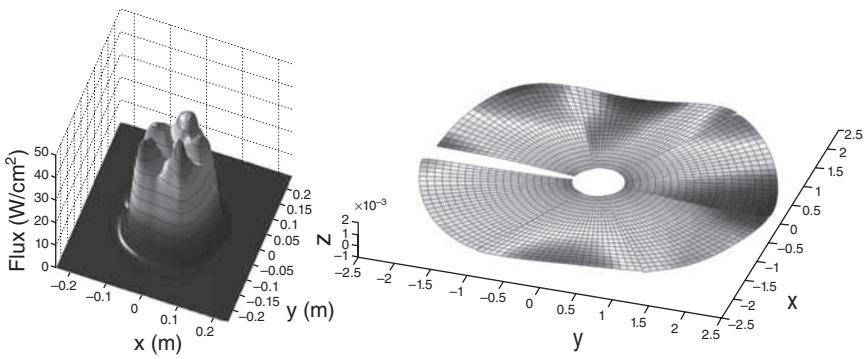

9.33 Isolated effect of reflector element tilt.

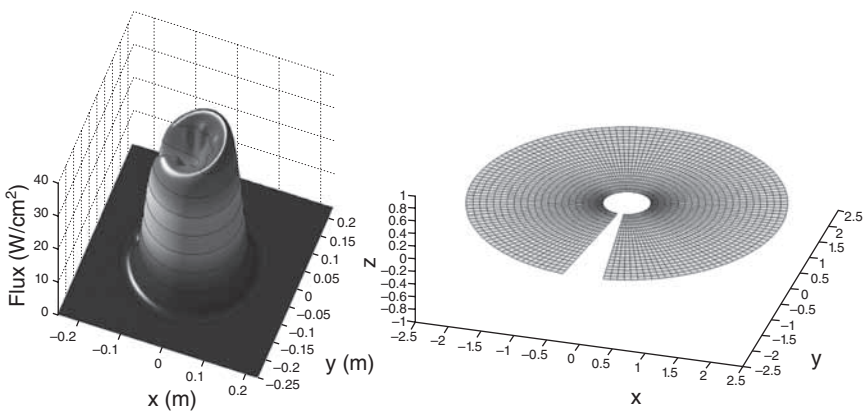

9.34 Isolated effect of target misalignment from optical axis.

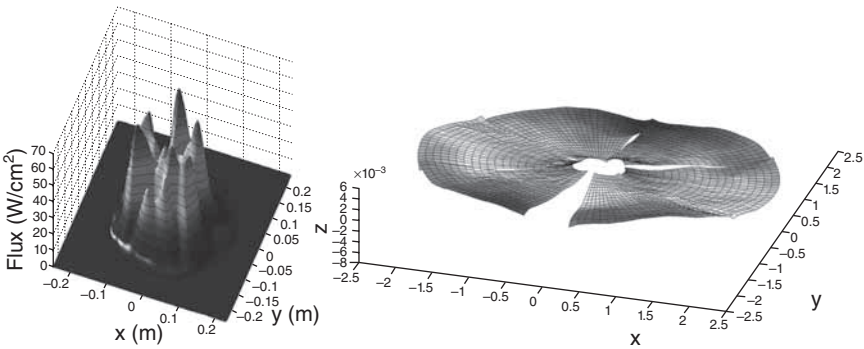

9.35 All errors plus dead weight and wind.

9.6.4 Strategies for site assembly and alignment

The cost of site assembly and alignment is an important fraction of the total system cost, thus it is important to find an efficient solution. The number of units to be erected on a site plays a prominent role in the decision on assembly strategy. Large installations allow for extensive tooling and machinery, while small clusters or even single system erection call for leaner methods.

For medium to large plants, a site workshop is erected as is common practice with parabolic trough collectors.

Automation is of course a way to reduce required manpower; the automotive industry is the oft-cited standard. However, the conditions for use of robots, for example, are different in a site assembly workshop: it usually runs for a relatively short period which increases the share of run-in, the environmental conditions like temperature changes and soiling are harder to create and the availability of personnel and spare parts for correction of failures is worse. Therefore, deployment of automated processes has to be well planned.

For one of the most critical assembly steps, joining and aligning of reflector elements, at least the following principles can be differentiated:

- use of precise jigs for the concentrator structure assembly ensures that the mirror supports are exactly in place,
- mirrors placed on a precision jig, imprecise support structure attached to the mirrors via a tolerance compensating joining method,
- building the structure from precise parts with low play in the joints results in a precise assembly and mirror supports at the right positions,
- less precise structure with adjustable mirrors and a suitable alignment procedure (Andraka *et al.*, 2010).

Also, transportation of dish assemblies from the site workshop into the installation field and mounting on the prepared foundation or pylon have to be organized efficiently. Trucks or special vehicles and mobile cranes are employed for this purpose.

Finally, fast and standardized commissioning procedures with little personnel demand are required. For large plants, commissioning can be conducted in sections according to the construction progress, making use of the modular character of decentralized power generation. Thus parts of the plant can already produce energy during plant construction and reduce interim financing.

9.7 Future trends

9.7.1 Decentralized applications

For a long time, parabolic dish and dish Stirling systems have been regarded mainly as an option for decentralized applications in the range of some kW to some MW. However, most of the product developments in recent years focus on large installations from 10 MW to almost 1 GW. The reasons are, on the one hand, that cost prognosis leads to the expectation that competitiveness with parabolic trough and PV can be achieved and that the market in many countries requires bulk solar power. On the other hand, operational experience with dish Stirling technology spread over more than 25 years has been collected with prototypes usually run under test conditions. Commercial applications are different in many aspects, thus lessons learned from prototypes cannot be directly transferred. Furthermore, the number of units under test has always been small. The number of operational hours collected so far has not been sufficient for maturing such a complex system and for achieving the targeted reliability and low maintenance and repair. Since the business plans and the market demands do not allow for extensive further testing in small and medium size installations, teething troubles have to be expected. Resolving future issues and implementation of necessary retrofitting would be very costly in decentralized applications. Large installations allow for better supervision of the systems and reduce the costs of unplanned maintenance and repair.

Dish Stirling systems are suitable for decentralized applications but it can be expected that this market will be served at a later stage when the technology has matured and has proven reliability and low maintenance costs.

9.7.2 System size

Most of the present dish Stirling product developments range between some kW and 25 kW. Going for small units increases relative cost for

components like electrics, controls and field cabling. For the same installed power, more parts have to be assembled. On the other hand, small size raises the number of produced parts and may enable thresholds in production volume to be reached for large mass production, especially for manufacturing technologies known from the automotive industry. The Infinia 3 kW system is an example of this path, where stamped parts are used for much of the frame. Also, wind moments on small dishes and thus loads for the drive system reduce more than proportionally with decreasing dish surface area. Wind moments also affect the dish structure and lead to reduced specific mass (kg/m^2 of projected concentrator area). In contrast, large systems have the benefit of lower part count to be assembled but they suffer from increasing specific mass.

The economic optimum in size depends on many variables. Many designers found that there is an optimum size in the range of 10–25 kW_{el}, corresponding to dish projected areas of 50–120 m^2. However, today we see commercial and pre-commercial dish and dish Stirling systems in very different sizes. The upper end is marked by the ANU Big Dish with 400 and 500 m^2; HelioFocus of Israel is also developing a very large dish. These systems have solar-chemical reactors or receivers that provide steam. The lower end is marked by the Infinia dish Stirling system with 3 kW and 15 m^2. Especially for dish Stirling, a major design driver for selecting the system size is always the availability of suitable engines which sometimes overrides what has been found to be the theoretical optimum.

9.7.3 Energy storage

A major advantage of centralized solar thermal power plants as parabolic trough and power tower systems is the possibility to add thermal storage. The storage option allows for increasing the capacity factor which is an important criterion in an electrical power distribution system with limited transmission line capacities and without sufficient electrical storage. It is even more important for the dish Stirling technology since their thermal inertia is low and electrical power output directly follows the solar radiation. Developing thermal storage for dish engines would therefore be very helpful to gain share in future markets.

There are two options for a thermal storage: it can be located at the engine itself or it might be a central unit in a power plant. A small local storage has the issue that it increases the engine dead weight. Since with today's storage technologies a useful storage capacity of at least some hours at nominal load means a multiple of the engine mass, this requires adding substantial extra material into the engine support structure, thus increasing loads on dish drives and bearings. Furthermore, small storage has an unfavourable surface-to-volume ratio and thus high thermal losses from thermal

conduction through the insulation result. A central storage solution faces the issue of transporting high temperature heat over considerable distances and across movable joints to accommodate the dish movement. Keeping thermal losses over all the lines to the storage low is a challenge.

Both storage options require a high temperature level to supply the engines; with typical Stirling engine working gas temperatures between 600 and 700°C, the storage temperature needs to be even higher to overcome required temperature differences for the heat transfers. So far no dish Stirling system with thermal storage has been published, which also indicates the sizeable technical and economic difficulties. Therefore the storage option is attractive, but there are still doubts whether viable technical and economic solutions can be found.

9.7.4 Hybrid operation

Similar to plants with thermal storage, hybrid solar power plants allow for de-coupling solar incident power and electric energy generation. In many cases, they can benefit from better feed-in tariffs, i.e. by avoiding losses of increased rates during demand peak times. The feasibility of hybridizing dish Stirling units has been proven in some projects (Laing and Reusch, 1998; Moreno *et al.*, 1999), but to date hybrid dish Stirling systems have not left the experimental stage. Perhaps the most challenging task is to find a technical solution for the conflictive demands of solar receivers and fossil or biomass-fired heaters at reasonable cost. With known solutions, the loss in efficiency compared to solar only systems and/or complexity and cost are too high.

If an efficient and reliable hybrid system at reasonable cost can be developed in the future, this could open considerable market opportunities. Today, it seems that this will not be achieved in the short term.

9.8 Conclusion

The parabolic dish concentrator development over the last 25 years has demonstrated an impressive diversity of designs and solutions. While many systems apply a Stirling engine as a PCU, others generate heat to be supplied by other thermodynamic cycles. Two-axis solar concentration allows for high upper process temperatures and the highest conversion efficiencies of all solar concentrating technologies. On the other hand, the reflector geometry demands more in terms of manufacturing and the bi-axial tracking to the sun requires additional effort. There is still a considerable variety of designs and a large span of concentrator sizes with present developments. First commercial products are going to enter the market and will have to prove their technical maturity and economic viability. Thermal storage and

hybrid operation are attractive options to improve economic viability but are technically challenging and not yet proven.

9.9 Sources of further information and advice

Mancini, T., Heller, P., Butler, B., Osborn, B., Schiel, W., Goldberg, V., Buck, R., Diver, R., Andraka, C. and Moreno, J. (2003) 'Dish-Stirling systems: an overview of development and status', Journal of Solar Energy Engineering, 125 (2), 135–151.

Stine, W.B. and Diver, R.B. (1994) 'A compendium of solar dish/Stirling technology', Report SAND93-7026. Sandia National Laboratories, Albuquerque, NM.

9.10 References and further reading

Andraka, C.E. (2008) 'Cost/performance tradeoffs for reflectors used in solar concentrating dish', Proc. 2nd International Conference on Energy Sustainability, August 10–14, Jacksonville, FL.

Andraka, C., Diver, R., Adkins, D., Rawlinson, S., Cordeiro, P., Dudley, V. and Moss, T. (1993) 'Testing of Stirling Engine Solar Reflux Heat-Pipe Receivers', Proc. 28th Intersociety Energy Conversion Conf. (IECEC), Atlanta, GA, August.

Andraka, C., Adkins, D., Moss, T., Cole, H. and Andreas, N. (1995) 'Felt-Metal-Wick Heat-Pipe Receiver', Solar Engineering 1995, Proc. ASME/JSME/JSES Int. Solar Energy Conf., Maui, HI, March.

Andraka, C., Yellowhair, J., Trapeznikov, K., Carlson, J., Myer, B. and Stone, B. (2010) 'AIMFAST: An Alignment Tool Based on Fringe Reflection Methods Applied to Dish Concentrators', Proc. SolarPACES 2010 Conference, Sepember 21–24, Perpignan, France.

Bean, J.R. and Diver, R.B. (1995) 'Technical Status of the Dish Stirling Joint Venture Program', Proc. 30th IECEC, Orlando, FL, pp. 2.497–2.504.

Buck, R., Heller, P. and Koch, H. (1996) 'Receiver Development for a Dish-Brayton System', Proc. ASME Int. Solar Energy Conference, San Antonio, TX, April.

Diver, R.B., Andraka, C., Rawlinson, K., Moss, T.A., Goldberg, V. and Thomas, G. (2003) 'Status of the Advanced Dish Development System Project', ASME 2003 International Solar Energy Conference (ISEC2003), March 15–18, Kohala Coast, Hawaii.

EPRI Report (1986) 'Performance of the Vanguard Solar Dish Stirling Engine Module', Electric Power Research Institute, AP 4608, Project 2003-5.

Gallup, D. and Mancini, T. (1994) 'The Utility-Scale Joint-Venture Program', Proc. 29th IECEC, August 7–12, Monterey, CA.

Gordon, J. (2001) *Solar Energy, The State of the Art, ISES Position Papers*, James & James, London.

Jaffe, L.D. (1988) 'A review of test results on solar thermal power modules with dish-mounted Stirling and Brayton cycle engines', *Journal of Solar Energy Engineering*, 110, 275–281.

Kaneff, S. (1991) *The White Cliffs Project – Overview for the period 1979–89*. NSW Office of Energy, Sydney, Australia.

Koshaim, B. (1986) 'Report: Fifty KW Solar Membrane Concentrator', The SOLERAS Program, Saudi Arabian National Center for Science and Technology.

Laing, D. and Reusch, M. (1998) 'Design and Test Results of First and Second generation Hybrid Sodium Heat Pipe Receivers for Dish Stirling Systems', Proc. ASME International Solar Energy Conference, Albuquerque, NM.

Lopez, C. and Stone, K. (1992) 'Design and Performance of the Southern California Edison Stirling Dish', Solar Engineering, Proc. ASME Int. Solar Energy Conf., Maui, HI, April 5–9.

Lopez, C. and Stone, K. (1993) 'Performance of the Southern California Edison Company Stirling Dish', SAND93-7098, Sandia National Laboratories, Albuquerque, NM.

Lovegrove, K., Burgess, G. and Pye, J. (2011) 'A new 500 m^2 paraboloidal dish solar concentrator', *Solar Energy*, 85 (4), 620–626.

Mancini, T., Heller, P., Butler, B., Osborn, B., Schiel, W., Goldberg, V., Buck, R., Diver, R., Andraka, C. and Moreno, J. (2003) 'Dish-Stirling systems: an overview of development and status', *Journal of Solar Energy Engineering*, 125 (2), 135–151.

Moreno, J., Rawlinson, S., Andraka, C., Mehos, M., Bohn, M.S. and Corey, J. (1999) 'Dish/Stirling Hybrid receiver Sub-Scale Tests and Full-Scale Design', 34th Intersociety Energy Conversion Conference, Vancouver.

SouthWest Solar (2011) http://www.swsolartech.com/ accessed December 2011.

Stine, W. (1993) 'An International Survey of Parabolic Dish Stirling Engine Electrical Power Generation Technology', Solar Engineering, Proc. ASME/ASES Joint Solar Energy Conf., Washington, D.C.

Stine, W.B. and Harrigan, R.W. (1985) *Solar Energy Fundamentals and Design: with computer applications*. John Wiley & Sons, New York.

Stine, W.B. and Diver, R.B. (1994) 'A compendium of solar dish/Stirling technology', Report SAND93-7026. Sandia National Laboratories, Albuquerque, NM.

10

Concentrating photovoltaic (CPV) systems and applications

S. HORNE, SolFocus Inc., USA

Abstract: This chapter is a summary of the state of the art of concentrating photovoltaic (CPV) systems, discussed from several viewpoints. It begins with an abbreviated history of the technology, then continues to a discussion of the characteristics, market, and system design. A short piece on future trends concludes. Because of its complex nature, this chapter is limited to a qualitative introduction to this interesting and growing field, and assumes a general familiarity with photovoltaics.

Key words: concentrating photovoltaic systems (CPV), multi-junction photovoltaic cells, optical systems, acceptance angle, spectral transfer function, two-axis tracking, levelized cost of energy, high volume manufacturing.

10.1 Introduction

Concentrating photovoltaic (CPV) systems operate by using an optical assembly to concentrate light onto a photovoltaic (PV) cell. In other words, they entrain a large area of solar energy onto a small cell, which operates at an irradiation level many times greater than that of direct, unconcentrated sunlight. A PV cell's conversion efficiency actually improves somewhat with increasing irradiation levels (Olson *et al.*, 2007), and will deliver much more power when used under concentration than when operated under direct sunlight. CPV technology exploits this to significantly reduce the cost of energy by amortizing the cost of the cell and attendant optics, housings and tracking systems over the high energy output. In practice, concentration ratios (while there are several definitions, broadly the ratio of the irradiance on the cell to the irradiance at the entrance aperture of the concentrator), generally expressed in 'suns', fall into two general groupings. Low concentration photovoltaic (LCPV) devices operate between 1.25 and approximately 40 suns, and high concentration photovoltaic (HCPV) devices have been built between 250 and 1,700 suns. Devices with concentration levels between HCPV and LCPV (medium concentration photovoltaic devices or MCPV) have not received much attention, mainly due to their economics, as will be illustrated later.

CPV can be applied with any of the CSP concentrator system types that have been discussed in other chapters (trough, tower, linear, Fresnel or dish). The concentrators are, however, designed specifically for the CPV application. Fresnel lens approaches are also applied to CPV.

This chapter introduces CPV systems from several different viewpoints, and describes their role in the solar marketplace.

10.1.1 Historical summary

While CPV technology has been under development for many years, commercialization has been elusive as technical and reliability difficulties dominated the development of this seemingly simple idea (Rosenthal and Lane, 1991). In addition, the rapidly maturing silicon panel market with its head start of many decades raised significant barriers to market entry. Swanson (2002: 449–452) illuminates the dilemma facing the CPV industry in greater detail than is possible here, and explains why the expected increase in commercial investment did not occur during that period. Sala and Luque (2007: 1–11) characterize the period up to the late 1990s as one dominated by academic leadership, with some product development progress being made by only a small number of companies, Arco Solar (Rosenthal and Lane, 1991), Amonix and Solar Systems Australia being three examples.

Within the past ten years, though, advances in the efficiency of practical high-performance multi-junction cells, first described by Olson and Kurtz (1993) from the US National Renewable Energy Labs (NREL), have reignited interest in HCPV. These cells, first developed for the space applications market and using materials other than silicon, promise conversion efficiencies of well over 40% but at a cost extremely prohibitive for use in standard panels, at one sun. The *only* possible application for these cells in a terrestrial environment is in a HCPV system. Significantly, this rebirth occurred at a time of great interest in energy prices and sustainable practices, much of it coming from the worldwide venture capital community, seeking a post-internet boom market. In addition, by the time the investment industry started to seriously analyze CPV, these cells had passed the stringent reliability standards of the space industry, and had amassed millions of successful cell-hours of operation. This confluence of performance promise, interest in renewable energy sources, and positive reliability data emboldened the investment industry, and an explosion in new HCPV companies occurred in the first few years of the century. This was soon followed by investments into the cell segment itself, as meaningful progress had been made on new cell morphologies and related technologies (Miyashita *et al.*, 2007), building on the pioneering work at NREL.

The LCPV segment also received significant interest. Improvements in silicon cells, while not as spectacular as those in multi-junction cells, were

important to this segment of the industry. The combination of efficiencies in the 18% range and low fabrication costs allowed for designs that made economic sense. Though a smaller segment than HCPV, LCPV has attracted high-quality commercial representation.

While all concentrator optics are constrained by the physics of reflection, refraction and total internal reflection (TIR), within these limits the relatively new field of non-imaging optics (NIO) pioneered by Welford and Winston (1989) added opportunity for innovation. Significant performance and manufacturability improvements have been realized by applying NIO, and the pathway to practical, deliverable products has become much more navigable. As a result, many new CPV companies have worked to merge NIO with the new cells, and a large range of designs have recently appeared at both ends of the concentration range, further contributing to what was an already well prototyped field.

Today, the leading companies in CPV have matured their products, have commissioned high-volume production lines and have amassed large amounts of data from operating installations. The focus for many of these companies is now on proving their bankability and product reliability, as larger commercial opportunities become available.

Currently, there are over 20 active CPV companies, and Table 10.1 summarizes the status of the leaders. Note that a more detailed description of the techniques used by many of these companies appears later in this chapter, as does a sample of product photographs.

After a long gestation, CPV is starting to meet its promise. Swanson (2002: 449–452) declared that CPV is 'a long range option of vital importance to the energy security of the world. Cost analyses indicate that it certainly has the possibility of becoming the low-cost PV approach in large installations.' That long-range timeframe is upon us.

10.2 Fundamental characteristics of concentrating photovoltaic (CPV) systems

To understand the appeal of the technology and the contribution it can make to the already large offering of solar technologies, it is necessary to understand its characteristics. Some central concepts are discussed in this section.

10.2.1 Acceptance angle

Regardless of the concentration level or optical method used, a CPV system can be thought of as telescope placed in front of an efficient PV cell. Only light entering this telescope will reach the cell and be converted to electricity, which presents a limitation not seen in standard flat plate or one-sun

Table 10.1 Photovoltaic concentrator manufacturers in or close to production as of August 2010

Company	System	Installations (completed or under construction; not announced)
SolFocus	High concentration, multi-junction cell, glass, point-focus reflective optical array	8 MW
Amonix	High concentration, silicon cell, acrylic, point-focus refractive (Fresnel lens) array	Approx. 9 MW
Amonix	High concentration, multi-junction cell acrylic, point-focus refractive (Fresnel lens) array	0.38 MkW
Entech	Medium concentration, silicon cell, single acrylic line focus refractive (Fresnel lens) module	Approx. 0.2 MW
Concentrix	High concentration, multi-junction cell, glass/silicone point-focus refractive (Fresnel lens) array	1.7 MW
Opel	High concentration, multi-junction cell, point-focus refractive (Fresnel lens) array	0.33 MW
Solar Systems/ Silex	High concentration, multi-junction cell, large single piece glass point-focus reflector (parabolic) system	Approx. 1 MW
Emcore	High concentration, multi-junction cell glass/silicone, point-focus refractive (Fresnel lens) array	1.0 MW
Skyline Solar	Low concentration, silicon cell, large single piece aluminum line focus reflective system (DSMTS system, described later)	0.1 kW

systems. Because of this, a concentrator system possesses a field of view or *acceptance angle*, which is inextricably linked to the concentration ratio. For the general rotationally symmetric concentrator, the relationship for the maximum achievable geometric concentration ratio, as previously discussed in Chapter 2, is derived by Welford and Winston (1989: 27) to be:

$$C_g = \left(\frac{n_{out} \sin \phi}{n_{in} \sin \theta} \right)^2 \qquad [10.1]$$

where C_g is the maximum possible concentration ratio, n_{out} is the index of refraction of the output medium of the concentrator, ϕ is the half-angle of the edge ray emerging from the concentrator output, n_{in} is the index of

refraction of the input medium of the concentrator, and θ is the half-angle of the edge ray entering the concentrator: the acceptance angle.

Rearranging this equation for acceptance angle gives:

$$\theta = \sin^{-1}\left(\frac{1}{n_{in}}\sqrt{\frac{(n_{out}\sin\phi)^2}{C_g}}\right) \quad [10.2]$$

From inspection, the maximum theoretically attainable acceptance angle would occur for $\phi = 90°$, when the output rays are allowed to emanate over the entire hemisphere from the concentrator's exit aperture. A concentrator of 1,000 suns, operating in air ($n = 1$) with a final concentration stage constructed of low-iron glass ($n_{out} = 1.5$, approximately) would have an acceptance angle of ±2.7°. However, since PV cells exhibit an approximate cosine relationship between input angle and conversion efficiency (Spectrolab, 2010), in practice this number is not attainable, as the high angle light would not be efficiently utilized. If the largest admissible output half-angle is taken to be at the point at which the cell output power is 90%, or ±26°, the acceptance angle is reduced to ±1.2°.

Because of this, CPV systems are mostly sensitive to the direct component of the sun's radiation only – that which emanates directly from the sun and is not reflected, refracted or scattered by the atmosphere or terrestrial objects. The term used to describe the direct or beam power is *direct irradiance*. In practice, as a design approaches the workable limit for acceptance angle, it becomes more expensive and, possibly, less efficient. Central to all concentrator design is the interesting and difficult challenge of the four-way trade between efficiency, cost, manufacturability, and acceptance angle.

10.2.2 Principles of photovoltaic devices

CPV systems convert light to electricity through the use of a photovoltaic cell, and their electrical characteristics run parallel to those of standard, flat silicon solar panels. While an adequate treatment of the physics of photovoltaics is far outside the scope of this chapter, an introduction to the topic is warranted. For a complete development, Green (1998) is very concise.

Photovoltaic devices comprise semiconductor materials that convert light to electricity in a very direct manner. These devices are made from crystalline materials deliberately 'doped' with impurities that donate additional weakly bonded electrons to the crystal. When in their unexcited state, these electrons occupy a range (or band) of energies called the valence band. If one of these electrons gains sufficient energy from, for example, an interaction with a photon, it enters a higher energy band called the conduction band. Energies in the conduction band exceed those allowed in the valence band by an amount defined by the bandgap of the crystalline material. The bandgap represents a forbidden energy zone, over which the electrons

effectively jump. The bandgap is primarily a function of the materials (e.g., silicon, gallium arsenide, and germanium to name a few) and temperature. Bandgaps are expressed in electron volts (eV), the amount of energy needed to move one electron through a potential of one volt. In order to excite an electron from the valence to the conduction band, a photon must have energy at least equal to the bandgap. Photon energy in excess of the bandgap is wasted as heat. Once in the conduction band, excited electrons are highly mobile, and can be directed out of the material to an electrode, forming a DC electric current.

Crucial to the extraction of the electrons from the crystal lattice is the structure formed by combining two types of semiconductors, namely n-type and p-type, into a diode arrangement, commonly called a photodiode when used for electricity generation. Without this, any freed electrons would quickly fall back into the valence band, giving up their energy as heat or radiation via a multitude of complex processes grouped under the general term recombination. Recombination exists right through the crystal lattice, but at the surface is particularly strong. The design of the diode and its manufacturing processes can minimize but not fully eliminate recombination.

Photons have energies that are inversely proportional to their wavelength. Photons of blue light (wavelengths on the order of 400 nm to 470 nm) are more energetic than photons of red (620 nm to 750 nm), and are generally absorbed closer to the surface of a semiconductor. Photons with energies greater than the bandgap will be able to produce an electric current, the surfeit energy they contain being given up thermally and lost. Because of this, and also because highly energetic photons are more subject to surface recombination, as photon energy increases – or wavelength decreases – from the minimum value required to activate a bound electron, device conversion efficiency decreases.

Similarly, other photons within the solar spectrum having energy less than the bandgap energy cannot promote an electron from the valence band to the conduction band. Instead, these photons pass through the material, eventually to be adsorbed in large fraction and converted to waste heat via various unwanted processes inherent in semiconductor materials.

Taken together, the above two mechanisms will cause the device's conversion efficiency to peak at a particular wavelength, and to exhibit sensitivity within a specific range of wavelengths only, dependent on the characteristic bandgap energy. Kurtz and Geisz (2010: A75) describe the optimized bandgap for the solar spectrum to be approximately 1.4 eV. Monocrystalline silicon (c-Si) has a bandgap of 1.11 eV, which is very close, and is one reason why silicon has dominated the photovoltaic industry to date. The characteristics of silicon can be seen in Fig. 10.1, where the efficiency is plotted against the wavelength of light. Also shown on the graph is the

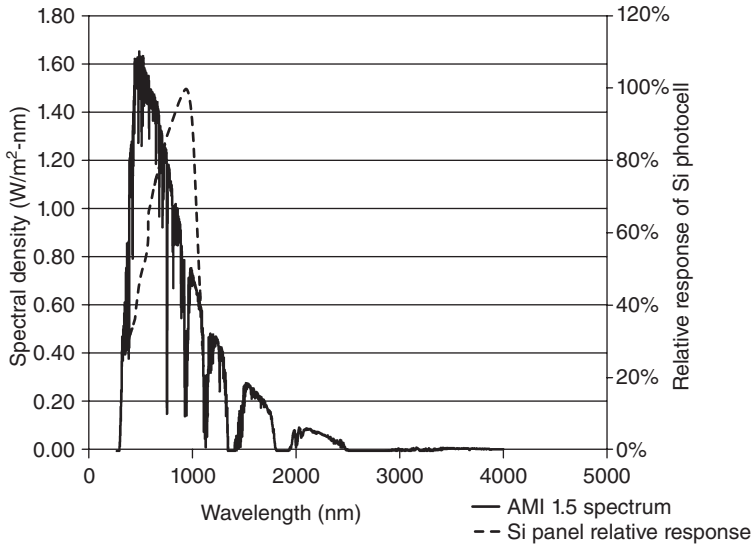

10.1 AMI 1.5 spectrum, overlaid with silicon junction conversion relative efficiency plot.

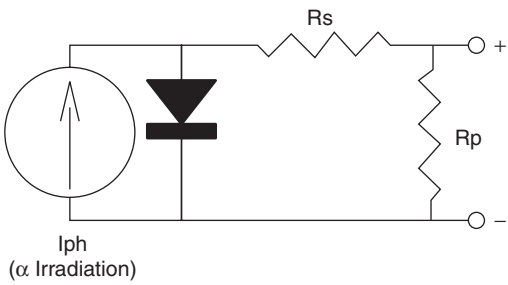

10.2 Single-junction solar cell, equivalent circuit.

spectrum of the sun under AMI 1.5 conditions. This is a standard spectrum, and is the result of the modification of the sun's native spectrum by 1.5 times the standard atmospheric depth, which occurs with the sun 48° above the horizon (chosen as a reasonable average estimate for the entire day). As can be seen, silicon's characteristics limit to converting a portion, but not all, of the sun's incident energy to electricity, leading to the upper bound efficiency. Green (1998: 89–90) shows this limit to be approximately 27%.

At the device level, the photodiode can be modeled by the equivalent circuit of Fig. 10.2, with the relationship between voltage and current shown in the solid curve in Fig. 10.3 (commonly called an IV curve). The product of the current and voltage produces a power–voltage curve, shown as a

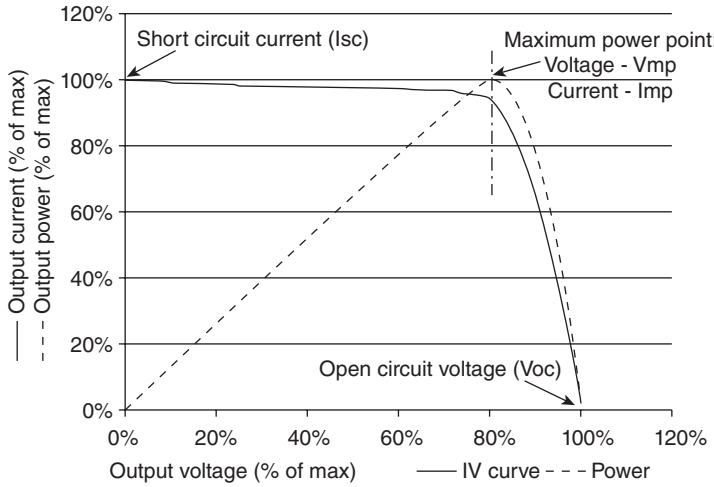

10.3 IV and power curves, photovoltaic junction under illumination.

broken curve in this figure, and which illustrates one important aspect of the application of these devices: they need to operate at the correct voltage, the maximum power point voltage (or Vmp), or they will not produce their maximum output. This maximum power point is continuously searched for by photovoltaic power management systems, for example inverters.

Parasitic series and parallel resistances (Rs and Rp in Fig. 10.2) will cause departure from ideal photodiode characteristics, and a figure of merit called the fill factor has been developed as a single valued 'quality factor'. Equal to the product of Vmp and Imp, divided by the product of Voc and Isc, the higher the value of the fill factor, the 'squarer' the IV curve is, and the closer to ideal the device is. The fill factor in practice, even for photodiodes with very low Rs and very high Rp, cannot reach the maximum of 100% since the ideality factor of the diode itself contributes to the rounding of the IV curve. The departure from ideality arises from various leakage mechanisms in the p/n junction, some inherent to semiconductors operating above absolute zero, and others due to undesired impurities and imperfections in the crystalline material.

As mentioned above, concentrator systems have output characteristics that are very similar to standard PV systems, although the particular cells used have somewhat higher fill factors than silicon. Recognizable stringing systems are used, and for the most part, standard inverters are employed. Direct irradiance varies more than global irradiance, so the diminished acceptance angle when compared to flat panels causes concentrator outputs to be more variable. This can be seen in data presented in Fig. 10.4, where a change in the direct irradiance (DNI) component is plotted against the

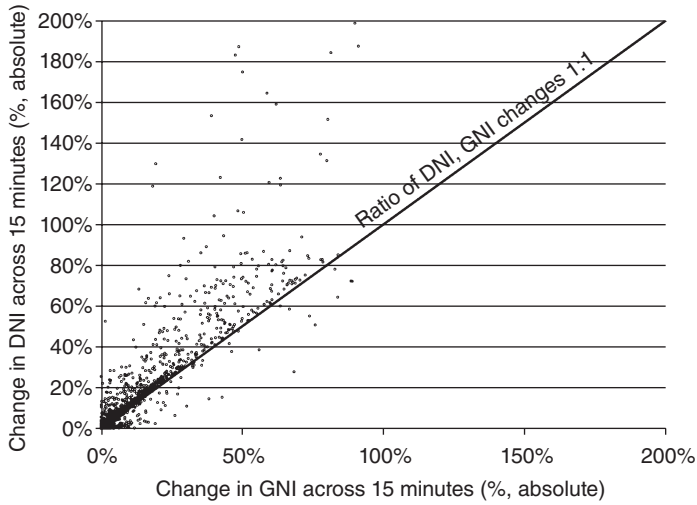

10.4 Change in the direct component of global irradiance vs the change in global irradiance.

equivalent change in global irradiance (GNI). For the vast majority of changes in the global value, the direct component is affected to a much greater extent.

As for all photovoltaic systems, concentrators do not intrinsically have any hold-over capacity or storage. They produce power when the sun is shining only, and generally their use is backed up by other generation assets, for example the grid or a local generation plant. Recent intensive research into large scale electrochemical storage has started to yield very interesting results however, and it is expected that economically viable, direct electrical storage will significantly mitigate this limitation within a few years. For an introduction to this rich field, the reader is encouraged to read Baxter (2006).

10.2.3 Maintenance

The most common maintenance activity for a concentrator will be cleaning the environment-facing optical surfaces, for example the mirrors on an exposed mirror system. This is because they have a limited acceptance angle, and will be more sensitive to light scattered by dust deposited on their surfaces than unconcentrated systems. While this is very site dependent, HCPV companies have found that an average of four times per year is adequate, and it will be somewhat less for LCPV. Exposed mirrors will be more sensitive than systems where the external optical element is transmissive, for example, a window. The vast majority of CPV systems are

passively air-cooled, which means that the only water requirement is for cleaning. In addition, the systems that present a flat, glass face to the atmosphere can be mechanically cleaned using a 'squeegee' – a standard window cleaning device based on a sponge and rubber wiper blade (as opposed to being deluge-washed), which further reduces the amount of water used during operation. With a squeegee, also, the purity of the water is not nearly as stringent as it is for deluge, where deposits from evaporation have to be regularly removed by other means. It has been estimated by SolFocus, one manufacturer of HCPV equipment (where the first optical surface is a window), that their cleaning needs are less than 15 litres of water per megawatt-hour.

The majority of the balance of maintenance is associated with the tracker. Mechanical systems need regular maintenance, but if well designed, this is limited to a biannual lubrication only.

10.2.4 Energy payback and recyclability

As CPV systems are being used to offset dirtier sources of energy, it is important to understand exactly how clean they are. CPV systems stand apart from other forms of solar in two distinct ways. First, they are predominantly assemblies of optics and support mechanisms, with very small amounts of active photovoltaic material. Per unit area, the amount of energy used to fabricate the cells (whether silicon or multi-junction) dominates over the manufacture of other materials, such as glass, aluminum and steel. For CPV, the small area of cell material compared to the area of system will drive down energy payback time relative to standard PV. Reich-Weiser *et al.* (2008) calculated the energy payback time for the SolFocus SF-1100 concentrator panel at 0.7 years, for example, against 2.2–2.7 years for silicon and 2.2–3.9 years for CSP under equivalent analysis. Second, again because concentrators are predominantly an assembly of common materials, they are highly recyclable, and over 95% of a typical system can re-enter the manufacturing stream at end of life.

10.3 Characteristics of high concentration photovoltaic (HCPV) and low concentration photovoltaic (LCPV) devices and their applications

10.3.1 HCPV-specific characteristics

Optical considerations

High concentration ratios can only be reached by point focus systems, so the acceptance angle will be approximately constant around the optical axis.

This means that all HCPV systems must track the sun in both azimuth and elevation, and the smaller the acceptance angle is, the more accurate the tracking has to be. Acceptance angle, then, is a vitally important figure of merit for an HCPV system. Moreover, workable acceptance angles are really only possible by invoking the science of NIO, and practically only by employing multiple-element optical systems (Winston *et al.*, 2005: 1–45). Single element optics and those employing classical designs, such as found on some central tower solar thermal plant, will require two to four times the accuracy required of a well-designed NIO system.

Acceptance angle also plays a role in the energy harvested by an HCPV system, commonly quoted as the ratio of generated energy to peak power (kWh/kW_p). Under non-ideal conditions for HCPV, circumsolar radiation – measured from the sun's limb out to approximately 10° from the solar axis – can be significant. Thomalla *et al.* (1983) calculated that under conditions of high cirrus clouds, for example, circumsolar can be several percent of the sun's irradiance at 0.5° from the axis. Energy harvest will be lost under these weather conditions if the circumsolar irradiation falls outside the acceptance angle. In general, HCPV systems are considered to be sensitive to the direct irradiance or beam radiation only (Lorenzo 2002: 905), though in practice all have some circumsolar performance. The term used to describe the beam energy is direct normal insolation (DNI), usually expressed in kWh/m^2-day.

Two-axis tracking

Given that HCPV systems must track the sun in two axes, they do not suffer from 'cosine loss', the decrease in output that comes from energy striking the cell at large angles from the normal. This effect decreases the energy harvest from fixed tilt flat panels, with power production approximating a cosine output with the maximum centered local solar noon. CPV, on the other hand, has a broad daily output characteristic which is extremely useful towards the end of the day, as it is usually coincident with some of the highest daily electricity demand times. To counteract this, there are examples of silicon panels mounted on two axis trackers, but their lower output has made this a difficult economic proposition. More commonly, the more efficient silicon panels are effectively mounted on single-axis trackers, with a fixed latitude tilt.

Where pedestal style trackers are used (Fig. 10.5), their shape and spacing guarantee that there is no place on the field that is permanently shaded. This has become an important issue with permitting authorities, many of whom are concerned with minimal land disturbance, and whether native vegetation can be re-established after construction. Linear trackers, used in both the CPV and concentrating solar power (CSP) industries, and

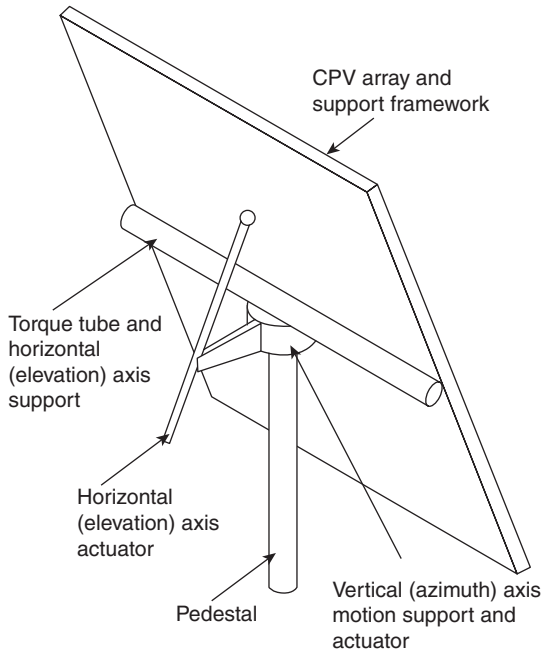

10.5 Pedestal or azimuth-elevation tracker.

stationary rack-mounted systems will cause permanent shading in some areas, and disturb the local ecosystem in a significant manner.

A downside to two-axis tracking is that, to minimize early morning and late evening shading by one system of another, they should be spaced further apart than stationary installations. Ground cover ratios (the ratio of the total area of PV to the area of land on which it is installed) of between 17% and 22% are common. While less than the 30% to 50% found in stationary systems, because of high CPV output, this still results in very competitive land use.

Multi-junction cells

HCPV systems can uniquely exploit the recently developed technology of multi-junction cells. An overview of these cells follows.

As mentioned above, many semiconductor materials are photo-active, and when used to form photodiodes (or 'junctions'), can produce useable power. The bandgap of the semiconductor determines the part of the solar spectrum the cell is sensitive to, which in turn ultimately dictates the maximum efficiency.

To break the barrier of single-photodiode efficiencies, research into a stack of electrically series-connected photodiodes with each photodiode or junction composed of a different semiconductor material has been underway for several years. The top junction – the one the light sees first – is of the largest bandgap material, absorbing and converting only the highest energy photons to power. Photons with a lower energy are transmitted through the first junction to the next, which is composed of a material with a lower bandgap. This structure is repeated until the entire solar spectrum is covered. If the junctions are constructed in a way that their photocurrents are identical, the total power is simply the sum of the power generated by each junction. Theoretical work shows a fundamental limit to efficiency of around 65% (Kurtz and Geisz, 2010: 75) for stacks of this type.

Practical multi-junction cells currently have three junctions, and with some exceptions, the different designs use very similar materials. The first junction, constructed epitaxially, is of InGaP and has a bandgap of 1.8–1.9 eV; the middle junction is also epitaxially constructed and is of GaAs with a bandgap of 1.3–1.4 eV. The bottom junction is usually diffused into Germanium and has a bandgap of 0.7 eV. Efficiencies have climbed dramatically over the past few years, from 25% in 1990 to 42% in 2010 (Kurtz and Geisz, 2010: 74), and recent work on cells having greater than three junctions is beginning to yield results over 40%.

In addition, their efficiency is relatively independent of their operating temperature. Unlike silicon cells, with coefficients of around –0.4%/C (Green, 1998), modern multi-junction cells can be in the range of –0.07%/C (Spectrolab 2010). Because of this, to a very large extent, the cooling system in a concentrator is designed to maintain the cell within its specified operating temperature range only, and not to maximize output. CPV fields show little output degradation with increasing ambient temperatures, and they are economically very attractive for hot, dry desert conditions, where daytime temperatures can reach over 50°C.

Nothing comes for free, however, and several intrinsic issues must be addressed with any of these complex cells. First, if the different junctions are stacked on top of one another, a parasitic diode will be formed between them. These parasitic diodes will seriously impair the performance of the overall structure, and must be eliminated. This is done by inserting tunnel diodes between the main junctions, isolating the individual photodiodes.

Second, when correctly biased at their maximum power point, each junction operates as a current source. Because of this and their series electrical connection, they must be sized to generate identical photocurrents, as the resulting current from the stack will be equal to that of the junction with the least current generation. This makes them more spectrally sensitive than single-junction cells, and since the sun's spectrum is not constant during the day, it is inevitable that most of the time one or more of the junctions will

underperform and dictate the device's photocurrent. Because of this, well-designed CPV systems will exhibit a daily efficiency variation of a few percent, and significant design attention must be paid to the concentrator optical transfer function, since it modifies the incoming energy spectrum (McDonald and Barnes, 2008). It is worth noting here that recent research into the bandgap-widening effect of nano-structures, for example quantum dots or quantum wells, has met with success, and will serve to lower the spectral sensitivity of the cell, and increase overall energy harvest.

The above two concerns, along with other practical crystallography issues result in a very complex device with long technical development times, and ultimately a high intrinsic product cost. The output from a multi-junction cell is large, and can be exploited economically effectively only by HCPV systems.

It is worthwhile underscoring one final point, briefly visited above. Despite years of development and reliable operation in space, multi-junction cells are still technically young, with room for performance improvement. Currently commercially available cells have efficiencies of approximately 38.5% at 25°C, and some companies are demonstrating cells at around 42%. Notwithstanding the spectral issues mentioned above, enormous gains can be made in performance, and several reputable firms have three- to five-year product roadmaps that border on 50% efficiency. Indeed, the history of the multi-junction cell is one of steady, concerted performance gain year on year. Efficiency increases are a very strong lever in the cost of HCPV systems. Not only do the concentrators themselves become less expensive for a given power output, but with fewer systems to install per megawatt, balance of plant and operating and maintenance (O&M) costs will also decrease.

10.3.2 LCPV-specific characteristics

As mentioned above, LCPV systems occupy concentration ratios of between 1.25 and 40. Because of their low concentration, they can use designs that have lower achievable maximum concentration ratios, like parabolic troughs (Swanson, 2002: 479–482), linear Fresnel reflectors, the compound parabolic concentrator (CPC), (Winston *et al.*, 2005: 50–89) or the V-trough (Sangani and Solanki, 2007). These two-dimensional concentrators can be thought of as concentrating in one axis only, the other axis operating at one sun. In addition, their acceptance angle in the concentration axis is large compared to HCPV systems.

If the concentration is very low, for example around 2–2.5 suns, the acceptance angle in the constrained direction will be above 23.75°, which is the tropical latitude plus the angular radius of the sun. If the concentrator is positioned carefully, the sun's arc during the entire year will fall

within the acceptance angle, and the system will not need to track. For a theoretical treatment, see Luque (1989: 305). For cost reasons, these systems are usually constructed as V-troughs or possibly as a compound parabolic trough.

As concentration increases from 2.5 to, say, 10 suns, concentrators can be tracked by making seasonal adjustment only. Twice per year they are moved so that for the following six months, the sun's arc will fall within their acceptance angle of down to 12°. Continuing from 10 suns, the tracking requirements become increasingly more stringent, but still needing movement in one axis only.

Another consequence of the high acceptance angle is the ability of the LCPV system to operate with circumsolar and, in the very low concentration systems, most of the diffuse light. As a result, an LCPV system will have a smoother output response than an HCPV system under intermittently cloudy conditions.

For all of the above, there is a significant challenge to the design, fabrication and operation of an LCPV system: cost. Because of the low concentration levels used, LCPV systems cannot overcome the cost hurdles presented by high performance multi-junction cells, and so use silicon cells. The lowered output in turn demands that very inexpensive optics, thermal management and tracking systems be employed, since there is not as much power over which the support structures and mechanisms can be amortized. In principle, any low cost photovoltaic technology, for example thin film, could be used, but achievable optics and tracker costs have still mandated using high efficiency mono-crystalline silicon. In addition, because of the lower output, there are constraints on the amount of effort that can be expended on system maintenance, with the result that the very inexpensive systems also have to be quite reliable.

10.3.3 Medium concentration photovoltaic devices (MCPV)

From the interest shown at both ends of the concentration scale, there is ample evidence that viable products can be built and operated. There is no evidence yet of domination of HCPV over LCPV or vice versa, but more of differentiation into market segments. Interestingly though, there appears to be little work being done on equipment with concentration ratios between 50 and 200.

At the low end, parabolic troughs can operate above 40 suns, but they have a theoretical maximum concentration predicted by NIO to be around 100 suns and as they reach this limit, tolerances and accuracy requirements render them expensive, but with an output too low for effective amortization. In the solar thermal space, the mechanical and hydraulic advantages of troughs have caused designs to be refined around 80 suns, though there

is still a practical and cost limit significantly below what is theoretically possible.

At the high end of the spectrum, dual-axis tracking and multi-junction cells are the norm. As concentration decreases below, say, 250 suns, systems still need the trackers for accuracy, but the decreased power density increases the cost per unit power. At some point the high cost of the cell cannot be justified and the switch to silicon must be made. But with the lowered output, the two-axis tracker cannot be justified. One concentrator company operated a point focus system at around 150 suns with silicon for several years, but economics caused them to increase the concentration and migrate to a triple-junction cell.

In summary, the occupancy of both ends of the concentration landscape is due mainly to cost optimization. HCPV systems have sufficient output over which to amortize their relatively complex designs, while LCPV systems rely on non-stringent requirements for their optics and trackers, leading to low cost.

Now with a basic understanding of the characteristics of concentrator systems, their place in the market can be assessed.

10.3.4 Application to the market

The viable solar market spans an enormous range of geographies and weather systems, significantly complicated by access to transmission assets, finance, construction resources and power users or offtakers. Government at all levels and semi-government institutions, such as utilities add a further and important complication. In addition, while the residential rooftop market dominated the growth of the solar sector for many years, as the reliability of photovoltaics has been proved and costs shown to be increasingly attractive, interest in large installations has become common. Usually ground-mounted and increasingly in hot, dry areas of the world (e.g., around the Mediterranean), solar power stations of up through hundreds of megawatts are now under development, and will be in operation well before the end of the decade. The result is a rich set of competitive ecosystems that favor one or another of the many technologies available today. The question is: Where are concentrators appropriate?

The very low concentration devices – those that don't track – will find use alongside standard silicon panels. Their economic arguments usually center around panels with outputs similar to standard panels, but at lower cost because they use less silicon. Decreased acceptance angle when compared to standard panels makes them more sensitive to light scatter, and hence they will have to be cleaned more often, and they will be of limited use in very hazy conditions. This will apply pressure for larger installations, where the operation can be amortized over a larger number of panels, for

example on commercial rooftops. In addition, because they don't need to track, low concentration devices are probably the only viable concentrator for rooftop applications. A small number of companies have been developing higher concentration systems for rooftop application, but the economics have been shown to be risky, especially in the urban environment with significant levels of atmospheric scattering. The relatively low output of the stationary systems means they will be less competitive against higher concentration devices, so they will probably not find large use in field-mounted situations.

Tracking LCPV systems – those from 10 to 40 suns – have the advantage over HCPV in that they are less sensitive to manufacturing tolerances, but are disadvantaged in output density. While having higher output than stationary concentrators, their mechanical complexity and maintenance requirements will probably prohibit them from rooftops. Their output levels combined with wide acceptance angles, though, will make them ideal for distributed generation in the urban environment. Maintenance requirements and the complexity associated with installing mechanical systems will apply commercial pressure to install tracking LCPV systems in fields of at least tens to hundreds of kilowatts, so that O&M tasks can be carried out cost effectively. At the high end of LCPV, care must be taken with location, as the acceptance angle, combined with the pressure for very low manufacturing cost, is sufficiently small as to disadvantage them in areas of high diffuse radiation. Like HCPV, the top end LCPV systems will be limited to areas of high DNI.

HCPV systems have the highest power density of any photovoltaic technology. They also require the most complex, expensive tracking systems, and have the lowest acceptance angle. HCPV equipment will be economically advantageous when aggregated into power stations of hundreds of kilowatts through to many megawatts, and will be operated in areas of high DNI – the 'sun belt' regions. Specifically, their high power output under elevated ambient temperatures coupled with very small water use (and, in many cases, the ability to use untreated water), means that HCPV is ideally suited to hot, dry climates. This is a market niche for CPV which is, however, very large, and growing fast. Market research shows this to be approximately 50% of the ground-mount solar marketplace, or 20% of the total available market.

10.4 Design of concentrating photovoltaic (CPV) systems

The preceding discussion on the characteristics of the technology and its entry points to the market now sets the stage for an introduction to the design elements and challenges for a concentrator. The basic issues at the

heart of any CPV design are introduced in this section, and a small set of example products are described.

10.4.1 Levelized cost of energy

Ultimately, a CPV plant is a financial instrument, and investors will make technology and project partner choices based on a return analysis. In addition, since a solar plant provides an annuity throughout its lifetime, any investor will require an accurate assessment of its ongoing financial performance against expectations. An effective metric that provides both of these needs is the levelized cost of energy (LCOE). LCOE has been introduced in Chapter 2; it is an important metric for CPV system design as it is with any CSP technology (Short *et al.*, 1995). Fundamentally, it is a calculation of the lifetime cost of energy for any generating plant, brought back to net present value and includes all fixed and marginal costs, degradation in output, projected repair and replacement costs, and inflation and discount rate estimations. Expressed as ¢/kWh, this type of calculation can uniquely be used to compare technologies, for example CPV against PV, hydroelectric or fossil fuel generation. Short *et al.* (1995) define LCOE as 'that cost that, if assigned to every unit of energy produced (or saved) by the system over the analysis period, will equal the Total Lifecycle Cost (TLCC) when discounted back to the base year.'

The formal definition for LCOE, if tax issues are not considered, can be expressed as:

$$LCOE = \frac{NPV_{LCC}}{\sum_1^N (E_i/(1+DR)^i)} \qquad [10.3]$$

where E_i is the energy output in year i, N is the amortization period, DR is the discount rate, and NPV_{LCC} is the net present value of lifecycle costs, which is given by:

$$NPV_{LCC} = \sum_{i=1}^{N} \frac{C_i}{(1+DR)^i} \qquad [10.4]$$

where C_i is a cost during period i.

For a CPV system, the cost cashflows can be categorized as (Nishikawa and Horne, 2008):

- the cost of installing the CPV/concentrator system which will essentially be a single investment in year zero
- the cost of installing balance of systems (BOS), i.e. inverters, civil works, etc., will also be a single large investment in year zero
- the annual operation and maintenance cost.

Bringing back all costs and generation to net present value allows the comparison of different technologies with different financial structures and lifetimes to be made at the time of a potential investment.

The quantification of energy and not operating power is central to the theme of LCOE. While it is common to use installed capacity-centric costs ($/W or $/kWe) when discussing solar plant of all types, it has two very important drawbacks. First, the rating schemes for the various technologies are not the same. As explained by Melia *et al.* (2010), because of the way the rating conditions are defined, a 300 W HCPV panel will actually produce 300 W at 20°C and under 850 w/m^2 direct irradiance (the rating irradiance). The rating conditions are different for silicon panels, however, with the result that an identically labeled poly-silicon panel will produce 264 W under its rated condition of 1,000 w/m^2 global irradiance. These differences are due to test practicalities, but if used in the design phase, will lead to power plant of very different sizes being built, with different up-front investments and different energy harvests.

Second, the specific energy, a metric used to indicate the ability of a technology to harvest energy, and defined as the ratio of kWh_{annual} to kW_{rated}, varies considerably by technology. There are many reasons for this, including whether a technology is mounted on a tracking system, the size of the temperature dependence on output, geographic spacing of systems, the acceptance angle and their susceptibility to soiling. As an example, a CPV system with a very narrow acceptance angle might produce as much power when directed on the sun as one with a wider one, but over the course of the year, the larger acceptance angle system will admit more circumsolar radiation, will be less susceptible to tracking errors, alignment issues and foundation movement. The product with the larger acceptance angle will harvest more energy, returning a greater annuity to the investor. So, using a power-based metric tells very little of the investment story, and eliminates the ability to choose between technologies or project equipment suppliers.

LCOE is gaining ground as a standard metric, largely due to the US Department of Energy and NREL investing significant effort in publicizing its value and producing tools for its use. The reader is advised to investigate the Solar Advisor Model (SAM) from NREL, and explore its supporting documentation (Gilman *et al.*, 2008).

10.4.2 General system design goals

Generally, the overall design goal of a CPV system is to produce a product that minimizes the LCOE in the chosen geography. Within that simple statement, however, lie many challenges and trade-offs. The first is that of scale.

To a first order approximation, regardless of efficiency, all PV technologies need to be fabricated and deployed in very high volume. Consider a 30 MWP_{dc}-rated CPV power plant with equipment operating at 27% efficiency, and a concentration ratio of 500 suns. At that efficiency, the input power would have to be 1.1×10^8 W to satisfy the output requirements. At the 850 w/m^2 irradiance rating, 1.3×10^5 m^2 of concentrator area would be required which, at 500 suns, means 2.6×10^2 m^2 of cell. A common size for a concentrator cell is 7.5 mm on a side, for approximately 0.56 cm^2, so 4.7 million of these cells would be installed in the plant. Each of these cells will require electrical connections, cooling, alignment, a share of the optical system and eventually to be integrated on a tracker of workable dimensions. Given the sheer numbers associated with this moderately sized plant, it should be clear that very high volume manufacturing, in the scale of the automotive industry, for example, is needed for successful CPV deployment.

Luckily, most photovoltaic concentrator designs, while seemingly complex, lend themselves exceptionally well to standard high volume manufacturing techniques as used, for example, in the automotive or electronics industries, with their attendant low costs of production. They are essentially an assembly operation, as opposed to thin film, for example, where thousands of square meters of complex vacuum deposited material must be produced.

Further, despite the complexity of CPV systems, they must be able to operate within accepted reliability norms for solar, usually guaranteeing 80% output after 25 years. A very good understanding of degradation mechanisms at work in any concentrator design is of paramount importance, as is the ability to accurately measure them. While this might seem to be a difficult task for a new technology, two things must be considered. First, because concentrators are assemblies, their components and assembly methods can be designed and tested separately for reliability. Second, if designed well, many of the subsystems use techniques, materials and assembly methods adopted from other industries with years of experience. Test protocols, design advice and degradation data are all available to guarantee a reliable system. An aluminum drawn backpan for a concentrator, for example, can use techniques from the automotive industry where simulations, materials choices and test techniques can all guarantee 25-year longevity.

Finally, performance is important, and the paramount concept is, as mentioned above, minimizing the LCOE of the product. This metric is informed by all other performance parameters and in turn will inform the financial performance of the field.

There are many degrees of freedom with concentrator design, and as a result, many different styles of product have emerged. So many, in fact, that

categorization has been virtually impossible beyond those of HCPV and LCPV. Adding to the confusion is the fact that there are still many unexplored design pathways. Observing some trends, however, one can make some necessarily imprecise generalizations. The rest of this chapter will describe these general categories. A small set of examples will be used for illustration.

System granularity

System granularity refers to the overall architecture, and whether the concentrator is composed of an array of small concentrators (usually each irradiating a single cell), or a single, large optic, powering an array of cells. There are instances of both approaches, covered in the examples below. An array of small concentrators is by far the most common approach, as it lends itself better to modern manufacturing techniques.

Optical method

The optical method may be refractive, reflective, or catadioptric (which employs both refractive and reflective techniques). The former two are the most common, with refractive Fresnel systems being favored by many. Cassegranean reflectors are being pursued by a smaller number of companies, as are single reflective optics. Catadioptric non-imaging optical elements are sometimes used as the last stage of a complex concentrator. One example of a complete concentrator of this type was designed and prototyped at Universidad Polytechnic Madrid (Swanson, 2002: 492–494) though it has not been commercialized. The optical design will drive all other aspects of a concentrator design, from thermal management through to the manufacturing processes that come available.

Tracking type

There are many mechanical styles of tracking systems. Degree of concentration will largely determine whether single- or double-axis tracking is chosen. Beyond this, there are not a strong set of criteria. Each appears to have advantages and disadvantages, none of which appear to be overwhelming. Tracker types generally fall into three broad categories:

1. Azimuth/elevation tracking systems (see Fig. 10.5 above) sit on top of a pedestal or pole, with one axis rotating vertically (azimuth) and the other horizontally (elevation). Polar tracking systems are a subset of this, where one of the axes, usually the azimuth, is inclined at the local latitude angle.

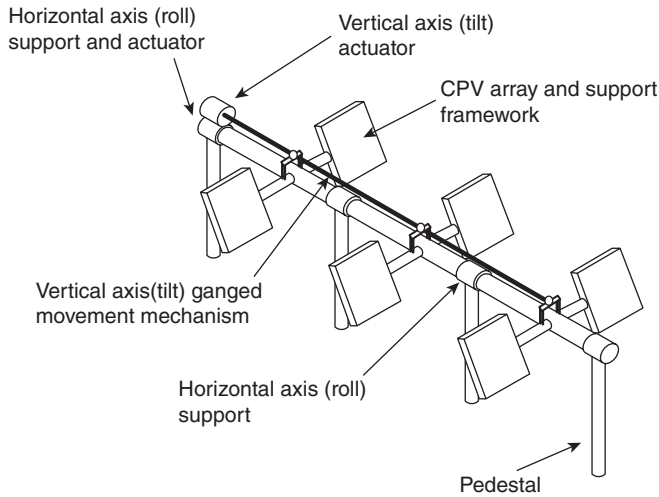

10.6 Tilt-roll tracker.

2. Tilt/roll systems have one horizontal axis and a second, attached to the first, at a right angle to it. An example of a tilt/roll tracker is shown in Fig. 10.6.
3. Finally, carousel trackers are a special form of the azimuth/elevation tracker, but are very compact, and possibly suitable for rooftop mounting. They are mechanically complex, however, and present a manufacturing and tolerancing challenge.

There are multiple means to control or steer tracking systems. First, movement is commonly driven by electric motors, though there are several examples of hydraulically actuated systems on the market. Control system algorithms vary from using external sensors, to sampling the output of the concentrator itself, to dependence on an ephemeris equation. While there remains a great deal of variation on the market, a combination of ephemeris plus monitoring the concentrator output appears to be the most practical method.

Trackers are a complex topic, especially when the issues of wind, local building codes, structural vibrations, logistics, deployment, and lifetime are considered. Details are, unfortunately, beyond the scope of this single chapter on CPV.

Environmental control methodology

CPV systems need to include thermal management of the cell. Despite the high efficiencies of multi-junction cells, currently still over 50% of the

incident energy is converted to heat, which must be removed in order to maintain reliability. In general the trend is towards passive, dry cooling, where the thermal energy is conducted away from the cell, then radiated and convected to the atmosphere. Active air cooling schemes have been tried on some systems, but generally the need for reliability and low maintenance costs mandate against them. Concentrators with larger optical systems and those with very large concentration ratios generally must use active cooling, which can include heat pipes and fluid reticulation.

Additionally, there is a need to protect the optical systems from the elements. Fresnel lenses with their fragile teeth and generally deep valleys would lose efficiency rapidly if employed in the outside environment. They are almost universally enclosed within a housing, where the front window is flat, and the lens elements are moulded or embossed onto the inner, protected surface. Reflective systems have more leeway, and several designs have external mirrors, in the same manner as solar thermal technologies. Several reflective technology companies still choose to house the mirrors, however, further protecting them.

In general the environment inside the housing is maintained through the use of passive air filtration, though active drying techniques have been seen.

Cell management

The immediate area around the cell itself is a technical and financial challenge. Within a few millimeters of the cell, thermal management must be carried out, robust electrical connections made, a bypass diode mounted, mechanical alignment carried out, and possibly very high incident solar flux managed, regardless of the alignment of the concentrator. There have generally been two approaches to these multiple challenges. The first has been to simply mount the cell or an assembly consisting of the cell and bypass diode on the concentrator superstructure, and complete the construction around it. In the second approach, a 'receiver', which consists of the cell or cell array and related thermal, electrical, and optical components, is assembled separately and mounted as a subassembly to the concentrator in an independent manufacturing step.

Both approaches have their advantages, generally in the manufacturing arena, and there are examples of both in the market.

10.5 Examples of concentrating photovoltaic (CPV) systems

Following are examples of some of the CPV systems that have been built in significant volume or are under development.

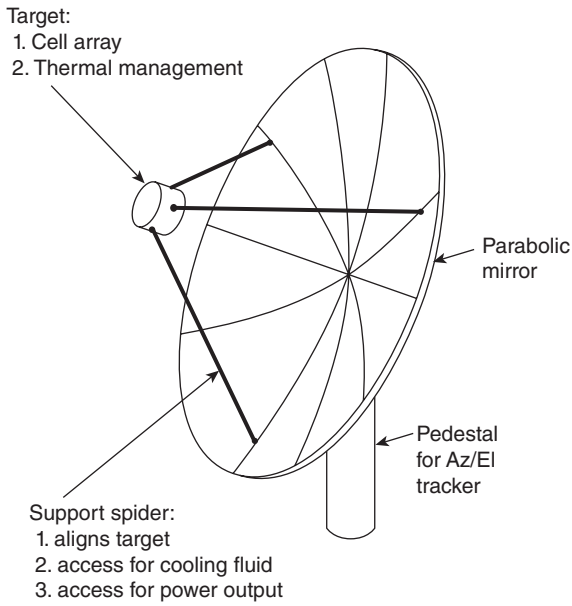

10.7 Point focus, imaging paraboloidal concentrator.

10.5.1 HCPV single dish reflective

Many early HCPV concentrators were built to a design common to optical and radio telescopes: the point focus, imaging paraboloid (Fig. 10.7). Solar Systems of Australia has commercialized one version, a large single reflecting optic of approximately 15 m in diameter, targeting an array of water-cooled multi-junction cells (Fig. 10.8). Several significant installations have been operating for some years in the center of Australia, powering remote grids and demonstrating the efficacy of the approach.

These systems are optically highly efficient, because they use only a single reflective element to achieve the necessary concentration. In addition, the optics are external, and not enclosed within a housing, so there is no transmission loss through a front window. Being reflective, they do not suffer from chromatic aberration. This architecture, though, while delivering high peak power, suffers from a limited acceptance angle. Because it is a single-element imaging system, as shown by Welford and Winston (1989: 31–51), the attainable acceptance angle for a given concentration will be much less than that of a non-imaging design, practically between 25% and 50% of what is possible. The system, then, needs to very accurately track the sun, and will be susceptible to atmospheric scatter.

Energy conversion by an array of cells mandates the use of liquid cooling, but also allows it, since relatively expensive pumps, filters, valves, radiators

10.8 Example of a point focus imaging paraboloidal concentrator from Solar Systems, Australia.

and piping can be amortized over a large power output. This is in contrast to the array-based systems described later, which, with an optical element per cell, are limited to mainly passive cooling. The parasitic energy required by the active cooling system, however, can rob several percent of the harvested energy from the system. While less than the 10% estimate for most thermal systems, this loss is significant. There are further compromises to consider also.

First, the interaction of the multi-cell target, and the inherently non-homogeneous illumination received from the reflector will decrease output due to mismatched cell photocurrents between the different cells in each series connected string. This effect can be minimized by the use of a blocking diode per cell, but cannot be eliminated. This spatial variation in power delivered to the cells will vary over time as the system tracks the sun, so an optimum electrical connection architecture for the cells is difficult to realize.

Second, the cells produced by all current manufacturers include a busbar on the light-facing side of the cell, for the negative terminal. There are no back-side contacts, as in some high-performance silicon cells. The area presented by the busbar and associated electrical connection does not itself

generate electricity, and represents a harvest loss that can be higher than 5%. This issue can theoretically be minimized by the use of reflectors on top of the cell busbars, but to the author's knowledge, this has not been tried.

Finally, the exposed mirrors will lose more power for a given amount of soiling than will any system where the external interface is a transmissive element, for example a Fresnel lens or a flat window (Vivar *et al.*, 2008). This is because not only will a particle of dust shade incident light, it will also scatter light reflected from a nearby area of the mirror.

Field examples use segmented mirrors to improve installation viability, and the mirrors are fabricated from glass, metalized on the second surface. This helps with the need for high precision optical alignment processes in the field, but by no means eliminates this somewhat slow and skilled task. Mirrors constructed in this manner for the solar thermal industry can withstand years of mechanical cleaning, but especially with the new non-metallic protective layers mandated by environmental laws, still have questionable longevity when used outdoors (Kennedy *et al.*, 2007).

The remainder of the system consists of a space-frame mirror mount attached to an azimuth/elevation tracker.

So, while optically efficient, energy harvest in a single dish reflective HCPV system presents a number of issues, its acceptance angle is quite low, and it will be more sensitive to contamination than most other types.

10.5.2 HCPV Fresnel lens array

In this approach, a Fresnel lens (either refractive or catadioptric) is mounted on a housing to entrain light to a photovoltaic cell or cells. Figure 10.9 shows a classic refractive Fresnel lens design. The reader is directed to Leutz and Suzuki (2001) for an excellent treatment of the complete genre of Fresnel lenses. The design is straightforward, though because the optical path is not folded (a possibility only if using reflectors), it yields a deep system with somewhat stringent mechanical tolerance requirements.

The vast majority of Fresnel systems are constructed as assemblies of small concentrators within an enclosure, with one cell per optical system. Usually the front of the enclosure is the lens or a series of lenses and support members. While the lenses themselves can be fabricated in large geometries, their size is chosen in consideration of the target concentration, the cell size and its thermal management requirements, and the maximum reasonable depth of the enclosure. Using one cell per optical assembly minimizes problems encountered from inhomogeneous illumination. The cells themselves can withstand a surprising degree of non-homogeneity with low efficiency loss (Katz *et al.*, 2006), and it is easier to balance the radiation on each cell in a string through the use of a dedicated optical system than by illuminating an array of cells from a single optic.

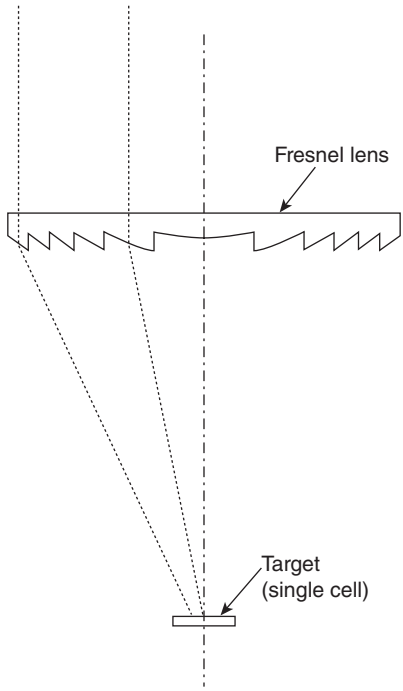

10.9 Cross section, refractive Fresnel lens concentrator.

The main benefit of a concentrator of this type is its high optical efficiency through the use of a single optical element, or two in the case where a non-imaging final stage is used. However, while a simple system, the Fresnel lens does exhibit losses that are hard to overcome. First, the teeth of the Fresnel system have to be made very accurately in order to achieve high concentration. Rounding at the teeth tips and filling in of the intervening valleys due to manufacturing imprecision can cause light scattering, and mechanical requirements for efficient mold operation can cause obstructions in the light path. In addition, an anti-reflective coating can be placed only on the flat part of the Fresnel and not the toothed surface, which contributes a further energy loss through unwanted reflection.

These relatively simple, high-efficiency optics do not yield the best acceptance angle, so these concentrators, while possessing high peak power, need to track the sun quite accurately to minimize output variations. The acceptance angle limitation also means they are more susceptible to large particulate aerosols, for example those found in cirrus clouds.

In addition, chromatic aberration, in which the refraction of the light through the lens is frequency dependent can lead to losses if not properly

managed. The effect of chromatic aberration is to alter the spectral balance on the cell, with a resulting energy conversion loss.

Most of the above problems can be minimized through careful design. Swanson (2002: 488) shows a domed lens that eliminates the tip losses, for example, and Leutz and Suzuki (2001: chapter 6) illustrate many methods in great detail. There are several Fresnel systems that minimize these problems, and lens efficiencies approaching 90% are possible (Leutz and Suzuki, 2001: 118).

Fabrication of the lens has split into two camps: poly(methyl methacrylate) (PMMA, or acrylic) and silicone-on-glass (SOG). PMMA has the longest history and is the easiest to fabricate, usually by embossing the lens elements onto a flat sheet of PMMA. Good mechanical tolerances can be achieved, and the process is fast, and scalable to high volume production. A PMMA lens, though, suffers from surface and internal degradation (Rainhart and Schimmel, 1974), and is known to be susceptible to damage from mechanical cleaning (e.g., with a squeegee) and stain-causing airborne pollutants.

SOG lenses are fabricated by casting the Fresnel lens elements onto one face of a sheet of glass using a clear silicone gel. Silicone bonds well to glass, and the mechanical structures formed are at least as accurate as with PMMA. In addition, the lens has a durable outside face of glass and does not suffer the degradation problems of PMMA. While questions still exist about the robustness, scalability and ultimate cost of lenses built this way, they are becoming more common in Fresnel concentrators.

The balance of the concentrator is made by forming a backpan, which contains the cells or receivers, alignment mechanisms for the lens array, any environmental control (e.g., filters or air dryers), and the means for attachment to a tracker. While it is usually fabricated from metal, at least one backpan has been prototyped from injection-molded plastic, and a system with an all-glass backpan is undergoing commercialization.

A significant advantage of the optical array architecture is that the majority of the high precision operations are carried out in the factory and not in the field. The receiver's size and components lend themselves to assembly on standard electronic assembly lines (including the use of high-speed pick-and-place equipment). The low number of part types intrinsic in an array-based design also allow for highly automated assembly, and automotive style manufacturing lines using six-axis robots are becoming common. The result is that completely operational, tested modules are shipped to the field, requiring a minimum amount of in-field alignment. Installation is possible by supervising locally sourced labor with a minimum of training. Depending on the ultimate size of each module, their installation on the tracking system can be done with locally sourced equipment.

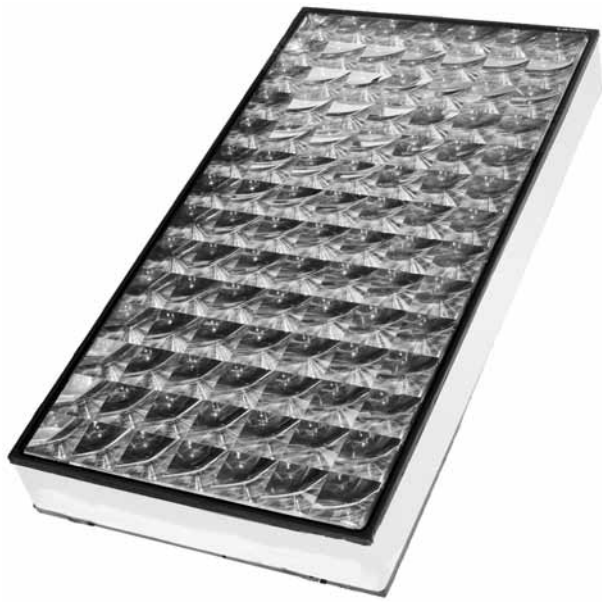

10.10 Example of a refractive Fresnel lens concentrator from Concentrix GmbH, Germany.

Fresnel concentrators are the most common of all, with the most mature companies being able to show several years of field experience. Concentrix GmbH, a spin-out from the Fraunhofer laboratories is one such leader, with their advanced silicon-on-glass FLATCON© concentrator. Figure 10.10 shows one module of their system. Several of these modules are integrated on the support frames of their proprietary dual-axis tracker to produce a system of approximately 6 kW rated power. Concentrix has installed a significant number of systems globally, and operates a 25 MW/year manufacturing plant.

10.5.3 HCPV complex reflective

Cassegrain optical geometry can be used to produce a concentrator system with very compact geometry, with wide acceptance angle and good efficiency (Fig. 10.11). In this design, a converging primary mirror entrains light on a diverging secondary, which in turn focuses on the entrance to an NIO final stage concentrator. Having the optical path 'folded' in this manner produces a system that can be more than three times more compact than a Fresnel system for a given input optic size. In general, mirrors are more efficient than refractors, and make possible the introduction of a larger

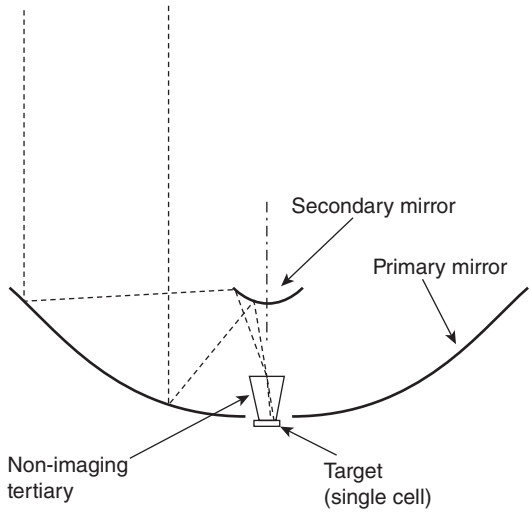

10.11 Cross section, reflective cassegrainean concentrator coupled to a non-imaging tertiary.

number of optical surfaces between sun and cell without large power loss. This increases flexibility when making efficiency, energy harvest, and manufacturability tradeoffs, over that of simpler systems.

Like Fresnel systems, this approach lends itself to being constructed as assemblies of small concentrators with one cell per optical system and with the use of prefabricated receivers. The optical system's size is also chosen for reasons similar to the Fresnel: concentration, cell size and thermal management technique. The folded optical path greatly reduces the bulkiness of the assembled system, which benefits assembly, logistics, and fielding.

With careful design, excellent efficiencies can be achieved, approaching what is possible with simpler systems. The larger number of optical surfaces directly trades against the throughput efficiency limits of the Fresnel lens and in principle the difference can be small. In practice, however, since very high quality reflective surfaces are expensive, Fresnels are usually somewhat more efficient than cassegrain reflectors, at least when considering only the transport of light through the optical system. Because of the use of reflection as opposed to refraction, however, the cassegrainean system delivers its efficiency with barely a trace of chromatic aberration and, especially at high concentration ratios (e.g., 1,200 suns), this can greatly mitigate the throughput loss as the spectral/spatial characteristic of the output light is better matched to the cell.

In addition, the complex optics allow acceptance angles reasonably close to the practical limit, and within its acceptance angle the output can be

made more uniform than that of more simple optical systems, which exhibit a more sinusoidal response over angle. Gordon (2010), for example, illustrates two reflective surfaces being tailored to produce an aplanatic system, that greatly minimizes coma, an optical aberration that deteriorates acceptance angle. As a result, a cassegrainean HCPV system will be less susceptible to scattering by suspended aerosols, and will be less sensitive to manufacturing tolerances and moderate tracking errors.

It is also worth noting that with the array approach, the reflectors are generally placed behind the window of a housing, rendering a flat, easy to clean surface and further decreasing the susceptibility of the concentrator to soiling.

The main drawback is the complexity of the system, which mandates a refined approach to volume manufacturing, including a well thought out automation strategy. While many prototype cassegrainean concentrators have been built over the years, a marriage between design and automated processes has only recently been successful.

Reflectors can be constructed of many different materials and using many techniques, since light need not necessarily be transmitted through the optical element. Importantly, in order to transmit the entire spectrum the multi-junction cell is sensitive to, there are a limited number of practical options for the reflecting material, which usually employs silver, or spectrally enhanced silver or aluminum. There are other significant tradeoffs in the combinations of materials and techniques, and their importance depends somewhat on the overall design. There is not, currently, a single obvious methodology. Table 10.2 illustrates the advantages and disadvantages of some of the more common materials and forming techniques.

As in practical Fresnel systems, the design is rounded out with a backpan. Because of the compactness afforded by a folded optical path, it can be fabricated from a simple stamping operation, yielding an inexpensive and robust subassembly. All of the manufacturing advantages associated with array-based architectures described above apply, and multi-megawatt/yr manufacturing plants have been shown to be inexpensive and fast to start up. Operating and tested concentrator panels are delivered to the field site, and the large acceptance angle minimizes requirements for planarizing the panels on the array frame. This speeds the overall installation process.

The SF-1100 from SolFocus Inc. is one example of a commercially ready system. Based on slumped glass mirrors, the optics are protected inside a glass and drawn metal housing. Twenty-eight of these modules are aggregated on a proprietary dual-axis tracker, to yield 9.2 kW under rated conditions (Fig. 10.12). The company has over three years of operation on its equipment and runs a 30 MW/year, highly automated production line. SolFocus has installed globally, and has shown that locally sourced labor and equipment can efficiently build a solar power plant based on the SF-1100.

Table 10.2 Comparison of reflector fabrication techniques

Base material	Forming technique	Metalizing technique	Advantages	Disadvantages
PMMA	Vacuum forming	Front surface, vacuum deposition	Lightweight	Hydrophilic material. Ag adhesion issues. CTE mismatch with most protective coatings.
PMMA	Injection mold	Front surface, vacuum deposition	Lightweight Large array fabrication	Hydrophilic material. Ag adhesion issues. CTE mismatch with most protective coatings. Needs very good mold quality.
Polyolefin or polycarbonate	Injection mold	Front surface, vacuum deposition	Hydrophobic Lightweight Large array fabrication	Most expensive option. Ag adhesion issues.
Glass	Slumping	Rear surface, liquid deposition	Hydrophobic Least expensive Good Ag adhesion	Difficult to fabricate an array of mirrors.
Aluminum	Drawing	Electro-deposition, with or without a base layer of polymer or glass frit	Lightweight, robust	Good surface finish is very difficult to achieve.

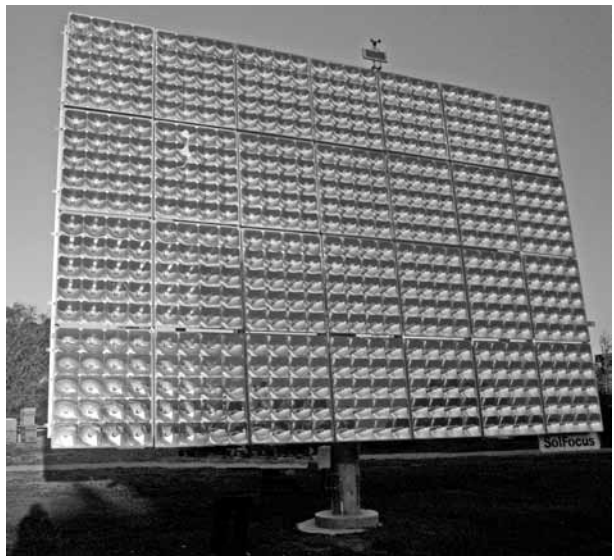

10.12 Example of a reflective cassegrainean concentrator from SolFocus Inc., USA.

10.5.4 LCPV reflective

There are a modest number of LCPV systems under development, including the V-trough non-tracking concentrator. This design can be thought of as an inexpensive silicon panel, and with few restrictions, can be used interchangeably. Because of the similarity to standard panels, the V-trough will not be considered here. Instead, we will consider a tracking example, a system similar to that of Benitez *et al.* (1997) called the dielectric single-mirror two stage (DSMTS) concentrator, and which is under commercialization.

This device operates at concentration sufficiently low that a point focus optical system is not needed, and a less expensive linear design can be employed. In addition, single-axis tracking is sufficient. It consists of two trough-shaped reflecting elements, arranged to direct light onto each other's strip receivers' mounted reflector edges, as shown in Fig. 10.13. Because of the low concentration, the optical target area is too large for the use of multi-junction cells to be economically viable, and high performance silicon cells are used instead. This is a very low cost approach that allows the reflector to be the alignment and mounting device for the receivers.

With only a single optical element, the optical efficiency will be quite high, and being a trough, the irradiation on the cells will be uniform in the lengthwise direction. Because of the low concentration (approximately 40 suns), the acceptance angle will be reasonably large, and the system can be tracked on an inexpensive tilt/roll system. In addition, the wide acceptance

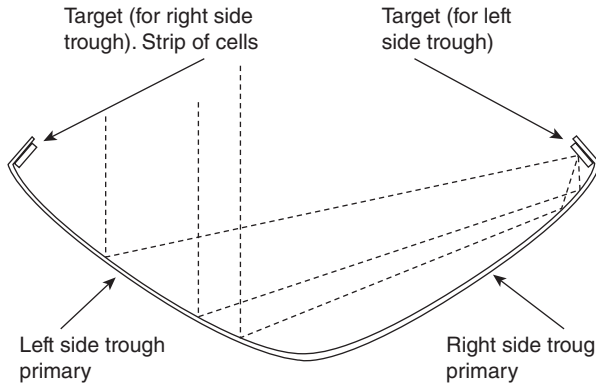

10.13 Cross section, reflective DSMTS linear concentrator.

angle will allow some of the diffuse radiation to reach the cell, and as a result, this system should see service in the urban environment.

Limiting the output is, in first place, the performance of the silicon cell itself. With the high temperature coefficient and rated efficiencies around 17%, the cell is only half as efficient as the best multi-junction cell, which puts large cost pressures on the optics and mechanical structure. Second, because of the high flux on the cells, efficiency loss due to temperature rise occurs, and must be minimized by the use of a very inexpensive but effective thermal management system on the back side of the receivers. These constraints have been sufficiently extreme to render most attempts at LCPV unsuccessful until recently.

The mirrors can be fabricated from rolled aluminum sheet. The limited frequency response of the silicon cells allows this, and is in contrast to most HCPV systems, where any reflecting surface must be constructed of silver, for wide bandwidth reflection. The aluminum sheet can be both the mirror and the support structure. In addition, low concentration allows for more lenient fabrication tolerances, making forming of the mirror using standard automotive manufacturing techniques feasible.

Skyline Solar is producing a concentrator based on these techniques, and has successfully installed at several pilot-sized sites. A fairly new entrant to the industry, they are combining the inherent advantages of LCPV with a mature understanding of high volume manufacturing to produce their high gain solar system. Figure 10.14 is a photograph of one of their systems.

In summary, as can be seen, there are significantly different approaches to concentrators. The above represent a very incomplete list and is based on the subset of designs that are furthest along in commercialization. There are many other ideas and technologies still under development, and a sampling of industrial trends follows.

10.14 Example of a reflective DSMTS concentrator from Skyline Solar Inc., USA.

10.6 Future trends

The CPV industry is maturing, with several companies deploying well-developed products, manufactured on high-volume, automated assembly lines and complete with high-quality warranties and documentation. The industry has its first set of qualification standards (IEC62108), and the CPV Consortium, formed in 2008, now has many members representing the entire supply and deployment chain.

Interestingly though, there is still a lot of basic technical research to be done, especially in the areas of optics, high-performance cells, tracking systems and algorithms, and as a result, the field is still attracting the attention of academic institutions and startup companies worldwide.

The push to commercialization has opened up new fields of research, as the drive to manufacture, deploy and successfully operate the equipment has increased. Now that significant installations are being undertaken, new topics receiving research attention include the interaction of concentrators and the electricity grid, the effect of weather statistics, and the development of highly deployable designs.

Therefore, future trends in the industry are beginning to look quite complex as the research landscape widens, not decreases. A very brief overview of some of the trends follows.

10.6.1 New generation optical systems

Optical systems, at least practical systems for HCPV products, can still benefit from efficiency and acceptance angle improvements. While the more common designs described earlier are being honed for

cost, performance and reliability, there are a few new approaches under development. As mentioned above, Universidad Polytecnic Madrid has demonstrated a unique and efficient optical system for use by small (on the order of 1 mm^2) multi-junction cells. This effort has not proceeded past the prototype stage, however, and has proven difficult to fabricate. If perfected, this approach promises the best acceptance angle for a given amount of concentration.

Very flat concentrators using TIR have been described (Karp *et al.*, 2010), and are being commercialized by at least one company. Constructed of PMMA, they show promise of low cost, albeit with degraded optical efficiency due to long optical path lengths. At present there are no commercially available systems of this type.

10.6.2 Next generation cells

Several companies are marrying the technology of nanostructures (quantum wells and quantum dots) to the semiconductor junctions of multi-junction cells. These structures provide the designer some control over the bandgap of the junction, to tune it for maximum efficiency. Interestingly, nanostructures can widen the bandgap of a junction, rendering it less spectrally sensitive and possibly allowing a larger energy harvest over the daily spectral variation. No cells with these new structures have yet been commercialized.

Further, different alloys are being experimented with for the junctions themselves. The traditional materials used for multi-junction cells were arrived at by use of relatively low-cost epitaxy techniques, primarily metal organic chemical vapor deposition, and selection of materials that are lattice-matched. If some of these constraints are lifted, for example moving to molecular beam epitaxy, more complex alloys can be produced, with interesting PV properties. Several companies are pursuing this path, and are working through the problems associated with defects and mechanical strain induced by material groups that have different lattice constants.

The ability to form light traps from nanostructures and/or change the direction of light so that it traverses a longer path through the cell is being researched. This will allow more efficient anti-reflection coatings to be developed, and significantly, will allow these coatings to accept light over a much larger input angle than the current generation of cells. This will open the door to higher system concentration ratios.

10.6.3 System level research

CPV systems are interacting with the environment in larger numbers, prompting research in several fields. Most of this work is new, and aimed

at improving energy harvest, including a better understanding of the effects of weather and the interaction with the electricity grid.

For example, CPV systems produce a variable output, because of their dependence on DNI (see Fig. 10.4 and associated explanation above). This could lead to grid stability difficulties when, for example, intermittent clouds modulate the output of a large CPV plant (e.g., 50 MW) that contributes significantly to local generating capacity. A geographically dispersed 50 MW CPV plant – say ten 5 MW systems positioned along a transmission line – would mitigate this effect. The question is, what is the optimum spacing, how geographically sensitive is it and how is the spacing determined?

Another area undergoing scrutiny is that of inverter granularity. An inverter may be provided per panel, per string, per system, per field subset and finally, per field. At one extreme, it is reasonably simple to show that if it were possible to produce an inverter or DC power management device per cell, energy harvest would be maximized. This is also, though, the most complex solution, and potentially the least reliable and most expensive. At the other extreme, a field-level inverter is large, inexpensive and efficient. Energy harvest suffers, however, from the interaction of a large number of electrically paralleled strings in which the adverse effects of module performance variability and daily system-to-system shading cannot be mitigated. This tradeoff is under investigation by several power management companies with a view to optimizing architecture.

There are many other examples of research being done at the system level that will positively influence the industry in the near future. As a result, it is expected that the improving trends in performance and cost will continue into the foreseeable future.

10.7 Conclusions

Photovoltaic concentrators are a relative young technology, but have established commercial credentials. While several companies are arguably well down the commercialization path, there are still many newcomers to the scene, and there is a visible intellectual churn within the arena. Because of its youth, the industry enjoys the benefit of potential for improved performance and decreased cost, which is spurring investment, research, and development.

Concentrators are ideally suited to automotive manufacturing techniques, since they are predominantly an assembly operation. Automotive capital equipment is readily available, inexpensive and well tried. Systems are often assembled from components that have analogs in other industries, and employ materials that have been in use for many years. Thus, despite their relatively recent appearance on the photovoltaic scene, if well designed, they can be robust and reliable.

These factors have contributed to a rapidly maturing industry that is capable of increasingly competitive electricity costs as volumes grow and new ideas are embedded in products. Sustained performance improvements and the greater adoption of automation will ensure the permanent place of CPV within the pantheon of solar technologies.

10.8 References and further reading

American Society for Testing and Standards (ASTM) (2008), 'ASTM G173-03(2008) Standard tables for reference solar spectral irradiances: direct normal and hemispherical on 37° tilted surface'.

Baxter R (2006), *Energy storage: A nontechnical guide*, PenWell.

Benitez P, Mohedano R, Miñano J (1997), 'DSMTS: a novel linear PV concentrator', *Photovoltaic Specialists Conference 1997*, 1145–1148.

Bett A, Dimroth F, Siefer G (2007), 'Multi-junction concentrator solar cells', in Luque A, Hegedus S, *Handbook of photovoltaic science and engineering*, John Wiley & Sons.

Gilman P, Blair N, Mehos, M, Christensen C, Janzou S (National Renewable Energy Laboratory), Cameron C (Sandia National Laboratories) (2008), 'Solar Advisor Model User Guide for Version 2.0', NREL technical report NREL/TP-670-43704.

Gordon J (2010), 'Aplanatic optics for solar concentration', *Optics Express*, 18 (S1).

Green M (1998), *Solar Cells. Operating principles, technology and system applications*, Prentice-Hall.

Karp J, Tremplay E, Ford J (2010), 'Planar micro-optic solar concentrator', *Optics Express*, 18 (2), 1122–1133.

Katz E, Gordon J, Feuermann D (2006), 'Effects of ultra-high flux and intensity distribution in multi-junction solar cells', *Progress in photovoltaics: research and applications*, 14, 297–303.

Kennedy C, Terwilliger K, Jorgensen G (2007), 'Further analysis of accelerated exposure testing of thin-glass mirror matrix', NREL report ES2007-36182.

Kurtz S, Geisz J (2010), 'Multijunction solar cells for conversion of concentrated sunlight to electricity', *Optics Express*, 18 (S1).

Leutz R, Suzuki A (2001), *Nonimaging Fresnel Lenses. Design and performance of solar concentrators*, Springer-Verlag.

Lorenzo E (2002), 'Energy collected and delivered by PV modules', in Luque A, Hegedus S, *Handbook of photovoltaic science and engineering*, John Wiley & Sons.

Luque A (1989), *Solar cells and optics for photovoltaic concentration*, IOP Publishing Inc.

McDonald M, Barnes C (2008), 'Spectral optimization of CPV for integrated energy output', *Proc SPIE*, Vol 7046, 704604.

Melia J, Horne S, Klaren A (2010), 'Rational ratings', *Proc 25th European Photovoltaic Solar Energy Conference*.

Miyashita N, Shimizu Y, Okada Y, Institute of Applied Physics, University of Tsukuba (2007), 'Effect of increasing nitrogen composition on the performance of GaAs/GaInNAs heterojunction solar cells', *Proceedings 22nd European Photovoltaic Solar Energy Conference*, 414–418.

Nishikawa W, Horne S (2008), 'Key advantages of concentrating photovoltaics (CPV) for lowering levelized cost of electricity (LCOE)', *Proc 23rd European Photovoltaic Solar Energy Conference*, 3765–3768.

Olson J, Kurtz S (National Renewable Energy Laboratories) (1993), Current-matched high-efficiency, multi-junction monolithic solar cells, US Patent number 5,223,043, issued Jun 29, 1993.

Olson J, Friedman D, Kurtz S (2007), 'High-efficiency III-V multijunction solar cells', in Luque A, Hegedus S, *Handbook of photovoltaic science and engineering*, John Wiley & Sons.

Rainhart L, Schimmel W (1974), 'Effect of outdoor aging on acrylic sheet', *Solar Energy*, 17, 259–264.

Reich-Weiser C, Dornfield DA, Horne S (2008), 'Environmental assessment and metrics for solar: case study of SolFocus concentrator systems', IEEE PV Specialists Conference, San Diego.

Rosenthal A, Lane C (1991), 'Field test results for the 6MW Carrizo solar photovoltaic power plant', *Solar Cells*, 30, 563–571.

Sala G, Luque A (2007), 'Past experiences and new challenges of PV concentrators', in Luque A, Andreev V, *Concentrator photovoltaics,* Springer.

Sangani C, Solanki C (2007), 'Experimental evaluation of V-trough (2 suns) PV concentrator system using commercial PV modules', *Solar Energy Materials and Solar Cells*, 91, 453–459.

Short W, Packey D, Holt T (1995), *A manual for the economic evaluation of energy efficiency and renewable energy technologies,* National Renewable Energy Laboratory, March.

Spectrolab (2010), CDO-100-C3MJ Concentrator Solar Cell data sheet. Available from http://www.spectrolab.com/DataSheets/PV/CPV/CDO-100-C3MJ.pdf.

Swanson R (2002), 'Photovoltaic concentrators', in Luque A, Hegedus S, *Handbook of photovoltaic science and engineering*, John Wiley & Sons.

Thomalla E, Köpke P, Müller H, Quenzel H (1983), 'Circumsolar radiation calculated for various atmospheric conditions', *Solar Energy*, 30 (6), 575–587.

Vivar M, Herrero R, Martínez-Moreno F, Moretón I, Antón I, Sala G (2008), 'Effect of soiling in PV concentrators: mechanisms of light dispersion and real field performance of soiled flat modules and CPV's', *Proc 23rd Photovoltaic Solar Energy Conference, Valencia, Spain*, 142–145.

Welford W, Winston R (1989), *High collection nonimaging optics*, Academic Press.

Winston R, Miñano J, Benítez P (2005), *Nonimaging optics*, Elsevier.

11

Thermal energy storage systems for concentrating solar power (CSP) plants

W.-D. STEINMANN, German Aerospace Center, Germany

Abstract: The integration of thermal energy storage systems enables concentrating solar power (CSP) plants to provide dispatchable electricity. The adaptation of storage systems both to the solar energy receiver system and the power cycle of the plant is essential. Three different physical processes can be applied for energy storage: sensible heat storage in solid or liquid media, latent heat storage using phase change material and thermochemical energy storage. This chapter gives an overview of the various technical concepts developed for thermal energy storage in CSP plants and describes their states of development, their potentials for use and their performances.

Key words: thermal energy storage, sensible energy storage, molten salt, steam accumulator, latent heat energy storage, phase change material.

11.1 Introduction: relevance of energy storage for concentrating solar power (CSP)

This chapter provides a survey of the status and current developments of storage technology intended for integration into CSP plants. CSP plants already have an inherent storage capacity in the thermal mass of the working fluid and of components such as absorbers, heat exchangers and tubes. Storage units extend this capacity by storing the energy provided by the solar receiver that is not immediately used by the thermal process of the CSP plant. During discharge, the storage unit provides heat to the thermal process and thereby replaces all or part of the solar collector. The possibility of integrating cost-effective local storage capacity is one of the most distinct advantages of CSP over other renewable energy technologies. Storage can be integrated in CSP system designs in a manner that delivers benefits with minimal or zero impact on overall system efficiency and cost of energy, in distinction to technologies such as photovoltaics, which must first generate electricity and then add the extra investment and efficiency loss of a complex independent electrical storage subsystem.

CSP can profit from storage in various ways:

- Electricity generation can be shifted to periods with high demand thus increasing the value.

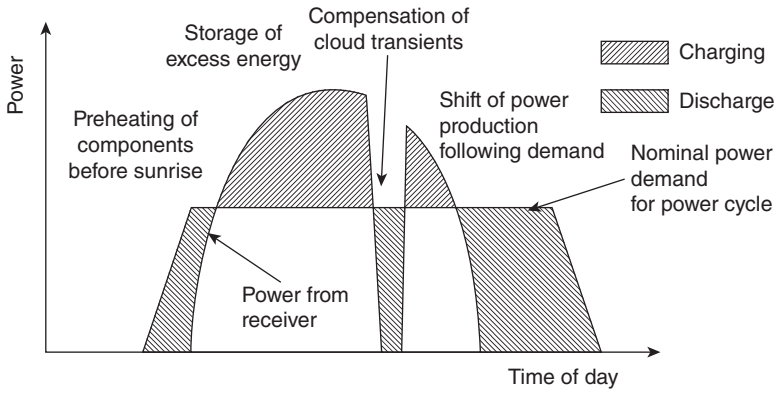

11.1 Various functions of thermal storage in a CSP plant.

- The capacity of external backup systems needed to compensate the mismatch between availability and demand can be reduced; fossil-fired backup systems have significant investment costs; the low thermal efficiency of these systems diminishes the benefit of electricity generation from renewable energy sources.
- Improved efficiency by avoiding transients in the power cycle due to clouds.
- Reduced start up period by preheating of absorber systems using energy provided by the storage system (Fig. 11.1).

The economic advantages of storage integration into CSP plants in the south-western US are described by Sioshansi and Denholm (2010). The most important conclusion is that generally storage improves the cost efficiency of CSP plants, but the degree of improvement varies over a wide range depending on the technology and project-specific assumptions made. This study also addresses the option to shift the power production to periods with lower ambient temperature thus increasing the efficiency of the power cycle.

The majority of today's commercial thermal storage systems used in industry and solar heating are operated at temperatures below 100°C and show storage capacities of less than 1 MW_{th}. Storage systems intended for CSP differ from these systems in two main aspects: CSP and solar process heat applications demand a temperature range between 120 and 1000°C, introducing specific requirements regarding corrosion and thermal stability of materials. Another characteristic of CSP applications is the huge capacity of storage units. A 50 MW_{el} parabolic trough power plant requires about 1 GWh_{th} storage capacity for a seven-hour operation time. Since the energy density of thermal storage systems is limited by physical constraints, typical CSP storage systems require several tens of thousands tons of storage

material. Due to the large quantities of storage material, the capital costs of thermal storage systems are usually dominated by their material costs. Fluctuations in market prices therefore limit the accuracy of cost estimations.

It is self-evident that a thermal energy storage system aims to minimize the losses in stored energy subject to cost constraints. However, in comparing systems, the issue of temperature differences and the associated loss of potential to generate power must also be considered. Every thermal system must be charged with a heat source at a higher temperature than itself and then will return heat to a working fluid at a temperature lower than itself. The efficiency of power generation reduces with lower temperature inputs, so the presence of the energy storage system may either force lower temperature, lower efficiency power generation, or force higher temperature operation of solar receivers to compensate, with a consequent increase in receiver losses.[1]

Basic storage concepts can be classified into three main groups according to the physical concept used for heat storage. While today's commercial storage systems apply sensible heat storage, the development of direct steam generation in the absorbers has sparked research activities aiming at high temperature latent heat storage systems, which have now reached an advanced status of maturity. The third main group comprises the application of reversible chemical reactions and sorption processes. Usually, this group is denoted as chemical energy storage. In the following sections, the various storage concepts which have been developed within the three main groups will be described.

11.1.1 Current commercial status of storage technology

Research on storage systems has accompanied the evolution of CSP technology almost from the beginning. Table 11.1 gives a survey of storage systems integrated into experimental and commercial CSP plants. Today, many commercial CSP plants already include storage capacity. The development of storage systems for CSP is characterized by a large variety of basic concepts reflecting the diversity of absorber systems, heat transfer media and power cycles used in solar thermal power plants. The identification of the optimal concept for a given application depends on the specific boundary conditions including working fluid, temperature range, storage capacity, power level and reaction time.

[1] In the language of thermodynamics, direct losses of energy are quantified via a 'thermal' or 'first law' efficiency. The effects of unavoidable temperature drop are quantified with a 'second law' or 'exergetic' efficiency.

Table 11.1 Survey of selected storage systems integrated in commercial and experimental CSP facilities

Project	Concept	Concentrator type	Max temperature	Thermal capacity	Start of operation
Eurelios (Italy)	Two-tank molten salt, steam accumulator	Tower/heliostat	430°C	0.5 MWh_{th}	1981
SSPS (Spain)	Two-tank liquid sodium	Tower/heliostat	530°C	1.0 MWh_{th}	1981
Nio central receiver (Japan)	Steam accumulator	Tower/heliostat	250°C	3.0 MWh_{th}	1981
Solar One (USA)	Thermocline with thermal oil	Tower/heliostat	300°C	28 MWh_{th}	1982
CESA-1 (Spain)	Two-tank molten salt	Tower/heliostat	340°C	3 MWh_{th}	1983
Themis (France)	Two-tank thermal oil Two-tank molten salt	Tower/heliostat	450°C	40 MWh_{th}	1984
SEGS-1 (USA)	Two-tank thermal oil	Trough	305°C	120 MWh_{th}	1984
TSA (Spain)	Packed bed with air	Tower/heliostat	700°C	1 MWh_{th}	1993
Solar Two (USA)	Two-tank molten salt	Tower/heliostat	565°C	110 MWh_{th}	1996
PS10 (Spain)	Steam accumulator	Tower/heliostat	245°C	20 MWh_{th}	2006
Andasol-1 (Spain)	Two-tank molten salt	Trough	385°C	1,010 MWh_{th}	2009
Solar Tres/Gemasolar (Spain)	Two-tank molten salt	Tower/heliostat	565°C	2,300 MWh_{th}	2011

11.2 Sensible energy storage

In sensible heat storage systems, variations of the stored energy ΔQ_{12} are dependent on the variation of the mean temperature (T) according to:

$$\Delta Q_{12} = m \int_{T_1}^{T_2} c(T)\, dT$$

where m is the mass and c the mass specific heat capacity. The capacity of sensible heat storage systems is limited by the available temperature difference $T_1 - T_2$ and physically by the specific heat capacity of the storage material. Using water as an example, since it is the substance with the highest specific heat capacity per mass of all liquids and solids, the maximum storage capacity for sensible heat storage systems is in the range of 0.11 kWh_{th}/kg for a temperature difference of 100 K. Compared to chemical energy sources (e.g. petrol 11.5 kWh_{th}/kg), thermal storage systems require large masses due to a low storage density.

The development of a sensible heat storage system starts with the selection of the storage material. Systems using liquid storage media can be distinguished from systems using solid storage media. Another criterion for classifying storage systems is the concept chosen for transferring solar energy to the storage material. For direct storage systems, the heat transfer fluid used for absorbing the solar radiation is also used as storage medium. Indirect storage systems use a storage medium that is different from the heat transfer fluid. Figure 11.2 shows a classification of various concepts for sensible heat storage. These concepts are discussed in detail in the following sections.

11.2.1 Liquid storage media: two-tank concept

The two-tank storage approach is illustrated in Fig. 11.3. As the name implies, a liquid medium is cycled between a hot tank and a tank at a lower temperature which is referred to as the 'cold tank' despite being still at several hundred degrees. Table 11.2 shows various liquid media and properties relevant for thermal energy storage. The simplest way to store sensible heat in a liquid is to connect inlet and outlet of a heat transfer process to two separated volumes held at different temperatures. This approach is widely used for low temperature applications using water as storage medium in vertical single tanks with a separation of the hot and cold volumes by thermal stratification. Due to the large volume needed for CSP applications, two separate storage tanks are usually preferred instead of a single vertical tank. If a non-pressurized heat transfer fluid (HTF) is used in the absorbers, the direct storage of this heat transfer fluid is a straightforward solution,

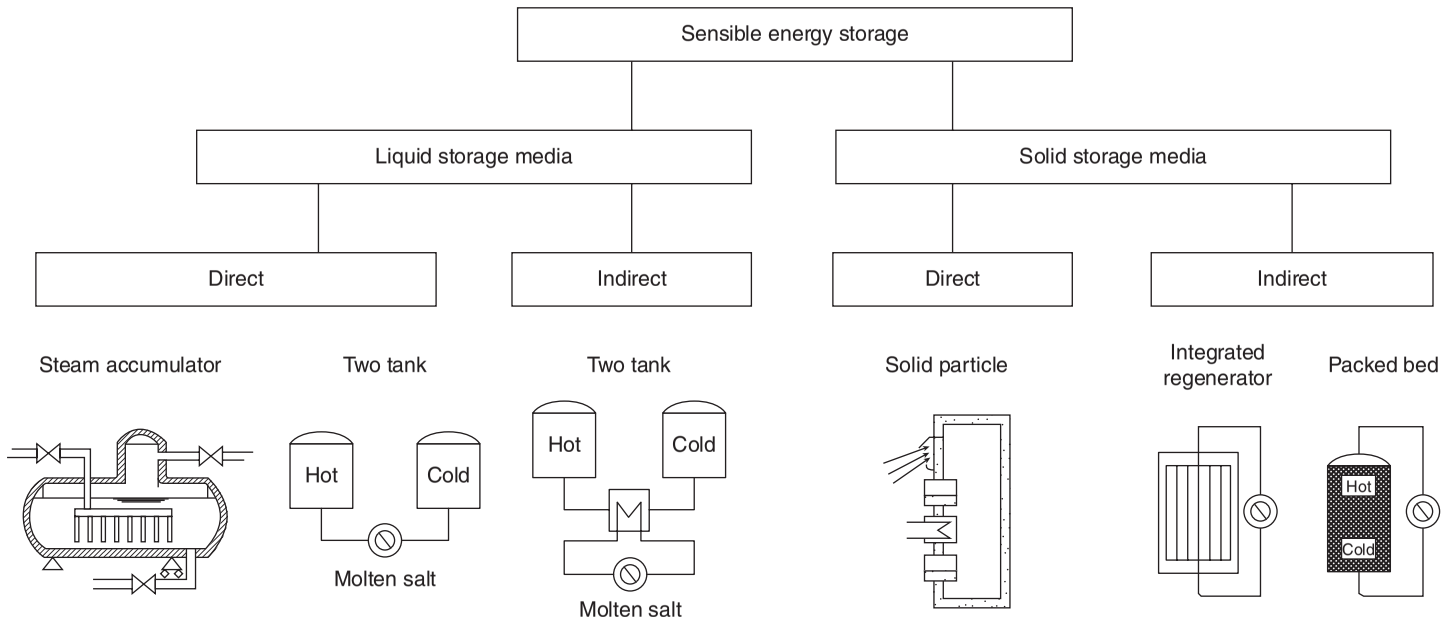

11.2 Concepts for sensible heat energy storage.

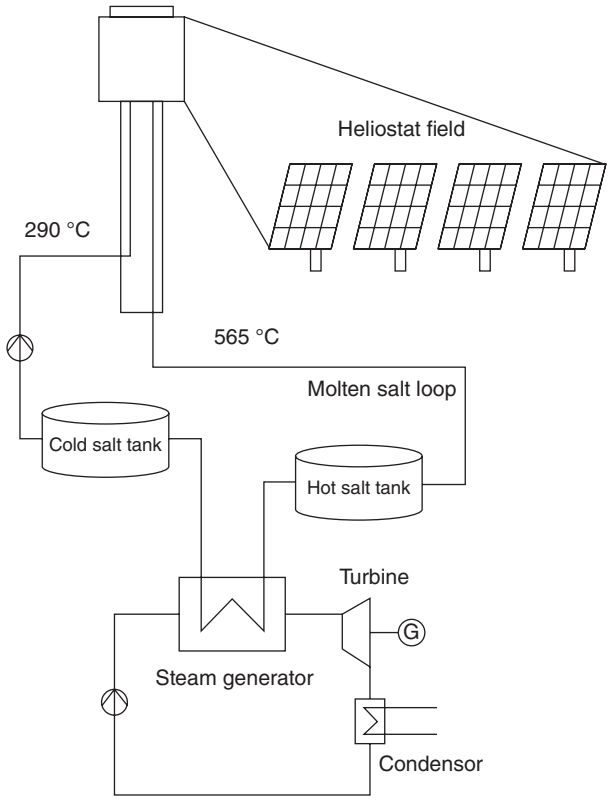

11.3 Simplified scheme of central receiver with two-tank storage concept.

provided that the HTF is inexpensive. The SEGS I parabolic trough power plant used direct storage of thermal oil operated between 240°C and 307°C (Pilkington Solar Int., 2000). Due to the limited maximum temperature, flammability and the high costs, thermal oil is not considered an attractive option. Molten salts represent an alternative already known from other applications (Bohlmann, 1972; Silverman and Engel, 1977). Mixtures of nitrates have been preferred so far for energy storage in molten salts. The major drawback of molten salt systems is the allowable operating temperature range, which is limited by the freezing point at the low end and the onset of thermal decomposition at the high end. Freezing within the storage tanks must be avoided, since due to the low thermal conductivity, re-melting is extremely complex. The corrosivity of molten salts increases with temperature; storage tanks exposed to higher temperatures require more expensive materials. The two-tank concept using molten salt was successfully demonstrated within the Solar Two project, using 1,400 tons of molten

Table 11.2 Examples for liquid media for sensible heat storage. Note that the thermo-physical data is indicative for the materials classes and also varies with temperature

Medium	Density (kg/m^3)	Specific heat capacity (kJ/kg/K)	dyn. viscosity (kg/ms)	Temperature difference = 100 K	
				Volume spec. storage density (kWh_{th}/m^3)	Capacity specific media costs (€/kWh_{th})
Saturated water (250°C, 40 bar)	798	4.865	1.06exp-4	100	–
Mineral oil (<320°C)	800	2.4	3.5exp-4	53	15
Synthetic oil (<400°C)	755	2.4	1.6exp-4	50	60
Nitrate salt (220°C <, <570°C)	1,950	1.5	3.4exp-4	81	20

salt between 565 and 290°C. Figure 11.3 shows a simplified scheme of a solar receiver using molten salt both as working fluid and storage medium. A detailed description of this storage system is provided by Pacheco (2002). The direct two-tank concept is also used for the 16-hour storage system of the Gemasolar project owned by Torresol Energy (Fig. 11.4).

In an indirect storage system, the molten salt (for example) used as storage medium is different from the HTF used in the absorbers. This concept is chosen if the specific costs of the HTF are higher than the costs of the storage medium (e.g. molten salt). The separate loops are connected by a heat exchanger. The first commercial two-tank molten salt storage unit integrated into the Andasol-1 plant is an indirect concept using 28,500 tons of binary nitrate salt operated between 292 and 386°C (Relloso and Delgado, 2009). The basic concept is illustrated in Fig. 11.5.

11.2.2 Liquid storage media: steam accumulator

Liquid water is an attractive storage medium due to its high specific heat capacity, low cost and compatibility. For temperatures exceeding 100°C, water must be pressurized to be used as liquid storage medium. Steam accumulators (Fig. 11.6) provide saturated steam during discharge (Goldstern, 1970). The energy for generating saturated steam is taken from a pressurized water volume in the saturated liquid state. Since the temperature of the saturated steam depends on the temperature of the liquid water

11.4 Two-tank storage system of the 17 MW_{el} Gemasolar central receiver plant. © by Torresol Energy. Reproduced with permission from Torresol Energy, Spain.

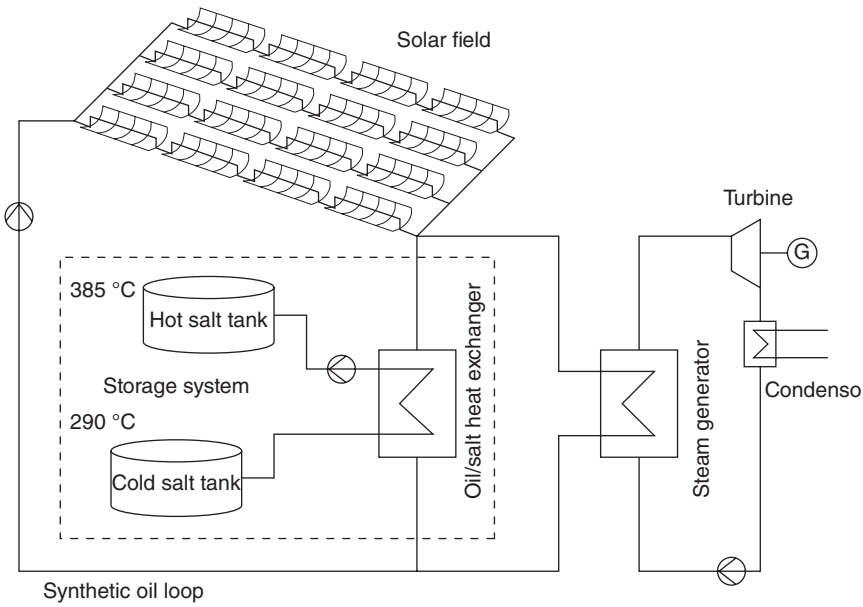

11.5 Simplified scheme of a parabolic trough plant using thermal oil as HTF with an indirect two-tank molten salt storage concept.

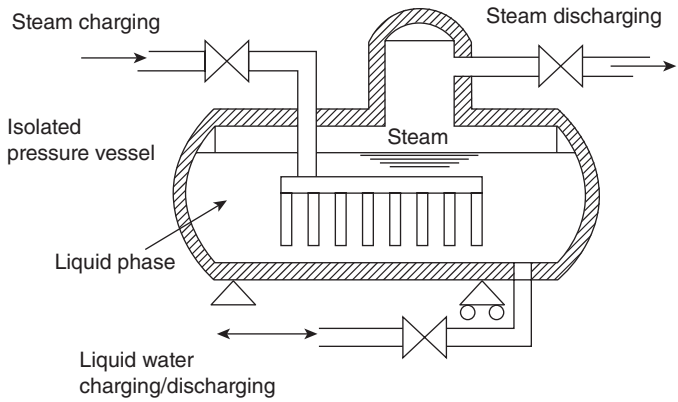

11.6 Scheme of a steam accumulator.

volume, the pressure of the saturated steam provided by the storage system decreases during the discharge process. The mass of the saturated liquid water remaining inside the steam accumulator is large compared to the mass of the saturated steam provided during the discharge process. Assuming a constant mass m_{liquid} of saturated liquid water inside the steam accumulator, the thermal energy provided during discharge from pressure P1 to pressure P2 can be estimated to be:

$$\Delta Q_{12} = m_{liquid} c_{liquid} \left(T_{sat}(P1) - T_{sat}(P2)\right)$$

where T_{sat} is the pressure dependent saturation temperature and c_{liquid} is the mean specific heat capacity of liquid water. Figure 11.7 shows the volume specific amount of steam provided by a steam accumulator dependent on initial pressure and pressure drops (Steinmann and Eck, 2006).

Steam accumulators are charged by feeding steam into the liquid volume. The temperature of the liquid volume is increased by condensation of the steam. While steam accumulators have fast reaction times, the storage capacity is usually limited economically by the costs of the pressure vessel. Since steam accumulators provide steam almost instantly for a short period, this concept can be used as buffer storage to compensate for short cloud transients.

Steam accumulators are widely used in process industry in the temperature range between 100 and 200°C. The application of steam accumulators for large-scale CSP plants was described by Gilli and Beckmann (1976). Some experimental CSP plants such as Eurelios (Strub *et al.*, 1984) and the Japanese central receiver plant at Nio (Tani *et al.*, 1986) used steam accumulators. The PS10 central receiver power plant, representing Europe's first commercial CSP plant starting operation in 2007, uses steam accumulators

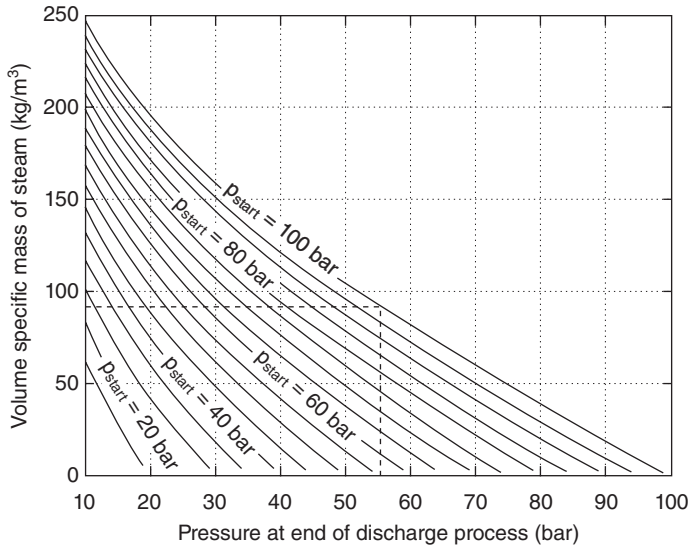

11.7 Volume specific mass of saturated steam provided by steam accumulator for different initial pressures and pressure drops. Dashed line indicates example with initial pressure = 100 bar and final pressure 55 bar; steam accumulator delivers approx. 90 kg saturated steam per m^3 storage volume.

as buffer storage. Four tanks with a total storage capacity of 20 MWh enable a 50% load operation of the 11 MW_{el} for about 50 minutes. The storage system is charged with saturated steam at 45 bar provided by the central receiver.

11.2.3 Solid media storage concepts

The application of solids as storage media is motivated mainly by cost aspects (Table 11.3). The material costs for concrete, per unit energy stored, for example, are in the range of 10–20% of the corresponding costs for molten salt, and maintenance costs are also expected to be lower for solid media storage systems. Additionally, there are no problems resulting from freezing, evaporation or leakages. Cost-effective solid storage materials show low thermal conductivities representing the main challenge for the implementation of an effective storage concept. Various options have been suggested to overcome the heat transport limitations of the storage material. The goal of these options is to reduce the path for heat transfer from the bulk of the storage material to the transfer medium.

Table 11.3 Examples for solid media for sensible heat storage. Note that data given is indicative

Material	Density (kg/m^3)	Specific heat capacity (kJ/kg/K)	Thermal conductivity (W/mK)	Temperature difference = 100 K	
				Volume specific storage density (kWh_{th}/m^3)	Capacity specific media costs (€/kWh_{th})
Aluminium	2,700	0.945	200	70.8	90
Concrete	2,200	0.72	1.5	44	5
Cast iron	7,200	0.5	35	100	70
Rock	2,500	0.8	1.0–3.0	55	–

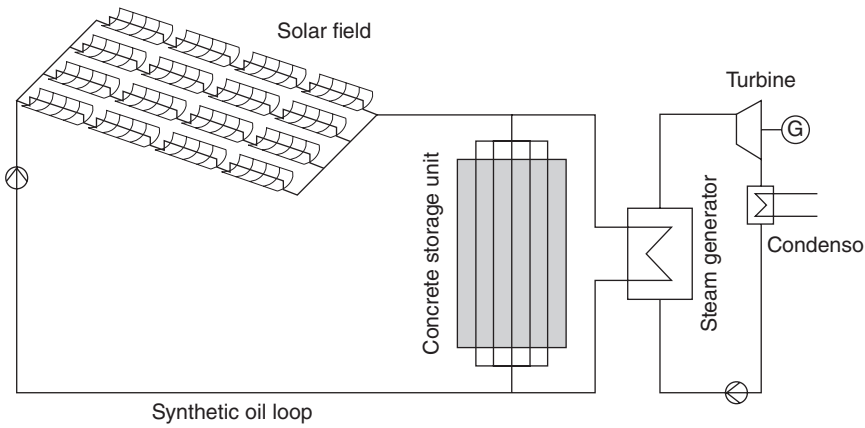

11.8 Simplified scheme of parabolic trough plant using thermal oil as HTF with a concrete storage unit.

11.2.4 Solid media with integrated heat exchanger

For pressurized heat transfer fluids, a parallel pipe tube register is usually integrated into the storage volume. Various castable storage materials such as concrete or castable ceramics have been investigated for this approach. A test unit was installed at the Plataforma Solar de Almería, Spain, and connected to parabolic trough collectors (Figs 11.8 and 11.9). This system was designed for a thermal power of 350 kW_{th} and a capacity of 400 kWh_{th}, operated with thermal oil at a maximum temperature of 390°C. A second test unit intended for storage cycles of 6–8 hours also having a capacity of 400 kWh_{th} was connected to a test rig to allow investigation of the long-time behaviour (Fig. 11.10). Operated with thermal oil between 300 and 400°C,

11.9 Concrete storage module (PSA-Almeria) before installation of insulation.

11.10 Concrete storage module (400 kWh_{th}) connected to test rig, before installation of insulation.

more than 300 cycles have been performed without any degradation (Laing *et al.*, 2009a). The same basic design has also been used for a storage unit intended for operation with superheated pressurized steam (100 bar) at maximum temperatures of 500°C (Laing *et al.*, 2009b). The specific investment costs for a storage unit with a capacity of 1100 MWh_{th} are estimated to be in the range of 34 €/kWh_{th} (Bahl *et al.*, 2009).

Currently, the focus of the ongoing development is on options to reduce the investment costs. These costs are dominated by the heat exchanger embedded in the storage volume. Various options to increase the effective

heat conductivity within the storage material have been investigated. The homogeneous addition of materials having a high thermal conductivity has not shown a significant potential for cost reduction. In another approach, additional heat transfer structures are integrated into the storage material to reduce the number of tubes needed for the heat exchanger.

11.2.5 Packed bed

In a direct contact storage system, there is no intervening wall between heat transfer fluid and storage medium. Particles of storage material are packed into a container, the HTF passes through the particles. Direct contact heat transfer allows extensive volume specific heat transfer areas. The effective flow cross section can be large, thus reducing pressure losses, especially for gaseous HTFs. Storage material and HTF must have the same pressure and must be compatible. A packed bed storage system is integrated into the Solar Power Tower Jülich. This experimental central receiver plant uses air at atmospheric pressure as heat transfer medium. The storage is cycled between 120 and 680°C and has a storage capacity of almost 9 MW_{th} (Zunft *et al.*, 2010).

Direct contact storage systems can also be operated with liquid HTFs. Here, the main aim is to displace expensive liquid storage media by cost-effective solids. This approach was chosen at the Solar One central receiver plant, using a mixture of thermal oil, sand and gravel stored in a single tank. The hot fluid at the top is separated from the cold fluid at the bottom by buoyant forces. This thermocline system is charged by feeding hot thermal oil into the top of the tank. During the discharge process, hot oil is taken from the top of the tank, pumped through a heat exchanger and returned to the bottom of the tank. Due to the selected thermal oil the maximum temperature of heat provided by this system was about 315°C. The thermocline concept was also investigated using molten salt as the HTF (Pacheco *et al.*, 2002).

11.2.6 Solid particles

Receivers with direct absorption of concentrated solar radiation in solid particles are considered to be an attractive solution for solar chemistry applications requiring high temperatures (Siegel and Kolb, 2008). Basically, this approach can also be chosen as an energy storage system. While the direct absorption of solar energy in non-pressurized solid storage materials is an attractive option, various issues have to be addressed before commercial scale CSP applications are possible. The long-term stability of the particles must be ensured, the parasitic load needed for the transport of the particles must be considered. The piping for the transport of the particles

will experience significant mechanical loads at high temperatures; heat transfer from the particles to the working fluid of the power cycle is complex (Tan and Chen, 2010).

11.3 Latent heat storage concepts

Latent heat storage systems employ the enthalpy change of a substance passing through a phase change (usually solid to liquid) to store energy. The most prominent advantage of storage concepts using the latent heat associated with the change of state of the storage material is the option to store energy within a narrow temperature range close to the phase change temperature. In CSP technology the development of absorbers directly generating steam has sparked interest in latent heat storage systems. Here, the application of storage concepts using sensible heat storage is usually not cost effective. This can be seen in Fig. 11.11. If a steam process is used both for charging and discharging a sensible heat store, the charging steam system will need to run with a much higher saturation temperature (i.e. at

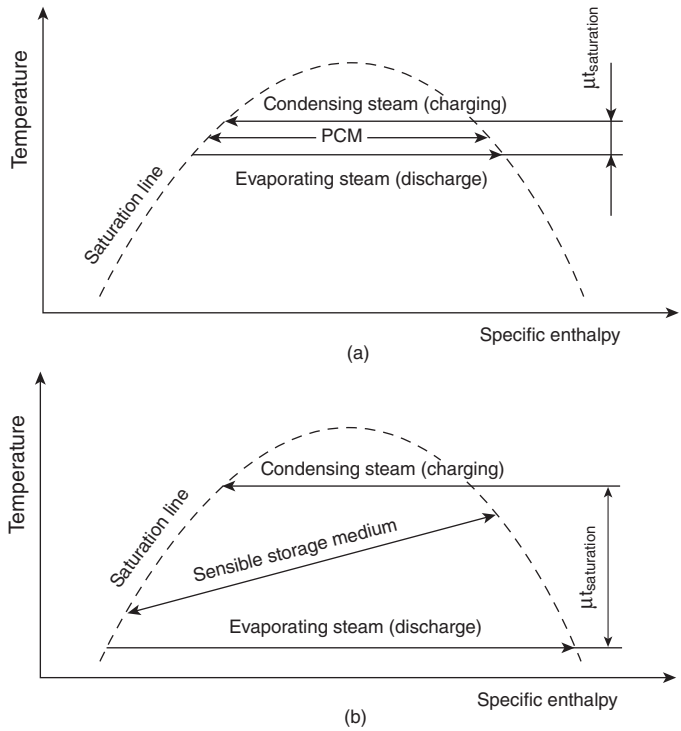

11.11 Necessary reduction of saturation temperature for a system using steam as working fluid. Comparison of latent heat storage concept (a) and sensible heat storage concept (b).

a much higher pressure) than the discharging steam in order for the heat transfers to take place. The steam with recovered energy will have considerably reduced power generation potential (exergy) compared to the charging steam. If the latent heat of vaporization for the steam is stored and released by an appropriately matched latent heat-based energy store, with the superheat component met by a sensible heat store, then this large exergy loss can be avoided. The development of a latent heat storage system starts with the selection of the phase change material (PCM). The temperature of the phase change should correspond to the specific application. Usually, this demands that the melting temperature of the storage material is close to the saturation temperature resulting from the desired steam turbine operating pressure. The phase change process should be physically and chemically reversible, i.e. no change of the melting temperature or melting enthalpy should occur over many cycles. For CSP and solar process heat application using direct steam generation in the absorbers the range for the melting temperature for candidate PCMs is between 120 and 340°C. Table 11.4 lists materials showing melting temperatures in this temperature range. Further relevant physical criteria for storage materials are the specific heat of fusion and the thermal conductivity.

Metals such as tin or lead can be excluded as PCMs due to cost aspects. A characteristic of the remaining candidate materials is a low thermal conductivity. Consequently, the development of PCM storage systems requires the identification of cost-effective heat transfer concepts to overcome the limitations resulting from poor heat conductivity of the storage material. The various PCM storage concepts can be distinguished by the approach to ensuring a sufficient heat transfer between storage material and heat transfer fluid (Fig. 11.12). These concepts involve the addition of other materials to the PCM volume. The volume specific costs of these additional materials should be compared to the volume specific costs of PCM (approx. 1600 €/m^3) to estimate the acceptable fraction for additional materials. PCM storage concepts are usually more complex than sensible heat storage systems, since the storage material often undergoes a significant volume change during the phase change. These concepts are discussed in turn in the following sections.

11.3.1 Phase change material (PCM) concept with extended heat transfer area

The average distance for heat transfer within the PCM is limited in this approach. By using finned tubes, the effective surface of the tube is extended. The aim is to replace expensive pressure pipes by less expensive non-pressurized thermally conductive structures. Finned tubes used in PCM storage differ from finned tubes applied in heat exchangers in several ways:

Table 11.4 Examples for PCM with melting temperatures in the temperature range relevant for CSP

PCM	Melting temperature (°C)	Density (kg/m^3)	Thermal conductivity (W/mK)	Heat of fusion (kJ/kg)	Volume specific latent heat (kWh_{th}/m^3)	Capacity specific media costs (€/kWh_{th})
KNO_3-$NaNO_2$-$NaNO_3$(eu)	142	2,000	0.5	60	33	65
KNO_3-$NaNO_3$(eu)	222	2,000	0.5	100	55	28
Tin	232	7,200	60	59	118	600
$LiNO_3$	252	1,800	0.6	360	180	60
$NaNO_3$	306	1,900	0.5	175	96	14
Lead	327	11,300	35	23	72	100

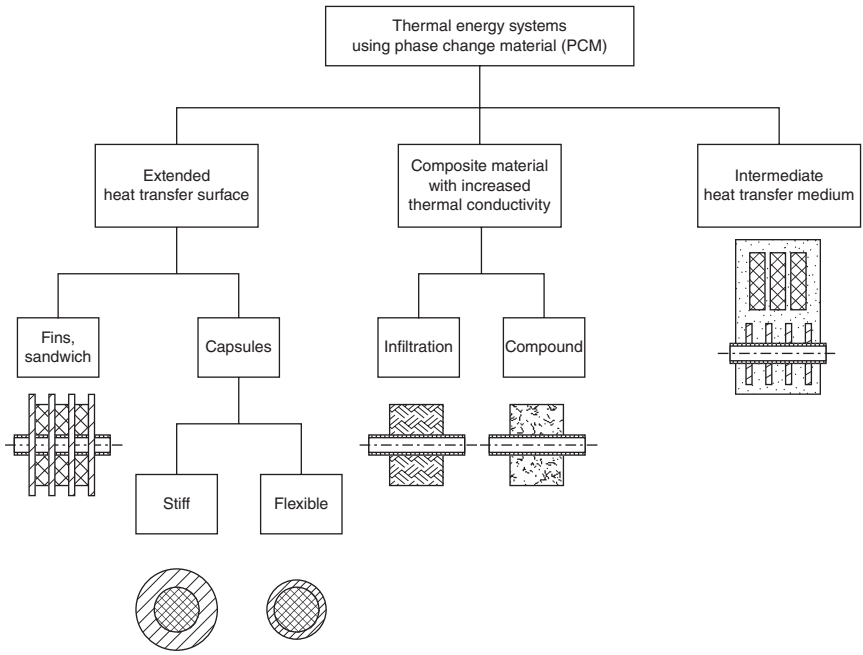

11.12 Concepts for latent heat energy storage.

Table 11.5 Materials for extended surface heat transfer

Material	Thermal conductivity (W/mK)	Density (kg/m^3)	Volume specific material costs (€/m^3)
Aluminium	200	2,700	7,000
Graphite foil	150	1,000	9,000
Carbon steel	30	7,800	14,000
Stainless steel	20	7,800	19,000
Copper	350	8,800	35,000

the distance between parallel tubes is larger than that of conventional heat exchangers, the material of the fins must be corrosion resistant in a PCM (e.g. molten salt) environment and the fins must be able to withstand thermomechanical stress resulting from the volume variation of the PCM within a small temperature range during phase changes. The material used for the fins (Table 11.5) is of specific importance: while steel is used for the pressurized tubes due to its strength, steel does not represent an optimal choice for the fins due to high volume specific costs and moderate thermal conductivity. Alternatively, fins can be made of aluminium or graphite (Fig. 11.13). Both

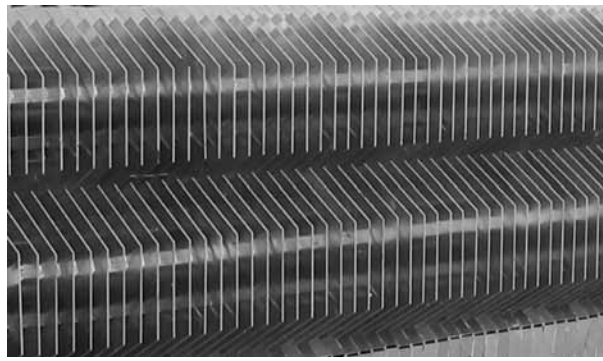

11.13 Heat exchanger for PCM storage with high fins made of aluminium.

materials show comparatively high thermal conductivity and lower volume specific costs. The temperature range for these fin materials is limited if nitrates are used as PCM by corrosion resistance (aluminium <400°C, graphite <250°C), but regarding the range of the saturation temperature for water, aluminium can completely cover the relevant temperature range. The feasibility of the finned tube concept embedded in PCM (sandwich concept) has been demonstrated in various DLR research projects using fins made of either graphite or aluminium (Table 11.6; Steinmann and Tamme, 2008). A PCM storage unit with a capacity of 700 kWh_{th} has been designed for operation with steam at 100 bar using fins made of aluminium (Laing *et al.*, 2010) (Fig. 11.14). This storage unit was integrated into a test loop connected to the power plant Litoral of Endesa in Carboneras, Spain.

The macro-encapsulation of PCM is another option for increasing the heat transfer area. Here, capsules filled with PCM are stacked in a pressure vessel. Macro-encapsulated low temperature PCMs are commercially available for cooling and low temperature applications. For CSP applications, capsules with metallic walls must be used (Fig. 11.15). Basically, containers for PCM can be either thin-walled (flexible) with equal pressure inside and outside or thick-walled (stiff) with different pressures. For systems using molten salts, the walls must have a minimum thickness to ensure a sufficient life expectancy regarding corrosion aspects. Consequently, a design using flexible containers is not possible for nitrates as the PCM. A significant drawback of stiff capsules is the necessity to include a gas volume to compensate for the expansion of the PCM during melting (Steinmann and Tamme, 2008). About 60% of the volume inside the pressure vessel can be filled by PCM capsules. A laboratory-scale test unit was designed and manufactured by DLR. Cylindrical capsules containing a total mass of 4.5 kg of $NaNO_3$-KNO_3 (eutectic) were stored in a pressure vessel (Fig. 11.15).

Table 11.6 PCM test storage units developed by DLR, using the sandwich concept

Identification	Max. power (kW)	Thermal capacity (kWh_{th})	PCM	Mass PCM (kg)	Melting temperature (°C)	HTF
DISTOR I	2	3.5	KNO_3-$NaNO_3$(eu)	130	225	Thermal oil
PROSPER	15	7	KNO_3-$NaNO_2$-$NaNO_3$(eu)	400	145	Steam
DISTOR II	100	55	KNO_3-$NaNO_3$(eu)	2,000	225	Steam
ITES-Lab	5	8	$NaNO_3$	140	306	Thermal oil
PROSPER PLUS	200	200 sensible + latent	KNO_3-$NaNO_2$-$NaNO_3$(eu)	5,500	145	Thermal oil
ITES	700	700	$NaNO_3$	14,000	306	Steam

11.14 PCM storage unit using fins made of aluminium, 700 kWh_{th} thermal capacity, operated with steam at 100 bar, integrated into a test loop connected to the power plant Litoral of Endesa in Carboneras, Spain.

11.15 Pipe segment with containers filled with PCM (macro-encapsulation).

Although the feasibility of the concept was proven by experiments, this approach was not pursued any further due to economic aspects. Regarding costs, the macro-encapsulation of PCM is not very attractive due to the limited effective volume share of the storage material and the significant amount of steel needed for the capsules and the pressure vessel. An additional problem is the necessity to ensure a high quality sealing of the capsules, since contamination of the steam due to leakages must be avoided.

11.3.2 Composite material with increased thermal conductivity

The effective thermal conductivity can be increased by the homogeneous addition of a material showing a high thermal conductivity. Highly conductive particles can be dispersed in the PCM. In another approach, PCM is integrated into matrices made of aluminium or graphite. Both these concepts require the addition of significant amounts of highly conductive materials. Since the contact surface between PCM and additives is large, corrosion problems increase for nitrates and limit the maximum temperature. Mainly due to cost aspects, this approach does not seem very promising.

11.3.3 Intermediate heat transfer fluid

An intermediate 'heat pipe' system based on the evaporation and condensation of a suitable intermediate heat transfer fluid can be used to transfer energy between a heat exchanger and the PCM. In this concept, the heat transfer area of the heat exchanger can be smaller than the outer heat transfer area of the PCM, and oversizing of the heat exchanger can be avoided. Since the temperature difference between the steam in the heat exchanger and the PCM undergoing a phase change should be minimized, the intermediate heat transfer fluid should also undergo a phase change between the liquid and the gaseous state. During the charging process, steam is condensed in the heat exchanger, which is covered by the liquid phase of the intermediate heat transfer fluid. The energy released during the condensation is used to evaporate the heat transfer fluid. The saturation temperature of the intermediate heat transfer fluid is lower than the condensation temperature of the steam but higher than the melting temperature of the PCM. When the gaseous intermediate heat transfer fluid contacts the surface of the PCM, it condenses and transfers the energy associated with the phase change to the melting PCM. During the discharge process, the intermediate heat transfer fluid evaporates at the surface of the PCM and transfers the heat to the steam by condensation at the surface of the heat exchanger. Essential for this concept is the identification of the intermediate heat transfer fluid. The temperatures for boiling and condensation

must be adapted to the temperature range of the steam and the melting temperature of the PCM. Further details are given by Adinberg and Epstein (2007).

11.4 Chemical energy storage

Chemical energy storage systems utilize the enthalpy change of a reversible chemical reaction. The interest in these systems is motivated mainly by the option to store energy at higher densities than other types of thermal storage. The possibility of storing the reactants at ambient temperature, so minimizing thermal losses, is also attractive. Although this potential was identified early in the evolution of CSP technology (Ervin, 1977; Williams and Carden, 1978; Brown *et al.*, 1992), chemical energy storage systems are currently in an earlier stage of maturity, and economic issues and system aspects demand further investigations. As with all energy storage systems, the overall energetic and exergetic efficiency of closed loop systems must be considered.

11.4.1 Reversible chemical reactions

The basic concept of chemical energy storage is to absorb excess heat in an endothermic reaction. The reaction products are stored separately. During the discharge process, the reaction products are recombined exothermically and the heat of reaction can be used. The concept is illustrated schematically in Fig. 11.16.

Catalytic gas–gas reactions represent one group of reactions considered for energy storage. An example for this group is the CH_4 reforming-methanation reaction, which originates from activities aiming at the storage of heat generated from nuclear energy:

$$CH_4\ (\text{gas}) + H_2O\ (\text{gas}) \leftrightarrow CO\ (\text{gas}) + 3\ H_2O\ (\text{gas})$$

The endothermic reforming reaction is carried out in the solar receiver at temperatures between 800 and 1200°C. The products are cooled to ambient temperature and stored at high pressure. The reaction is reversed in the methanator system providing heat in the temperature range of 350–700°C. There is a large body of work addressing the feasibility of this concept, culminating in a demonstration system using a volumetric receiver installed on a solar central receiver reaching a power level of 480 kW (Epstein *et al.*, 1996; Abele *et al.*, 1996). The storage system shows a storage density of about 45 kWh_{th}/m^3. The group at CSIRO in Australia are continuing to investigate the solar driven endothermic half of the system for the purposes of 'open loop' solar value adding to natural gas (Stein *et al.*, 2009). Another example is the dissociation of ammonia:

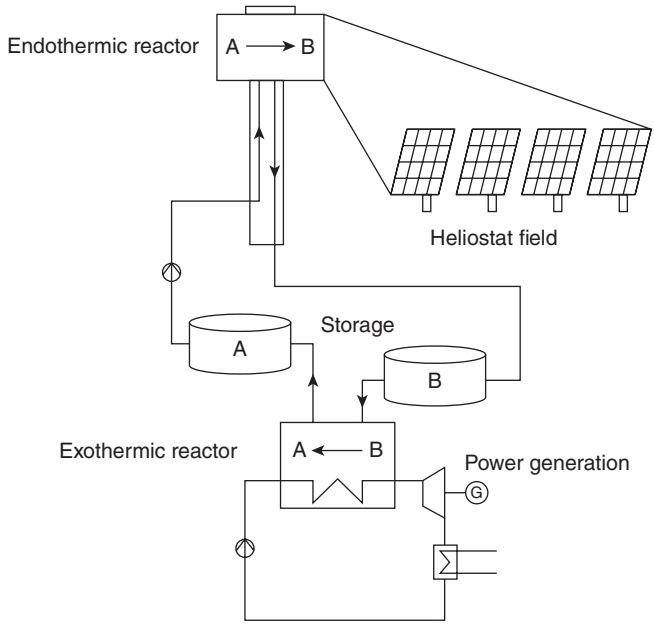

11.16 Schematic of a reversible chemical energy storage system.

$$NH_3 \leftrightarrow 1/2\ N_2 + 3/2\ H_2$$

which has been extensively investigated by the Solar Thermal Group at the Australian National University (ANU) (Lovegrove *et al.*, 2004). A receiver was operated at a power level of 15 kW with solar energy provided from a dish system. In order to enhance reaction rates in the exothermic ammonia synthesis reaction, system pressures up to 30 MPa are proposed. At 10 MPa, the volumetric storage capacity is in the range 40 kWh_{th}/m^3. One of the major advantages of the ammonia-based system is that the heat recovering exothermic reaction is the well-known Haber Bosch process, employed on a major scale around the world for fertilizer and explosives production. Hence there is large-scale proven reactor technology already commercially available.

Thermal dissociation of solids and liquids can also be applied for energy storage. By addition of solar heat to a liquid or solid, a gas is released. During the discharge process, the synthesis of the dissociation products provides energy. One example of this kind of reaction is the dehydration/hydration cycle:

$$Ca(OH)_2 \leftrightarrow CaO + H_2O$$

The storage capacity of this system is in the range of 300 kWh/m^3 (Schaube *et al.* 2010). There is a large number of active investigations of solar-driven

chemical processes aimed at producing fuels and useful chemical products. These approaches are also forms of energy storage in a general sense. Such applications are covered in detail in Chapter 20.

11.4.2 Sorption heat storage

A sorption process can be considered to be a chemical reaction system based on weaker chemical bonds than the covalent bonds encountered in the systems described above. In a sorption heat storage system, the sorbent is heated during the charging process and vapour is desorbed from the sorbent. During discharging, vapour at a lower temperature is adsorbed (solid sorbent) or absorbed (liquid sorbent) and heat at a higher temperature level is released. Most research activities on sorption heat storage aim at heating applications at low temperature ranges. An example for a medium temperature application is the reaction of NaOH and water, which has recently been considered for seasonal storage of solar heat (Weber and Dorer, 2008). This chemical reaction system has been demonstrated driving a steam locomotive, the 'caustic soda locomotive' described by Riedler (1883).

11.5 Selecting a storage system for a particular concentrating solar power (CSP) plant

Storage systems intended for application in CSP plants must not only minimize energy seepage to the environment, but avoiding exergy losses is also critical. This requires the minimization of temperature differences within the driven heat transfer during charging and discharging. The storage system must be adapted both to the receiver system of a CSP plant and to the thermodynamic cycle. The identification of the optimal basic storage concept represents the first step in selecting a storage system for a specific CSP application. Due to the early stage of development and the lack of pilot-scale demonstrations for chemical energy storage, only sensible heat storage and latent heat storage are currently considered here. These two concepts should be regarded as complementary rather than competing. For the absorber concept using two-phase working fluids (e.g. wet steam), latent heat storage systems should be preferred due to their capability to store the energy provided by the condensation of the working fluid within a narrow temperature range. Sensible heat storage systems should not be applied here, since the saturation pressure of the steam provided during the discharge process must be reduced significantly compared to the charging process, which causes efficiency losses that are not acceptable for CSP applications. Steam accumulators are the exception to the rule: saturated or slightly superheated steam is used to increase the sensible energy of the pressurized water used as storage medium.

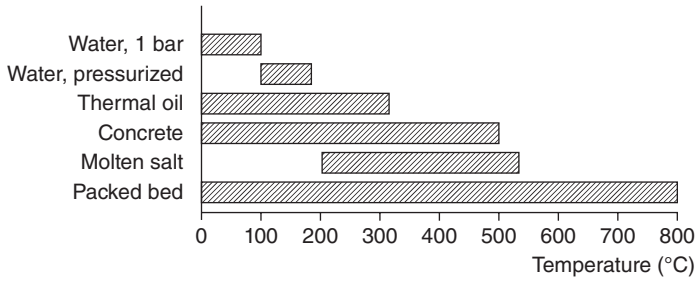

11.17 Characteristic temperature range for various sensible heat storage concepts.

For CSP systems using single-phase working fluids (e.g., thermal oil, molten salt, air) undergoing significant temperature variations in the absorber, sensible heat storage is usually preferred. Latent heat storage does not offer any important advantage here; the higher volume specific storage density is usually not relevant for CSP plants. If sensible heat storage is chosen as the basic storage concept, a further criterion for the identification of the optimal storage concept is the temperature range of the specific application. Figure 11.17 shows the characteristic application range for the various concepts based on sensible heat storage. While for some concepts, the maximum temperature is below the maximum temperature required for some CSP applications, storage concepts using molten salt must avoid operation near the freezing temperature of the storage material. Table 11.7 gives an overview of sensible heat storage concepts and their specific pros and cons.

11.6 Future trends

Today's commercial scale CSP plants use either two-tank molten salt storage systems or steam accumulators. This choice is mostly influenced by the operational experience already existing for these two concepts. While this approach represents a low-risk solution, these two storage concepts also show a low potential for further cost reductions. The technical feasibility of integrating large-scale thermal storage with CSP plants has been proven by the Andasol and PS10 facilities. Current research activities focus on various aspects:

- further reduction of capital and operating costs
- adaptation to advanced power cycles with higher efficiencies at increased temperature levels
- improved operability.

Table 11.7 Summary of sensible heat storage concepts

Concept	Advantages	Disadvantages
Two-tank (molten salt)	• Provides heat at constant temperature during discharge • Good behaviour at partial charge • Option for using storage medium as working fluid in the solar field as well	• Risk of irreversible freezing • Complex initial filling procedure • Limited potential for further cost reductions resulting from technical improvements • Total costs strongly dependent on costs of storage medium • Tank volume approx. two times the volume of the storage material
Thermocline (molten salt)	• Cost reduction possible with partial substitution of molten salt by low cost filler material • Only single tank needed	• Risk of irreversible freezing • Complex initial filling procedure • Filler material must be compatible with molten salt • About 30% of the storage volume cannot be used due to thermal boundary layer
Solid media with embedded heat exchanger	• Cost reduction due to low cost storage material • No risk of freezing • Pressurized working fluid can be used directly without intermediate heat exchanger	• Temperature decreases during discharge • Repair or maintenance of embedded heat exchangers difficult • Thermomechanical stress between heat exchanger and storage medium must be considered
Steam accumulator	• Low response time • High volume-specific power • Substantial operating experience in process industry	• Temperature not constant during discharge process • Cost attractive only for small pressures • Large pressurized vessels necessary • Limited storage capacity
Packed bed with air as heat transfer fluid	• No heat exchanger necessary • Suitable for high temperatures • Low risk potential • Substantial operating experience in process industry	• Pressure losses might be critical • Combination with solar absorbers using liquid heat transfer fluids difficult • Distances between solar receiver and storage must be limited
Falling particle	• Direct absorption of solar radiation	• Only experience from lab-scale experiences available • Parasitic loads needed for transportation of large masses might be critical • Mechanical loads of heat exchanger for solids at high temperatures might be critical

Storage systems are investigated on two different levels: while system analysis deals with the interaction of storage units with the other components of a CSP plant, detailed research on various storage concepts aims at cost reduction by more efficient material usage based on an improved understanding of the heat transfer processes in the storage system.

11.6.1 System analysis

System analysis aims at the identification of requirements for storage systems to allow for an optimal integration into various kinds of CSP plants. Based on simulations of the annual performance of a specific CSP application, correlations between storage capacity and cost benefit can be developed. These correlations enable the definition of cost targets for storage systems. Estimates of acceptable costs for a storage system should also consider efficiency benefits resulting from the integration of a storage system. Efficiency benefits can result from an operation strategy which profits from the possibility to reduce off-design operation of the power plant by using storage capacity. The development of new operation and control strategies for CSP plants with integrated storage capacity is essential for exploiting the full potential of storage technology.

11.6.2 Further development of existing storage concepts

With capital costs in the range of 35–50 €/kWh$_{th}$, two-tank molten salt systems provide a benchmark for acceptable investment costs for sensible heat storage concepts. Various aspects should be considered here: costs should only be compared for systems with the same temperature range, identical discharge duration and the same reaction time. For storage systems operated at higher temperatures, higher investment costs are acceptable, since the heat provided by the storage system is usually used in a power cycle showing a higher thermal efficiency. While steam accumulators show high capacity-specific investment costs, these systems are attractive for compensation of fast transients due to their short reaction times. Since the costs for the pressure vessels become prohibitive at temperatures exceeding 250°C, future applications of steam accumulators are probably limited.

A typical capital cost structure for two-tank molten salt concepts is shown in Fig. 11.18 (Kelly and Kearney, 2006). The costs are clearly dominated by the share required for the molten salt; the cost reduction potential for the other components is considered limited. The estimated maximum cost reduction for concepts requiring only a single tank for both hot and cold molten salt volume is only in the range of 10%, since only the less expensive cold tank can be eliminated. On the other hand, single tank concepts are usually more complex and require additional effort to separate the hot and

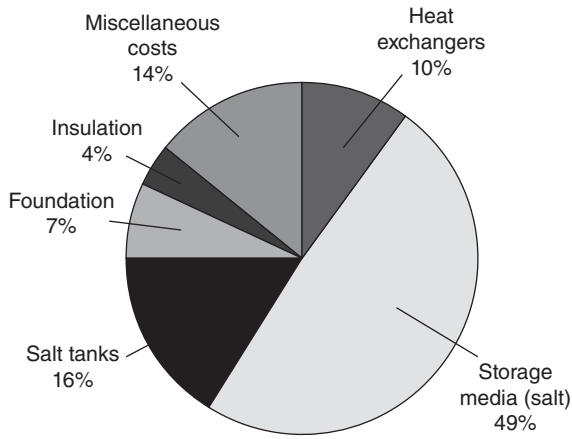

11.18 Capital cost structure for two-tank molten salt storage concept.

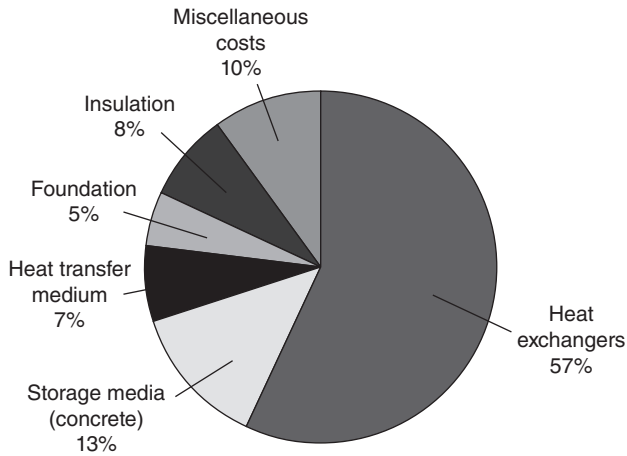

11.19 Capital cost structure for concrete storage concept.

cold volumes. The replacement of the binary nitrate salt used currently by an alternative liquid is one option to reduce costs, but so far no promising substance has been identified. Substitution of molten salt by a less expensive filler material (thermocline concept) represents a promising option for cost reduction, but the long-term compatibility of the materials must be ensured.

Solid media energy storage systems show a significant potential for cost reduction due to the low costs of the storage material (WANDA, 2006) (Fig. 11.19). Mandatory for the economic success of these systems is the development of cost-effective heat transfer concepts. The cost benefit of solid

storage material must not be outweighed by the costs of the equipment for heat transfer, so the acceptable amount of material needed for heat transfer structures integrated into the storage material is limited. The only latent heat storage concept to be demonstrated successfully so far in the 100 kW power range is the sandwich concept using fins made of either aluminium or graphite.

For the sandwich concept, the cost share of the PCM is currently estimated to be in the range of 20–25%. For the embedded heat exchanger, an optimized material usage and the integration of manufacturing aspects are expected to result in significant cost reductions. The improved design of containers and manifolds is also assumed to offer a further potential to reduce costs.

While chemical energy storage concepts show a significant theoretical potential for future cost-effective storage systems, additional research and development is required to provide the basis for commercial applications. The long-term reversibility of the reactions must be ensured. The overall energetic and exergetic efficiency must be evaluated. The energy flow schemes are usually more complex than for other basic storage concepts and the integration of energy flows which are not linked to the storage material is often essential for the efficiency of a chemical storage concept. Cost estimations must also consider investments for pressure vessels and heat exchangers, which are often large for CSP applications.

11.7 Conclusion

The plurality of thermal storage technology reflects the diversity of CSP systems. There is no storage concept that can be identified as the universal best solution for all applications; the selection depends strongly on the specific requirements regarding heat transfer fluid, temperature range, power cycle and tariff structure. The pairing of storage concept, solar absorber and power cycle is essential for successful storage implementation.

Thermal storage technology for CSP applications has made significant progress both in commercial application and development. For CSP systems using single-phase heat transfer fluids, two-tank molten salt storage systems with capacities in the GWh_{th} range have become a proven standard solution. Since the potential for cost reductions is limited for molten salt systems, there is still a demand for innovative storage solutions with a better cost efficiency. The application of cost-effective solid storage materials is a promising approach for fulfilling this requirement; efficient concepts for the transfer of thermal energy between solid storage material and the working fluid are needed.

Efficient storage for CSP systems using two-phase fluids as the heat transfer medium in the absorbers requires charging and discharging within

a narrow temperature range, which cannot be done cost efficiently with sensible heat storage. Latent heat energy storage for CSP applications has matured in recent years, and pilot systems using phase change materials are being operated with steam in the 100 bar range providing up to 700 kW_{th} during discharge. The application of finned heat exchangers embedded in the phase change storage material has proven to be a concept that provides the necessary power densities. Ongoing research activities focus on cost reductions of the heat exchangers and identification of additional storage materials fulfilling the requirements in terms of costs, compatibility with the heat exchanger materials and cyclic stability.

11.8 Acknowledgement

The author would like to thank Torresol Energy for providing the picture of the Gemasolar storage system.

11.9 References

Abele, M. *et al.* (1996) 'Test results of a receiver reactor for solar methane reforming and aspects of further applications of this technology', *Proceedings of the 8th Solar Paces Conference*, June, Cologne.

Adinberg, R. and Epstein, M. (2007) 'Conception and design of a thermal energy storage system', *Proceedings of the 5th IASME/WSEAS Int. Conference on Heat Transfer, Thermal Engineering and Environment*, Athens, Greece, 25–27 August.

Bahl, C., Laing, D., Hempel, M. and Stückle, A. (2009) 'Concrete thermal energy storage for solar thermal power plants and industrial process heat', *SolarPaces Conference 2009*, Berlin.

Bohlmann, E.G. (1972) 'Heat transfer salt for high temperature steam generation', Oak Ridge National Laboratory report ORNL-TM-3777.

Brown, D., LaMarche, J. and Spanner, G. (1992) 'Chemical energy storage system for SEGS solar thermal power plant', *Journal of Solar Energy Engineering*, 114(4), 212.

Epstein, M. *et al.* (1996) 'Solar experiments with a tubular reformer', *Proceedings of the 8th Solar Paces Conference*, June, Cologne.

Ervin, G. (1977) 'Solar heat storage using chemical reactions', *Journal of Solid State Chemistry*, 22, 51–61.

Gilli, P.V. and Beckmann, G. (1976) 'Design and economy of solar plants with integrated thermal energy storage', *Solar Energy, Proceedings of the UNESCO/WMO Symposium, Geneva*.

Goldstern, W. (1970) *Steam Storage Installation*, Pergamon Press, Oxford.

Kelly, B. and Kearney, D. (2006) 'Thermal storage commercial plant design study for 2-tank indirect molten salt system', Final Report, NREL.

Laing, D., Lehmann, D., Fiss, M. and Bahl, C. (2009a) 'Test results of concrete thermal energy storage for parabolic trough power plants', *Journal of Solar Energy Engineering*, 131, 041007.

Laing, D., Bauer, T., Lehmann, D. and Bahl, C. (2009b) 'Development of a thermal energy storage system for parabolic trough power plant with direct steam generation', *Proceedings of Energy Sustainability 2009*, San Francisco.

Laing, D., Bahl, C. and Fiss, M. (2010) 'Commisioning of a thermal energy storage system for direct steam generation', *Proceedings of the SolarPACES 2010 conference*, 21–24 September, Perpignan, France.

Lovegrove, K., Luzzi, A., Soldiani, I. and Kreetz, H. (2004) 'Developing ammonia based thermochemical energy storage for dish power plants', *Solar Energy*, 76, 331–337.

Pacheco, J.E. (2002) 'Final test and evaluation results from the Solar Two project', Sandia report SAND2002-0120.

Pacheco, J.E., Showalter, S.K. and Kolb, W.J. (2002) 'Development of a molten-salt thermocline thermal storage system for parabolic trough plants', *Journal of Solar Energy Engineering*, 124, 153–159.

Pilkington Solar International GmbH (2000) 'Survey of thermal storage for parabolic trough power plants', NREL/SR-550-27925, DOI 10.2172/765081.

Relloso, S. and Delgado, E. (2009) 'Experience with molten salt thermal storage in a commercial parabolic trough plant. Andasol-1 commissioning and operation', *SolarPaces 2009*, 15–18 September, Berlin.

Riedler, A. (1883) 'Die Honigmannsche Dampflokomotive mit feuerlosem Natronkessel', *Zeitschrift des Vereines Deutscher Ingenieure*, 27, 729–750.

Schaube, F., Woerner, A. and Tamme, R. (2010) 'High temperature thermo-chemical heat storage for CSP using gas-solid reactions', *Proceedings of the SolarPACES 2010 conference*, 21–24 September, Perpignan, France.

Siegel, N. and Kolb, G. (2008) 'Design and on sun testing of a solid particle receiver prototype', *Proceedings of Conference for Energy Sustainability*, 10–14 August, Jacksonville.

Silverman, M.D. and Engel, J.R. (1977) 'Survey of technology for storage of thermal energy in heat transfer salt', Oak Ridge National Laboratory.

Sioshansi R. and Denholm P. (2010) 'The value of concentrating solar power and thermal energy storage', Technical Report NREL-TP-6A2-45833.

Stein, W., Edwards, J., Hinkley, J. and Sattler, C. (2009) 'Solar thermal steam reforming', in Garche, J. (ed.), *Encyclopedia of Electrochemical Power Sources*, Elsevier, Amsterdam, pp. 300–312.

Steinmann, W.D. and Eck, M. (2006) 'Buffer storage for direct steam generation', *Solar Energy*, 80, 1277–1282.

Steinmann, W.D. and Tamme, R. (2008) 'Latent heat storage for solar steam systems', *Journal for Solar Energy Engineering*, 130, 41–45.

Strub, A.S., Gretz, J. and Palz, W. (1984) 'Eurelios, the 1 MW_{el} experimental solar thermal electric power plant of the European Community', *Solar R&D in the European community, Series B, Thermomechanical solar power plants*, 1.

Tan, T. and Chen, Y. (2010) 'Review of study on solid particle solar receivers', *Renewable and Sustainable Energy Reviews*, 14, 265–276.

Tani, T., Ikeda, N., Tanaka, T., Marukawa, A., Wakamatsu, S., Horigome, T., Saishoji, T. and Fukuda, K. (1986) 'Results and evaluation of the 1 MW solar thermal electric power plant at Nio', in Becker M. (ed.), *Solar Thermal Central Receiver Systems, Vol. 1*, Springer Verlag, Berlin.

WANDA (2006) 'Pre-kommerzielle Entwicklung der WESPE Speicher-Technologie für den Einsatz in ANDASOL Kraftwerken', final report, Wanda-Project.

Weber, R. and Dorer, V. (2008) 'Long-term heat storage with NaOH', *Vacuum*, 82, 708–716.

Williams, O.M. and Carden, P.O. (1978) 'Screening reversible reactions for thermochemical energy transfer', *Solar Energy*, 22, 191–193.

Zunft, S., Haenel, M., Krueger, M., Dreissigacker, V., Göhiring, F. and Wahl, E. (2010) 'Juelich Solar Power Tower – Experimental evaluation of the storage subsystem and performance calculations', *Proceedings of the SolarPACES 2010 conference*, 21–24 September, Perpignan, France.

12

Hybridization of concentrating solar power (CSP) with fossil fuel power plants

H. G. JIN and H. HONG,
Chinese Academy of Sciences, China

Abstract: This chapter summarizes developments in solar hybridization in conventional fossil fuel plants. Drawing on examples of both experimental and commercial plants, the chapter reviews the potential of hybrid solar/thermal power systems and outlines the various arrangements and methods used in hybrid solar/fossil fuel processes. Several new hybridization systems are also introduced, before future challenges for technological improvements in hybridization are discussed.

Key words: hybrid solar/fossil thermal power generation, thermal hybridization, hybridization principle and method.

12.1 Introduction

The operation of concentrated solar thermal power plants involves a number of state-of-the-art technologies; however, questions still remain regarding the installation of systems with a capacity of over 100 MW, and the ability to bring costs down in order to facilitate widespread use.

A variety of different technologies are considered as methods for improving the solar-to-electric efficiency of solar thermal power systems and of reducing cost, but most of these technologies have to contend with theoretical and practical limitations. When collected solar thermal energy is used at a higher temperature, the thermal cycle has high conversion efficiency, while the solar collectors have reduced efficiency and are expensive to produce. On the other hand, when collected solar thermal energy is used at a lower temperature, the solar concentrators are cheaper to produce, but the efficiency of the thermal cycle is significantly reduced.

Another key issue for solar-only thermal power plants is dispatchability. The intermittent nature of solar energy sources can be overcome by the use of some form of energy storage. The recent advances in the field of energy storage systems are discussed in detail in Chapter 11. Another viable means of addressing the dispatchability problem is the integration of concentrated solar thermal power (CSP) in a conventional fossil plant. Hybridization

offers great potential in allowing the cost-effective exploitation of solar energy on a scale commensurate with energy requirements.

Hybridized power plants can be divided into two categories: those using thermal integration and those using thermochemical integration. In thermal integration processes, hybridization uses solar energy to heat water, saturated or superheated steam in combination with fossil fuel combustion. In thermochemical hybridization, fossil fuels are used as chemical reactants, while solar energy serves as the process heat to upgrade or decarbonize the fossil fuel to produce a cleaner fuel. Thermal hybridization is already used for industrial application, while thermochemical hybridization is still at the experimental and demonstration stage.

In contrast to solar-only thermal power plants, a solar hybrid plant can utilize the existing infrastructure of a conventional power station, thereby reducing the investment in equipment lowering the cost of power production. At the same time, it allows the problem of the intermittent nature of solar energy to be avoided. In addition, using solar energy in existing fossil plants goes some way to alleviating fossil fuel shortage and to reducing greenhouse emissions, especially CO_2. Thus, in the short and medium term, the development of hybridized solar and fossil fuel power plants is a practical means of accelerating the adoption of solar thermal power technology on a larger scale.

This chapter describes the forms of solar/fossil fuel hybridization involving coal and natural gas, and examines the various methods of integration. Hybridization technology, integration system design, and equipment are all discussed, along with a look forward to future promising developments in solar hybridization technology.

12.2 Solar hybridization approaches

There are a number of different basic approaches to solar/fossil fuel hybridization. The following sections of this chapter address several of these that have already been used in commercial plants, along with some advanced concepts that are still under development.

12.2.1 Fossil backup and boosting of solar thermal plants

Many solar thermal power plants use fossil fuel as a source of backup energy in the absence of sunlight; this is the most common form of hybridization. The nine commercial solar electric generating systems (SEGS) have a combined capacity of 354 MW and are the most mature and successful of the solar-hybrid pure Rankine cycles. These systems use parabolic trough solar collectors and synthetic oil in a collector loop to transfer thermal energy to Rankine cycle turbines via heat exchangers. Backup gas-fired

boilers are used when the temperature of the steam is below that required by the steam turbines.

12.2.2 Solar-aided coal-fired power plants

Solar hybridization with coal-fired steam production is suitable for countries with large coal resources, such as China and Australia. The solar heat can be easily integrated into coal-fired power plants, to work in parallel with the boiler or feedwater heaters. For example, solar heat can be used to replace the extraction of steam from the turbine to heat the feedwater. This technology could be a particularly attractive option for repowering older coal-fired power plants with a capacity of less than 300 MW. One key advantage of this system is the enhancement of the output of a coal-fired power plant without the need to oversize the steam turbine.

12.2.3 Integrated solar combined cycle (ISCC) plants

Conventional combined cycle power plants use a gas turbine (Brayton) cycle in which the fossil fuel is combusted in series with a steam-based Rankine cycle. This kind of fossil fuel power plant offers the highest conversion efficiency of all the widely used fossil-fired power generation technologies.

In an ISCC plant, the concentrated solar heat is introduced into the gas-fired 'combined cycle' power plant where the solar heat replaces or adds to the exhaust gas from the gas turbine to produce saturated or superheated steam. ISCC systems seek to add solar steam to the steam cycle of such plants, with a view to achieving the benefits of both the pure solar input and the fossil input with the highest efficiency possible.

12.2.4 Advanced systems

Advanced hybridization systems are those in which solar heat and Brayton cycles are integrated in order to convert solar energy into electricity, in contrast to the systems mentioned above, in which solar energy is combined with the conventional Rankine cycle. There are two main categories of advanced hybrid power plants. In the first, solar heat is introduced to preheat the compressor discharge air in the gas turbine cycle, while the second relies on the hybridization of solar heat with decarbonization of the fossil fuel via decomposition, steam reforming or gasification to produce a cleaner fuel, also known as a 'solar fuel'. The hybridization of solar thermochemical sources with fossil fuels is outside the scope of this chapter. The production of solar fuels is discussed in detail in Chapter 20. Hybridization via pre-heating compressed air has been demonstrated by the German

Aerospace Center (DLR) and Plataforma Solar de Almería (PSA), among others, and is discussed further in Section 12.6.

12.2.5 The role of different concentrators

A hybrid system can be constructed by adding solar collectors to a conventional fossil fuel power plant. This provides only a modest fraction of the solar energy needed for a large stand-alone fossil-fired plant. The cost effective design of the solar concentrator field is a key aspect, and is closely related to the establishment of a good match between solar heat, the concentration ratio of the concentrator and the requirements of the power plant. Usually, the concentrated higher temperature solar heat (above 500°C) requires a dish or tower collector; while the concentrated lower temperature solar heat (below 500°C) requires a parabolic trough or linear Fresnel. The following sections briefly introduce these main types of concentrators.

Parabolic dish

This system involves a parabolic dish-shaped reflector with the receiver located at the focal point of the dish. Its concentration ratio is about 1,000–3,000, and the operating temperature of the receiver is approximately 750–1,000°C [1, 2]. A great deal of the research carried out on dish systems is centred around their application to Stirling engines; however, it has also been shown that direct steam generation can be achieved. These systems could provide steam at up to the highest temperatures and pressures found in a fossil-fueled plant. Dish systems are presented in detail in Chapter 9.

Solar tower

A solar tower system involves a large heliostat field with a single receiver mounted on a tall tower positioned at its center. The working substances used in the receiver can include water/steam, molten salts, liquid sodium and air. Its concentration ratio is usually in the range of 150–1,500 and the operating temperature is about 300–2,000°C. Like dishes, tower systems have the potential to provide steam at the highest pressures and temperatures within a conventional power plant, either directly or via a heat transfer fluid. These systems are described in detail in Chapter 8.

Parabolic trough

In this system, parabolic trough-shaped mirror reflectors are used to concentrate sunlight onto receiver tubes placed in the trough's focal line. The

operating temperature of a trough receiver ranges between 50 and 500°C. For example, a heat transfer fluid of synthetic thermal oil can be heated to approximately 400°C [3], while the molten salt that is used as a heat transfer fluid in, for example, the Archimede project in the south of Italy, can be heated from 290°C to 550°C [4]. Direct steam production using trough systems is also at an advanced stage of development. The steam that is produced either directly or indirectly with troughs will not be at as high a temperature as that produced from tower or dish systems; however, it can be applied at various points within a steam cycle. Parabolic trough systems are dealt with in Chapter 7.

Linear Fresnel reflector (LFR)

In an LFR system, as discussed in Chapter 6, strips of mirrors rotate around independent parallel axes to reflect sunlight onto a fixed linear receiver [5]. Its reflector array is a line focus similar to that found in a parabolic trough system. The operating temperature is between 50 and 300°C and the concentration ratio is about 10–40 [6]. For example, in Puerto Errado Thermosolar Power Plants located in Spain, water is heated from 140°C to 270°C through LFR collector strings [7]. A case study of the application of LFR systems to a coal-fired power plant is given in Chapter 13.

12.3 Fossil boosting and backup of solar power plants

The best known fossil backup solar power technology is the famous nine solar electric generating stations (SEGS) plants built between 1984 and 1991, by the American/Israeli Company, Luz International, in the Mojave desert in California. The SEGS plants started with an initial 14 MW, followed by six plants of 30 MW, finally reaching a capacity of 80 MWe in the last two units. In total, they provide 354 MW of reliable capacity which can be dispatched to the Southern California grid [8]. Figure 12.1 shows the SEGS III–VII plants located at Kramer Junction.

12.3.1 Process integration and design

The flow sheet of a SEGS plant is shown in Fig. 12.2. The heat transfer fluid (HTF) is heated up to 393°C through the parabolic trough collector field and returns to a series of heat exchangers, where the fluid is used to generate high-pressure superheated steam at 100 bar and 371°C. After passing through the HTF side of the solar heat exchangers, the cooled HTF is recirculated through the solar field. The superheated steam is then fed to a conventional reheat steam turbine to produce electricity. The exhaust steam from the turbine is condensed and returned to the heat exchangers and

12.1 SEGS III–VII plants located at Kramer Junction (A.R. Akradecki; reproduced under the Creative Commons Attribution-Share Alike 3.0 Unported license).

feedwater pumps to be transformed back into steam. Given sufficient solar input, the plants can operate at full power using solar energy alone.

A receiver tube for direct steam generation is being developed, manufactured and tested at elevated steam temperatures by SCHOTT [10]. The receiver tube can withstand a higher operation pressure of up to 120 bar, compared to the state-of-the-art HTF receiver tubes, which are designed to work at only 40 bar; similarly, it can tolerate an increase in the operation temperature from 395°C to 500°C. These advances will lead to significant improvements in the solar-to-electric efficiency of solar power plants.

12.3.2 Dispatchability

To enable these plants to achieve a rated electric output during periods of low solar radiation, such as overcast conditions or at night, a backup natural gas-fired capability can be used to supplement the solar output. This fossil backup capability allows the SEGS plants to be fully dispatchable. All of the existing SEGS plants are hybrid solar/natural gas designs that can take up to 25% of their annual energy from the natural gas plant. Fossil energy can be used to superheat solar generated steam (SEGS I), from 307°C out of the solar field to 415°C, resulting in increased efficiency in the Rankine cycle. When insufficient solar energy is available, fossil energy can also be used in a separate fossil-fired boiler to generate steam (SEGS II–VII), or

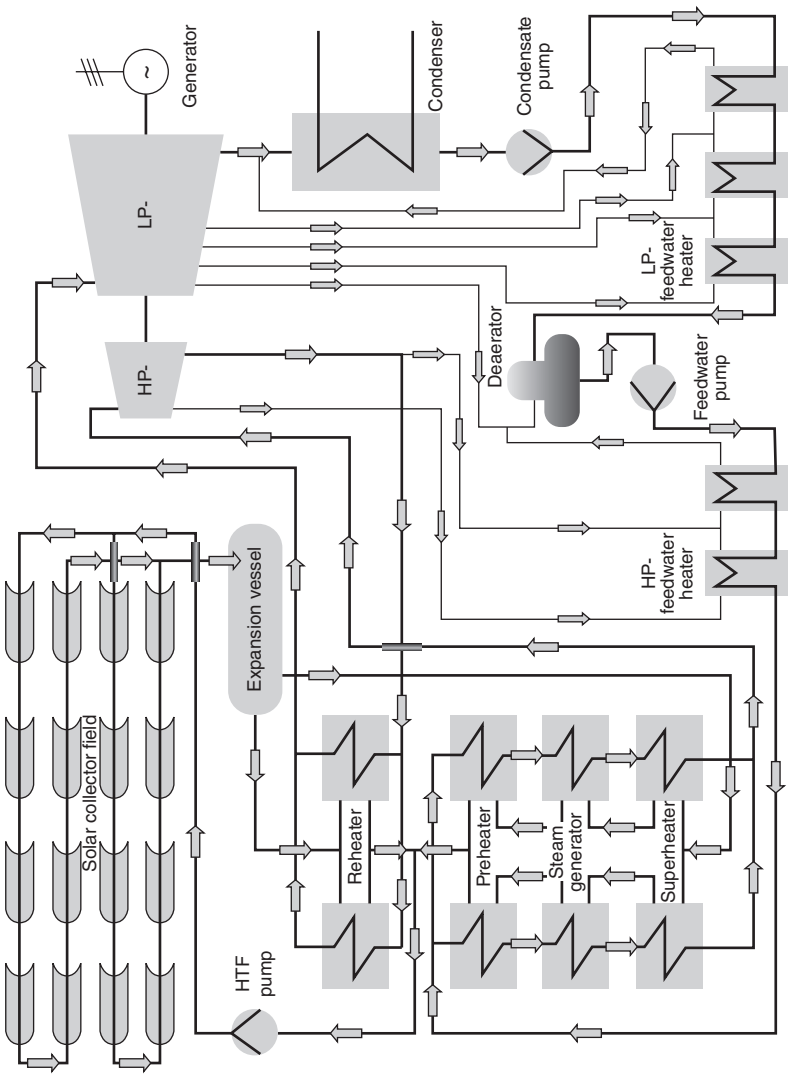

12.2 Flow diagram of the SEGS plant for pure solar mode (reproduced with permission from Ref. [9]).

used in an oil heater in parallel with the solar field (SEGS VIII–IX). The data relating to the SEGS power plants is given in Table 12.1.

12.3.3 Economic effect

Table 12.2 gives a comparison of the economic performance of trough plants in solar-only operation mode and hybrid operation mode. The cost information presented is outdated and should only be used to establish how the various system configurations relate to each other. The cost of power quoted for the 30 MWe SEGS VI trough plant is 0.17 $/kWh for a solar-only plant and 0.141 $/kWh for the hybrid plant with 25% fossil backup in 2002. In plants planned for the near future, the solar-to-electric efficiency is expected to improve by approximately one-third over the original SEGS plants, in large part due to new solar receivers and the use of ball-joint assemblies. Unit capital costs are lower because of the larger plant capacity and the more efficient solar field, which helps to reduce the size of the solar field required. The levelized cost of energy (LCOE) is reduced to 0.11 $/kWh for a solar-only plant and 0.096 $/kWh for the hybrid plant. Overall, hybridization of solar energy with fossil fuel makes the electricity cost of a solar power plant 12–17% lower than if solar-only mode was employed.

12.4 Solar-aided coal-fired power plants

In contrast to the fossil backup technology, the hybridization of solar energy with coal-fired power plants reduces reliance on fossil fuels and allows outmoded conventional power stations to be updated.

12.4.1 Hybridization process and arrangement

Three different arrangements used in solar-aided coal-fired power plants [13], are shown in Fig. 12.3.

- *Solar-aided with boiler drum*: In this hybridization arrangement, the solar collector field is operated in parallel with the boiler. The solar heat at around 400°C converts the feedwater from the economizer of the boiler into saturated steam which is then returned to the drum of the fossil-fired boiler.
- *Solar combined with feedwater*: In this arrangement, solar energy at around 300°C acts as a heat source to preheat the feedwater, instead of using extracted steam from the turbine. The solar field is connected in parallel with the powerhouse feedwater heaters. The solar heat at 300°C can raise the temperature of the feedwater to that required for the

Table 12.1 SEGS power plant data from NREL (from reference [11])

Plant name	Net output (MW)	Solar field outlet (°C/bar)	Solar field area (km^2)	Solar turbine efficiency (%)	Solar field thermal efficiency (%)	Solar-to-electric efficiency	Dispatchability
SEGS IX	80	390/100 reheat	0.484	37.6	50	13.6	HTF heater
SEGS VIII	80	390/100 reheat	0.464	37.6	53	14	HTF heater
SEGS VII	30	390/100 reheat	0.188	37.5	43	12.3	Gas boiler
SEGS VI	30	390/100 reheat	0.194	37.5	43	12.4	Gas boiler
SEGS V	30	349/40	0.251	30.6	43	10.2	Gas boiler
SEGS IV	30	349/40	0.230	30.6	43	10.2	Gas boiler
SEGS III	30	349/40	0.230	30.6	43	10.2	Gas boiler
SEGS II	30	316/40	0.190	29.4	43	10.7	Gas boiler
SEGS I	13.8	307/35	0.083	31.5	35	9.3	3-hour TES

Table 12.2 Solar-only and hybrid operation comparison (from reference [12])

Site: Kramer Junction	30 MW SEGS plant		Near-Term Trough Plant	
	Solar-only	Hybrid (25%)	Solar-only	Hybrid (25%)
Plant size, net electric (MW)	30	30	50	50
Collector aperture area (km^2)	0.188	0.188	0.312	0.312
Thermal storage (h)	0	0	0	0
Solar-to-electric efficiency (%)	10.6	10.7	13.9	14.1
Plant capacity factor	22.2	30.4	29.2	39.6
Capital cost ($/kW)	3008	3204	2745	2939
O&M cost ($/kWh)	0.046	0.034	0.024	0.018
Fuel cost ($/kWh)	0	0.013	0	0.01
LCOE (2002$/kWh)	0.17	0.141	0.11	0.096

boiler, usually around 220°C. The steam that does not need to be extracted is further converted in the turbine, and more output work is therefore generated from the steam turbine compared to the amount generated before hybridization using the same amount of input coal. In this way, this conventional coal-fired power plant is updated to a larger capacity system without incurring substantial costs.

- *Solar aided with superheater*: This arrangement involved the use of solar heat to produce part of the superheated steam which is then injected into the steam turbine. The solar collector field is operated in parallel with the boiler.

Of the above three arrangements, the combination of solar heat with feedwater is the easiest to implement. This solar-aided technology can update repowered coal-fired power plants with a capacity of below 300 MW, giving them greater capacity. Unlike solar-only thermal power plants, this solar hybridization power technology does not require solar energy storage equipment. Also, the existing feedwater heaters are operated in parallel with a solar-driven feedwater heater. In this way, the hybridized power plant can be guaranteed to be operated at full capacity even in the case of low solar radiation.

12.4.2 Case study design

The hybridization of solar energy with coal-fired power technology is suitable for countries rich in coal resources such as China. In northwest China, a large number of old coal-fired power plants with small capacity

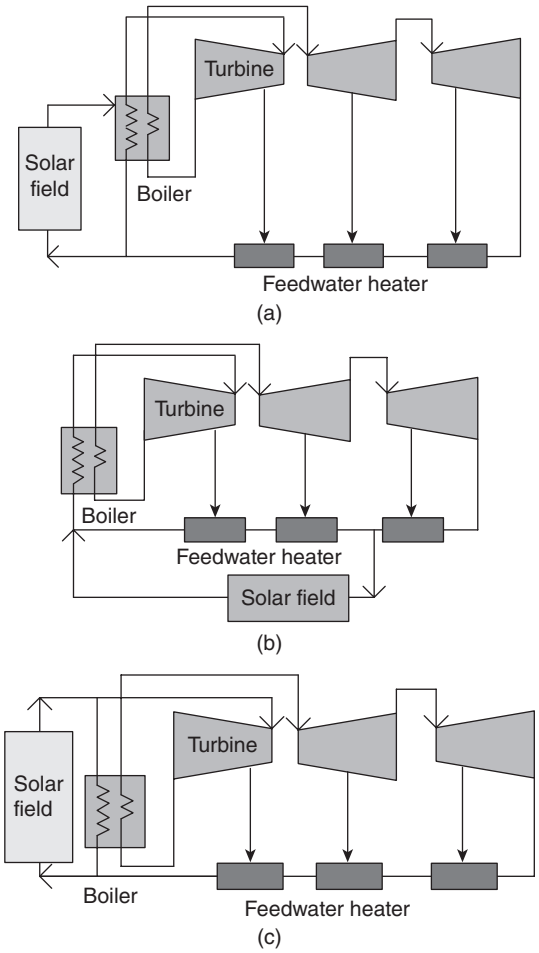

12.3 Schematics of three solar-aided coal-fired processes: (a) boiling process; (b) feedwater heating process; (c) boiling and feedwater heating process.

are still in operation, leading to high levels of environmental pollution. The northwest of China, especially the Xinjiang region, is rich in solar energy with 2,550–3,500 hours of sunlight per year and a high average solar radiation of 5,430–6,670 MJ/m^2/year [14]. Figure 12.4 shows the design flow-sheet for a hybridization system that could be implemented in a 135 MWe coal-fired power plant in the city of Kashi in the Xinjiang region, where there is an annual average of 3,037 hours of sunshine [15].

In this typical design, both the two high-pressure heaters and four low-pressure heaters in the existing 135 MW coal-fired power plant are still maintained. These are operated in parallel with the solar feedwater heating

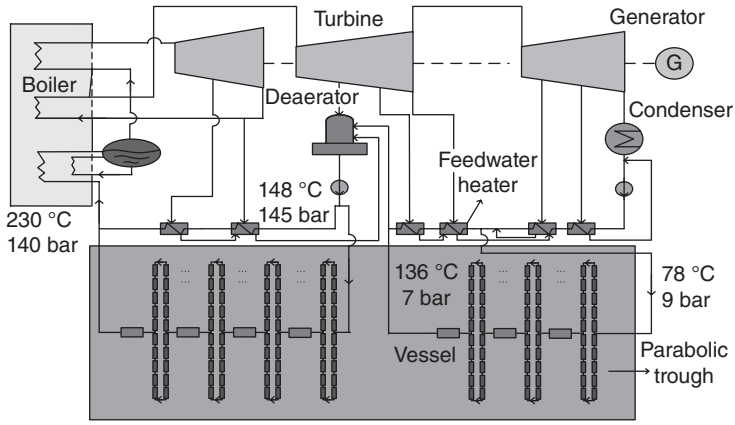

12.4 A design flow-sheet for the typical 135 MW solar hybrid coal-fired power plant in Xinjiang, China.

collector which consists of parabolic trough concentrators, vacuum tube receivers, and heat exchanger. The concentrated solar heat at around 300°C substitutes the high-pressure extracted steam to heat the feedwater to 230°C, before it is injected into the economizer of the boiler. When the direct normal irradiation (DNI) decreases, the total mass flow of the feedwater and the inlet temperature of the regenerative subsystem may be maintained at the same levels that were employed before repowering. However, the flow of the feedwater in the solar collector is decreased, while the flow in the previous feedwater heaters is increased in order to maintain a constant inlet temperature for the boiler economizer. In this way, this repowered plant may be operated at fully-rated output during periods of low solar radiation.

From a design perspective, the overall power output of this hybrid system increases the capacity of the coal-fired power plant from 135 MW to 152 MW, reducing the coal consumption from 319.75 g to 284.24 g/kWh. This increased output is a consequence of the use of solar energy. On the other hand, looking at the conversion of solar energy into electricity, this increase in capacity of 17 MW is equal to the capacity of an equivalent solar-only power plant. The annual solar-to-electricity efficiency in this hybrid plant can reach 15%, about 3 percentage points higher than the state-of-the-art SEGS VI technology [11].

It is estimated that the typical unit capital cost would be almost 2,007 $/kW: this is lower than that of the 30 MW SEGS plant in standard configuration, which has costs close to 3,000 $/kW[12]. The preliminary evaluation of investment needed for this plant is listed in Table 12.3.

It is worth noting that the temperature range of the concentrated solar heat at 300°C is usually used for heating water, rather than to generate

Table 12.3 Preliminary evaluation of investment

Total investment cost	Million $	34.78
Operation and maintenance (O&M) cost	Million $	0.70
Annual average coefficient of device investment (CRF)	$	0.12
Annual cost of device investment	Million $	4.09
Net increased generation power	MWe	17.08
Increased electricity	Million kWh/y	52
Net increased profit	Million $/y	3.70
Payback period	Y	9.39
Solar-generation cost	$/kWh	0.09
Specific investment cost	$/kW	2,007

electricity. Fortunately, hybridization of a solar system with a coal-fired power plant may allow low-grade solar heat to provide electricity.

12.4.3 Potential of systems in China

By the end of 2009, the total installed capacity of traditional coal-fired plants in China is estimated to be 599 GW. Small units (~300 MWe) were estimated to generate approximately 30.57% or 183 GW [16]. If these conventional plants are converted into solar-aided coal-fired systems, assuming 2,500 h per year of sunlight, it is estimated that coal consumption will be reduced by 16.2 million tons per year.

In China, several academic institutes and companies are promoting the industrial application of this kind of solar hybrid plant. For example, the Institute of Engineering Thermophysics, Chinese Academy of Sciences, and North China Electric Power University are developing the technology needed for system integration. Power generation companies, such as Datang, Huadian, Guodian and others, have begun pre-feasibility studies for hybrid plants to be built in Northwest China. In the short term, solar hybridization plants have been designated a high priority technology and their development is supported by the Ministry of Science and Technology and the National Natural Science Foundation of China. They are acknowledged as an appropriate and practical option for solar thermal power plants in China.

12.5 Integrated solar combined cycle (ISCC) power plants

This section will examine integrated solar combined cycle power technology (ISCC). This technology integrates solar energy into the steam cycle of a combined cycle power plant. The steam generated by solar heat may be

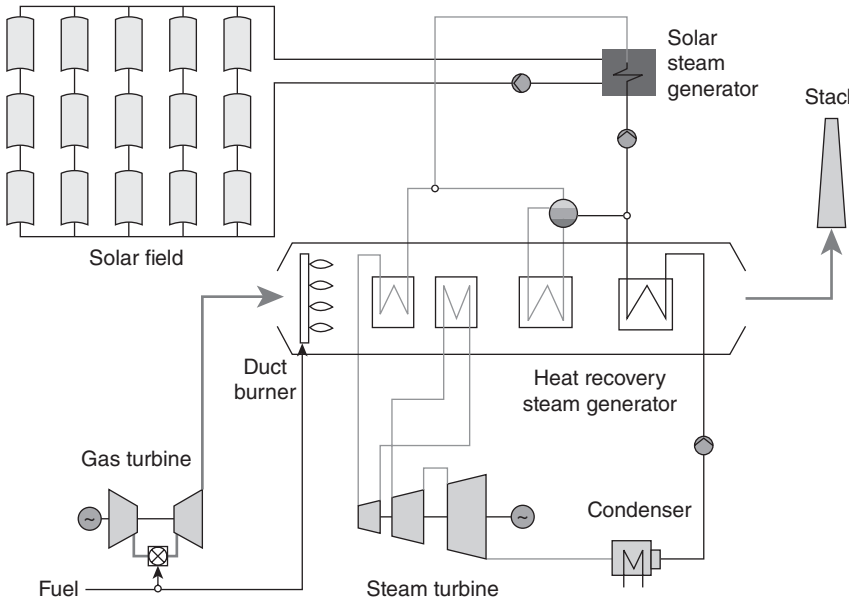

12.5 Diagram of an ISCC power plant with a single-pressure-reheat steam cycle ([17], reproduced with permission).

injected into different parts of the heat recovery steam generator (HRSG) or directly into the steam turbine of the combined cycle. A schematic diagram of an ISCC plant [17] is shown in Fig. 12.5.

The main feature of this approach to solar hybridization is that additional steam cycle power is generated without burning any additional fuel; that is, all the additional power generated in the steam cycle of the combined cycle is 'free' from a fuel perspective. To achieve this, the size of the steam turbine may be increased relative to the unit that would be used in a pure gas-fired application. At times of zero solar input, the oversized steam turbine runs at part load. Solar thermal input can also be used to reduce the fuel consumption of an ISCC plant. In this approach it is the gas turbine that runs at part load when solar input is available. Note that reducing the fuel consumption of the gas turbine also reduces its power and exhaust energy.

When planning to integrate steam generated by solar energy into a combined cycle, two main questions must be considered: (a) How much solar energy should be integrated into the combined cycle? and (b) Where is the best place in the steam cycle to inject the solar generated steam? The best means of integrating steam that is generated by solar technology is obviously highly dependent upon the steam conditions that can be generated by that technology. The following sections discuss how various solar technologies can be integrated into combined cycle power plants.

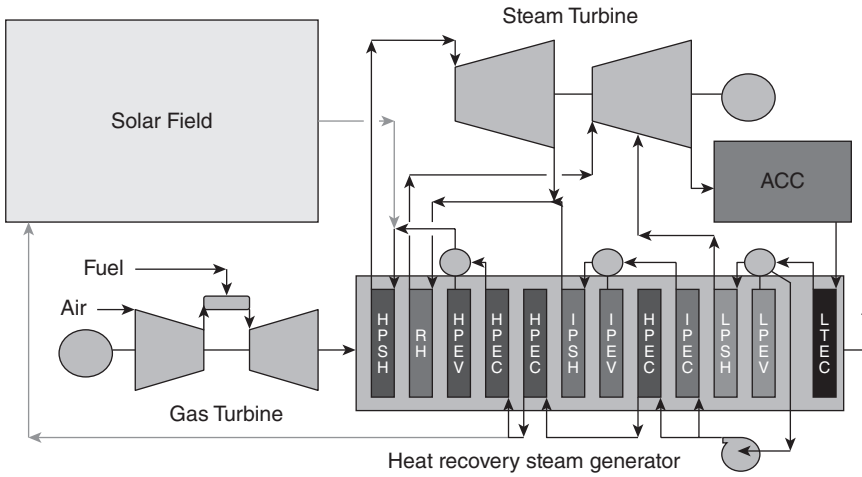

12.6 A medium temperature solar IGCC. (HPSH: high-pressure superheater; RH: reheater; HPEV: high-pressure evaporator; HPEC: high-pressure economizer; IPSH: intermediate-pressure superheater; IPEV: intermediate-pressure evaporator; IPEC: intermediate-pressure economizer; LPSH: low-pressure superheater; LPEV: low-pressure evaporator; LTEC: low temperature economizer; ACC: air cooling condenser) ([18], with permission).

12.5.1 Process integration and design

ISCC technology can be categorized into three types on the basis of its fluid temperature capability: high temperature: >500°C; medium temperature: 400°C; low temperature: 250–300°C. The medium temperature type has been most widely implemented, and will be discussed first.

Medium temperature solar technology

The most common medium temperature solar technology makes use of a parabolic trough. The integration of extra high-pressure saturated steam into an HRSG is also proposed in integrated gasification combined cycle (IGCC) plants (Fig. 12.6). The parabolic trough systems can generate steam up to ~380°C. Sending out heated feedwater from the HRSG is also very common in IGCC plants. Note that it is important to take the feedwater supply to the solar boiler from the proper location in the steam cycle. The most convenient location for this is from the discharge of the HP feedwater pump. Similar to what is observed in SEGS plants, the HTF leaving the steam generator is at ~290°C. The feedwater temperature should be ~260°C to maximize the heating of feedwater in the HRSG and minimize the heating of feedwater in the solar field.

High temperature solar technology

Solar tower systems can generate superheated steam at high pressure and up to 565°C. These conditions potentially allow solar generated superheated steam to be directly admitted into the HP steam line to the steam turbine. In addition, steam can be reheated in the power tower along broadly the same lines as in an HRSG. This allows minimal impact on the HRSG as the superheating and reheating of the solar steam is carried out in the solar boiler.

Low temperature solar technology

To date, most linear Fresnel systems have been used to generate saturated steam at up to 270°C/55 bar. This pressure is too low to allow integration into the HP system of the steam cycle. In this situation there are two options: either generate saturated steam at ~30 bar and admit to the cold reheat line, or generate steam at ~5 bar and admit it to the LP steam admission line.

12.5.2 Major equipment design

The design mainly involves the integration of the solar field input with the combined cycle equipment, particularly the HRSG, steam turbine and heat sink.

Heat recovery steam generator (HRSG)

It is clear that in most cases the steam generated by the solar field needs to be re-injected into one of the HRSG sections. One major challenge in the selection process would be the sizing of this particular section of the HRSG. Both the fossil and solar generated steam could be accommodated; alternatively, the section could be sized for only the fossil part [19].

Steam turbine

One of the major decisions in the selection of the amount of solar generated steam (for a given CSP technology) is the sizing of the steam turbine, which is connected to both the steam mass flow and pressure. The variation in these two aspects, particularly during night-time or evening operation, will affect the cycle efficiency. The volumetric flow to the turbine should be kept close to design value.

Balance of plant (BOP)

The contribution of the solar generated steam also affects the BOP components such as pumps, motor control centers (MCC), piping and cabling.

If the purpose of the solar generated steam is to augment the power output of the plant, then the electrical generator must also be able to cope with the increased capacity. Due to water scarcity the heat sink (condenser cooling) in these plants is more often an air cooled condenser (ACC) rather than a conventional wet cooling tower. In either case, the heat rejection load is increased or modified for the given ambient conditions.

12.5.3 Typical demonstration plant and project

One of the first ISCC plants to be built was Yazd Solar Thermal Power Plant in Iran [20], which became operational in 2009. The plant comprises two gas turbine units with nearly 150 MW capacity each, one steam unit with nearly 150 MW capacity, together with a solar thermal unit with 17 MW equivalent capacity. With a total capacity of 467 MW, the Yazd power plant [21] was the eighth largest solar power plant in the world at the start of 2010.

In Ain Beni Mathar, Morocco, an ISCC project of 472 MW is being built, supported by Global Environmental Facility [22], as shown in Fig. 12.7. The plant includes a parabolic trough solar component of 20 MW (180,000 m^2) with an expected annual net production of 3.538 GWh. The solar output is estimated at 1.13% of the annual production, representing 40 GWh per year. The plant started electricity production in May 2011.

Abener has recently constructed a second ISCC power plant in Hassi'Mel, Algeria. The complex comprises a 130 MW combined cycle, with a gas turbine power in the order of 80 MW and a 75 MW steam turbine. A 25 MW solar field, requiring a surface of around 180,000 m^2 of parabolic

12.7 IGCC plant in Ain Beni Mathar, Morocco (from [22], with permission from Elsevier).

mirrors, is the source of non-fossil energy. Nearly $140 million has been invested in the project, and it is the first privately financed solar thermal plant in North Africa [23]. The plant started to produce electricity in July 2011.

In Egypt, a plant with a total capacity of 140 MW [24] is currently under construction. It has a large solar contribution of 30 MW and is supported by Global Environmental Facility with a $50 million grant. It is due to start production on December 30, 2012.

In Italy a solar field of 30 MW is being added to an existing power plant with a 700 MW capacity. The United States is in the process of building an ISCC plant in Victorville, CA, with three others planned in California and Florida. In Mexico an ISCC project was approved by Global Environmental Facility in 2006 and in India a 150 MW ISCC plant [20] is being planned with a solar contribution of 30 MW.

In 2010, US utility group Florida Power and Light (FPL) opened the first hybrid solar thermal facility in the US to connect to an existing combined cycle power plant at the Martin Next Generation Solar Energy Center [25]. The CSP installation with a capacity of 75 MW is the largest of FPL's solar facilities and consists of approximately 180,000 mirrors over roughly 500 acres at the existing plant location, which currently produces up to 2.8 GW.

Table 12.4 shows ISCC projects currently at an advanced stage of development [20].

There is a practical issue with ISCC systems: namely that when solar energy is not available, the steam turbines have to run at part load and thus with reduced efficiency. In other words, solar steam is only supplied during some 2,000 of the 6,000–8,000 operating hours of the combined cycle. This means that the solar share obtainable is less than 10%; as a result ISCC systems are only considered to have short-term prospects [26].

12.6 Advanced hybridization systems

Advanced hybridization refers to the combination of solar energy with a gas turbine cycle. There are two main categories: systems that use solar heat to preheat the compressor discharge air in a gas turbine cycle; and those that use solar heat to decarbonize fossil fuel for electricity generation. The latter also involve high-temperature and mid-temperature thermochemical hybridization processes. Here, we focus on the solar preheating of air and mid-temperature solar thermochemical hybridization technology.

12.6.1 High-temperature solar air preheating

The concentrated solar power can be used to heat pressurized air in a gas turbine before it enters the combustion chamber. There is thus no need to

Table 12.4 ISCC projects under development

Country	Technology	Capacity (MWe)	Solar capacity (MWe)	Solar share	DNI (kWh/m^2/y)	Construction status at December 2011
Iran, Yazd	ISCCS PT	467	17	3.6%	2,500	Complete
Algeria, Hassi R'mel	ISCCS PT	150	25	16.7%	2,300	Well advanced
Morocco, Ain Beni Mathar	ISCCS PT	472	20	4.2%	2,300	Well advanced
Egypt, Kuraymat	ISCCS PT	140	40	28.6%	2,400	Well advanced
Florida Power and Light	?	?				Complete
US, Victorville, CA	ISCCS PT	563	50	8.9%	2,200–2,600	?
US, Indiantown, FL	ISCCS PT	1,125	75	6.7%	–	?
Italy, Siracusa	ISCCS PT	730	30	4.1%	2,100	?
US, Palmdale, CA	ISCCS PT	570	50	8.8%	2,200–2,600	?
Mexico, Sonora State	ISCCS PT	500	30	6.0%	2,600	?

use fossil fuels to preheat the air from 300°C to 1200°C, and the solar heat is converted with all the high thermal efficiency of a modern recuperated or combined gas turbine cycle.

Solar air preheating has great potential to reduce the costs of solar thermal power. In addition, the concept could be applied to a wide range of power levels (from 1 to 100 MW) [27]. Projects involving solar air preheating are discussed below.

Typical projects

The SOLGATE project investigated the concept of combining solar energy with fossil fuel in a hybrid plant, and showed its feasibility by proving that a gas turbine could be modified to allow dual operation. Tests were carried out at different operating temperatures, which resulted in different solar shares and varying electricity generation costs. In the EU-funded SOLGATE project demonstrated at the Plataforma Solar de Almería (PSA) [28], pressurized air temperatures of up to 960°C were achieved at the receiver exit.

The aim of the closely related REFOS project is to develop, build and test modular pressurized volumetric receivers under operating conditions representative of those encountered when receivers are integrated with gas turbines. The main focus of the project is the testing of solar air preheating, accompanied by basic research into materials. The project is led by DLR and carried out in cooperation with CIEMAT, Spain, and G+H, Germany. A diagram of a REFOS project principle [27] is shown in Fig. 12.8.

A pressurized volumetric air receiver with a secondary concentrator has been developed and successfully tested at the PSA, Spain. A number of receiver modules, each of which consists of a pressurized receiver unit and a secondary concentrator with a hexagonal entrance aperture (see the

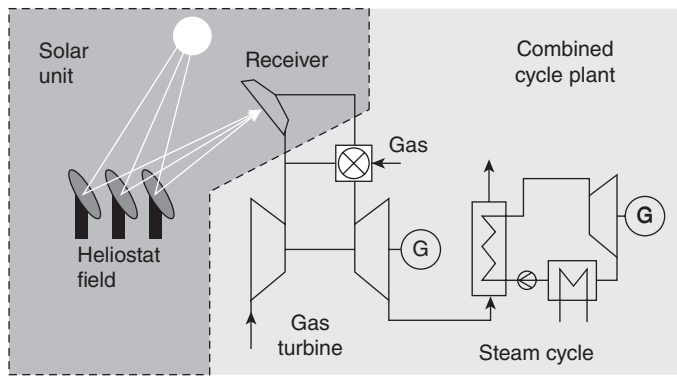

12.8 Solar air preheating system (from [27], with permission).

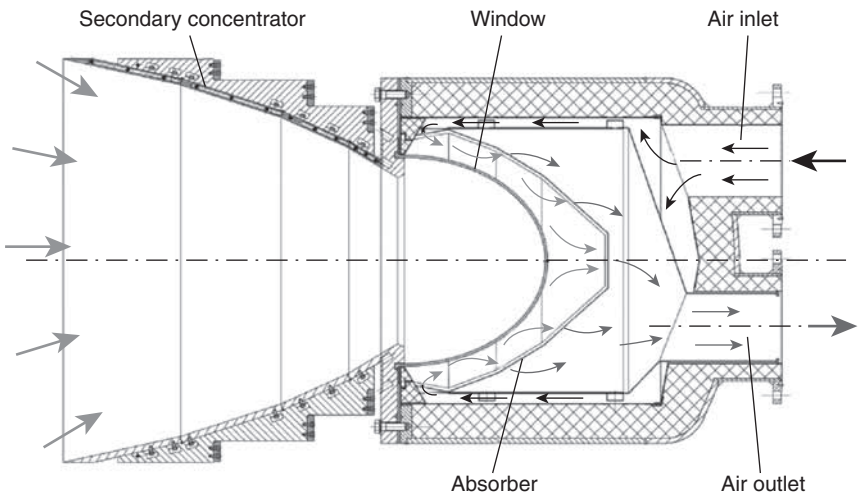

12.9 REFOS Receiver module (from [27], with permission).

REFOS receiver module [27] in Fig. 12.9) were placed on the tower of a solar plant.

Since pressurized air receivers in solar tower plants can heat compressed air in a gas turbine to temperatures up to 1,000°C, it is theoretically possible to achieve a solar share of 40–90%, and annual solar shares of up to 30% as a base load. Results from a test rig [27], simulating a 30 MWe solar hybrid gas-turbine plant with a pressurized volumetric air receiver, show that the thermal solar share is 28.6% for daytime operation and 15% for full-time operation; the corresponding net solar-to-electricity efficiency is 18.1% and 15.3%, respectively.

Economical potential

The investment required for a hybrid plant depends on the power level of the plant and on the solar share proposed; the solar share itself is governed by the maximum exit temperature of the receiver. The current evaluation shows [27] that for a 30 MWe solar hybrid gas turbine plant with a pressurized volumetric air receiver, the potential solar LCOE is $0.1275–$0.1367/kWh.

If using modern gas turbine systems in recuperation or combined cycle mode, the conversion efficiencies for solar heat will be increased to over 50%. For a given solar share, this results in a reduced heliostat field size and in lower overall costs for the solar aspect of the investment, compared to the investment needed for solar steam generation. Thus, solar gas turbine systems are expected to have great potential for market success in the medium term [29].

12.6.2 Solar thermochemical hybridization plant

Chapter 20 addresses solar fuels in detail. Any solar-derived fuel can be used in a combined cycle power plant with a suitably modified combustion system. One of the most obvious strategies in the short term is solar-driven natural gas reforming. This could be carried out together with combined cycle power generation which would otherwise burn natural gas directly.

Case study of medium temperature thermochemical hybridization

This section briefly discusses one example of a cost-effective mid-temperature solar thermochemical hybridization plant. Figure 12.10 shows the arrangement of the mid-temperature solar thermochemical hybridization combined cycle using methanol decomposition proposed by the group in which the authors of this chapter currently work, at the Institute of Engineering Thermophysics, Chinese Academy of Sciences [30]. It is composed of two main integrated processes: a solar thermochemical process at around 200–300°C and a gas turbine combined cycle with dual-pressure heat recovery steam generation. The solar thermal heat collected at 200–300°C supplies the heat required for methanol decomposition. The solar fuel produced with syngas (CO and H_2) acts as a fuel to drive the combined cycle, which

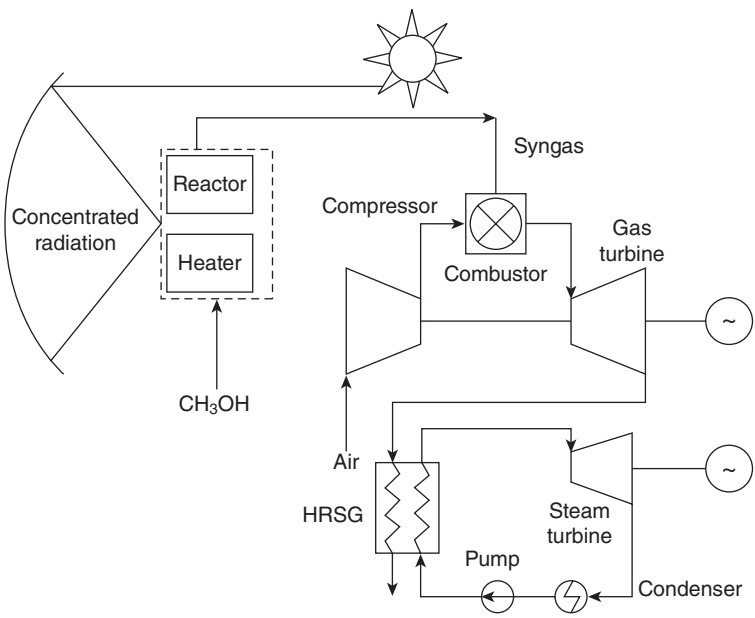

12.10 Schematic of the new solar/methanol combined cycle hybrid plant.

then produces electricity. The net solar-to-electric efficiency is expected to be about 35%, which is related to the energy-level upgrade of mid-temperature solar heat to a high level of chemical energy in the fuel [31].

Key equipment

The parabolic tubular solar receiver/reactor is the most important element of this mid-temperature solar hybridization technology. A 15 kW mid-temperature solar receiver/reactor prototype has been manufactured and fabricated [32–34], as shown in Fig. 12.11.

(a)

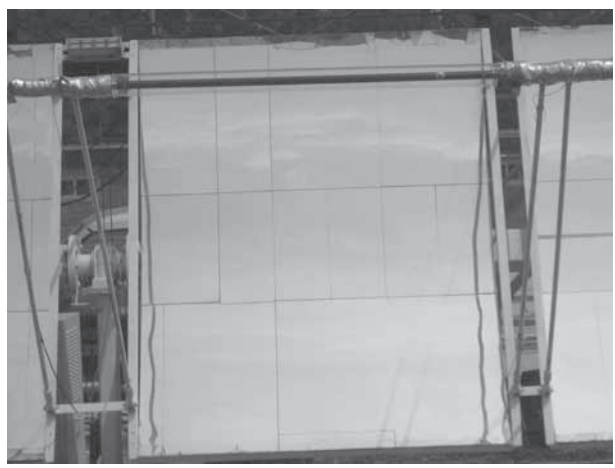

(b)

12.11 Photograph (a) and close-up (b) of the 5 kW solar receiver/reactor prototype.

The prototype consists of 30 m^2 parabolic trough solar fields, with a concentration ratio of 30, and an axial copper reactor tube enclosed by an evacuated transparent glass envelope. The tubular receiver/reactor is positioned along the focal line of a one-axis tracking parabolic trough concentrator oriented in an east-west direction. The National Natural Science Foundation of China has supported this research into the basic scientific issues surrounding this mid-temperature solar thermodynamic hybridization process, and the related technological developments are supported by the National High Technology Research and Development Program of the Ministry of Science and Technology of the People's Republic of China. The technology can also be applied in co-generation power, cooling, and heating using gas turbines, and may represent a viable starting point for the rapid development of economical solar thermochemical power generation technology in the short term.

12.7 Conclusions and future trends

The hybridization of solar technology with conventional power generation technology is an extremely promising energy system and is likely to provide a major share of renewable bulk electricity production in the near future. It has enormous potential to be economically superior to solar-only plants using the same field size. Current research predicts that annual thermal solar shares could be as high as 40–65%, with levelized solar energy costs much lower than those of solar-only technology.

Currently, almost all existing hybrid solar and fossil fuel plants suffer from the relative expense of the process. The greatest challenge facing researchers and engineers today is to work towards a truly standardized primary technology for solar energy use. The areas with most potential for improvements are in the efficiency of the energy system itself and in the manufacturing costs of the different components, which must be substantially reduced.

Currently, one of the most realistic approaches is the repowering of existing coal-fired plants using solar thermal energy to replace extracted turbine steam. The most significant impact will be seen in larger power plants with a capacity of more than 100 MW, and this could drive the rapid development of the cost-effective implementation of solar electricity, especially for countries rich in both coal and solar energy resources, such as China, Australia, and the United States. The key issue in this approach is the integration of concentrator technology and steam turbines with a flexible system configuration. The basic goal is to develop sufficient, cheap hybrid solar–thermal power technology with scalable efficiencies of 15–20% in solar-to-electricity conversion.

With regard to future developments in solar hybridization systems, emphasis needs to be placed on highly integrated systems, rather than on

those that are simply annexed to existing plants. Future systems need to consider resource hybridization, energy conversion hybridization, and system simplification, as well as co-pollutant control and cascade utilization of both concentrated solar energy and fossil fuel energy.

12.8 Acknowledgements

This study was supported by the Natural Science Foundation of China (No. 50836005) and the National Basic Research Program of China (973 Program) (No. 2010 CB 227301).

12.9 References

[1] Stine W., Diver R., 'A Compendium of Solar Dish/Stirling Technology'. Sandia National Laboratories, Albuquerque, NM, 1994.
[2] Groenendaal B., 'Solar Thermal Power Technologies'. Monograph in the framework of the VLEEM Project, 2002.
[3] Lippke F., 'Simulation of the part-load behavior of a 30 MWe SEGS plant'. Solar Thermal Technology Department and Sandia National Laboratoires, 1995.
[4] http://www.nrel.gov/csp/solarpaces/project_detail.cfm/projectID=19.
[5] Grena R., Tarquini P., 'Solar linear Fresnel collector using molten nitrates as heat transfer fluid', *Journal of Energy*, 2011, 36: 1048–1056.
[6] Singh P., Ganesan S., Yadava G., 'Performance study of a linear Fresnel concentrating solar device', *Journal of Renewable Energy*, 1999, 18: 409–416.
[7] http://www.nrel.gov/csp/solarpaces/project_detail.cfm/projectID=46.
[8] Brakmann G., Aringhoff R., Geyer M., Teske S., 'Concentrated solar thermal power now: Exploiting the heat from the sun to combat climate change, Greenpeace/ESTIA/Solar Paces, 2005.
[9] Stuetzle T., Blair N., Mitchell J.W., Beckman W.A., 'Automatic control of a 30 MWe SEGS VI parabolic trough plant'. Solar Energy Laboratory, University of Wisconsin-Madison, 2001.
[10] Eck M., Eickhoff M., Feldhoff J., *et al.*, 'Direct steam generation in parabolic troughs at 500°C – First results of the Real-Diss project'. Concentrating Solar Power and Chemical Energy Systems. SolarPaces, 2011, Granada, Spain.
[11] National Renewable Energy Laboratory, 'TroughNet: Solar parabolic power network', 2008.
[12] Price H., Kearney D., 'Reducing the cost of energy from parabolic trough solar power plants'. National Renewable Energy Laboratory. International Solar Energy Conference, Hawaii, 2003.
[13] Odeh S., 'Unified model of solar thermal electric generation systems', *Journal of Renewable Energy*, 2003, 28: 755–767.
[14] http://scitech.people.com.cn/GB/6772011.html.
[15] Hong H., Zhao Y., Jin H., 'Proposed partial repowering of a coal-fired power plant using low-grade solar thermal energy', *International Journal of Thermodynamics*, 2011, 14(1): 21–28.
[16] http://www.ndrc.gov.cn/jjxsfx/t20100713_360615.htm.

[17] Dersch J., Geyer M., Herrmann U., *et al.*, 'Trough integration into power plants – a study on the performance and economy of integrated solar combined cycle systems'. *Journal of Energy*, 2004, 29: 947–959.
[18] Anon., Renewable energy: The future of power generation, *Engineering Review*, September 2009 http://www.engrreview.com/Editorial_pages/2009/sep_09/power_technofocu-07.html (accessed December 2011).
[19] Kelly B., Herrmann U., Hale M., 'Optimization studies for integrated solar combined cycle systems'. Proceedings of Solar Forum 2001.
[20] http://www.zawya.com/story.cfm/sidZAWYA20101220044922.
[21] Siemon B., Alice D., 'Defining the techno-economic optimal configuration of hybrid solar plants'. Universiteit Gent Faculteit Economie en Bedrijfskunde Academiejaar, 2008–2009.
[22] http://www.nrel.gov/csp/solarpaces/project_detail.cfm/projectID=43.
[23] http://www.nrel.gov/csp/solarpaces/project_detail.cfm/projectID=44.
[24] http://www.nrel.gov/csp/solarpaces/project_detail.cfm/projectID=65.
[25] http://www.fpl.com/environment/solar/martin.shtml.
[26] Geyer M., 'International Market Introduction of Concentrated Solar Power – Policies and Benefits'. IEA SolarPACES Implementing Agreement. Proceedings of ISES Solar World Congress 2007: Solar Energy and Human Settlement.
[27] Buck R., Bräuning T., Denk T., *et al.*, 'Solar-hybrid gas turbine-based power tower systems (REFOS)', *Journal of Solar Energy Engineering, Transactions of the ASME*, 2002, 124: 2–9.
[28] Garcia P., Ferriere A., Flamant G., *et al.*, 'Solar field efficiency and electricity generation estimations for a hybrid solar gas turbine project in France', *Journal of Solar Energy Engineering, Transactions of the ASME*, 2008, 130: 0145021–0145023.
[29] Schwarzbözl P., Buck R., Sugarmen C., *et al.*, 'Solar gas turbine systems: design, cost and perspectives', *Journal of Solar Energy*, 2006, 80: 1231–1240.
[30] Hong H., Jin H., Ji J., *et al.*, 'Solar thermal power cycle with integration of methanol decomposition and middle-temperature solar thermal energy', *Journal of Solar Energy*, 2005, 78(1): 49–58.
[31] Hong H., Liu Q., Jin H., 'Solar hydrogen production integrating low-grade solar thermal energy and methanol steam reforming', *Journal of Energy Resources Technology, Transactions of The ASME*, 2009, 131(1): 0126011–01260110.
[32] Jin H., Sui J., Hong H., *et al.*, 'Prototype of middle-temperature solar receiver/reactor with parabolic trough concentrator', *Journal of Solar Energy Engineering, Transactions of The ASME*, 2007, 129(4): 378–381.
[33] Liu Q., Hong H., Yuan J., *et al.*, 'Experimental investigation of hydrogen production integrated methanol steam reforming with middle-temperature solar thermal energy', *Journal of Applied Energy*, 2009, 86(2): 155–162.
[34] Hong H., Liu Q., Jin H., 'Operational performance of the development of a 15 kw parabolic trough mid-temperature solar receiver/reactor for hydrogen production', *Journal of Applied Energy*, 2012, 90(1): 137–141.

13

Integrating a Fresnel solar boiler into an existing coal-fired power plant: a case study

R. MILLAN, J. DE LALAING, E. BAUTISTA, M. ROJAS and F. GÖRLICH, Solar Power Group GmbH, Germany

Abstract: A Fresnel solar boiler is used to investigate the influence of a superheated-steam generating solar add-on on the overall performance of a 350 MW coal-fired power plant in two promising places for this type of technology. The solar boiler supplies steam to the preheating stages of the power block in order to reduce the steam extraction from the turbine. The focus of the investigation is the evaluation of the potential of using not just a single but several points of supply for solar steam. Different combinations of solar steam management are analyzed concerning their thermodynamic performance, and potential to save fossil fuel and thereby reduce the carbon footprint of power generation.

Key words: coal-fired power plant, Fresnel solar boiler, solar add-on, feedwater heating, internal rate of return (IRR), electricity production cost, emission reduction.

13.1 Introduction

Coal-fired power plants produce electricity using a steam turbine. Retrofitting existing coal-fired power plants is a low-cost option for solar thermal systems, as most of the existing system can be used. Solar add-ons can be a way to simultaneously expand the use of solar energy and trim carbon footprints [1]. The implementation of a solar system into the power plant does not affect the steam cycle or the electrical efficiency during the periods of low irradiation, since the fuel supply can be adjusted (within operating limits) according to the thermal energy available from the solar system.

The integration of a concentrating solar power (CSP) plant into an existing steam-based power plant is readily achieved with a direct steam generating system. In that way it can be directly connected to the steam cycle and does not require additional heat transfer media and heat exchangers. Any of the CSP technologies could be applied to this end, however this chapter presents a case study based on the use of linear Fresnel technology. Fresnel systems are linear concentrators that use an array of parallel long mirrors moving to maintain a linear focus on a fixed linear receiver mounted on towers. Fresnel systems are discussed in detail in Chapter 6. The linear

Fresnel system offers the ability to conveniently generate direct steam, either saturated or superheated.

The aim of this case study is to demonstrate and assess the potential fuel and cost savings that can be achieved by retrofitting a linear Fresnel system in an existing coal-fired power plant.

13.2 Description of options considered as variables selected for the case study

13.2.1 Coal-fired power plant

A regenerative steam power cycle, with a six-stage feedwater heating system (five close feedwater heaters and one open feedwater heater and reheat), was used as the basis for this case study; see the process flow diagram (PFD) in Fig. 13.1. This simplified PFD represents a typical design of coal-fired power plants installed in many locations. High pressure (HP), intermediate pressure (IP) and low pressure (LP) turbine stages are mounted on a single shaft coupled to the generator. Steam is reheated in the boiler following expansion in the HP turbine, before returning to the IP turbine, which serves to prevent excessive condensation of liquid in the LP turbine. In a regenerative cycle, the feedwater is heated progressively in a series of feedwater heaters (FWH) which involve heat exchange with steam bled off from the turbines at various points in such manner that in each case the steam used is

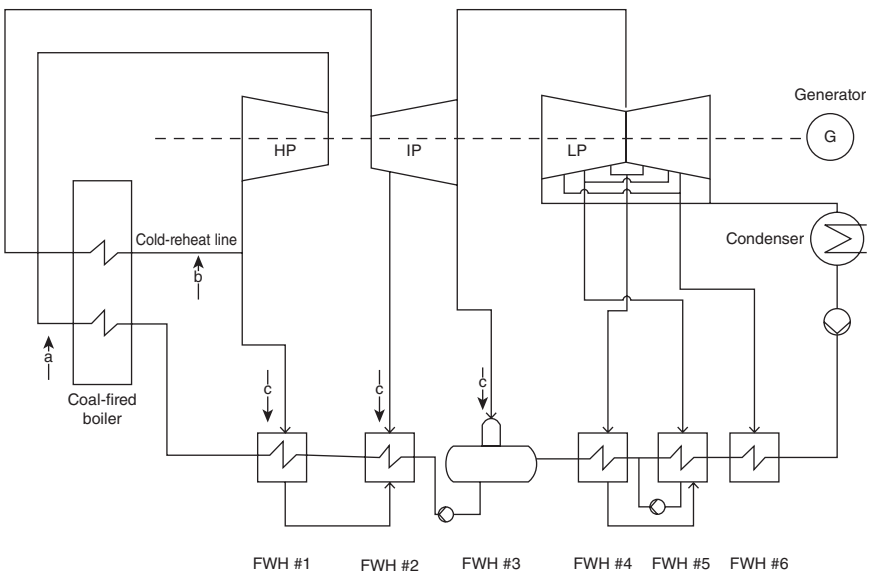

13.1 Process flow diagram of the coal-fired power plant with possible solar steam injection points marked a, b and c.

of sufficient temperature to drive the necessary heat transfer. FWH #3 is an open feedwater heater that mixes steam directly into the feedwater.

The chosen electric capacity of the coal-fired power plant is 350 MW. The temperature of the water/steam working fluid varies from around 50°C up to over 500°C, giving a wide temperature range for the possible integration of the solar system.

13.2.2 Modes of operation when integrating solar steam

The boundary conditions of a retrofitting concept are set according to the tolerance of the power plant's components. In 'augmentation' mode, the purpose is to increase the production of electricity by moving the operation of the turbine-generator set beyond its nominal operating point. Most systems can typically work at up to 112% of nominal capacity. The boiler continues operating at nominal full load. If the plant 'fuel conversion efficiency' is defined as the ratio between the electricity produced and fossil primary energy, then the final effect is increased plant efficiency as more electricity is produced with the same amount of fuel burnt. In 'fuel-saving' mode, the boiler operates below its full load point. The solar steam is added to the main flow in such a way that the turbine receives enough steam to continue operating at its nominal point. In this case the net effect is that the same electricity is produced with less fuel.

13.2.3 Solar steam insertion points

Main steam line

There are several considerations regarding the injection point (point 'a' in Fig. 13.1). The most simplistically obvious option is to add the solar steam to the main steam line. However, this is technically challenging, as the steam quality has to be assured to avoid condensation inside the turbine that might damage it. Another important point is the operational temperature of the turbine; state-of-the-art linear concentrator solar thermal systems can reach up to a maximum of 450°C superheated steam whereas the operational temperature of the common turbines used today is around 550°C. This implies the use of additional superheaters to boost the temperature of the solar steam. Otherwise, the decrease in efficiency due to lower steam temperature can override the desired efficiency increase effect.

Cold reheat line

In this case solar steam would be injected into the exit steam flow from the HP turbine, prior to reheat in the boiler (point 'b' in Fig. 13.1). For solar

boilers with the capacity to produce superheated steam, this method of insertion provides significant additional benefits, due to the net increase in efficiency obtained as a result of the lower energy requirement of the steam to reach the turbine operating conditions. This effect is directly related to the solar boiler temperature: the higher, the better.

Feedwater heater

Another suitable option is to replace or reduce the steam bled from the turbines for the feedwater heater with the solar steam (points 'c' in Fig. 13.1). Usually, to increase efficiency, the turbine is bled to allow preheating of the water entering the boiler. The same effect is obtained if solar energy is used to preheat the water, allowing the turbine to extract more power from the inlet steam. This has the advantage that it is one of the least invasive methods of retrofitting, because it avoids complex boiler integration issues [2].

Due to the benefits given above, this integration concept is used in the case study. The high pressure and intermediate pressure bleed extractions from the turbine are replaced by the solar steam generated and the fuel-saving mode is applied. Although different types of heat transfer fluids can be used in a Fresnel system, the use of water/steam, known as 'direct steam generation', is less risky, more efficient and requires less investment.

If the goal is simply to heat feedwater, the option of directly passing the feedwater through the solar boiler or else using any other sort of heat transfer fluid in heat exchangers for the purpose is valid. The disadvantages of not using water/vapour as heat transfer fluid are:

- addition of heat exchangers → more expensive
- decrease of efficiency due to the addition of heat exchangers
- fluids, like salt or thermoil, are not environmental friendly and are expensive.

13.2.4 Solar steam generation

In principle, all of the CSP technologies, trough, tower or Fresnel could be used as solar add-ons to existing power stations. With these collector types, either direct steam generation or a range of heat transfer fluids could be used. The technology selected for this case study is superheated steam – Fresnel solar boiler, since it has been demonstrated that it can provide the highest steam conditions and matches the bleed extractions from the turbine.

The Fresnel solar boiler considered, based on the systems produced by the German company Solar Power Group GmbH, consists of 120 collector modules. Each collector module has a mirror surface of about 1,400 m^2 distributed in 24 rows that concentrate the light onto a horizontal pipe,

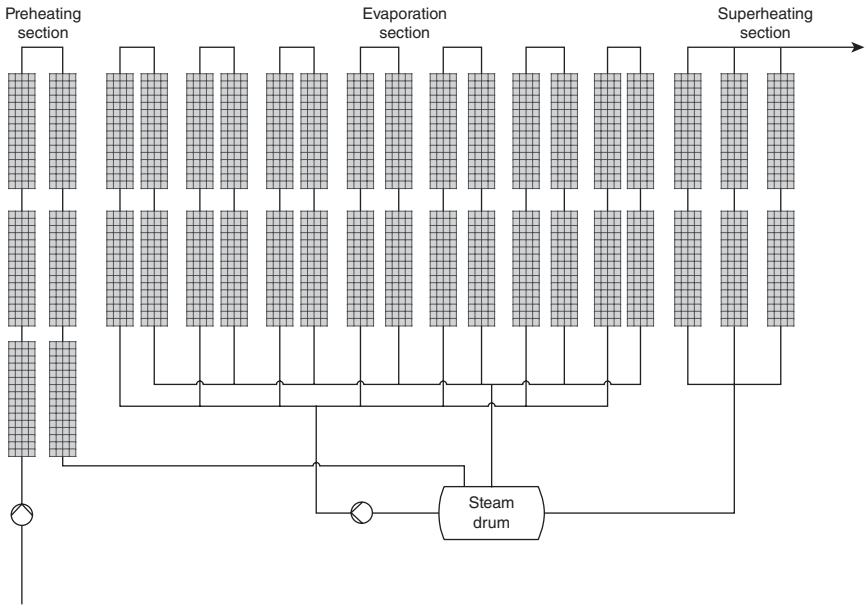

13.2 Different sections of the Fresnel solar boiler.

located 8 m above, through which water/steam circulates. Each row is 96 m long and comprises 16 mirrors.

The solar collector field is divided into three sections, analogous to a regular fossil-fired boiler. In the preheating section, the feedwater is heated up to a temperature close to the evaporation point at the operating pressure and then sent to the steam drum. In the evaporation section, the feedwater coming from the steam drum is gradually evaporated. This section is designed to have a certain degree of steam wetness at its outlet, meaning that part of the flow is still in liquid phase. To ensure dry steam conditions at the entrance of the superheating section, the wet steam coming out of the evaporation section is separated in the steam drum. The temperature of the steam is further increased in the superheating section up to the desired outlet condition. The arrangement of the three different sections of the solar field is shown in Fig. 13.2.

13.2.5 Integration of the Fresnel solar boiler into the coal-fired power plant

The Fresnel solar boiler is integrated into the existing coal-fired power plant by installing it in parallel to the existing high and intermediate pressure (HP/IP) feedwater heater steam bleed lines (see Fig. 13.3). This arrangement allows high flexibility since the maximum solar energy input can be

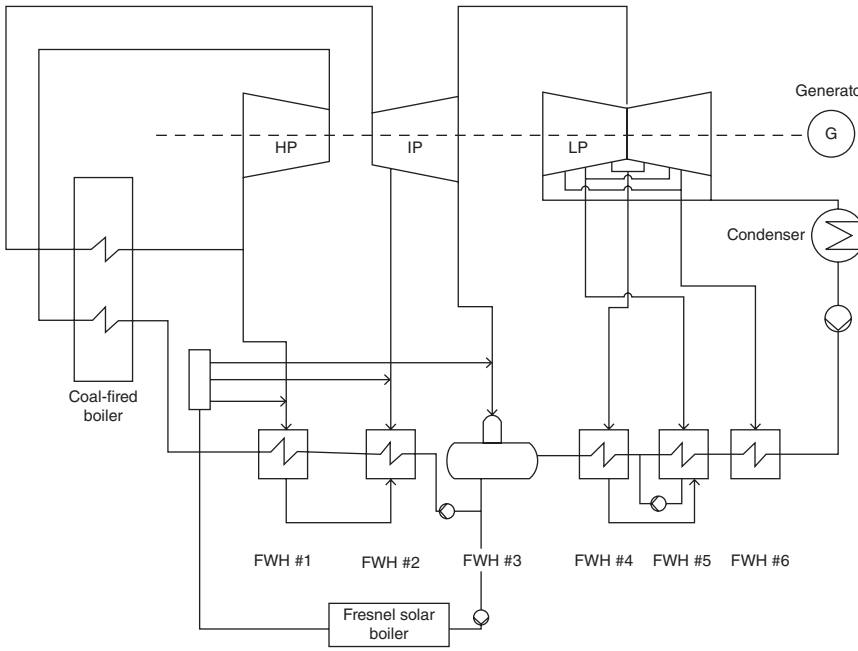

13.3 Process flow diagram showing the integration of the Fresnel solar boiler into the coal-fired power plant.

used and low solar heat input can be compensated independently of the required load demand.

The economic impact and the electrical output improvement of reducing the HP/IP extraction steam is much higher than for the LP extraction steam [3]. For this reason, the solar system is designed to replace the bleed extractions from the steam turbine for the HP and IP feedwater heaters, FWH #1 and FWH #2 respectively. The open feedwater (FWH #3) supplies the solar field with the required feedwater. The amount of feedwater that is pumped to the solar field depends not only on the feedwater heater demands, but also on the availability of solar irradiation. The working temperature and pressure of the solar field are given by the operating conditions of the FWH #1, thus the steam flow is throttled before entering into the FWH #2 and #3.

Regarding the distribution of the solar steam to the preheating system, two cases have been analysed: one that gives priority to the FWH #1 demand and the other that supplies the same amount of heat to FWH #1, #2 and #3.

Case A: Steam flow to feedwater heaters distributed by priority

The steam coming out of the superheating section is distributed to the feedwater heaters according to a given priority, with FWH #1 having the

Table 13.1 Conditions at locations selected for the study [4]

Location	Average ambient temperature[a] (°C)	Average relative humidity[a] (%)	Available sun hours per year (h)	Annual direct normal irradiation (kWh/m^2)
Site 1	32	17	2,480	2,300
Site 2	27	44	2,280	1,950

[a] Average ambient temperature and relative humidity during the sun hours.

highest. First, the demand of FWH #1 is covered; any surplus is fed into FWH #2. In case the steam generated by the solar field exceeds the requirement of FWH #1 and #2, FWH #3 receives the surplus steam produced. The bleed extractions from the turbine ensure that sufficient steam is provided to the feedwater heaters regardless of the output of the solar field.

Case B: Split steam flow to the feedwater heaters

In this case, a steam header splits the outlet steam of the solar field into three streams with the same steam flow rate. The outlets are connected to FWH #1, #2 and #3. The three outlet flows of the header have the same composition and specific enthalpy as the header's inlet (but as noted above, steam is throttled to adjust its pressure before passing to FWH #2 or #3). As in case A, the bleed extractions from the turbine ensure that sufficient steam is provided to the feedwater heaters regardless of the output of the solar field.

13.2.6 Power plant locations

Suitable locations for concentrating solar power plants are especially arid and semi-arid regions where the annual direct normal irradiation is above 1,700 kWh/m^2. For the purposes of this study, two globally representative specific locations in high solar areas were used for the analysis. The solar irradiation of the selected locations is shown in Table 13.1.

13.3 Assessment of the solar add-on concept

13.3.1 Technical assessment

The technical assessment comprises a comparison regarding the thermodynamic performance, fossil fuel saving and CO_2 emission avoidance of the two different cases in the two proposed locations.

Solar add-ons can either enhance the plant net output or reduce the fuel consumption, as discussed previously. Since the base case is a hypothetical existing plant and it is uncertain how much additional steam the steam turbine and generator could handle, the target is to reduce the fuel consumption and not to increase the electricity production. Thus, the fuel saving mode is used. The solar field is designed in such a way that its peak production does not exceed the heat demand of the HP/IP feedwater heaters at nominal load conditions of the power plant.

Power plants, such as the one presented in this paper, often follow daily load fluctuation from full load down to the minimum turbine load. In order to simplify the simulations, the plant is assumed to be a base load plant with the turbine running at full load continuously.

For the evaluation of the hybrid plant performance, the Thermoflex software [5] was used. Thermoflex is a simulation environment of steady state of power plants. It is a modular program which offers the opportunity to design and simulate combined cycles, conventional steam power plants, and thermal power systems, among others. Its extensive library of components also includes the elements required to simulate solar thermal power systems.

The development of a model is carried out in two steps. In the first step, 'design mode', the thermodynamic design criteria (working parameters) are determined. In second step, 'offdesign mode', the size of the components and the logic of their controls are established. Once the model is in offdesign, the performance of the system at different operating conditions, such as the weather data, can be evaluated.

Based on the hourly resolution of the meteorological data supplied by METEONORM [4] – DNI, sun position, ambient temperature, atmospheric pressure and relative humidity – the annual performance of solar add-ons to the coal-fired power plant was assessed by calculating steady state for each hour of the year. The number of collector modules and thereby the available mirror surface were kept constant for all simulations. The same applied for the base model of the conventional coal-fired power plant. The simulations also take into account the geometry of the solar field, position of the sun, irradiation level, ambient temperature and relative humidity. The solar steam production varies according to the feedwater heater demands and solar irradiation. The electricity production of 350 MW was regulated by adjusting the coal consumption of the boiler. The inputs, outputs and design parameters for the simulations are summarized in Table 13.2.

Figure 13.4 shows the amount of thermal energy generated by the solar field in sites 1 and 2.

The type of steam extractions used is uncontrolled or non-automatic extraction, the pressure and the flow vary as a function of the load [6, p. 224]. Therefore, slight variations in the demand of the feedwater heaters can be seen in Fig. 13.4, which is acceptable.

Table 13.2 Inputs, outputs and design parameters for the simulations

	Inputs (METEONORM data)	Design parameters	Outputs
Fresnel solar boiler	→ DNI → Solar azimuth angle → Solar zenith angle → Ambient temperature	→ Number of modules (120)	→ Solar steam mass flow
Power plant	→ Ambient temperature → Relative humidity	→ Electricity production (350 MW)	→ Fuel mass flow → Steam mass flow of the bleed extraction 1, 2 & 3

As shown in Fig. 13.4, in case A, the heat demand of the FWH #1 is covered for about 1,500 hours completely by the solar boiler, while for FWH #2 approximately 50 full-load hours are covered, in both locations. The amount of solar energy provided to the FWH #1 (a) is higher than to the FWH #2 (b) and #3 (c). Whereas in case B, none of the feedwater heater demands is fully covered by the solar system, not even at the highest intensity, where only ~70% of the demand of FWH #1, #2 and #3 is covered. At lower irradiation levels, the solar energy provided to the three FWHs diminishes proportionally.

Solar add-on results in a relative plant coal conversion efficiency (expressed as electricity generation per thermal input from coal combustion) improvement up to 1.6% and 1.5% at sites 1 and 2, respectively. The increment in efficiency implies lower fuel consumption and therefore higher CO_2 emission avoidance. In both regions, case A has a higher impact on the overall performance of the plant than case B, since the HP bleed extraction from the turbine has been totally substituted by the solar system (see Fig. 13.5).

13.3.2 Economic assessment

Add-ons based on solar direct steam generation have an impact on generation costs, among others, due to the associated fuel savings derived from their implementation. The expected effect on the electricity production cost depends on the value of the equivalent fuel savings. The analysis is based on the contribution of the solar field to electricity generation. Aside from fuel, generation costs include the amortized costs of the solar collectors and their operation. Revenues assumed from electricity sales are based on the calculated solar contribution to electricity production.

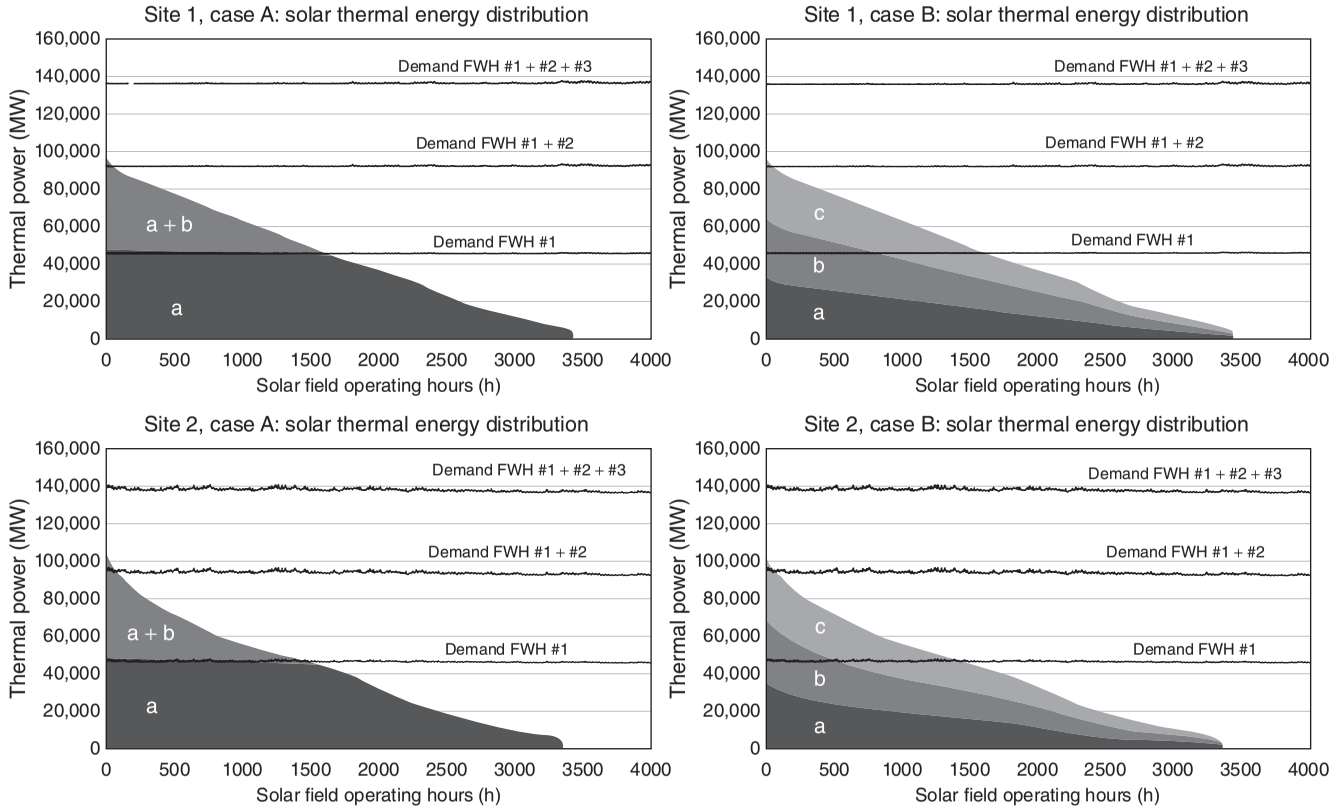

13.4 Solar thermal energy distribution in the selected locations.

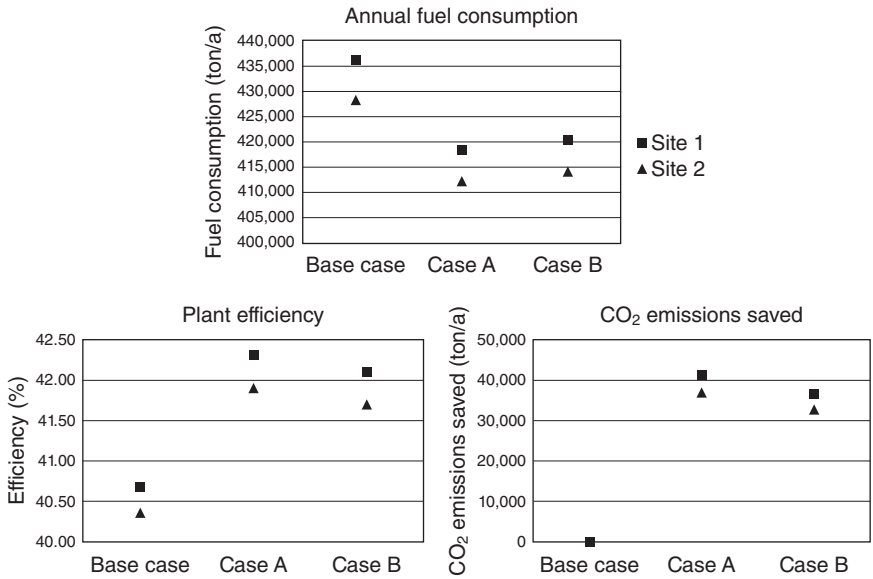

13.5 Performance of the hybrid power plant coal energy conversion efficiency, coal fuel consumption and CO_2 emissions saved for Site 1 (DNI = 1,950 kWh/m^2/year) and Site 2 (DNI = 2,300 kWh/m^2/year).

The economic analysis of the solar add-on was based on a strategy that integrates all revenues in an overall compensation tariff T:

$$T = T_{feed\text{-}in} + FS + C_{CO_2}$$

where T is the overall compensation applicable to solar add-ons (€/kWh). $T_{feed\text{-}in}$ is the feed-in tariff for solar thermal generation, which includes the base electricity price (considering only the solar contribution) and the incentives (€/kWh), FS is the component due to fuel savings derived from the operation of the solar field (€/kWh) and C_{CO_2} is the credit support due to CO_2 emission avoidance (€/kWh). Assumptions of the economic model of the solar powered add-on are shown in Table 13.3.

Several assumptions were considered in order to select the values for the base scenario.

- The feed-in tariff was selected to be lower than the current feed-in tariff in Spain but higher than the generation cost.
- Fuel price is an average of the international coal price over 10 years.
- Although a fix CO_2 emission avoidance credit has not been established, the European Union Emissions Trading Scheme (EU ETS) has analysed it and suggested a carbon credit of around 20 €/ton CO_2 [7]. In order to have a conservative calculation, 25% less was assumed.

Table 13.3 Assumptions of the economic model of the solar powered add-on

Financial assumptions	
Total solar field cost	€71,700,000
Equity ratio	100%
Depreciation	25 years
Annual indexation of feed-in tariff	2%
Inflation rate	2%
Discount rate	6.5%
Base scenario	
Feed-in tariff	0.16 €/kWh
Fuel price for savings	60 €/ton
CO_2 emission avoidance	15 €/ton-CO_2

Only the electricity generation contribution from solar steam generates revenues according to $T_{feed\text{-}in}$. The electricity produced conventionally is not taken into account for revenues nor the fuel costs derived from it. The economic calculation is focused on the cost of the equipment added to the plant and its operation. All other operations and maintenance (O&M) costs of the conventional plant are excluded from the analysis.

This model assumes that out of the total electricity generated by the turbine, there is a fraction associated with the presence of the solar add-on. The difference in fuel consumption attained when the solar field is operated corresponds to a certain thermal power that is indirectly put into the system by solar steam production. By means of the plant's electric efficiency, this is related to an equivalent 'solar' electric output, which is used to assess the solar field's effective generation costs. The results of the plant's performance under the aforementioned scenarios are compared in Table 13.4.

The higher annual DNI site enables the add-ons to obtain a higher thermal output, since more solar hours at the site let the system achieve a higher solar share for the related electricity production. Both facts imply a higher potential for fuel savings and thus for emission avoidance.

The use of a steam flow priority header (case A) is highly recommended to allocate the thermal production of the solar field to achieve a higher reduction in fuel use and thus a design with better economic performance. With regard to site selection, generation costs are expected to be up to 0.02 €/kWh higher at the lower DNI site studied.

The inclusion of solar add-ons in the plant's layout can be paid off in nine years at the high DNI site under these assumptions, leading to a higher internal rate of return (IRR). The reference framework assumes a feed-in tariff of 0.16 €/kWh which allows solar field implementation within a reasonable IRR, electricity production cost and payback time ranges. The

Table 13.4 Results of the economic model of the solar powered add-on by site

Location	Site 1		Site 2	
	Case A	Case B	Case A	Case B
Technical assumptions and results				
Solar share of total generation	1.60%	1.42%	1.43%	1.26%
Collector modules	120			
Major overhaul (13 years)	5% of total investment			
Boiler efficiency	88%			
Fuel savings[a]	17,805 ton/a	15,771 ton/a	16,005 ton/a	14,115 ton/a
CO_2 emission avoidance	41,207 ton/a	36,500 ton/a	37,043 ton/a	32,668 ton/a
Financial results				
Total investment	€71.700,000			
NPV	€44,949,859	€32,384,669	€33,530,952	€21,916,192
IRR	12,91%	11,23%	11,38%	9,78%
Discounted payback period	8 years	9 years	9 years	10 years
Electricity production cost	0.136 €/kWh	0.152 €/kWh	0.150 €/kWh	0.169 €/kWh
Revenues per kWh				
→ CO_2 crediting system	0.013 €/kWh	0.013 €/kWh	0.013 €/kWh	0.013 €/kWh
→ Fuel saving	0.022 €/kWh	0.022 €/kWh	0.022 €/kWh	0.022 €/kWh
→ Feed-in tariff	0.160 €/kWh	0.160 €/kWh	0.160 €/kWh	0.160 €/kWh
Total	0.195 €/kWh	0.195 €/kWh	0.195 €/kWh	0.195 €/kWh

[a] Assumed low heating value (LHV) of the coal =24,466 kJ/kg.

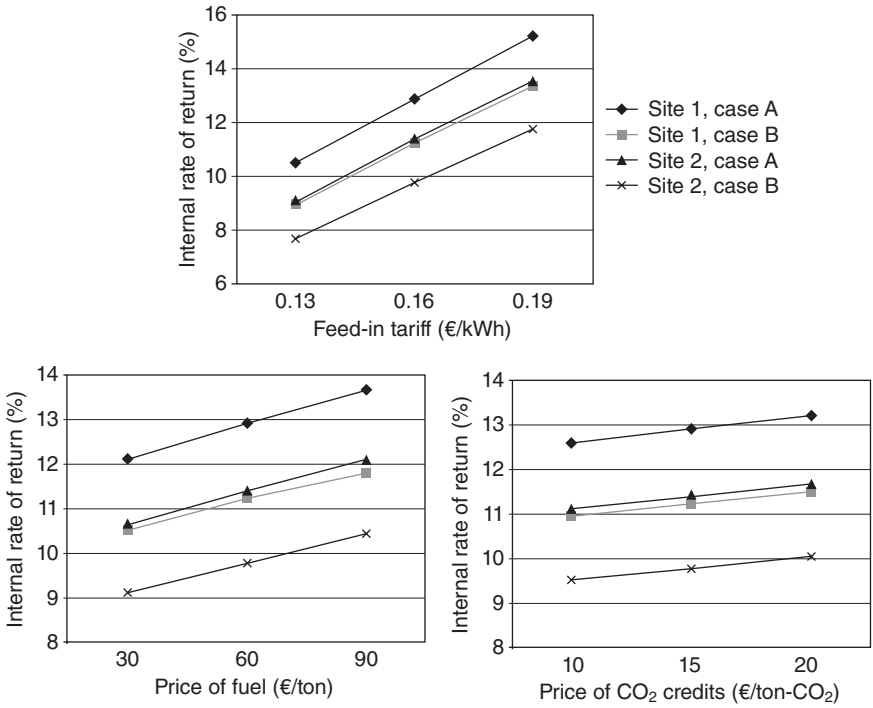

13.6 Variation of the project IRR to equity.

advantages coming from fuel savings and CO_2 credits represent a 0.035 €/kWh additional support.

The sensitivity of the results to the revenue contributions is relevant to knowing how profitable the implementation of the solar add-ons will be under different scenarios (e.g., price variation of fuel and CO_2 credits). The results are shown in Figs 13.6 and 13.7. The range of the analysis was constrained to about ± 25% difference in feed-in tariff and to the latest trends in coal prices. The price of carbon credits is likely to be adjusted according to the country's regulations.

Since the sale of solar electricity has the biggest share in the proposed revenue system, the feed-in tariff is the driving force of the analysis. In the range of about ±25%, the feed-in tariff can modify the IRR up to 2.5 percentage points. Likewise, it can impact the payback period by one to two years, depending on the site rather than on the add-on's configuration. The economics of including solar add-ons in the plant layout are more sensitive to the price of fuel saved than to the price of carbon credits. The changes that the discounted payback time is subjected to by varying the price of fuel or CO_2 in some cases (see Fig. 13.7 (b) and (c)) are not perceived, since the variations are smaller than one year.

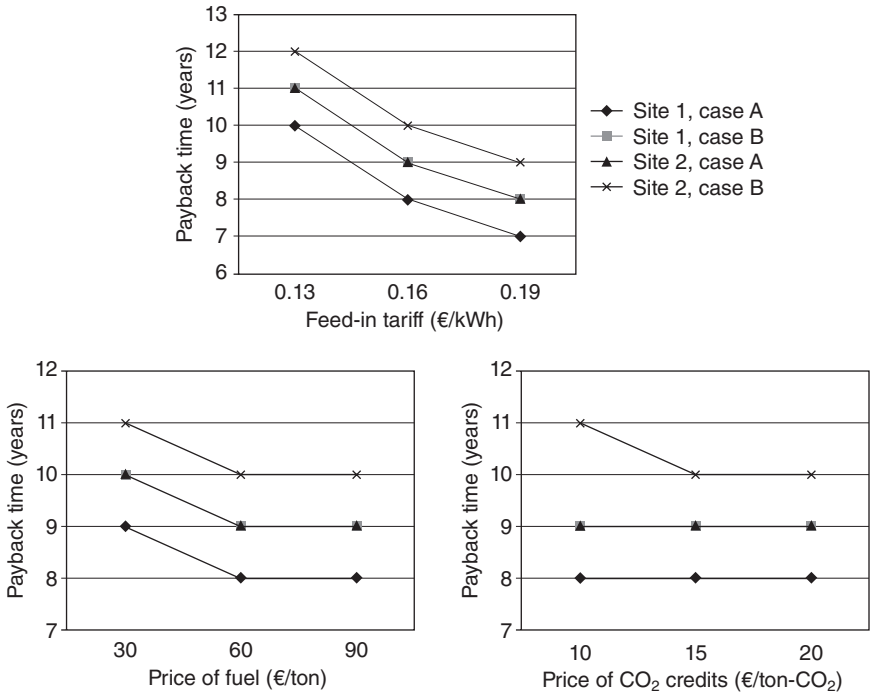

13.7 Variation of the discounted payback time.

13.4 Conclusions

The optimum scenario for the most economic introduction of solar add-ons to existing power plants is, not surprisingly, for sites with the highest DNI. Diverting the solar steam with priority to the HP feedwater heater (case A) maximizes the use of the solar heat input, achieving a reduction of fuel consumption that is equivalent to a rise in solar share of electricity generation of up to 0.2%.

The assumption to use a base load power plant for the case study leads to a relative low solar share. For peak load plants, the solar add-ons will have a higher impact on the overall performance of the plant, since their capacity factor is lower and their time of operation is comparable to those of the solar add-ons, avoiding the potential that solar production has to be wasted when the power plant is out of operation.

A feed-in tariff as low as 0.16 €/kWh allows the implementation of solar field add-ons in a payback time frame of 8–10 years in a high DNI site, depending on the system configuration. In this context the IRR remains close to 13%, even in case of price volatility of coal or carbon credits.

The feed-in tariff of the assumed revenue scheme is up to 0.14 €/kWh lower than, for instance, the current tariff for solar thermal in Spain (0.27 €/kWh). This scheme includes the support provided by CO_2 emission avoidance and the fuel savings (a characteristic advantage of the configuration of the solar add-ons).

13.5 References

[1] Morin G., Lerchenmüller H., Mertins M., Ewert M., Fruth M., Bockamp S., Griestop T., Häberle A. (2004), 'Plug-in strategy for market introduction of Fresnel-collector', SolarPaces Conference.
[2] Ugolini D., Zachary J., Park J. (2009), 'Options for hybrid solar and conventional fossil plants', *Bachtel Technology Journal*, 2, 1, 1–11.
[3] Yang Y.P., Cui Y.H., Hou H.J., Guo X.Y., Yang Z.P., Wang N.L. (2008), 'Research on solar aided coal-fired power generation system and performance analysis'. *Science in China Series E: Technological Sciences*, 51, 8, 1211–1221.
[4] Meteonorm, meteorological database developed by Meteotest, www.meteotest.ch.
[5] Thermoflex, thermodynamic tool developed by Thermoflow, www.thermoflow.com.
[6] Black & Veatch (1996), *Power Plant Engineering*, New York, Springer.
[7] Committee on Climate Change (2009),'Meeting Carbon Budgets – the need for a step change', Progress report to Parliamentary Committee on Climate.

14

The long-term market potential of concentrating solar power (CSP) systems

S. J. SMITH, Pacific Northwest National Laboratory and University of Maryland, USA

Abstract: This chapter will examine the conditions under which thermal concentrating solar power (CSP) systems might play a larger role in the global energy system during the twenty-first century. CSP technologies, such as parabolic troughs or power towers, have a large advantage over other solar technologies in that they offer the potential for firm power delivery, mitigating intermittency issues. These systems require relatively cloud-free conditions to operate, however, which limits their geographic applicability.

Key words: concentrating solar power, electric generation.

14.1 Introduction

Concentrating solar power (CSP) systems are at a transition point in their development. As discussed in Chapter 1, installed capacity in 2012 is close to 2 GWe following several years of rapid growth. With average capacity factors averaging around 40%, total annual energy generation is still only of the order of one large coal-fired power station. Nonetheless, this is sufficient to establish CSP as a serious industry and continued growth is predicted. While the current contribution is relatively small, as the number of CSP plants built increases, the expectation is that, following general historical trends in technology development, costs are likely to fall as the production of CSP plant components becomes more streamlined, operating procedures are standardized, and plant designs improved.

As with most renewable technologies, the largest determinant of the cost of electricity generated using CSP is the capital cost. The extent to which these costs fall over time will, therefore, be a principal determinant of CSP market share. Water availability, site characteristics, financing options, transmission capability, and the cost of alternative technologies will also all play a role in determining CSP market potential. The role of these factors will be discussed below. The general considerations below apply to all thermal CSP technologies: trough, dish, tower and Fresnel; however, with parabolic trough technologies being the most commercially mature and widely deployed, some of the specific analysis is focused on trough systems.

Published by Woodhead Publishing Limited, 2012

14.1.1 The role of concentrating solar power (CSP) systems in the electric system

One key feature of thermal CSP plants is that they are generally constructed as hybrid units, whereby an auxiliary boiler or other heating unit using natural gas,[1] can be used to heat the working fluid and power the generation system. With a relatively small additional capital expense, CSP plants are, therefore, capable of producing predictable power. The auxiliary system can be operated during a short cloudy period during the day or during entire cloudy days when the system would otherwise not be operational. This provides an inherent advantage over many other renewable energy technologies in that intermittency of the solar resource is mitigated with little capital cost. Although fuel costs are incurred, which will be discussed later, CSP hybrid plants can be conceptually considered much like conventional fossil electric generation technologies in terms of their dispatchability. The topics of energy storage and hybridization are covered in detail in Chapters 11 and 12, respectively. Many commercial plants are now also in operation incorporating large-scale thermal energy storage, which allows solar operation into the evening.

CSP plants will operate within electricity markets that can be simplistically considered to consist of base, intermediate, and peak load segments.[2] Base load plants are run nearly 24 hours a day, as exemplified by large coal and nuclear plants. Intermediate plants are generally brought on line when loads begin to increase during the day, with natural gas turbines (combined cycle and conventional) often serving this load segment. Peaking plants operate only during the highest demand periods, which in sunny regions is generally during mid-day and evening in the summer. These power plants are used only a relatively small fraction of the year. In the nomenclature of the field, their capacity factor is low. This favors plants with low capital costs even if efficiency is lower than in intermediate plants. Open cycle natural gas or oil combustion turbines are generally used for the purpose of supplying peaking power as these offer low capital cost and a short start-up time.

CSP technologies are well suited to supply intermediate and base load market segments. Most current CSP plants operate only during the day and are best considered as intermediate load plants. Intermediate load comprises around 15–20% of total electricity demand in energy terms and this

[1] Whilst natural gas has been used nearly exclusively for backup purposes to date, in principle any fuel could be used, including biomass.

[2] Markets in some jurisdictions (Eastern Australia, for example), have actually moved to the concept of a continually varying cost of electricity based on supply and demand estimates for short future time intervals.

defines the maximum market for CSP plants without large amounts of thermal storage. As discussed further below, thermal storage is not necessarily essential to initial penetration in the intermediate electric power segment, although storage does lower costs somewhat and expands the maximum portion of intermediate load that can be economically served by CSP technologies.

Base load generation is the largest market segment, comprising around three-quarters of total electric generation in the United States, for example. CSP plants with around 12 hours of thermal storage could provide base load power, which offers the largest potential role for CSP technologies. Note that base load CSP plants would still require hybrid operation in order to provide power during cloudy days. While the cost of electricity from a base load CSP plant with storage could be comparable to that from a CSP plant serving intermediate loads due to longer hours of operation (see below), the cost of competing generation options is also lower for the same reason. In other words, the capacity factor of a base load plant is higher than an intermediate load plant. While CSP plants are currently competitive in some intermediate generation markets, capital costs will likely need to fall further to compete as base load generators.

14.2 Factors impacting the market penetration of concentrating solar power (CSP)

14.2.1 System cost and performance

The primary factor that determines the role of any electric generation technology is the cost of energy. Levelized cost of energy (LCOE) has been introduced in Chapter 2. Reiterating, for CSP a simplified LCOE calculation is:

$$\mathrm{LCOE} = \frac{(C_0 + \mathrm{O\&M}_{fixed})F_R}{PF_c} + \frac{c_{fuel}}{\eta_{conversion}} + \mathrm{O\&M}_{variable} \qquad [14.1]$$

where P is the nominal design point capacity of the system, F_c is the capacity factor (the annual average fraction of nominal capacity achievable), O&M are operation and maintenance costs that are split between those that are in proportion to generation (variable, expressed in the same units as the LCOE) and those that are fixed annual costs (expressed as a fraction of capital cost per year), C_0 is the total initial capital cost, C_{fuel} is the per unit energy cost of any fuel used in a hybrid system, $\eta_{conversion}$ is the conversion efficiency of fuel to electricity, and $F_R \equiv \left(\frac{DR(1+DR)^n}{(1+DR)^n - 1} \right)$ is the capital recovery factor (sometimes called annualization factor).

Published by Woodhead Publishing Limited, 2012

The dominant factors in determining CSP costs are the total capital cost and financing assumptions, represented by the C_0 and F_R terms in Eq. [14.1]. Solar resources are dispersed, requiring large collector areas, which leads to substantial initial capital costs. For a CSP trough plant, the collector field and associated equipment comprise over 50% of total capital costs, with the power block and the balance of the system accounting for less than 50%. Cost reduction for CSP, therefore, rests largely on reducing collector costs.

Given the importance of capital costs for CSP systems, the capital recovery factor plays a critical role in determining the net cost of energy. Zhang and Smith (2008) examine a number of key variables using a financial model developed by NREL and show that the debt-to-equity ratio, investment tax credits, and depreciation schedules can all have a substantial impact on the CSP LCOE. For example, changing from a 20- to a 5-year depreciation schedule (in the United States formally termed 'modified accelerated cost recovery system', or MACRS) lowers the LCOE by 60%. One caveat is that lenders often require a certain minimum annual debt service and some lower cost financing assumptions do not meet these requirements.

Policies are in place in many regions that lower the effective cost of capital-intensive renewable energy technologies through incentives such as investment tax credits or feed-in tariffs. One issue that may be relevant in the long term is that the total cost of some policy incentives could become large as the deployment of CSP and other renewables increase. A robust scenario for widespread use of CSP technologies depends on costs becoming sufficiently low that policy incentives can play a smaller role. The addition of a price on carbon has a limited impact on long-term CSP penetration. While a carbon price will increase average electricity generation costs, this increase can be relatively small in many scenarios (Clarke *et al.*, 2007), in large part due to the many current and potential future options for low-carbon generation. As discussed below, the need for some sort of backup for cloudy days (Zhang *et al.*, 2010) means that CSP backup fuel costs also will increase under a carbon policy. The combination of these two effects means that the imposition of a carbon price may have only a relatively modest impact on CSP deployment. As discussed in Section 14.3, however, if CSP capital costs continue to fall, CSP can make a substantial contribution to world energy supplies.

Any increase in efficiency linearly reduces generation costs. As a thermal system, the primary means of increasing efficiency is to increase operation temperatures. Power tower and dish systems tend to operate at higher temperatures and, therefore, have higher efficiencies, although capital costs are currently higher than for trough systems. Reducing thermal losses is an additional way of increasing system efficiency.

The availability of water is an important issue for CSP systems as the majority of the areas with suitable solar resources, that is, with few cloudy days, have limited water resources. While some water is needed to wash mirror and reflector surfaces and to make up water lost during operation of the power system, the largest water use is for evaporative cooling. Evaporative cooling is the most common method of lowering outlet temperatures in thermal power plants in order to maximize efficiency. While fossil fuel thermal plants can generally be located in proximity to water sources, CSP plants need to be located in areas with suitable solar resources. Use of evaporative cooling is the lowest generation cost option, but this presumes sufficient water, often groundwater, is available.

The alternative to evaporative cooling is either dry cooling or a hybrid system where water is used for partial cooling and/or only at critical times to meet high demand. These options can reduce water use dramatically, but with a reduction in efficiency and additional capital costs. Lower efficiency can be compensated with a larger solar field (WorleyParsons, 2008), which also increases the capital cost. A general figure for the cost penalty for use of dry cooling is 10% (Stoddard *et al.*, 2005; Kelly, 2006); however, Stoddard *et al.* (2005) note that the impact of dry cooling on system performance 'can vary considerably depending on site factors and system configuration.' Note that in extremely arid regions, even the more modest water requirements of CSP plants with dry cooling systems might be problematic.

Power tower CSP plants operate at higher temperatures, which would lead to a lower efficiency penalty for dry cooling (DoE, 2008). In the future, power tower plants might operate at very high temperatures allowing the use of gas turbines, perhaps eliminating the need for cooling entirely (Heller *et al.*, 2006; Angelino and Invernizzi, 2008), although if combined cycle operation is pursued for maximum efficiency, some cooling requirement would remain. In either case, power tower CSP or dish plants might ultimately be a particularly preferred option in areas with water limitations.

From an economic perspective, CSP is still a relatively new technology in that production volumes are low, system components are not yet standardized, and technological improvements are possible in many areas. Reductions in costs are generally observed to occur as deployment of a technology expands. This is often captured as a 'progress ratio', which reflects the amount costs are observed to decrease as a function of production volume. A value of 0.8 is commonly quoted, which means that costs are observed to decline to 80% of their original value with a doubling of cumulative experience (Dutton and Thomas, 1984).

While such cost decreases are often interpreted as 'learning by doing', many effects are operating simultaneously making these observations difficult to interpret. As noted in the literature review of Clarke *et al.* (2006a), 'no single source dominates the process of technological change.' They

conclude that research and development (R&D) and learning-by-doing within an industry play a role, but 'spillover', or positive impact of technological advancements in other industries, can also play a strong role. A spillover technical change exogenous to a specific industry that lowers costs will lead to larger deployment (due to lower costs) without, necessarily, any direct connection between production volume and cost decreases. The use of a progress ratio formulation to represent cost decreases over time can, therefore, be misleading because factors other than deployment over time can result in cost decreases. While there is broad agreement that there is substantial scope for cost decreases for CSP technologies, the ultimate limit that costs might actually decrease to in the future is uncertain.

There have been a number of investigations of CSP cost reduction potential. Sargent and Lundy (2003) have carried out a detailed 'bottom up' cost reduction potential study for trough and tower plants. For trough plants, for example, potential cost reductions included technological improvements to reduce losses and increase efficiency; manufacturing and scale efficiencies associated with volume production and size scale-up; and the development of more advanced thermal storage technologies. On this basis they projected a levelized cost of energy for trough plant costs falling from ~13 cents/kWhr in 2003 to 8 cents/kWhr in 2020. Inflating their costs to 2010 USD, their projections have power tower costs ultimately falling below trough costs, to 7 cents/kWhr by 2020. Their costs, assuming a 10% investment tax credit (ITC), are expressed in nominal dollar terms (see Short *et al.*, 2005; costs presented in real dollar terms are approximately 25% lower). All 2020 costs refer to baseload plants with ~12 hours of thermal storage.

The Sargent and Lundy cost projections appear to have been overly optimistic, in part perhaps because the assumed increases in production volumes since 2003 did not actually occur. Kutscher *et al.* (2010) estimate the cost of current parabolic trough plants to be 24 cents/kWhr, falling to 13 cents/kWhr in 2020 under a set of assumptions for across-the-board technological advances and changes in financing assumptions. Similarly, Kolb *et al.* (2011) present an assessment of the technological advances necessary to decrease power tower costs from a currently estimated value of 19 cents/kWhr to 10 cents/kW/yr in 2020. Major improvements identified include moving to higher temperature operation with supercritical cycles and improvements in heliostat manufacture, design, and associated systems. Note that these roadmap exercises identify improvements that are considered technologically plausible and are not predictions of future technology performance.

As a final note, cost of energy, while central, is not the only characteristic that will ultimately be of importance. The ability to meet load under all but exceptional circumstances is an essential characteristic of any

fully-developed electric generation system. If electricity generation moves away from a nearly complete reliance on dispatchable plants, system stability may become an even more critical issue. Note that a recent analysis of the issue (Eto *et al.*, 2010), finds that system stability in the US, in terms of quality of frequency control, appears to have declined for reasons other than renewable generation. While the economic mechanisms by which system stability will be maintained are still in flux in many regions, hybrid CSP plants provide firm power and, therefore, make a substantial contribution to system stability. CSP plants with thermal storage are likely to have additional benefits as flexible generation that can assist in accommodation of more variable solar or wind resources. The nature of these interactions and the potential role of flexible generation such as hybrid CSP plants with thermal storage is an active subject of research.

14.2.2 Solar irradiance characteristics

The quality of solar irradiance at a specific site has an obvious impact on CSP performance. CSP systems require direct sunlight, also termed direct normal irradiance (DNI) (see Chapter 3), and cannot operate during cloudy days. To first order, the cost of electricity from a CSP plant is inversely proportional to the amount of direct normal radiation at the plant site. There are further characteristics, however, that are also important for CSP costs. As noted by Zhang *et al.* (2010), the cost of backup operation in a hybrid plant is likely to become a larger portion of total costs over time as capital costs of CSP plants fall and if fuel costs increase (particularly under a climate policy). It is, therefore, useful to characterize solar irradiance with two quantities: the average direct irradiance during operational days, and the number of non-operational days, that is, days during which direct irradiance is too low to operate the plant (low DNI days). While average annual direct normal irradiance varies substantially, the average direct irradiance during operational days varies much less from location to location.

An estimate of the average number of non-operational days (low DNI days) is shown in Plate III (between pages 322 and 323) as estimated by Zhang *et al.* (2010) using data from NASA (Chandler *et al.,* 2004) and the US National Solar Radiation Database. Africa and the Middle East are particularly well suited for CSP, as are Australia, the southwest North America, and portions of South America and Asia.

Except for scheduled maintenance, auxiliary heating will generally be required on low DNI days in order to meet load. Locations with a larger number of low DNI days will, therefore, incur increased fuel costs and will tend to have a larger cost of energy as a result.

Of particular importance are the spatial correlation characteristics of low DNI days. Large-scale weather patterns can cause cloudy conditions

over large areas, potentially rendering all CSP plants in that area non-operational at the same time. The hybrid generation capacity of CSP plants is particularly important in this situation so that demand can still be met by these plants.

The seasonal distribution of low DNI days will also have an impact on costs. In the continental US, for example, an analysis of NREL persistence data finds that cloudy days are three times as likely in the winter as in the summer in generally sunny areas (Zhang *et al.*, 2010). In mid-latitudes, the impact of low DNI days in winter is smaller than in other seasons as loads are lower in the winter and there is excess capacity available that may be able to substitute for CSP plants on days when irradiance is not sufficient for CSP operation. In tropical regions there can be issues related to large-scale weather patterns, such as the monsoon season, where extended times of cloudy weather could necessitate use of backup systems. Zhang *et al.* (2010) find preliminary evidence that CSP technologies could play a significant role even with a relatively large number of cloudy days, essentially as fuel extending technologies with substantial operation of the hybrid backup system.

14.2.3 Thermal storage

Electricity demands need to be met instantaneously, requiring supply and demand to be matched at all times. As discussed in Chapter 11, the addition of thermal storage to CSP plants allows solar energy to be collected and used at a later time when solar irradiance might not be sufficient to meet demands.

CSP plants serving intermediate loads do not necessarily need thermal storage to be competitive. At low penetration levels, there is sufficient additional capacity in the energy system to meet demand during times when the CSP plant is not operational. Zhang *et al.* (2010) found that CSP plants without thermal storage do not suffer significant economic penalties until CSP is supplying greater than 40% of intermediate + peak demand under an assumption of optimal operation of the electric system. After this point the cost of CSP power increases due to two effects: increased use of auxiliary heat to supply power, particularly during evening times, and increased dumping of potential output, due to mismatch between potential CSP generation and demand. This analysis implies that substantial CSP deployment can occur while thermal storage systems are researched and further developed.

As more CSP plants are brought on-line, the addition of thermal storage, however, can mitigate these factors such that most intermediate load can be served by CSP plants without substantial cost increases due to either dumped power or increased auxiliary heating operation. With the addition

of thermal storage, the solar field is built larger than needed to operate the power block at peak capacity. The excess energy is then stored and can be used in the evening when load is still high but sunlight is not available. The overall cost of energy is also lowered slightly because the fixed cost of the power block is averaged over a larger amount of generation.

The addition of thermal storage could enable an even larger expansion of CSP potential if sufficient thermal storage, about 12 hours, is added such that a CSP plant can supply base load power around the clock. Presumably, once thermal storage is developed and successfully deployed for intermediate plants, the barriers for deployment of thermal storage to enable base load plants will be relatively small. The primary challenge at this point will be cost. CSP systems operating as base load plants will have a higher total capital cost as compared to intermediate plants, due to the cost of larger thermal storage capacity and a larger solar field. Countering the increase in capital cost will be a larger capacity factor. The net cost depends on the relative costs of the power block, solar field, and thermal storage systems. Base load power, however, is inherently less valuable in the marketplace than intermediate power, and CSP base load plants will need to compete with other low-cost base load electricity sources including fossil plants (with or without CO_2 capture and storage), wind, and geothermal.

The relative advantage of CSP plants as base load as compared to intermediate plants will also depend on factors such as seasonal load shapes and solar irradiance characteristics in a particular region. Note that the presence of thermal storage in CSP plants could also be valuable as a method of buffering variations in output from other renewable generation such as wind or solar PV. The potential value of these services is only beginning to be assessed.

Comparison between electric and thermal storage

It is useful to briefly consider the potential role of photovoltaic (PV) technologies, which use the same solar resource, and the potential benefits of electricity storage for PV as compared to thermal storage in CSP systems. Denholm and Margolis (2007a) perform an analysis of the role of PV technologies by combining hourly information on solar irradiance and electric system load for the ERCOT region, which encompasses most of the state of Texas in the United States. As the fraction of load supplied by PV increases, a larger portion of potential PV supply is wasted due to mismatch between PV supply and demand. This increases the net cost of PV power as less power per unit can be sold. Around 5–10% of the system load can be supplied by PV if 60% of the remaining generation in the system is flexible enough to accommodate variable PV output, and the cost increase due to wasted PV output is limited to 25%.

Published by Woodhead Publishing Limited, 2012

In a follow-up study, the impact of load shifting and electricity storage technologies was examined (Denholm and Margolis, 2007b). The ability to shift load during the day substantially increases the potential for PV to supply power, perhaps doubling the amount of load that could potentially be supplied by PV if 10% of load could be shifted from one portion of the day to times when PV is available. The incorporation of electricity storage technologies also increases the potential role for PV. The incorporation of the ability to store 4 hours of system load, for example, allowed PV to supply close to 20% of system load, albeit with some loss of energy due to losses in the electric storage system.

While both PV and CSP systems benefit from energy storage, there are a number of differences between electricity storage as might be used with a PV system, or other renewable generation, and thermal storage systems as would be used for CSP plants. Thermal storage in a CSP system is fully integrated which leads to lower energy losses and can lead to a cost reduction as the power block components are downsized relative to the solar field. For a PV system with electricity storage, on the other hand, the storage system is a separate addition with presently high capital costs and larger energy losses.

Thermal storage is highly efficient, with losses of the order of 1% quoted, as compared to current best efficiencies of 80–90% for load leveling electrical storage applications (Divya and Østergaard, 2009), with additional losses from power/inverter electronics. An energy loss is equivalent to the need to scale up the solar field to compensate for lost energy, and this must be considered alongside the direct capital cost of the storage technology.

The capital costs for thermal storage are also much smaller than current electric storage technologies. For near-term future thermal storage, NREL (2005) implies a typical capital cost of $350/kWe of overall system capacity. A comprehensive review of the costs of electricity storage has not been performed, although there is consensus that compressed air energy storage (CAES) technology is currently one of the most cost-effective utility scale technologies for electric energy storage. The capital costs of CAES are quoted in the range of 500–1,000 $/kWe, larger than the capital cost of thermal storage integrated with CSP. Battery technologies are even more expensive on a capital cost basis and, further, have an additional cost disadvantage due to relatively short lifetimes. A battery with a lifetime of 4–5 years is three times as costly on a levelized basis as a system with a lifetime of 20–30 years, considered as a simple discounted cost. The comparison of storage technologies is, however, complex: clearly capital costs increase with the number of hours of storage capacity, and there are also variable O&M costs. Chapter 11 deals with these issues in more detail.

Published by Woodhead Publishing Limited, 2012

Neither thermal storage nor CAES technologies are widely deployed, however, and current cost estimates must be considered uncertain. Costs of any of these storage technologies could fall as experience is gained. As also discussed in Section 14.4, integration of thermal storage is an important characteristic, as this allows CSP technologies to supply a large fraction of electric load demand.

14.2.4 Long-distance transmission

In the near term, when CSP plants are supplying a relatively small portion of total demand, power generation from CSP plants will need to be fed into local and regional transmission systems. In regions with good solar resources, solar irradiance levels are spatially fairly uniform, aside from localized effects such as areas with coastal clouds. This means that, in principle, there is substantial flexibility in locating solar plants in a manner convenient for connection to transmission lines. This means that, with respect to transmission, connecting CSP resources to supply local to regional grids may not be substantially more difficult than for conventional thermal plants, although in many locations any new transmission development can encounter opposition. Note, however, that CSP plants have a larger footprint than most conventional generation technologies, which can pose issues for plant siting.

Over the longer term, however, CSP plants located in areas with good solar resources could supply power to more distant regions. The major issue for CSP will then be long-distance transmission. In the United States, for example, solar resources suitable for CSP are located in the south-west portion of the country, whereas the load centers are widely distributed. There are sufficient resources in the southwest to supply a large portion of load for the entire country (Fthenakis *et al.*, 2009). For this to occur, however, substantial augmentation of long-distance transmission would be needed. Similar situations exist in Europe, where the best areas for CSP plants are in Spain, or more ambitiously across the Mediterranean Sea in North Africa, whilst much of the load is in the north, and in China, where good quality resources exist in the interior western desert regions, whilst the majority of the load is in the east.

As an indication of the spatial concentration of CSP resources relative to loads, Table 14.1 shows the fraction of population in various world regions that are located in areas with high-quality resources (Zhang *et al.*, 2010). This is a rough lower limit to the fraction of load that CSP might be capable of supplying in each region because some load centers in cloudy areas might be geographically close to areas with good resource. While a few countries have essentially no high-quality solar resources suitable for CSP, most of

Table 14.1 Fraction of population in each region located in areas with the indicated level of annual average direct solar irradiance during operational days (Zhang *et al.,* 2010)

Fraction of regional population in areas with high quality direct solar irradiance resource		
	>7 kWh/m^2/day	>6 kWh/m^2/day
USA	12%	20%
Canada	0%	0%
Western Europe	4%	22%
Eastern Europe	0%	2%
Japan and South Korea	0%	0%
Australia and NZ	17%	43%
Former Soviet Union	8%	14%
China	1%	17%
Middle East	39%	93%
Africa	23%	62%
Latin America	12%	41%
Southeast Asia	11%	28%
India	13%	56%

the countries/continents in Table 14.1 have some areas with suitable resources. In most if not all cases, however, substantial transmission will be required to serve loads outside of the sunny areas. If an enhanced transmission infrastructure was in place that allowed generation from sunny regions to be used at load centers elsewhere, this would substantially increase the total potential market share for CSP systems.

The cost of long-distance transmission infrastructure can be large, but if a large fraction of a region's load is to be supplied, then the amortized cost can be small relative to generation costs. A major barrier to large electric transmission projects is often public acceptance, particularly if new transmission corridors would be needed or if transmission lines would need to be constructed through areas with significant natural or cultural resources. Transmission line corridors can also contribute to fragmentation of ecosystems, which can decrease their resilience to climate change.

As a point of comparison, note that the situation is very different for wind resources, which are not only also dispersed but also highly spatially variable. Wind turbine output varies as the cube of wind speed, so turbines are best placed in specific areas with high winds. These areas may or may not be located with convenient access to local and regional transmission capability. The ability to connect to *regional* transmission is a more salient issue for utilization of wind resources as compared to solar. An enhanced *long-distance* transmission infrastructure, however, could increase both solar and wind solar deployment. The cost, broadly construed, of additional

Published by Woodhead Publishing Limited, 2012

long-distance transmission capacity would need to be weighed against the value of additional CSP (or wind) as compared to other alternatives.

14.2.5 Climate policy

The widespread use of fossil fuels, along with land-use changes, have led to the increase of atmospheric carbon dioxide concentrations from a pre-industrial level of around 280 ppmv to over 380 ppmv in 2005 (Forster *et al.*, 2007). This, along with changes in other atmospheric constituents, has resulted in an increase in the net radiative balance in the atmosphere, termed radiative forcing. This will result in an increase in global mean temperatures and consequently other climatic changes, although the magnitude of those changes remains uncertain. Concern over the potential for climate change led 194 countries to adopt the Framework Convention on Climate Change (FCCC) with an ultimate objective of 'stabilization of greenhouse gas concentrations in the atmosphere at a level that would prevent dangerous anthropogenic interference with the climate system'. Reaching this goal will require a major reduction in the use of fossil fuels in a manner that releases carbon dioxide, and other greenhouse gases, into the atmosphere. One option for the continued use of fossil fuels for electric power generation is the use of coal or natural gas with carbon dioxide capture and geological storage (CCS), a technology already in use, albeit at smaller scales than would be needed to address carbon dioxide emissions.

Whilst there is much debate on the most economically efficient method to limit the emission of greenhouse gases, there is a general consensus from economic analysis that placing a charge, or carbon tax, on net emissions of greenhouse gases would ultimately be needed to achieve large emissions reductions. Note that a cap and trade system, if ideally implemented, is economically equivalent to a carbon tax. This will increase the cost of fossil-fuel generation relative to no or low-carbon generation technologies. The use of natural gas to fuel auxiliary backup for CSP plants, however, will also result in greenhouse gas emissions, and the impact of this cost will be addressed in Section 14.3.3.

The impact of a climate policy on CSP market potential will depend on the availability and cost of alternative low-carbon technologies. Considering first the base load segment, there are a number of low-carbon generation options including: nuclear, coal or natural gas with CCS, biomass, wind, and geothermal. CSP base load plants will need to compete on a cost basis with these technologies for market share.

The options are more limited in the intermediate generation segment. Fossil plants with CCS are an option, but will be relatively expensive given the lower capacity factor when supplying the intermediate segment. PV is

one of the few renewable technologies that naturally supplies intermediate loads. CSP may be more attractive than PV for this segment in many cases both on a cost of energy basis but also due to the ability of CSP to supply firm power into the evening when PV is not operating. The impact of a climate policy on CSP market share is examined further below.

14.3 Long-term concentrating solar power (CSP) market potential

14.3.1 Methods for projecting future market potential

It is now common in the energy field to produce projections of the market potential for various technologies. The term 'projection' is used deliberately here, because forecasts of the coupled technological-social system, at least in any deterministic sense, are not possible in the same manner as, for example, the weather can be forecast (Craig *et al.*, 2002). Projections are, however, still useful as aids to thinking and planning. In general, projections of future deployment levels will vary widely because deployment of any technology will depend on not just the cost of that technology, but the costs of all other competing technologies, demand growth, and potential changes in policy. There will be a particularly wide range of potential pathways for a relatively new technology such as CSP.

Energy projections range from quantitative analysis based on expert judgment to formal energy-system models. Models used for energy-system projection fall into two general categories: technology-based 'bottom-up' models and 'top-down' economic models. The track record of such projections is decidedly mixed (Craig *et al.*, 2002). However, while 'all models are wrong, some are useful' (attributed to the industrial statistician George Box). Energy projections can be used as guides to thinking about a system and examining the consequences of different assumptions, and it is under this philosophy that we approach this topic.

Projections vary not only in their methodology, but also in their purpose. Integrated energy-systems models generally consider economic competition between various available options, considering factors such as demand growth, stock turnover, and resource costs. More schematic scenarios, such as the 'vision of future [CSP] deployment' presented by the International Energy Agency (IEA, 2010) provide a general quantitative and qualitative outline reflecting the authors' judgments as to what could happen under favorable conditions.[3] We consider below insights using scenarios from one quantitative model.

[3] In many cases, such scenarios are based on quantitative models and analysis, although in the case cited here the quantitative basis for the projections is not given.

14.3.2 The global climate assessment model (GCAM)

The projections below use the global climate assessment model (GCAM, formally MiniCAM), which is an integrated model of the economy, energy supply and demand technologies, agriculture and land-use, carbon-cycle, and climate designed to examine long-term, large-scale changes in global and regional energy systems. The GCAM is one of a class of model known as integrated assessment models, which are used to examine systems level interactions relevant, in this case, to climate and energy policy (Clarke *et al.*, 2007). The GCAM operates over a 100-year time-scale, allowing an examination of the potential long-term role of CSP in the energy system. An explicit representation of CSP technologies has recently been implemented within this model (Zhang *et al.*, 2010), which makes this model particularly relevant for this chapter.

The GCAM is intended to bridge the gap between 'bottom-up' technology models and 'top-down' macroeconomic models (Kim *et al.*, 2006). By allowing a greater level of detail where needed, while still allowing interaction between all model components, the framework allows a high degree of technological detail while retaining system-level feedbacks and interactions. The model has a strong focus on energy supply technologies and has recently been expanded to include a suite of end-use technologies. The GCAM was one of the models used to generate the Intergovernmental Panel on Climate Change (IPCC) SRES scenarios (Nakicenovic and Swart, 2000), the recent RCP scenarios (Moss *et al.,* 2010), and numerous national and international assessment and modeling activities (Edmonds *et al.*, 2004; Smith and Wigley, 2006; Clarke *et al.*, 2006b, 2007).

The model uses inputs such as labor productivity growth, population, fossil and non-fossil fuel resources, energy technology characteristics (cost, performance, resource availability), and productivity growth rates to project energy supplies and demands by fuel (such as oil and gas) and energy carriers (such as electricity), agricultural supplies and demands, emissions of greenhouse gases and other radiatively important compounds, and global climate changes.

14.3.3 The future context for CSP

The first step in considering the potential role of any technology is to examine the larger context. There are many possible future pathways for the energy system and only a limited number can be discussed here. We will examine results from global scenarios developed by the GCAM model, focusing in this section on general results that will impact the potential for CSP technologies. Scenarios such as these provide a consistent context for examining the role of technologies over a future where prices and demand

Table 14.2 Current and projected electricity demand for various world regions (billion kWhr)

Region	2005	2050	2100
USA	4,266	6,459	9,195
Canada	622	867	954
Western Europe	3,188	4,763	5,311
Eastern Europe	496	1,190	1,560
Japan and South Korea	1,480	1,829	1,697
Australia and NZ	293	527	611
Former Soviet Union	1,391	3,414	5,271
China	2,577	11,048	17,290
Middle East	639	3,420	6,161
Africa	563	4,128	12,243
South and Latin America	1,140	3,754	9,644
South and East Asia	858	7,628	15,640
India	699	5,609	14,793
Global	18,211	54,635	100,371

may change substantially from present conditions. The scenarios presented here are based on the socioeconomic scenarios from Clarke *et al.* (2007). Results from a reference case scenario, with no climate policy, and a climate policy scenario will be presented.

The scale of electricity demand sets the overall size of the potential market for CSP technologies. Table 14.2 shows total electricity demand for a number of world regions from the GCAM reference case scenario. Global electricity demand increases substantially with most of the increase in industrializing regions of the world. The magnitude of the increase in demand in these regions in particular is uncertain, but it is clear that there is a desire in these regions for increased access to modern energy services that will be filled in large part by increased electricity production. After 2020, in this projection, electricity generation in developing countries will exceed that of the currently more industrialized regions. By 2050 electricity generation is projected to expand by an average of 60% in already industrialized regions as compared to over 500% in the rest of the world. The currently industrialized regions are listed in the top portion of Table 14.2 (the USA through to the former Soviet Union). While many assumptions affect the absolute values of these projections, including the assumption of continued economic growth in many developing countries, a large increase in electricity generation is a common feature of future scenarios (Clarke *et al.*, 2007).

A general increase in electricity demand expands the potential market for CSP power. Globally, however, the potentially large increases in developing countries has particular relevance for CSP technologies because a

Published by Woodhead Publishing Limited, 2012

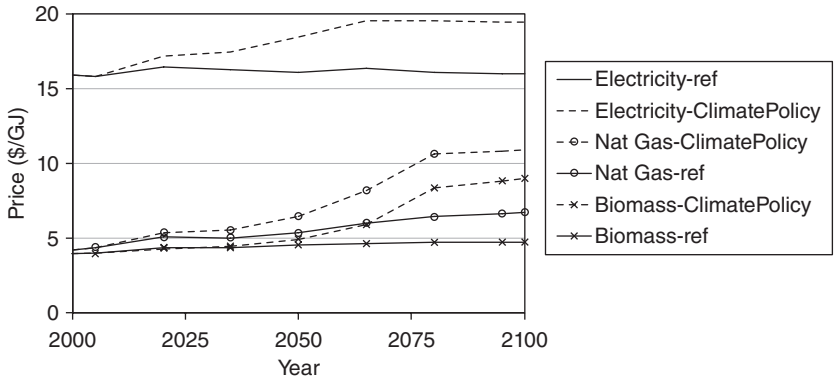

14.1 Wholesale US energy prices under a reference scenario with no climate policy (solid lines) and a scenario where climate forcing is stabilized by the end of the century (dotted lines, see text). Prices are in $2005 constant dollars per GJ.

larger fraction of the population in these regions live in sunny areas. While only 16% of the population in industrialized regions lives in areas with high-quality solar resources for CSP (>6 W/m^2, Table 14.1), the figure for developing regions is 40%. The increase in electricity demand in these countries, therefore, creates a large potential market for CSP technologies. One substantial barrier in poorer regions, however, is often lack of access to capital, which can be due to the perceived risk associated with international investments in these regions. Limitations associated with capital financing are a particular problem for capital-intensive technologies such as CSP.

Many options are potentially available to supply these growing electricity demands. The economic context for CSP technologies includes the price paid for electricity and the cost of fuel – either used for auxiliary heating or for use in competing electricity generation technologies. Figure 14.1 shows projected US wholesale electricity, natural gas, and biomass prices over the century for a reference and climate policy case. The reference case includes technological change and a central set of socioeconomic assumptions, but no explicit action to limit greenhouse gas emissions (Clarke *et al.*, 2007).

The climate policy case meets a target of 4.5 W/m^2 radiative forcing in 2100 (Clarke *et al.*, 2007; Moss *et al.*, 2010), which in this scenario, requires a carbon price that increases to 20 $/TC (tonne of carbon) in 2020, 80 $/TC in 2050, and 300 $/TC by the end of the century.[4] All monetary quantities

[4] Two units are commonly used for carbon prices, per unit mass of carbon and per unit mass of carbon dioxide. $1/tonneC = $0.27/tonne$CO_2$.

Published by Woodhead Publishing Limited, 2012

are in $2005 constant dollars. In this idealized scenario, a price on carbon is assumed to be applied to all fuels and all terrestrial carbon in all regions. This results in global greenhouse gas emissions that are 50% below 2005 values by 2095. Global emissions increase over the next few decades, driven largely by emissions in developing countries, to peak around 2035 at 45% above 2005 values. Emissions in the United States in 2050 are 20% below 2005 values.

Under the reference case with no climate policy, natural gas prices are projected to increase over the long term due to a combination of increased demand and a need to use resources with higher extraction costs, even with the assumption of technological changes that decrease extraction costs relative to today. Biomass prices remain relatively flat in the reference case due to limited demand, which can be supplied in this scenario largely by relatively low-cost waste and residue sources (Gregg and Smith, 2010). Electricity prices are higher than primary fuel prices (exemplified by natural gas) due to losses in energy conversion and the capital costs of electricity generation technologies. Reference case electricity prices are fairly stable over the century due to competition as additional electricity generation technologies are introduced, including CSP, and due to assumed improvement for all technologies over time.

Under the climate policy scenario, fossil fuel technologies are charged a price on any carbon dioxide that is released into the atmosphere as a result of combustion or other use, and this price is included in the values given in Fig. 14.1. As the cost of fossil fuels increases, low-carbon technologies become more competitive. These effects are seen in Fig. 14.1, where natural gas prices are higher in the climate policy case due to the impact of this carbon charge (the curve in the figure is based on the assumption that all carbon in natural gas is vented to the atmosphere). Biomass prices also increase due to increased demand for low-carbon fuels combined with higher land prices due to the assumption that terrestrial carbon stocks are valued equally to fossil fuel carbon (Wise *et al.*, 2009). In the climate policy case, natural gas prices increase by 60% relative to the reference case by the end of the century and biomass prices increase 90% relative to the reference case. Electricity prices also increase, but only by 20% relative to the reference case. This is due to the number of technology choices available whereby lower carbon technologies such as wind, nuclear, PV, CSP and fossil with CCS are used to lower carbon emissions from electricity generation. Note that these are generation, or equivalently, wholesale prices. The change in delivered energy prices at the consumer level will be smaller as distribution costs will not change much between the two cases.

In a scenario exercise such as this, the exact results depend on the modeling approach and assumptions made. What is often of most use are the

general insights that can be drawn from such an analysis. Differences between two scenarios, for example, are often more robust than absolute values. The increase in prices under a climate policy constraint, for example, is a general feature of such scenarios. The relatively modest increase in electricity price under a carbon policy as shown above is typical of other models, although higher near-term increases are seen in some cases (Clarke *et al.*, 2007).

One general conclusion from economic modeling studies is that, while the increase in electricity prices over time makes renewable technologies more attractive, this increase is not sufficient to move a technology with a small market share to a position with a large market share. Technologies that have a substantial market share under a carbon policy were already viable at the same point in time without a climate policy. A technology that is not already competitive at a given point in time, e.g., with only a small market share, will not gain a large portion of a market solely due to a carbon price. The primary key to a large market share in the long term for CSP is lower technology costs.

We note that the one exception to the above discussion is carbon capture and geologic storage, which is generally not economically viable in the absence of a carbon policy. Without a carbon policy, there is no value in capturing CO_2 and injecting it into deep underground geological formations. Only a sufficiently high carbon price makes the extra costs of CCS technology justifiable. Renewable electricity generation technologies, in contrast, produce a product that has economic value in all scenarios.

The scenario results in Fig. 14.1 show an aggregate electricity price. In reality electricity generation costs differ by market segment, even though this difference is not always transmitted to consumers. Overall, the price paid for all generation segments increases over time under a climate policy. A separate detailed analysis of electricity prices by sector indicates that there is a differential impact of a carbon policy on electricity segment prices, with the price paid for peak electricity generation increasing more than the price for off-peak (base load) generation (Luckow *et al.*, 2009; Wise and Dooley, 2005). In a scenario with a 50% reduction in greenhouse gas emissions in 2050, off-peak (e.g., base load) prices increase by 21% from 2005 to 2095 with peak prices increasing by 37% over the same period. These figures are only illustrative: actual values will depend on technology costs and other market conditions at any point in time.

The context for CSP within these scenarios is one where continued technological change brings into play a number of competitive electrical generation options and increasing performance from existing technologies. With policies to reduce greenhouse gas emissions in place, however, the electric system is one of the first sectors to become largely decarbonized (Clarke *et al.*, 2007). This increases electricity prices modestly, with much larger

increases in primary fuel costs. The discussion now turns to scenario results specifically for CSP technologies.

14.3.4 Long-term scenario results for CSP

We now examine the potential role of CSP over the twenty-first century both with and in the absence of a climate policy. We first examine CSP results from the scenarios described in Zhang *et al.* (2010) as produced by the GCAM model. As discussed above, a primary determinant of CSP market share is capital cost and this applies to model simulation results as well. For the reference analysis results presented here, total CSP capital costs were assumed to fall from USD4,500/kW in 2010 to USD3,500/kW in 2050 and USD2,500/kW in 2100 for CSP plants serving intermediate and peak loads (a decline of 0.6% per year over the century). These cost assumptions are exogenous to the model and based on NREL assumptions (NREL, 2005) with updated solar multiple and solar field estimates (Zhang *et al.*, 2010). Costs for base load plants are slightly larger due to the larger solar field and larger thermal storage capacity. This is a conservative estimate of technology advancement, and larger declines in cost are possible, particularly with dedicated efforts toward research, development, and deployment. A second 'advanced technology' scenario was also analyzed, where capital costs fall to USD1,500/kW by the end of the century, or 60% of the reference case costs. These assumptions are used as 'what if' scenarios to examine the potential role of CSP if future costs were to follow these pathways.

Figure 14.2 shows global CSP generation under the two technology cases, each also run with the climate policy case described above. This analysis assumed only limited expansion of current inter-regional transmission capability such that CSP generation was largely consumed within sunny regions with good solar resources. Even with this assumed limitation, CSP generation increases by the end of the century to 7% of total US generation in the reference case and to 14% of total US generation in the advanced technology case, where capital costs were assumed to decrease at a faster rate. Compared to the United States, CSP supplies a larger fraction of electric generation in the Middle East, Africa, and India in these scenarios (Zhang *et al.*, 2010). In the regions with the best resources, CSP is serving a large portion of intermediate loads. The increase in market share in the advanced technology case occurs in base load and intermediate segments. The reference technology case results here for the US are broadly similar to those of Blair *et al.* (2006) who, in a more spatially detailed analysis, projected a reference case scenario where CSP supplies approximately 2.75% of total US generation capacity in 2050.

CSP market share also increases under a climate policy. One factor that limits the increase in CSP under a carbon policy is that the cost of CSP

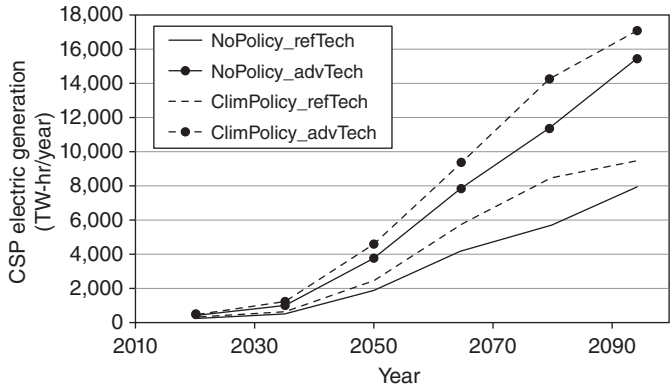

14.2 Projected global electric generation from CSP thermal technologies under two assumptions for technology costs (reference and advanced), combined with two assumptions for a climate policy (see text).

auxiliary heating also increases under a carbon policy (Fig. 14.1). In some cases, by the end of the century these cost increases are sufficient that CSP market penetration under a climate policy is similar to that in the reference case. The influence of auxiliary heating on CSP costs is discussed in detail in the next section.

The IEA 'vision' for CSP (2010) projects a potential 2050 generation of 5,000 TW-hr. This is much larger than the reference case technology deployment in the scenarios shown here, but similar to the advanced technology case where CSP capital costs were assumed to decrease. In the projections shown here, the combination of a climate policy and lower capital costs results in an even larger 2050 deployment of nearly 5,000 TW-hr.

14.3.5 The role of hybrid output under a climate policy

The capability of hybrid CSP plants to supply firm power through use of auxiliary heating is a critical characteristic of these systems. Due to this capability, a large portion of electric demand can be supplied even though solar irradiance can vary during a day, from day to day and from season to season. A key to this capability is the relatively low capital cost of auxiliary operation. The capital investment necessary to provide this hybrid operation is the cost of a boiler or heating element. This compares to the cost of a stand-alone backup system, for example a combustion turbine or battery system, where an entire generating unit would need to be purchased at a much larger cost.

Natural gas auxiliary systems are the preferred option at present. A biomass boiler is more expensive and somewhat less efficient than a natural

gas turbine. Over time in the reference scenario, however, as natural gas prices increase, biomass auxiliary input becomes more attractive. We estimate that the net cost of biomass and natural gas backup systems become comparable toward the end of the century in these scenarios. Costs for biomass backup could be comparable today in regions with high natural gas prices and convenient biomass sources. Further, in areas with limited natural gas distribution infrastructure, biomass backup systems may also be the most attractive option.

The implementation of a climate change policy can change the context for auxiliary operation. The cost of both natural gas and biomass fuel will increase, increasing the overall cost of CSP generation. The increase is modest before 2050 in this scenario, with auxiliary generation costs 40–100% higher than current levels by the end of the century. Note that the presence of thermal storage does not eliminate the need for auxiliary operation during cloudy days, although this can reduce the need for auxiliary operation on operational days.

The role of auxiliary backup operation in contributing to CSP plant costs has been little studied. In part this is because current CSP plants are generally located in regions with very favorable solar resources with a low number of non-operational days and also because auxiliary operation costs are currently a small portion of total plant costs. As capital costs fall, however, auxiliary operation costs will become a larger fraction of total costs (and even more so if natural gas prices increase). Zhang *et al.* (2010) find that auxiliary operation costs in regions with high-quality resources increase from 7 to 8% currently to around 20% of total system costs by the end of the century. Further, if CSP plants begin to be located in regions with less than ideal resources, auxiliary operation costs will be an even larger fraction of total costs. In regions such as the United States, this will represent a tradeoff between building more transmission capability to transmit power from higher quality resource areas and, instead, locating plants with somewhat higher operating costs closer to load centers.

14.3.6 Role of photovoltaics (PV) compared to CSP

Overall, in sunny areas with a small number of cloudy days, CSP systems have the potential to supply a large portion of intermediate, and ultimately, base load generation if costs fall to competitive levels. PV in these same regions can also serve intermediate loads, although CSP may have a larger ultimate potential due to relatively low-cost thermal storage and the presence of auxiliary backup capability.

It is worth noting that most PV systems, however, are usable in areas with a moderate amount of cloudy or hazy days, that is, where a large portion of solar irradiance may be scattered instead of direct. CSP systems are

generally not economic in such areas. PV systems can also be installed in small increments and in a manner compatible with existing land uses, for example on residential rooftops, while thermal CSP systems need dedicated land with suitable resources and infrastructure.

It is likely that both CSP and PV systems will be in use in sunny areas, with additional deployment of PV systems in areas where CSP is not feasible. The initial rate of deployment of CSP and PV systems will depend largely on their relative costs. The manufacturing processes and materials used for PV and CSP systems are quite different and it is difficult to predict their relative cost paths. If the cost of both PV and CSP systems continues to fall, then the largest market share may ultimately go to CSP systems due to their more favorable characteristics regarding integration into the electric system. This, of course, could change if the costs of battery or other electricity storage technologies fall dramatically.

While the discussion has focused on trough and power tower CSP systems, dish systems are also being developed and deployed. To date, the key commercial activity with parabolic dish systems involved receiver-mounted Stirling engines. Dish systems that focus sunlight on high performance photovoltaic cells have also been deployed commercially. One advantage of these systems is that water use is far lower than steam Rankine CSP systems since condenser cooling is not required. These systems are also highly modular, making them potentially attractive for distributed uses or installation in difficult terrain. A disadvantage of such systems is that thermal storage is not an easy option (although this is under consideration, see Chapter 11). Hybrid operation with backup gas firing is under development for Stirling engines, but not yet commercially mature. This means that, at present, the issues and limitations involved in integration of these systems into the electricity grid are essentially identical to those discussed above for PV systems.

14.4 Summary and future trends

Even though the first thermal CSP plants have been operating for 25 years, CSP is in the early stages of widescale deployment. Overall, the industry has been on a growth trajectory since the late 2000s, with an increasing number of plants being built and more in the planning stages. As with any technology at this stage, there is likely to be substantial improvements in manufacturing, construction, and operation processes as deployments increase.

Scenarios with steady, but relatively modest, decreases in costs over time point to a substantial role for CSP in sunny regions over the coming decades. Of course deployments will be even larger if technological advances and economies of scale allow costs to decrease at even faster rates.

Published by Woodhead Publishing Limited, 2012

The expansion of CSP in the electric system begins with CSP plants serving intermediate daytime loads. The successful development and deployment of thermal storage will allow CSP plants to operate into the evening hours and thereby serve an even larger share of intermediate loads. The next phase in the expansion of CSP would be the implementation of sufficient thermal storage to allow round the clock operation and thereby supply base load power.

A key characteristic of thermal CSP systems is their provision of reliable power through the use of low-cost hybrid-backup systems. This makes thermal CSP one of a limited number of technologies that can supply firm intermediate (e.g., daytime through evening) power with low net carbon emissions. An attractive feature of CSP is the combination of hybrid-backup systems, which allow power generation even during cloudy days, combined with thermal storage, which allows solar energy generation to be flexibly supplied to match demand. This combination mitigates the inherent intermittency of solar so that CSP plants can reliably supply a large portion of electric demands. Thermal storage is also valuable in supplying services such as ramping and load leveling to the electric system, particularly in conjunction with intermittent renewable generation such as wind and solar PV. If, in the future, solar energy technologies begin to supply large portions of the electricity market, these system integration issues will become more important and may increase the relative value of CSP technologies.

This growth trajectory will require a reduction in CSP capital costs, particularly to supply base load power. The extent to which this will occur is difficult to predict; while some level of reduction is likely to come from economies of scale as the CSP industry grows, additional technological advances are also likely needed for large cost reductions to occur. Cost declines are most likely in the solar-specific portions of the CSP plant, since the power block of current thermal CSP systems represents a mature technology with many decades of development. Both trough and power tower CSP systems have large numbers of identical components, making these ideal candidates for cost reductions through economies of scale. Material science advances may play a role as well in terms of development of less expensive materials with optical, thermal, and mechanical properties suitable for CSP components.

Even if CSP capital and operating costs fall to a point where CSP is a preferred generation option in sunny locations, a significant uncertainty is the availability of long-distance transmission. Except for tropical regions (Table 14.1), many load centers are not located in areas with high-quality solar resources. Enhanced long-distance transmission would allow CSP generation to be delivered to distant load centers and greatly increase the potential market share for CSP generation in most regions.

Published by Woodhead Publishing Limited, 2012

While substantial investments in long-distance transmission capacity would increase costs, the primary issues for increased transmission are political, social, and, in some areas, ecological. Large transmission projects can be controversial due to visual and other proximity impacts, perceived risks, and trans-boundary issues, as would be the case for proposals to build solar plants in northern Africa to supply loads in Europe. Due to these issues, the preferred location for transmission projects can be areas with low population densities, where a new set of impacts such as habitat fragmentation can arise. Note that the availability of alternative electric generation options will affect the attractiveness of transmission. Most current electric generation plants can be located relatively close to load centers. Under a carbon constraint in particular, fossil-fueled generation would either be reduced or required to be located such that geological carbon storage can be used. This may increase the need for an enhanced long-distance transmission system, which would increase the market opportunities for CSP technologies. Overall, however, it is difficult to predict if the long-distance electric transmission capability necessary to allow regional use of CSP power outside of sunny regions will be built in the future.

Policies to reduce greenhouse gas emissions will have multiple impacts on CSP. CSP is one of the few renewable technologies well suited to supplying firm intermediate power, making this market segment particularly attractive for this technology. The cost of auxiliary heating fuels, however, will increase in a carbon-constrained world, in turn increasing the net cost of CSP. As CSP technologies mature and capital costs fall, the role of auxiliary heating as a component of operating costs will become more important. The same considerations apply to base load power generation, although there are more potentially cost-effective low-carbon options for base load as compared to intermediate load. The role of auxiliary heating in CSP systems has only begun to be examined, however, particularly in situations where CSP supplies a large share of electric supply. Finally, climate change itself could alter the character of solar resources due to changes in cloudiness as well as changing the water resources required for evaporative cooling.

Solar resources, particularly the number of non-operational days per season, need improved characterization in order to better estimate auxiliary heating needs and CSP performance in general. Electric system simulations with increasing levels of CSP penetration are also needed to better characterize auxiliary heating requirements under different system configurations, supply technology and demand management options, and fuel and carbon prices. Such simulations would also be useful for evaluating the potential economic value of CSP plants with thermal storage in a system with large amounts of wind and solar power.

Although not discussed in detail here, thermal CSP systems might also play a role in supplying process heat and chemical fuels production (see Chapters 19 and 20). Cost is a particular challenge here since process heat can often be provided relatively inexpensively by natural gas or other fuels. The use of CSP for desalination (Trieb and Müller-Steinhagen, 2008) is a particularly interesting possibility given the coincidence of high levels of solar irradiance in arid areas that often lack freshwater resources. Backup operation might not be a substantial consideration for desalination plants if sufficient water storage was available to accommodate cloudy days.

14.5 Sources of further information and advice

14.5.1 Long-term socio-economic scenarios

Clarke, L., J. Edmonds, J. Jacoby, H. Pitcher, J. Reilly, and R. Richels, 2007. Scenarios of Greenhouse Gas Emissions and Atmospheric Concentrations. Report by the US Climate Change Science Program and approved by the Climate Change Science Program Product Development Advisory Committee (United States Global Change Research Program, Washington, DC).

14.5.2 Electricity storage

http://www.electricitystorage.org/
http://www.sandia.gov/ess/

14.6 Acknowledgements

The author is indebted to past and current members of the integrated assessment modeling group at the Joint Global Change Research Institute for the development of the GCAM modeling system, results from which are featured in this chapter. The discussion in this chapter also benefited greatly from previous joint work with Dr Yabei Zhang. The author would also like to thank Patrick Luckow for helpful comments.

14.7 References

Angelino, G. and C. Invernizzi, 2008. 'Binary conversion cycles for concentrating solar power technology', *Solar Energy*, 82, 637–647.

Blair, N.M., Mehos, W. Short, and D. Heimiller, 2006. 'Concentrating Solar Deployment System (CSDS) – A New Model for Estimating US Concentrating Solar Power (CSP) Market Potential.' Proceedings of the Solar 2006 Conference, 9–13 July, Denver, CO.

Chandler, W.S., C.H. Whitlock, and P.W. Stackhouse, Jr., 2004. 'NASA climatological data for renewable energy assessment', *Journal of Solar Energy Engineering*, 126 (3), 945–949.

Clarke, L., J. Weyant, and A. Birky, 2006a. 'On the sources of technological change: assessing the evidence', *Energy Economics*, 28 (5–6), 579–595.

Clarke, L.E., M.A. Wise, J.P. Lurz, M. Placet, S.J. Smith, R.C. Izaurralde, A.M. Thomson, and S.H. Kim, 2006b. 'Technology and Climate Change Mitigation: A Scenario Analysis.' PNNL-16078.

Clarke, L., J. Edmonds, J. Jacoby, H. Pitcher, J. Reilly, and R. Richels, 2007. Scenarios of Greenhouse Gas Emissions and Atmospheric Concentrations. Report by the US Climate Change Science Program and approved by the Climate Change Science Program Product Development Advisory Committee (United States Global Change Research Program, Washington, DC).

Craig, P.P., A. Gadgil, *et al.*, 2002. 'What can history teach us? A retrospective examination of long-term energy forecasts for the United States', *Annual Review of Energy and the Environment*, 27, 83–118.

Denholm, P. and R. Margolis, 2007a. 'Evaluating the limits of solar photovoltaics (PV) in traditional electric power systems', *Energy Policy*, 35, 2852–2861.

Denholm, P. and R. Margolis, 2007b. 'Evaluating the limits of solar photovoltaics (PV) in electric power systems utilizing energy storage and other enabling technologies', *Energy Policy*, 35, 4424–4433.

Department of Energy, 2008. Concentrating Solar Power Commercial Application Study: Reducing Water Consumption of Concentrating Solar Power Electricity Generation (Report to Congress).

Divya, K.C. and J. Østergaard, 2009. 'Battery energy storage technology for power systems – an overview', *Electric Power Systems Research*, 79, 511–520.

Dutton, J. and A. Thomas, 1984. 'Treating progress functions as a managerial opportunity', *The Academy of Management Review*, 9 (2), 235–247.

Edmonds, J.A., J.F. Clarke, J.J. Dooley, S.H. Kim, and S.J. Smith, 2004. 'Modeling greenhouse gas energy technology responses to climate change', *Energy*, 29 (9–10), 1529–1536.

Eto, J.H., J. Undrill, P. Mackin, R. Daschmans, B. Williams, B. Haney, R. Hunt, J. Ellis, H. Illian, C. Martinez, M. O'Malley, K. Coughlin, and K.H. LaCommare, 2010. 'Use of Frequency Response Metrics to Assess the Planning and Operating Requirements for Reliable Integration of Variable Renewable Generation', Lawrence Berkeley National Laboratory, LBNL-4142E.

Forster, P., V. Ramaswamy, P. Artaxo, T. Berntsen, R. Betts, D.W. Fahey, J. Haywood, J. Lean, D.C. Lowe, G. Myhre, J. Nganga, R. Prinn, G. Raga, M. Schulz, and R. Van Dorland, 2007. Changes in atmospheric constituents and in radiative forcing. In: *Climate Change 2007: The Physical Science Basis. Contribution of Working Group I to the Fourth Assessment Report of the Intergovernmental Panel on Climate Change* (Solomon, S., D. Qin, M. Manning, Z. Chen, M. Marquis, K.B. Averyt, M. Tignor, and H.L. Miller, eds. Cambridge: Cambridge University Press.

Fthenakis, V., J.E. Mason, and K. Zweibel, 2009. 'The technical, geographical, and economic feasibility for solar energy to supply the energy needs of the US', *Energy Policy*, 37 (2), 387–399.

Gregg, J.S. and S.J. Smith, 2010. 'Global and regional potential for bioenergy from agricultural and forestry residue biomass', *Mitigation and Adaptation Strategies for Global Change*, 15 (3), 241–262.

Heller, P., M. Pfänder, T. Denk, F. Tellez, A. Valverde, J. Fernandez, and A. Ring, 2006. 'Test and evaluation of a solar powered gas turbine system', *Solar Energy*, 82 (7), 637–647.

IEA, 2010. Technology Roadmap Concentrating Solar Power. International Energy Agency, Paris.

Kelly, B., 2006. Nexant Parabolic Trough Solar Power Plant Systems Analysis: Comparison of Wet and Dry Rankine Cycle Heat Rejection. NREL/SR-550-40163.

Kim, S.H., J. Edmonds, J. Lurz, S.J. Smith, and M. Wise, 2006. 'The ObjECTS framework for integrated assessment: hybrid modeling of transportation', *Energy Journal*, Special Issue #2, 63–91.

Kolb, G.J., C.K. Ho, T.R. Mancini, and J.A. Gary, 2011. Power Tower Technology Roadmap and Cost Reduction Plan. Sandia National Laboratory, SAND2011-2419.

Kutscher, C., M. Mehos, C. Turchi, and G. Glatzmaier, 2010. Line-Focus Solar Power Plant Cost Reduction Plan. National Renewable Energy Laboratory, NREL/TP-5500-48175.

Luckow, P., M.A. Wise, and J.J. Dooley, 2009. 'Deployment of CCS technologies across the load curve for a competitive electricity market as a function of CO_2 emissions permit prices', 10th International Conference on Greenhouse Gas Control Technologies, Amsterdam, Netherlands. PNNL-SA-70032.

Moss, R.H., J.A. Edmonds, K. Hibbard, T. Carter, S. Emori, M. Kainuma, T. Kram, M. Manning, J. Meehl, J. Mitchell, N. Nakicenovic, K. Riahi, S. Rose, S.J. Smith, R. Stouffer, A.M. Thomson, D. VanVuuren, J. Weyant, and T. Wilbanks, 2010. 'The next generation of scenarios for climate change research and assessment'. *Nature*, 463, 747–756.

Nakicenovic, N. and R. Swart, 2000. *Special Report on Emissions Scenarios* Cambridge: Cambridge University Press.

National Renewable Energy Laboratory (NREL), 2005. Potential for Renewable Energy in the San Diego Region, Appendix E, August.

Sargent and Lundy, 2003. Assessment of Parabolic Trough and Power Tower Solar Technology Cost and Performance Forecasts. National Renewable Energy Laboratory, Golden, CO, NREL/SR-550-34440.

Short, W., D.J. Packey, and T. Holt, 2005. A Manual for the Economic Evaluation of Energy Efficiency and Renewable Energy Technologies. National Renewable Energy Laboratory, NREL/TP-462-5173.

Smith, S.J. and T.M.L. Wigley, 2006. 'Multi-gas forcing stabilization with the GCAM', *The Energy Journal*, Special Issue #3.

Stoddard, L., B. Owens, F. Morse, and D. Kearney, 2005. New Mexico Concentrating Solar Plant Feasibility Study. Draft Final Report, Black & Veatch.

Trieb, F. and H. Müller-Steinhagen, 2008. 'Concentrating solar power for seawater desalination in the Middle East and North Africa', *Desalination*, 220, 165–183.

Wise, M.A. and J.J. Dooley, 2005. 'Baseload and peaking economics and the resulting adoption of carbon dioxide capture and storage systems for electric power plants'. In: *Greenhouse Gas Control Technologies, Volume I* (Rubin, E.S., D.W. Keith, and C.F. Gilboy, eds). Oxford: Elsevier Science, pp. 303–311.

Wise, M.A, K.V. Calvin, A.M. Thomson, L.E. Clarke, B. Bond-Lamberty, R.D. Sands, S.J. Smith, T.C. Janetos, and J.A. Edmonds, 2009. 'Implications of limiting CO_2 concentrations on land use and energy', *Science*, 324, 1183–1186.

Published by Woodhead Publishing Limited, 2012

WorleyParsons, 2008. FPLE – Beacon Solar Energy Project: Dry Cooling Evaluation. WorleyParsons Report No. FPLS-0-LI-450-0001.

Zhang, Y. and S. Smith, 2008. 'Long-Term Modeling of Solar Energy: Analysis of CSP and PV Technologies'. Pacific Northwest National Laboratory report PNNL-16727.

Zhang, Y., S.J. Smith, G.P. Kyle, and P.W. Stackhouse Jr., 2010. 'Modeling the potential for thermal concentrating solar power technologies', *Energy Policy*, 38, 7884–7897.

Published by Woodhead Publishing Limited, 2012

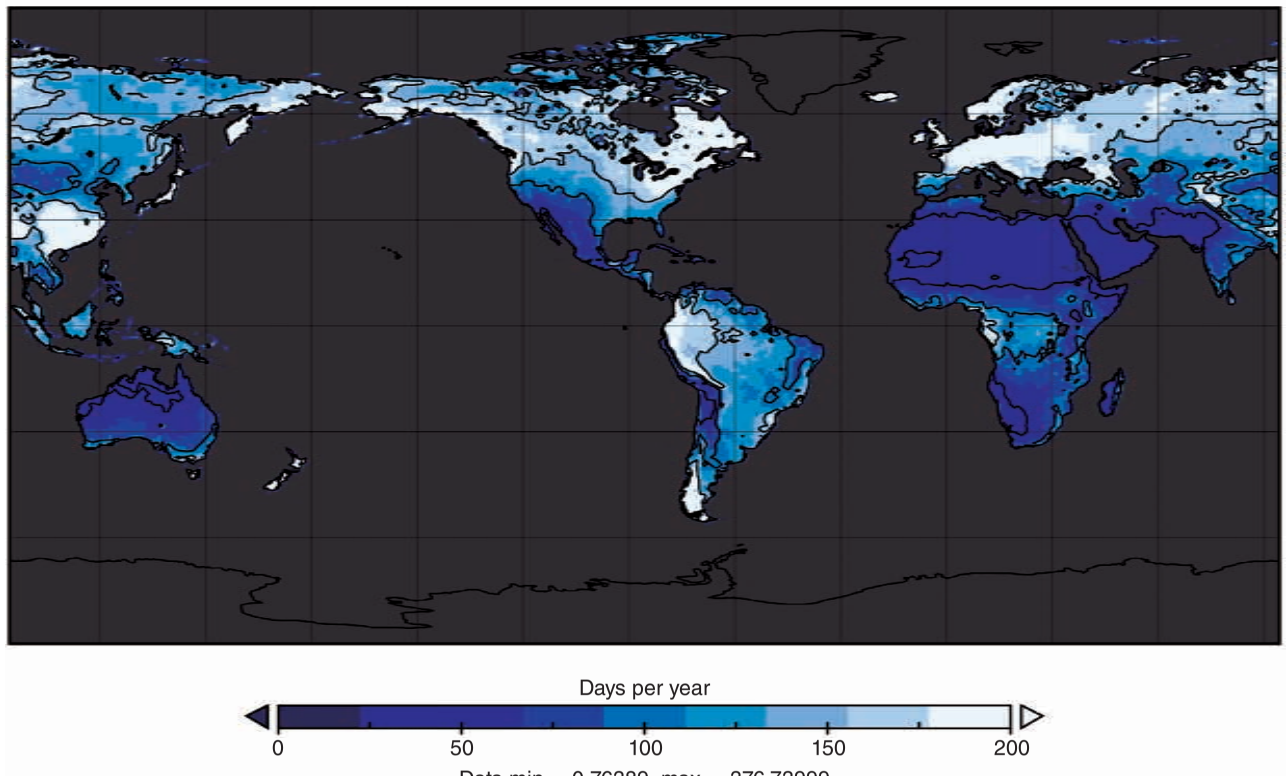

Plate III Estimate of the number of days where direct solar irradiance is too low to operate a thermal CSP plant (Zhang *et al.*, 2010). The dark shaded regions indicate areas with less than 100 low DNI days per year, which are areas particularly well suited for CSP.

15

Absorber materials for solar thermal receivers in concentrating solar power (CSP) systems

W. PLATZER and C. HILDEBRANDT,
Fraunhofer Institute for Solar Energy Systems, Germany

Abstract: In this chapter, different approaches and properties of absorber coatings for receivers in parabolic trough and linear Fresnel collectors are discussed. The receiver is a central and crucial element determining the optical efficiency of the conversion of solar radiation on the one hand, and the heat losses on the other. High solar absorptance and low thermal emittance in the temperature range of operation are important. The exact definitions of these key characterizing parameters are given. As the receivers should retain their performance over many years of operation, degradation processes and service lifetime are important as well.

Key words: absorber coatings, receiver tubes, selective absorbers, high-temperature stability, degradation.

15.1 Introduction

In the solar field of a solar thermal power station, the receiver is a central and crucial element in the technology chain, determining the efficiency of the conversion of solar radiation into heat. In this chapter we will discuss absorber materials used for solar thermal receivers, with an emphasis on linearly concentrating solar collectors.

15.1.1 Receivers for linearly concentrating collectors

Two basic collector types of line focusing systems are used. The first is the parabolic trough collector (PTC), which tracks the diurnal position of the sun with the complete parabolic mirror structure, and the second is the linear Fresnel collector (LFC) where the parabolic mirror shape is split up into mirror facets according to the Fresnel principle. This has consequences on the receiver design. All receivers are based on steel tubes coated with a more or less black, i.e. highly absorbing coating. Whereas the PTC receiver for constructional reasons (weight distribution) rotates together with the mirror structure in the focus of the parabolic trough, the LFC's mirror facets are usually mounted horizontally on the ground each

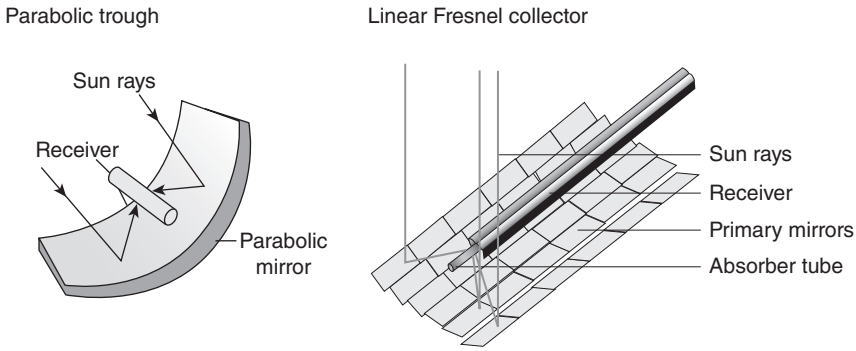

15.1 Principles of parabolic trough (left) and linear Fresnel collectors (right).

individually tracking the sun, and concentrating the light on a receiver construction above the mirror field (Fig. 15.1). Trough systems are discussed in detail in Chapter 7 and linear Fresnel systems in Chapter 6.

Within the absorber tubes a heat transfer fluid (HTF) is circulated to transport the heat generated to a consumer load (typically a power generation system). In order to convert solar radiation into sensible heat efficiently, the absorber tube surfaces should have a very low reflectivity and correspondingly high absorptivity.

15.1.2 Ideal selective absorber

The surface of an ideal selective absorber is black (i.e., completely absorbing) in the solar wavelength range between 0.3 μm and 2.5 μm approximately. In order to reduce the thermal heat losses via emitted radiation from the absorber tubes, the surfaces should ideally have a very low emissivity for the wavelengths that they emit.

Absorber surfaces are governed by the basic principles of optical behaviour of materials. Key to this are two principles:

- the absorptivity of a surface at a particular wavelength (i.e., the fraction of incident radiation that it absorbs) is equal to its emissivity at the same wavelength (the amount of radiation it emits expressed as a fraction of the amount that an ideal black body would emit)
- all the radiation incident on a surface must either be absorbed, reflected or transmitted, so absorptivity, transmissivity and reflectivity must sum to 1.

The key to the idea of a selective surface is that the wavelengths that a hot solar receiver will emit are different from the solar spectrum wavelengths. Whilst absorptivity must equal emissivity at each specific

wavelength, they can and do vary with wavelength. As a consequence the ideal reflectance function of an effective so-called selective solar absorber is a step function between a minimum value of reflectance (hence high absorptivity) in the solar wavelength range and a high reflectance (hence low emissivity) in the infrared (IR) thermal radiation range (see Fig. 15.2). Ideally the lower reflectance limit would approach 0% while the upper limit would be 100%; however, in reality these values cannot be achieved. Perfect gold surfaces have reflectance values in the IR of nearly 98%, whilst blackened surfaces with 98% are also possible. For lower temperatures there is no energetically significant overlap between the thermal emission spectrum of a body (with the blackbody spectrum according to Planck being the upper limit) and the solar spectrum. A critical wavelength λ_{crit} for the step function can be defined which separates the two respective wavelength regions. For higher temperatures, however, the thermal emission spectrum is shifted towards shorter wavelengths which implies an increasing overlap of the spectra. Therefore the critical wavelength has to be optimized with respect to solar absorptance and thermal emittance for different operating temperatures.

In determining an optimal critical wavelength and designing surfaces, the issue of concentration ratio also needs to be considered. A high level of concentration on a receiver means that the relative area for thermal loss via emitted radiation is smaller, overall efficiency will be enhanced more by increases to absorptivity than by decreases to thermal emissivity. For example, for a parabolic trough (Eurotrough type) due to the concentration, a loss of 0.01 of absorptance can reduce the solar gains per receiver length up to about 50 W/m. For a corresponding reduction in emissive power, the emittance would need to change approximately three times as much.[1]

When the critical wavelength of the ideal reflectance step function is varied (see Fig. 15.2), the integrated values of solar absorptance α_S and of thermal emittance ε_{IR} for a specific temperature change due to different overlap with solar and thermal spectra (Fig. 15.3). For a low value of the critical wavelength, a part of the solar spectrum overlaps with the high reflectivity, and therefore solar reflectance increases – and due to the basic principles solar absorptance decreases. When the critical wavelength exceeds the maximum wavelength of significant solar radiation (at about 2.6 μm) a further increase leaves the integrated value constant.

In contrast, the infrared emittance rises with increasing critical wavelength, as a part of the low reflectivity/high absorptivity curves enters the infrared region where the thermal spectrum is significant. Consequently,

[1] Based on a tubular receiver with 70 mm diameter. The radiation heat loss increases about 50 W/m in the relevant temperature range 350°C when emissivity changes from 11% to 8%.

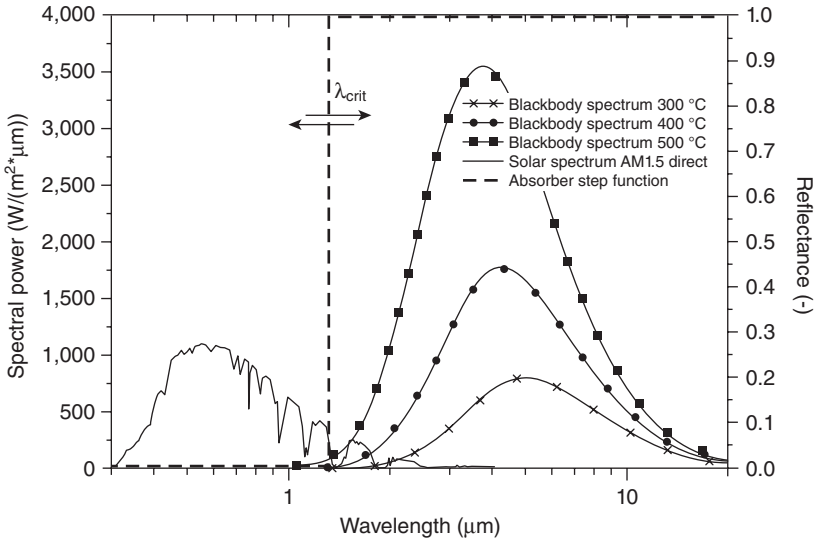

15.2 Reflectance of an ideal selective solar absorber together with standard solar spectrum (AM1.5 direct, not concentrated) and blackbody spectra (300°C, 400°C, 500°C).

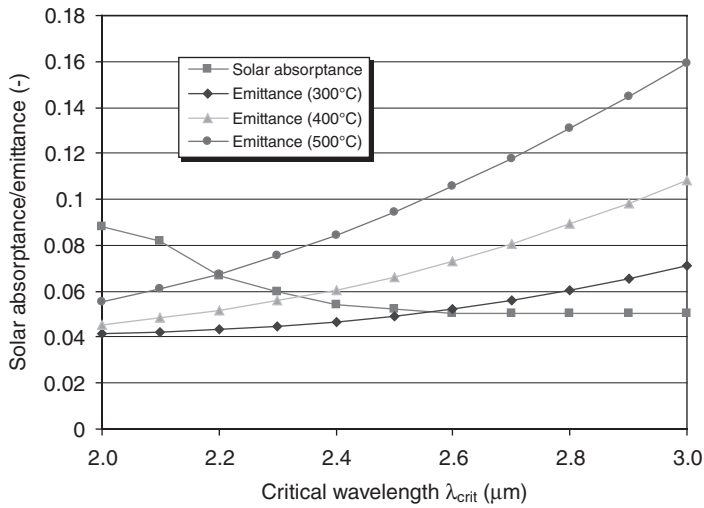

15.3 Solar absorptance and thermal emittance for absorber temperatures 300°C, 400°C and 500°C vs critical wavelength of an ideal selective absorber (step function) with short wavelength reflectance 0.04 and long wavelength reflectance 0.96.

shifting the critical wavelength to higher values in order to gain a higher absorption will always result in a higher emittance for a given temperature.

One emittance curve is only valid at a specific temperature, as emittance is a function of temperature. Furthermore, when the critical wavelength changes, the overlap with the Planck function for a specific temperature also changes. This effect can clearly be seen in Fig. 15.3.

15.1.3 Evacuated and non-evacuated receivers

As convective thermal losses also have to be minimized for high efficiency, in PT collectors a vacuum receiver is typically used. A transparent glass tube is placed around the absorber tube, connected in a flexible way to the steel tube and the space between absorber and glass tube is evacuated. For the LFC the receiver is in a fixed position above the mirror field. Therefore due to the buoyancy of warm air, an insulated cavity with opening viewing the ground can be used in order to reduce thermal losses due to natural convection. It is advisable, however, to close the cavity with a cover glass in order to avoid convective losses due to wind. In such a cavity receiver, we do not necessarily need evacuated tube receivers, and hence air-stable absorber tubes can be used instead. In fact, most LFC designs today do not use vacuum receivers, and further discussion of LFC receivers can be found in Chapter 6. A second use of the cavity can be that the inner surface is mirrored and the cavity shaped to reflect radiation not hitting the absorber tube directly onto the absorber. With a mirror casing the cavity, this makes a secondary concentrator (the mirror field being the primary concentrator).

15.1.4 Point focus receivers

The receivers for point focus concentrators such as dishes and central receivers (see Chapters 8 and 9) typically operate at much higher temperatures (500–800°C) and corresponding concentrations (500–5,000) than do linear systems. This significantly complicates the issue of producing a useful selective absorber. The critical wavelength is shifted to substantially shorter wavelengths, resulting in substantial overlap of the solar and thermal spectra. In addition, the effect of the loss of 1% of solar absorptance is greatly increased. At a surface temperature of 600°C and a concentration of 1,000, a loss of absorptance of 0.01 will lose 10 kW/m^2, requiring a decrease of the thermal emittance by 0.30 to break even. At a surface temperature of 800°C and a concentration of 3,000, the equivalent numbers are 0.01, 30 kW/m^2, and 0.40. So in practice non-selective absorbers are used for coating tower receivers black.

Table 15.1 Maximum fluid temperatures and related pressures for general categories of heat transfer fluids

Fluid	Max. fluid temp. (°C)	Typical fluid pressure (bar)
Synthetic thermo-oil	393	20–50
Molten salts	550	20–50
Steam	480	120

15.1.5 Optical and thermal operating requirements

For linearly concentrating systems, the operating requirements on the tube receivers are dependent on the chosen heat transfer fluid of the solar field which determines the maximum temperature. For the three general types of the fluid currently used, different maximum fluid temperatures and fluid pressures are listed in Table 15.1.

The operating pressure in the solar field for thermo-oil and molten salt is due to the required pumping power to drive the fluid through the field and is therefore dependent on the solar field design and hydraulics. Steam is used as the heat transfer fluid where it is generally intended to be the working fluid in a power cycle, thus high pressures are dictated by the requirements of the turbine chosen. If steam is intended for process heat applications, elevated pressures are likely to be chosen to improve heat transfer, reduce pressure drop and increase the boiling temperature. Due to the higher pressure of steam fluid, the wall thickness of the absorber tubes has to be increased compared to the other fluids. In addition, the heat transfer from inner tube surface to the fluid is relatively low for dry steam. As a consequence, the temperature differential is larger between the absorber coating and the fluid itself, depending on the momentary heat flux. For the absorber system therefore the thermal stresses can be larger for direct steam generation even when the operating temperature of the circulating fluid is the same as for thermo-oil.

The intensity distribution on the absorber surface also has an impact on the stresses on the absorber system. Due to the concentrator system usually one side of the absorber tube receives an overwhelming fraction of the total irradiation on the tube. For PT, the outside part of the pipe receives just unconcentrated radiation (say 900 W/m^2), whereas the side facing the reflector on average receives around 35–40 kW/m^2. For linear Fresnel receiver designs with a secondary concentrator, the difference between the downward facing side and the upper side of the tubes might not be so extreme; however, the thermal stresses associated with the local surface temperatures being above fluid temperatures are appreciable. These

temperatures depend on the thermal conductivity and thickness of the steel tube wall as well as the thermal resistance of the fluid boundary layer inside the tube. Local excess temperatures approaching 70–80 K compared to the steam temperature have been calculated for a stainless steel absorber for a linear Fresnel collector, with about 30 K of the temperature difference occurring over the wall thickness [1]. On the opposite side of the upper tube for the same case only a few degrees Kelvin excess temperature are predicted. This means that the temperature distribution around the absorber tube has an azimuthal variation of 60–70 K. A coating has to be able to cope with the mechanical stresses associated with that in addition to the effects of the average high receiver temperature.

15.2 Characterization of selective absorber surfaces

As noted above, the performance of a candidate solar absorber can be characterized by its solar absorptance and thermal emittance. Using Kirchoff's law, spectral absorptance or emittance can be expressed in terms of total reflectance $\rho(\lambda,\theta)$ for opaque (zero transmissivity) materials:

$$\alpha(\lambda, \theta) = 1 - \rho(\lambda, \theta) \quad [15.1]$$

$$\varepsilon(\lambda, T) = \alpha(\lambda, T) \quad [15.2]$$

where $\rho(\lambda,\theta)$ is the sum of both collimated (specular) and diffuse reflectance, λ is the wavelength, θ is the incidence angle of light, and T is the given temperature. Development of spectrally selective materials depends on reliable characterization of their optical properties.

15.2.1 Determination of thermal emittance

Using standard spectrophotometers, solar reflectance is usually measured in the 0.3–2.5 μm wavelength range at near-normal angle of incidence. Similarly in the infrared range above 2 μm emittance is determined by measuring near-normal reflectance with an integrating sphere, and by using Eqs [15.1] and [15.2]. This may lead to unrealistic low predictions because the effective emittance relevant for radiation heat transport is systematically underestimated. The reason is that the property determined from normal-hemispherical reflectance is the normal emittance, which is usually smaller than hemispherical emittance relevant for the overall radiative heat loss of a surface. An alternative is the calorimetric measurement of radiative heat loss of a surface in vacuum at the relevant temperature. Whereas spectral reflectance can be measured at room temperature, total emittance has to be measured at elevated temperatures. An average emittance over a wavelength range is frequently reported from reflectance data weighted with blackbody curves:

$$\varepsilon(T) = \frac{\int_{\lambda_{\min}=0}^{\lambda_{\max}=\infty} \varepsilon(\lambda, T) \cdot e_B(\lambda, T) d\lambda}{\sigma \cdot T^4} \quad [15.3]$$

where $\sigma = 5.67 \times 10^{-8}\,\mathrm{Wm^{-2}K^{-4}}$ is the Stefan–Boltzmann constant and $e_B(\lambda,T)$ is the spectral irradiance of a blackbody curve from

$$e_B(\lambda, T) = \frac{c_1}{\lambda^5 \cdot \left[\exp\left(\frac{c_2}{\lambda \cdot T}\right) - 1\right]} \quad [15.4]$$

where $c_1 = 3.7405 \times 10^{+8}\ \mathrm{W\mu m^4 m^{-2}}$ and $c_2 = 1.43879 \times 10^{+4}\ \mu\mathrm{m\ K}$ are Planck's first and second radiation constants, respectively (see ref. [2]). The actual performance of an absorber at high temperatures may not correspond to the calculated emittance. This is because small errors in measured ρ can lead to large errors in small values of ε. Calculating the emittance from spectral data taken at room temperature assumes that the spectral characteristics do not change with increasing temperature. This is only valid if the material is invariant, for example does not undergo a phase change (as do some titanium-containing materials), break down or undergo oxidation (as do paints and some oxide coatings) at higher temperatures. It is important before using high-temperature emittance calculated from room temperature data that the calculated data is verified with high temperature emittance measurements for each selective coating. Therefore, it is preferable to also measure the total emittance at the operating temperatures and conditions [3]. In addition, measurement errors might lead to differences to the direct calorimetric measurement.

Emittance is a surface property and depends on the surface condition of the material, including the surface roughness, surface films, and oxide layers. Coatings typically replicate to some degree the surface roughness of the substrate. Therefore to facilitate development, it is important to measure the emittance of each coating–substrate combination as well as the uncoated substrate when developing a solar selective coating. Furthermore, selective coatings can degrade at high temperatures because of oxidation, high humidity or water condensation on the absorber surface (hydratization and hydrolysis), atmospheric corrosion (pollution), diffusion processes (interlayer substitution), chemical reactions, and poor interlayer adhesion [4].

15.2.2 Determination of solar absorptance

Using the spectrally measured reflectance as described in the previous section, we may determine similarly the solar absorptance by integration using a standard solar spectrum as weighting factor.

$$\alpha_S = \frac{\int_{\lambda_{\min}=0}^{\lambda_{\max}=2.6} [1-\rho(\lambda,T)]\cdot e_S(\lambda)\,d\lambda}{\int_{\lambda_{\min}=0}^{\lambda_{\max}=2.6} \cdot e_S(\lambda)\,d\lambda} \qquad [15.5]$$

where $e_S(\lambda)$ is a suitable solar standard spectrum. As concentrating collectors use direct irradiation only, a direct solar spectrum should be taken. The proposed standard spectrum here is ASTM G173-03 AM1.5 Direct Normal [5].

15.3 Types of selective absorbers

Selective absorber surface coatings can be categorized into several distinct types based on different physical principles: (a) intrinsic, (b) semiconductor–metal tandems, (c) multilayer absorbers, (d) multi-dielectric composite coatings, (e) textured surfaces, and (f) selectively solar-transmitting coating on a blackbody-like absorber. Whereas the first two principles need only one homogeneous material, the other ones work with layers of different optical properties.

Intrinsic absorber coatings use a material having intrinsic properties that result in the desired spectral selectivity. Semiconductor-metal tandems absorb short wavelength radiation where photon energy is above the semiconductor bandgap and have low thermal emittance as a result of the metal layer. Multilayer absorbers use multiple reflections between layers to absorb light and can be tailored to be efficient selective absorbers. Metal-dielectric composites – cermets – consist of fine metal particles in a dielectric or ceramic host material. Textured surfaces can produce high solar absorptance by multiple reflections among needle-like, dendritic, or porous microstructure. Additionally, selectively solar-transmitting coatings on a blackbody-like absorber are also used but are typically used in low-temperature applications. These constructions are shown schematically in Fig. 15.4(a)–(f), respectively, and are discussed in greater detail below.

15.3.1 Intrinsic absorbers

Intrinsic selective absorbers consist of a single material with intrinsic selective property of the material. No naturally occurring material exhibits intrinsically ideal solar-selective properties, only some roughly approximate selective properties. Intrinsic properties are found in transition metals and semiconductors, but both need to be greatly modified to serve as an intrinsic absorber. Examples include the transition metal tungsten W [7] and a series of semiconducting materials, for example MoO_3-doped Mo [8], Si doped

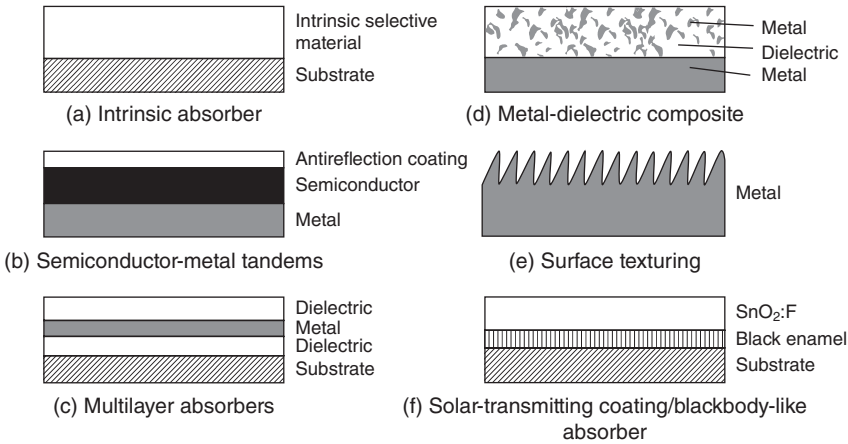

15.4 Schematic designs of six types of coatings and surface treatments for selective absorption of energy [6].

with B, HfC [9], ZrB_2 [10], SnO_2 [9] among others. Hafnium carbide (HfC) could be useful as an absorbing selective surface at elevated temperatures because of its high melting point. However the absorptivity of HfC has to be increased e.g. by an antireflective (AR) layer. Using Zirkonium bromide ZrB_2 one can reach the best selectivity with $\alpha = 88\%$ and $\varepsilon(100°C) = 8\%$, which may be even inproved by a Si_3N_4-AR-Layer to $\alpha = 93\%$ and $\varepsilon(100°C) = 10\%$ [10].

Intrinsic absorber materials are usually structurally very stable but optically less effective than other types of selective absorbers. Therefore historically, research on intrinsic absorbers has not been very productive because there are no ideal intrinsic materials; but the intrinsic materials are finding increasing use as a component in high temperature absorber multilayers and composite coatings.

15.3.2 Surface texturing

Surface texturing is a common technique to obtain higher absorption due to optical trapping of solar energy. When surfaces are textured with a lateral dimension close to the wavelength to be absorbed, they appear as a series of cavities. Thus using structures smaller than 1 μm they absorb solar energy, whereas for longer wavelengths the texture cannot be resolved and appears highly reflective and mirror-like to thermal energy. The emittance can be adjusted (higher or lower) by modifying the microstructure of the surfaces with ion-beam treatments. The selective properties depend on the ratios of mean height deviations and the autocorrelation distance to the wavelength [11].

Needle-like, dendrite, or porous microstructures on the same scale as the wavelength of the incident radiation exhibit both wavelength and some directional selectivity. The surface of the microstructure must be protected from damage caused by surface contact or abrasion. Selection of a material having a high intrinsic absorption coefficient can further optimize the absorptance. A number of methods exist to prepare textured microstructures [9], for example:

- liquid–solid phase separations
- lithography in combination with ion-etching
- unidirectional solidification of eutectic alloys
- lithography with X-rays
- ion-exchange reactions between metals – isothermal transport occurs between two metals where the difference in the work function (ΔE_w) is >0.2 eV (e.g., Cu-Ni alloy).
- vapour–liquid–solid (VLS) mechanism grows in a controlled way, whiskers on substrates from the liquid alloy zone at the interface (e.g., Si, Ge, III–V whiskers)
- vapour deposition – the condensation of a metal or compound from the gas phase onto a substrate by chemical vapour deposition (CVD) or physical vapour deposition (PVD) (e.g., Ni-Al_2O_3, Ni)
- oxidation of metals at high temperature – the growth of whiskers on metals by the oxidation process in air or O_2 at high temperature (400–850°C) (e.g., Fe_2O_3-Fe, steel; CuO-Cu, phosphor bronze; ZnO-Zn, brass; W; Ni; Mo).

These techniques can be useful in texturing selective surfaces. Examples for absorber surfaces are dendritic tungsten or structured copper, nickel or stainless steel surfaces [12]. Typical values are $\alpha = 92\%$ and $\varepsilon(100°C) = 22\%$. Using nickel, which is not stable at high temperatures, the emittance can be as low as $\varepsilon(100°C) = 10\%$ [6].

15.3.3 Semiconductor–metal tandems

Semiconductors with bandgaps from about ~0.5 eV to 1.26 eV, corresponding to wavelengths of 2.5 μm to 1.0 μm, absorb short wavelength radiation and are transparent to longer wavelengths. Hence an underlying metal provides low emittance to give the desired spectral selectivity to semiconductor–metal tandems. Semiconductors of interest include Si (1.1 eV), Ge (0.7 eV), and PbS (0.4 eV) [7]. An antireflection treatment (coatings or porous surfaces) is needed because the useful semiconductors have high refractive indices resulting in large detrimental reflectance. Si-based designs produced by CVD are well known that are suitable for mid- to

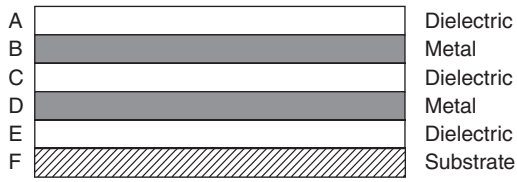

15.5 Schematic designs of multilayer absorber film structure [6].

high-temperature applications [13]. Best values to be reached are quoted as $\alpha = 91\%$ and $\varepsilon(100°C) = 9\%$ [6].

15.3.4 Multilayer absorbers

Multilayer absorbers or multilayer interference stacks consist of many alternating thin layers of transparent dielectric layers and semitransparent metallic or semiconducting layers (Fig. 15.5). The lowest opaque thick coating has to be metallic in order to provide a low emittance. The alternating thin-layer stack is optimized for high solar absorption while being transparent to longer wavelengths. Thus the stack can be designed in order to become an efficient selective absorber.

The basic physics of multilayer absorbers is well understood, and computer modelling can predict the optical properties given by an optimum multilayer design of candidate materials [14], provided adequate optical constants for the thin films are available. Multilayer interference stacks have high solar absorption, low thermal emittance, and are stable at elevated temperatures (≥400°C) depending on the materials used. Several multilayer absorbers using different metals (e.g., Mo, Ag, Cu, Ni) and dielectric layers (e.g., Al_2O_3, SiO_2, CeO_2, ZnS) have been cited in the literature for high-temperature applications [6]. A very well-known example is the AMA-coating (Al_2O_3-Mo-Al_2O_3) with an absorption $\alpha = 92–95\%$ and $\varepsilon(20°C) = 6–10\%$ [15].

15.3.5 Metal-dielectric composite coatings (cermets)

These absorbers consist of an anti-reflection (AR) layer on top of a composite layer, which is highly absorbing in the solar region (i.e., black) and transparent in the infrared region (IR), deposited onto a highly IR-reflective metal substrate. The highly absorbing metal-dielectric composite, or cermet, consists of fine metallic nanoparticles in a dielectric or ceramic matrix. These films are transparent in the thermal IR region, while the absorption in the solar region is either due to interband transitions in the metal or small particle resonances. The cermet layer may have uniform metal content but graded profiles are preferable to enhance absorption. The

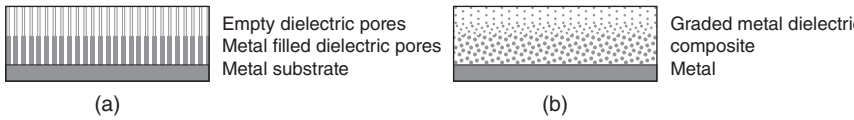

15.6 Schematic designs of two different metal-dielectric solar selective coatings.

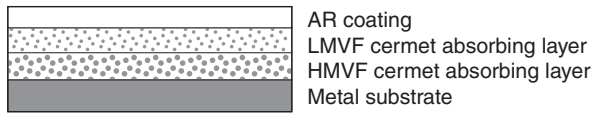

15.7 Schematic design of double-cermet film structure [6].

metal-dielectric concept offers a high degree of flexibility, and the solar selectivity can be optimized by proper choice of constituents, coating thickness, particle concentration, size, shape, and orientation. The solar absorptance can be boosted with a suitable choice of substrates and AR layers, which can also provide protection (e.g., from thermal oxidative degradation). A variety of techniques, such as electroplating, anodization, inorganic pigmentation of anodized aluminum, CVD, and co-deposition of metal and insulator materials by PVD, can produce the composite coatings.

In cermets, solar absorptance is mainly determined by the response of the absorbing particles. There is a shift of the absorption and scattering cutoffs to larger wavelengths when the particle radius, r, increases. This effect is accompanied by a reduction in the scattering and absorption efficiencies roughly proportional to r^{-1} [16].

In a graded cermet (Fig. 15.6(b)), the reflectance from the cermet is reduced by gradually increasing the metal volume fraction, hence the refractive index, as a function of depth from the surface to the base of the film. A double-cermet film structure has been developed similarly increasing the absorption of a homogeneous cermet layer like the graded cermets [17]. Solar radiation is effectively absorbed internally and by phase interference in double-cermet solar coatings.

Further, it is easier to deposit the double-cermet selective coating than graded-cermet layer selective surfaces. The typical double-cermet layer film structure from surface to substrate consists of the following (Fig. 15.7): an AR layer that enhances solar absorption; an absorbing layer composed of two homogeneous cermet layers, a low-metal-volume fraction (LMVF) cermet layer on a high-metal-volume fraction (HMVF) cermet layer; and a metallic infrared reflector layer to reduce substrate emittance [17]. High selectivity can be achieved with these absorber types. Typical values are $\alpha = 95\%$ and $\varepsilon(100^{\circ}C) = 5\%$ [6].

15.3.6 Selectively solar-transmitting coating on a blackbody-like absorber

A selectively solar-transmitting coating on a blackbody-like absorber is the last concept. Here the low-emitting surface is the top layer, which transmits radiation in a wavelength selective manner. This solar-transmitting coating can be a highly doped semiconductor (e.g., SnO_2:F, SnO_2:Sb, In_2SO_3:Sn, and ZnO:Al) over an absorber with a proven long-term durability. Some low-temperature flat-plate collectors have used black enamel as the absorber material [13]. Highly doped semiconductors may be useful with high-temperature black absorber materials. The selectivity, however, is limited for this type of coating.

15.3.7 Other considerations

Several physical principles and a wide range of different production methods can be used to produce solar selective absorbers. The selectivity and corresponding optical properties are very important for assessing the relevance for CSP applications. However, other factors like stability and cost of production must certainly be considered. Multilayer cermet absorber coatings seem to be the most flexible and selective class of high temperature absorber coatings used up to now. Although intrinsic properties of the coatings (materials chosen, number of barrier layers and contact layers, thicknesses and number of different layers as well as gradients) are important for the optical properties and the stability of a material, other factors add to that. The roughness and purity of the substrate surface, the substrate material and phase transitions have large impacts on the practical applicability of an absorber coating type. Production processes have to be stable and controlled in order to guarantee the homogeneous long-term performance of selective absorbers at elevated temperatures. As a consequence, good laboratory results cannot automatically be transformed into good products. Nevertheless, laboratory research and numerical optimization and modelling of absorber coatings can stimulate development. A large number of historical approaches for selective absorbers in the medium temperature (150–250°C) and high temperature range (>250°C) have been reviewed [6]. Tables 15.2 and 15.3 give an overview of these findings.[2]

[2] Note: some minor flaws exist especially when specifying the substrate material. For example, the absorber coating for the Solel receiver has not been produced on Ni or Al, but using a Mo-IR-mirror and a stainless steel tube as substrate. TurboSun had no copper tubes as substrate but used glass tubes. The PT-Al_2O_3 coating which is stable in air has not been produced on copper, but on a PT-IR-mirror on stainless steel or glass. Another approach was on Mo- and W-IR-mirror deposited on highly alloyed steels. Nevertheless the tables give a very good overview on the multitude of possible absorber coating approaches.

Table 15.2 Mid-temperature selective surfaces (from [6])

Rank	Material	Substrate	Fabrication	Absorptance	Emittance ε (100°C)	Stability (°C) vacuum	Stability (°C) air	Commercial product
2	TSSS[a]	Al	Paint	0.92	<0.015		<135	Solariselect
2	PbS	Al	Evaporation Pyrolysis	0.93–0.99	0.21–0.10		200	
2	$NiCrO_x$	SS[b] Cu/Polyamide	Sputtering	0.8 0.92–0.93	0.14 0.06		<200 <200	
2	Colored SS	SS	Chemical conv.	0.62–0.93	0.1		<200	SEL, INCO
	Black nickel							
2	NiS-ZnS	Ni coated steel	Electrodeposition	0.88–0.96	0.03–0.10		<200	Maxorb
3	Ni-Sn	Cu	Electrodeposition/ Sol-gel	0.92–0.98	0.08–0.25		300	Black Crystal
	Graphitic films							
3	a-C:H/Cr	Cu	MF-pulsed	0.92	0.025		250	
	a-C:H	Al	PVD/PECVD	0.876	0.061		250	
3	Ge *in silicon* Si *binder* PbS	Cu or SS	Paint	0.91 0.83 0.96	0.7 0.7 0.7		300	
3	Ag dielectric	Al	Biomimetic sol-gel				300	
3	*Black copper* $BlCu\text{-}Cu_2O:Cu$	Cu	Electrodeposition	0.97–0.98	0.02	370	250	
3	*Black chrome* $Cr\text{-}Cr_2O_3$	Ni-Cu Cu steel	Electrodeposition	0.97	0.09	400	350	MIT ChromeCoat
3	$Mo/\ Cr_2O_3$			0.95	<0.30		425	Energie Solaire
3	TiN_xO_y	Cu	ARE	0.92	0.06	400		Thermomax
2	$CuFeMnO_4$/silica	Glass,Si	Sol-gel	0.6	~0.29–0.39			
1	Cr,Fe,Mo,SS,Ta Ti,W silicides	Bulk Cu Sputtered Cu	DC reactive Sputtering	0.76–0.82 0.81–0.86	0.02–0.3		400 250	
1	Cr,Fe,Mo,SS,Ta, Ti, W carbides	Bulk Cu Sputtered Cu	DC reactive Sputtering	0.76–0.81 0.81–0.86	0.02 0.035–0.06		400 250	
3	$Ni\text{-}NiO_x$	Al	Reactive sputtering	0.096	0.10		300	Sunstrip
3	Ni pigmented Al_2O_3	Al	Anodization	0.85–0.97	0.08–0.21		300–400	Tekno Term Energi Showa

Rank = should material be investigated for CSP applications 1 = Yes, 2 = No, 3 = Maybe
[a] TSSS = thickness-sensitive spectrally selective; [b] SS = stainless steel.

Table 15.3 High-temperature selective surfaces (from [6])

Rank	Material	Substrate	Fabrication	Absorptance	Emittance ε (100°C)	Stability(°C) vacuum	Stability (°C) air	Commercial product
2	Ni-Al_2O_3/SiO_2AR	Mo-Ni-SS	RF sputtering	0.94	0.07	500	350–400	
2	Co-Al_2O_3			0.94	0.04			
3	Mo-Al_2O_3	NI or Al	RF sputtering	0.96	0.16 (350)	350–500		Solel
1	W-Al_2O_3	Steel	RF sputtering	0.97–0.98	0.1–0.07 (400)			Solel
	W-Al_2O_3		CVD	0.85		500		[20]
1	Pt-Al_2O_3	PT SS/glass	RF sputtering		0.04		600	[15, 21] [22]
1	Al_2O_3-Pt-Al_2O_3	Mo/W alloy		0.90–0.98	0.08		600	
	Double					500		
1	Mo-Al_2O_3	Cu	DC-sputtering	0.96	0.06 (350)	350–500		TurboSun (glass)
2	SS-AlN	50		0.95	0.10 (350)	500		
3	Mo-AlN			0.92–0.94	0.08–0.10 (350)	500		
1	W-AlN							
	Quasicrystals							
1	Multilayer	Cu,Si		0.90	0.025	500	400	
1	Cermet			0.86–0.92	0.031–0.05	550		
3	Si_3N_4/Si-Ge/Ag	SS, Si	CVD	0.890	0.0389 (300) 0.0545 (500)		650 (He)	
1	Ni:SiO_2 Cr:SiO	Al, Cu	Reactive DC sputtering	0.90–0.96	0.03–0.14		400–800 (Ar)	
3	Al-AlN_x-AlN	SS	Reactive DC	0.97	0.10	500		
2	CuO	Cu, SS	Electroplating	0.91	0.18		>400	
1	Ag/CuO/Rh_2O_3/CeO_2//	SS	Organo-metallic spray	0.9	0.1	700	500	
1	CeO_2//Ag/Pt/CuO/Rh/ Rh_2O_3//Ag/Pt			0.86–0.88	0.1	775	550	

1	CeO_2//CuO/CoO/Mn_2O_3//Pt			0.88–0.92	0.06–0.12	700	500
	Black cobalt						400–650
1	Co_3O_4/Co			0.96–0.92	0.71–0.017		
3	Ni-Co_3O_4/Co			0.95	0.10		
	Black moly		CVD	0.94	0.30 (500)	500	350
1	Mo-MoO_2						
	Black tungsten		CVD	0.83	0.15	800	
1	W-WO_x						
1	Au/TiO_2	SS	Sol-gel	0.85	0.01(400)	>500	
3	Au/MgO	Mo/SS	RF sputtering	0.90–0.93	0.04–0.1		400
3	ZrC_xN	Al		0.85	0.074 (325)	600	125
3	Al_2O_3/ZrC_xN_y/Ag			0.91	0.05 (325)	700	175
1	ZrO_x/ZrC_x/Zr	SS		0.90	0.05 (20)	700	
3	TiN	Cu,Al	DC reactive sputtering	0.80	0.14–0.40		500
1	$Ti_{1-x}Al_xN$						750–900
3	M_bO_c+$M'Fe_2O_4$	Ni-Mo alloy	Painting Arc plasma	>0.90	>0.45		700 1060
3	VB_2, NB_2, TaB_2, TiB_2,ZrB_2,LaB_6, WSi_2,$TiSi_2$	Glass	DC-reactive sputtering	0.99	0.95–0.97	2300–3040 (MP)	
1	Si_3N_4 AR-ZrB_2	ZrB_2	CVD	0.88–0.93	0.08 to 0.10		500
3	Masterbeads® paint			0.93			>1000
2	C-Textured Cu	Cu		0.9	0.04(20)	400	
2	Textured Ni	Ni		0.92 ± 0.2	0.09 ± 0.02		>300
1	Textured SS			0.93 ± 0.02	0.22 ± 0.02	>440	
3	Textured Cr	SS		0.80–0.90	0.10–0.30		>500
1	W whiskers	Cr		0.98	>0.26	550	
1	Mo, Rh, Pt, W, HfC, Au						>600
1	NiO_x, CoO_x						800

Also promising results with very good stability in vacuum and high optical efficiency for temperatures up to 500°C have been reported for cermets of tungsten W and molybdenum Mo in Al_2O_3, in combination with an aluminium Al or copper IR-mirror and an AR layer of AlN on glass by Zhang [18] and Zhang and Shen [19].

These tables give a very good overview of the multitude of possible absorber coating approaches. However, stability, as quoted by the research papers used as the basis for these tables, does not necessarily mean long-term stability. Different concepts of 'stability' have been used, which makes the temperatures quoted for stability indicative rather than directly comparable.

15.4 Degradation and lifetime

15.4.1 Degradation processes

Absorber coatings of the various sorts that have been discussed are precisely formulated to achieve the optical properties that are desired. They must operate at elevated temperatures, subject to temperature fluctuations and need to achieve long lifetimes to be practically useful. Surface temperatures experienced during operation which exceed the production temperatures of the absorber systems may lead to structural reordering within the materials, diffusion and redox reactions. The optical properties will usually change as a consequence. High temperatures above 400°C pose a special challenge, because kinetics for most processes are much faster at higher temperatures. A short overview of degradation processes is given here based on reference [1].

Diffusion processes

Principally there are different kinds of diffusion processes. Diffusion of atoms along interstitial lattice sites or lattice vacancies plays a minor role if the material in question exhibits lattice disorder like grain boundaries or dislocations. The diffusion along these defects is several orders of magnitude faster and is also called 'short circuit diffusion' [23]. Sputtered layers may also have a high porosity. The diffusion of molecules, for example of oxygen from air, may take place.

Diffusion processes may take place between substrate and absorber systems or within the individual layers. In cermet layers, even the diffusion within the cermet itself changes the gradient of constituents and therefore the optical properties of the system.

In order to prevent or at least substantially reduce the diffusion of atoms, e.g. from the substrate (Fe, C) into the IR-mirror layers, barrier layers can be prepared. Oxides as such, for example, Al_2O_3 have been used for these

layers. High density of the barrier layer and continuous layer formation is important. These layers have to cope also with thermal expansion and stresses of the substrates because cracks will destroy the barrier functionality. A different approach is taking a thick IR-mirror metal layer as barrier.

Oxidation

The oxygen in air is obviously a threat for degradation due to oxidation in high temperature absorbers. Metallic layers of the IR-mirror and the metallic particles in the cermet layer are subject to oxidation. Barrier layers between the surrounding air and the absorber system have to prevent oxygen diffusion without destroying the desired optical properties of the absorber system.

Redox reactions

Redox reactions are important in cermet layers even in vacuum. During the production of a reactively sputtered cermet Me_1/Me_2-oxide, e.g. a Mo/Al_2O_3-cermet, the metallic constituent Me_1 (Mo) usually is also partially oxidized whereas the second metal Me_2 (Al) is not completely oxidized. During a tempering process, redox reactions drive the system towards chemical equilibrium, i.e. the oxidized Mo will be reduced and give the oxygen to the metallic aluminium. The size and shape of metallic particles in a cermet might also change. All these processes provoke strong spectral changes in the reflection spectrum and hence a change in solar absorptance and thermal emittance.

Thermo-mechanical stresses

The temperature differences occurring within the high temperature receivers, on the one hand, and also even for homogeneous temperature fields, produce unequal thermal expansion coefficients of adjacent layers which may lead to thermally induced stresses on the individual layers. This in turn may induce flaking or chipping off of layers. Cracks develop and barrier layers are destroyed locally. The problems may be ameliorated by introducing special adhesion layers between problematic materials.

Other environmental stresses

Apart from the mechanisms described above, of course, a number of other environmental stresses may deteriorate the optical properties of an absorber system reversibly or irreversibly. For instance, for non-hermetically sealed receivers open to air, humidity and even dust, a number of reactions may occur. For example, dust on a hot receiver may fasten on the surface

irreversibly. Condensation of humidity during cold periods (night-time) in combination with gases like sulphur or carbon oxide may produce acids which attack the surface layers of the absorber. Sulphur itself can be a problem, e.g. for silver IR-mirrors, if the oxide is reduced. If near to an ocean, salt may react aggressively with both steel and absorber system.

Although accelerated testing [4] may try to incorporate all effects conceivable, there will always be a risk that the exposure in the real environment will have additional effects. The conditions at a specific location may be different from what is expected in a standard atmosphere, and also interactions between different mechanisms may not be the same as in a test. Nevertheless it is important to develop methods for estimating long-term stability and predicting service lifetime as far as possible to reduce the risks for degradation and failure.

15.4.2 Long-term stability and lifetime

In addition to the initial efficiency, long-term stability is an important requirement for absorber coatings. Complex designs of absorber coating systems are frequently susceptible to changes with temperature exposure. However, these changes may even help to improve the performance of a freshly produced absorber system. Tempering processes may improve the optical properties, but should stop after a short period of time. Slowly continuous changes, on the other hand, are likely to lead to long-term performance reduction and have to be quantified and eliminated.

In order to quantify 'degradation' of an absorber system, a so-called performance criterion (PC) is required. For flat-plate collector selective absorber testing (i.e., non-concentrating, 1–2X sunlight intensity) such a criterion has been developed [4]. The PC describes the influence in the change of solar absorption ($\Delta\alpha_s$) and emittance ($\Delta\varepsilon$) on the solar fraction:

$$\mathrm{PC} = -\Delta\alpha_S + 0.25 \cdot \Delta\varepsilon \leq 0.05 \qquad [15.6]$$

It provides a single quantifiable parameter for maximum acceptable degradation. Service lifetime testing for this criterion is performed by exposing the absorber coatings of flat-plate collectors for 200 h at 250°C. If the material survives, it is then exposed for 75 h at 300°C, followed by 600 h at 40°C/95% relative humidity (RH), then 85 h at 60°C/95%RH [4]. After exposure testing, the emittance is typically measured at 100°C.

No similar criterion has been developed up to now for testing the service lifetime of high temperature absorbers for CSP applications. It is obvious that for concentrating collectors a change in the absorptance is even more important than for non-concentrating collectors. On the other hand, emittance at higher temperatures is more important due to the Stefan–Boltzmann law. Therefore, taking C as the concentration factor and f as the

factor describing the higher operating temperatures compared to flat-plate hot water collectors, we would suggest as a first approach to a PC for concentrating collectors:

$$\begin{aligned} \mathrm{PC} &= -\Delta\alpha_S + \frac{0.25\cdot f}{C}\cdot\Delta\varepsilon \le 0.05 \\ f &= \frac{\sigma\cdot\left(T_{op,CSP}^4 - T_{amb}^4\right)}{\sigma\cdot\left(T_{op,FPC}^4 - T_{amb}^4\right)} \\ T_{op,CSP} &= 273.2 + 340\,K \\ T_{op,FPC} &= 273.2 + 60\,K \\ T_{amb} &= 273.2 + 25\,K \end{aligned} \qquad [15.7]$$

where T_{amb} is ambient temperature, T_{op} is operating temperature of the solar system, and the subscripts FPC and CSP stand for flat-plate collector and concentrating collector for solar thermal power, respectively.

Thermal stability is sometimes based on the thermal properties of the individual materials or the processing temperature parameters. Durability or thermal stability is typically tested by heating the selective coating, typically in a vacuum oven or in air at elevated temperatures, for a relatively short duration (thousands of hours) compared to the desired lifetime (25–30 years). This procedure of accelerated indoor testing may pose problems if cascaded processes and interactions during exposure occur [6]. Degradation of high temperature absorbers usually changes the reflectance spectrum significantly and causes increasing emittance; therefore, optical properties are sensitive indicators for monitoring degradation with exposure.

15.5 Examples of receivers for linearly concentrating collectors

15.5.1 Vacuum tube receivers for parabolic trough power stations

At the moment there are two main commercial providers of vacuum receivers for parabolic trough power stations: Schott Solar CSP GmbH (Germany) [24] and Siemens (Germany), formerly Solel Solar Systems (Israel) [25]. The constructions of their receiver units are shown in Fig. 15.8.

Both absorber coatings are stable in vacuum up to a maximum operating temperature of 400°C. The absorber tube is covered by a borosilicate glass tube to keep the vacuum and to reduce the heat losses. A publication by Lanxner and Elgat of the Siemens-Solel predecessor LUZ from 1990 [20] describes the production of the absorber tubes at that time. Polished stainless steel tubes (mean roughness index $R_a < 0.2$ μm) are heated in vacuum for 10 minutes at a temperature of 600°C. Then the coating system consist-

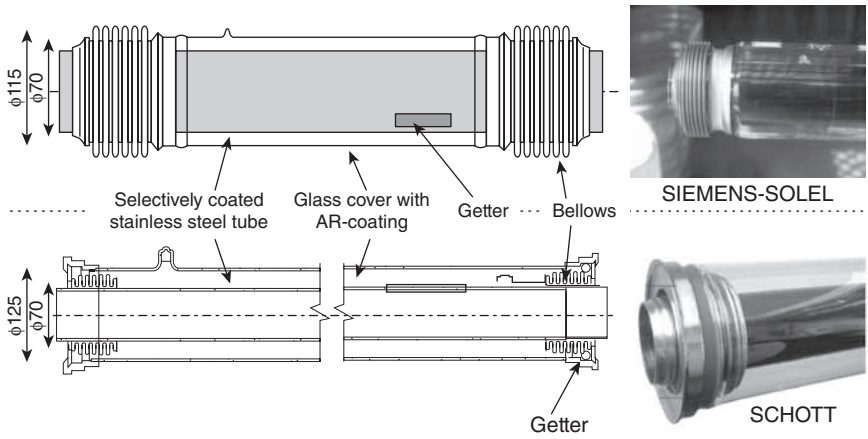

15.8 Vacuum tube receivers.

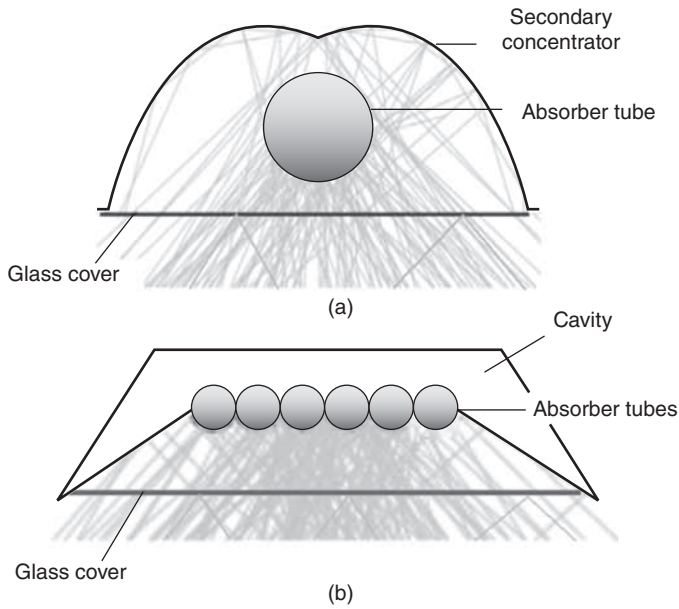

15.9 Receiver design for linear Fresnel (a) single tube receiver (b) multi-tube cavity receiver.

ing of Al_2O_3 diffusion barrier, the Mo-IR-mirror, the Mo/Al_2O_3-cermet and the SiO_2 AR layer is deposited on the tube. While the absorbers can withstand a month at elevated temperature of 600°C in vacuum, the intrusion of air leads to degradation. The absorber has a quoted performance of $\alpha = 96\%$ and $\varepsilon(350°C) = 17\%$. Further development and optimization led to an increased absorptivity of 97% and lower emittance of 10% according

to the manufacturer (400°C) [26]. Measurements by NREL on two samples found optical properties $\alpha = 94–95\%$ and $\varepsilon(350°C) = 13–15\%$ earlier [27]. Since then, improvements have led to the better result.

The company Schott CSP GmbH also has improved their first vacuum receiver PTR-70 (2004), for which they guaranteed $\alpha = 95\%$ in combination with $\varepsilon(380°C) = 14\%$, and have offered the improved product in the market since 2008. The coating according to [27] is similar to the LUZ coating, but not identical. Recent measurements by NREL [28] show a much lower heat loss. The emittance derived for 380°C is close to 9%. Similarly for the UVAC receiver from Siemens, the emittance has been reduced to below 9% (for 400°C) [29].

Of the many different approaches for absorber systems from the literature, we describe two interesting approaches below.

Based on a patent [30] published in 2005, ENEA developed a DC (direct current) sputtered absorber system of a 500 nm thick W or ZrN IR-mirror, a cermet of TiN_x, ZrN_x or HfN_x in AlN. The AR layer is made from AlN or Al_2O_3. The absorber coating is stable in vacuum up to 580°C and reaches $\alpha > 95\%$ and $\varepsilon(580°C) < 12\%$. It is specially developed and used at the moment for receivers with molten salt as a heat transfer fluid (HTF), because with this HTF operating temperatures up to 560°C are feasible in contrast to the HTF thermo-oil. The company Archimede Solar produces a vacuum receiver for molten salt technology under licence from ENEA for temperatures up to 550°C. The values quoted in the product description are $\alpha = 95\%$ in combination with $\varepsilon(400°C) = 10\%$ and $\varepsilon(580°C) = 14\%$ [31].

15.5.2 Air-stable receivers

For the application in air, at the moment no commercial products for absorber tube for use above 300°C operating temperature are available (see Fig. 15.9). The well-known black chrome degrades at temperatures above 350°C [6]. Another commercial steel absorber is produced by the Chinese company Himin Solar Energy, which quotes emissivities of $\varepsilon(300°C) = 10\%$ [2].

There are many concepts for absorbers for temperatures above 350°C on a laboratory scale. One of the most stable material candidates for absorber systems is platinum (Pt). Many authors describe it as a stable IR-mirror and, embedded in Al_2O_3, it forms stable cermet [15], [22], [32]. The most extensive investigations describe the influence of different process parameters on the stability of the system Pt-IR-mirror, Pt/Al_2O_3-cermet and Al_2O_3 AR-layer on glass and on stainless steel with an Al_2O_3 diffusion barrier. Sputtering with RF (radio frequency) produces better results than DC. Also sputtering with higher substrate temperatures seems to be beneficial for stability and low emittance. However, platinum is an extremely expensive material, and secondly RF sputtering is slow, which makes a commercial

production process expensive. Also the substrate heating requires longer production times and additional investment costs. Highly alloyed substrates are necessary which are too expensive for receiver tubes.

Therefore less expensive materials and processes are still required. Substrates used should be only stainless steel tubes and not extremely expensive materials. The suitability of many other materials Cr, Mo, Ni, and Ta has therefore been investigated as IR-mirrors. One problem is the relatively fast oxidation in air for these materials, although the embedding in the cermet layer helps. Silver (Ag) is an excellent IR-mirror and as a noble metal has a relatively low tendency for oxidation. The main degradation mechanism is the formation of Ag_2S through reaction with H_2S in air [33]. Also the thin layers tend to agglomerate at temperatures above 200°C [34]. Therefore protection and adhesion layers are needed to stabilize Ag in the system. Using that approach absorber coatings on stainless steel tubes with $\alpha > 95\%$ and $\varepsilon(450°C) < 12\%$ could be produced but they do not have long-term stability for testing temperatures of 500°C [1]. However, based on the emissivity of polished stainless steel, a CrOx cermet in combination with a SiOx-AR layer was stable for 3,000 hours at 500°C. The optical properties reached for such a system were $\alpha = 94\%$ and $\varepsilon(450°C) = 18\%$ [1].

15.6 Conclusion

As efficiencies of the solar thermal power stations are intimately connected to high operating temperatures, research and development will further try to raise the limits of temperatures. For linearly concentrating collectors, molten salt receivers are a promising option for operating temperatures up to 550°C. Therefore further efforts will be undertaken in order to produce commercially viable receiver systems. It is important to keep in mind both the major constituents of the absorber tube, the steel substrate and the absorber coating. Both components have to cope with high temperatures, and of course also with other stresses. Corrosive interaction between molten salts and steel, suitability for treatment before coating and of course cost are major issues in the selection of substrates.

On the other hand, there seems to be a divergence of collector specifications. Collectors for very high temperatures are one trend, collectors with reduced temperature, pressure or performance specifications are another trend. The dichotomy of two approaches in solar thermal energy systems is also applicable in solar thermal power: low cost solutions with reduced efficiencies compete against highly efficient high cost systems. Low temperatures in the operation reduces the efficiency of the power plant; however, it might reduce the problems for selecting cost-effective steel substrates, reduce material costs as a consequence and enhance the

long-term stability in spite of a cheaper product. Therefore when the market is expanding and booming, probably more and more targeted commercial receiver systems will emerge.

15.7 References

[1] Hildebrandt, C., Hochtemperaturstabile Absorberschichten für linear konzentrierende solarthermische Kraftwerke, Dissertation, Universität Stuttgart (2009).

[2] http://www.himinsun.com/6-coated-steel.html (accessed 17.1.2011).

[3] Brunotte, A., Lazarov, M. and Sizmann, R., 'Calorimetric measurements of the total hemispherical emittance of selective surfaces at high temperatures', in A. Hugot-Le Goff, C. G. Granqvist, and C. M. Lampert (eds), *Proc. SPIE*, 1727, 149–160 (1992).

[4] Brunold, S., Frei, U., Carlsson, B., Möller, K. and Köhl, M., 'Accelerated life testing of solar absorber coatings: testing procedure and results', *Solar Energy*, 68, 4, 313–323 (2000).

[5] ASTM G173-03(2008) Standard Tables for Reference Solar Spectral Irradiances: Direct Normal and Hemispherical on 37° Tilted Surface.

[6] Kennedy, C. E., Review of Mid-to High-Temperature Solar Selective Absorber Materials, Technical Report NREL/TP-520–31267, National Renewable Energy Laboratory, Colorado, USA (2002).

[7] Agnihotri, O. P. and Gupta, B. K., *Solar Selective Surfaces*, Wiley-Interscience, New York, (1981).

[8] Seraphin, B. O., in B. O. Seraphin (ed.), *Topics in Applied Physics, Vol. 31*, Springer-Verlag, Berlin (1979), pp. 5–56.

[9] Seraphin, B. O. and Meinel, A. B., in B. O. Seraphin (ed.), *Optical Properties of Solids: New Developments* (North Holland, Amsterdam (1976), pp. 929–971.

[10] Randich, E. and Allred, D. D., 'Chemical vapor-deposited ZrB2 as a selective solar absorber', *Thin Solid Films*, 83, 393–398 (1981); Randich, E. and Pettit, R. B., 'Solar selective properties and high temperature stability of CVD ZrB2', *Solar Energy Mater.*, 5, 425–435 (1981).

[11] Cuomo, J. J., Ziegler, J. F. and Woodall, J. M., 'A new concept for solar energy thermal conversion', *Appl. Phys. Letters*, 26, 10, 557–559 (1975).

[12] Zhao, S., Spectrally selective solar absorbing coatings prepared by dc magnetron sputtering, Dissertation, Universität Uppsala, Uppsala (2007).

[13] Granqvist, C. G. (ed.), *Materials Science for Solar Energy Conversion Systems*, Pergamon Press, Oxford (1991).

[14] Born, M. and Wolf, E., *Principles of Optics*, 6th edn., Pergamon, Oxford (1980).

[15] Thornton, J. A., Penfold, A. S. and Lamb, J. L., 'Sputter-deposited Al_2O_3/Mo/Al_2O_3 selective absorber coatings', *Thin Solid Films*, 72, 101–109 (1980).

[16] Arancibia-Bulnes, C. A., Estrada, C. A. and Ruiz-Suárez, J. C., 'Solar absorptance and thermal emittance of cermets with large particles', *J. Phys. D: Appl. Phys.*, 33, 2489 (2000).

[17] Zhang, Q.-C. and Mills, D. R., 'Very low-emittance solar selective surfaces using new film structures', *J. Appl. Phys.*, 72, (7), 3013 (1992); Zhang, Q.-C., Mills, D. R. and Monger, A., US Patent No. 5,523,132, 4 June 1996.

[18] Zhang, Q. C., 'Recent progress in high-temperature solar selective coatings', *Solar Energy Materials and Solar Cells*, 62, 63–74 (2000).
[19] Zhang, Q. C. and Shen, Y. G., 'High performance W-AlN cermet solar coatings designed by modelling calculations and deposited by DC magnetron sputtering', *Solar Energy Materials and Solar Cells*, 81, 25–37 (2004).
[20] Lanxner, M. and Elgat, Z., 'Solar selective absorber coating for high service temperatures, produced by plasma sputtering', *Proc. SPIE*, Vol. 1272, Optical Materials Technology for Energy Efficiency and Solar Energy Conversion IX (1990).
[21] Schön, J. H., Binder, G. and Bucher, E., 'Performance and stability of some new high-temperature selective absorber systems based on metal/dielectric multilayers', *Solar Energy Materials and Solar Cells*, 33, 403–416 (1994).
[22] Vien, T. K., Sella, C., Lafait, J. and Berthier, S., 'Pt-Al_2O_3 selective cermet coatings on superalloy substrates for photothermal conversion up to 600°C', *Thin Solid Films*, 126, 17–22 (1985).
[23] Heumann, T., *Diffusion in Metallen*, Springer, Berlin (1992).
[24] http://www.schottsolar.com/de/produkte/solarstromkraftwerke/schott-ptr-70-receiver (accessed 17.1.2011).
[25] http://www.siemens.com/press/en/pressrelease/?press=/en/pressrelease/2009/renewable_energy/ere200911017.htm (accessed 17.1.2011).
[26] SOLEL [online], http://www.solel.com/files/UVAC.pdf (accessed 17.01.2008).
[27] Kennedy, C. E. and Price, H., 'Progress in development of high-temperature solar-selective coating', *Proceedings of ISEC2005*, 2005 International Solar Energy Conference, Orlando, FL (2005).
[28] Burkholder, F. and Kutscher, C., Heat Loss Testing of Schott's 2008 PTR70 Parabolic Trough Receiver, Report NREL/TP-550-45633, May 2009.
[29] http://www.energy.siemens.com/co/en/power-generation/renewables/solar-power/concentrated-solar-power/receiver.htm#content=Technical Data (accessed 17.1.2011).
[30] Schutzrecht WO2005/121389 A1 (22.12.2005). ENEA – Ente per le nuove tecnologie, l'energia e l'ambiente. Pr.: RM2004A000279 (7.6.2004).
[31] http://www.archimedesolarenergy.com/receiver_tube.htm (accessed 17.1.2011).
[32] Sella, C., Bichri, A., Martin, J. C., Lafait, J., Driss-Khodja, K. and Berthier, S., 'Adjustable optical properties of coatings based on cermet thin films near the percolation threshold', *Physica A*, 157, 555–560 (1989).
[33] Graedel, T. E., 'Corrosion mechanisms for silver exposed to the atmosphere', *J. Electrochem. Soc.*, 139, 1963–1970 (1992).
[34] Hollingsworth Smith, P. and Gurev, H., 'Silicon dioxide as a high temperature stabilizer for silver films', *Thin Solid Films*, 45, 159–168 (1977).

16

Optimisation of concentrating solar power (CSP) plant designs through integrated techno-economic modelling

G. MORIN, Novatec Solar, Germany

Abstract: Simulation helps the understanding and prediction of real CSP plants in terms of economic, energetic and operational aspects. This chapter first reviews established approaches for simulation and design optimisation of CSP plants. Following this, a new multivariable optimisation approach is presented.

A deeper look into the interdependencies of solar field, storage and power block shows that mutual subsystem influences can be very strong and also indirect. It is important to consider such interdependencies, for example when an optimised solar field operation temperature is determined. Until now, iterative calculations using several programs are necessary to assess mutual influencing effects. Alternatively, the new integrated software approach, as presented here, can address this complexity through integral modelling and a powerful multi-variable optimisation algorithm. This approach is applied to a state-of-the-art parabolic trough plant using a two-tank molten salt storage. However, the approach and even most of the results are also applicable to other CSP systems.

Key words: simulation, optimisation, plant design, storage, parabolic trough, power block.

16.1 Introduction

Simulation is essential to support decisions related to investment in CSP plants and to design CSP plants because simulation helps the prediction of the economic, energetic and operation characteristics of a real plant installation. This chapter reviews established approaches to modelling and design optimisation for CSP plants. Specifically, a new method for design optimisation of solar thermal power plants is presented in Sections 16.3–16.6. This approach integrates the energetic and the economic simulation of an entire power plant on component level as well as a multi-parameter optimisation algorithm which allows optimisation of the relevant design parameters of the plant. To illustrate the method and the results that can be obtained, this approach is applied to a state-of-the-art parabolic trough plant using a two-tank molten salt storage. However, the approach and even most results are also applicable to other CSP systems.

16.2 State-of-the-art in simulation and design of concentrating solar power (CSP) plants

Today, different methodologies and software tools for simulating CSP plants are available, depending on the scope of the simulation. An overview of the different approaches is given in the following sections.

16.2.1 Energy yield calculations

The most important difference between the energy yield calculation of conventional power stations and solar thermal power plants is the unsteady solar resource. Even if no clouds reduce the amount of available direct solar irradiance, the sun position (relative to the collector orientation) influences the collector efficiency and hence the thermal output of the collector field. Therefore, it is not sufficient to calculate a mean annual energy yield based on an assumed amount of annual full load hours, as is often done for conventional power stations.

For the energetic simulation of solar thermal power plants there are methods for performing short-term dynamic simulations with high time resolution (e.g., time-step one second). Such tools focus on understanding plant dynamics and developing control parameters of the collector and/or the power plant. Examples of such dynamic simulation tools are the program library *DissDyn* of the German Aerospace Centre (DLR) or *ColSim* by Fraunhofer ISE. A comparative description of both programs for use in direct steam generating line-focusing collectors is given in Hirsch *et al.* (2007). The flow in the tube is sub-divided in small control units (tube segments) to model transient flow effects appropriately. Thereby, dynamic effects such as temporarily differing mass flows at collector inlet and outlet due to differences in density can be simulated which helps to develop suitable control strategies. In order to model such effects in sufficient detail, high spatial and time resolution is required which results in significant calculation time which is often higher than real time (i.e., simulating one hour of plant operation takes more than one hour to simulate).

Therefore, on the other hand, the calculation of the energy yield of representative periods of one year or several years use 'pseudo steady-state' calculations that are based on hourly discretisation with simplified consideration of dynamic effects. Today, there are basically two philosophies for implementing this:

1. The approach from CSP research institutes is based on rather detailed simulation of the solar block – solar field and storage (if used) – and characteristic curves to describe the power block for the conversion ratios of thermal to electric power. Examples are the *System Advisor*

Model (*SAM*) (System Advisor Model, 2009) from the National Renewable Energy Laboratory (NREL), *Greenius* (Greenius Free Software, 2010) from the DLR and HTW Berlin and a version of *ColSim* which simplifies the dynamics (Mertins, 2008), from Fraunhofer ISE. Initially, *ColSim* was developed to simulate the dynamic behaviour of solar thermal systems and to develop control strategies for them (Wittwer, 1999). From 2002 on, the functionality of *ColSim* was extended to simulate solar thermal power plants energetically, but based on reduced complex consideration of dynamic effects (no plug flow consideration) (Mertins, 2008; Morin, 2011).

2. In the last two years, software providers for modelling conventional thermal power stations have also started expanding their simulating capabilities towards CSP plants; examples are *Thermoflex* (Griffin *et al.*, 2009), *Ebsilon* (Pawellek *et al.*, 2009) and *IPSEpro* (IPSEpro, 2010). According to the current state of the art, all these tools have two things in common: due to their historic background they offer detailed power block models, and the fact that they calculate the entire thermal cycle of the CSP plant for each time step. Due to the thermodynamic calculations which imply the solution of complex equation systems, these tools are rather slow in computation time. One annual yield calculation (hourly resolution) on a state-of-the-art PC lasts in the order of hours, whereas the above-mentioned tools *SAM*, *Greenius*, and *ColSim* need only a few seconds.

A process towards international standardisation of energy yield calculations for CSP plants has started under the umbrella of IEA-SolarPACES. In March 2010, a workshop on modelling the annual performance of solar thermal power plants was held at NREL in the USA where different approaches were presented and a road-map towards comparative calculations, program validations and standardisation was initiated (Solar PACES, 2010).

Although the various tools have differences in the models used, all of them calculate the energy yield along the energy conversion chain: direct solar irradiation, optically absorbed solar power, thermal power, electric gross power, and electric net power.

16.2.2 Economic simulation

Some modelling approaches focus only on energetic simulation of the plant. Others also integrate an economic model. The economic models vary depending on the scope of the simulation. In most cases, the impact of technical variations can be evaluated by calculating specific energy production cost (levelised cost of energy; LCOE) (e.g. Mertins, 2008; Morin *et al.*,

2009). Other approaches integrate a complete cash flow analysis of a plant, including energy-political incentives like feed-in-tariffs or tax credits, time-dependent electricity sales prices and cost of capital (debt and equity financing) (e.g. System Advisor Model, 2009). Basically, any commercial actor in the solar thermal power market – be it project developer, general contractor for building the plant, plant operator or original equipment manufacturer – has their own economic model to evaluate financial feasibility and profitability of a project according to their respective business practice.

16.2.3 Design process for solar thermal power plants

Today, the design of CSP plants is determined by performing several subsequent calculations, usually applying multiple tools that model different technical sub-systems or plant economics. Using the tools that model some aspect or sub-system of the CSP plant, parameters of interest are varied and optimised by parameter studies. At the system level, the main parameters that are usually optimised with respect to techno-economic criteria are solar field size (cf. e.g. Dersch *et al.*, 2009; Morin *et al*, 2009; Montes *et al.*, 2009) and – where storage is used – storage size (Blair *et al.*, 2008).

The above-mentioned System Advisor Model (SAM) is one tool that incorporates both the energetic and the economic simulation of a CSP plant. SAM has greatly evolved over the past few years through generous funding by the US Department of Energy. SAM has probably become the most widely used CSP simulation tool (for plant yield and plant economics), not only by an increasing number of established CSP actors (e.g. engineering consultants and technology providers) but also by less technically oriented CSP actors such as project developers or actors in the financial sector. SAM offers an easy-to-use graphical user interface and a large variety of predefined technology settings for selection (and optional adaptation) by the user (see Fig. 16.1).

Depending on site and technology parameters, SAM calculates the hourly and annual energy yield of the plant based on hourly weather data. Beyond energetic data, SAM can also be used to evaluate projects economically based on levelised cost of electricity (LCOE) or a cash flow analysis. These economic performance criteria include investment cost, operation and maintenance (O&M) cost, the plant lifetime, debt and equity financing, electricity and fuel prices, fiscal and other parameters. A basic optimisation feature helps varying plant design parameters to search for parameter configurations which optimise an objective function such as LCOE.

One drawback of SAM is that power block efficiency calculations are performed based on static parametric power block equations which are not based on a physical power block model. Since power block integration

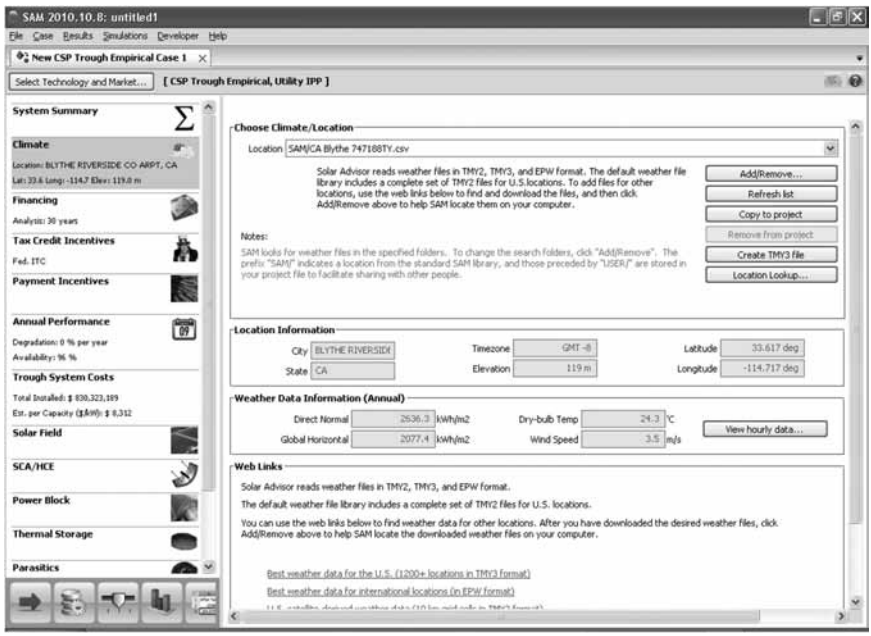

16.1 Screenshot of NREL's System Advisor Model for simulating CSP plants energetically and economically.

is a very project-specific issue (depending on plant size, availability of cooling water, power block integration concept of solar field, optional co-firing), the SAM default power block data needs to be critically revised and/or generated on a case-by-case basis using other simulation tools which are dedicated to power block simulation (e.g. *Thermoflex* or *Ebsilon*; see above).

The following sections present an approach to overcome the above-mentioned drawbacks of the existing tools such as cumbersome power block data generation in combination with slow power block simulation, and the difficulty of solving the multi-dimensional optimisation problem in designing CSP plants.

16.3 Multivariable optimisation of concentrating solar power (CSP) plants

As mentioned in Section 16.2, simulation and optimisation of plant designs today occurs using multiple tools and approaches. Designing CSP plants is a multivariable optimisation task because many design parameters can be (and should be) varied and optimised on a project-specific basis. But so far,

no method or software has been available that integrates the mutual effects of power block and solar block at system level. Hence the mutual interdependencies cannot be assessed easily.

An integrated techno-economical simulation and optimisation approach (including power block optimisation), which has not been available so far, has been developed by Morin (2011) and its main features are presented in the subsequent sections. This approach can help in quickly finding a well-designed project-specific plant concept. This helps project developers to quickly reach a good project design and project evaluation, e.g. for sales support. Thereby, person-months of concept engineering or – in case this is not feasible – sub-optimal (and expensive) plant designs can be avoided. Furthermore, such a tool can provide specifications for detailed component engineering at an early planning stage, based on a top-down approach in the sense that the overall plant design is optimised first.

Designing commercial power plants always aims at finding the most economic plant design under a given set of boundary conditions. Decision makers will look at economic performance numbers such as the Levelised cost of energy (LCOE) or the net present value (as previously introduced in Chapter 2).

Technical design determination for CSP plants is project-specific in the sense that a power plant has to be designed according to the specific requirements like solar site conditions, cooling water availability, nominal power and regulations for fossil co-firing. Depending on these conditions, the subsystems have to be designed and dimensioned, i.e. the solar field, power cycle, condenser, and, if used, heat storage and/or boiler for co-firing. All these factors can be considered as variables of a multi-parameter optimisation problem. These design parameters influence both cost and energy yield. A few examples are given to explain relevant interdependencies.

- For a given power block size, a larger solar field increases the amount of full load hours but also increases costs for investment as well as for operation and maintenance (O&M).
- Higher operating temperatures increase the efficiency of the thermal cycle but also raise heat losses in the solar field.
- Large heat transfer surfaces in the condenser will raise both efficiency and cost. However, the cost of the solar field will influence condenser design. Condensers in CSP plants are likely to be designed larger than condensers for conventional power plants of the same size because the solar heat is relatively expensive due to the high investment costs for the solar collector.

Today, an economic evaluation of a plant concept is usually done after a technical design concept has been developed. By carrying out these steps sequentially, the following problems arise:

- Optimising a plant layout with respect to economic decision criteria requires different tools – and maybe even different persons such as specialised engineers and financial experts. Iterative loops of design calculations and evaluations are time-consuming and expensive.
- It is likely that significant optimisation potential remains undetected, since there is a high number of mutually influencing variables.
- Experts in financial analysis and engineers with different specialties, such as solar field or power block, face the risk of pursuing their particulate aims without considering the overall cost performance of the plant.

The new package *OPTISIM* has recently been developed by this author and others (Morin, 2011; Richter, 2010; Gutjahr, 2009; Strelow, 2007). It aims to combine the advantages of the above-mentioned detailed power block modelling tools on the one hand with the fast annual yield calculations on the other, in order to perform design optimisations (see Figs 16.2 and 16.3). The *OPTISIM* package consists of *ColSim,* for the energetic simulation of the solar field and the thermal storage, of *Thermoflex* (in combination with the cost estimation feature *PEACE*) for simulating the power block energetically and economically and of other, mainly freely available, software tools for multi-parameter optimisation, database communication and economic plant modelling.

The new approach helps to fully explore the optimisation potential in the design phase of a plant, by considering all relevant site-specific, technical and economic factors simultaneously. This integrated methodology allows for calculation of the site- and design-specific electricity yield. In parallel, financial performance figures such as investment costs or LCOE are calculated.

This program is coupled with a suitable time-efficient optimisation algorithm in order to optimise simultaneously several design and operation parameters that have an influence on the energetic and economic system quality. The quality function – e.g. the LCOE – and the number of variable parameters used in a simultaneous optimisation can be chosen according to specific requirements. Examples of such parameters are solar field size, power block configuration, condenser size, condenser part load operation, solar field design parameters, as well as temperature and pressure levels.

The simulation and optimisation model is applicable to power plants based on parabolic trough and linear Fresnel collectors, solar-only and hybrid plants, plants with or without thermal storage, for direct steam generation or use of a heat transfer medium.

16.3.1 New methodology for integrated plant optimisation

Figure 16.2 shows the methodology that is used in this new approach. First of all, a set of technical and economic parameters has to be chosen to

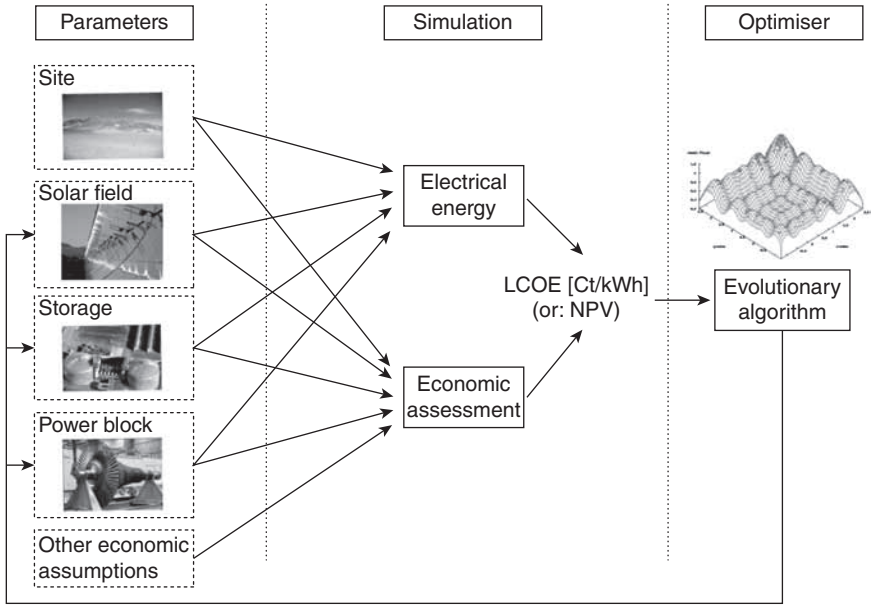

16.2 General structure of the techno-economic system simulation and optimisation model (illustration arrangement: author, single photos/graphs from top to bottom, left to right: Atacama desert, 2009; Relloso and Delgado, 2009; Siemens, 2010; Strelow, 2007).

simulate a power plant configuration. The parameters refer to power plant site, power block, collector, storage (if used) and other economic assumptions. Some of the parameters are fixed, independent of plant design, e.g. site and irradiation data. Variable parameters are optimised simultaneously by an evolutionary algorithm with respect to the objective function. The variables depend on the optimisation requirements; an example for a variable parameter is the solar field size. All these assumptions are used to calculate the annual energy yield for a representative time period (e.g. a year), based on hourly values. As opposed to conventional power plants, the permanently changing sun position and solar irradiation level require detailed annual energy yield calculations. Based on the economic assumptions, mean annual cost is calculated. Both technical and economic simulation results are combined in an objective function, e.g. the LCOE, which indicates the economic quality of the system layout.

A multi-parameter optimisation method is then used to optimise the relevant plant parameters with respect to the objective function. The optimiser solves steady-state operating parameters (e.g. live steam temperature or live steam pressure) but also the structure of the plant, e.g. different process designs with different number and arrangement of feedwater

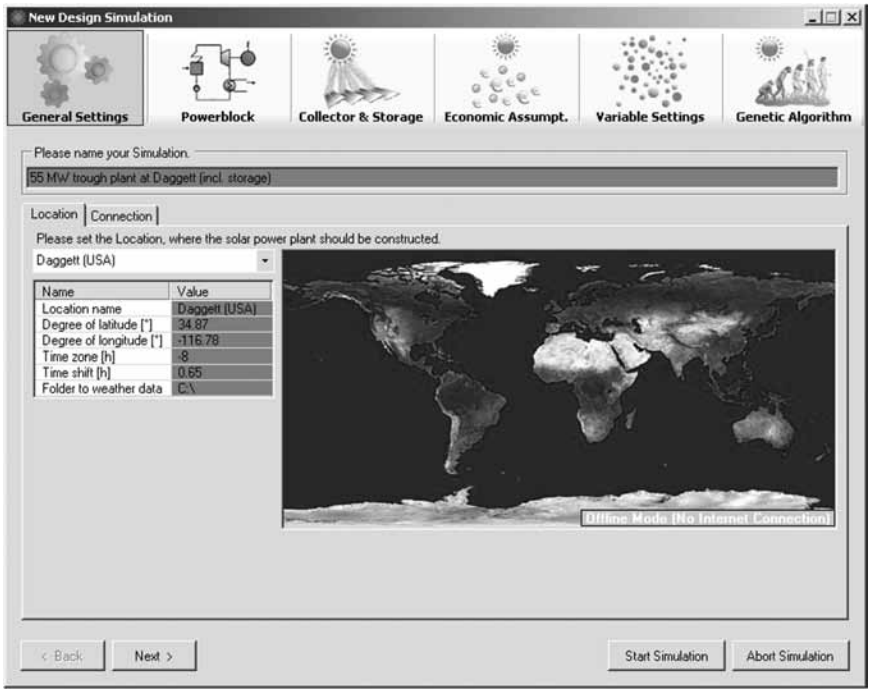

16.3 Graphical user interface for integrated simulation and optimisation software package *OPTISIM,* aiming at integral techno-economic design optimisation through fast but detailed power block modelling in combination with solar simulation and a multi-parameter optimiser.

heaters and reheat section (0, 1 or 2 reheat sections). A graphical user interface (GUI) has been developed (see Richter, 2010) to make the simulation settings and to observe the progress of the optimisation (see Fig. 16.3).

16.3.2 Overview of optimisation methods

There are several different multi-parameter methods available. In order to assess the applicability to CSP plant optimisation, we have to look more closely at our optimisation problem. The objective function, which in the example described below is the LCOE, has the following properties:

1. The LCOE function is non-linear.
   Example: the solar field size influences the LCOE non-linearly (Morin *et al.*, 2004).

2. The LCOE function is not continuously differentiable.
   Example: the solar field size is defined by an integer number of collector loops with a standard length. This results in a step function.
3. The LCOE function may have several local minima.
   Reason: It cannot be ruled out that the LCOE has several local optima due to the interactions of technical and economical models. When optimising several process structures at once (for which the *OPTISIM* software is principally developed; cf. Fig. 16.3 and Richter, 2010), the LCOE function has several local minima: e.g., a process with reheat (or even double reheat) will have higher optimal live steam pressures than processes without reheat.

Most methods for multi-parameter optimisation search for the nearest optimum, which is a local optimum but not necessarily a global optimum. Examples for such methods are the Simplex method, gradient methods, the Newton method or the widely used Levenberg-Marquart-Algorithm. Since such methods do not fulfil the above-mentioned third requirement (global optimisation), they were not further considered in the context of this work.

To date, there are no methods available that can ensure globally optimising an objective function with the properties mentioned above. But there are several methods which in principle address the aim of global optimisation, e.g. the multiplicator method of Lagrange (mathematical optimisation), and the stochastic methods: Monte Carlo methods and evolutionary algorithms. Evolutionary algorithms conduct a stochastic but systematic search for improvement analogous to biological evolution. A configuration is characterised by a so-called individual. Several individuals form a population which evolves from generation to generation. Evolutionary algorithms have the big advantage over global optimisation algorithms that the optimisation and the model are separate which results in a clear interface which is easy to handle (more easy to handle than mathematical methods which often aim at differentiation of the objective function). Further details on different optimisation algorithms can be found in Morin (2011).

In the context of the *OPTISIM* software, an evolutionary algorithm (*GAlib* from *MIT*, see Wall, 1996) was used for multi-parameter optimisation. The respective algorithm settings as used in Section 16.4 are described in detail in Morin (2011).

16.4 Case study definition: optimisation of a parabolic trough power plant with molten salt storage

In this section, the techno-economic modelling and optimisation of a typical case of commercial interest is presented: a 50 MW_{el} parabolic trough power

plant using thermal oil as heat transfer fluid, a two-tank molten salt thermal storage and a power block using an air-cooled condenser – for the Southern Californian site Daggett. Parabolic trough plants have been introduced in Chapter 7 and further discussion of molten salt energy storage can also be found in Chapter 11.

Section 16.4 describes the optimisation task defined by eight technical decision variables that are of interest when designing such a plant. Section 16.4.2 presents an overview of the models used to describe the solar thermal power plant technically and economically. The optimisation algorithm that is used to solve the multi-parameter optimisation problem for finding an optimal plant configuration is described in detail in Morin (2011). The optimisation results are described, validated and discussed in Section 16.5.2–16.6.9.

16.4.1 Definition of optimisation task

The case study examines a 50 MW_{el} parabolic trough power plant, similar to the *Andasol-1* power plant (see Fig. 16.4). The reference plant uses thermal oil as heat transfer fluid (HTF) and a molten salt thermal storage. As opposed to the *Andasol* plants, an air-cooled condenser and a Californian site in the Mojave Desert is assumed.

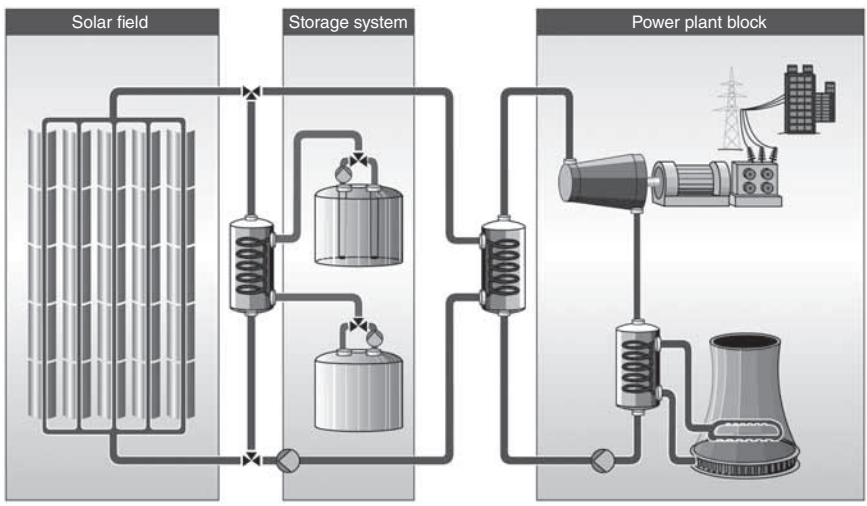

16.4 Sketch of the reference plant design based on the *Andasol-1* power plant in Andalucía, Spain. The thermal storage uses molten salt as storage medium which is stored in a cold tank and/or a hot tank (from Sven Moormann, Solar Millennium AG, pers. comm. 2009).

The Andasol-1 plant is located near Guadix in Southern Spain and uses a thermal storage utilising 28,500 tons of liquid salt equivalent to 7.5 hours of full load operation and a solar field with a total surface of 510,000 m^2. The power-block model, is based on the specifications of an operating 30 MW_{el} CSP plant in California (Lippke, 1995), but upscaled to 50 MW_{el}. The cycle has a live steam temperature of 370°C, a design condenser pressure of 0.08 bar, one reheat section and six feedwater heaters. An air-cooled condenser instead of a wet cooling condenser has been used and no fossil co-firing was considered. The overall reference case specifications are indicated in Table 16.3 in Section 16.5.1.

The reference design was then optimised for the site characteristics of Daggett in Southern California, USA (weather data retrieved from http://rredc.nrel.gov/solar/old_data/nsrdb/tmy2/). The main difference between the sites in Spain and California is the available solar irradiation. Whereas the *Andasol* site has an average direct normal irradiance (DNI) of 2,136 kWh/(m^2a) (Sven Moormann, Solar Millennium AG, pers. comm., 2009), Daggett has 2,791 kWh/(m^2a), hence roughly 30% more solar irradiation.

Starting from the reference design, the following eight variables are simultaneously optimised, with the indicated purpose:

1. Solar field size – A larger solar field increases the power block full load hours but also increases dumping of thermal energy due to capacity limitations of the power block and of the storage (so-called upper dumping).
2. Distance between parallel collector rows – Larger distance between parallel collector rows reduces mutual shading of collector rows and therefore improves optical efficiency. On the other hand, cost of land of header piping increases with larger distance.
3. Storage capacity – Larger storage increases the operating hours of the power block and limits hours with low-efficiency part-load operation of the power block. But higher investment is needed. The size of storage is defined in tons of liquid salt.
4. Upper solar field temperature – Higher temperature leads to higher power block efficiency; but also solar field efficiency drops due to increased heat loss.
5. Upper temperature difference in oil-to-water/steam heat exchangers – The Californian reference plant described in Lippke (1995) assumes a terminal temperature difference (TTD) of 20 K between hot oil and hot steam. Smaller TTD can increase the efficiency of the power block because the live steam temperature rises (or reduces solar field temperature and hence heat loss). However, an argument in favour of a large TTD in the heat exchanger is that at given live steam temperature,

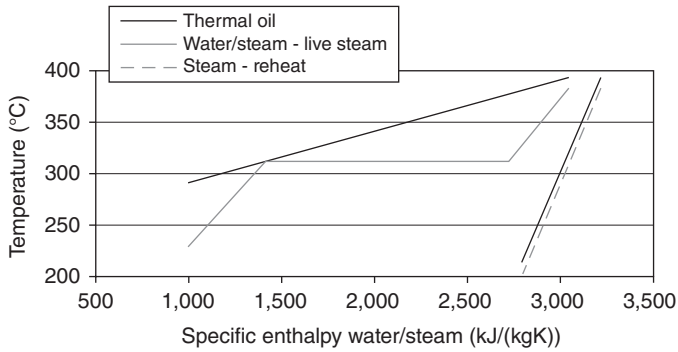

16.5 Assumed properties of the oil-to-water/steam heat exchangers in the T-Q diagram. The pinch point at beginning evaporation – temperature of oil minus temperature of boiling water – is assumed to be 2.9 K according to Lippke (1995).

a large TTD will lead to low solar field oil inlet temperature (cf. Fig. 16.5), and hence the HTF pumping power decreases.

6. Live steam pressure – For each process configuration, an efficiency-optimal live steam pressure relates to a given live steam temperature (examination of optimal pair of live steam temperature and pressure can be found in Morin, 2003). Additionally, too high pressures must be avoided because of condensation at the outlet of the high pressure turbine (danger of water droplet erosion).
7. Reheat pressure – With the herein assumed rule of equal temperature rise in all feedwater heaters, the parameter 'reheat pressure' determines not only the reheat pressure itself but implicitly serves for calculating the final feedwater temperature. Like the live steam pressure, the reheat pressure leads to a Carnotisation of the heat cycle because both variables lead to a rise in temperature at which the (solar) heat is transferred to the water steam cycle. One side restriction is that the reheat pressure level must be chosen such that the steam dryness requirements are met at the outlet of the high pressure steam turbine and of the low pressure turbine (danger of water droplet erosion in final turbine stages). Final feedwater temperature and reheat pressure have an influence on lower oil temperature and hence on pumping power parasitics and energetic storage capacity.
8. Size of air-cooled condenser – Larger cooling systems lead to higher power block efficiency but also to higher investment cost. Large air-cooled condensers have high auxiliary power consumption. The optimal condenser size in the sense of a trade-off between cost and performance is searched for.

16.4.2 Applied energetic and economic plant models

The integrated techno-economic design optimisation methodology can in principle be applied with any technical and economic models and assumptions. All models used in the calculations presented in this chapter allow for quantitative consideration of the effects described in Section 16.4.1 and are described in detail in Morin (2011).

Energetic plant model

The technical model of the plant describes the relevant energetic mechanisms in order to calculate the energy production of the plant under a set of side restrictions. The principle methodology is summarised as follows. The model used here is applicable for different time resolution steps but by default uses hourly resolution. For each hour of the year the following steps of calculation are performed.

Based on the calculated sun position and the available DNI data, the optical collector performance is calculated. After subtraction of heat loss and thermal inertia effects – when heating up (or cooling down) – the thermal energy, that the solar field can provide (potential) is calculated. First, the solar field performance is calculated surface-specifically, referring to the collector aperture. The total field performance is calculated by multiplying the surface-specific performance by the total solar field surface. The total solar field surface in m^2 is rounded to an integer value of collector loops which is the standardised collector module in a large solar field.

The HTF heated by the solar field is used to provide thermal energy to the power block or to load the storage, in case the power block already runs at full load. If the energy cannot be used within the plant, it may even be dumped by de-focusing mirrors, e.g. when storage is full and the power block already runs at full load. Then, the potential solar output is reduced. In principle, co-firing using fossil or biogenic fuels is possible (see Morin *et al.*, 2004; Lerchenmüller *et al.*, 2004; Bockamp *et al.*, 2003). In the calculations presented in this work, hybrid co-firing is not considered. The power block receives a thermal energy flow from the solar field and/or storage and converts it into electric energy at certain efficiency depending on the power block operation conditions. Storage is discharged when the solar field cannot supply nominal steam mass flow to the power block. By subtraction of the auxiliary power consumption needed to operate the components, the net power production is calculated.

The energy conversion chain for the calculation steps described is shown in Fig. 16.6 . Each of these instantaneous values can be integrated in order

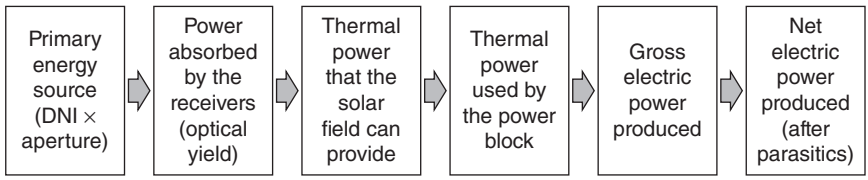

16.6 Energy conversion steps.

to obtain annual values of energy. Annual values are usually more suitable measures for design comparisons.

For the case study, the calculation steps described – except for the thermodynamic cycle calculation which is performed with *Thermoflex* (Thermoflow, 2009) – are performed in *ColSim*.

A special focus has been put on assessing effects of power block variables on the system. For this, each design was calculated thermodynamically. Beyond this, for each design, an off-design look-up table was calculated thermodynamically to assess the effect of thermal load, ambient temperature and live steam temperature on performance. Designs with high moisture content at the turbine outlet (endangering the turbine through droplet erosion) are given a high LCOE value in order to sort them out for the optimisation process.

A method for air-cooled condenser operation that maximises the net energy yield for each operation point was developed and applied. This is necessary to evaluate large condensers adequately because they realise favourably low condenser pressures but have, on the other hand, relatively high auxiliary power consumption: Especially at low load cases and low temperatures, cooling cell units need to be turned off to maximise net plant yield (instead of gross plant yield).

All models and assumptions used in the calculations presented here are described in detail in Morin (2011). The main technical assumptions are given in Table 16.1.

Economic plant model

Beyond the energetic model of a power plant as described above, the plant is also modelled economically because in many cases, performance and cost are inversely related. By calculating the levelised cost of electricity, a techno-economic figure of merit is available that considers the effect of any (modelled) technical modification on cost efficiency of the plant.

The LCOE is used as the techno-economic decision criterion according to which plant design is evaluated and optimised. A simplified version of LCOE calculation for a CSP plant with no fuel cost was given in Chapter 2 as:

Table 16.1 Main technical assumptions

General plant characteristics	Value/Magnitude
Site / DNI	Daggett, CA (USA) 2791 kWh/(m^{2}a)
Nominal gross electrical output	55.0 MW
Nominal gross efficiency of the power block	Depending on process parameters, 37.6 $MW_{el,gross}/MW_{th}$ for reference design in Fig. 16.3
Solar field properties	
Collector type	*Skal-ET*
Aperture width per collector	5.77 m
Optical efficiency relative to DNI on mirror aperture	75.0%
Average cleanliness/field availability	0.97%/99%
HTF temperature at inlet	Depending on live steam pressure, pinch point and HTF outlet temperature
Receiver thermal losses	New Schott-PTR70 (2008)
HTF pressure drop in solar field	Depending on solar field size and mass flow, according to Arias *et al.*, 2009
Specific thermal losses of field piping	Depending on SF temperature (10 W/m² at 340°C)
Auxiliary power consumption	
Auxiliary power consumption of solar field	Depending on HTF pressure drop and HTF mass flow (resp. HTF temperature rise)
Auxiliary power of storage	0.003 MW_{el}/MW_{th}
Auxiliary power consumption of power block	Depending on power block design (optimised ACC part load operation)

$$\mathrm{LCOE} = \frac{(F_R + O\&M_{fixed})C_0}{PF_c} + O\&M_{variable} \qquad [16.1]$$

where P is the nominal design point capacity of the system; F_c is the capacity factor (the annual average fraction of nominal capacity achievable), $O\&M$ are operation and maintenance costs (including insurance) that are split between those that are in proportion to generation (variable) and those that are fixed annual costs, C_o is the total initial capital cost, and $F_R \equiv \left(\frac{DR(1+DR)^n}{(1+DR)^n - 1} \right)$ is the capital recovery factor (sometimes called annualisation factor) with n being the plant's lifetime and DR the discount rate, i.e. the cost of capital. The discount rate reflects a weighted cost of capital for financing construction of the plant and operation of the plant with mixed debt and equity financing.

If O&M costs are expressed only as fixed costs, the LCOE expression can also be written in terms of the levelised annual cost (LAC), the sum of the

Table 16.2 Main economic assumptions

Investment cost	Value/Magnitude
Specific costs of the collector (incl. HTF and HTF heat exchanger)	260 €/$m^2_{aperture}$
Specific header piping cost	1000 €/m_{header}
Specific investment of storage system (incl. heat exchangers)	Depending on size; for reference design of 28.5 kt: 1009 €/t
Specific investment of power block	Depending on design; for the reference design: 800 €/$kW_{el,gross}$
Specific land costs (land and site preparation)	7 €/m^2
Surcharge for engineering, EPC, project management and risk	20%
Annual insurance costs relative to total invest	1%
Useful life and amortisation period	30 years
Interest rate	8%
Operation and maintenance	
Annual costs per employee	48,000 €/a
Total no. of employees excl. solar field	30
Specific no. of employees for solar field	0.030 × 1/1000 m^2
Specific water consumption	295 l/$MWh_{el,net}$
Annual replacement costs (as % of investment costs)	1%
Total plant availability	0.96

constant annuity of the investment costs (investment costs times annuity factor), the annual O&M (including insurance) costs:

$$\mathrm{LCOE} = \frac{(F_R + O\&M)C_0}{PF_c} = \frac{\mathrm{LAC}}{PF_c} \qquad [16.2]$$

The investment costs for the power block are derived from the cost estimates of Thermoflex's cost estimation module PEACE. The full economic model used to generate the results of this case study can be found in Morin (2011).

For this comparative technology assessment, this LCOE methodology provides enough detail. For more detailed analysis, tax might be considered, especially when tax credits are applicable and might lead to a shift in importance of invest and O&M cost. Other potential decision criteria, such as the internal rate of return (IRR) or the net present value (NPV), refer to cash flow and profitability of a project including the incoming payments from the sale of electricity. The main economic assumptions used are summarised in Table 16.2.

16.5 Case study results

16.5.1 Results of optimisation by varying solar block variables only (the classical approach)

As described above, different approaches for designing power plants exist with no development known so far that integrates all sub-system models in one tool in combination with a multi-parameter optimiser. One approach which is pursued by several widely used tools such as *SAM* and *Greenius* is to assume fixed power block parameters and to vary only parameters that are related to solar field and storage. This section emulates tools such as *SAM* and *Greenius* by varying only the solar block variables which such tools are able to do (but no power block variables).

Based on the reference configuration as defined in Table 16.3, the solar field size, the storage size and the row spacing between parallel rows was optimised using *ColSim* by varying these three solar block variables. This was done in order to compare the results obtained with the results obtained by the integral optimisation including the variables that also affect the design of the power block (see Section 16.5.2, below). The results of optimising the solar block variables only are shown in Table 16.3.

Table 16.3 LCOE and variable values for the reference configuration as described in Section 16.4.1 in comparison with the optimised solar block variables

LCOE (result)		Reference design	Optimal design obtained by this classical approach
LCOE or variable	Optimisation spectrum		
		14.33 €ct/kWh	14.12 €ct/kWh
1 Cumulated collector aperture A_{col}	100 tm^2–2,000 tm^2	510 t m^2	556 t m^2
2 Distance between collector loops	8.66 m–40.39 m	17.3 m	22.1 m
3 Storage size	0–50 k tons	28.5 t tons	38.0 t tons
4 Upper solar field temperature (oil)	–	391°C	391°C (not optimised)
5 Temperature difference hot oil to steam	–	20 K	20 K (not optimised)
6 Live steam pressure	–	100 bar	100 bar (not optimised)
7 Reheat pressure	–	17.1 bar	17.1 bar (not optimised)
8 Design temperature (ACC press. 0.08 bar)	–	30°C	30°C (not optimised)

The LCOE obtained by this classical approach is 14.12 €ct/kWh, hence a reduction of 1.5% relative to the reference design, which is mainly based on the *Andasol* design. Hence, the design, which was presumably optimised for the Spanish *Andasol* site based on similar models and assumptions, remains close to optimal even for the site in California, under the assumed set of models and assumptions. The next section quantifies the additional improvements that can be achieved when also the power block is optimised, beyond solar block optimisation.

16.5.2 Results of optimisation by varying solar and power block variables simultaneously

This section presents the results from the techno-economic plant optimisation, including power block variables. First, the definition of the optimisation task is described and the results of the optimisation calculations are presented. The optimisation procedure itself is then evaluated and the following question is then addressed: Is the optimum found really the global optimum?

All LCOE numbers calculated in the context of this work have the purpose of relative indications, in order to evaluate the methodology presented here. Absolute LCOE values for real power plants may deviate considerably because the cost of components and complete power plants undergo strong volatility due to current market dynamics. Hence, the LCOE values are to be treated as indicative only, and express a relative rather than an absolute value.

One more general remark to plant optimisation: generally, it is not possible to calculate the design that is optimal under any set of side restrictions. The optima found only apply for the described models herein and the set of assumptions that were used. The method can in principle be applied to any decision problem in CSP engineering, but the results will always depend on the quality of the models and assumptions.

Optimised plant configuration

Table 16.4 shows the parameters chosen as starting configuration (cf. definition of optimisation task in Section 16.4.1) and their optimisation ranges, the optimum found from Section 16.5.1 (solar block only) as well as the optimum found by varying solar field and power block parameters together.

By optimising the parameters within the indicated range, the LCOE of the starting configuration as defined in Table 16.4 could be improved from initially 14.33 €ct/kWh down to 13.47 €ct/kWh. This is an improvement of 6.0% compared to the 1.5% improvement when only the solar block

Table 16.4 Variable values for the starting configuration (incl. references) and resulting optimal configuration for the Southern Californian site Daggett

LCOE (result)		Reference design incl. reference	Optimal design (solar block only as per Table 16.3)	Optimal design (solar and power block)
LCOE or variable	Optimisation spectrum			
		14.33 €ct/kWh	14.12 €ct/kWh	13.47 €ct/kWh
1 Cumulated collector aperture A_{col}	100 tm^2–2,000 tm^2	510 t m^2 Solar Millennium (2009)	556 t m^2	559 t m^2
2 Distance between collector loops D	8.66–40.39 m	17.3 m Solar Millennium (2009)	22.1 m	21.9 m
3 Storage size	0–50 k tons	28.5 t tons Solar Millennium (2009)	38.0 t tons	33.3 t tons
4 Upper solar field temperature (oil)	340–393°C	391°C Lippke (1995)	391°C (not optimised)	392.9°C
5 Temperature difference hot oil to hot steam	2–30 K	20 K Lippke (1995)	20 K (not optimised)	2.2 K
6 Live steam pressure	65–150 bar	100 bar Lippke (1995)	100 bar (not optimised)	98.7 bar
7 Reheat pressure	5–30 bar	17.1 bar Lippke (1995)	17.1 bar (not optimised)	10.6 bar
8 Design temperature (ACC press. 0.08 bar)	10–38°C	30°C (own assumption)	30°C (not optimised)	24.1°C

variables are optimised (Section 16.5.1). Hence, the reference design (similar to *Andasol-1* but with Californian dry cooling power block and in California) shows significant potential for improvement. This example shows that power block effects must not remain unconsidered when a CSP plant design is being developed.

Table 16.5 presents energetic and economic results of both the start configuration and the power block optimised configuration from this section. The results presented in Table 16.5 are discussed in Section 16.6. But before that, it will be checked whether the optimum configuration found is really optimal (see below), especially given that eight variables have been optimised simultaneously.

Table 16.5 Energetic and economic results for the starting configuration and for the optimal configuration

Results	Reference design	Optimal design
LCOE	14.33 €ct/kWh	13.47 €ct/kWh
Total investment	269 M€	288 M€
Net annual electrical yield	229 GWh/a	260 GWh/a
Investment solar field	139 M€	154 M€
Investment power block	43.9 M€ (798 Eur/kW_{el})	36.7 M€ (668 Eur/kW_{el})
Investment storage	28.9 M€	33.0 M€
Investment land	12.3 M€ (land used: 1756 tm^2)	16.8 M€ (land used: 2397 tm^2)
Annual O&M cost	4.90 M€	5.16 M€
Annual net electric efficiency ($Q_{DNI} \rightarrow E_{el,net}$)	16.1%	16.7 %
Upper dumping of solar thermal energy (due to full storage)	4.1%	3.0%
Annual thermal efficiency ($Q_{DNI} \rightarrow Q_{PB}$)	47.4%	49.1%
Annual power block efficiency ($Q_{PB} \rightarrow E_{el,gross}$)	37.1%	36.6%
Auxiliary power consumption (total/PB/SF/storage) (% of generator power)	8.6% / 6.0% / 2.0% / 0.5%	7.3%/ 5.1% / 1.5% / 0.6%
SF lower oil temperature/final feed water temperature/SF temperature rise	287°C / 236°C / ΔT_{oil} = 104 K	275°C / 209°C / ΔT_{oil} = 118 K
Storage efficiency (due to heat loss/exergetic eff. by reduced steam temperature in PB)	98.52% / 99.25%	98.61% / 99.11%
Annual optical efficiency ($Q_{DNI} \rightarrow Q_{opt}$)	56.3%	57.5%

Evaluation of the stochastic optimisation process applied

Evolutionary algorithms are based on stochastic variables and the optimisation process itself is scarcely traceable. Hence, this section addresses the question to what extent the optimisation results depend on coincidence and whether the results are reproducible and plausible.

Looking at the optimised configuration above, the question is whether the starting configuration, which is similar to *Andasol* starting configuration, for this optimisation biases the process of optimisation because the starting individual has not evolved from complete coincidence but can be considered as a fairly good starting configuration. To assess this, the same optimisation was repeated twice but with no starting configuration.

As a result, virtually the same LCOE was achieved in all three optimisation runs, but with minor deviations in the configuration of parameters. Starting from these three optimised configurations, sensitivities for each of the variables were performed (see Fig. 16.7). This was done for two reasons:

1. to assess if the LCOE can be further decreased by varying the parameters 'manually'
2. in order to understand techno-economic influences.

The sensitivity assessment confirms that, for each variable, the local optimum is found and thereby confirms proper functioning of the optimisation algorithm applied to this optimisation problem. The influences of the variables on plant performance and cost are discussed in Section 16.6.

16.6 Discussion of case study results

In this section, the optimisation results and the sensitivity assessments from Section 16.5.2 are discussed and causally explained.

Before addressing power block-related aspects – such as the visually striking steep LCOE rises in some of the graphs in Fig. 16.7 – the solar block variables are discussed first because the interdependencies are less complex than the interaction of solar and power block variables. Solar block variables include the solar field size, distance between parallel collector rows and storage size. Then, the variables on the power block side and at the interface between solar block and power block are examined.

In the subsequent interpretations, the optimisation results are analysed using the optimal configuration found in 'optimisation 1' (cf. Section 16.5.2), unless another case is mentioned explicitly.

16.6.1 Optimal solar field size

When comparing and quantifying the different influencing factors on LCOE, it is useful to normalise them with respect to the optimum point of

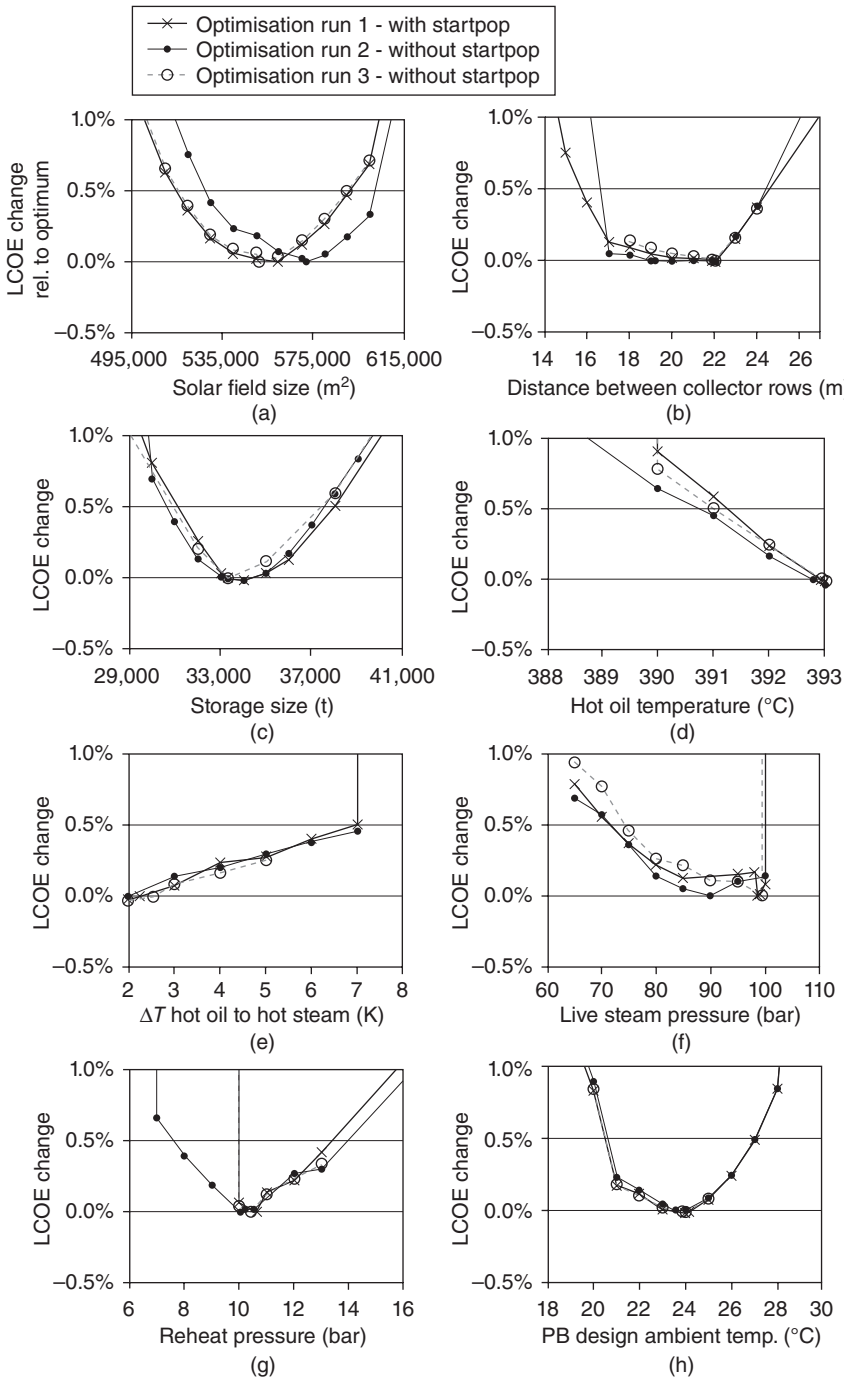

16.7 LCOE sensitivity of each variable near the optima found. All other variables are kept constant in each sensitivity assessment.

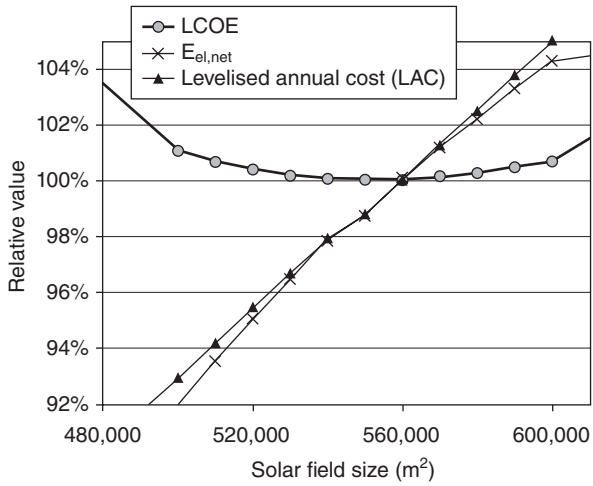

16.8 Relative influence of solar field size on LCOE and on its two constituents, annual levelised cost (enumerator) and net electricity production (denominator), normalised to the minimum LCOE point.

minimal LCOE (cf. Fig. 16.8). The LCOE is the fraction of levelised annual cost and net annual electricity yield $E_{el,net}$ (cf. LCOE definition above). In Fig. 16.8 it can be seen that the levelised annual cost (LAC) increases almost linearly with the solar field size which results from the fact that investment but also O&M cost models consider proportional influence of solar field size. The slight deviations from this linearity result from the rounding of solar field size to an integer number of collector loops. For example, for the optimum solar field size of 559,000 m^2, 163 loops are calculated, for 560,000 m^2, too.

Disregarding this rounding (many loops), the net electricity yield ($E_{el,net}$) is a concave function. The LCOE minimum is where both LAC and net electricity yield have the same gradient:

$$\frac{\partial E_{el,net}}{\partial A_{Coll}} \stackrel{!}{=} \frac{\partial LAC}{\partial A_{Coll}} \qquad [16.3]$$

where $E_{el,net}$ is the annual net electricity yield of the plant, A_{Coll} is the total collector aperature and LAC is the levelised annual cost.

With the help of Fig. 16.9 it can be explained why the electricity production is non-linear. The potential of solar thermal power delivery ($Q_{th,sol.pot.}$) is the amount of annual solar thermal energy that the solar field can provide. It is only a theoretical number because in practice the instantaneously used thermal power (Q_{PB}) is limited by the capacities of the power block and of the storage. $Q_{th,sol.pot.}$ increases proportionally with the solar field size. Q_{PB}

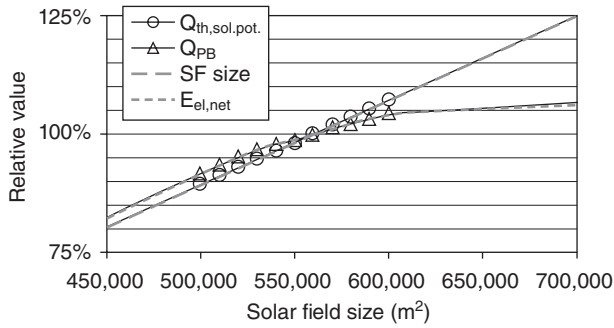

16.9 Potential of solar thermal power delivery by the solar field and thermal power that is actually used in the power block, normalised to the minimum LCOE point.

is the thermal power that is actually used in the power block. Q_{PB} is almost proportional to net electricity production. Minor deviations are caused by a shift from power block part load operation (lower efficiency) to more hours of full load operation with larger solar fields and by increased auxiliary power consumption due to higher pumping energy needs in a larger solar field.

The difference between $Q_{th,sol.pot}$ and Q_{PB} are – to a minor part – the storage heat losses which amount to only 1.4% (cf. Table 16.5) and are (almost) independent of the solar field size. Since the storage only provides as much thermal energy to the power block as it can take, the storage capacity is the limiting factor. The dumping of solar thermal energy due to full storage is the so-called 'upper dumping'. It amounts to 3.7% for the optimum configuration and increases to 5.8% for a solar field size of 600,000 m^2 which is only 7% larger than the optimum solar field size. For the upper limit of the optimisation range of 2 million m^2, the upper dumping would even amount to 62%.

To summarise: a larger solar field will always yield more electric energy production but, for a given set of side restrictions such as power block, weather data and investment cost, there is an optimum when further increasing the solar field size is economically no longer useful.

16.6.2 Optimal distance between parallel collector rows

The investment cost of the headers and cost of land change linearly with header length. When the collectors are spaced further apart, the headers need to be enlarged accordingly to connect the loops. The LAC dependency of the row distance reflects this linear investment influence of row distance (see Fig. 16.10). The optical efficiency respectively optical yield Q_{opt} of the

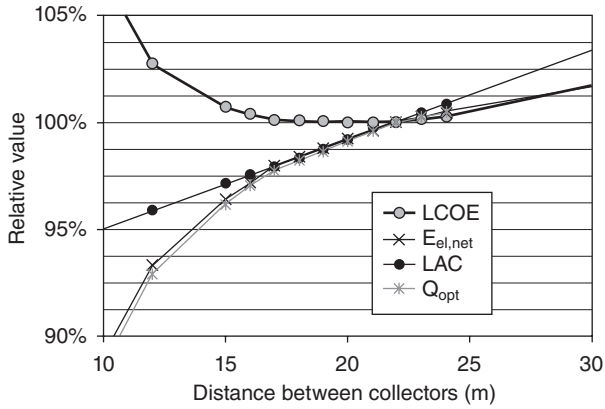

16.10 Main energetic and economic influences of distance between parallel collector rows, normalised to the minimum LCOE point.

solar field increases with increased distance between parallel collector rows because mutual row-shading is reduced (see also Table 16.4). This effect is transferred directly to net electric output of the plant.

The LCOE influence of row distance between the collectors is very limited in a wide range from 17 to 22 m with a minimum at 22 m. The reference design which uses two collector widths of spacing between two collectors (cf. Section 16.5.2) results in a 0.1% higher LCOE compared to this optimum of 22 m. Hence, other relevant aspects such as availability of land or total plant investment cost might play a more dominant role than the option of saving 0.1% in LCOE.

16.6.3 Optimal storage size

Figure 16.11 shows the influence of storage size on the main parameters. Whereas the solar thermal energy potential $Q_{th,sol.pot.}$ is constant for all storage sizes (assuming constant solar field size), the thermal energy that is actually used in the power block (Q_{PB}) increases with storage size – with almost equal gradient as net electricity production $E_{el,net}$. The reason is that dumping of excess solar energy can be reduced from 24% for storage size of 10,000 tons to 0% for the maximum assessed storage size of 50,000 tons.

But with storage size, storage investment increases, too. For the LCOE optimal storage size of 33,300 tons, upper dumping amounts to 3.0%. For this storage size and the given temperature difference between hot tank and cold tank (design conditions) of 118 K, the energetic storage capacity is 1635 MWh, which corresponds to 13 hours of full load capacity. Due to this large storage size, the plant produces 260 GWh of net electricity per year which corresponds to 5,100 equivalent full load hours of the plant or

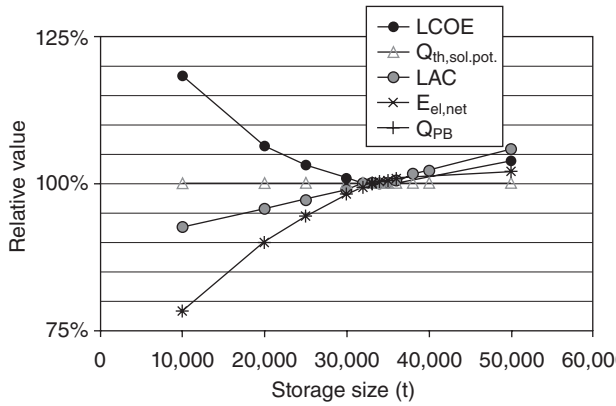

16.11 Main energetic and economic influences of storage size, normalised to the minimum LCOE point.

an annual capacity factor of 58%. Note that storage size and solar field size strongly depend on each other. In this sensitivity analysis, solar field size was kept constant.

The optimum storage size applies for the models and assumptions described in Morin (2011) (e.g. specific cost of the storage system (incl. heat exchangers) of 990 €/tons of salt). If these assumptions are changed, the size of the storage will change significantly. If storage cost is too high, the use of storage might even be completely rejected (no storage).

16.6.4 Steam quality limitations (punishments)

The most striking visual effects in some of the graphs in Fig. 16.7 is the virtually perpendicular LCOE increase for some variables, e.g. the LCOE influence of hot oil temperature, heat exchanger ΔT, live steam pressure and reheat pressure. This steep increase indicates punished configurations, for which the LCOE is set to 100 €ct/kWh, due to steam quality violations. These violations are explained as follows.

Unacceptable steam quality at high pressure turbine exit

High live steam pressure in combination with low reheat pressure (and/or low live steam temperature) leads to unacceptable steam properties at the high pressure turbine exit (before reheat) (See Figs 7.4(f) and (g)). Looking at the sensitivity of reheat pressure for optimisation 2 confirms this: the optimal live steam pressure found here (cf. Fig. 16.7(f)) is 90 bar compared to 99/100 bar for the other two optimised designs. This allows for more

flexibility for reducing the reheat pressure level as can be seen in Fig. 16.7(g).

Unacceptable steam quality at low pressure turbine exit

In principle, the low pressure steam quality restriction is violated for the combination of high reheat pressure, low reheat temperature (here equal to live steam temperature) and low condenser pressure. The design condenser pressure is assumed constant here for all designs.

Looking at the LCOE sensitivities of the ΔT in the heat exchanger (in Fig. 16.7), it is not immediately obvious whether a steam quality violation in the high pressure turbine or in the low pressure turbine caused the punishment. In principle it could be both.

For the hot oil temperature, this is different. Given that the process with lower live steam pressure (optimisation 2) accepts lower temperatures, the results indicate that again it is the high pressure turbine where the steam quality limit is violated.

16.6.5 Optimal upper solar field temperature

Looking at the sensitivities in Fig. 16.7, it is obvious that an increase temperature up to the assumed limit of 393°C is beneficial. The upper temperature limit was chosen according to material stability restrictions for the thermal oil used (Solutia, 2008). Disregarding material stability issues, an interesting question is up to what temperature this LCOE trend can be extrapolated until the heat loss in the collector compensates gains on the power block side from further temperature increase. This can give indications for the optimal operating temperatures when using other heat transfer fluids such as molten salt or direct steam generation. Often, it is claimed that an increase in operating temperatures increases plant efficiency and plant economics. This assessment shows that this statement is only valid for temperatures up to 500°C in a state-of-the-art parabolic trough plant. However, operating temperatures of 540°C and above which are usually applied in fossil steam plants are not beneficial here.

Figure 16.12 shows the influence of the solar field operating temperature on energy production and LCOE. Again, the starting point was the optimised design from optimisation 1 (cf. Fig. 16.7). For better visual comparability, 390°C instead of 393°C was chosen as the reference temperature in Fig. 16.12. Both LCOE and net plant efficiency (in this context equivalent to $E_{el,net}$) show their optimum for 500°C upper fluid temperature. Whereas power block efficiency increases in the assessed temperature range up to 640°C, the efficiency of the collector (equivalent to $Q_{th,sol,pot.}$) decreases progressively because radiative thermal losses become significant for high

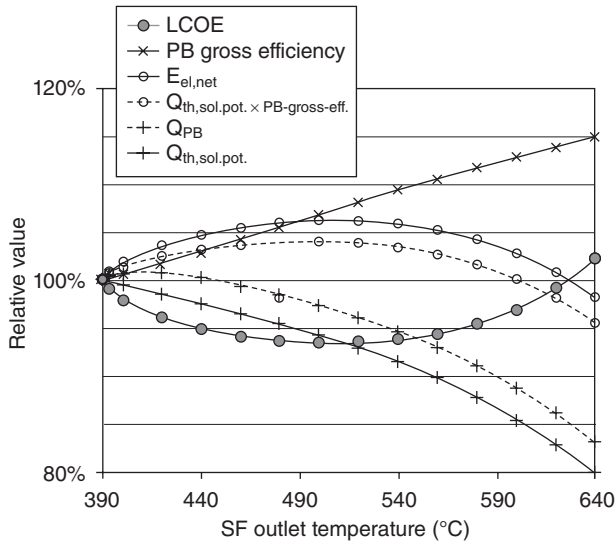

16.12 Influence of upper HTF temperature (at SF outlet) on annual efficiencies and LCOE, normalised to the minimum LCOE point.

temperatures. When looking at the two dotted functions, it is apparent that not only collector and power block influence the optimal operating temperature: the difference between the collector efficiency (equivalent to $Q_{th,sol.pot.}$) and Q_{PB} is attributed to the storage. Storage to some extent compensates the collector efficiency decrease because its energetic capacity increases (physical storage size assumed constant). The energy stored in 1 kg of storage medium increases if it is not only heated by 100 K (up to 380°C) but by 150 K and more. This leverage effect of storage in favour of higher temperatures can also be noted when comparing $E_{el,net}$ and the product of collector efficiency and power block efficiency (dotted line with '+'), the latter corresponding to the gross electricity production of a PTC plant without storage. For both, the optimum is 500°C, but the storage configuration benefits more from higher temperature: increasing the upper solar field temperature from 390°C to 500°C will lead to an LCOE improvement of 6.3% (with storage). Without storage, this benefit is only 4.0%.

The effect of increased solar field outlet temperature on storage is assessed in Fig. 16.13. Assuming the same fixed storage size in tons of storage medium, the energetic storage capacity increases linearly with the upper solar field temperature because a higher ΔT between hot and cold storage medium increases energetic storage capacity. According to the assumed temperature model, storage design temperatures scale directly with solar field temperature. The increase in energetic storage capacity also

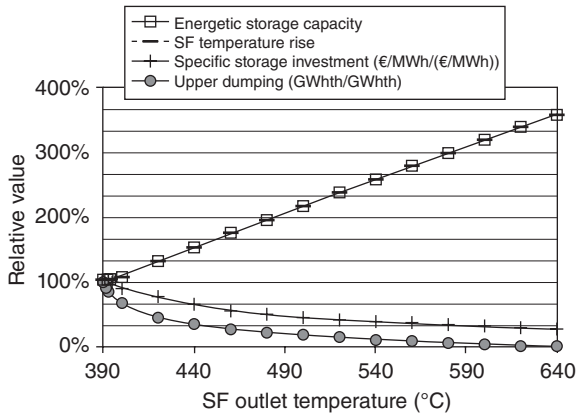

16.13 Relative change of storage-related parameters by increasing the upper solar field temperature (constant mass of storage medium), normalised to the minimum LCOE point.

implies reduced storage investment in €/MWh and reduced dumping of solar thermal energy due to full storage from initially 4.2% for 390°C down to 0% for HTF temperatures above 600°C.

The calculated optimal temperature of 500°C will be lower:

- for sites with lower DNI (e.g. for European sites) because relative heat loss will be higher
- for higher receiver heat loss than assumed (PTR70 from the company Schott; Burkholder and Kutscher, 2009), e.g. with part of the receivers being degraded or with other (older) receivers showing higher heat loss.
- for plants without storage.

To summarise, in a temperature range where costs can be assumed independent of temperature, the optimal operating temperature is an efficiency optimisation problem between power block efficiency and solar field efficiency. Other factors that show an influence on optimal operating temperature are energetic storage capacity and solar field parasitics.

16.6.6 Optimal terminal temperature difference of oil-steam heat exchanger

At first glance, the influence of the terminal temperature difference of the oil-steam heat exchanger (HE-ΔT) – the difference between the hot oil and the hot steam – looks somewhat similar to the LCOE dependency of the hot oil in Fig. 16.7: the hotter the oil respectively the live steam, the better. However, the gradient of both curves is different. Figure 16.14 explains the

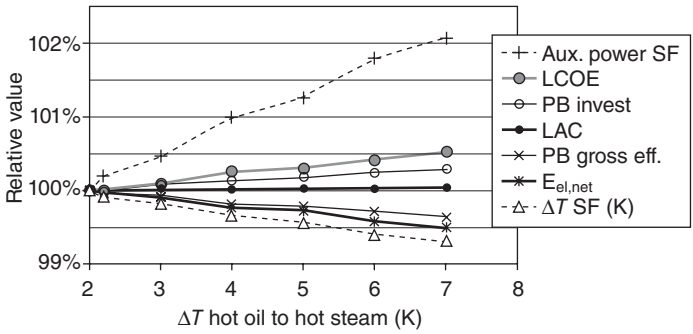

16.14 Influence of the terminal temperature difference of the oil-to-steam heat exchanger on energetic and cost aspects, normalised to the minimum LCOE point.

effects caused by a change in HE-ΔT. The LCOE change is almost exclusively attributed to the change in net electricity production $E_{el,net}$. A minor contribution comes from the change in investment cost. Due to reduced power block efficiency that accompanies an increased terminal temperature difference, less power is generated and more heat has to be rejected by the condenser which, as a consequence, is dimensioned larger.

The decreasing net plant output ($E_{el,net}$) in turn is attributed mainly to the decrease in gross power block efficiency due to lower steam temperatures. However, this does not fully explain the change in net efficiency. For the reheat oil-to-steam heat exchanger, the same terminal temperature difference at both the hot and the cold end of the heat exchanger was assumed. Therefore, the oil temperature at the cold end of the reheat section increases slightly with higher ΔT assumed. The resulting change in solar field temperature rise is also shown in Fig. 16.14. Since the pumping power for the HTF depends by the power of three on the temperature difference (model used: Arias *et al.*, 2009), the auxiliary power consumption in the solar field increases accordingly with lower HE-ΔT. Additionally, storage capacity decreases with higher ΔT (cf. Section 16.6.3).

Still, the question is not answered, why a change in HE-ΔT has only half the quantitative effect compared to a change of hot oil temperature (Fig. 16.7). The increase in power block efficiency and the decrease in specific power block cost with higher live steam temperature are the same in both cases. However, the temperature rise in the solar field is different. Whereas in the HE-ΔT variation, the solar field temperature rise decreases from 118 K (for HE-ΔT = 2 K) to 117 K (for HE-ΔT = 7 K) due to an increase in cold reheat temperature, this effect is different for hot oil temperature variation. An increase of hot oil temperature faces a slight decrease in cold oil temperature because the T(Q)-line for the HTF of the main heat adder

(cf. Fig. 16.5) is getting steeper and the final feedwater temperature remains constant. Hence, a decrease in hot oil temperature from 393 to 390°C results in a decrease in solar field oil temperature rise from 118 K to 114 K. The implications on auxiliary power consumption and storage efficiency are favourable for an increase in hot oil temperature but unfavourable for a decrease in the HE-ΔT.

One general remark with respect to the optimum found, of quite low terminal temperature difference of the heat exchanger (2 K): the lower (and optimal) value of 2 K was derived from the pinch at the evaporator inlet (cf. Fig. 16.5) (Lippke, 1995). But, heat exchanger costs are included in the solar field costs. Hence, the assessed variations of the heat exchangers are only considered with their energetic effects but not with changes in cost. Given that heat exchanger costs for the oil-to-steam heat exchangers amount to only a minor fraction of total plant investment and that the LCOE optimum depends on the gradient of LAC of the plant, neglecting this cost influence of heat exchanger design leads to a limited distortion of the results. But the observed monotonic trend towards low terminal temperature difference will definitely apply only for a limited temperature range if a more detailed cost model, which also considers cost influences of HE design variations, is applied.

16.6.7 Optimal live steam pressure

The effect of varying live steam pressure is rather complex and involves many different effects which are shown in Fig. 16.15. Since a live steam pressure above 100 bar violates the steam quality limitations (cf. Fig. 16.7(d)) this defines the upper limit of the assessed interval. The lower limit is defined by the variable range.

Both net electric output ($E_{el,net}$) and LAC improve over the assessed range, and therefore LCOE decreases, too. The basic driver for efficiency increase is the power block efficiency which increases for higher live steam pressures. Higher live steam pressures contribute to a so-called Carnotisation (thermodynamic optimisation) of the heat cycle. But this effect is mitigated by two effects:

- Decreased thermal energy delivery Q_{PB} with higher pressures: The amount of thermal energy actually delivered to the power block decreases with higher pressure. The reason for this is an increased solar field inlet temperature with higher pressures, increasing from 256 to 276°C (upper temperature 393°C), resulting from the oil-to-water-steam heat exchanger. The pinch point there limits the lower solar field temperature for higher pressures. As a consequence, heat loss in the solar field increases slightly (cf. line $Q_{th,sol.pot.}$). But the larger effect is

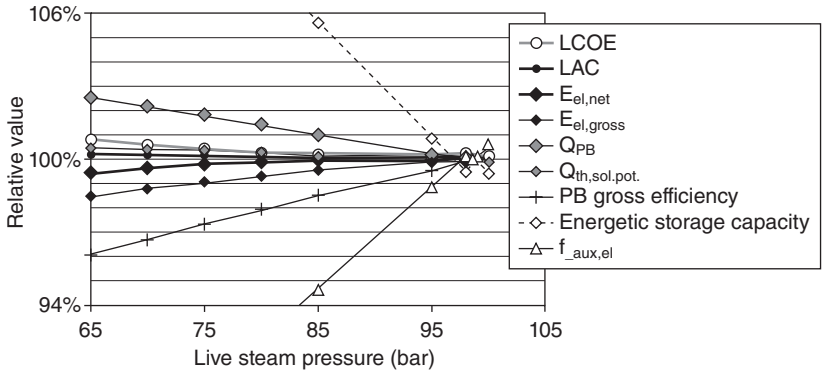

16.15 Performance and cost parameters influenced by varying live steam pressure – all other parameters are kept constant, normalised to the minimum LCOE point.

that upper dumping increases due to decreasing energetic storage capacity.

- Increased auxiliary power consumption ($f_{\_aux,el}$) with higher pressures: Comparing net power production ($E_{el,net}$) and gross power production ($E_{el,gross}$), the auxiliary power consumption is reduced with increased pressures. Responsible for this is again the lower temperature rise in the solar field respectively the higher pumping power in the solar field ($f_{\_aux,el}$ in Fig. 16.15).

LAC is almost constant over the assessed range. The slight decrease results from reduced power block investment through efficiency increase (smaller condenser because reduced amount of heat to be rejected to ambience).

To summarise, the LCOE optimum results mainly from increasing power block efficiency with pressures up to 100 bar. But the sensitivity of LCOE to live steam pressure is very limited. This can also be noted when comparing the significant difference in optimal live steam pressures found by the three optimisation runs (cf. Fig. 16.7).

16.6.8 Optimal reheat pressure

Compared to live steam pressure, reheat pressure has a greater impact on LCOE, (cf. Fig. 16.7(g)). As opposed to all other sensitivity calculations which were performed using 'optimisation 1' (in Fig. 16.7), here 'optimisation 2' was chosen, because a broader spectrum of non-punished configurations can be assessed. Figure 16.16 shows the LCOE and its constituents, levelised annual cost (LAC) and net electricity production ($E_{el,net}$). From

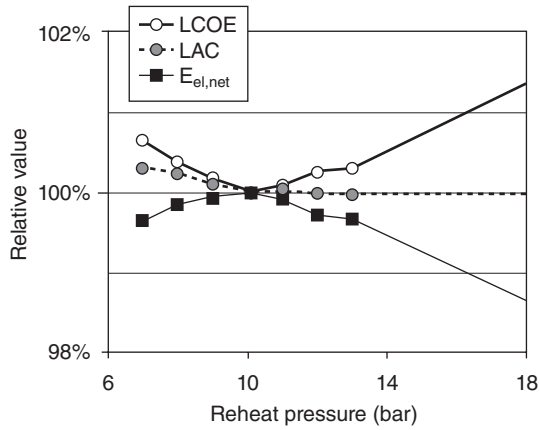

16.16 LCOE and its constituents levelised annual cost and net electricity production, normalised to the minimum LCOE point.

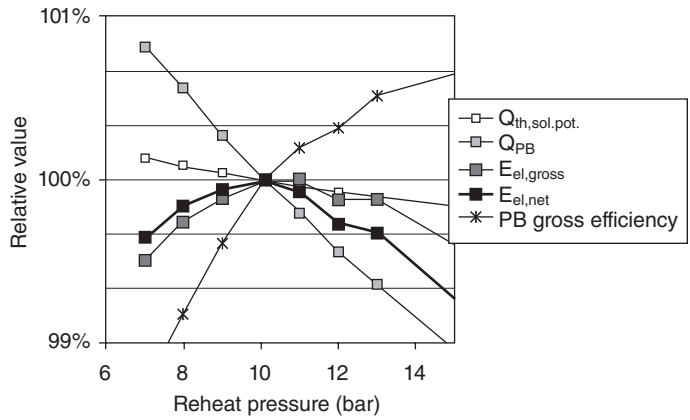

16.17 Different energy conversion steps are influenced positively and negatively by rising reheat pressure. All functions are normalised to the minimum LCOE point.

Fig. 16.16 it can be concluded, that – again – electricity output $E_{el,net}$ and not cost (LAC) is primarily responsible for the LCOE minimum because LAC hardly changes in the assessed interval. Therefore, net electricity production is broken down into its constituents in Fig. 16.17.

Sticking to the top-down assessment and starting with analysing the energy conversion steps to net electric power production $E_{el,net}$, gross electric power $E_{el,gross}$ minus auxiliary power is used to calculate net electricity production. Net power production shows a lower gradient $\partial E_{el}/\partial p_{reheat}$ than

gross power over the entire range of the analysis (7–30 bar). This indicates increasing auxiliary power consumption: auxiliary power consumption increases steadily from 6.9% to 8.2% of gross power production. This is owed mainly to auxiliary power increase in the solar field (1.3% to 2.2% of gross power). Again, the reason is increased SF pumping parasitics because of an increased mass flow in the solar field resulting in turn from a decreased ΔT of the HTF from 135 K to 103 K with higher reheat pressures. The respective cold oil temperature rises from 265 to 290°C which is a consequence of a rise in final feedwater temperature from 188 to 272°C and a temperature rise of the cold reheat steam (by evaporation pressure rise) from 165 to 234°C.

Gross power in turn is the product of thermal power to power block (Q_{PB}) and power block efficiency (line 'PB gross efficiency' in Fig. 16.17). Power block efficiency rises considerably over the entire range, especially given that the final feedwater temperature rises with the reheat pressure with the assumed feedwater heater design rules (cf. Section 16.4.1).

The steep decrease in thermal power production (Q_{PB}) with live steam pressure is also significant. The increased heat loss in the solar field due to higher solar field temperature hardly contributes to this effect (cf. line $Q_{th,sol.\ pot.}$ in Fig. 16.17). Responsible for the difference between solar thermal potential and energy used by the power block for electricity production is storage and power block upper limitations.

Storage losses, both heat losses and exergetic losses, are very small and almost constant in the assessed range. But the dumping of solar thermal energy increases from 2.3% to 6.3%. This is due to decreasing energetic storage capacity which is proportional to the SF temperature rise. Hence, again, the change in energetic storage capacity through increased temperature difference between solar field inlet and outlet is important and is strongly influenced by reheat pressure and final feedwater temperature.

16.6.9 Varying the power block design ambient temperature

When the so-called cold end of the power block, the condenser, is designed, this occurs usually by assuming a hypothetical ambient temperature for which the objective condensing pressure is achieved. According to these assumptions, the heat transfer surfaces of the condenser and the mass flows in the condenser are calculated. In reality, the ambient temperature during operation differs in most cases from this design temperature. Choosing the right design ambient temperature is a task that should be site-specific and is discussed in this section.

For the design point of the power block, the condenser pressure is assumed to be 0.08 bar which corresponds to a condensing temperature of

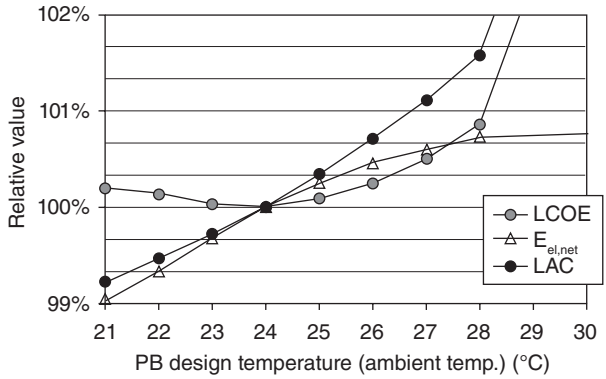

16.18 Power block design temperature (design condenser pressure 0.08 bar): influence on net electricity generation $E_{el,net}$, total plant cost (LAC) and LCOE, normalised to the minimum LCOE point.

41.5°C. Optimising the design ambient temperature for the power block hence means optimising the exergetic efficiency of the condenser: the larger the condenser, the higher is the net plant efficiency but also the cost of the condenser and consequently the cost of the total power plant.

In this context, it is important that part load operation of the air cooled condenser is adapted to maximise net power block output, because of high auxiliary power consumption for the fan operation. A method to account for load-adapted fan operation was developed and applied to account for this effect (see details in Morin, 2011).

Figure 16.18 shows the influence of the design ambient temperature on LCOE and on the two constituents of the fractional LCOE value: the net plant output ($E_{el,net}$) and the levelised annual plant cost (LAC). The LCOE becomes minimal where both net plant output ($E_{el,net}$) and levelised annual plant cost (LAC) have the same gradient, given that LAC is a concave function and $E_{el,net}$ a convex function near the LCOE optimum. The steep gradient of plant cost (LAC) and LCOE above the design temperature of 28°C results from the dramatically increasing cost of the condenser which needs to be dimensioned very large in order to realise the required condenser pressure at higher ambient temperature.

The net electricity production ($E_{el,net}$) rises with larger condensers (higher design ambient temperature) but this increase declines for high temperatures because auxiliary consumption of large condenser fans induce an electric energy consumption which is over-proportionally increasing with the design temperature.

For the optimal design temperature, which is 24.1°C – under the given (weather) conditions – the terminal temperature difference of the condenser is 17.4 K (= 41.5°C – 24.1°C).

Comparing both reference design and optimum design on pages 513–515 the reduced condenser size results in reduced auxiliary power consumption for the power block (condenser fans) and in lower specific investment in the power block.

16.7 Conclusions and future trends

Simulation is essential to support decisions related to investment in and design of CSP plants, because simulation helps the prediction of the economic, energetic and operational characteristics of a real plant installation. This chapter has given an overview of state-of-the-art simulation of CSP plants. The new method for design optimisation of solar thermal power plants that has been presented integrates the energetic and the economic simulation of an entire power plant on a component level as well as providing a multi-parameter optimisation algorithm which allows relevant design parameters of the plant to be optimised. A strong focus is set on the detailed assessment of the power block in the context of modelling the entire plant.

This integrated techno-economic modelling and optimisation method was applied to a special optimisation case: the optimisation of a parabolic trough power plant using thermal oil as heat transfer fluid and a two-tank molten salt storage. Starting from a plant design that is similar to the Andasol-1 power plant but transferred to a different site, the LCOE could be reduced by 6.0%, In contrast, varying solar block variables (describing solar field and storage) only, as today's commonly used tools such as SAM do, leads to an improvement of only 1.5% in this example.

The applied optimisation algorithm proved to work very reliably to optimise the eight-dimensional optimisation problem presented here. Based on the models used and the assumptions made, the following results were obtained. Optimising the solar field size, the row spacing between parallel collector rows and the physical size of the storage is a trade-off between net electricity production (the larger the better) and cost (the larger the more expensive). The additional electricity production decreases with increased values of the respective parameters (concave function) whereas the cost increases almost linearly. As a consequence, a clear and single optimum for the specific energy production cost exists. Whereas LCOE reacts very sensibly to variations in solar field size and storage size, the effect of row spacing variations is limited.

Beyond these three pure solar block variables, five variables were optimised that induce changes in power block design: solar field outlet temperature, terminal temperature difference of the oil-to-steam heat exchangers, live steam pressure, reheat pressure including feedwater heating section and condenser size. All defined variables are not only theoretically variable but show flexibility when a commercial power plant is designed.

The calculations show that designing the condenser to project-specific conditions has a very high impact on total plant economics. The availability of water, cost of the condenser itself but indirectly also the cost structure of the rest of the plant require a case-specific optimisation. For the air-cooled condenser assumed here, a temperature difference between ambient air and condensation of 17 K turned out to be LCOE-optimal under the assumptions used. For all other above-mentioned variables which induce changes in power block design, it could be shown that the implications on the temperature rise in the solar field have a very important effect. High SF temperature rise reduces auxiliary power consumption for the pumping of the heat transfer fluid in the solar field which depends by the power of three on mass flow and which is a significant energy consuming factor. High SF temperature rise also increases the energetic capacity of the storage medium through higher temperature difference between the hot and cold tanks.

It was also shown that it is beneficial to increase the operating temperature beyond the limits which today's oil-based heat transfer fluids allow (approx. 400°C). However, for a parabolic trough plant, increasing temperatures beyond 500°C, as representatives from the conventional power sector often claim, is likely to be neither energetically nor economically beneficial.

Today, power plant designs are developed by several sub-system calculations from different experts (solar field, power block, finance). Optimising a plant layout usually requires several iterations between those contributing actors. The integrated techno-economic simulation and optimisation approach presented here may help to ease today's time-consuming assessments and iterations. It may also help discover additional optimisation potential by simultaneous multi-variable optimisation and by an integrated consideration of inter-dependencies of the sub-systems which may otherwise remain undetected when the sub-systems are optimised sequentially.

The optimisation approach presented here has been demonstrated using a specific set of tools, one specific plant model and one specific set of cost and performance assumptions. Further examples to which this integrated techno-economic simulation and optimisation approach – but with adapted models and assumptions – may be applied include:

- optimisation of layouts for other configurations such as linear Fresnel collector power plants based on direct steam generation
- optimisation of cash-flow oriented performance numbers such as internal rate of return as opposed to LCOE or
- structural optimisation as presented in Richter (2010) in the sense of number of feedwater heaters and number of reheat sections.

Today, many different tools are used for the simulation of solar thermal power plants. This multi-variable optimisation method in combination with

a detailed techno-economic plant model – including power block simulation – can in principle be transferred to any kind of optimisation task, to any plant model, and even to any kind of simulation software.

16.8 Acknowledgements

The work described in this chapter is an extract from a PhD thesis (Morin, 2011). The work and the thesis were carried out at the Fraunhofer Institute for Solar Energy Systems ISE (Freiburg, Germany), mainly within the project 'OPTISIM', funded by the German Ministry of Environment, Nature Conservation and Nuclear Safety (BMU) under the number FKZ 0325045 and co-funded by Fraunhofer ISE (2008–2010). The author would like to thank the funding institutions for supporting this development. In particular, the author would like to thank Torsten Gutjahr, Pascal Richter and Martin Strelow for their contributions in the development of the integrated optimisation software. Representatively for the discussions with *Flagsol*, the author would like to thank Dr.-Ing. Ulf Herrmann for giving input on practically relevant modelling and design parameters. The author would also like to thank Prof. Dr. Reinhard Leithner (University of Braunschweig), Prof. Dr. Volker Wittwer and Dr. Peter Nitz, both of Fraunhofer ISE, for giving valuable comments to improve the PhD thesis of Gabriel Morin, and implicitly this article.

16.9 References

Arias, DA, Gavilán A, Russel M (2009) 'Pumping Power Parasitics in Parabolic Trough Solar Fields', Proceedings of 15th International SolarPACES Symposium, 14–18 September 2009, Berlin.

Atacama desert (2009), picture from: http://www.ipantalla.com/wp-content/uploads/2009/03/desierto-atacama.jpg (accessed 27 April 2010).

Bockamp S, Griestop T, Fruth M, Ewert M, Lerchenmüller H, Mertins M, Morin G, Häberle A, Dersch J (2003) 'Solar Thermal Power Generation', Conference Paper, PowerGen Europe.

Blair N, Mehos M, Christensen C (2008) 'Sensitivity of Concentrating Solar Power Trough Performance, Cost, and Financing with the System Advisor Model', Proceedings of 14th International SolarPACES Symposium, 4–7 March, Las Vegas, NV.

Burkholder F, Kutscher C (2009) 'Heat Loss Testing of Schott's 2008 PTR70 Parabolic Trough Receiver'. Technical Report NREL/TP-550-45633, May.

Dersch J, Morin G, Eck M, Häberle A (2009) 'Comparison of Linear Fresnel and Parabolic Trough Collector Systems – System Analysis to Determine Breakeven Costs of Linear Fresnel Collectors', Proceedings of 15th International SolarPACES Symposium, 14–18 September, Berlin.

Greenius (2010) Greenius Free Software from FHTW Berlin and DLR, available at: www.f1.htw-berlin.de/studiengang/ut/downloads/greenius/index.html (accessed 15 March 2010).

Griffin P, Huschka K, Morin G (2009) 'Software for Design, Simulation and Cost Estimation of Solar Thermal Power and Heat Cycles', Proceedings of 15th International SolarPACES Symposium, 14–18 September, Berlin.

Gutjahr T (2009) Solarthermische Kraftwerke: Simulation und Optimierung von Kraftwerksprozessen unter Verwendung eines geeigneten Optimierungsverfahrens und eines kommerziellen Kreislaufsimulationsprogramms. Diploma thesis at HTWK Leipzig and Fraunhofer ISE.

Hirsch T, Berger M, Morin G (2007) Softwarevergleich zur Wärmeträgerregelung, Projekt Fresdemo technischer Abschlussbericht zu AP 4.1, August 8, project funded by MAN Ferrostaal and German Ministry of Environment under the number FKZ 16UM0069.

IPSEpro (2010) IPSEpro model library Solar Thermal (CSP_Lib), see: http://enginomix.net/products/ipsepro-model-libraries/solar-thermal/ (accessed 15 March 2010).

Lerchenmüller H, Mertins M, Morin G, Häberle A, Bockamp S, Ewert M, Fruth M, Griestop Th, Dersch J (2004) 'Fresnel collectors in hybrid plants with high solar shares', Proceedings of EuroSun conference, Freiburg, Germany.

Lippke, F (1995) 'Simulation of the Part Load Behaviour of a 30 MW SEGS Plant', Technical report SAND95-1293, Sandia National Laboratories, Albuquerque, NM.

Mertins M (2008) Technische und wirtschaftliche Analyse von horizontalen Fresnel Kollektoren. PhD thesis urn:nbn:de:swb:90-138844, available at: http://digbib.ubka.uni-karlsruhe.de/volltexte/1000013884 (accessed 7 January 2010).

Montes MJ, Abánades A, Martínez-Val JM (2009) 'Performance of a direct steam generation solar thermal power plant for electricity production as a function of the solar multiple', *Solar Energy* 83, 679–689.

Morin G (2003) 'Auslegung und Wirtschaftlichkeitsanalyse eines solarthermischen Kraftwerks auf der Basis von linearfokussierenden Fresnel-Kollektoren. Diploma thesis at University Karlsruhe, supervised by Fraunhofer Institute for Solar Energy Systems and E.ON Engineering GmbH, April.

Morin G (2011) Design Optimization of Solar Thermal Power Plants. PhD thesis, University Braunschweig and Fraunhofer ISE, April, published by Fraunhofer-Verlag.

Morin G, Lerchenmüller H, Mertins M, Exert M, Fruth M, Bockamp S, Griestop T, Häberle A (2004) 'Plug-in Strategy for Market Introduction of Fresnel-Collectors', Proceedings of 12th International Symposium SolarPACES, 6 October, Oaxaca, Mexico.

Morin G, Dersch J, Eck M, Häberle A, Platzer W (2009) 'Comparison of Linear Fresnel and Parabolic Trough Collector Systems – Influence of Linear Fresnel Collector Design Variations on Break Even Cost', Proceedings of 15th International SolarPACES Symposium, 14–18 September, Berlin.

Pawellek R, Löw T, Hirsch T (2009) 'EbsSolar – a solar library for Ebsilon Professional', Proceedings of 15th International SolarPACES Symposium, 14–18 September, Berlin.

Relloso S, Delgado E (2009) 'Experience with Molten Salt Thermal Storage in a Commercial Parabolic Trough Plant. Andasol-1 Commissioning and Operation', Proceedings of 15th International SolarPACES Symposium, 14–18 September, Berlin.

Richter P (2010) Simulation und Auslegungsoptimierung solarthermischer Kraftwerke unter Einsatz evolutionärer Algorithmen und neuronaler Netze. Diploma thesis at Fraunhofer ISE and RWTH Aachen, January.

Siemens (2010) Steam turbine picture from Siemens press picture, available at: www.siemens.com/press/en/presspicture/ (accessed 27 April 2010).

Solar Millennium (2009) Solar Millennium AG, Erlangen, personal e-mail communication by Sven Moormann, Head of Corporate Communications, 13 October 2009.

SolarPACES (2010) SolarPACES Task I workshop on modeling of the annual performance of solar thermal power plants, 2 and 3 March 2010, at NREL, Golden, CO. Participants: Abengoa Solar (Arias D, Russel M, Price H), DLR (Dersch J, Eck M, Pitz-Paal R), EPRI (Bedilion R), Enginomix (Erbes M), Evonik (Pawellek R), Flabeg (Nava P), Flagsol (Benitez D), Fluor (Wadman G), Fraunhofer ISE (Morin G), Kearney&Associates (Kearney D), NREL (Blair N, Burkholder F, Dobos A, Mehos M, Renne D, Turchi C, Wagner M), Sandia (Ho C, Kolb G), SkyFuel (McMahan A), Solar Millennium (McKee J), Thermoflow (Griffin P).

Strelow M (2007) Einsatz numerischer Optimierungsverfahren zur Wirkungsgrad-Maximierung des Dampfkraftprozesses solarthermischer Kraftwerke. Diploma thesis at University Braunschweig and Fraunhofer ISE, April.

System Advisor Model (2009) SAM Version 2009.10.13, software developed and distributed by the National Renewable Energy Laboratory, available at: https://www.nrel.gov/analysis/sam/ (accessed 15 March 2010).

Thermoflow (2009) Software Thermoflex, Version 19.0.1 from April 24 2009, software developed and distributed by Thermoflow Inc., www.thermoflow.com (accessed 23 February 2010).

Solutia (2008) Fluid Therminol® VP-1 heat transfer fluid by Solutia (product information brochure) available at www.therminol.com (accessed 24 January 2010).

Wall M (1996) GAlib: A C++ Library of Genetic Algorithm Components, version 2.4, Documentation Revision B, August 1996, Mechanical Engineering Department, Massachusetts Institute of Technology, Copyright © 1996 Matthew Wall, all rights reserved, available at: http://lancet.mit.edu/ga/ (accessed 9 March 2010).

Wittwer C (1999) *ColSim* – Simulation von Regelungssystemen in aktiven solarthermischen Anlagen. PhD thesis, available at: http://digbib.ubka.uni-karlsruhe.de/volltexte/41499 (accessed 7 January 2010).

17

Heliostat size optimization for central receiver solar power plants

J. B. BLACKMON, University of Alabama in Huntsville, USA

Abstract: This chapter presents a parametric analysis of heliostat cost as a function of area for a representative solar central receiver power plant. Results show that heliostats in the range of approximately 25 to 40 m^2 have a substantially lower cost per unit area than the current base line 148 m^2 heliostat considered by the US Department of Energy (DOE), based on their cost data. The analysis is based on allocating costs into three categories: a constant cost per unit area; a cost per unit area that is dependent on the imposed load on the structure, drive units, etc., as a function of area; and a cost that is essentially fixed, irrespective of heliostat size.

Key words: heliostat, cost, optimum size, solar central receiver.

17.1 Introduction

Central receiver based systems have been introduced in detail in Chapter 8. Heliostats are a major element of the cost of central receiver plants, estimated to be of the order of 50% of the total installed system cost (Kolb *et al.*, 2007). Thus, significantly reducing heliostat cost is critical to achieving some degree of economic parity between solar and carbon-sequestered base load coal power plants, which is part of current US policy (Holdren, 2010). Intermediate and peak power generation market value is higher, and this offers a more attractive opportunity for solar central receiver systems, but base load capability is also needed. The fundamental impediment of high up-front installed costs for the system has made it difficult for solar central receiver developers to compete in the utility market. Achievement of the goal of an established, cost-competitive solar central receiver industry has remained elusive for over 30 years. Success is dependent on reducing the cost of the single most important subsystem: the heliostat.

This chapter reviews past development efforts around heliostat design and then presents an analysis of the heliostat size optimization problem. The optimization presented is applied to a specific set of assumptions; however, the principle of the approach could be applied under other assumptions. The approach is also applicable to the cost optimization of the solar field elements from any of the CSP technologies.

17.1.1 Progress in the development of heliostats

Over the last several decades, heliostat designs have primarily used conventional glass and steel, pedestal-mounted elevation-azimuth designs, but alternatives include 'ganged heliostats', carousel heliostats on tracks, stretched membrane reflectors, inflatable enclosures, etc. Various examples are shown in Fig. 17.1. The US Department of Energy (DOE) studies conducted by Sandia National Laboratories Albuquerque (SNLA) resulted in the base line glass-steel/elevation-azimuth (el/az) heliostat being about 150 m^2 in area; the most specific version of this base line is the 148 m^2 Advanced Thermal Systems (ATS) heliostat (Kolb *et al.*, 2007), which was used to develop the DOE installed cost of \$211/m^2 in 2010 dollars for sustained, high volume production. As with many el/az designs, a linear actuator is used for elevation, and a multi-stage gear system is used for the azimuth. Information on these heliostats is available from various sources (Kolb, 2006; Kolb *et al.*, 2007; Falcone, 1986; Jones, 2006; Dietrich *et al.*, 1982; Winter *et al.*, 1990), including numerous websites maintained by solar central receiver companies, such as eSolar, BrightSource, Abengoa, etc.

Starting with initial heliostat efforts in the early 1970s up to today, there has been a general tendency to increase the heliostat size from about 12 m^2 to approximately 150–200 m^2, and even up to 320 m^2, with several counter-examples of much smaller heliostats, primarily in the past several years.

The tendency to favor larger heliostats during this period has apparently been based in part on the assumed advantages of 'economies of scale'. This trend is seen in various design studies and analyses (Kolb, 2006; Kolb *et al.*, 2007; Falcone, 1986; Jones, 2006; Dietrich, *et al.*, 1982; Winter *et al.*, 1990). This trend has also been seen in other solar power systems, such as the 320 m^2 (or, 334 m^2, depending on version) Amonix concentrating photovoltaic system (www.amonix.com). This system was also proposed by Arizona Public Service for modification to a heliostat, but that plan was not completed. Another expected benefit with larger heliostats was that the fixed costs for a heliostat could be spread over a larger area, thus reducing the cost per unit area. Other factors may have played a role in this general trend, such as availability of custom drive units potentially offering high performance and low cost, or relaxing design criteria to achieve lower costs by increasing the reflector area to the maximum allowable for a given drive unit. These studies covered primarily specific designs, and cost considerations for these designs. Only recently have intrinsic cost vs. size considerations been available in the literature (Kolb *et al.* 2007, and an earlier discussion in the Sandia Heliostat Handbook, 1982). Figure 17.2 shows the trend of heliostat size as a function of area, compiled from Kolb (2006), Kolb *et al.* (2007), Falcone (1986), Jones (2006), Dietrich *et al.* (1982), Winter

SAIC 50 m^2
Stretched Membrane

Martin Mariettta Solar One and
Solar Two (39.9 m^2)

CSIRO National Solar Energy
Centre Solar Towers, 4.5 m^2

SAIC Stretched Membrane 145 m^2

APS PV Concentrator 320 m^2
(Plan was to convert to Heliostat)

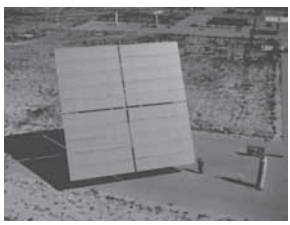

Advanced Thermal
Systems (ATS) 148 m^2

ASM SBP/Steinmüller 150 m^2

BrightSource-Ivanpah 14.4 m^2

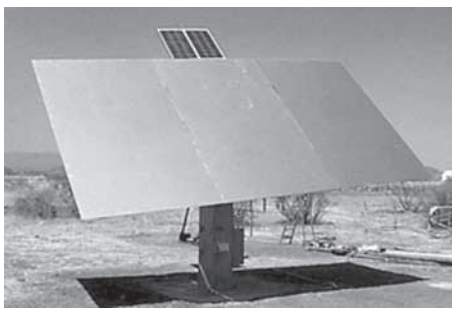

GHER S.A. HELLAS 01 19.2 m^2

Esolar Sierra Sun Tower 5 m^2

17.1 Representative heliostat designs and sizes (Kolb *et al.,* 2007).

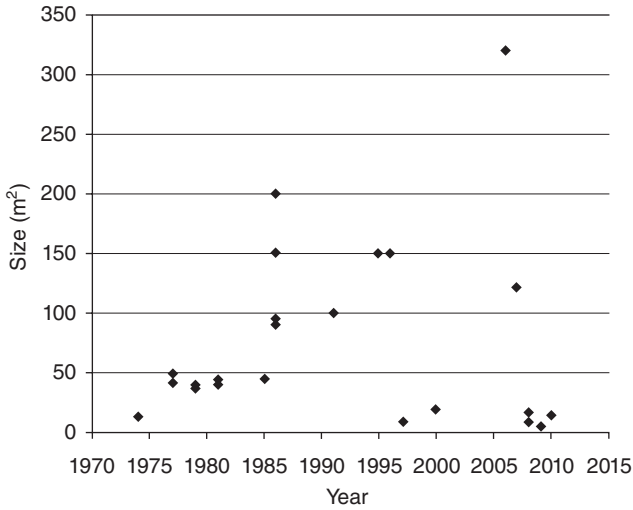

17.2 Heliostat size trend 1970 to 2010.

et al. (1990), Blackmon (2008), California Energy Commission (2007) and various manufacturers websites (BrightSource, eSolar, CSIRO); these programs are summarized in Table 17.1. Note that this summary captures selected prototypes and several commercial developments. There are undoubtedly other prototypes that have been constructed by various groups in this period, but this selection is representative of the range of sizes and the general trend over the last 35 years or so.

Figure 17.2 and Table 17.1 illustrate substantial variations in design approaches and costs. This variation in size is remarkable; of 32 designs only six are less than about 15 m^2 and sixteen are approximately 50 m^2 or above and nine of these are about 100 m^2 or above. If the assumptions of economies of scale, and, in effect, relatively high fixed costs on a per heliostat basis are true, then the larger heliostats would be the preferred choice. This fixed cost per heliostat aspect may have been at least partially supported by relatively high electronic costs needed for each heliostat during the early period of heliostat development. If, however, the fixed costs associated with a heliostat are not a substantial fraction of the total cost, then the reverse would be true. That appears to be the case, especially with far lower electronic costs available today. Finally, costs are typically based on a relatively well-established, if not fully commercialized, central receiver industry. Actually, the initial costs to form this industry would be higher, and thus can pose a major impediment to market entry and commercialization. It remains to be seen if lower initial costs can be achieved by aggregating costs over high production volumes through large power purchase agreements.

Table 17.1 Selected heliostat development programs 1970 to 2010

Year (approximate)	Program	Prime contractor or location	Size (m^2)
1970	Trombe Heliostats	France	45
1973–1974	National Science Foundation	University of Houston/McDonnell Douglas	13.4
1975–1977	Pilot Plant	Boeing	48
	System Research	Martin Marietta	41
	Experiment	Honeywell	40
		University of Houston/McDonnell Douglas	31.4
		University of Houston/McDonnell Douglas	37.5
1977–1979	Central Receiver Test Facility (SNLA)	Martin Marietta	37.2
1978–1979	Pilot Plant Prototypes	Martin Marietta	39.9
		University of Houston/McDonnell Douglas	44.5
1979–1981	Second Generation	Boeing	43.7
	Heliostat	Martin Marietta	57.4
		University of Houston/McDonnell Douglas	56.9
		Arco (Northrup)	57.8
1980–1981	Pilot Plant (Solar One)	Martin Marietta	39.9
1981–1986	Large Area Heliostat	University of Houston/McDonnell Douglas	90
		Arco	95
		Arco	150
		Solar Power Eng. Co.	200
1984–1986	Stressed Membrane (SM)	Solar Kinetics Inc	150
		Science Applications	150
1990	Stressed Membrane (SM)	Science Applications International Corp.	100
mid-1990s	SM, but with Glass	Solar 2/Spain	150
mid-1990s	USISTF High Concentration Solar Central Receiver	University of Houston/McDonnell Douglas/HiTek Services	9.2
mid-1990s	ASM-150	Steinmüller (Germany)	150
1995–2000	Gher S.A. Hellas 01	Gher S.A. (Spain)	19.2
2006	Existing Amonix PV Tracker Converted to a Heliostat	APS (Proposed)	320
2006–2007	PS-10 and PS-20	Planta Solar (Abengoa, Spain)	121
2006–2008	Carpe Diem HelioCA 16	DLR	16
2006–2008	SHP (Australia)	DLR-Julich, Germany	8
2007	CSIRO (Australia)	CSIRO National Solar Energy Centre Solar Towers	4.5
2009	BrightSource	Solar Energy Development Center, Rotem, Negev, Israel	14.4
2010	eSolar Sierra SunTower	eSolar, Inc (Five 1 sq. meter)	5

An example of one type of size growth is seen in the study conducted at McDonnell Douglas (Dietrich *et al.*, 1982). There it was concluded that the cost of that heliostat was reduced by increasing the area, and keeping the same structure and drive unit, with some relatively minor changes. This conclusion was based primarily on determining that the angle of attack of the high wind condition for horizontal stow could be reduced from 10 to 6.5°, and that it was cheaper to replace damaged heliostats, rather than design for a 25-year life with a worst case wind condition. This approach, however, did not address the fundamentals of heliostat loads vs size, and it did not keep the design load conditions constant. Other examples are noted, including a study to increase the size of the stretched membrane (SM) heliostat from 50 to 150 m^2 to decrease cost (Kolb *et al.*, 2007); it was concluded that this did not reduce cost and the effort was not continued. Note that the ATS design is based on strength, not stiffness. If strength, not stiffness, is used, then gravity bending or sagging becomes an issue with larger heliostats. This would 'make large heliostats less costly on an optics-corrected basis than they will be in reality' (Kolb *et al.*, 2007).

Sandia determined in 2006 that 'The ATS heliostat is the low cost baseline in the U.S.' (Kolb *et al.*, 2007). Their reported cost for this heliostat is \$126.49/m^2 for 50,000 units per year and \$164/m^2 for 5,000 units per year. These costs are presumed to be for the 5,000th and 50,000th units per year, respectively, with no further reduction due to learning curve effects. The DOE requires that solar generating cost be determined using the System Advisor Model (SAM 3.0). They state that the current DOE baseline heliostat is 150 m^2 with a cost of \$211/m^2 (DOE, 2009). This cost is based on the ATS heliostat. However, the detailed cost breakdown and production quantity are not available; it may be presumed that the cost differences compared to the ATS heliostat are at least partly attributable to broader considerations, such as market entry conditions, with lower production rates, as well as initial startup costs, inflation escalation from 2006 to 2010, and perhaps additional costs being included, such as for site preparation, permits, and various financial cost factors.

17.2 Heliostat design issues and cost analysis

17.2.1 Design issues

Using NREL's System Advisor Model (SAM) with the \$211/m^2 as a constant value, the generation cost for a solar central receiver system with 75% capacity factor is 13.2 cents/kWh. Reducing the cost of the heliostat can substantially reduce the generation costs as determined by SAM, but the key is determining the conditions that make this possible. This aspect is addressed in the following by first allocating the costs into three categories.

O&M, learning curve, and optical performance cost impacts are then considered. In the following cost analysis the Sandia ATS base line heliostat values are used for the hardware installed cost (Kolb *et al.*, 2007). These values are used in part because they represent the base line design, and this study is the most thoroughly considered public analysis available. The costs are then allocated into the three categories to account for their relationship to the size and number of heliostats.

Heliostat cost minimization challenges are compounded by the issues of market entry. The first plants must bear most, if not all, of the startup costs, of which a major factor is associated with the heliostat factory as well as the installed cost of the heliostats.

Thus, the decision process for commercially successful market entry involves numerous heliostat cost aspects. Among these are the basic design concept; production rate; intrinsic cost of the heliostat as a function of its size; manufacturing learning curve effects; optical performance as a function of size; trade-off of custom designs against commercial off-the-shelf components; degree of assembly conducted in the field vs in the factory; trade off of performance vs cost; and use of low-cost labor vs investment in automated production, to list a few. Heliostat performance issues include factors such as tracking accuracy, stiffness, wind loads, gravity bending, and optical performance, such as reflectivity and reflector surface slope error or 'waviness', together with mirror module design and size. Higher performance should lead to improved capture of solar energy at the receiver, but above some level, the associated heliostat cost increases lead to a diminishing return. The operations and maintenance issues must also be factored into the heliostat cost, using net present value, to comprehensively determine the optimum design and its initial cost. Typically O&M costs are treated separately from the heliostat installed cost and these are combined to determine the levelized cost of energy (LCOE), but the net present value approach allows O&M to be included in the comparison of heliostat designs and sizes.

The size optimization analysis presented in this chapter uses the DOE base line heliostat design and the associated costs as determined for this design (Kolb *et al.*, 2007) as a starting point, but with the use of three cost categories into which the costs are allocated, not an overall cost.

For this analysis, the three categories of costs are:

- *Category 1: Constant costs per unit area*, which are essentially independent of heliostat size or number, for a given size plant and total production quantity;
- *Category 2: Size-dependent costs* that are determined by the loads imposed, and that decrease the cost per unit area as the area decreases; and

- *Category 3: Fixed costs for components* used on each individual heliostat, irrespective of its size; for a given size field this fixed cost per heliostat increases linearly with the number of heliostats, and thus increases the cost per unit area as the size decreases, and vice versa.

Category 1 is for constant cost per unit area hardware, such as mirrors, which are essentially identical whether installed on a large or small heliostat, with only the number changing. Category 2 is for costs per unit area that are dependent on the imposed loads, such as the structure, pedestal, foundation, drive units, motors, etc., and therefore can be shown to be functions of area. Category 3 is for costs that are constant, such as for encoders, processers, etc., and are the same irrespective of heliostat size.

Two approaches are examined to reduce the heliostat installed hardware costs. The first approach is to decrease the size of the current base line heliostat in the DOE program, but retaining its basic design; this involves a parametric analysis of Category 2 for size, and Category 3 for the number of heliostats for a particular field size. The decrease in size reduces the loads, primarily from wind, expressed as the imposed moment (e.g., product of force due to wind or gravity times a characteristic moment arm). It is shown that the lower load for the smaller heliostat decreases the hardware weight and cost, on a per unit area basis, and the higher numbers of smaller heliostats increases the Category 3 costs. In general, the Category 3 costs are much lower than those for Category 2.

It is shown in the following that appropriately allocating the cost of the various components of the base line heliostat used in DOE studies and considering the cost and weight dependence on the imposed moment result in a reduced cost per unit area, and a substantially smaller heliostat, even without reducing the Category 1 constant cost per unit area or the Category 3 fixed cost of hardware required for each of these base line heliostats, irrespective of their size. However, as the size is reduced even further, to very small heliostats, the Category 3 fixed costs become dominant, and the cost per unit area increases, but in between these two extremes lies the minimum cost per unit area. The size reduction also improves the optical performance, and the larger number of heliostats allows substantial learning curve cost reductions as well. To further take advantage of this size effect, a second approach is considered.

The second approach is to reduce Category 3 fixed costs that are attributable directly to an individual heliostat, irrespective of its size, and by appropriately allocating a part of these costs into the other two categories. These costs are composed primarily of the electronics, such as processors, position sensors, limit switches, motor electronics, etc. The challenge is to develop heliostat designs with much lower Category 3 costs. By reducing these fixed costs, it is seen that there is not only a reduction in the total cost, but there

is also a leveraging effect that increases the cost reduction by further reducing the optimum heliostat area, and thus gaining additional benefit in terms of decreased moment and weight per unit area, additional learning curve benefits, and additional optical performance. This leveraging effect leads to a lower cost per unit area and it leads to a somewhat smaller overall field reflector area, and somewhat greater cost reduction through the learning curve effect. Successfully employing these two approaches can decease the hardware installed cost of the heliostat design on a per unit area basis.

There is another issue: operations and maintenance (O&M) costs, and how these are allocated to the heliostat. The approach to deal with this issue is complex and is not treated here explicitly. Rather, it is treated as a cost parameter, and is based on a reasonable percentage of the levelized cost of energy (LCOE) for the solar plant. The net present value (NPV) of O&M costs on a per area basis is determined. This NPV O&M cost is included with the installed hardware cost, rather than adding this O&M cost separately to the LCOE as is usually done. The observation of the importance of fixed costs per heliostat, irrespective of size, points to a means for reducing the total installed cost of the heliostat, including O&M, when it is treated together with heliostat installed cost. Similarly, some of the O&M costs are associated with Category 1 and 2 costs. The key is to appropriately allocate the heliostat hardware installed costs and the NPV O&M costs into the three major cost categories.

For the case considered here, using the DOE base line heliostat costs, an overall reduction of about 30–40% is seen for the cost per unit area. These costs correspond to a heliostat size range of the order of 25–40 m^2, compared to the DOE base line heliostat of about 150 m^2. The purpose, however, is not to show that a particular heliostat design or area results in the lowest cost, but to show an analytical method of treating the various aspects contributing to the total heliostat cost for any design. How these aspects of imposed load, learning curve, optical effects, and O&M are considered in the heliostat design is therefore one of the most important decisions facing the central receiver developer.

A cost analysis is then presented for a representative plant based on allocating heliostat costs into the three categories and generating a family of curves for cost per unit area vs area for heliostat installed cost. Additional effects are considered for reducing cost through improved optical performance and garnering the benefits of learning curve effects. These effects are then combined, including allocated O&M costs, to illustrate the overall cost per unit area dependence on heliostat area, for the same delivered thermal energy at the receiver. These analyses show the importance of the Category 2 costs that are dependent on load, and the Category 3 fixed cost associated with a heliostat, irrespective of its number or size. Decreasing the size

clearly has a major impact on reducing the cost, but further cost reductions are provided if the design has low fixed cost. Reducing this fixed cost provides an additional potential path forward for development of lower cost heliostats because of the leveraging effect on the minimum cost being at an even lower heliostat area.

17.2.2 Introduction to cost analysis

For a given heliostat design there is a minimum for the cost per unit area vs area. For example, it is shown in the following that for a large heliostat, such as the Sandia base line ATS design, decreasing the size from 148 m^2 offers cost advantages, since the costs for each item (drive, structure, etc.) are reduced by the size-dependent effect. Conversely, fixed costs per heliostat (e.g., processors, position sensors, limit switches, etc.) become important on a cost per unit area basis as the heliostat size decreases and thus the number of heliostats required increases. These essentially fixed costs, irrespective of size, are a modest *fraction* of the baseline ATS heliostat costs relative to the drive unit, structure, reflector, pedestal, etc., but their cost *impacts* become significant as the size is reduced.

Other costs that are not directly associated with individual heliostats can also be important factors, such as centralized ('master') control systems, civil engineering site preparation, heliostat foundation surveying, initial costs associated with a production factory and how this cost is amortized over the heliostat production. Some of these may be considered part of the heliostat subsystem cost and thus could be assigned to it in some cost studies. Again, these are difficult to consider in detail here, and are highly dependent on heliostat designs and detailed cost studies for those designs. Therefore, the basic approach here is to use the costs from Kolb *et al.* (2007) and treat these costs parametrically. In addition, O&M costs that can be specifically associated with heliostats need to be included with the hardware installed cost within the appropriate cost categories.

Therefore, representative costs including both hardware installed costs and O&M are used in a parametric analysis of the cost per unit area as a function of the heliostat area and the number of heliostats. Representative values for O&M costs are allocated into the appropriate cost categories. Typically the heliostat installed costs do not explicitly include O&M in determining the minimum cost per unit area and the resulting area. However, it is useful to include O&M as part of the installed cost, because it allows these costs to be appropriately allocated into the three categories, and then treated quantitatively. This approach should be beneficial to the developer in better understanding the effect of heliostat sizes on the minimum heliostat cost per unit area. This alternative approach is developed further below.

For smaller heliostats, the improved optical performance as a function of size results in a reduced total field reflective area for a given plant thermal energy intercepted by the receiver, and this too reduces total cost of the heliostat subsystem, and can reduce tower and receiver costs as well. For example, smaller heliostats could have virtually no spillage losses with large receivers, and negligible spillage losses with smaller receivers, and thus the smaller, lower cost receiver could be an option. With smaller receivers the lower weight and wind load conditions would result in a lighter, lower cost tower. The manufacturing learning curve cost reduction effect also tends to favor smaller heliostats, and may be further improved by having access to components already in mass production. However, costs that are essentially constant for a particular component used on each heliostat increase the cost per unit area as the area decreases. Together these various aspects can be used to estimate how heliostat costs can be minimized by consideration of size, for a particular design, and the leveraging effect of design changes, especially those that lower the constant costs per heliostat. In order to have a consistent comparison, it is assumed that surface slope, tracking and calibration errors remain unaffected by size though this may not be the case in practice.

The purpose of the following categorization and analysis is to consider these relationships and how they can be used to reduce costs. It is found that the cost of the baseline ATS heliostat design is reduced substantially for a smaller area *even though its individual item costs are not changed*. Further reductions in cost are then examined parametrically.

Consider first the three cost categories applied to the installed hardware cost of the SNLA ATS base line heliostat.

17.3 Category 1: costs constant per unit area irrespective of heliostat size and number

The primary cost per unit area that is essentially constant, virtually irrespective of the heliostat size and number of heliostats, is the reflective material, most commonly a second surface silvered glass reflector used in many of the heliostat programs, and in particular, the ATS design. The principles of this analysis are applicable to other reflective materials such as polymeric film. There are differences in designs, and quoted costs, from different manufacturers; however, the cost per unit area for a given total quantity can be assumed essentially constant, irrespective of the size or number of heliostats, for a particular type of glass reflector module delivered in commercial quantities (Kolb *et al.*, 2007). Typically, there will either be a glass substrate to support the mirror (i.e., thin mirrored glass bonded to a thicker glass laminate, foam or composite backing, etc.) or mirrored glass of sufficient

thickness can be directly bonded to a support structure, with a given span between the members to ensure appropriate stiffness and strength. The baseline ATS heliostat has 1 mm thick mirrors bonded to a 3 mm thick glass to form a corrosion resistant laminate. Conversely, for the same stiffness and strength, a thicker glass mirror can be bonded directly to the steel support structure and a mirror backing paint used. Both approaches have been proven by tests and field use by various companies since the late 1970s, and curved glass mirrors bonded directly to support structure are used extensively with various trough plants.

The mirror module cost per unit area varies depending on source and quantity, but this capital cost is essentially independent of the heliostat size. In effect, the same mirror module can be used for a wide range of heliostat areas, simply by using more or less of these; only the number of modules per heliostat changes, but not the total number. The ATS module cost was based on the Gardner mirror and was determined to be $\$23.06/m^2$ for 50,000 units per year and $\$26.50/m^2$ for 5,000 units per year. (Dollar values are approximate 2006 USD.) It should be noted that this cost, even with additional factors for overhead, production, assembly, and profit, is less than $\$35/m^2$ or about 20% for the 5,000 units cost of the base line ATS heliostat; mirror reflector costs are thus an important, but not the major cost parameter.

There may be some reduction in price for larger orders, but this is a minor effect when considering a given field area, and determining for this field the optimum heliostat size. For example, in data provided by Pilkington, the cost decreases at about 9% as the quantity is doubled from 100,000 to 200,000, then 200,000 to 400,000, and from 400,000 to 800,000 (Kolb *et al.*, 2007). For our purposes, this cost dependence on total quantity is not the issue; an increase in the number of heliostats, for essentially the same total field area, would have, to first order, the same mirror cost/m^2. This cost decrease with quantity is included later below, in the learning curve analysis, but care must be taken to not include a learning curve reduction for the mirrors from an increased number of heliostats, if the total mirror module area is essentially the same.

Thus, this mirror cost/area is assumed to be constant, irrespective of heliostat size, for a *given total field area*. The overall heliostat cost/area in the parametric analysis changes substantially depending on the size, but the mirror module part of this total cost/area remains essentially the same, for a given type of mirror, available from a high production commercial supplier.

There are other minor cost/area components that are essentially constant, independent of the heliostat area or the number of heliostats. These are much less than the mirror cost/area, and are noted later in the discussion of the cost allocation into the three categories.

17.4 Category 2: size dependent costs

Representative basic equations are shown below for the weight of loaded structures and mechanical hardware. All of these weights are shown to have essentially the same relationship with heliostat size and imposed loads and performance requirements. It is also shown that for the same basic component, the cost is approximately linearly proportional to the weight. The same approach also applies for the determination of the size, weight, and thus cost of certain O&M equipment, including installation. For example, larger heliostats will require larger, heavier equipment for foundations, heliostat lifting and installing, washing, etc.

In principle, it can be shown that the imposed moment on the heliostat for a constant wind speed induced load is related to the area to the three-halves power. This so-called 'three-halves power law' is typically applied to the moment imposed on a structure, but it is shown below that it also applies to drive units, motors, pedestals, foundations, etc. Thus, the majority of the heliostat hardware follows this 'three-halves power law'. As a result, the moment/area is approximately proportional to the square root of the area (for uniform wind speed). Representative structural and mechanical elements of a heliostat are shown to agree with this cost, weight, and moment per unit area relationship in the following.[1]

17.4.1 Structure

Both strength and stiffness requirements are typically considered in heliostat designs. Both can be shown to be dependent on the so-called 'three-halves power law'. For a constant wind speed with height the imposed wind load force, F, on the heliostat is proportional to the wind pressure, P, times the reflector area, A. Assuming a characteristic moment arm can be associated with the square root of the area, a representative moment is this force times the square root of the area. Thus, a characteristic moment is given by:

$$M = FA^{1/2} = PA^{3/2} \quad [17.1]$$

and the moment per unit area, M/A, is:

$$M/A = PA^{1/2}. \quad [17.2]$$

These expressions relate the ability of the heliostat to move against high imposed wind loads, such as for stowing, or for surviving high winds while stowed, and is a major design criterion for strength. To be consistent, the pressure, P, is assumed constant for all heliostats in this example. This

[1] In this analysis all heliostats in a field are assumed to be identical; any second order effects, such as the possibility that heliostats experience different average wind loads depending on location within the field, are neglected.

expression is similar to that determined in Kolb *et al.* (2007), where the maximum stress in the components as the size changes is related to bending moment. There, with tubes and I-beams, cost is proportional to weight and weight is proportional to bending moment; thus both are found to scale as the third power of the chord. Since the chord is nominally the square root of the area, the moment, weight, and cost per unit area are proportional to the square root of the area.

The second basic criterion is the heliostat stiffness; it must achieve a certain optical and tracking performance, and that requires that the support structure and tracking system are sufficiently stiff to maintain acceptable power interception at the receiver. For consistency, this stiffness is assumed to be the same for the different sizes of heliostats because that provides the same basic optical performance under the design load.

17.4.2 Reflector support structure stiffness

Reflector support structure stiffness is related to the deflection for a particular span under a given load. The load can be a point load, F, at the end of the beam, or a constant or distributed load over the beam, or a load at the center, etc. The only difference is in the constant, m, with the deflection, d, given by $d = FL^3/mEI$, where, for a simple beam of modulus E, length L, cross-sectional area of height h and width, b, the moment of inertia I is given by $bh^3/12$ (Baumeister and Marks, 1967).

The small angle associated with deflection is approximately d/L, and thus, for the same angular deflection, corresponding to the same optical performance relative to the reflected rays, with the load exerted on one end of this cantilevered beam ($m = 3$):

$$d/L = FL^2/3E(bh^3/12) = 4FL^2/Ebh^3. \quad [17.3]$$

With the force, $F = PA = PL^2$, where P is the wind pressure and L is the length of one side of the square heliostat, which is the length of the beam, then:

$$d/L = 4PAL^2/Ebh^3 = 4PL^4/Ebh^3. \quad [17.4]$$

It can be seen that with the same basic heliostat design, and thus geometric similarity, doubling the length, width, and depth, with the same wind pressure P, produces the same angular deflection, since the factors of 2 cancel. The weight of the beam is ρbhL, where ρ is the density of the beam. Thus, the weight per unit reflector area (assuming that the area is L^2) is:

$$W/A = \rho bhL/A = \rho bhL/L^2 = \rho bh/L = \rho bh/A^{1/2} \quad [17.5]$$

For comparison of similar configuration heliostats, b and h are related to L by a constant. Thus, $b/L = h/L = C$, and $W/A = \rho C^2 A^{1/2}$. Again, weight per

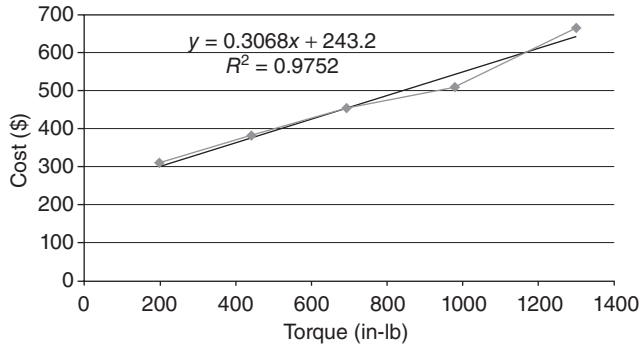

17.3 Representative gear reducer cost vs output torque. Data from McMaster Carr (http://mcmaster.com/), costs in 2010 USD.

unit area is proportional to the square root of the area. For basic structural steel, for a particular shape and type, the cost is proportional to the weight. Thus, cost per unit area varies as the square root of the area when stiffness (angular deflection) is constant for varying heliostat sizes, just as this same relationship holds for equal stress, as noted in Kolb *et al.* (2007).

17.4.3 Representative drive units

Using representative gear reducer cost and torque data, a linear relationship is found, as shown in Fig. 17.3. The torque is related to the imposed moment, and thus Fig. 17.3 shows that the cost/area for a representative drive unit is linear with imposed moment/area, which is proportional to the square root of the area. However, using data directly from catalogs needs to be validated, since it is not clear that equal stress and safety factors are used. There are also instances in which drive unit assemblies use elements that have higher or lower load capability. For example, a cited load bearing capability for linear actuators may not be equal for all the elements, and there can be substantial life cycle differences. When this effect is corrected, by reducing the stated load capability to correspond to the same stress for the given linear actuator screw cross-sectional area, then the actuator weight becomes linear with the output worm torque, as shown in Fig. 17.4.

Past quotes from various suppliers have illustrated that the cost is essentially proportional to the weight, for similar production quantities, and thus to the square root of the area, but those quotes are not included here, since only catalog costs are openly available. There are also instances in which a linear correlation is an approximation. For example, in Fig. 17.5, bearing weight is better correlated with a polynomial. In this case, the weight increases more rapidly with moment than for a linear relation.

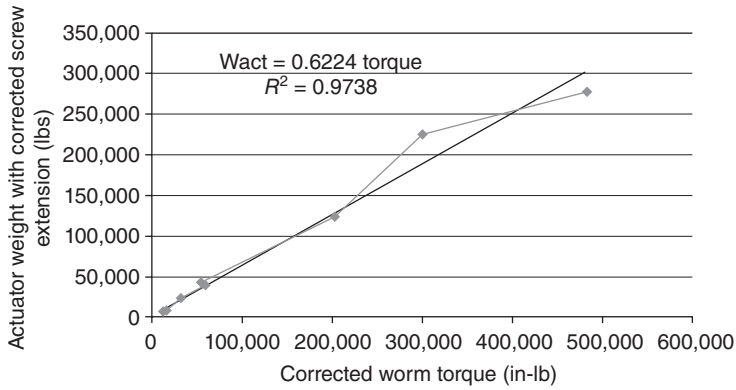

17.4 Actuator weight vs corrected worm torque. Data from Duff Norton (http://www.duffnorton.com/).

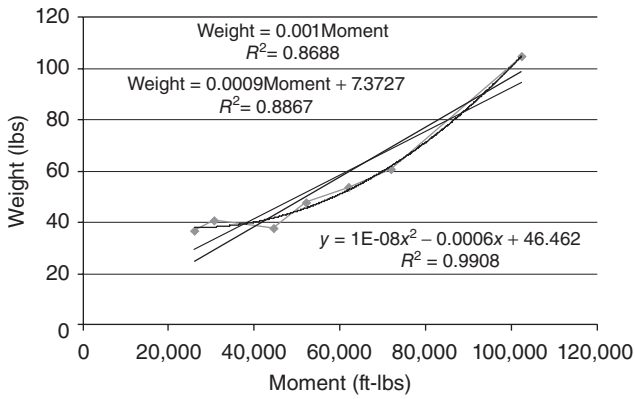

17.5 Bearing weight vs moment. Data from Kaydon (http://www.kaydon.com/)

There are other issues, in that the linear actuator screw travel distance varies as well as the load, as the heliostat size changes. Also, in some cases there is a fixed cost factor, especially for ordering single quantities from catalogs, such that the linear relationship of cost vs torque has an intercept at some non-zero cost. This constant cost aspect is related to the general tendency for virtually all production items to have both fixed and variable costs. This aspect is not treated here, but should be included with a more detailed cost per unit area analysis for a particular heliostat design. The existence of a non-zero intercept for the cost curves does not change the general parametric approach, and is best done with real cost quotes for an actual system, for a realistic number of heliostats. Clearly, there can be

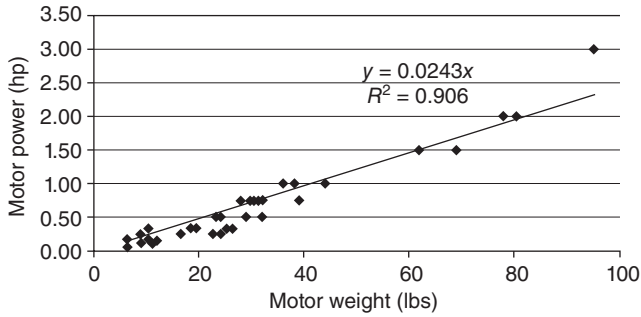

17.6 DC motor power vs weight.

some exceptions to this linear relationship, depending on production quantity, demand, etc. These factors are not amenable to analysis since such data are unavailable. Overall, however, there is a general tendency for the weight to vary linearly with the imposed moment or torque, and, where available, it is found that cost for a particular type of component varies linearly with weight.

Motor power is torque times motor rotational rate (e.g., rpm). The motor rpm is related to the required angular rotational rate of the heliostat through the gear ratio; both rotational rate and gear ratio are assumed to be constant for heliostat parametric size comparisons. For example, the same angular rotational rate required for emergency stow of the heliostat is assumed for the selected heliostat design for all sizes. There are many variations in types of motors, frame size, voltage, ancillary controls, production rates, suppliers, etc., which can affect cost, but overall, the motor horsepower and torque are linearly related to the motor weight, and the motor price is linearly related to the horsepower and/or torque. These approximate linear relationships are shown in Figs 17.6 and 17.7. Since price is proportional to torque, and torque is directly related to imposed moment through the gear ratio, motor price per unit area is again proportional to the square root of the area.

17.4.4 Foundation or pier

For the same basic configuration, soil bearing pressure, and imposed load, the weight of both the soil removed for a representative augered pier and the weight of the pier foundation, per unit heliostat area, are proportional to the square root of the heliostat area. This is shown as follows.

For simplicity, the soil bearing pressure in the lateral direction can be assumed to be constant with depth. Having a more complex relationship, or just a simple linear relationship with depth, does not change

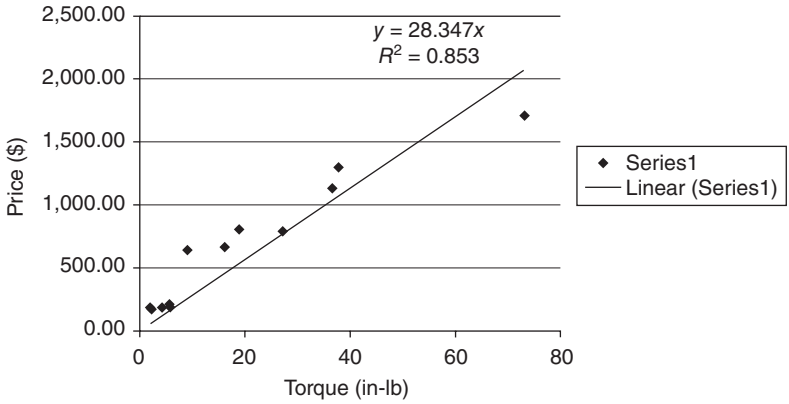

17.7 DC motor price vs torque. Data from Grainger (http://www.grainger.com/). Prices in 2010 USD.

the fundamental parametric relationship. It is also not important, for a parametric relationship comparing the effects of heliostat area, to have the heliostat foundation assumed to be set in 'bedrock' at the bottom, and rotating about this base as the pivot point, or rotating at the mid-point, or any other point, assuming that the characteristics of the soil are the same irrespective of depth. Although the soil conditions can vary widely with site and depth, these issues are not addressed here; they are more appropriately dealt with for a specific design and site. But the basic parametric relationship is instructive.

The force on the heliostat from the wind is proportional to the wind pressure difference times the heliostat area. The overturning moment is this force, times a characteristic moment arm; that moment arm may be the distance from the center of pressure to the pivot point.

Assuming constant soil pressure, the elemental moment provided by the reaction force of the soil at a distance y below ground level, for an elemental depth, dy, and a diameter, D, is approximated by:

$$dM = P_s D y dy \qquad [17.6]$$

where P_s is the soil bearing pressure.

Integrating over the characteristic moment arm, L,

$$M = P_s D L^2/2. \qquad [17.7]$$

Assume that the heliostats have the same geometric relationship for the distance from the center of pressure from the wind to the pivot point. Thus, $x = cH$ where c is a constant and H is the height (and width, for a square heliostat). The wind-induced moment, or overturning moment, for a wind pressure P and heliostat area A is then $Fx = PAx$, and this is equal to the

soil bearing moment, $P_s D L^2/2$. Again, with the same basic heliostat configuration, there is geometric similarity, and L/D is a constant, n. Thus:

$$P_w AcH = P_s D n^2 D^2/2. \quad [17.8]$$

Grouping the coefficients $c/2n^2$ as one constant, k, and using $A = H^2$, we have:

$$PA_h kA^{3/2} = P_s D^3, \quad [17.9]$$

or,

$$D^3 = (P/P_s)kA^{3/2} \quad [17.10]$$

Both the weight of the soil removed and the weight of the concrete and steel pier are proportional to the volume of the foundation, V, or,

$$V = \pi D^2 L/4 = n\pi D^3/4 = n\pi(P/P_s)kA^{3/2}/4. \quad [17.11]$$

The volume of the soil removed, or the volume of the pier, per unit area of the heliostat, is thus

$$V/A_h = n\pi(P/P_s)kA^{1/2}/4, \quad [17.12]$$

and the volume per unit area is proportional to the square root of the area.

Since the cost of the soil removal, and the manufacturing material cost of the foundation (concrete and steel rebar, etc.) are approximately proportional to the volumes, it can be concluded that the cost per unit area of the foundation and pier are approximately proportional to $A^{1/2}$. There are of course alternatives to this foundation and pedestal design, such as using a pedestal that is driven into the ground, or carousels, or 'ganged' heliostats, etc., but it is the type used for the DOE baseline heliostat and has been used with the majority of heliostats. The purpose here is to illustrate that the basic materials and effort required for the foundation and pedestal are related to the heliostat size, and for a representative pedestal and foundation, the 'three-halves' power law effect is a reasonable expression for parametric analysis purposes. This relationship would be replaced by more detailed expressions if available for a specific design.

In Kolb *et al.* (2007), the motor wiring harness (control box to motors and encoders) is treated by assuming that the length of the harness is proportional to the pedestal height. It is further assumed that half the cost is in the wire, while the remainder is in connectors and labor. However, the wiring cost is also dependent on the gauge or in effect the wire cross-sectional area. For the lower motor power required with smaller heliostats, the wire cross-sectional area would be less, and the amount and cost of wire would be less on a unit length basis. A portion of the heliostat wiring can thus be allocated into Category 2, though the relationship with area is not ascertained.

Thus, Category 2 costs per unit area for the structure, electromechanical components, foundation, and pier are shown to be approximately proportional to the square root of the area for a parametric comparison that is based on equal stress, safety factor, configuration, imposed wind loads (i.e., wind speed), materials, and properties.

17.5 Category 3: fixed costs for each heliostat and other costs

17.5.1 Category 3: fixed costs for each heliostat

There are costs that are fixed for each heliostat. Prime examples are the processor, position sensors (e.g., encoders), limit switches, etc., associated with controlling each heliostat. For example, an encoder of a particular design could be used on virtually any heliostat, irrespective of its size. These costs on a per unit area increase as the size of heliostats decreases because the number of heliostats increases. Thus, cost/area varies inversely with the area. With a relatively large number of heliostats, this cost, which appears to be minor for a large heliostat, can become a major cost/area factor for small heliostats. This fixed cost per heliostat works against very small heliostats. Conversely, this fixed cost per heliostat is also one of the justifications for increasing the heliostat area and is especially important if this cost is high.

17.5.2 Costs distributed among the categories

There are also costs that must be distributed among these three categories, because they share some aspects of all three. For example, the drive unit has electrical wiring that can be related to motor power and size of the heliostat as a Category 2 cost, but it requires field wiring as well. For a given field size, a fraction of the field wiring costs would involve trenching and installing electrical (and, often, fiber optic) cables throughout the field. Ancillary wiring from these primary cables to individual heliostats would be with smaller wires. With smaller heliostats the total power required would be less even though there are a larger number of heliostats. This is seen by noting that the power per unit area is less for the smaller heliostats, and thus even though there are more of these than for a larger heliostat, the total power required is estimated by multiplying the same total field area times the power per unit area. Therefore the main power cables into the field would be conducting lower current, and thus would be smaller. With more, smaller heliostats, more wiring and connections would be required, but this wiring would be higher gauge (smaller diameter) since the smaller heliostats would have lower current flow.

Some of this installation cost would be associated with the number of heliostats, and would increase as the size is decreased. The wire gauge or wire diameter would be determined by the motor power on each heliostat, and this can be shown to be a function of the torque and rotational rate, and thus is determined by the imposed moment. With smaller heliostats, there are more rows of heliostats, and thus more trenching and wiring is required. At the heliostat there is wiring connected to the motor that must be connected to the field wiring; this wiring length and gauge is also determined by the size of the heliostat and the motor power. Depending on the type of motor used, there may also be additional electronics; this would be partially determined by the motor power and voltage and the number of heliostats. For these reasons, some fraction of the drive electrical and field wiring costs are associated with the 'three-halves power law' relationship and some are associated with the number of heliostats. For simplicity it is assumed that the drive electrical cost is evenly divided between the category for cost/area dependent on imposed moment and cost/area dependent on number of heliostats. With a given design, this simple approximation would be replaced with a more detailed allocation.

Cost/area for the field wiring is estimated by assuming that one-third of the cost is associated with the overall size of the field, irrespective of the number of heliostats or their size. In effect, the cost for trenching and installing the primary wiring is assumed to depend in part on field size. One-third is determined by the heliostat motor horsepower, and thus the imposed moment. One third is linear with the number of heliostats, since additional labor and electrical connections are required as the number of heliostats increases. This allocation is for illustration purposes; a more quantitative approach would be needed in a detailed cost study for a specific design.

Field alignment/checkout is assumed to consist of tasks involving electrical continuity, operation, and positioning the reflector to ensure the beam will meet the aim point on the receiver. A part of the cost/area for field alignment/checkout is assumed to involve costs that are essentially constant, irrespective of the number of heliostats. For example, the beam characterization system used at Solar One had four tower mounted targets, four field cameras in enclosures, processors, control interfaces to the master control, radiometers, and ancillary hardware and equipment. These types of costs are assumed to be essentially constant, and dependent primarily on the field size. It could be argued that some fraction of this cost is constant irrespective of heliostat size and number or irrespective of the field size, but for this representative analysis, this type of constant cost for the system is not considered. Such costs could be considered separate from any heliostat cost category, and more properly placed under a separate cost category, such as balance of plant or master control. The remaining

cost/area for field alignment/checkout is dependent on the number of heliostats, especially for initial alignment/checkout after installation. Again for simplicity, field alignment/checkout cost/area is evenly divided into Category 1 and Category 3. The latter effect can be assumed to represent primarily the labor to initially align an individual heliostat, which is assumed to be essentially the same irrespective of the heliostat size.

17.6 Cost analysis as a function of area: the case of the 148 m^2 Advanced Thermal Systems (ATS) glass/metal heliostat

17.6.1 Installed cost/area analysis

The cost breakdown from Kolb *et al.* (2007) is shown in Table 17.2 for both the stretched membrane and the ATS glass/metal heliostats. This table assumes 50,000 units/year, which corresponds to annually adding approximately 1 GWe.

Since the stretched membrane design is not a major contender at this time, and its costs are higher than the ATS design, it is shown for reference purposes but is not considered further. Table 17.3 shows the costs of the various heliostat items for 5,000 and 50,000 heliostats/year.

Table 17.2 Heliostat prices (2006 USD) given 50,000 units/year (from Kolb *et al.*, 2007)

	150 m^2 stretched membrane heliostat price per unit area ($)	148 m^2 ATS glass/metal heliostat price per unit area ($)
Mirror module	42.99	23.06
Support structure	19.08	21.21
Drive	26.67	27.11
Drive electrical	1.76	1.78
Controls	1.87	1.94
Pedestal	16.73	16.96
Total direct cost	109.11	92.06
Overhead/profit (20%)	21.82	18.41
Total fabricated price	130.93	110.47
Field wiring	7.30	7.40
Foundation	2.30	2.28
Field alignment/checkout	2.41	6.34
Total installed price	142.94	126.49

Table 17.3 Heliostat prices (2006 USD) for ATS heliostat at 5,000 and 50,000 units/year (from Kolb *et al.*, 2007)

Item	Cost/m^2 5,000/yr ($)	Cost/m^2 50,000/yr ($)
Gear drive	48.65	27.11
Mirror module	26.50	23.06
Torque tube assembly	11.85	10.78
Truss assembly	7.43	6.75
Cross bracing	4.04	3.68
Controls and cabling	2.09	1.90
Drive motors and limit switches	2.67	1.78
Pedestal	18.66	16.96
Fabrication and direct cost	121.89	92.02
Overheat/profit (20%)	24.38	18.40
Total fabrication cost	146.27	110.42
Foundation	2.56	2.33
Field wiring	8.14	7.40
Field assembly and checkout	6.97	6.34
Total installed cost	163.94	126.49

The reason stated in Kolb *et al.* (2007) for the 20% overhead/profit on the bare production cost of the fabricated mirror module and structure components was 'to account for the business needs of the heliostat manufacturer.' Rather than apply the overhead and profit only to the bare production or direct costs, a revised version of this cost breakdown is used herein with this factor applied to the total cost, as shown in Table 17.4. This results in a slightly higher total installed price of $129.71 for 50,000 units/year and $167.41 for 5,000 units/year, but this is only for the purposes of this analysis. The issue of whether this price reflects realistic overhead rates and profit is not addressed.

The cost/area for the 148 m^2 ATS heliostat (Kolb *et al.*, 2007) is distributed into the three cost/area categories in Table 17.5 for both 5,000 and 50,000 units/year, including the 20% profit factor. The mirror module cost/area is in Category 1 as a constant value. One-third of the field wiring is in this category and one-half of the field alignment/checkout. The overhead/profit factor of 20% is applied for this category. Category 2 has the support structure, drive, one-half the drive electrical, one-half the controls, pedestal, one-third of the field wiring, and foundation; again, the overhead/profit factor of 20% is applied to this category. Category 3 has one-half the drive electrical, one-half of the controls, one-third field wiring, and one-half field alignment/checkout, with the overhead/profit factor of 20%. Other distributions for these categories can of course be easily selected; this could be determined for a particular design by its developer. The distribution used here is simply to illustrate the effect and provide insight into the importance

Table 17.4 Revised heliostat prices (2006 USD) with overhead and profit for total installed cost (from Kolb *et al.*, 2007)

Item	Cost/m^2 5,000/yr ($)	Cost/m^2 50,000/yr ($)
Gear drive	48.65	27.11
Mirror module	26.50	23.06
Torque tube assembly	11.85	10.78
Truss assembly	7.43	6.75
Cross bracing	4.04	3.68
Controls and cabling	2.09	1.90
Drive motors and limit switches	2.67	1.78
Pedestal	18.66	16.96
Fabrication and direct cost	121.89	92.02
Foundation	2.56	2.33
Field wiring	8.14	7.40
Field assembly and checkout	6.97	6.34
Installation cost (no overhead/profit)	17.67	16.07
Fabrication and direct + installation	139.56	108.09
Overhead/profit (20%)	27.91	21.62
Total installed cost	167.47	129.71

of Categories 2 and 3. The total cost for each component is not changed, it is simply distributed into the categories. Rationales for these distributions are provided below.

DOE (2009) defines a 150 m^2 baseline heliostat with a cost of \$211/m^2 as the baseline for cost analysis purposes; this cost is substantially higher than that from Kolb *et al.* (2007) of \$126.49/m^2 for 50,000 units/year, or the revised cost of \$129.70/m^2 shown in Table 17.2. This difference may be due in part to the lower expected production rate for first plants, as well as other factors, such as inflation between 2006 and 2009–2010, or perhaps a higher profit and overhead, etc. However, since that cost breakdown is not available, the results from Kolb *et al.* (2007) are used to develop a parametric relationship for total cost/area. It appears that the referenced costs on an annual basis are considered to be constant for these two production rates and do not decrease further due to additional 'learning curve' effects.

Now consider the costs for the 5,000 units/year case as shown in Table 17.5. The Category 1 cost/area is constant at \$39.24/m^2. The Category 2 cost/area varies as the square root of the area. Thus, Category 2 cost/area = $KA^{1/2}$.

Consider the drive electrical, controls, and field wiring associated with the ATS heliostat; the total, with overhead/profit, is 1.2(2.67 + 2.09 + 8.14) = \$15.48/m^2. For the 148 m^2, this is \$2,291. It is hard to justify that a cost this high could be associated solely with the heliostat, irrespective of its size. That is why these costs are distributed as shown in Table 17.5.

Table 17.5 Cost/area for heliostat elements distributed into three categories for 5,000 and 50,000 units/year, costs in 2006 USD (based on data from Kolb *et al.*, 2007)

Allocation for 5,000 units/yr	148 m^2 ATS glass/metal heliostat price per unit area	Category 1	Category 2	Category 3
		Costs/area that are constant irrespective of heliostat area or number of heliostats	Costs/area dependent on imposed moment	Costs/area that are constant for each heliostat irrespective of area (i.e., depend on number)
	($)	($)	($)	($)
Mirror module	26.50	26.50		
Support structure	23.32		23.32	
Drive	48.65		48.65	
Drive electrical	2.67		1.33	1.34
Controls	2.09		1.05	1.05
Pedestal	18.66		18.66	
Field wiring	8.14	2.71	2.71	2.71
Foundation	2.56		2.56	
Field alignment/checkout	6.97	3.49		3.49
Total installed cost/area	139.56	32.70	98.28	8.58
Overhead/profit (20%)	27.91	6.54	19.66	1.72
Total installed price/area	167.47	39.24	117.93	10.29
Fraction category to total cost 5,000 ATS 148 m^2 heliostats		0.234	0.704	0.061
Allocation for 50,000 units/yr				
Mirror module	23.06	23.06		
Support structure	21.21		21.21	
Drive	27.11		27.11	
Drive electrical	1.78		0.89	0.89
Controls	1.94		0.97	0.97
Pedestal	16.96		16.96	
Field wiring	7.40	2.47	2.47	2.47
Foundation	2.28		2.28	
Field alignment/checkout	6.34	3.17		3.17
Total installed cost/area	108.08	28.70	71.89	7.50
Overhead/profit (20%)	21.62	5.74	14.38	1.50
Total installed price/area	129.70	34.44	86.26	9.00
Fraction category to total cost 50,000 ATS 148 m^2 heliostats		0.266	0.665	0.069

Now, as an illustration of the size effect, consider the Category 2 costs in Table 17.5 and reduce the area from, say, the base line value of about 150 m^2 to 50 m^2; this decreases the Category 2 cost of \$117.93/m^2 by a factor of the square root of three, to \$68.09/m^2. Category 3 costs would be increased by a factor of three to account for having three times as many heliostats, and thus the \$10.29 would increase to \$30.87. The total cost/area would then be the sum of the Category 1, 2, and 3 costs, or \$39.24/m^2 + \$68.09/m^2 + \$30.87/m^2 = \$138.20/m^2, compared to the \$167.47/m^2 cost. This is a reduction of about 17.5%. Not yet included in this potential reduction are (1) the learning curve effect, which can be of the order of 5–10% cost reduction for each doubling in the number of units and (2) the optical improvement. These are treated in a following section. Also, this example was for illustration purposes; it is not the minimum cost. That is determined later below.

It is instructive to consider a second example, to illustrate that the heliostat cost/m^2 is highly sensitive to the fixed cost for an individual heliostat. Consider now that all of the drive electrical and controls in Category 3 are shifted into Category 2, leaving only one-third the field wiring and one-half of the field alignment/checkout in Category 3. This allocation is shown in Table 17.6. The rationale for moving more of the electrical costs from Category 3 into Category 2 is that this cost could be directly associated with a mass produced motor that requires only simple on-off controls and has embedded in it the position sensor; for example, this could be a stepper motor with automatic counts for position sensing.

Repeating the same approach as used in the first example, we assume again that the heliostat is 50 m^2, and thus the cost/area for Category 2 is reduced (122.80/$3^{1/2}$), giving \$70.90/m^2. There are three times as many heliostats, and thus the Category 3 cost increases to 3 * 5.44/m^2 = \$16.32/m^2. The total cost for the three categories is \$39.24/m^2 + \$70.90/m^2 + \$16.32/m^2 = \$126.46/m^2. Now the reduction in cost, compared to the base line cost of \$167.47, is about 24.5%.

A third example is provided in Table 17.7. Note that in all cases the costs for the ATS heliostat from Kolb *et al.* (2007) have not been reduced; they have simply been allocated into the three categories with different assumptions. The primary difference is in the relative amount of costs that are essentially fixed for each heliostat, irrespective of its size, which are moved into another category. Rather than repeat the illustration, the general results are plotted in Fig. 17.8, using the fractional costs associated with each category, and applying the same size and number corrections. A family of curves is obtained for these three examples. This family of curves shows that the minimum areas range from about 25 m^2 at \$115/m^2, to 35 m^2 at \$128/m^2 to 50 m^2 at \$138/m^2. Note that these costs do not include optical improvements achievable with smaller heliostats, or the manufacturing learning curve benefit, nor do they include the additional O&M costs. The

Table 17.6 Cost/area for heliostat elements distributed into three categories with lower costs in Category 3

Allocation for 5,000 units/yr	148 m^2 ATS glass/metal heliostat price per unit area	Category 1	Category 2	Category 3
		Costs/area that are constant irrespective of heliostat area or number of heliostats	Costs/area dependent on imposed moment	Costs/area that are constant for each heliostat irrespective of area (i.e., depend on number)
	($)	($)	($)	($)
Mirror module	26.50	26.50		
Support structure	23.32		23.32	
Drive	48.65		48.65	
Drive electrical	2.67		2.67	
Controls	2.09		1.05	1.05
Pedestal	18.66		18.66	
Field wiring	8.14	2.71	5.43	
Foundation	2.56		2.56	
Field alignment/ checkout	6.97	3.49		3.49
Total installed cost/ area	139.56	32.70	102.33	4.53
Overhead/profit (20%)	27.91	6.54	20.47	0.91
Total installed price/ area	167.47	39.24	122.80	5.44
Fraction category to total cost 5,000 ATS 148 m^2 heliostats		0.234	0.733	0.042

results indicate that even with no reduction in the 'fixed' costs associated with the baseline heliostat, there is a substantial reduction in costs from the size-dependent loads effect. The cost reductions range from about 18 to 31% for these examples, again without the learning curve, optical performance effects, or O&M.

Figure 17.8 illustrates that simply re-allocating the costs associated with Category 3, *without directly reducing them for the base line ATS heliostat*, has a leveraging effect on the total heliostat cost/area reduction. Part of this reduction is through the size and load effect in Category 2, but much of the

Table 17.7 Cost/area for heliostat elements distributed into three categories

Allocation for 5,000 units/yr	148 m^2 ATS glass/metal heliostat price per unit area ($)	Category 1 Costs/area that are constant irrespective of heliostat area or number of heliostats ($)	Category 2 Costs/area dependent on imposed moment ($)	Category 3 Costs/area that are constant for each heliostat irrespective of area (i.e., depend on number) ($)
Mirror module	26.50	26.50		
Support structure	23.32		23.32	
Drive	48.65		48.65	
Drive electrical	2.67		2.67	
Controls	2.09		2.09	
Pedestal	18.66		18.66	
Field wiring	8.14	2.71	5.43	
Foundation	2.56		2.56	
Field alignment/ checkout	6.97	3.49		3.49
Total installed cost/ area	139.56	32.70	103.38	3.49
Overhead/profit (20%)	27.91	6.54	20.68	0.70
Total installed price/ area	167.47	39.24	124.05	4.18
Fraction category to total cost 5,000 ATS 148 m^2 heliostats		0.234	0.741	0.025

reduction results from the allocation of some of the Category 3 costs into Category 2. In principle, as Category 3 costs approach zero, dependence of Category 2 costs on the square root of the area forces the area, and hence cost for this category, to zero, leaving only the Category 1 constant cost/m^2 of about $39.24. This is of course unrealistic, but it does point to the potential of minimizing the total heliostat cost by minimizing the Category 3 costs, both by direct reduction and by allocating these costs properly. The key is to reduce costs that are essentially independent of the number or size of the heliostat, such that better advantage can be taken of the 'three-halves

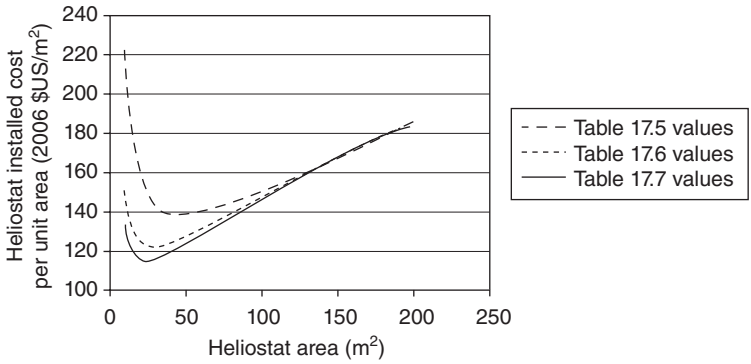

17.8 Heliostat hardware cost/area vs area for various allocations of ATS costs as shown in Tables 17.5, 17.6 and 17.7.

power law' effect. These costs are typically associated with the electronics for the processor, limit switch, motor electronics, position sensors, etc.

What is important about the Fig. 17.8 family of curves is that they illustrate how strong an effect 'fixed' costs per heliostat have on the total cost, even if some of these costs (here, for the ATS design) are not decreased directly, but more appropriately reallocated into Category 2. The combination of the 'three-halves power law' effect in Category 2 in combination with reducing the costs for the increased number of heliostats for Category 3 results in a substantially smaller heliostat area having the minimum cost/m^2.

The purpose of the analysis presented above was to use the well-established SNLA installed hardware costs for the US ATS baseline heliostat in order to assess the effect of size on heliostat hardware installed cost. The analysis illustrates that, based on this parametric analysis, simply reducing the size leads to substantial hardware installed cost reductions. The above analysis is also conservative, in several respects. It does not consider the aerodynamic coefficients for non-uniform, more realistic wind speed distributions (Colorado State University, 1987), which result in an area dependent exponent of the order of 0.6 to 0.7, not 0.5; this larger exponent further increases the impact of reducing the heliostat size on decreasing the cost per unit area. The above analysis also neglects the optical and manufacturing learning curve effects and it does not include the O&M effects. One concern of the heliostat developer is that the larger number of smaller heliostats would lead to unacceptably high O&M costs. This, too, may be one of the reasons that larger heliostats have been preferred over the last several decades. In the following, these are all incorporated into a parametric expression for the heliostat cost per unit area as a function of area, for the same total thermal power level.

17.7 Additional considerations in analysis of cost as a function of area for the 148 m^2 Advanced Thermal Systems (ATS) glass/metal heliostat

17.7.1 Operations and maintenance

O&M has several effects associated with size and number of heliostats. O&M can involve costs that increase with the number of heliostats, decrease, or remain constant. Some O&M costs are determined primarily by the size of the plant and are not directly related to the heliostat size. For example, to first order, the number of technicians and logistics personnel required is primarily a function of the plant size, but there may be a larger number of these required for a field of small heliostats with a substantially larger number of units compared to essentially the same output power from a field of large heliostats.

It should be noted, however, that the net present value of O&M costs must be a relatively small part of the total installed cost, or the solar central receiver cannot be cost effective. With cost factors such as these unknown, or difficult to determine analytically, it is still instructive to include their effect parametrically. We treat this O&M uncertainty by assuming that it is relatively small for a competitive solar plant and that these O&M costs will be included parametrically as part of the installed costs. With this approach, the heliostat developer can use a specific detailed cost study for a specific design to estimate the effect of increasing or decreasing the heliostat size.

O&M is usually added to the overall system cost as a net present value (NPV) for the LCOE or as a NPV for the stacked cost of the total system 'installed'. For a parametric analysis of the total costs associated with the heliostat, a different approach is helpful. In order to allocate the total installed cost into the three categories, the NPV for O&M must be determined on a per unit area basis. There are no validated data for O&M for a heliostat field, and few examples. However, in correspondence with NREL (Turchi, pers. comm., 2010) a method has been developed that can be used for parametric purposes. The NPV of the O&M for a central receiver has been estimated and is shown in Table 17.8. The data below (and prior chart) are from the System Advisory Model for a wet-cooled tower case.

For this plant, the NPV of the O&M is of the order of $101 m, or about 14.3% of the total plant cost. Considering the hardware costs associated with the storage, balance of plant, heliostat, tower, receiver, and power plant, this total is about $398,000,000. The heliostat cost is about 49% of this cost. This example illustrates that the assumption that the heliostat cost is about 50% of the total system installed hardware cost is a reasonable estimate. The various financial costs (contingency, indirect, insurance, and taxes) are assumed to be proportionally distributed among the hardware

Table 17.8 System Advisory Model (SAM) levelized cost of energy for wet-cooled 100 MWe Rankine cycle tower case

Site cost ($)	19,294,200	2.7%
Storage cost ($)	46,588,200	6.6%
Balance of plant cost ($)	37,950,000	5.4%
Heliostat cost ($)	193,907,000	27.5%
Tower cost ($)	12,449,000	1.8%
Receiver cost ($)	44,310,900	6.3%
Power plant cost ($)	63,250,000	9.0%
Contingency cost ($)	41,775,000	5.9%
Indirect cost ($)	113,503,000	16.1%
Present value of O&M ($)	101,206,000	14.3%
Present value of Ins. and Prop. Tax ($)	31,468,400	4.5%
	705,701,700	

From Turchi, pers. comm. (2010).

and O&M costs. The O&M cost is therefore distributed essentially equally among the hardware elements, and thus about half of the O&M is allocated to the heliostat. However, it should be noted that this approach does not address the likely wide variation in O&M costs that are associated with the different subsystems. Different O&M costs can be used in detailed design studies, but for simplicity, this simple allocation based on capital costs is used. To first order then, the NPV of the O&M is approximately 7.15% of the installed hardware cost for the heliostat, before the various contingency factors are applied. Thus, this value is used with the equivalent installed hardware cost values from the Kolb *et al.* (2007) study. Note that the installed hardware costs from this study also do not have these contingency factors. This approach is taken for consistency in the comparisons that follow below. For the 5,000 units/year case, with $\$167.47/m^2$, the 7.15% O&M is thus $\$11.97/m^2$. This O&M cost per unit area is then added to the installed cost of the hardware for the base line SNLA ATS heliostat. The total cost is $\$167.47/m^2 + \$11.97/m^2 = \$179.44/m^2$.

Next, this O&M cost is allocated into the three categories. The allocation here is primarily as an example, since there are few data available to enable this allocation to be made accurately. Again, a more detailed design study would address this allocation. However, it is apparent that much of the O&M cost for a solar field is associated with activities such as general and administrative (G&A) costs and overheads. These activities include supervisory/management roles and responsibilities, including O&M oversight, review, approval, work scheduling, permitting, codes and standards, certifications, training, safety (and associated processes, procedures, equipment, etc.), personnel (records, evaluations, time sheets, HR issues, etc.), regulatory compliance, audits, business operations (e.g., cost accounting,

invoicing, contracts/sub-contracts, reports, etc.), data acquisition and archiving, etc.

O&M activities typically involve 'hands-on' activities, such as heliostat control, washing, and remove and replace and/or repair of components that have failed or are scheduled for replacement. O&M may also involve periodic inspections, safe work practices (lock out/tag out, interlocks, etc.), decontamination of soil due to spills (wash solution, lubricants, etc.). O&M also involves logistics/spares/inventory control for equipment and tools, upkeep/housekeeping, etc.

Overall, the majority of the O&M activities are likely associated with the size of the power plant. Some of the activities are associated with aspects that are related to the number of heliostats, irrespective of their size, and some are associated with the size of the heliostat. For example, the equipment to wash the heliostats will be in part a function of the heliostat size; larger wash trucks and longer booms are needed, for example, with larger heliostats, and vice versa. However, to first order, approximately the same reflector area must be cleaned, and therefore this part of the O&M cost is relatively insensitive to the heliostat size. Access to very small heliostats that are closely packed may be an issue, especially close to the receiver, but for heliostats as small as, say, 10 m^2, the minimum distance between rows would be of the order of about 7 m, to avoid contact along diagonals of the reflectors. This is more than enough space for wash trucks of the order of less than 3 m in width. Conversely, small heliostats such as e-Solar allow two rows to be washed per pass by facing one row rearward. Replacement of the motors/drive units for very large heliostats is somewhat harder than for small heliostats, and may require special tools, fixtures and lifting equipment, compared to more generic equipment for small heliostats, and simply removing such components by hand. Conversely, some of the time and labor associated with remove-and-replace operations is essentially constant, and with a greater number of units to remove and replace, there would be a greater total time and cost.

These are all aspects well beyond a parametric analysis and would also be associated with a particular design, time and motion studies, field experience, etc. Therefore, in order to provide some insight into the O&M impact on total installed cost, it is assumed that the same three categories are appropriate, and that the majority of the O&M costs are associated with the plant size and basic G&A and overhead functions, and are therefore relatively insensitive to the heliostat size and number. Thus, Category 1 O&M costs are estimated to be 60% of the total O&M. Category 2 and 3 are then assumed to be equal, with 20% each. The O&M cost per unit area value of \$11.97/m^2 is thus assumed to be 60% or \$7.18/m^2 for Category 1 and 20% or \$2.39/m^2 for each of Categories 2 and 3. These values are added to the installed cost for the base line heliostat. The corresponding

percentages of O&M relative to the total cost per unit area of \$179.44/m^2 are:

- Category 1 O&M = 4%
- Category 2 O&M = 1.3%
- Category 3 O&M = 1.3%.

These values are used to estimate the cost per unit area as a function of area, together with the other effects, such as optical performance and learning curve. Note, however, that in keeping with the basic assumptions used by Kolb *et al.* (2007) to develop an installed hardware cost per unit area, the additional financial costs that are used to develop a complete LCOE are not considered here; that is more properly conducted as a more detailed cost analysis for a particular plant design.

17.7.2 Optical performance

In principle, there is some loss in optical performance with larger heliostats for given receiver size. This is primarily due to direct spillage from the larger reflected beams with a given tracking/beam error and by having greater off-axis aberration losses. This effect results in greater total field reflector area with larger heliostats, compared to smaller heliostats, for the same power incident on the receiver. This reduction in heliostat area directly improves the system cost of the plant with a given receiver because the increase in optical performance increases the total annual energy. Secondary improvements can also occur with smaller heliostats. For example, having a receiver with a lower mass and area, and thus lower cost, coupled with a lower mass and cost tower can result from this change. There would also be some slight performance improvement in the receiver, since there would be less radiation and convective loss for the smaller area, assuming the same surface temperature. Since the receiver and tower costs are of the order of about 8% of the total plant cost (or about 14% of the hardware installed cost), some slight improvement in cost can occur from these effects. However, these effects are not considered here.

Direct optical performance effects are treated by Kolb *et al.* (2007) for a representative field. DELSOL was used to determine the total field reflective area for the same annual absorbed power as for the base line case of a 150 m^2 heliostat, at a cost of \$150/m^2. A linear fit to the data for field area was determined as:

$$\text{Field area} = 75.7 * (\text{heliostat area in m}^2) + 229{,}359\ \text{m}^2. \qquad [17.13]$$

Expressing this as a ratio, or correction factor, F, the field area for a given heliostat area, $A_{\text{heliostat}}$, compared to that for the base line heliostat is:

$$F = 75.7A_{\text{heliostat}} + 229,359/240,714$$
$$= 0.000314A_{\text{heliostat}} + 0.953. \quad [17.14]$$

For very small heliostats, Eq. [17.14] shows that the total field area is about 5% less than for the base line heliostat case. This small optical correction factor will be used in the parametric estimate for the total heliostat cost as a function of area.

17.7.3 Learning curve effects

The effect of so-called 'learning', 'experience', or 'progress ratio' curves can have a significant impact on the costs. This effect is especially important for production of the first central receiver system, since the startup costs associated with a production plant must be borne in large part by the first power plants under contract. In addition, there is a diminishing return aspect; it becomes more difficult to continually reduce the costs beyond a certain minimum value, if for no other reason than the tendency of this curve to asymptotically approach the cost of the raw materials. These 'learning curve' effects need to be considered in the aggregate, not just for the *n*th heliostat, because the market must pay for the first, relatively high cost plant, and thus the initial costs for startup production and the relatively high costs for the first heliostats are important considerations.

The learning curve is typically expressed as the cost, $C(n)$, of the *n*th unit in terms of a learning curve fraction, f, raised to the power of the number of doublings (the learning curve is based on number of units produced rather than m^2 produced). The importance of this is seen by an example. Assume that the number of smaller heliostats produced is of the order of four times that of the larger, for the same total reflective area in the field. For example, having a 37 m^2 heliostat, compared to the base line 148 m^2 ATS heliostat, would potentially have a substantial cost reduction just from the increased production. Since a 90% learning curve corresponds to a 10% reduction in cost as the number of units is doubled, then the total cost of the *n*th smaller heliostat would be reduced to 0.9^2 times the first unit cost on a per unit area basis. The overall field cost reduction due to this effect is determined by the appropriate expression for the total cost for all heliostats, not just as comparison between the *n*th unit cost for different numbers of units. This approach follows.

Consider first the number of doublings, n, and the total number of units, N. A typical expression for the cost of the unit, $C(N)$, corresponding to the number of units is given as $C(N) = C(1)f^n$, where $C(1)$ is the cost of the first unit. Expressed in terms of $n = \log_2(N)$,

$$C(N) = C(1)f^{\log_2(N)}. \quad [17.15]$$

For, say, two doublings, with a 90% learning curve, $C(8) = C(1)(0.9)^{\log2(4)} = C(1)(0.9)^2$, as in the example above.

For the parametric analysis, the learning curve effect for N heliostats, based on the price for the 5,000th heliostat, is the ratio of these expressions from Eq. [17.15]:

$$C(N)/C(5{,}000) = f^{\log 2(N)/\log 2(5{,}000)}. \quad [17.16]$$

The cost for the 5,000 units/year is shown by Kolb *et al.* (2007) to be \$164/m^2. As shown in Table 17.4, a somewhat higher value of \$167.47 m^2 is used, with slight modifications due to having the overhead and profit applied to all of the heliostat cost. It appears that the Kolb *et al.* (2007) value is for the cost for the 5,000th unit. However, the first unit cost has to be \$611/m^2 to have \$167.47 for the 5,000th heliostat, assuming a 90% learning curve. Programming the above expression into a simple spreadsheet, the total cost for the first 5,000 units is \$146,043,000, with an average cost per unit area of \$197.36/m^2. (Note also that this value is much closer to the DOE value of \$211/m^2, and may be part of the reason for the cost differences noted above.) In principle, producing a larger number of smaller heliostats, of the same basic design, should result in a cost saving. To first order, for the example shown above for the 37 m^2 heliostat, the total cost reduction, based on learning curve effects could be estimated to be about 19%, or \$27,748,816.

Figure 17.9 shows the average cost per unit area of a heliostat, based on the ATS heliostat and assuming a 90% learning curve. This curve is obtained from a spreadsheet that sums and averages the cost of each heliostat; a trend-line gives this cost per unit area to very good agreement, with an R^2 value of essentially 1. The same reduction of 10% occurs for the average cost as the number is doubled as for the nth unit cost. The use of the average cost is more appropriate for determining the cost of a given size field.

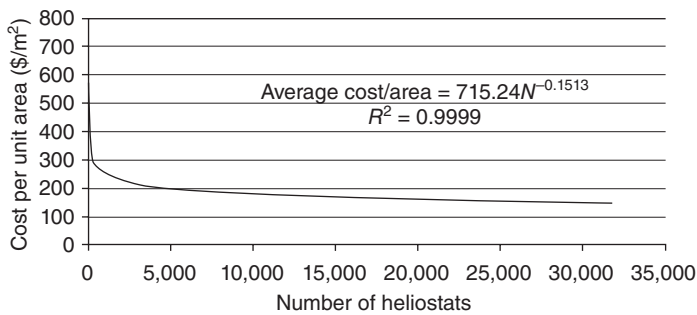

17.9 Average installed cost per unit area vs area for the SNLA/ATS heliostat. First unit cost = \$611/m^2, 5,000th unit cost = \$167.41/m^2, 90% learning curve.

However, this average cost is not used in the comparison costs, in part to be consistent with the values in Kolb *et al.* (2007).

The trend-line for the average cost per unit area for this case is:

$$C_{\text{average}}/A_{\text{heliostat}} = 715.24N^{-0.153}, \text{ in } \$/\text{m}^2. \quad [17.17]$$

Clearly, just on the basis of potential learning curve cost reductions, size effects are significant, especially for the early plants.

However, it is important to distinguish the learning curve effect that is used for the number of heliostats with that for a total increase in the quantity. The cost per unit area decreases for a given total field reflector area, if more heliostats are produced, *but only for those parts of the heliostat that benefit from the learning curve effect*. As noted earlier, the mirror module cost/area, for a given quantity or field reflector area, is essentially constant. Therefore, the learning curve effect of smaller heliostats (but a higher number) should only be applied, for a given field area, to hardware costs that can be reduced by increasing the production number. Thus, reductions would not be included for Category 1 (i.e., the mirror modules and a few other costs), but would be included for Category 2 and 3 costs.

The consideration now is how to apply all of these effects:

- cost categories
  - Category 1: constant costs per unit area, for a given field area,
  - Category 2: cost per unit area reductions due to decreased heliostat size, and
  - Category 3: fixed costs irrespective of heliostat size that increase as heliostat size decreases and the number increases;
- O&M effects (distributed into the appropriate categories);
- optical performance improvements that can reduce the heliostat field area; and
- learning curve effects.

Finally, it was noted earlier that the 'three-halves power law' corresponds to a uniform wind speed, whereas Colorado State University (1987) shows that the wind speed varies with height and turbulence effects such that the aero-coefficients for wind load are higher. Thus, instead of moment per unit area varying as $A^{0.5}$, it varies as approximately $A^{0.65}$. The larger exponent makes larger heliostat moment per unit area for structure, drive units, etc., even higher, and thus cost per unit area increases more rapidly with size increases, and vice versa.

All of these effects are now combined, using the same basic assumptions on costs as given in Kolb *et al.* (2007), to produce plots of the overall cost per unit area as a function of area. Again, only the 5,000 heliostat/year case is considered.

First, the assumptions used in Table 17.5 are followed, but with various revisions. The cost per unit area for Category 1, $C_{\text{cat 1}}$, from Table 17.5 is \$39.24/m^2; to this is added the O&M cost of \$7.18/m^2, giving:

$$C_{\text{cat 1}} = \$46.42/\text{m}^2. \quad [17.18]$$

The cost for Category 2 is the sum of that from Table 17.5, \$117.93, plus the O&M cost determined above of \$2.39/m^2, giving \$120.32/m^2. This Category 2 cost per unit area, $C_{\text{cat 2}}$, is used to determine the cost per unit area based on heliostat area, $A_{\text{heliostat}}$, relative to that for the ATS heliostat, using the expression:

$$C_{\text{cat 2}} = \$120.32/\text{m}^2\,(A_{\text{heliostat}}/148)^{0.65}. \quad [17.19]$$

For a 37 m^2 heliostat, the Category 2 cost is reduced to \$48.87/m^2, using the wind speed exponent of 0.65 for a variation in speed with height, compared to \$60.16 if the constant wind speed exponent of 0.5 were used.

Category 3 cost per unit area, $C_{\text{cat 3}}$, is determined from the number of heliostats, but with the correction for the slight reduction in number due to improved optics for the same total thermal power incident on the receiver. First, from Table 17.5, assuming the plant size corresponds to 5,000 148 m^2 heliostats, the cost per unit area is added to the O&M cost per unit area of \$2.39/m^2 giving, for the ATS 148 m^2 heliostat, $C_{\text{cat 3}}$ = \$10.29/m^2 + \$2.39/m^2 = \$12.68/m^2. Thus, the Category 3 total dollar value for the ATS 148 m^2 heliostat, including O&M, is \$1,876.64. For 5,000 ATS heliostats, the total Category 3 cost is \$9,383,200. In general, the number of heliostats, $N_{\text{heliostats}}$, is the field area divided by the heliostat area; the field area is reduced by the F factor from Eq. [17.14]. Thus, the F factor is used to modify the field area assumed here, 5,000 heliostats × 148 m^2 = 740,000 m^2, giving:

$$\begin{aligned} N_{\text{heliostats}} &= 740{,}000F/A_{\text{heliostat}} \\ &= 740{,}000(0.000314A_{\text{heliostat}} + 0.953)/A_{\text{heliostat}} \end{aligned}$$

or,

$$N_{\text{heliostats}} = 232 + 705{,}220/A_{\text{heliostat}}. \quad [17.20]$$

The number of 37 m^2 heliostats would be 19,280, somewhat less than the 20,000 using just the area ratio. The Category 3 costs are increased as the heliostat area is reduced. The Category 3 cost for this example is 19,280 ∗ \$1,876.64 = \$36,181,619, almost four times that for the ATS total cost. The cost per unit area using this total cost is given as \$36,181,619/(19,280 ∗ 37) = \$50.72/m^2; it is also simply the total dollar value cost for the ATS heliostat, divided by the heliostat area. Thus, Category 3 cost per unit area is given by:

$$C_{\text{cat 3}} = \$12.68(148/A_{\text{heliostat}}), \text{ in } \$/\text{m}^2. \quad [17.21]$$

The total cost for a 37 m^2 heliostat, for Category 1, 2, and 3, is \$46.42/m^2 + \$48.87/m^2 + \$50.72/m^2 = \$146.01/m^2. This is 18.6% less than the 179.44/m^2 cost for the ATS heliostat, obtained by adding the O&M NPV cost per unit area to the installed hardware cost of \$167.44/m^2.

Now consider, for this example, the manufacturing learning curve effect. For the 37 m^2 heliostat, there are about four times as many heliostats that are produced for this first plant; these two doublings correspond to a reduction of $0.9^2 = 0.81$ for the nth heliostat. This factor is applied only to Categories 1 and 2, now giving a total heliostat cost per unit area of \$46.42/m^2 + \$39.58/m^2 + \$41.08/m^2 = \$127.08/m^2. With learning curve included, as well as optical performance effects, the total heliostat installed cost is reduced by 29.2%. This is a representative example, but it is not the minimum. Also, in this example, the cost from Kolb *et al.* (2007) is essentially assumed to be constant for the 5,000 heliostats; at this point, cost is not the average over the n heliostats, as shown in Eq. [17.17] and Fig. 17.8. The same basic approach used in Kolb *et al.* (2007) is retained at this point such that the comparison can be consistent, and determined primarily by the costs in each category, together with the optical effect correction factor and the learning curve applied to the nth heliostat.

Now the same basic approach used to generate the family of curves in Fig. 17.7 is followed, but with the revised cost per unit area values based on Eqs [17.16] and [17.18]–[17.20]. Using the values in Tables 17.5, 17.6, and 17.7, and adding to the appropriate category the allocated O&M gives a series of values. These values are then revised on the basis of the aero-coefficient effect, with cost per unit area proportional to $A^{0.65}$; this revision is applied to Category 2 values. The optical effect on the field area is applied to determine the number of heliostats for each area. The learning curve effect (e.g., Eq. [17.16]) is applied to Categories 2 and 3, since, for a given size field and intercepted power at the receiver, or approximate total reflector area, the glass cost is essentially constant. The resulting values are shown in Fig. 17.10.

The results shown in Fig. 17.10 include several factors not included in Fig. 17.8. The effect of the higher exponent for the loads effect, the learning curve, and the relatively small effect from the improved optics combine to produce a range of minimum cost heliostat areas that varies from about 25 m^2 to 40 m^2. These are based on the ATS cost data, allocated into the three categories delineated in Tables 17.5, 17.6 and 17.7, with the addition of the O&M costs. The results shown in Fig. 17.10 for the minimum cost condition are slightly lower than those shown in Fig. 17.8, even though O&M costs are included. By far the most important effect is from Category 2 the moment, weight, and cost per unit area and the dependence on area to an exponent of either 0.5 or 0.65. The leveraging effect of allocating some of the costs associated with Category 3 into Category 2 is notable. This

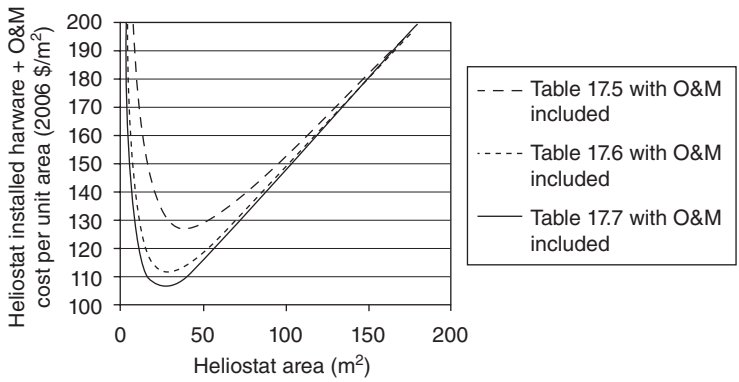

17.10 Heliostat hardware cost/area vs area for various allocations of ATS costs, with no reduction in cost/area for each heliostat component. O&M allocation, optical effect, and learning curve included.

effect shows that a means for reducing overall heliostat costs is to reduce the costs that are essentially fixed, irrespective of heliostat size. In the above cases, the total costs for the ATS heliostat components were not reduced, they were simply reallocated. This conservative approach shows that there may be further reductions in heliostat cost per unit area that result from decreasing the fixed costs in Category 3 relative to the ATS results. These would be associated with smaller heliostats. Designs that can achieve substantial cost reductions for position sensing, controller logic, and other costs that are essentially independent of heliostat size will have an important impact through the combination of cost dependence on moment, together with optical performance and learning curve.

It should be noted that the results of Figs 17.8 and 17.10 are based on changing the size of an assumed basic design (ATS). It would be unrealistic to build such a design down to sizes of just a few m^2 and so the values at the extreme high gradient section of these curves at the small size end of the spectrum are not meaningful, it is the position of the optimal point that is of most interest. Alternative designs, such as very small ganged heliostats, will likely have different cost allocations. They could be analyzed to find their optimal size in a similar manner.

17.8 Conclusion

The parametric analysis that has been presented indicates that carefully considering heliostat size is an important aspect of reducing overall LCOE. This type of parametric analysis can be used by the heliostat developer to

find the area resulting in the minimum cost per unit area for any particular design. The effect of applying this type of analysis has a significant impact on heliostat cost. In the specific case analyzed, the cost per unit area reductions for the minimum cost areas (25–40 m^2), compared to the cost for the base line area (148 m^2), are of the order of 30–40% The total installed cost, including NPV of the O&M, for the base line heliostat is approximately \$180/m^2. For a field of 5,000 of these heliostats, the cost would be \$133 m. A cost reduction of the order of 30–40% is approximately \$40–53 m, for one plant. Although this analysis has been done in 2010 USD, the optimum areas and fractional cost improvements only depend on the initial allocation of costs to categories and so are independent of time and currency.

If a heliostat with major design differences to the baseline ATS design were examined using the same approach, different optimum areas would no doubt result. Similar size-based cost optimizations could be applied to the solar field elements of troughs, dishes or linear Fresnel systems, with expected additional insights into the appropriate sizes for these designs.

17.9 References

Baumeister, T. and Marks, L.S. (1967), *Standard Handbook for Mechanical Engineers*, 7th edn, McGraw-Hill, New York.

Blackmon, J.B. (2008), 'Tri-Lateral Noor al Salaam High Concentration Solar Central Receiver Program', Final Report, March. Conducted under DOE Grant Number DE-FC36-02GO12030, DOE Golden Field Office, Beth H. Dwyer, Contract Officer.

California Energy Commission (2007), Ivanpah Solar Electric Generating System 2007-AFC-05 (PR announcement on the web in 2007).

Colorado State University (1987), 'Mean and Peak Wind Load Reduction on Heliostats'. Colorado State University, September. Subcontract XK-6-06034-1. SERI/STR-25303212. DE-87012281.

Dietrich, J.J., Knowles, R.K., Stone, K.W., Steinmeyer, D.A. and Nourse, J.H. (1982), 'Optimization of the Second Generation Heliostat and Specification', SAND 82-8181, May. Contract DE-AC0476DP00789.

DOE (2009), DOE Financial Assistance Funding Opportunity Announcement, Baseload Concentrating Solar Power Generation, DE-FOA-0000104, CFDA Number 81.087, issued July 15, 2009.

Falcone, P.K. (1986), *A Handbook for Solar Central Receiver Design*, Sandia National Laboratories, Albuquerque, NM.

Holdren, J.P. (2010), 'Science & Technology Priorities and Policies in the Obama Administration'. Remarks for The Council of Science Society Presidents, Washington DC, 3 May.

Jones, S. (2006), 'Heliostat Cost-Size Relationships'. Sandia National Laboratories, July.

Kolb, G. (2006), 'Brief History of USA Heliostat Development', June. Sandia National Laboratories.

Kolb, G.J., Jones, S.A., Donnelly, M.W., Gorman, D., Thomas, R., Davenport, R. and Lumia, R. (2007), 'Heliostat Cost Reduction Study', Sandia Report SAND2007-3293, June.

Winter, C.J., Sizemann, R.L. and Vant-Hull, L. (1990), *Solar Power Plants*, Springer Verlag, New York.

18

Heat flux and temperature measurement technologies for concentrating solar power (CSP)

J. BALLESTRÍN, CIEMAT – Plataforma Solar de Almería, Spain and G. BURGESS and J. CUMPSTON, Australian National University, Australia

Abstract: Heat flux and temperature are two fundamental quantities to be determined in the design of solar receivers for concentrating solar power (CSP) plants. Heat flux measurement allows the determination of the efficiency of solar receivers; a range of radiometers and calorimeters have been developed for this purpose. To provide accurate spatial resolution, the camera target approach has been widely applied by concentrating solar thermal (CST) R&D groups. Temperature measurement is also very important; contact thermometry of solar irradiated material surfaces has limitations at very high temperatures, and infrared measurement is the most reliable alternative. However, reflected solar radiation can be an important source of error in this non-contact methodology. This chapter presents some of the most modern systems to measure both heat flux and temperature.

Key words: heat flux measurement, radiometer, calorimeter, temperature measurement, pyrometer, infrared camera, solar blind.

18.1 Introduction

CSP plants collect solar radiation using reflective or transmissive optical elements that concentrate the radiation to a focal region where it is directly converted into thermal or electrical energy. Concentrating solar thermal (CST) systems perform the task by collecting the concentrated solar radiation in a high temperature receiver. This receiver should be designed to maximise thermal efficiency, defined as the ratio of the thermal power absorbed by the receiver to the incident radiant power falling on the receiver aperture (Carasso and Becker, 1990). This is done by minimising thermal losses from the receiver due to conduction, convection, and radiation (further comprising reflection and re-radiation). The basic trough, linear Fresnel, tower and dish concentrator types are covered in detail in Chapters 7, 6, 8 and 9, respectively. The basic principles around thermal losses and performance are covered in Chapter 2.

The design and characterisation of such receivers involve gathering detailed knowledge on heat transfer pathways into and out of the receiver and the heat transfer fluid (HTF). Firstly, receiver geometry will be determined by the spatial variation and extent of incident solar flux within the region of maximal focus, otherwise known as the focal region, where the receiver will be placed. To do this, it is desirable to obtain accurate and spatially detailed profiles of the solar flux within the focal region. Flux profiles are also important for determining concentrator performance. Optical concentration ratios range from around 80 : 1 for linear systems up to around 20,000 : 1 for high accuracy point focus systems. This translates to flux levels from 80 kW/m^2 up to 20,000 kW/m^2.

Radiometers and fluid-heating calorimeters are basic devices that can be used for direct measurement of incident heat flux in a particular location within the focal region, incorporated in ways that depend on the type of concentrator and the level of solar concentration. Alternatively, indirect measurement of solar flux is performed using remote cameras and reflective targets that are placed within the focal region for detailed images of the flux profile, sometimes calibrated using direct flux measurement with radiometers. Ray tracing based on measurements of concentrator surface topology can also be used to create simulated flux distributions, which can be used for further analysis.

Once a receiver is installed, thermometry can provide temperatures that aid in characterising the performance of the receiver. Contact methods have limitations so appropriate pyrometers and infrared cameras are used to determine temperatures and heat losses due to radiation. In advanced applications, receiver temperatures in excess of 1,000°C are encountered.

These tasks can present significant challenges to the engineer, particularly when working with high solar concentrations and high temperatures that can damage materials placed within the focal region. As such, the objective of this chapter is to provide a summary of techniques and existing technologies that have been used in obtaining flux profiles for different concentrator types.

18.2 Heat flux measurement

Concentrated flux is measured to determine the total amount of energy incident on a receiver aperture, or to examine the detail of the spatial distribution of the focal region flux. The most common approaches to flux measurement (sometimes known as flux mapping) are: the use of radiometers, calorimeters and photographic analysis of focal region images on diffusely reflecting targets, also known as the camera-target method. Flux distributions can also be modelled through characterisation of the concentrator surface and ray tracing of solar radiation reflected from it.

18.2.1 Radiometers

Radiometers are instruments that have an electrical response that varies with the incident radiation, in this case the concentrated solar flux. In CST applications, they are installed directly in the focal region and provide a single spatial point of measurement. Such devices detect radiation using either thermocouples or photodiodes. The current produced by a photodiode is proportional to the incident flux of photons, enabling direct measurement of solar flux over the area of the detector. A thermocouple is a junction between two conductors that converts a temperature difference into a potential difference via the thermoelectric effect. In a radiometer application, one of the conductors is joined to a heat sink that is held at a constant temperature, while the other conductor receives radiation.

Gardon and Kendall radiometers are commercially available designs suitable for detection of concentrated solar flux. A comparison between the Gardon and Kendall radiometers and the SUNCATCH calorimeter (described below) determined that the Kendall radiometer was the most reliable of the three (Kaluza and Neumann, 2001). As such, the Kendall radiometer is sometimes used for calibration of other radiometers and calorimeters. Gardon radiometers have the advantages of a wider angle of acceptance, a small size, mechanical robustness, and a faster response time than the Kendall radiometer (Hernandez *et al.*, 2006; Ballestrín *et al.*, 2006), but their accuracy is typically ±3%.

Gardon radiometer

The Gardon type radiometer (Gardon, 1953) is often used for measuring concentrated solar flux because of its robustness and simplicity. The transducer of this sensor is a differential thermocouple measuring the temperature difference between the centre and the circumference of a thin circular foil disk. The disk is bonded to a circular opening in a cylindrical heat sink. The standard foil is made of constantan and the heat sink is copper (Fig. 18.1). These materials produce an output, which is directly proportional to the absorbed heat flux. This radiometer has a response time (1/e) of around half a second that limits the maximum acquisition rate to 1 Hz. The exposed face of the sensors is covered with a black coating (e.g., Zynolite® with 94% of emissivity). These water-cooled circular foil heat flux sensors are designed for applications with longer measurement times. The water flow continuously removes the absorbed heat.

Kendall radiometer

The Kendall radiometer was developed at NASA's Jet Propulsion Laboratories (JPL) primarily for the detection of solar intensity and is therefore

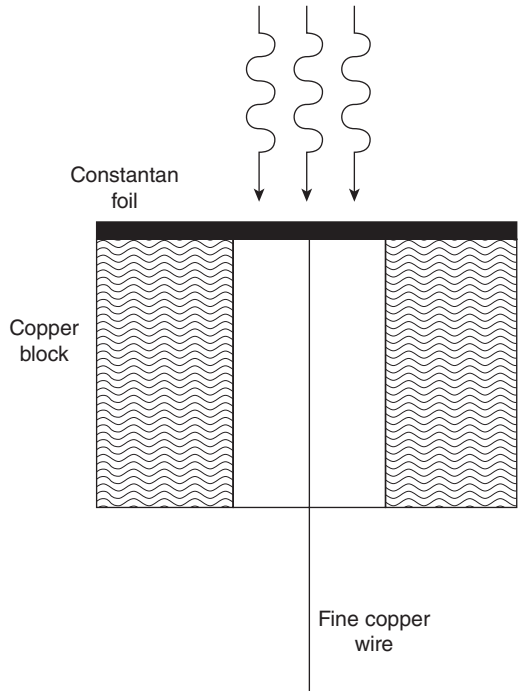

18.1 Gardon radiometer.

accurate for wavelengths corresponding to the solar spectrum (Kendall and Berdahl, 1970). The incident solar radiation is directed into a cavity that is coated with a highly absorptive lacquer so that it approximates closely a black-body cavity. The walls of the cavity are thermally connected to a large heat sink by a thermopile, providing a voltage proportional to the difference in temperature between the cavity wall and the heat sink. The voltage is calibrated against a voltage from a similar cavity that is connected to the heat sink the same way but is not subject to any radiation (Fig. 18.2). Heat flux measurements taken with this device have an uncertainty of ±0.3% with a response time of around 7 s.

Double cavity radiometer

A novel radiometer has been developed by Parretta *et al.* (2007). It comprises two integrating spheres connected physically in series, so that incident light must interact with both spheres before detection (Fig. 18.3). It has been developed for fast-response small-scale investigation of points in the flux profile for a large range of concentration ratios. This detector is able to measure a wide range of solar intensities, from a few suns to

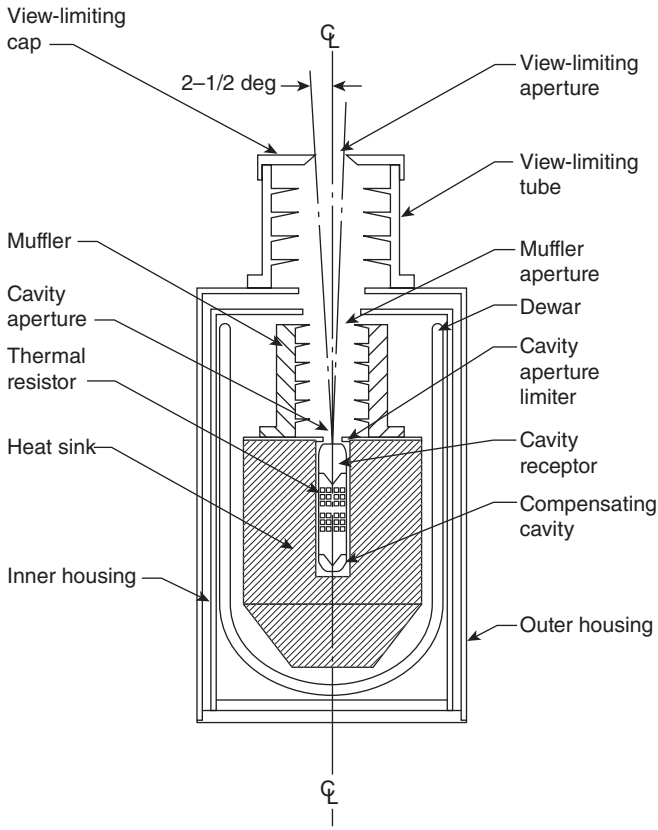

18.2 Kendall radiometer (Kendall and Berdahl, 1970).

thousands of suns, and is capable of determining absolute incident solar power. The large range of detection is achieved through proportional adjustment of the input aperture and the aperture between the integrating spheres in order to allow an appropriate amount of light to reach the photodiode detectors. A spectrometer is also included at the output sphere in order to measure the spectrum of light after propagating through the two-sphere configuration.

Heat flux microsensors

A thin thermopile sensor called the heat flux microsensor (HFM) was described by Hager *et al.* (1991) and is manufactured by Vatell Corp. (Vatell Corporation, 2002). Because it is made with thin-film sputtering techniques, the entire sensor is less than 2 mm thick (Fig. 18.4). The thermal resistance

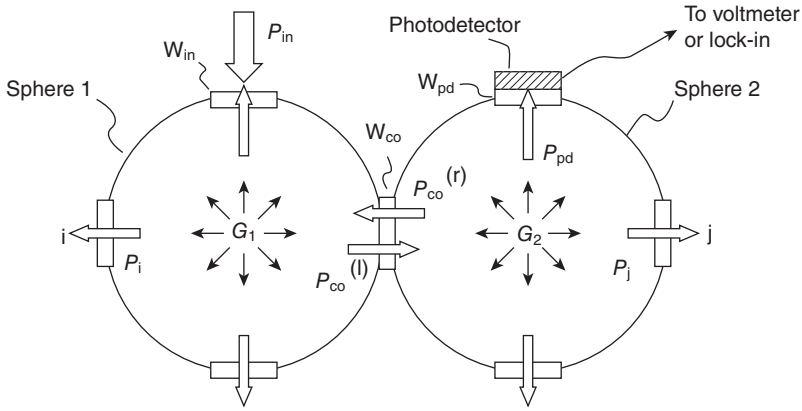

18.3 Double cavity radiometer (Parretta *et al.*, 2007).

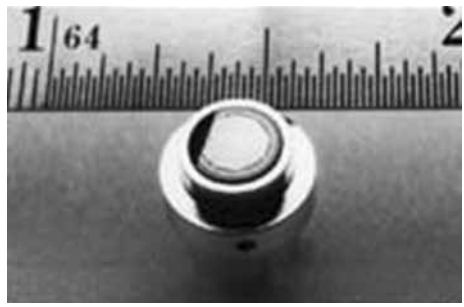

18.4 Heat flux microsensor.

layer of silicon monoxide is also sputtered directly onto the surface. The resulting physical and thermal disruption of the surface due to the presence of the sensor is extremely small. Use of high-temperature thermocouple materials allows sensor operating temperatures to exceed 800°C for the high-temperature models. They are best suited for heat flux values above 1 kWm^{-2}, with no practical upper limit. Because the sensor is so thin, the thermal response time is less than 10 ms, giving a good frequency response well above 1 kHz. A temperature measurement that is integrated into the sensor is very useful for checking the heat flux calibration and determining the heat transfer coefficient. The high temperature and fast time response capabilities are useful for aerodynamic applications, combusting flows in engines and propulsion systems, and capturing high-speed events such as shock passage. This rapid response also offers advantages in measurement of CST receiver transients.

18.2.2 Calorimeters

As with radiometers, calorimeters can be placed directly into the focal region. Calorimeters are used to determine solar flux by the measurement of heat transferred to a cooling fluid that passes through them. A well-designed calorimeter can transport almost all of the incident solar radiation (with minimal reflection loss) to the cooling medium (Estrada *et al.*, 2008), providing absolute measurement. As a general rule, calorimeters are large aperture devices that measure the total flux incident on an area; however, smaller units that provide finer spatial resolution are also possible.

CAVICAL and SUNCATCH calorimeters

The Mexican-designed CAVICAL calorimeter is constructed from two cones; one of copper, for high conductivity, which forms a cavity into which the concentrated solar radiation is directed, and a surrounding cone that has an insulated rear surface in order to minimise heat loss from the cavity. The front of the cavity corresponds to the large end of the cones, and an aperture is placed over this end to allow concentrated radiation into the cavity while minimising heat loss due to convection (Fig. 18.5). Cooling

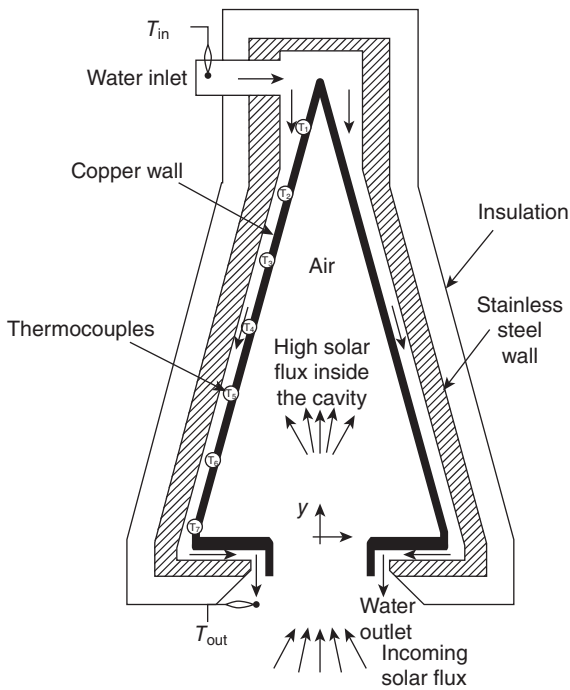

18.5 CAVICAL calorimeter (Pérez-Rábago *et al.*, 2006).

water flows in between the two cones. Thermocouples are located between the cones in order to measure the heat transfer to the water from the irradiated copper cone. The range of measurement for incident flux density is approximately 50–2,000 suns (Estrada *et al.*, 2008). Tests carried out on the CAVICAL calorimeter at the PSA solar furnace, in Almería, Spain were reported by Pérez-Rábago *et al.* (2006). A theoretical study of the CAVICAL copper-wall temperatures was conducted and compared with values recorded by the thermocouples within the calorimeter wall. Theoretical values differed from experiment by a maximum of 6%.

Another calorimeter with a double-cone design is the SUNCATCH, developed at DLR Cologne. Cooling channels are milled within the thick copper inner cone, and the outer cone insulates this high conductivity mass from the environment. The measurement accuracy of the SUNCATCH calorimeter depends inversely on the average incident flux: at 5,000 suns it is approximately ±0.5%, at 1,000 suns it is ±1%, with the error rising steeply at lower concentrations (Groer and Neumann, 1999).

Camera-target method

The camera-target method is an indirect measurement of the flux profile, but offers a high level of spatial resolution. It is widely applied in the CST R&D community.

A diffusely scattering target which either transmits, or more commonly, reflects incident light, is generally placed parallel to the receiver aperture or perpendicular to the axis of the concentrator, as near as possible to the focal plane. The light reflected off this target is then recorded with the use of a camera, generally with a charge-coupled device (CCD) sensor (Figs 18.6 and 18.7). The camera image files must have a highly linear response, which is not the case with images produced by common consumer grade digital cameras[1]. Analysis of this recorded image gives a relative intensity distribution of the flux profile at the plane of the target, which can be calibrated using an absolute measurement device such as a radiometer. The camera-target method offers fast data retrieval and a large number of data points captured simultaneously.

The surface of the target used in the camera-target method should ideally be perfectly diffuse, i.e. having zero specular reflectivity, and diffuse reflectivity which obeys Lambert's cosine law. Radiation reflected from such a surface has the same observed radiance regardless of the observation angle, so that light arriving at different incidence angles on the target (i.e., from

[1] 'Range compression' is used to make such images appear more natural to the human eye. Some consumer grade cameras can produce 'raw' files without range compression, but specialist 'machine vision' cameras are nevertheless preferable for flux mapping work.

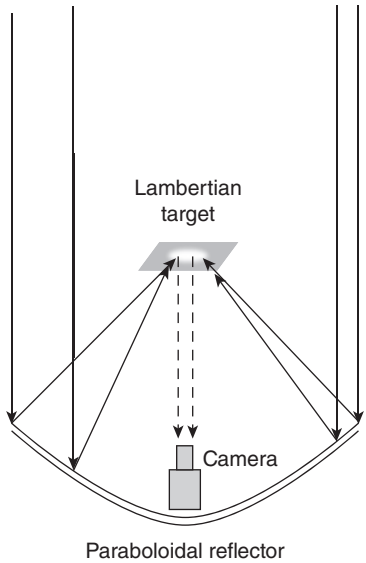

18.6 Camera-target method.

18.7 Image created on a diffuse cooled target by the Australian National University SG4 dish concentrator, with most of the dish reflective area covered in order to reduce the flux on the target (dark filters on the camera lens are used to make some of the focal region detail visible).

different regions of the collector) is imaged with equal weighting. For reliable flux determination using the camera-target method, a surface with diffuse reflectance within ±5% of ideal Lambertian reflectance, for all incident angles up to the rim angle of the collector, should be used. Reflectivity profiles for thermally-stable Lambertian surfaces are given by Neumann

and Schmitt (2003). For accurate quantitative analysis, the camera CCD array must be calibrated in order to obtain accurate relative flux intensities from the image.

In order to determine the absolute flux across the recorded distribution, a calibrated radiometer can be embedded in the target surface at a given point in the flux profile to provide a reference to which the rest of the profile can be compared. This will be observed in the image as a dark spot, and interpolation of the image grey values is required over this region, for calibration to the flux recorded by the radiometer. Such interpolation can, however, introduce significant uncertainty, as flux distributions at the focal region can exhibit very steep gradients (Ulmer *et al.*, 2002). Alternatively, the image intensity can be scaled by equating the integrated sum of the greyscale levels on the CCD array to the predicted total power incident on the target. The total power is given by the product of the solar irradiance, collector mirror aperture area, mirror reflectivity, and target intercept factor. The maximum total error of measurement for experiments conducted on the PSA solar dishes (Ulmer *et al.* 2002), using this calibration technique, has been determined at –6.2%, +10.6%.

A key issue when using this method with high concentration ratio systems is that the concentrated flux has the potential to overheat and damage the target. Water cooling of the target is a standard approach. Another technique is to move an uncooled target through the flux whilst a series of images are captured. In this approach a radiometer can be located just behind the plane passed over by the moving target. Another possibility is the use of Jupiter or the full moon as the light source. A detailed description of a camera-target system is given in Section 18.3.2.

Surface profile measurements and ray tracing

Optical modelling of the flux distribution is an alternative or complement to direct flux measurement. Measurements of the concentrator surface profile can be used as an input to a ray tracing program to model and predict the flux distribution. An appropriate sunshape (Buie *et al.*, 2003) and tracking uncertainty can be added to a ray-tracing analysis of the concentrator in order to predict the flux distribution before it has been directly observed, or for comparison to an observed profile. An advantage of this method is that it can be used to generate the three-dimensional flux distribution inside a receiver cavity. Parametric studies can also be readily carried out (e.g., the effect of sun position on the focal image at a central tower).

Measuring the surface profile of a solar concentrator is also useful in identifying aspects of the concentrator that contribute to the shape of a measured flux distribution. Gross concentrator errors arise from

misalignment of mirrors, gravitational sag in mirrors, wind distortion, thermal expansion, and manufacturing tolerances and defects. Photogrammetry is a useful tool for experimental determination of these types of concentrator errors (Shortis *et al.*, 2008; Shortis and Burgess, 2012). Any smaller aberrations on the mirror surface can be measured using deflectometry (Ulmer *et al.*, 2006) or laser scanning (Maccari and Montecchi, 2007). Individual sources of reflector error can be measured experimentally and added to the ray-tracing model. This allows investigation of the influence of particular errors and is a useful tool for concentrator optimisation.

Deflectometry is another technique for measuring the profile of reflective surfaces. Ulmer *et al.* (2006) obtained surface profiles, using colour-target distant-observer deflectometry measurements, of the DISTAL-II dish concentrator. The profiles were then used in a ray-tracing code implemented in MATLAB. The modelled flux distribution was in excellent agreement with the observed profile obtained using the ProHERMES system on the same solar collector (Plate IV between pages 322 and 323). For many purposes these results are considered accurate enough to replace flux-mapping altogether. Deflectometry measurements require a 'distant-observer' and, depending on the surrounding of the collector, are not always viable.

18.3 Flux mapping system case studies

The instrumentation and flux mapping techniques introduced above have been used in a number of different systems to measure concentrator flux distributions. Descriptions of a selection of flux mapping systems are given below.

18.3.1 Flux mapping at the Deutsches Zentrum für Luft- und Raumfahrt (DLR) solar furnace

The SCATMES and FATMES flux measurement systems employ the camera-target method for measuring the solar flux profiles of the DLR solar furnace in Cologne, Germany.

FATMES (Flux And Temperature MEasurement System) is a flux mapping system that comprises a Lambertian target that swings through the flux distribution (Neumann and Groer, 1996). During the sweep, a series of camera shots are taken and a complete flux image is built up. The short duration of the pass ensures the target does not heat up significantly and no active cooling is needed. A Kendall radiometer is used for determining the absolute flux (Fig. 18.8). A similar system is in use on a central tower at the CSIRO Energy Centre in Newcastle, Australia.

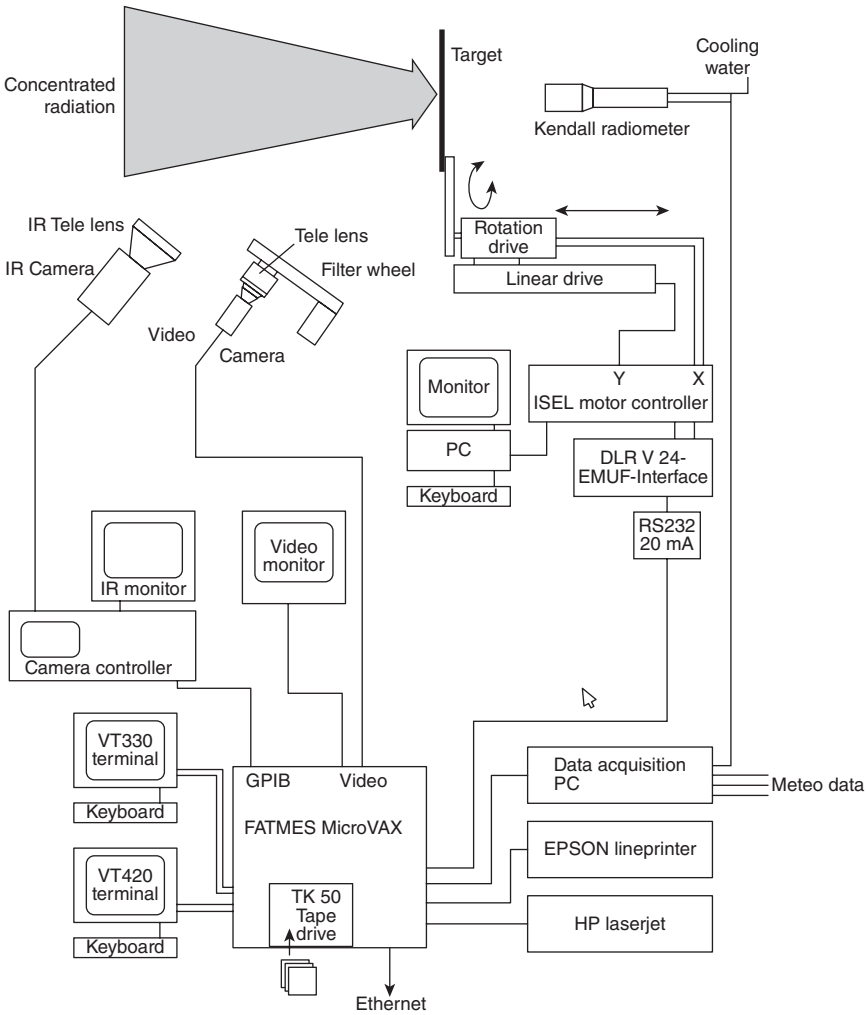

18.8 Flux mapping at the DLR solar furnace.

Subsequently, the SCATMES (SCAnning Target and MEasurement System) device for camera-target method of measuring concentrated solar flux was created as a more compact improvement to the FATMES system, more suitable for measuring the flux on a solar power tower. This system incorporates a moving bar that reflects light towards a CCD camera. The camera and bar are secured to the same mount such that their relative position remains constant. The estimated overall error in flux distributions recorded using this system is 4–7% (Neumann and Schmitz, 1999).

18.3.2 Heat flux measurement systems at the Plataforma Solar de Almería (PSA)

ProHERMES

The ProHERMES (Programmable HEliostat and Receiver MEasuring System) is a high accuracy flux mapping system that runs on a PC platform and has flexible programmability. This camera-target flux mapping system has been used with a portable flux mapping target in order to record the flux distributions from the DISTAL I, DISTAL II and EURODISH concentrators at PSA (Ulmer *et al.*, 2002). The planar target has a linear drive that enables motion along the direction of flux propagation.

ProHERMES 2A and MDF

A hybrid heat flux measurement system has been designed, constructed and mounted on top of the SSPS-CRS tower at the Plataforma Solar de Almería (PSA) to measure the incident solar power that is concentrated by a heliostat field on the flat aperture of the Hitrec II volumetric central receiver. There are two separate measurement systems, one direct and the other indirect; the direct system (MDF) utilises HFMs (heat flux microsensors), which enable measurements to be taken in a few seconds without water cooling; the indirect system (ProHERMES 2A) uses the camera-target method, with a water-cooled heat flux sensor used as a reference. ProHERMES 2A is the latest generation of concentrating solar radiation systems based on the indirect measuring procedure. A bar with heat flux sensors and Lambertian plates used in the camera method are mounted together in the same plane (Fig. 18.9). The combined unit is swung rapidly through the focal region for an instantaneous measurement in the same manner as the FATMES and SCATMES systems. A systematic comparison of the measured incident solar power and spatial heat flux distribution has shown good agreement. They are described in more detail below.

The MDF direct heat flux measurement system

The MDF system, incorporated in the swinging Lambertian target of ProHERMES 2A, is a linear array of fast-response, heat flux microsensor (HFM) radiometers with measurement uncertainties of ±3% (Ballestrín, 2002; Ballestrín and Monterreal, 2004). The flux distribution is scanned in a single sweep that takes approximately 2 seconds to perform. Measurements of the total power in the flux distribution calculated from the MDF data were reported to have an uncertainty of ±5–6%, after a degree of data processing (Ballestrín, 2002).

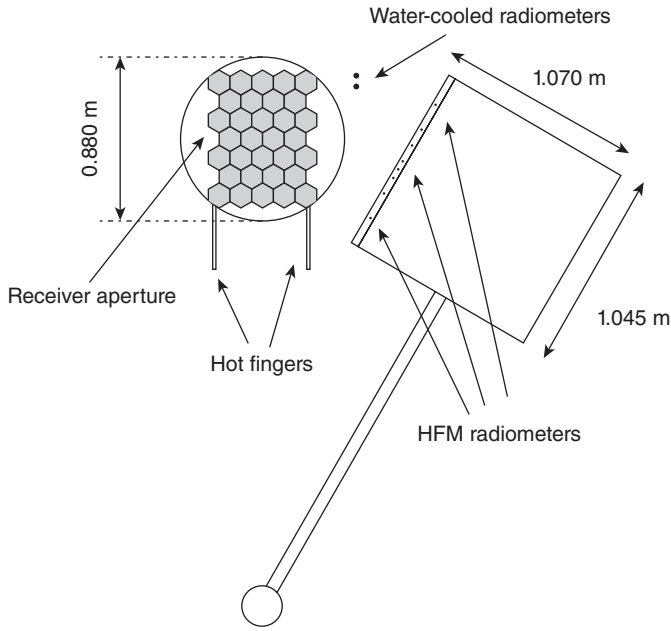

18.9 Hybrid heat flux measurement system at PSA. MDF and ProHERMES 2A systems.

The MDF system improves on the technical limitations of the previous direct heat flux measurement devices (Diessner, 1981; García, 1988). It consists of a number of Vatell heat flux microsensors mounted on a carbon steel moving bar. The distribution of sensors determines the spatial resolution in the direction perpendicular to the motion of the bar, in this case the vertical direction[2].

The measurement bar is moved in a plane 25 cm in front of the receiver aperture (Fig. 18.9), pivoting about a fixed point located centrally below the receiver aperture. The combination of a fast data acquisition system and an appropriate moving bar speed allows nearly instant measurement of the heat flux distribution, without water cooling and good spatial resolution in the horizontal direction.

The moving bar has eight HFM heat flux sensors, which are placed from the lower edge to the higher edge of the bar (Fig. 18.9) with average spacing of 100 mm. The sensors are more closely spaced in the middle of the bar, which traverses the peak of the flux distribution.

Two small rods made of carbon steel, so-called 'hot fingers', are placed at the edges of the receiver aperture. They are used as references which

[2] Here 'vertical' refers to the projection of the global vertical axis onto the plane of the receiver aperture.

give the time taken by the moving bar to scan the receiver aperture. A new electronic card has been designed to control the angular movement of the measurement bar of the latest version of the MDF system (Ballestrín *et al.* 2010a). An absolute optic encoder, with 16,384 pulses per revolution, is fixed on the bar axis. In principle, the card obtains up to 32 readings per second of the bar angular position, with a resolution of 0.02°; it also commands and controls the bar movement during the measurement process.

ProHERMES 2A indirect heat flux measurement system

ProHERMES 2A, a revision to the ProHERMES system, has been installed to measure the flux distribution of the SSPS-CRS solar power tower. The non-cooled Lambertian target (Fig. 18.9) swings in front of the receiver and intercepts the reflected concentrating beam as close to the receiver as possible in the so-called 'measurement plane'. A camera with a high resolution CCD sensor records the flux distribution at an appropriate point of the target passage. As with FATMES, the flux distribution is recorded as a composite image of many flux images taken as the target moves through the concentrated solar radiation. The overall uncertainty of the system for the total power into the receiver is less than 5%. Two heat flux sensors (Gardon radiometers) are placed very close to the receiver aperture (Fig. 18.9) to be used as heat flux reference by the CCD camera. The transducer of these sensors is a differential thermocouple measuring the temperature difference between the centre and the circumference of a thin circular foil disk.

Measurements have been performed simultaneously with MDF and ProHERMES 2A. There is good agreement between the measurements performed with the two systems, with a random deviation of less than 1%. The hybrid system incorporating two independent methodologies gives greater confidence in the measurements, and makes it possible to detect calibration changes.

PARASCAN

The PARASCAN (PARAbolic Trough Flux SCANner) flux mapping system is operated at the EuroTrough parabolic trough collector at PSA, which has a concentration ratio of 82 : 1 (Geyer *et al.*, 2002). It uses transparent Lambertian transmissive surfaces in front of arrays of photodiodes that are situated in front of and behind the tubular receiver (Fig. 18.10) (Riffelmann *et al.*, 2006). The photodiode arrays move along the linear receiver and record the flux distribution along the entire trough. The photodiode array in front of the receiver intercepts the total reflected solar energy from the trough, while the array behind the receiver detects the

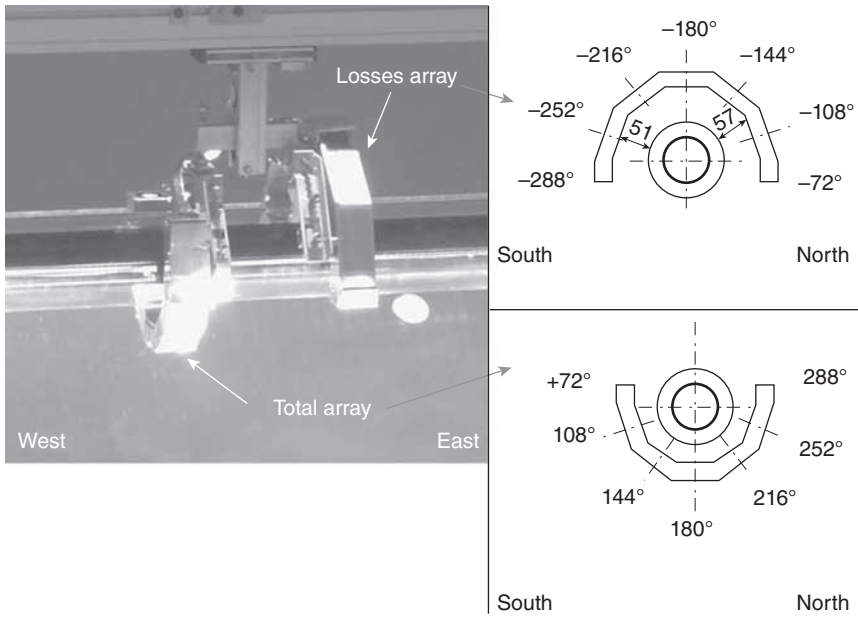

18.10 PARASCAN system (Riffelmann *et al.,* 2006).

amount of light not intercepted by the receiver. Measurements were conducted with a variety of concentrator tracking angles, and the changing intercept factor of the receiver, due to gravitational distortion as the trough tracks the sun, was determined (Lüpfert *et al.* 2007). The flux was also measured using the camera-target method in a plane perpendicular to the linear receiver. This enabled a comparison of results with those obtained using PARASCAN, and to photograph the concentrated rays as they pass into or past the receiver. An upgraded version, PARASCAN II, has been developed which uses optical fibres to transport the flux to remote photodiodes. It has a higher spatial resolution than PARASCAN (Lüpfert *et al.* 2007).

18.3.3 High concentration dish flux mapping

For very high concentration ratio systems, such as accurate paraboloidal dishes, producing a water-cooled target that can cope with the peak concentration regions is challenging. Camera-target flux mapping using either the Moon or Jupiter as the light source, rather than the sun, can be carried out more cheaply and safely, and gives an initial indication of the optical quality of a concentrator. This technique eliminates the requirement for a moving target or target cooling; however, neither the Jupiter nor Moon images provide a true solar flux distribution. Jupiter is effectively a point

source of light, and when imaged in the focal plane by the concentrator, the spread of the image gives an indication of the concentrator surface errors. The moon subtends approximately the same angle as the sun and its image will give a reasonable indication of the extent of the solar flux distribution, though its surface features will confound attempts to correlate the brightness of the image to the solar flux at any given point in the flux profile.

Lunar flux mapping has been utilised on the PETAL 400 m^2 dish at Ben-Gurion University, Sede Boqer campus, Israel (Biryukov, 2004), and the 500 m^2 'Big Dish' at the Australian National University, Canberra, Australia (Lovegrove *et al.*, 2011). In the case of PETAL, individual mirror panel measurements were taken, using the sun, by covering all panels except one (to avoid excessive heating of the target). A compound flux distribution was calculated from the individual panel measurements. This was compared with the expected solar flux distribution calculated from the Moon and Jupiter flux maps; all were found to be in good agreement.

18.4 High temperature measurement

Knowledge of surface temperatures is essential in many applications of concentrated solar radiation. Pyrometric temperature measurement of solar irradiated material surfaces is a good alternative to contact metrology, which has limitations at high surface temperatures (Schaffner *et al.*, 2003; Kraupl and Steinfeld, 2003; Hernandez *et al.*, 2003; Meier *et al.*, 2004; Osinga *et al.*, 2004; Hirsch and Steinfeld, 2004).

18.4.1 Contact measurement techniques

There are a number of standard approaches to contact measurement of temperature which find application in CST receivers, particularly for distributed measurement at a number of points. The three most common types of contact sensors are thermocouples, resistance temperature detectors (RTD), and thermistors. Thermistors are manufactured with a maximum usable temperature between 150 and 300°C. RTD sensors are generally more stable and accurate than thermocouples, but are less robust and have a temperature range up to the order of 650°C, compared to over 1,000°C for K-type thermocouples. Detailed descriptions of these and other temperature measurement technologies, with discussion of the methods used to obtain the highest possible accuracy, are given in Agilent Technologies (1980) and Baker *et al.* (1975).

Thermocouples consist of a pair of wires made from dissimilar metals which are joined at one end (Fig. 18.11(a)). If there is a temperature difference between the junction (which is used as the temperature probe) and the other ends of the wires, a small voltage is produced (e_{AB} in Fig 18.11(b)),

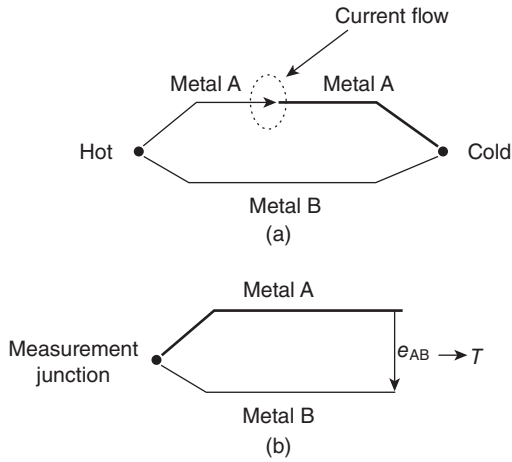

18.11 Measurement principle of a thermocouple.

which is dependent on the particular metals being used and on the temperature difference. Standard calibration curves give the temperature differential as a function of output voltage for a wide range of thermocouple material types; these curves are commonly built into data acquisition hardware.

In order to obtain an absolute measurement, the temperature at the ends of the wires (known as the 'cold junction') must be determined independently and added to the temperature differential. Data acquisition equipment usually has an internal temperature sensor for this purpose.

Thermocouples are classified according to the pair of metals employed and the temperature calibration range; 'K-type' thermocouples typically have ±2°C accuracy, up to a standard maximum temperature of 1,250°C. The insulation material on the thermocouple wires may, however, impose a lower maximum temperature. For example, polytetrafluoroethylene (PTFE) insulated sensors are rated to approximately 250°C, fibreglass insulation 350°C or higher and mineral insulation over 1,000°C. Other factors to take into account when choosing thermocouples are mechanical robustness and flexibility. Thermocouples can be enclosed in a stainless steel or Inconel sheath as a barrier or seal between the working fluid, or for protection against mechanical damage.

In order to measure the temperature of a working fluid, such as steam, at a point in a high temperature tubular receiver, thermocouples can be placed either in contact with the outer surface of the tube, or else in-line in the tube. Accuracy is generally reduced with external measurements, as there will be some thermal resistance and temperature difference between the fluid and the outer wall of the tube. The thermal time lag in the wall

material and the thermocouple itself may be of significance in accurate, rapid measurements. Attachment of a thermocouple can be effected by a spot weld or mechanical fastening. If a thermocouple is placed inside a receiver, care must be taken to ensure it is not in the direct path of the concentrated flux, which would affect the probe temperature.

18.4.2 Pyrometry

Pyrometry is the determination of surface temperatures via measurement of radiation flux emitted by the surface. Pyrometric temperature measurement of solar irradiated material surfaces is a useful alternative to contact measurement techniques at high temperatures. Pyroelectric detectors are the most common optical thermal detectors, as they are the most sensitive to thermal radiation and are fairly inexpensive. A pyroelectric detector contains a sensor made from a ferroelectric material which develops a change in polarisation in response to a change in its temperature. The polarisation state of the sensor, and therefore its temperature, can be measured as an electrical signal by electrodes placed either side of it. Radiation emanating from the surface of interest passes through a window in the detector and heats the sensor; the deviation of the sensor's temperature from ambient is then used to determine the temperature of the source material.

A difficulty with pyrometric temperature measurement is, however, that the detector responds to solar radiation which is directly reflected from the irradiated sample, as well as re-radiation. This problem is especially important in solar furnaces, where solutions have been proposed including:

- estimating the reflected radiation by varying the incident flux during temperature measurement
- determining the incident flux and the sample spectral reflectivity online (Tschudi and Morian, 2001)
- the use of pyrometry with band-pass filters centred on the atmospheric solar absorption bands of carbon dioxide and atmospheric water, which minimises or avoids this source of uncertainty (Tschudi and Morian, 2001; Hernandez *et al.*, 2004; Pfänder *et al.*, 2006).

In addition, determination of the real temperature requires accurate knowledge of the surface emissivity, as the temperature is determined on the basis of the current signal generated by the radiant surface compared to the signal generated by a black-body calibrator. Use of the solar absorption band with the shortest wavelength reduces the influence of the uncertainty of emissivity on surface temperature determination compared to longer wavelengths (Rohner and Neumann, 2003). This approach is similar to that used for infrared measurements of radiation from a receiver using a solar blind camera, discussed below.

A commercial pyrometer has been tested in the wavelength band around 1.4 μm in the solar furnace at the Plataforma Solar de Almería (PSA) in material treatment experiments with concentrated solar radiation (Ballestrín *et al.*, 2010b). This wavelength band is an atmospheric solar absorption band due to water steam, but solar radiation absorption is incomplete in this band. The pyrometer works well at temperatures over 800°C even through quartz windows, and has frequently been used in concentrated solar radiation experiments (Schaffner *et al.*, 2003; Kraupl and Steinfeld, 2003; Meier *et al.*, 2004; Osinga *et al.*, 2004; Hirsch and Steinfeld, 2004).

18.4.3 Solar blind infrared camera

A solar blind infrared (IR) camera employs an infrared detector which is made 'blind' to the solar spectrum by the use of appropriate filters. It is therefore relatively insensitive to radiation reflected from the surface of interest, with most of the detected radiation attributable to the radiation emitted by the heated surface. This enables an accurate determination of the surface temperature, providing that the emissivity is known and a calibration is made for ambient conditions.

An IR camera prototype was analysed in the PSA solar furnace (Ballestrin *et al.*, 2009). This camera was designed with three pass-band filters centred on 1,900, 2,700 and 4,300 nm in accordance with three atmospheric solar absorption bands centred on these three wavelengths. The problem with this technique is that special care must be taken with these filters if the camera is used at a distance or under ambient humidity conditions other than calibration.

A new IR camera based on an InSb detector has been designed. This detector works in the 1.5–5 μm spectral range and a software-controlled filter wheel enables the pass-band filters centred on 3,320 and 4,720 nm to be used (Fig.18.12), creating a solar blind IR camera.

Figure 18.12 shows the solar spectrum based on a MODTRAN code simulation (Anderson *et al.*, 1996), the solar reflected spectrum, two pass-band filters, black-body radiance at several temperatures, mirror reflectance, and quartz transmittance. Once the solar radiation is reflected by the heliostat mirror and concentrator, some solar radiation is reflected from the sample to the IR camera (Fig. 18.12). Fortunately this IR camera has two special pass-band filters, which avoid or minimise the reflected solar radiation from the sample. The low reflectivity of the mirrors over 3,000 nm (Rubin, 1985) allows defining wavelength bands where the solar radiation is almost negligible (Fig. 18.12).

These two filters are solar-blind (Fig. 18.12), and their wavelength bands are not in accordance with atmospheric solar absorption bands. This point

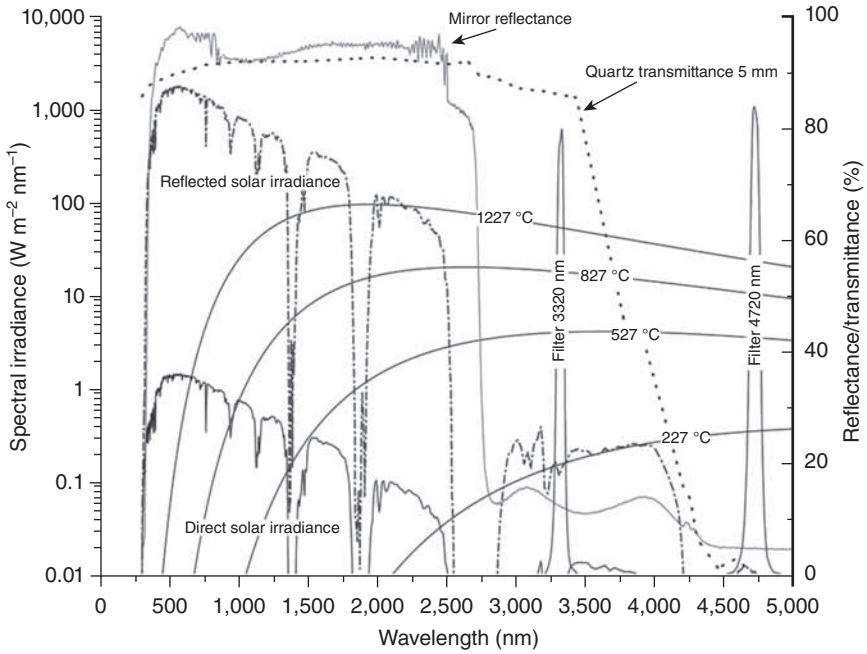

18.12 Solar spectrum based on a MODTRAN simulation, solar reflected spectrum, two pass-band filters, black-body radiance at several temperatures, mirror reflectance, and quartz transmittance.

makes it possible to measure temperature properly even if the camera is used at a distance or under ambient humidity conditions other than calibration. With the band-pass filter centred on 3,320 nm the camera measures properly through quartz windows. The temperature measurement performed using this filter must be increased using Planck's law correction due to the quartz attenuation (15%) of the detected thermal radiation. The filter centred on 4,720 nm allows the temperature of the quartz window to be measured. In both cases, the distortion of the reflected solar radiation on the temperature measurement decreases if the temperature of the sample increases (Fig. 18.12).

This solar blind IR camera, based on a standard camera, was designed by CIEMAT. The camera has an image size 640 × 512 pixels, a full frame rate up to 100 Hz per second, and an accuracy of ±0.02°C. The fast speed permits a very high thermal resolution even at short integration times. Features include self-test functions, focal length 100 mm, range zoom, recalibration, different outputs (serial interfaces, analogue outputs) and remote operation via personal computer.

18.5 Conclusions

After more than 20 years of research and development, heat flux and temperature measurement systems are more sophisticated and accurate, however, commercial solar tower plants have much larger aperture surfaces than the receiver prototypes tested in the past. Existing methods to measure the solar flux density in the receiver aperture face new challenges regarding the receiver size. Also, the requirements regarding costs, accuracy, spatial resolution, and measuring speed are different than in the past.

Flux density measurement on large-scale receivers is important, because this delivers the receiver input power, which is a parameter used in calculation of performance figures for the receiver and heliostat field. Moreover, continuous measurement of the flux density distribution facilitates efficient receiver operation and heliostat aiming control. Different receiver types and different requirements regarding the measurement purpose result in several possible solutions for flux and temperature measurement on large-scale receivers.

Direct and indirect flux measurement systems make use of heat flux sensors manufactured and calibrated by few companies. Confidence in the measurements of the incident power is based on the calibration of these sensors, whose accuracy is limited to ±3%. Reducing these bounds would represent a step forward in heat flux measurement in general and in concentrated solar power measurement in particular.

18.6 References

Agilent Technologies (1980), Practical Temperature Measurements, Application Note 290.

Anderson G P *et al.* (1996), Reviewing atmospheric radiative transfer modelling: new developments in high and moderate resolution FASCODE/FASE and MODTRAN. In *Optical Spectroscopic Techniques and Instrumentation for Atmospheric and Space Research*, Vol. II, Society of Photo-Optical Instrumentation Engineers.

Baker H, Ryder E, Baker N (1975), *Temperature measurement in engineering*. Omega Press, Stamford, CT.

Ballestrín J (2002), A non-water-cooled heat flux measurement system under concentrated solar radiation. *Solar Energy* **73** 159–168.

Ballestrín J and Monterreal R (2004), Hybrid heat flux measurement system for solar central receiver evaluation. *Energy* **29** 915–924.

Ballestrín J, Estrada C A, Rodríguez-Alonso M, Pérez-Rábago C, Langley L W, Barnes A (2006), Heat flux sensors: calorimeters or radiometers? *Solar Energy* **80** 1314–1320.

Ballestrín J, López M, Rodríguez J, Cañadas I, Marzo A (2009), A solar-blind IR camera prototype, *15th SolarPACES International Symposium*. Berlin, Germany.

Ballestrín J, Valero J and García G (2010a), One-click heat flux measurement device, *16th SolarPACES International Symposium*. Perpignan, France.

Ballestrín J, Marzo A, Cañadas I, Rodríguez J (2010b), Testing a solar-blind pyrometer. *Metrologia* **47** 646–651.

Biryukov S (2004), Determining the optical properties of PETAL, the 400 m^2 parabolic dish at Sede Boqer. *Journal of Solar Energy Engineering*, **126** 827–832.

Buie D, Monger A G, Dey C J (2003), Sunshape distributions for terrestrial solar simulations. *Solar Energy* **74** 113–122.

Carasso M and Becker M (1990), *Performance Evaluation Standards for Solar Central Receivers*, Springer-Verlag, New York.

Diessner F (1981), Operation manual for the measurement activities with heat flux distribution (HFD) system. DFVLR (Deutsche Forschungs- und Versuchsanstalt für Luft- und Raumfahrt), Cologne, Germany.

Estrada C A, Pérez-Rábago C, Ballestrín J (2008), Development of a conical cavity calorimeter for measuring highly concentrated solar flux. *14th SolarPACES International Symposium on Concentrated Solar Power and Chemical Energy Technologies.* Las Vegas, USA.

García G (1988), General description of the flux measuring system of the volumetric receiver, Internal report R-15/88GG. CIEMAT – Plataforma Solar de Almería.

Gardon R (1953), An instrument for the direct measurement of intense thermal radiation. *Review of Scientific Instruments* **24** 366–370.

Geyer M, Lupfert E, Osuna R, Esteban A, Schiel W, Schweitzer A, Zarza E, Nava P, Langenkamp J, Mandelberg E (2002), Eurotrough: Parabolic trough collector developed for cost-effective solar power generation. *Proceedings of 11th Solar PACES International Symposium on Concentrated Solar Power and Chemical Energy Technologies*, CD-ROM, Zurich, Switzerland.

Groer U and Neumann A (1999), Development and test of a high flux calorimeter at DLR Cologne. *Le Journal de Physique IV* **9** 643–648.

Hager JM, Simmons S, Smith, D, Onishi S, Langley LW, Diller TE (1991), Experimental performance of a heat flux microsensor. *Journal of Engineering for Gas Turbines and Power* **113** 246–250.

Hernandez D, Olalde G, Bonnier G, Le Frious F, Sadli M (2003), Evaluation of the application of a solar furnace to study the suitability of metal oxides to be used as secondary reference points in the range 2,000–3,000 degrees C. *Measurement* **34** 101–109.

Hernandez D, Olalde G, Gineste J M, Gueymard C (2004), Analysis and experimental results of solar-blind temperature measurements in solar furnaces. *Journal of Solar Energy Engineering* **126** 645–653.

Hernandez D, Ballestrín J, Neumann A (2006), First work by the flux and temperature measurement group (F.T.M) in the SOLLAB laboratory alliance. *Proceedings of the 13th SolarPACES International Symposium on Solar Thermal Concentrating Technologies*, Seville, Spain, Paper No. B6–S6.

Hirsch D and Steinfeld A (2004), Solar hydrogen production by thermal decomposition of natural gas using a vortex-flow reactor. *International Journal of Hydrogen Energy* **29** 47–55.

Kaluza J and Neumann A (2001), Technical brief: Comparative measurements of different solar flux gauge types. *Journal of Solar Energy Engineering* **123** 251–255.

Kendall J M and Berdahl C M (1970), Two blackbody radiometers of high accuracy. *Applied Optics* **9** 1082–1091.

Kraupl S and Steinfeld A (2003), Operational performance of a 5-kW solar chemical reactor for the co-production of zinc and syngas. *Journal of Solar Energy Engineering* **125** 124–126.

Lovegrove K, Burgess G, Pye J (2011), A new 500 m² paraboloidal dish solar concentrator. *Solar Energy* **85** 620–626.

Lüpfert E, Pottler K, Ulmer S, Rifflemann K J, Neumann A, Schiricke B (2007), Parabolic trough optical performance analysis techniques. *Journal of Solar Energy Engineering* **129** 147–152.

Maccari A and Montecchi M (2007), An optical profilometer for the characterisation of parabolic trough solar concentrators. *Solar Energy* **81** 185–194.

Meier A, Bonaldi E, Cella G M, Lipiński W, Wuillemin D, Palumto R (2004), Design and experimental investigation of a horizontal rotary reactor for the solar thermal production of lime. *Energy* **29** 811–821.

Neumann A and Groer U (1996), Experimenting with concentrated sunlight using the DLR solar furnace. *Solar Energy* **58** 181–190.

Neumann A and Schmitz A (1999), The new SCATMES device for measurement of concentrated solar radiation. *Journal of Solar Energy Engineering* **121** 116–120.

Neumann A and Schmitt G (2003), Review of optical properties for Lambertian diffusers in solar energy application. *Proceedings of ASME 2003 International Solar Energy Conference*, 231–242.

Osinga T, Frommherz U, Steinfeld A, Wieckert C (2004), Experimental investigation of the solar carbothermic reduction of ZnO using a two-cavity solar reactor. *Journal of Solar Energy Engineering* **126** 633–637.

Parretta A, Antonini A, Armani M, Nenna G, Flaminio G, Pellegrino M (2007), Double cavity radiometer for high-flux density solar radiation measurements. *Applied Optics* **46** 2166–2179.

Pérez-Rábago C A, Marcos M J, Romero M, Estrada C A (2006), Heat transfer in a conical cavity calorimeter for measuring thermal power of a point focus concentrator. *Solar Energy* **80** 1434–1442.

Pfänder M, Lüpfert E, Heller P (2006), Pyrometric temperature measurements on solar thermal high temperature receivers. *Journal of Solar Energy Engineering* **128** 285–292.

Riffelmann K J, Neumann A, Ulmer S (2006), Performance enhancement of parabolic trough collectors by solar flux measurement in the focal region. *Solar Energy* **80** 1303–1313.

Rohner N and Neumann A (2003), Measurement of high temperatures in the DLR solar furnace by UV-B detection. *Journal of Solar Energy Engineering* **125** 152–158.

Rubin M (1985), Optical constants and bulk optical properties of soda lime silica glasses for windows. *Solar Energy Materials* **12** 275–288.

Schaffner B, Meier A, Wuillemin D, Hoffelner W, Steinfeld A (2003), Recycling of hazardous solid waste material using high-temperature solar process heat. II: Reactor design and experimentation. *Environmental Science and Technology* **37** 165–170.

Shortis M R and Burgess G (2012), Photogrammetric monitoring of the construction of a solar energy dish concentrator. *Photogrammetric Engineering & Remote Sensing* **78** 519–527.

Shortis M R, Johnston G H G, Pottler K, and Lüpfert E (2008), Quality analysis for solar concentrators. *International Archives of Photogrammetry and Remote Sensing* **37** 81–87.

Tschudi H R and Morian G (2001), Pyrometric temperature measurements in solar furnaces. *Journal of Solar Energy Engineering* **123** 164–170.

Ulmer S, Wolfgang R, Heller P, Lüpfert E (2002), Beam characterization and improvement with a flux mapping system for dish concentrators. *Journal of Solar Energy Engineering* **124** 182–188.

Ulmer S, Heller P, Reinalter W (2006), Slope measurements of parabolic dish concentrators using color-coded targets. *Proceedings of the 13th SolarPACES International Symposium on Solar Thermal Concentrating Technologies*, Seville, Spain, Paper No. A7–S5.

Vatell Corporation (2002), Thermateq''-nology Newsletter. Available from: http://www.vatell.com/newsletter.htm.

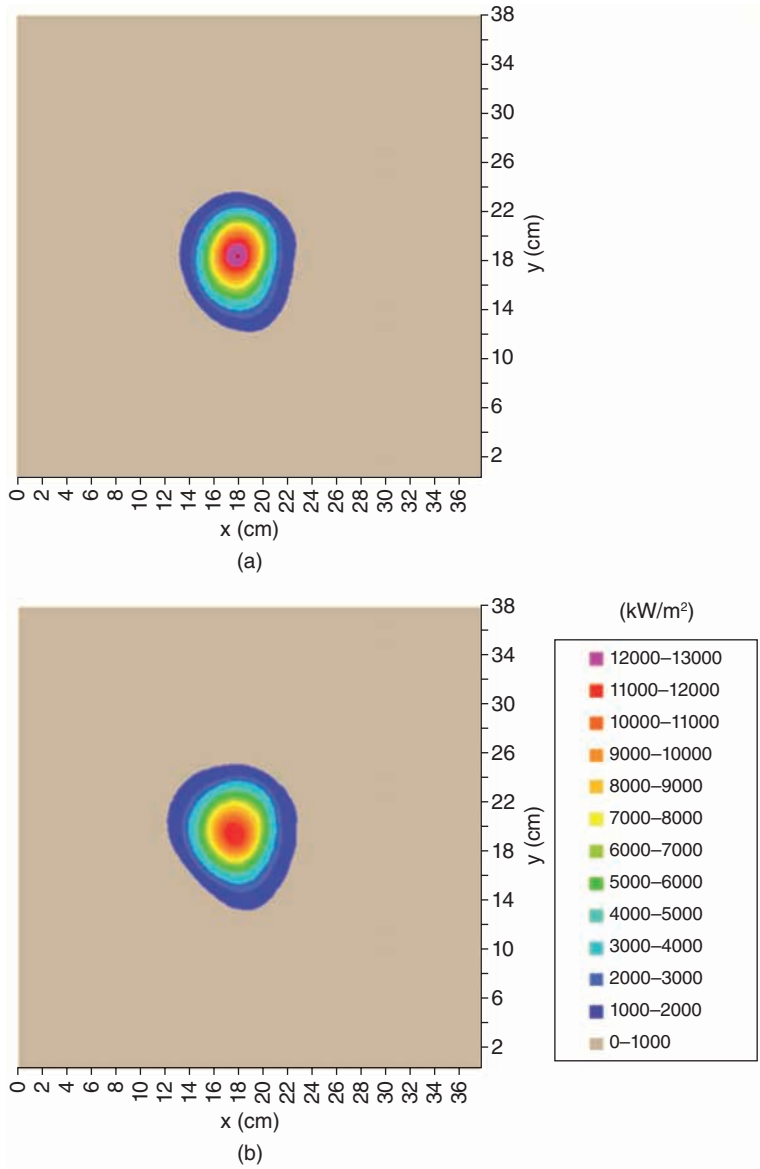

Plate IV (a) Calculated flux distribution in the focal plane and (b) measured flux distribution in the focal plane (Ulmer *et al.*, 2006).

19

Concentrating solar technologies for industrial process heat and cooling

A. HÄBERLE, PSE AG, Germany

Abstract: In addition to power generation, concentrating solar thermal (CST) systems can also be applied directly to process heat production. Today, the application of concentrating solar power (CSP) technologies for the generation of industrial process heat is a very small niche market; however, it offers an enormous fuel saving potential. The first projects were realized in the 1970s but it is only recently that several new developments were started in this field. Process heat is used at temperatures between 50 and 1,500°C, CST technologies have a role above 120°C and so far have not been applied above 400°C for this purpose. A major growth area is solar-driven cooling using thermally-driven cooling cycles. This chapter gives a brief overview about general system requirements and available solar technologies for process heat applications.

Key words: process heat, solar cooling, rooftop installation, system integration.

19.1 Introduction

Process heat accounts for approximately two-thirds of the final energy consumption of industry in Europe (Ecoheatcool, 2006). Industry uses heat in a wide temperature range starting as low as 50°C, e.g. for space heating, cleaning or washing. Operating temperatures between 100°C and 250°C can be found typically in the food, textile or chemical industry and up to higher than 1,500°C are used, e.g., for metallurgical processes.

A major share of that heat is at temperatures below 400°C and thus in a temperature regime that is accessible for state-of-the-art solar thermal technologies. However, compared to other applications of solar thermal collectors, concentrating or not, it is still the least developed with the fewest realized projects.

Solar generation of industrial process heat is a field with enormous and still untapped potential for the substitution of fossil fuels and thus CO_2 emission reduction. The application of concentrating solar thermal (CST) technologies for the generation of industrial process heat makes use of all the solar collector technology types, which were described in earlier chapters of this book. However, the typical system size and temperature level

of process heat projects differ from other CSP applications. As a consequence we find specific collector developments for small and medium scale applications, i.e. small troughs, small linear Fresnel and also dishes that are not suited for large-scale power generation.

This chapter gives a brief overview about general system requirements and available solar technologies for process heat applications.

19.2 Technology overview

19.2.1 Process heat

To cover the very high temperature end of process heat demand, solar technologies are still in their development phase. But up to 400°C solar collectors are an absolutely feasible commercial option. Temperatures below 120°C can be produced by non-concentrating collectors (flat plate collectors or vacuum tube collectors), which are on the market in a large variety of products. Thus the target operating temperature for concentrating collectors in the field of industrial process heat starts at temperatures of approx. 120°C (below that non-tracking collectors generally are simpler and cheaper).

The appropriate solar technologies for the sub 400°C market segments are linear concentrators like parabolic trough (discussed in detail in Chapter 7) or linear Fresnel collectors (discussed in detail in Chapter 6). A few groups also follow a point focusing (dish) approach customized for the purpose (dishes for power generation purposes are covered in Chapter 9). However, when looking at process heat applications it should be noted that not only are the typical temperature levels for industrial process heat lower than those for power generation, but also the power range is smaller. Typical systems can be as small as only a few hundred kW and mostly do not exceed several MW of peak thermal power. Of course there are exceptions, but a general rule is that the typical process heat project is much smaller than the hundreds of MW that are planned for power generation. The conclusion of lower operating temperature and smaller plant size is that smaller collectors can be used, which are also suitable for rooftop installation.

While the first pioneering projects date from the 1970s it was not until the first decade of the new century that a number of start-up companies defined industrial process heat as their target market and developed appropriate new products. A study of the IEA's joint SHC task 33 and SolarPACES task 4 'Solar Heat for Industrial Processes' extrapolated the solar potential for industrial process heat from five European countries and derived the total solar thermal potential for Europe to be 100–125 GW_{th} (see Table 19.1).

Table 19.1 Industrial heat demand and solar process heat potential for selected countries and for EU25

Country	Industrial heat demand (PJ/year)	Solar process heat potential (PJ/year)	Solar process heat potential (GWth)	Solar process heat potential (Mio. m² collector area)
Austria	137	5.4	3	4.3
Spain	493	17	5.5–7	8–10
Portugal	90	4	1.3–1.7	1.9–2.5
Italy	857	31.8	10	14.3
Netherlands	46	1.95	0.5–0.7	0.8–1
EU 25	6,881	258.2	100–125	143–180

Adapted from Vannoni *et al.* (2008).

19.2.2 Solar cooling

Solar cooling is an attractive application for solar process heat and currently the major market segment for the application of CST heat systems. Utilities recognize that summer peaking electricity demand in many countries is increasingly dominated by air conditioning from noon to late afternoon. This is exactly the time with the highest solar irradiation, so any technology transforming solar radiation to cold profits from the coincidence of high demand and optimum operation conditions.

A variety of solar cooling technologies have been investigated in the past, ranging from PV-driven vapour compression to the many options for thermally-driven cycles that produce cold and dehumidification. The race for the most economic, most reliable or most powerful technology is still open. However, it is clear that due to different boundary conditions there will not be the one superior technology, e.g., hot and humid conditions require a different solution than dry desert environments.

The most common cooling technology that is operated with solar thermal collectors is via absorption heat pumps. The thermodynamic principle is simple: heat at high temperature T_3 (from the collector) is used to 'pump' heat from a low temperature T_1 to an intermediate temperature level T_2. The low temperature is where the cooling takes place (taking heat away is the thermodynamic principle of 'cooling').

This is done by evaporating a refrigerant (at T_1) at low partial pressure, which is absorbed by a second working fluid (at T_2). External heat (at T_3) is used to regenerate the diluted solution. This means the refrigerant is boiled out of the solution (desorbed). Then it is condensed again (at T_2) so it can be provided to the evaporator as a liquid. Absorption and condensation are not necessarily at the identical temperature T_2, but it can be advantageous to design the cycle accordingly.

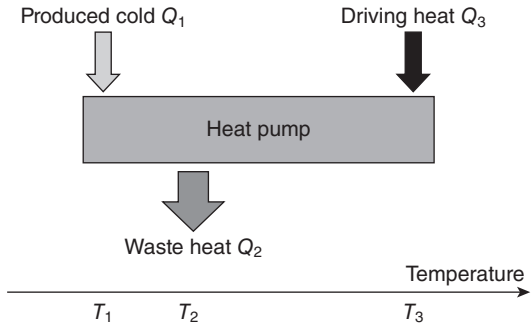

19.1 Heat flux for thermally driven heat pump.

The most commonly used working pairs are water/lithium bromide and ammonia/water, where in the one case water is the refrigerant and in the other case ammonia is the refrigerant.

Figure 19.1 illustrates this thermodynamic principle and defines the basic heat flux and temperature levels. The so-called coefficient of performance (COP) is then defined as the ratio of heat transfer from the cold space (Q_1) and driving heat (Q_3).

$$\text{COP} = Q_1 / Q_3$$

Both the driving heat and the pumped heat need to be rejected to the environment.

$$Q_2 = Q_1 + Q_3$$

The temperature difference between the useful cold and the rejected heat ($T_2 - T_1$) is called the temperature lift. The minimum cooling temperature and the maximum temperature lift are determined by the materials that are used as refrigerants and by the driving temperature that is available from the collector.

As a consequence of the second law of thermodynamics, it is a general rule that a high temperature lift, a low cooling temperature or a high COP can only be achieved with a high driving temperature. Thus concentrating collectors, with their higher temperature capability, have some advantages for solar cooling applications compared to stationary collectors in areas with a high direct normal irradiation.

Table 19.2 gives the typical parameters for heat pumps with LiBr/water and water/NH_3, which are the most commonly used refrigerants for absorption heat pumps. The higher COP of double and triple effect chillers is achieved by adding one or even two additional regenerator/condenser units to a single effect cycle. The waste heat of the high temperature condenser is then used to power the low temperature regenerator. Thus a

Table 19.2 typical parameters for NH_3 and LiBr absorption chillers

		H_2O/LiBr		NH_3/H_2O
	Single effect	Double effect	Triple effect	
Max. temperature lift	25 K	25 K	25 K	55 K
Temperature of Cold	5–20°C	5–20°C	5–20°C	–20°–20°C
Driving temperature	70–90°C	140–180°C	200–270°C	120–180°C
Max. COP	0.7–0.8	1.1–1.4	1.6–2.1	0.6–0.7

higher concentration of the solution can be reached without additional heat consumption but with the necessity of higher driving temperature for the initial cycle.

When looking a little closer at the time patterns of cooling demand and solar resource, it shows that a certain shift of the cooling demand towards the evening hours can appear, largely as a consequence of the thermal inertia of buildings. Also not all regions globally really have bright sunlight during noon in summer but are rather hazy and humid with the highest cooling load due to dehumidification of the air. In such cases the incorporation of either heat or cold storage can make sense. Often hybrid fossil solutions are preferred to extensive storage volumes because of their lower investments; however, in this case proper system design is especially important in order to avoid inefficient use of the fossil backup that might spoil the overall energy saving balance.

What was not elaborated in the above is that thermally driven heat pumps also need electricity for the operation of pumps or fans. This is a small but not negligible electricity consumption, which also needs to be considered for an overall energy balance (see Henning 2007 for further information).

19.3 Components and system configuration

19.3.1 Collector designs

A large variety of collector designs are available on the market, three of which are described below.

Linear concentrators: parabolic trough (PT)

Parabolic troughs (Fig. 19.2) are the best known and most established collector technology in this field. As stated earlier, the typical collector size for

19.2 Parabolic troughs for a solar cooling system in Newcastle, Australia (source: NEP Solar AG).

process heat is smaller than that designed for CSP applications. The typical aperture width is in the range of 1–2 m. The reflectors are typically based on aluminium or sandwich structures with polymer films or thin glass because the glass mirrors that are typically used in big troughs are not available with the small focal length of small troughs. This is not a technological issue but a matter of commercial availability. Thermally shaped glass mirrors will only be feasible once a certain sales volume is reached. A similar situation applies for the receivers. Vacuum receivers for unidirectional flow in large arrays[1] are not available yet in the dimensions needed for small PTs. However, the typically lower operating temperatures also allow for non-vacuum receivers, which are comparably easy to produce. Other advantages of small troughs are the low wind load, which even allows for rooftop installations and comparably little end losses for short collector rows.

Linear concentrators: linear Fresnel

Linear Fresnel collectors (Fig. 19.3) use an approximation of the ideal parabolic reflector consisting of many reflector facets, which typically are aligned horizontally. The big focal length allows for the use of flat glass mirrors, which have a long track record of withstanding even harsh desert conditions. Compared to parabolic troughs, linear Fresnel collectors typically have a bigger aperture per receiver unit, an even more reduced wind load and a higher ground usage ratio. These features are especially interesting

[1] So-called 'dewar'-type evacuated tube units as used in stationary hot water heating arrays are available but have not been successfully applied with PT concentrators.

19.3 Linear Fresnel collector for a solar cooling installation in Doha, Qatar (source: Industrial Solar GmbH).

19.4 Sheffler Dishes: solar steam cooking system at Brahma Kumaris, Rajasthan, India (source: Brahma Kumaris, 2007).

for rooftop installations and can compensate for the reduced optical efficiency due to the non-ideal reflector.

Point focus systems

There are a number of dish systems, especially in India, mostly for large-scale solar cooking installations. Compared to the dish reflectors described earlier in this book, these so-called 'Sheffler' dishes (Fig. 19.4) use a fixed focus to concentrate on. In that sense they can be classified as heliostats. The approach of the Sheffler dish is a simplified construction that uses as

much as possible local materials and handcraft. An interesting design detail of the Sheffler dish is its adaptation of the reflector's shape to the yearly change of the solar altitude. This allows for the use of a relatively simple polar axis mechanism for the daily tracking. The overall concentration ratios achieved are small by dish standards and similar to linear concentrators.

19.3.2 Heat transfer medium

The relatively low operating temperature of process heat applications sometimes allows for the use of pressurized water as heat transfer medium, which is attractive because of its good heat transfer parameters and cost efficient system components. Direct steam generation is an interesting option, because it offers the potential for highly efficient heat transfer and relatively lean system integration with conventional steam networks.

When high pressures are prohibitive for whatever reason, oil can be used as the heat transfer fluid (HTF). Compared to CSP applications, the temperature limits of synthetic oil usually are of no concern. What can be more problematic is the environmental safety issue that no oil must mix with drain water, etc., in case of spillage. Safety measures can add substantially to the system costs especially for rooftop installations. In principle, air is also an interesting HTF for process heat systems but has not been pursued widely yet.

19.3.3 Storage

Thermal storage is very important for achieving high solar shares even in hybrid solar/fossil process heat installations. Only very few applications fit so well to the solar resource that the need for storing solar heat might be negligible. In most cases several hours of full load storage operation are on the wish list of solar project engineers. Available storage technologies are discussed in detail in Chapter 11. They can be divided into sensible, latent and chemical heat storage technologies, which then have different pros and cons for different storage capacities and temperature levels. For low temperatures (up to 100°C), simple single water tanks are a cost-efficient storage solution, which are available in a large variety of sizes and design. Above 100°C, water storage needs to be pressurized, which adds substantially to the cost. This is why at a certain point other sensible storage materials like thermal oil become interesting. Sensible heat stores similar to those used in CSP plants (with a hot and a cold tank) are also an option when using pressurized water or synthetic oil as HTF.

Steam accumulators are conventional practice for short duration storage of solar steam. However, a substantial storage capacity for full load

operating quickly becomes prohibitively expensive with steam accumulators. Latent (phase change) or chemical heat stores are options under development for storing heat from solar steam. A number of material combinations are available for different operating temperatures. Especially in the temperature regime below 300°C, some seem to be close to commercialization (see Tamme *et al.*, 2008).

A favourable approach for cost-efficient system dimensioning during the present early phase of market development is the so-called fuel saver design, which limits the peak capacity of the solar system such that it just about meets the minimum continuous heat demand of the process. This will minimize shutdown periods of the solar system and also avoids the need for high storage capacities and consequently leads to minimum payback periods. Of course the flip side of this approach is that solar share is rather limited.

19.3.4 System integration

Solar components for the generation of industrial process heat are available with a broad spectrum of technologies. However, the optimum integration with conventional heating systems in sometimes quite complex production processes requires a thorough system analysis. It is not sufficient just to look at the integration of solar collectors because, according to the first law of thermodynamics, all heat that is fed into a process needs to be released to the environment afterwards. Often both the generation of heat and the later re-cooling create costs. This fact is not very obvious because sometimes the heat is dissipated without apparent effort (e.g., after bottle washing the hot bottles are simply left to cool down over a longer period of time), but in many cases the active cooling of a process (e.g., cooling of wort in a brewery) and possible heat recovery is important for the product and can drastically influence the overall system energy performance.

Heat rejection to the ambient is typically done with cooling towers, which are available with water evaporators or with dry fan coils. The performance of dry cooling is limited by the temperature of the ambient air, whereas wet cooling can get the fluid temperature down to close to the dew point of the ambient temperature. Especially for chillers with a small temperature lift, the temperature of heat rejection is a very important design parameter.

The first engineering exercise for the application of solar heat generation systems in industrial processes is the search for internal heat recovery options (which in some cases might even prove an additional solar heat source to be obsolete). During this exercise, so-called 'pinch analysis' (see Brunner *et al.*, 2008) is a method that looks at the temperature profile of all heat streams entering a process (heating) and those leaving the process (cooling). It yields the maximum heat recovery potential and the minimum

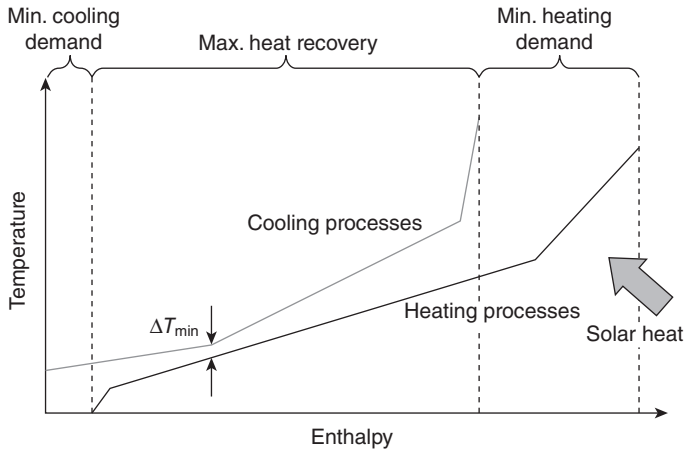

19.5 Pinch diagram, adapted from Brunner *et al.* (2008).

temperature at which a new heat generation system should be integrated (see Fig. 19.5). Of course, the second exercise usually is to bring together theory and reality. Poor overlapping of batch processes or physical distance might lead to high costs for internal heat recovery, which then again might favour additional solar heat sources.

The system integration of low temperature solar heat is typically in direct competition with heat recovery options. However, for regions with high direct solar insolation, the generation of high temperature heat is a feasible option, which is also suitable for retrofitting of existing plants. Figure 19.7 gives the hydraulic scheme of a built demonstration project for the integration of direct steam generation into an existing steam network. It is a cost efficient 'fuel saver' approach, which does not interfere with the production process itself.

19.3.5 Backup

The backup system in an industrial process heat system will typically simply be a fossil- or biomass-fired boiler. In this case the hydraulic integration with solar heat (steam or other) is relatively easy and solar heat generation will directly replace the burning of fossil fuel.

Looking at solar cooling, the situation is more complex because here the conversion efficiency of the thermally driven chiller plays an important role for the overall system efficiency. It is important to analyse the performance of the complete system on a yearly basis rather than only look at nominal load conditions. If, for example, a fossil-fired boiler is used as an auxiliary heat source for a solar cooling system with a single effect chiller, the yearly

solar share needs to be very high or the auxiliary operation will undo any fuel saving effect compared to a conventional state-of-the-art electrically driven vapour compression chiller. Substantial backup via an auxiliary boiler should only be used with highly efficient thermally driven chillers (e.g., double or triple effect absorption chillers).

19.4 Case studies

In this section, three case studies are described in more detail.

19.4.1 Direct steam generation for a production process in Germany

This case study is adapted from Krüger *et al.* (2011). In this project a parabolic trough collector field from Solitem has been mounted on the roof of an industrial production site in Ennepetal, Germany, to demonstrate the solar supply of saturated steam for an existing industrial steam network. The trough array is shown in Fig. 19.6. The solar system produces saturated steam at a pressure of 4 bar and a temperature of 143°C, which is fed into a steam line of the aluminium processing company Alanod. The solar field consists of 108 m^2 of parabolic trough collectors by the company Solitem.

Figure 19.7 gives an overview of the plant layout. Automatic operation starts when the solar radiation reaches a programmed level. When the feedwater enters the solar field, it first gets preheated to the evaporation

19.6 Collector field by Solitem at the Alanod factory in Ennepetal, Germany.

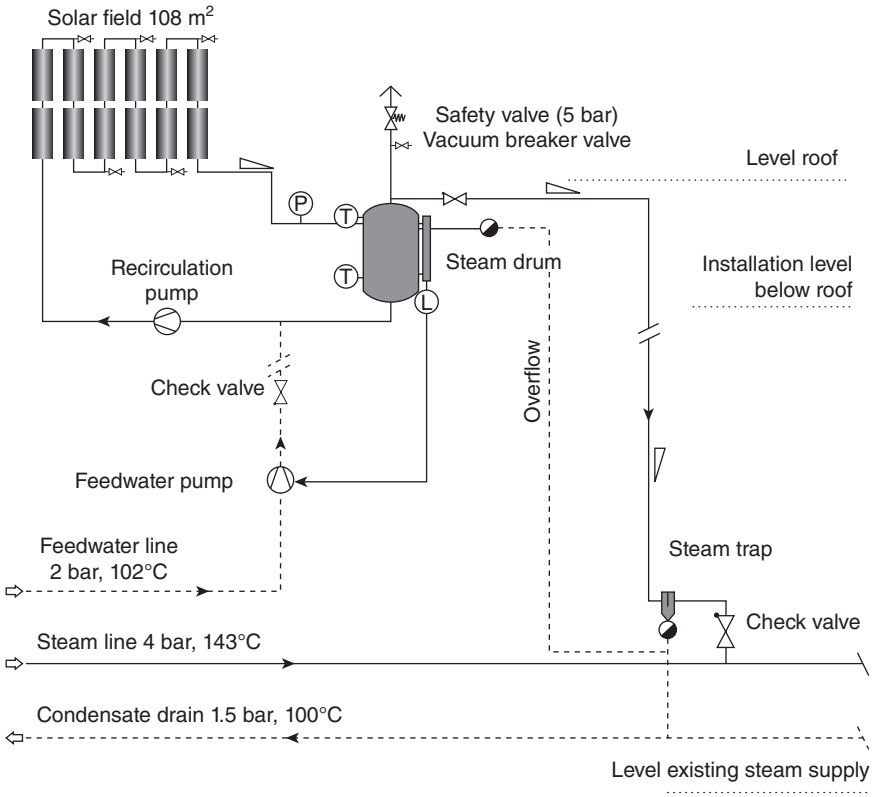

19.7 Hydraulic scheme for the integration of direct steam generating collectors into the existing steam network of a production facility in Germany (source: Krüger *et al.,* 2011).

temperature and then partly is evaporated in the serially connected collectors. The steam/water mixture leaving the solar field gets separated in a steam drum from where the steam flows to the main steam line of the production. A pump recirculates the water out of the steam drum back to the solar field. The steam needs to pass a check valve before entering the main steam line, thus it can only enter the steam line after reaching a pressure which is higher than in the steam line. Evaporated water is replaced by feedwater from the plant.

The main steam line supplies various consumers in the conveyer line for anodic oxidation treatment, such as degreasing and sealing baths. The solar plant has been operating since July 2010. Direct steam generation has proven to be a viable technology to supply saturated steam to an industrial steam network.

19.8 Fresnel collector field by Industrial Solar GmbH in front of showcase football stadium in Doha, Qatar.

19.4.2 Solar cooling with linear Fresnel collectors in Doha, Qatar

This case study is adapted from Zahler *et al.* (2011). A solar cooling system powered by a 700 kW concentrating solar collector field, manufactured by Industrial Solar GmbH drives the air-conditioning of a showcase football stadium in Doha, Qatar. The 1,408 m^2 Fresnel collector field (shown in Fig. 19.8) heats water at 16 bar pressure to temperatures of up to 200°C powering a double-effect lithium bromide absorption chiller.

A pressurized hot water storage with a volume of 40 m^3 allows for delayed operation of the absorption chiller to avoid operation during noon hours with high ambient temperatures thus reducing the water consumption of the wet cooling tower. The double-effect lithium bromide absorption chiller by the Indian company Thermax has a nominal cooling capacity of 750 kW. The cold is stored in tanks beneath the stadium and then distributed in the building (Fig. 19.9).

The circulation pumps allow the flow rate to be adjusted from 5 m^3/h to 30 m^3/h to maintain a nearly constant operating temperature throughout the day. This is of special importance as the collector loop is directly connected to a pressurized water storage with a volume of 40 m^3. The operating temperature of this heat storage is in the range between 140 and 200°C, which translates to a storage capacity of approx. 2,500 kWh.

The double-effect absorption chiller has a cooling capacity of 750 kW with a nominal COP of 1.39 and can be operated with pressurized water with a temperature between 160 and 180°C from the hot water storage. Alternatively, it can be fired directly with an integrated auxiliary burner.

The waste heat of the absorption chiller is rejected to the ambient using an open type cooling tower with a cooling power of approx. 1.3 MW. The

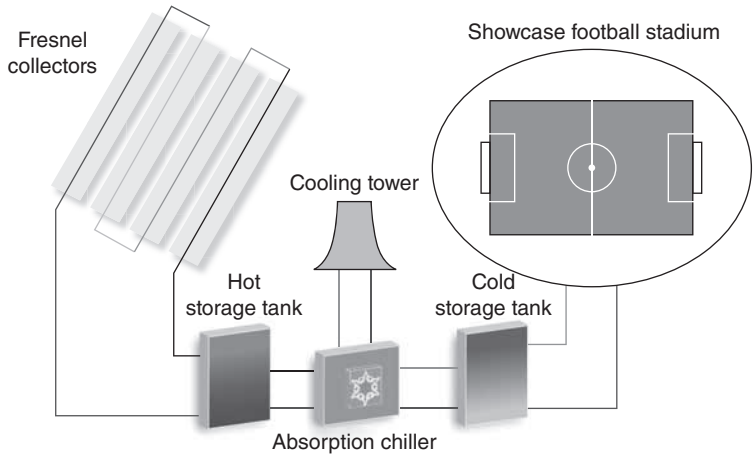

19.9 Scheme of the main components.

cooling water from the condenser and absorber of the chiller enters the cooling tower at a temperature of 39°C.

The evaporator of the chiller is connected via a cold water circuit to a PCM cold storage with a volume of 100 m^3. The total storage capacity of this tank is 5.780 kWh. Compared to a cold water storage of the same size with operating temperatures from 7 to 14°C, the sensible heat stored would be only 14% of the latent heat stored in the PCM storage. The PCM cold storage is connected to the ventilation system of the showcase stadium.

To realize a continuous air-conditioning of the stadium, which contains a large air volume, a high cooling power would be needed. However, the stadium is only intended to be used for a few hours at a time and not on two successive days. Therefore investment costs have been reduced by using a smaller air-conditioning system, which is operated several days ahead of a match and relying on the thermal inertia of the building to maintain conditions during use. The rooftop of the stadium can be closed during cooling down operation. Then during the game, which usually takes place in the evening hours, the rooftop can be opened.

Due to the high ambient temperature and humidity during daytime, it is difficult to reject the waste heat of the absorption chiller to the environment with a wet cooling tower. Therefore the collector heats a 40 m^3 hot water storage during peak solar hours for delayed operation of the absorption chiller. The chiller then cools down the PCM cold storage, which can store up to almost 8 hours of chiller full load operation until all of the PCM is solid.

19.4.3 Solar steam cooking system at 'Shantivan', the Brahma Kumaris complex at Taleti, Abu Road, India

This case study is adapted from Brahma Kumaris (2007) and Pilz (2012). In May 1997 a solar steam cooking system was installed at the Brahma Kumaris in the Academy for a Better World in Mt. Abu (see Fig. 19.4). The solar steam cooker typically produces 3,500 kg of steam per day, enough to cook two meals for 800 people. A scheme of the cooking system is shown in Fig. 19.10.

The parabolic dish concentrators were developed originally by Wolfgang Scheffler from Switzerland. At present the concentrators are manufactured locally by the Brahma Kumaris in Taleti, Abu Road, and by Deepak Ghadia, Eco Centre in Valsad, Gujarat, and several other places in India. The frame and support structure is a steel design. The sunlight is concentrated into a focus of 30 cm diameter at a distance of 4 m from the centre of the dish. A dish has a maximum output of 4.0 kW and reaches temperatures of up to 850°C in the focus. The mirrors are positioned in an accurate east-west alignment and tracking is done by means of counterweights and an electronic timer. In the evening, the system has to be manually reset into the morning position.

The steam for cooking is generated directly in a 12″ header pipe above the receivers. The receivers use the thermosyphon principle, so there is no need for a circulation pump. The header pipe acts as steam generator, steam storage and feedwater reservoir. The steam cooking system in Shantivan has succesfully operated over many years and has been reproduced in several other projects in India.

19.5 Future trends and conclusion

Low temperature solar thermal systems (water heaters) face increasing competition with photovoltaic (PV) driven heat pump systems. Also electricity production in large CSP plants sees PV as serious competition as long as storage is not needed. On the other hand, it is presently not competitive to use PV for direct electric heating. At temperatures above 80–100°C, which is a technical limit for vapour compression heat pumps, solar thermal collectors will be the most cost effective way to generate solar heat for quite some time to come.

The integration of solar boilers into the steam networks of industry will have enormous potential in the future. Some technical developments like direct steam generating collectors and commercial effects like economics of scale will cut costs on the solar side.

Similar to conventional boilers, the combination of heat production and electricity production in cogeneration units will offer opportunities to

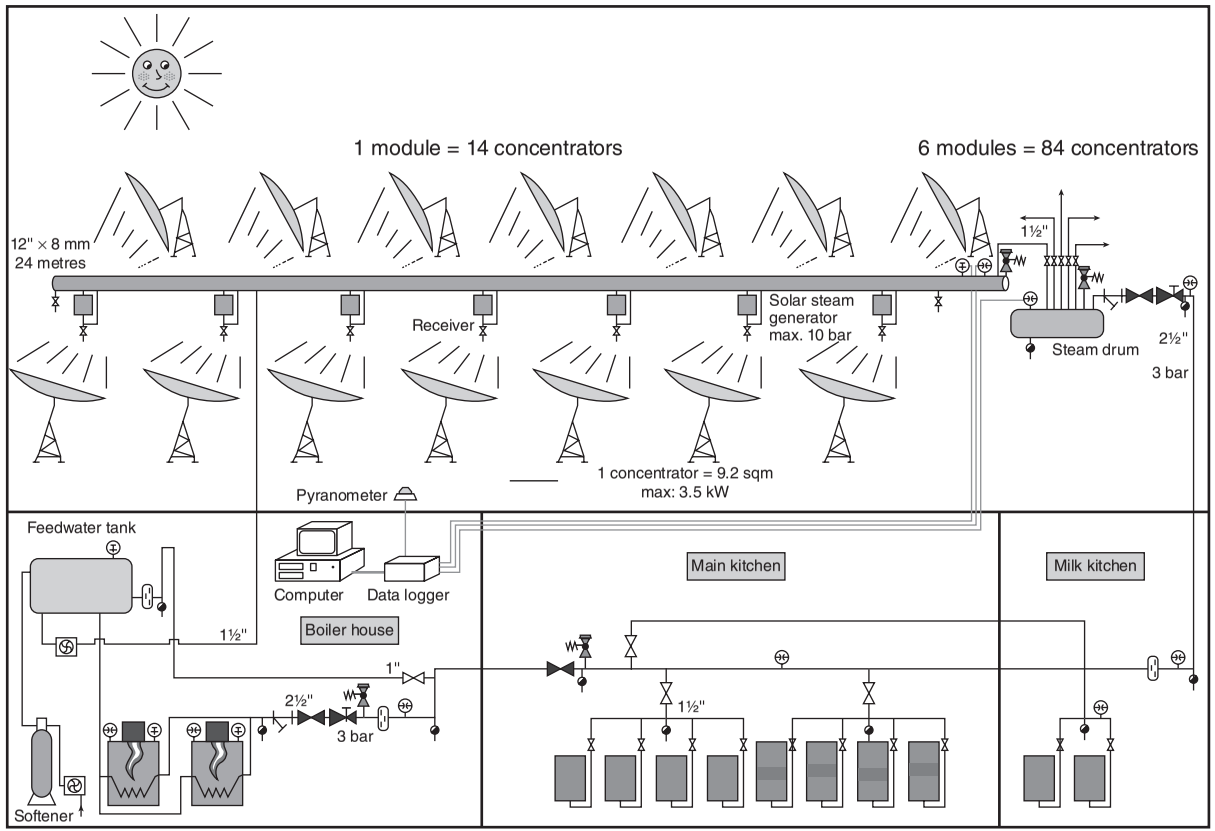

19.10 Scheme of the solar steam cooking system in Mt. Abu.

enhance energy efficiency and improve economics at the same time. Polygeneration means the combined production of three or more useful outputs. This can be, for example, the production of electric power in a turbine, the operation of an absorption chiller with the waste heat of the turbine and then subsequently the use of the rejected heat from the chiller in a low temperature application, e.g. the heating of a greenhouse. Also the integration of a desalination unit is an interesting option for polygeneration. Many other combinations of technologies and applications can be imagined. It will be the future challenge for engineers to find the cleverest energy-saving and cost-efficient designs.

Apart from electricity generation, concentrating solar thermal technologies are a feasible option to substitute the burning of fossil fuels in industrial process heat applications and to power thermally driven chillers in regions of the earth with a high share of direct insolation. While first pioneer projects were already realized in the 1970s, it is only in recent years that new product developments were started and new projects were realized. With rising and highly volatile energy prices being an increasingly important production factor in many industrial processes and cooling and refrigeration contributing to electricity peaks worldwide, this technology will eventually become a major energy and cost saving opportunity for industry.

19.6 Sources of further information and advice

IEA SHC, *International Energy Agency Solar Heating and Cooling Program.* www.iea-shc.org (accessed 02.01.2012).

Poship (2001), *The Potential of Solar Heat for Industrial Processes.* Available from http://www.solarpaces.org/Library/docs/POSHIP_Final_Report.pdf (accessed 02.01.2012).

PROCESOL II (2002), *Solar Thermal Plants in Industrial Processes, Design Guidelines.* Available from www.solarthermalworld.org (accessed 02.01.2012).

RHC-Platform, *European Technology Platform on Renewable Heating and Cooling.* www.rhc-platform.org (accessed 02.01.2012).

Weiss W and Biermeyer P (2009), *Potential of Solar Thermal in Europe.* Available from www.estif.org (accessed 02.01.2012).

Weiss W and Mauthner F (2011), *Solar Heat Worldwide.* Available from www.iea-shc.org (accessed 02.01.2012).

19.7 References

Brahma Kumaris (2007), *Prajapita Brahma Kumaris Ishwariya Vishwa Vidyalaya.* Available from www.solar.bkwsu.de (accessed 02.01.2012).

Brunner C, Slawitsch B and Giannakopoulou K (2008), *Industrial Process Indicators and Heat Integration in Industries*, Joanneum Research, Graz, Austria. Available from http://www.energytech.at/pdf/ieatask33_4_ipi.pdf (accessed 02.12.2012).

Ecoheatcool (2006), *Work Package 1, The European Heat Market, Final Report, IEE ALTENER Project*, Euroheat & Power, Belgium.

Henning H-M (2007), Solar assisted air conditioning of buildings – an overview. *Applied Thermal Engineering*, 27(10), 1734–1749.

Krüger D, Lichtenthäler N, Dersch J, Schenk H, Hennecke K, Anthrakidis A, Rusack M, Lokurlu A, Saidi K, Walder M, Fischer S and Wirth HP (2011), *Solar steam supply: Initial operation of a plant*, ISES Solar World Congress, Kassel, Germany.

Pilz J (2012), private communication, GoloPilz, Advisor Solar Energy, Brahma Kumaris, Mount Abu – 307501, Rajasthan, India.

Tamme R, Bauer T, Buschle J, Laing D, Müller-Steinhagen H and Steinmann W-D (2008), Latent heat storage above 120°C for applications in the industrial process heat sector and solar power generation. *International Journal of Energy Research*, 32, 264–271.

Vannoni C, Battisti R and Drigo S (2008), *Potential for Solar Heat in Industrial Processes*, IEA Task 33/IV. Available from www.iea-shc.org (accessed 02.01.2012).

Zahler C, Berger M and Louw J (2011), *Industrial Solar Fresnel Collectors powering the largest Solar Cooling system in the Middle East for a football stadium*, Solar-PACES, Granada, Spain.

20

Solar fuels and industrial solar chemistry

A. G. KONSTANDOPOULOS, Centre for Research and Technology Hellas, Greece and Aristotle University, Greece, C. PAGKOURA, Centre for Research and Technology Hellas, Greece and University of West Macedonia, Greece and S. LORENTZOU, Centre for Research and Technology Hellas, Greece

Abstract: The main advantage of concentrated solar power (CSP) is the production of carbon free energy. However, the problem is that the energy produced must be directly consumed. This could be dealt with by the chemical storage of solar energy in the form of an energy carrier such as hydrogen (H_2), which is transportable and can be used upon request. The available routes to produce solar hydrogen as well as different kinds of solar reactors known from the literature are presented. If solar thermochemical processes are used to decompose hydrocarbons (either biomass or fossil), the resulting mixture of hydrogen and carbon monoxide (CO) can be used as the feedstock for 'Fischer Tropsch'-based liquid fuel production, for diesel and gasoline replacements. In addition, the idea of combining solar H_2 with an actual waste such as carbon dioxide (CO_2) to produce renewable solar HC fuels is discussed. This is an attractive way to manage the problem of CO_2 storage and, at the same time, to create an intermediate step which is essential for the development of the appropriate infrastructure that could support the H_2 economy. Finally, some potential industrial applications of solar fuels and solar energy are described.

Key words: solar fuels, solar hydrogen, thermochemical water-splitting, carbon neutral fuels, solar fuel applications, solar reforming.

'the general struggle for existence of animate beings is not a struggle for raw materials – these, for organisms, are air, water and soil, all abundantly available, nor for energy which exists in plenty in any body in the form of heat, but a struggle for entropy, which becomes available through the transition of energy from the hot sun to the cold Earth' (Boltzmann, 1886).

20.1 Introduction

Since the industrial revolution at the end of the eighteenth century, the rate of use of fossil fuels has been growing continuously. Significant technological achievements that have led to an improvement in the standard of living were based on the extensive exploitation of carbonaceous fuels. The

developments that have taken place in many parts of the world in the last 50 years have led to a rapid increase in energy demand. The major contribution in covering global energy needs is derived from fossil fuels (coal, oil and natural gas). However, the energy crisis in the early 1970s, the fluctuations in oil price, the depletion of accessible oil deposits and the environmental effects of the use of fossil fuels (greenhouse gas emissions, accidental oil spills, etc.) have made it clear that at some point the world has to reduce its dependence on or even abandon the use of fossil fuels.

Over recent years, technology has made progress in the production of energy from alternative sources; however, still only a small fraction of fossil fuel use has been substituted. Much of our everyday life (transportation sector, industrial processes, etc.) is currently powered mainly by liquid hydrocarbon fuels (Fig. 20.1(a)). The term 'liquid fuels', refers to substances that at room temperature are in a liquid state and may 'fuel'/supply

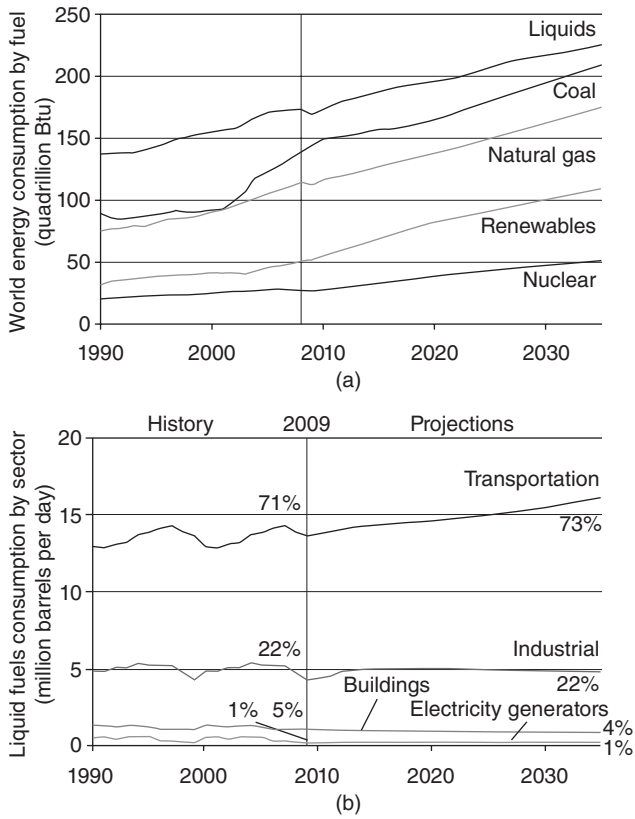

20.1 (a) World energy consumption by fuel (adapted from IEA (2011a); (b) Liquid fuels consumption by sector; historical data and projections up to 2035 (adapted from IEA (2011b).

processes with energy via combustion with air. The most widely used and commonly known liquid fuel is petroleum and all of its products. Besides petroleum products, liquid fuels may be derived from other hydrocarbon sources (e.g. coal or hydrocarbon gases converted to liquids) or any liquid fuel produced by the combination of hydrogen with carbon monoxide (syngas). Liquified petroleum gas ('LPG', composed mainly of propane), plays a minor but important role in the energy mix. It is a liquid at ambient temperatures if stored at modest pressure and is used extensively as an alternative transportation fuel. Liquified natural gas (LNG) is a rapidly growing means of transporting natural gas with less bulk by cooling natural gas to approximately –162°C at close to atmospheric pressure. Another form of natural gas used for transport is compressed natural gas (CNG).

The sector that is almost completely reliant on the use of liquid fuels is that of transportation (Fig. 20.1(b)). This reliance is related to the advantages that liquid fuels have over other energy sources existing in different states (gaseous and solid fuels). Liquid fuels have high energy density per volume, can be stored easily and used upon demand (when compared to electricity), are easier to transport and handle (compared to solid fuels) and require smaller volume of storage tanks (compared to gaseous fuels). On the other hand, the environmental 'cost' originating from the persistence in relying on conventional energy sources is continuously growing and is a major threat to the global climate. In addition, conventional sources of petroleum are widely acknowledged to be close to or past the 'peak' beyond which demand continues to outstrip supply and prices consequently continue to rise.

To avoid this inauspicious future, measures need to be taken that could include the substitution of the dominant conventional fuels by renewable energy sources such as solar energy. Part of this process will include the increasing electrification of the transport sector. However, the practical advantages of liquid fuels are compelling and the global investment in existing liquid hydrocarbon processes and infrastructure is enormous. Bioethanol and biodiesel offer completely renewable alternatives that are already in commercial application. However, it is clear that there are insufficient land and water resources for these to practically replace petroleum use completely.

Most of this book is directed at the use of concentrating solar thermal (CST) systems for the production of electrical power. This chapter looks at the possibility of using CST systems to produce alternative fuels that are either completely or partly derived from the solar energy input. In practice this means solar derived hydrogen and/or hydrogen-based compounds are the energy carrier.

Using CST systems to produce solar fuels not only offers a more environmentally benign alternative to petroleum-based fuels whilst preserving

their advantages, it also naturally addresses the need for energy storage that follows from the intermittency of solar radiation. However, the aim of the current chapter is not to focus on chemical processes for energy storage but rather on chemical processes for fuels. The interested reader should also consult Chapter 11 on energy storage.

20.2 Solar chemistry

Solar fuels are derived from 'solar' processes that exploit the energy of the sun, either in the form of heat or in the form of photons, to drive endothermic (energy storing) chemical reactions. All chemical reactions can proceed in either direction and energy is either absorbed (in the endothermic direction) or released (in the exothermic direction). The laws of thermodynamics dictate that at any given temperature or pressure, reactions will proceed until a state of equilibrium is reached where the rate of the forward reaction equals the rate of the reverse reaction:

$$A + B + \Delta H \Leftrightarrow C + D \qquad [20.1]$$

According to the principles of Le Chatelier and van't Hoff, a reaction in chemical equilibrium may be shifted, forward or reverse, by implementing a change in concentration, pressure or temperature, in a way that will force the reaction towards the direction of the reactants or the products in order to undo the change and bring the system back to equilibrium. For example, an increase in temperature will favor the direction of the endothermic reaction.

In addition to the underlying drive towards equilibrium conditions, the actual rates of reactions (forward, reverse or net) are determined by complex mechanisms. A simple but important concept to reaction rates is the idea of an 'activation energy', an amount of energy that the reactant molecules must have to escape from a current state and initiate a reaction to a new state irrespective of whether the final result is either the absorbing or releasing of energy. The activation energy is an energy barrier or 'hurdle' that must be cleared.

The rate of most reactions is increased as temperature increases, because more of the reactants receive the necessary energy to pass the barrier of the activation energy of a reaction. The influence of temperature on the rate of a reaction is described by the Arrhenius equation.

$$k = k_0 \cdot e^{-\frac{E}{RT}} \qquad [20.2]$$

where k_0 is the pre-exponential factor, E is the activation energy, R is the universal gas constant and T is the temperature.

The Arrhenius equation is related to the probability that reactants have sufficient energy to pass the activation energy barrier in order to achieve the production of the desired products. A more accurate form of the Arrhenius equation includes an additional temperature factor (Masel, 2001).

$$k = k_0 T \cdot e^{-\frac{E}{RT}} \qquad [20.3]$$

The energy barrier of a reaction can be lowered with the use of catalysts, that help the reaction to take place faster or at lower temperatures. Catalysts introduce a series of reaction steps that overall equates to the original reaction in effect and leaves the catalyst returned to its initial state, but each of which have lower activation energies. In the case of multistep processes, the rate of the overall reaction is determined by the slowest step which has the highest activation energy. This step is called the 'rate determining' step. By changing the factors that would increase the rate of the slowest reaction (e.g., the concentration of the reactants of the slowest reaction), the rate of the overall reaction would also increase.

20.2.1 Thermochemical and photochemical reactions

As mentioned above, the necessary energy for a reaction to take place can be provided thermally by an increase in temperature. Processes that are based on this kind of reactions are called thermochemical processes. An alternative way to provide the reactants with energy greater than the activation energy of a reaction is via direct absorption of photons of sufficient energy. As the intensity of light increases, the number of molecules absorbing photons of sufficient energy is increased with subsequent increase in the rate of the reaction. These are called photochemical processes.

In the case of thermochemical reactions a catalyst may play a significant role in the realization of the reaction. In the case of the photochemical processes, a photosensitizer is effectively a catalyst that enhances the absorption of photons of energy necessary for the initiation of the reaction.

In the context of CST systems, high radiation fluxes are expected by definition. Under such circumstances, photochemical reactions could take place if the radiation is allowed to access the reactants directly through a windowed reactor. However all photons not directly utilized would lead to heating of the reactants to very high temperatures and thermochemical reactions would consequently occur at high rates and so dominate. Thus this chapter is directed mainly at the utilization of solar thermochemical processes for the production of solar fuels and the storage of solar energy.

20.2.2 Applications of solar thermochemistry to fuel production

As was mentioned in the introductory paragraphs, the potential of the sun can be utilized for the production of solar fuels (i.e., solar hydrogen, solar hydrocarbons, alcohols and liquid fuels). Solar thermochemistry can be employed for the conversion of water and waste CO_2 into H_2 and CO, which are valuable building blocks for the production of synthetic fuels as well as other chemicals. The different pathways are summarized by Graves *et al.* (2011) in Fig. 20.2.

In the case of solar hydrogen, the technological maturity and the lack of necessary infrastructure do not allow its immediate large-scale application. On the other hand, solar hydrocarbons can play an intermediate role since they are a means of storing solar energy into a medium which has high energy density and can be more easily stored and distributed, using the current infrastructure, and applied in existing vehicles (Graves *et al.*, 2011).

Estimates by the IEA (2010) suggest that CSP facilities could begin providing competitive solar-only or solar-enhanced gaseous or liquid fuels by 2030, while by 2050 CSP could produce enough solar hydrogen to displace 3% of global natural gas consumption, and nearly 3% of the global consumption of liquid fuels. This seems a conservative prediction, as actual deployment is likely to be strongly affected by the progress of international oil prices.

The processes that can be employed for the synthesis of fuels with captured CO_2 and solar H_2 and CO as precursor reactants are common to the

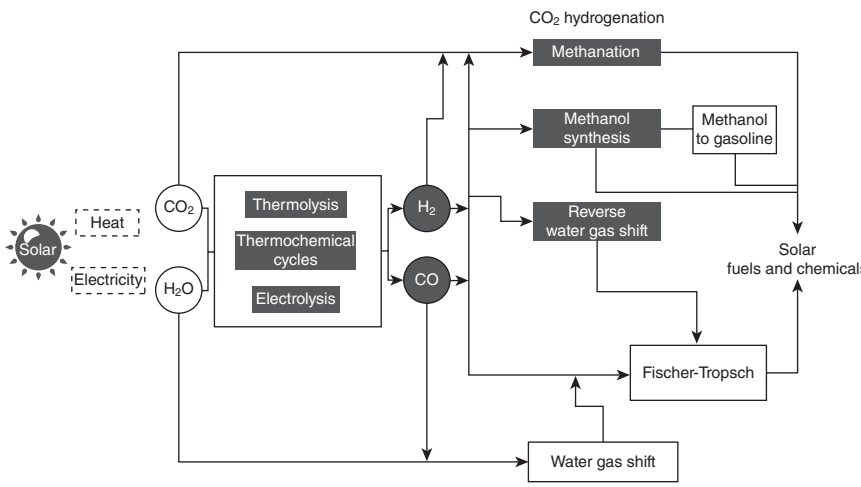

20.2 Pathways of CO_2 conversion to solar fuels (adapted from Graves *et al.,* 2011).

ones employed for the conventional fossil-based synthetic fuels and other chemicals. Thus all the downstream technology for solar liquid fuels is available.

20.3 Hydrogen production using solar energy

Solar hydrogen is a promising energy carrier (or solar fuel). Currently hydrogen (that is produced nearly entirely from fossil fuels) is used almost exclusively as a chemical in industrial processes (e.g. in ammonia synthesis and fertilizer production, in oil industries in refineries during hydrogenating processes and for the conversion of heavy and low crude oils into transport fuels) (Pregger *et al.*, 2009; World Nuclear Association and Hore-Lacy, 2009). It is projected that hydrogen use is going to increase, due to the increase in the exploitation of heavy hydrocarbons (Pregger *et al.*, 2009). Demand for hydrogen will increase rapidly, as it penetrates to other new sectors, such as transportation, generation of heat, electric power or mechanical energy (Pregger *et al.*, 2009). Conventionally hydrogen is synthesized via non-renewable processes that involve hydrocarbon reforming (usually natural gas reforming) or hydrocarbon pyrolysis.

Other more sustainable options under development are the production of hydrogen from biomass via gasification, pyrolysis, etc., biological hydrogen that can be produced by genetically modified microorganisms (algae, bacteria) via photolytic or aerobic (photo-fermentation) and anaerobic (dark fermentation) processes. However, the solar to hydrogen conversion efficiency is extremely low. Technologies that employ water as a primary raw material for hydrogen production are electrolysis, photoelectrolysis and finally thermochemical water-splitting which is discussed in detail in this chapter (Steinfeld and Meier, 2004, Holladay *et al.*, 2009).

All of the above processes require energy that can be provided from the sun. For the thermochemical approaches, the solar input can be provided by employing CST systems. As mentioned in the previous paragraphs, the utilization of CSPs can provide the required energy for natural gas reforming, towards hydrogen or syngas production. Additionally, hydrocarbon pyrolysis (e.g., natural gas cracking) for the production of hydrogen and carbon black can be conducted with the aid of concentrated solar radiation. Finally, a completely renewable production of hydrogen from water can be achieved with the aid of concentrated solar configurations that can provide the necessary energy either indirectly by supplying electricity to an electrolyzer or directly by supplying the required heat for the thermochemical water-splitting.

The production of hydrogen with the aid of solar energy has been the subject of investigation for several decades. Some exemplar studies were those of Bilgen *et al.*, (1977), Bilgen and Galindo 1981; Sibieude *et al.* (1982)

and Tofighi (1982). Comprehensive reviews on solar thermochemical processes and their potential on hydrogen production were conducted in Kodama and Gokon (2007), Steinfeld (2005), Steinfeld and Weimer (2010), Abanades *et al.* (2006), Perkins and Weimer (2004) and Möller and Palumbo (2001b).

The following sections provide more detail on the solar thermochemical routes to hydrogen production. For processes that begin with hydrocarbon feedstock, the products produced can be a mixture of hydrogen and carbon monoxide. This offers two options, either separation and use of pure hydrogen, or the further processing of the mixture to produce derivative fuels as discussed in Section 20.5.

20.3.1 Solar hydrogen from hydrocarbons

Natural gas steam reforming

The majority of the hydrogen produced globally derives from natural gas steam reforming, which is a well-established technology. Natural gas solar steam reforming (Eq. [20.4]) is based on the thermal decomposition of a mixture of methane and steam. The reaction also proceeds in parallel with the water gas shift reaction (Eq. [20.5]). The final amount of CO versus CO_2 in the product mix depends on the operation conditions and the catalyst used. Usual temperatures for the reactions fall within the range from 800 to 1,000°C, while the process also involves the separation of CO_2 from the product gases for pure hydrogen production. Reactors are typically tubular units with packed catalyst beds that use metal catalysts supported on ceramic pellets.

Reforming:

$$CH_4 + H_2O \rightarrow CO + 3H_2 \qquad \Delta H^0 = -206\ \text{kJ/mol} \qquad [20.4]$$

Water gas shift:

$$CO + H_2O \rightarrow CO_2 + H_2 \qquad \Delta H^0 = 41\ \text{kJ/mol} \qquad [20.5]$$

The combination of the conventional natural gas steam reforming with solar technologies is an efficient means of solar hydrogen production since it is an intermediate path until purely renewable solar processes are fully developed and debugged.

Solar steam reforming in a closed loop system was demonstrated by Anikeev *et al.* (1990), while one of the first attempts at combining solar energy with steam reforming was the ASTERIX project where a methane steam reformer was integrated into a solar facility in Almería, Spain (Böhmer *et al.*, 1991). A more recently developed technology which is currently at the state of completion and at a state of pre-commercial readiness,

is the one developed in Australia by CSIRO. The product of this technology is known as 'SolarGas' and is the result of the combination of solar energy with natural gas (Stein *et al.*, 2009, Rochlin *et al.*, 2011).

Natural gas cracking

Methane decomposition can be described by the following overall reaction:

$$CH_4 \rightarrow 2H_2 + C \qquad \Delta H^0 = 75\ \text{kJ/mol} \qquad [20.6]$$

The solar thermal non-catalytic cracking of methane for the production of hydrogen, requires very high temperatures to achieve a significant yield (>1200°C) (Abbas and Wan Daud 2010a, 2010b). For catalytic methane decomposition, various types of reactors and catalysts are proposed in literature. The solar reactors are divided in those that heat the reactants directly (Hirsch and Steinfeld, 2004; Kogan and Kogan, 2003a) and indirectly (Rodat *et al.*, 2010a, 2010b, 2011); there are reactors for continuous methane decomposition, fixed bed or fluidized bed reactors, etc. (Amin *et al.*, 2011). Besides solar reactors, plasma reactors are also encountered in the literature (Gaudernack and Lynum, 1998). With respect to the catalyst used for methane cracking, the most common are nickel-based catalysts (Zhang and Amiridis, 1998), but there are also iron- or cobalt-based catalysts (Avdeeva *et al.*, 2002), La_2O_3-promoted catalysts (Figueiredo *et al.*, 2010), etc.

Gasification of solid hydrocarbons

The third route to produce solar hydrogen (or solar gas mixtures in general, e.g. CO and H_2, etc.) from hydrocarbons besides reforming and cracking is by solar gasification of solid hydrocarbons such as coal (lignite, anthracite), biomass (wood, agricultural residues, aquatic biomass) and any kind of organic feed in general.

Coal can be gasified (Gregg *et al.*, 1980; Matsunami *et al.*, 2000) by reacting either with steam (Eq. [20.7]), or with carbon dioxide (Boudouard reaction, Eq. [20.8]).

$$(C) + H_2O \rightarrow CO + H_2 \qquad \Delta H^0 = 135.75\ \text{kJ/mol} \qquad [20.7]$$

$$(C) + CO_2 \rightarrow 2CO \qquad \Delta H^0 = 169.16\ \text{kJ/mol} \qquad [20.8]$$

Similar to the reactions followed for coal gasification is the reaction for biomass gasification which is described in a simplified equation in Eq. [20.9] (Melchior *et al.*, 2009), where only the main compounds of the reaction are shown (impurities such as sulfur and nitrogen are omitted from the reaction

scheme). A more general equation describing biomass gasification process is described in Eq. [20.10] (adapted from Lédé, 1999 and Balat *et al.*, 2009). Solar biomass gasification was demonstrated to be feasible when added in mixtures with coal during the 1970s and 1980s as a possible futuristic solution dealing with coal depletion issues (Gregg *et al.*, 1980). Since then, the feasibility of net biomass solar gasification has also been proven (Lichty *et al.*, 2010; Sundrop Fuels Inc., 2009).

$$CH_zO_y + (1-y)H_2O \rightarrow (z/2+1-y)H_2 + CO \qquad [20.9]$$

$$\text{Biomass} + O_2(\text{or air or } H_2O) \rightarrow CO, CO_2, H_2O, H_2, CH_4, \text{other CHs, tar, char, ash} \qquad [20.10]$$

The conversion of solid fuels to renewable liquid fluid fuels via solar gasification broadens their applicability.

20.3.2 Solar hydrogen from thermochemical water splitting

Direct thermal water-splitting (Eq. [20.11]) is a reaction that requires very high temperatures (>2000°C).

$$2H_2O + \text{Energy} \rightarrow 2H_2 + O_2 \qquad [20.11]$$

The reduction of the temperature of the water-splitting reaction can be achieved via thermochemical cycles based on redox pairs.

One of the earliest investigations for multi-step hydrogen production from water-splitting was by Funk and Reinstorm in the 1960s (Funk and Reinstorm, 1966). They evaluated the energy requirements and the possibility of employing two-step processes for water dissociation and hydrogen production by oxides and hydrides. The result of their investigation was that there were no compounds that could efficiently yield a two-step process for hydrogen production from water, provided that the temperature remained lower than 1100°C. Also they added that it is unlikely that a compound exists or can be synthesized that could yield a two-step chemical process superior to water electrolysis (Funk and Reinstorm, 1966).

Thermodynamically it was proven that the minimum number of thermochemical reaction steps to keep operation below ~730°C would be three (Abraham and Shhreiner, 1974). Carty *et al.* (1981) and McQuillan *et al.* (2005) have reported more than 200 thermochemical multi-step water-splitting reactions; however, only a few have proven to be feasible.

The processes currently receiving the greatest attention are based on two-step thermochemical cycles with redox materials that are usually oxides of multivalent metals (Steinfeld, 2005; Steinfeld and Weimer, 2010; Abanades *et al.*, 2006, Perkins and Weimer, 2004; Möller and Palumbo, 2001b; Tamaura

et al., 1995; Kodama, 2003). In the first step (water-splitting) a metal oxide, in its reduced state, is oxidized by taking oxygen from water and producing hydrogen (exothermic reaction) (Eq. [20.12a]), while in the second step (endothermic reaction), the oxidized redox material is reduced (regenerated) to be used again (Eq. [20.12b]):

$$MO_{red} + H_2O(g) \rightarrow MO_{ox} + H_2(g) \qquad \text{(exothermic)} \qquad [20.12a]$$

$$MO_{ox} \rightarrow MO_{red} + 1/2O_2 \qquad \text{(endothermic)} \qquad [20.12b]$$

In this way pure hydrogen is produced avoiding the need for high-temperature separation from oxygen and the formation of explosive mixtures.

Nakamura (1977) was the first to investigate the two-step thermochemical splitting of water with the use of iron oxide redox pairs. Thermodynamic analysis that was conducted in order to explore the potential of different metal oxide redox pairs for thermochemical water-splitting has revealed that some pairs are not appropriate for hydrogen production via water-splitting since they have very low hydrogen yields, while other pairs have extremely high regeneration temperatures that in some cases may even exceed their melting point. Most recent research activities focus on two-step metal oxide cycles that include the ZnO/Zn cycle (Möller and Palumbo, 2001a; Steinfeld, 2002) the SnO_2/SnO cycle (Abanades *et al.*, 2008) and the mixed oxides (Tamaura *et al.*, 1995, 1998, 2004; Kodama *et al.*, 2005, 2008; Ehrensberger *et al.*, 1995, 1996; Kaneko *et al.*, 2005, 2006a; Inoue *et al.*, 2004; Takahashi *et al.*, 2004; Agrafiotis *et al.*, 2005) cycles (based on iron oxide) with the addition of nickel, manganese, cobalt, aluminium-copper or zinc. Also several studies have been conducted for the enhancement of the latter mixed oxides to avoid sintering and coarsening via their deposition on ceramic materials like zirconia or yttrium stabilized zirconia (Kodama *et al.*, 2005; Gokon *et al.*, 2008a, 2008b; Ishihara *et al.*, 2008). Popular redox pairs that are investigated include oxides of manganese (Francis *et al.*, 2010), cerium (Abanades and Flamant, 2006b), while some rarer mixed oxides (Funk and Reinstorm; 1966; Sibieude *et al.*, 1982; Abanades *et al.*, 2006, 2008; Kang *et al.*, 2009; Lundberg, 1993; Steinfeld *et al.*, 1998a) such as tin, germanium, niobium, indium, cadmium and tungsten have also been tested.

Other thermochemical cycles that are extensively studied are the sulfur-iodine and the copper-chlorine cycles. Both these two cycles are utilizing a series of chemical steps of which the net result is the production of H_2 and O_2. The sulphur-iodine (SI) cycle, which was introduced by General Atomics (Norman *et al.*, 1982), requires temperatures within the intermediate steps exceeding 800°C, while the copper-chlorine cycles require lower temperatures (~500°C, Barbooti and Al-Ani, 1984).

20.4 Solar-thermochemical reactor designs

The design of solar thermochemical reactors has been an issue of research over the last three decades. Some of the most significant reactor designs are presented in the following paragraphs.

20.4.1 Multi-tubular solar reactors

For catalyzed reactions, reactors based on packed beds of porous solid catalyst particles are a standard approach in the chemical industry. Adaptation to solar operation via assembly of multiple tubes to form a receiver is an obvious approach. Stein *et al.* (2009) have followed this route for solar steam reforming, for example. Recently a thermal and optical analysis for the development of a multi-tubular reactor filled with mixed ferrite for hydrogen production via two-step water-splitting reactions by making use of mixed ferrites was reported (Martín *et al.*, 2011). This concept has some similarities with the fixed-bed set-up employed in laboratory-scale experiments for the evaluation of the redox activity of ferrites. In place of a furnace, the proposed concept utilizes a heliostat field to develop high enough temperatures. Instead of one tubular reactor, the proposed design consists of a semi-cylindrical cavity filled with a bundle of tubes, which is easily scalable by adjusting the size of the cavity, the number of tubes (each filled with the redox material) and the size of the heliostat field.

20.4.2 Volumetric cavity reactors

Cavity solar reactors (Fig. 20.3) were introduced in the work of Trombe *et al.* (1973), for melting of oxides, Flamant *et al.* (1980) for calcite decomposition, and Steinfeld *et al.* (1998b) and Haueter *et al.* (1999) for oxide reduction. As the name suggests, concentrated radiation enters a cavity aperture via a window. In Steinfeld *et al.* (1998b), a 5 kW continuous-feed, 'vortex' cavity reactor was designed for co-producing Zn and syngas, while in Haueter *et al.* (1999), a 10 kW rotating-cavity reactor, similar to the aforementioned design, was used for the decomposition of zinc oxide.

20.4.3 Cavity dual cell reactors

A 'rotary' type system (Fig. 20.4) that was designed for two-step thermochemical water-splitting cycles, had separate dual cells for the water-splitting and the regeneration. It was developed at the Tokyo Institute of Technology (Kodama and Gokon, 2007; Kaneko *et al.*, 2007) and consists of ceramic foams coated with the redox material and adapted on a cylindrical rotor. The reactor has two quartz windows through which the radiation

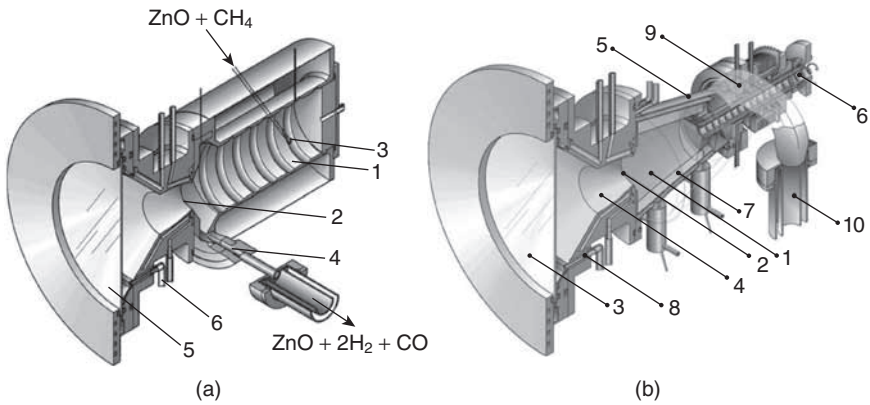

20.3 (a) Vortex reactor (Steinfeld, 2005) that consists of: 1 cylindrical cavity, 2 windowed aperture, 3 inlet port, 4 outlet port, 5 window, 6 auxiliary flow of gas for cooling and clearing the window; (b) Rotating cavity reactor (Steinfeld, 2005) consisting of: 1 rotating conical cavity-receiver, 2 aperture for access of concentrated solar radiation, 3 quartz window, 4 CPC for solar flux concentration increase, 5 (non-rotating) conical shell, 6 screw powder feeder, 7 layer of ZnO that insulates and reduces the thermal load on the inner cavity walls, 8 purge gas inlet, 9 gaseous product exit, 10 quench device.

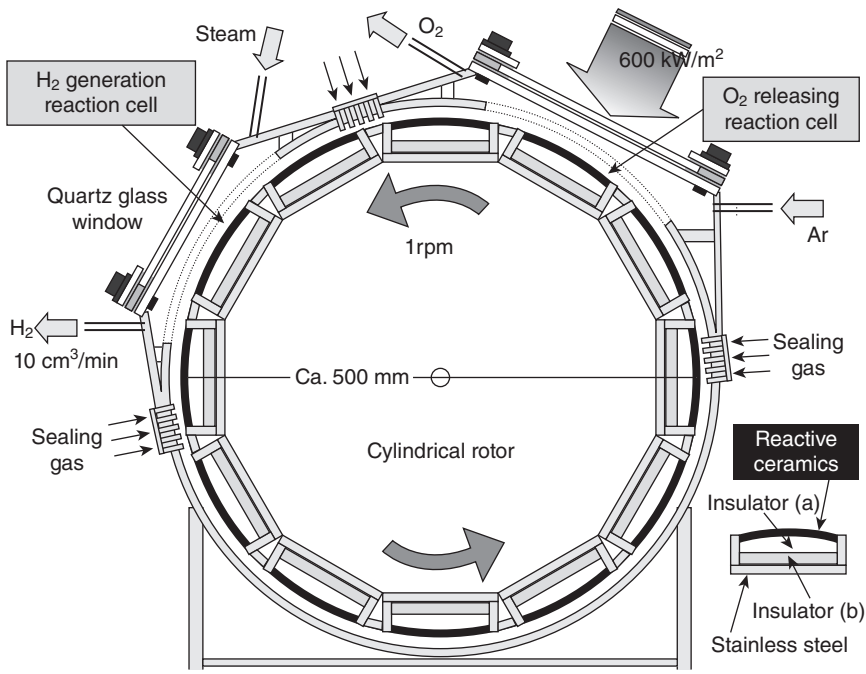

20.4 Cavity dual cell rotating reactor (Kaneko *et al.*, 2007).

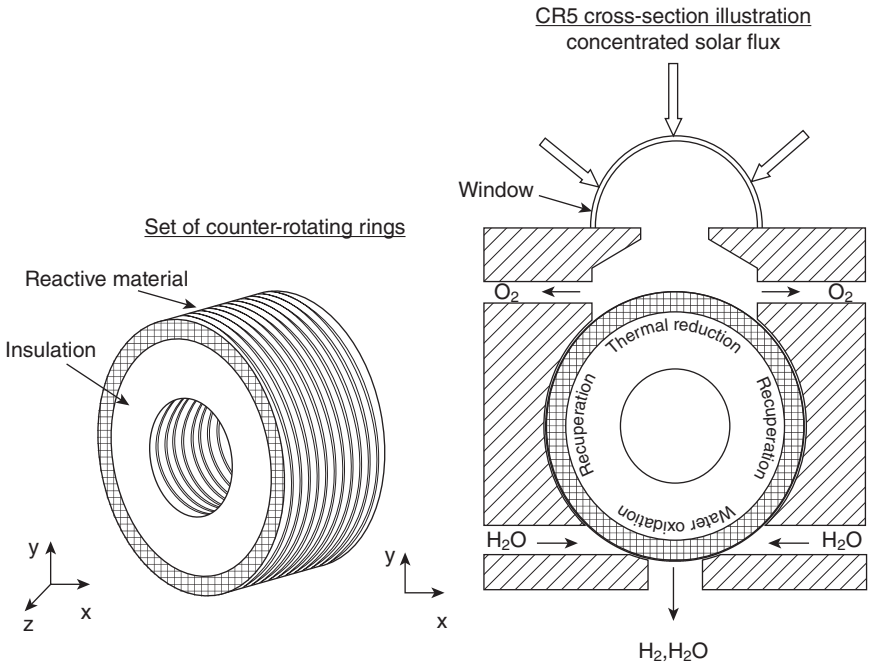

20.5 The CR5 rotating reactor consisting of rotating disks (Diver *et al.*, 2008).

enters. The first aperture is used as a 'preliminary heater' that heats the reactor up to temperatures suitable to perform the water reaction, whilst the second one heats the ceramic walls to higher temperatures suitable for thermal regeneration of the material (Kaneko *et al.*, 2006b).

20.4.4 Rotating disk reactors

Another type of rotating reactor (Fig. 20.5) is the CR5 developed at the Sandia National Laboratories (Diver *et al.*, 2008). The reactor is a receiver/reactor/recuperator that consists of counter rotating rings or disks. Robocast redox material in the form of fin segments is adjusted on the rotating disks. With the aid of the rotating disks, the redox material is alternately exposed to solar radiation for the regeneration step and water vapor for the water-splitting step.

20.4.5 Aerosol flow reactors

The high temperature aerosol flow reactor (AFR) (Fig. 20.6) has been employed for the production of ceramics and for solar methane dissociation

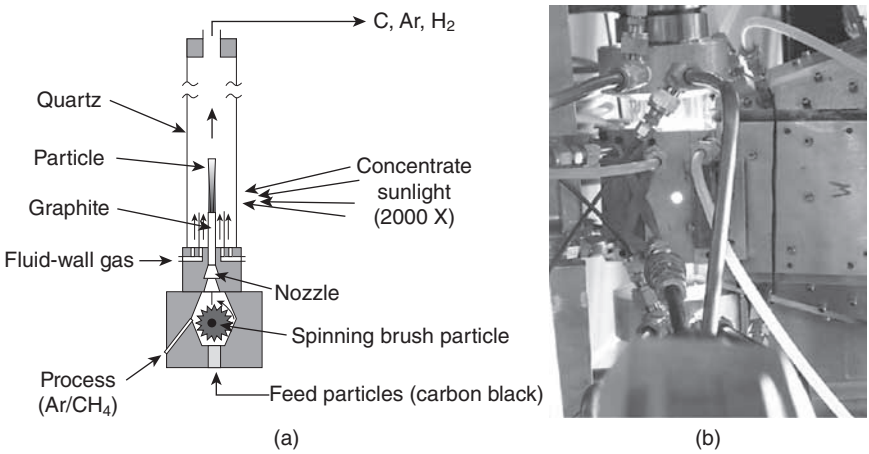

20.6 (a) Schematic of aerosol flow reactor (Weimer *et al.,* 2001); (b) installed solar thermal aerosol reactor (Dahl *et al.,* 2004).

(Perkins *et al.*, 2008). 'Proof-of concept' experiments were carried out for the dissociation of methane for hydrogen and carbon black production and the dry reforming of methane for syngas production (Weimer *et al.*, 2001). Use of an aerosol reactor for hydrogen production from water-splitting was presented in Funk *et al.* (2008) where Zn powder was introduced into a gas stream with the aid of a fluidized feeder and subsequently passed through an aerosol flow reactor. The Zn particles were hydrolyzed by water towards the formation of ZnO and hydrogen.

20.4.6 SOLREF reactor

A solar thermochemical reactor for the reforming of natural gas to hydrogen was designed, fabricated and operated in the scope of the European project SOLREF (Fig. 20.7). Based on the experience obtained in a previous project (SOLASYS), in which the 'proof-of-concept' of solar steam reforming was demonstrated, an advanced reactor was developed in the SOLREF project. The main purpose of this project is to develop and operate an innovative 400 kWth solar reactor consisting of a more compact and cost-effective reformer for such applications as hydrogen production or electricity generation.

Some of the aims of the SOLREF project were to achieve temperatures higher than 900°C to enhance the efficiency of the process and to enable the coupling of the reactor with the process for the production of pure hydrogen. Further development of the layout of the system and of the operational parameters is required to reach high efficiency, stability and

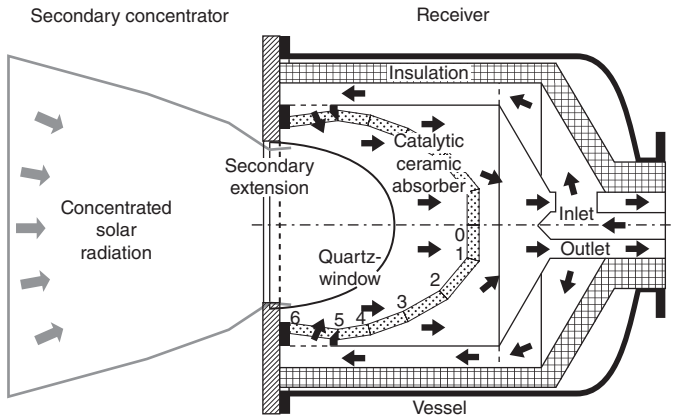

(a)

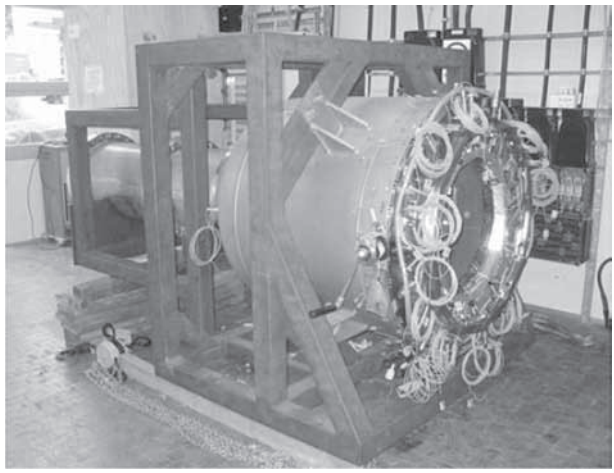

(b)

20.7 (a) Schematic of directly irradiated volumetric receiver-reactor (adapted from Möller, 2005) and (b) the actual SOLREF reactor assembled at DLR Stuttgart (adapted from Richter *et al.,* 2008).

high recovery rates of hydrogen and CO_2. Alternative feedstock (e.g., biogas and landfill gas) will also be investigated.

20.4.7 SOLHYCARB reactors

As mentioned previously, the solar thermal cracking of natural gas can be achieved in two types of reactors. In a direct heating reactor (Kogan and Kogan 2003b; Kogan *et al.*, 2005; Trommer *et al.*, 2004; Hirsch and Steinfeld, 2004; Abanades and Flamant, 2008; Rodat *et al.*, 2010b), the particles absorb

heat from solar radiation and the reactor is seeded for the increase of the adsorption and nucleation sites. The disadvantage of direct heating is the potential deposition of particles on the window of the reactor. In the indirect heating reactor (Dahl *et al.*, 2004; Wyss *et al.*, 2007; Rodat *et al.*, 2010b), the solar irradiation zone is separated from the reacting flow by an opaque wall that serves as a heat transfer medium that allows convection of heat from the solid wall to the gas flow. A weakness of the indirect configuration is that it demands higher temperatures due to the heat transfer wall (Abanades and Flamant, 2006a).

In the scope of the European project SOLHYCARB (http://www.promes.cnrs.fr/ACTIONS/Europeenes/solhycarb.htm), which aims at the production of hydrogen and carbon black nanoparticles from methane cracking, a 20 kW laboratory-scale reactor and a 50 KW pilot-scale reactor are being developed based on the indirect solar heating configuration (Fig. 20.8). The 20 kW solar reactor consists of a cubic blackbody-cavity receiver that absorbs the concentrated solar radiation through a hemispherical quartz window placed at the front. Inside the reactor's cavity, four graphite tubular reaction zones are arranged vertically. Each of the four consists of two concentric graphite tubes. The reaction gas first enters the inner tube and flows out through the space in-between the two tubes. This mainly serves to increase the gas residence time and the better preheating of the reactants (Rodat *et al.*, 2010b). The 50 kW pilot-scale reactor (Fig. 20.8(c)) was designed on the same principle. The reactor body is made of an aluminum shell (800 × 780 × 505 mm) and a water-cooled front face with a 13 cm diameter aperture for concentrated solar radiation entry. The radiation is absorbed by the graphite cavity (360 × 400 × 300 mm) that approaches black-body behavior. To avoid contact of graphite with the oxidizing atmosphere, the opening is protected by a domed quartz window (outer diameter of 360 mm) swept by a nitrogen flow to avoid overheating. The reaction occurs in seven horizontal graphite tubes (single tubes).

Typical results for the 20 kW and 50 kW solar reactors are illustrated in Fig. 20.9. Experimental data show clearly that complete conversion of methane is achievable in the solar reactors. However, the significant amount of C_2H_2 that is produced lowers the carbon yield (Fig. 20.9(b)). The production at pilot-scale is 200 g/h H_2 (88% H_2 yield), 330 g/h CB (49% C yield), and 340 g/h C_2H_2. The thermal and thermochemical performances of the pilot reactor (50 kW) are shown in Fig. 20.10.

20.4.8 HYDROSOL reactors

The hydrosol reactor was the first solar thermochemical reactor that produced on-sun (Roeb *et al.*, 2006b; Konstandopoulos and Lorentzou, 2010) solar hydrogen from the dissociation of water vapor via a redox-pair cycle.

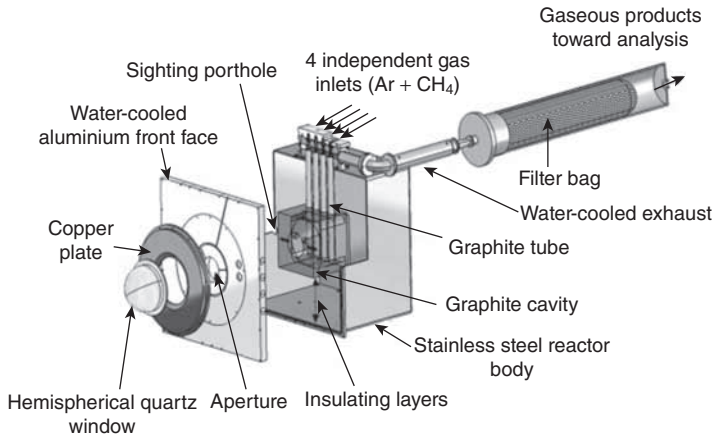

(a)

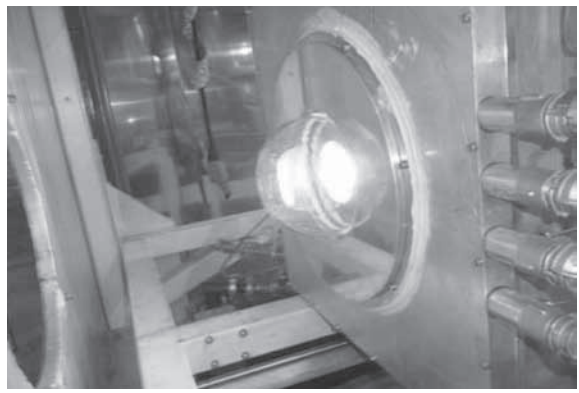

(b)

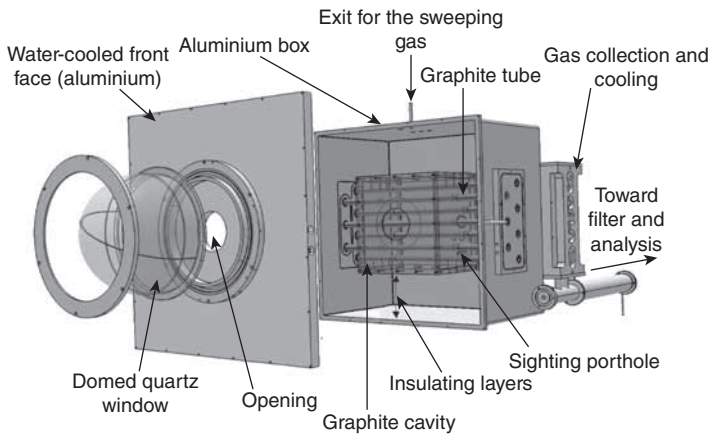

(c)

20.8 (a) Schematic of the 20 kW solar reactor and filter (Rodat *et al.*, 2010a); (b) close look at a 20 kW SOLHYCARB reactor aperture during cooling at CNRS-PROMES test rig (Richter *et al.*, 2008), (c) schematic of the 50 kW pilot solar reactor (Rodat *et al.*, 2010b).

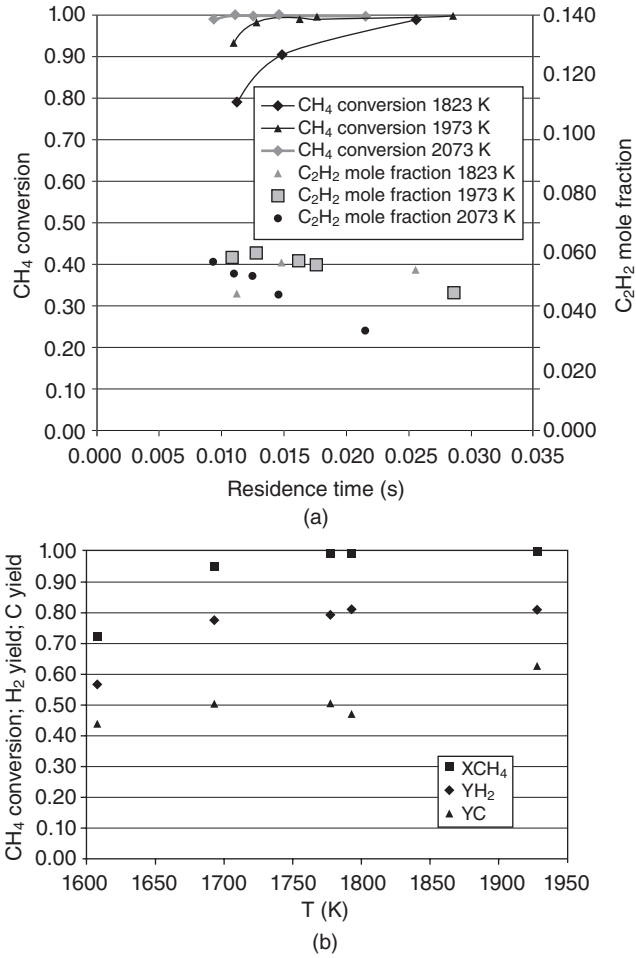

20.9 (a) Temperature dependence of CH_4 conversion and C_2H_2 off-gas mole fraction vs residence time (CH_4 mole fraction in the feed: 20%) in the 20 kW solar reactor (Rodat *et al.*, 2010a). (b) CH_4 conversion, H_2 yield, and C yield vs temperature for the 50 kW pilot solar reactor (Ar: 31.5 NL/min, CH_4: 10.5 NL/min), (Rodat *et al.*, 2010b).

The HYDROSOL reactor was developed during the homonymous European projects 'HYDROSOL' and 'HYDROSOL-II' (Konstandopoulos and Lorentzou, 2010) and was based on a concept similar to that of the automobile converters for catalytic applications and of volumetric receivers for concentrated solar radiation (Konstandopoulos *et al.*, 2005; Agrafiotis *et al.*, 2007a). The 'HYDROSOL' reactor contains no moving parts and is constructed from a refractory ceramic material, shaped into thin-wall honeycomb monoliths, optimized to absorb solar radiation and develop the

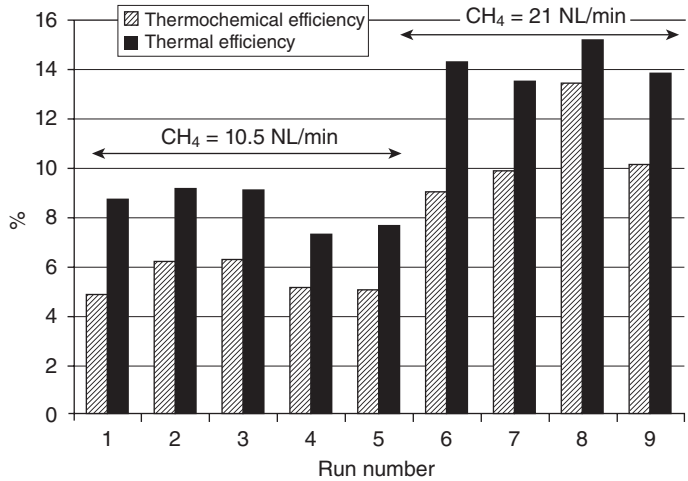

20.10 Thermochemical and thermal efficiencies of the pilot solar reactor (Rodat *et al.,* 2010b).

required high temperatures. The monolith channels are coated with an active water-splitting material and the overall reactor looks very similar to the familiar catalytic converter of modern automobiles.

When steam passes through the solar reactor, the coating material splits water vapor by 'trapping' its oxygen and leaving in the effluent gas stream pure hydrogen. In a subsequent step the oxygen 'trapping' coating is regenerated by increasing the amount of solar heat absorbed by the reactor and hence a cyclic operation is established in a single solar receiver-reactor (Fig. 20.11). The proof of concept was demonstrated on the solar receiver-reactor, HYDROSOL-I, at the solar facilities at the German Aerospace Center (DLR), where quasi-continuous solar-operated water-splitting regeneration cycles were achieved, producing the first ever solar hydrogen with monolithic honeycomb reactors (Konstandopoulos and Lorentzou, 2010; Roeb *et al.*, 2006a; Agrafiotis *et al.*, 2006a, 2006b, 2007b).

The next generations of HYDROSOL reactors were the HYDROSOL-I dual-chamber reactor (Roeb *et al.*, 2006a, 2009) and the 100 kW pilot-scale HYDROSOL-II reactor (Roeb *et al.*, 2011). All the reactors constructed within the two HYDROSOL projects can be seen in non-operational mode in Figs 20.12 and 20.13. HYDROSOL-I (Fig. 20.12) and the dual-chamber reactor (Fig. 20.13) were operated at the solar facilities in DLR, while HYDROSOL-II (Fig. 20.14) operates at the Plataforma Solar de Almería in Spain (PSA). Four major experimental campaigns have been carried out in the HYDROSOL-I and the dual-chamber reactors, to investigate, evaluate and iteratively optimize the water-splitting efficiency and regeneration capability of the nanostructured materials.

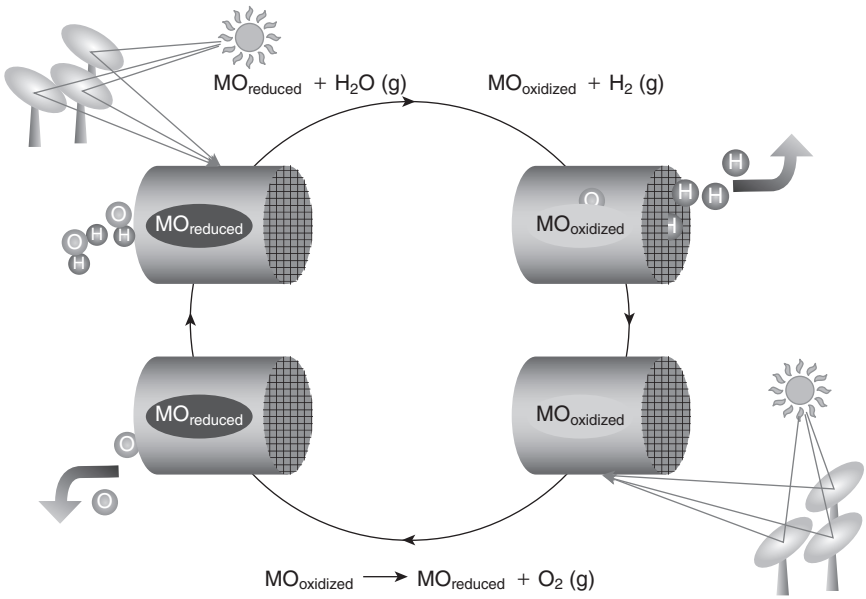

20.11 The HYDROSOL metal oxide thermochemical cycle for solar-water-splitting (Konstandopoulos and Lorentzou, 2010).

The first two campaigns were carried out in the 3 kW solar HYDROSOL-I reactor (Fig. 20.12). In the first campaign, the coated monoliths were able to react with water and produce solar hydrogen at 800°C and regenerate at 1200°C, for the first time (Fig. 20.12(b)). In the second campaign, multiple sequential water-splitting and regeneration steps were achieved (Fig. 20.12(c)).

The HYDROSOL-I dual-chamber reactor (Fig. 20.13), with its modular design, allowed continuous solar hydrogen production. While in one of the modules water-splitting took place, the other was regenerated. By switching the feed gas and controlling the amount of solar radiation that strikes each module, the regenerated part can be switched to the splitting mode and vice versa. Meeting the different heat demands for the two reactions (water-splitting and regeneration) that take place alternately in the two modules was achieved by providing two focal points (one on each module) with different flux density via re-alignment of the facets of a faceted solar concentrator at the solar furnace facility of DLR. In the third solar campaign, hydrogen was produced continuously for five days, which was the period that was available to the consortium for the use of the solar furnace (Fig. 20.13(c)).

The solar campaigns on the 100 kW pilot-scale HYDROSOL-II reactor (Fig. 20.14(a)) were conducted at the Plataforma Solar de Almería (PSA) in Spain (Fig. 20.15). This reactor also consists of two modules that

(a)

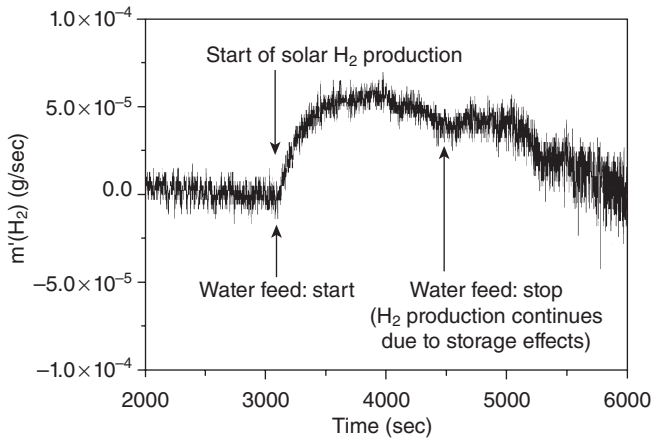

(b)

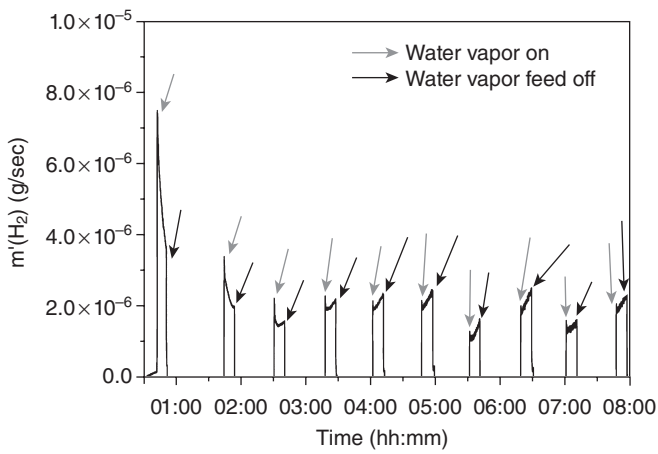

(c)

20.12 (a) HYDROSOL-I reactor (Agrafiotis *et al.*, 2005); (b) proof of concept – first solar hydrogen production (Konstandopoulos and Lorentzou, 2010); (c) multiple sequential hydrogen production cycles in the HYDROSOL-I reactor.

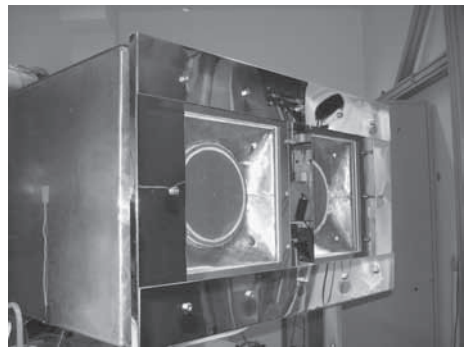

(a)

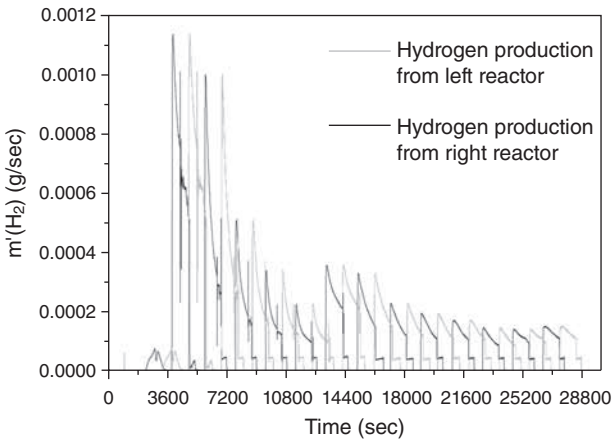

(b)

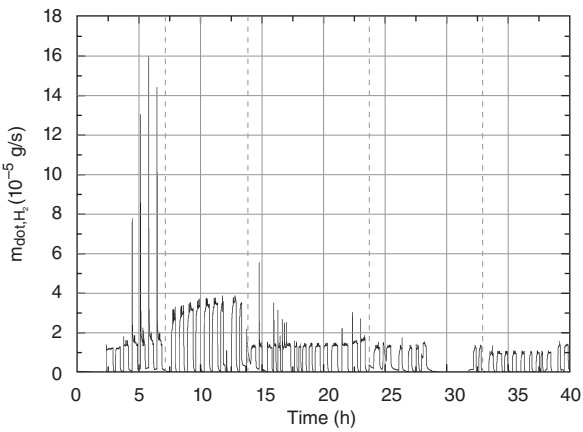

(c)

20.13 (a) HYDROSOL-I reactor dual chamber (Konstandopoulos and Lorentzou, 2010); (b) continuous hydrogen production from the two modules (Konstandopoulos and Lorentzou, 2010); (c) continuous hydrogen production for five sequential days performed with one sample.

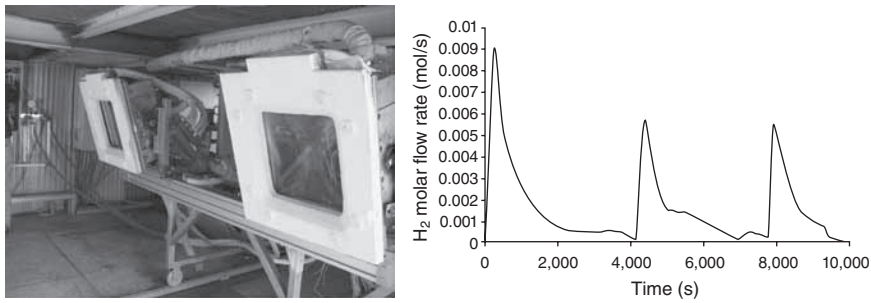

20.14 (a) HYDROSOL-II reactor (Konstandopoulos and Lorentzou, 2010); (b) solar thermochemical hydrogen produced from the pilot HYDROSOL-II reactor (Konstandopoulos and Lorentzou, 2010).

20.15 Solar tower facilities at the Plataforma Solar de Almería (PSA) in Spain (Konstandopoulos and Lorentzou, 2010).

alternately shift from the water-splitting to the regeneration mode. The control of the temperature of each module is achieved with strategic adjustment of the heliostat field (Fig. 20.16).

The development towards commercialization continues with the Hydrosol-3D project which focuses on the pre-design and design of a 1 MW solar demonstration plant. The options that will be investigated are the adaptation of the hydrogen production plant to an already available solar facility or the development of a new, completely optimized hydrogen production/solar plant.

20.5 Solar-derived fuels

By employing solar energy, solar hydrogen and CO_2, solar hydrocarbons can be synthesized. In this way solar hydrocarbons can play the role of a

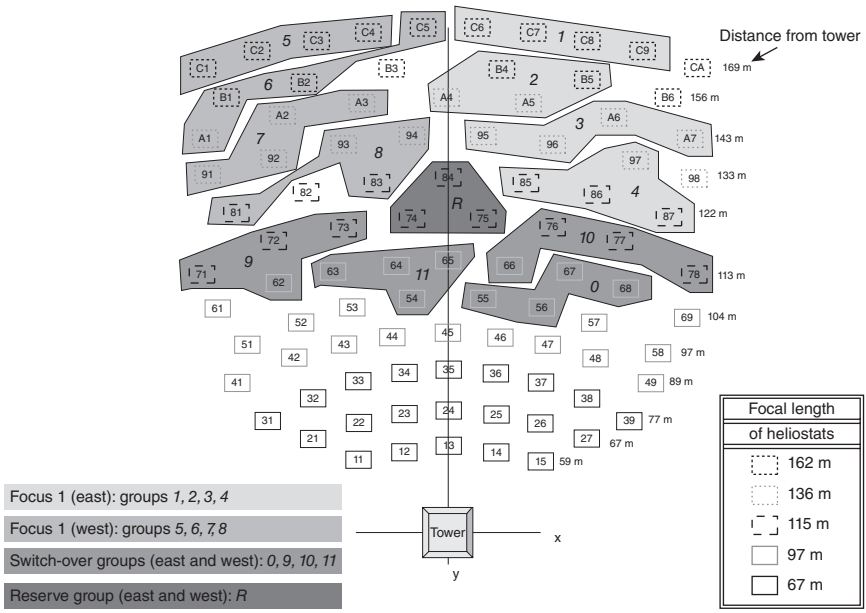

(a)

(b)

20.16 (a) Partitioning of the SSPS-CRS heliostat field at the PSA (Roeb *et al.*, 2011); (b) focus of solar radiation on the dual HYDROSOL-II reactor (Konstandopoulos and Lorentzou, 2010).

renewable energy carrier since they utilize solar energy and consume waste CO_2.

A very well-known technology that could be applied for the conversion of solar energy, hydrogen and carbon monoxide (e.g., from the solar decomposition of CO_2) into solar hydrocarbons is Fischer-Tropsch synthesis. The term Fischer-Tropsch is applied in a rather large variety of chemical processes used for the production of synthetic hydrocarbons (e.g., paraffins,

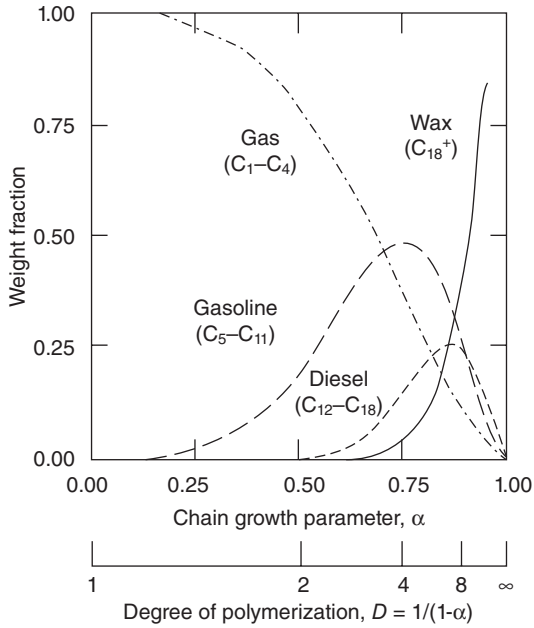

20.17 Product yield in Fischer-Tropsch synthesis (Perry, 2008).

olefins and alcohols, while depending on the reaction conditions or the catalyst used, other compounds may be produced) from synthesis gas (hydrogen and carbon monoxide) (Perry, 2008). Some of the most common reactions that might take place in a Fischer-Tropsch system are: Boudouard (Eq. [20.8]), water-gas shift (Eq. [20.13]), methanation (Eq. [20.14]) and reactions for the production of heavier hydrocarbons (Eq. [20.15]) (Opdal, 2006). The first two reactions (methanation and Boudouard) are considered undesirable, while the latter one (Eq. [20.15]) consists of the chain building reaction. In Fig. 20.17, the product yield of the Fischer-Tropsch processes is shown.

$$CO + H_2O \rightarrow CO_2 + H_2 \qquad \Delta H^0 = 41\ \text{kJ/mol} \qquad [20.13]$$

$$CO + 3H_2 \rightarrow CH_4 + H_2O \qquad \Delta H_{298K} = -247\ \text{kJ} \qquad [20.14]$$

$$nCO + 2nH_2 \rightarrow C_nH_{2n} + nH_2O \qquad [20.15]$$

The demonstration of the Fischer-Tropsch (F-T) processes at commercial scale dates back to around 1935, when Ruhrchemie A.G. was formed by a group of Ruhr companies that had in common the main objective of constructing the first commercial plant (Hall and Hsensel, 1945). In fact, the Ruhrchemie company at the time was the holder of the exclusive rights over the F-T process and the first plant was also used for the further

research and development of the technology. Later on (until 1945) Ruhrchemie A.G. was the owner of eight additional Fischer-Tropsch plants all built within Germany.

Currently one of the largest operators of F-T plants converting gas and coal into liquid fuels, and also a leading fuel provider in South Africa, is Sasol (Sasol, 2011). Another leading company in the field of F-T plants, is PetroSA company, which is also located in South Africa and operates a semi-commercial unit (http://www.petrosa.co.za/; Njobeni, 2011). Besides these two leading companies, there are several others that utilize F-T processes, thus proving the maturity of the technology on an industrial scale as well as the potential for further commercialization.

Where the solar fuel process has begun with the decomposition of a hydrocarbon, the production of syngas mixtures is a natural consequence. If production of Fischer-Tropsch liquids was to be pursued following production of pure hydrogen, a source of CO would also be needed. Separating CO_2 from the atmosphere is difficult because of the very low concentration levels.

If CO_2 emissions were not treated as chemical waste but rather as a raw material for the formation of energy-rich products, CO_2 could be incorporated in a cyclic operation, where after its production from carbonaceous sources, it would be reused as a storage medium of the solar energy that is abundant, renewable and freely dispensable. Zeman and Keith (2008) studied the issue of obtaining carbon-neutral hydrocarbons as a viable alternative to hydrogen or conventional biofuels, and investigated the economics of such an approach based on hydrogen generation from coal/fossil fuels in combination with carbon capture and storage (CSS) technology and CO_2 sourced from biomass or air capture and arrived at the conclusion that: 'the lack of a clear technological "winner" warrants equal attention and funding on all potential solutions' (Zeman and Keith, 2008). This is not unexpected, since it is clear that in any such scheme where, on the one hand, CO_2 is treated as waste that needs to be disposed of and, on the other hand, as a raw material that is being collected (worst as it may be in a very diluted form), one part of the process fights the other. In addition, hydrogen from fossil coal and similar sources can never be sufficient to turn the process economics around. Put simply, to synthesize hydrocarbon fuels we need a source of hydrogen and a source of carbon independent of each other.

Another alternative to synthesizing a fuel from pure hydrogen is to convert it to ammonia. This can be done using standard Haber Bosch ammonia synthesis (Eq. [20.16])

$$H_2 + N_2 \rightarrow NH_3 \qquad [20.16]$$

Ammonia liquefies at modest pressures and can be transported and handled using similar equipment to LPG. Operation of gas turbines and

internal combustion engines using ammonia as a fuel has been successfully demonstrated and is the subject of ongoing work (Dunn *et al.*, 2012).

20.5.1 Ongoing research into solar fuels

The 'European hydrogen and fuel cell roadmap' introduced by the European Commission considers hydrogen as the most feasible solution to achieve independence from fossil fuels. However, currently hydrogen production employs fossil fuels (i.e., natural gas), and therefore has the undesirable side effects of the use of carbonaceous materials. For this reason, the European roadmap (Fig. 20.18), which covers a timeframe until 2050, established the activities and strategies that should be supported for the development of the technologies for solar hydrogen. The main objective is to focus all efforts towards the determination of the most promising paths for renewable hydrogen production and to motivate politicians and encourage the private sector to invest in a clean and renewable future based on hydrogen (Meier and Sattler, 2009).

One of the most promising technologies for large-scale solar hydrogen production is, as mentioned above, the use of solar thermochemical processes based on concentrated solar power. There are numerous research groups around the world who are investigating different pathways with the aim of unveiling all possibilities and condensing the knowledge around solar hydrogen. Figure 20.19, reproduced from Meier and Sattler (2009), illustrates several solar thermal facilities around the world that are active in the area of concentrated solar thermochemical research.

A European Union-funded project with the acronym INNOHYP-CA that was completed in 2006 created a roadmap of the thermochemical processes for massive hydrogen production with the use of solar or nuclear energy (Fig. 20.20) (Meier and Sattler, 2009). Three phases were set for the development and, consequently, commercialization of the most promising technologies.

In the first phase, which runs up to 2015, technologies that are considered as an intermediate step towards completely renewable solar hydrogen production (such as solar steam reforming, solar carbon gasification, solar ZnO carbothermal reduction), are going to be demonstrated at the pilot scale. In the second phase, due to be completed by 2020, pilot-scale demonstrations of the most promising carbon-free thermochemical processes are going to take place. The third phase, which lasts until 2025, will focus on the improvement and demonstration of the zero-CO_2 processes that are proved to be economically feasible.

Other issues that are addressed in the INNOHYP-CA project are the need to further investigate the candidate thermochemical processes with respect to materials and component development as well as the possibility

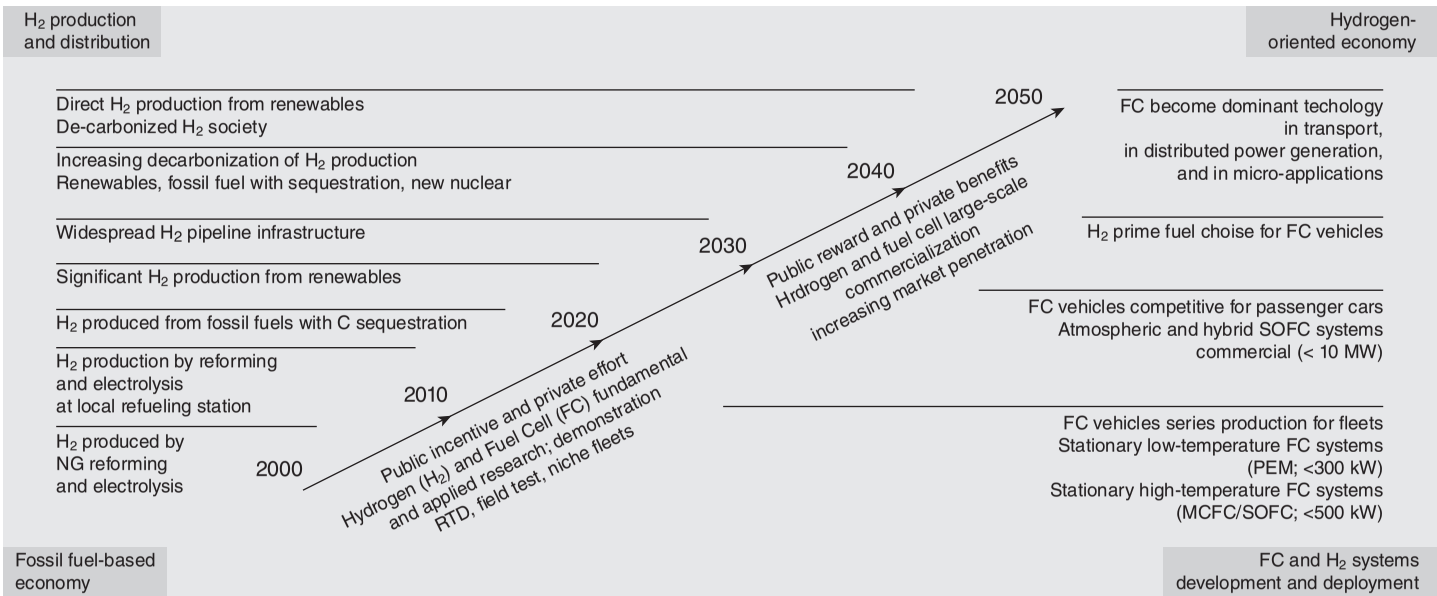

20.18 European hydrogen and fuel cell roadmap (Meier and Sattler, 2009).

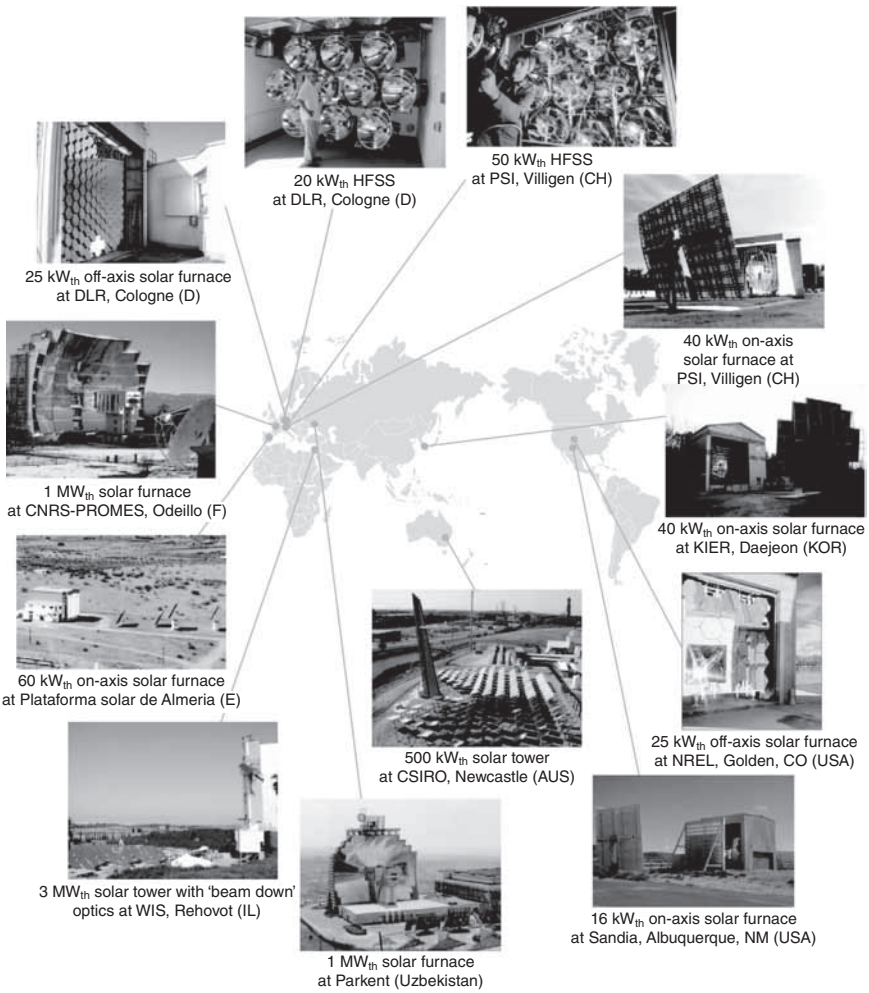

20.19 Solar thermochemical research around the world (Meier and Sattler, 2009).

of improvement of the existing concentrated solar facilities to be able to accommodate the thermochemical technologies that are developed. In the case of material development, there are several challenges that need to be overcome, such as the manufacturing of materials and components that will maintain their reliability under 'unfriendly' conditions (high temperatures, corrosive environment, etc.). In the case of solar facilities, the aim is to find a feasible way for the successful integration of the new technologies in the already existing solar infrastructure that would be upgraded and efficiently used (Meier and Sattler, 2009). The latter would be essential for the evaluation of the thermochemical processes on a large scale.

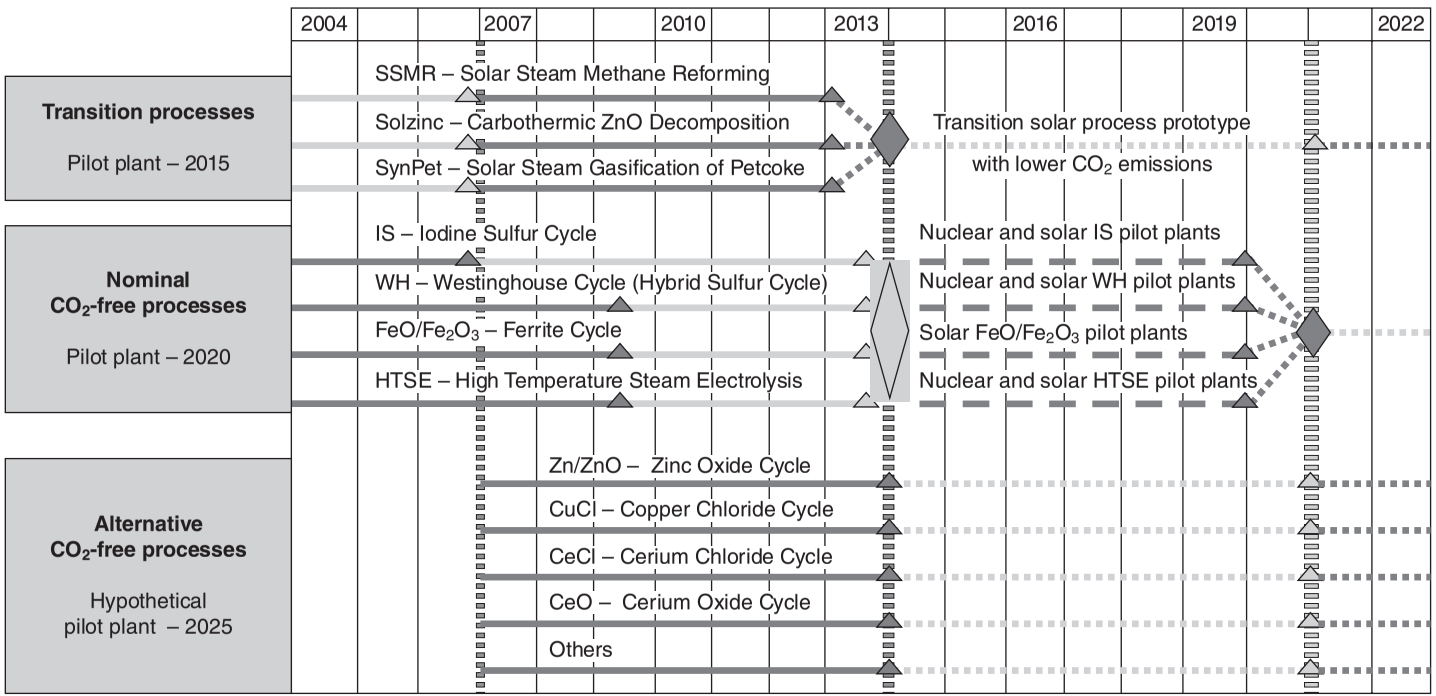

20.20 INNOHYP-CA roadmap for massive thermochemical hydrogen production with the use of solar or nuclear energy (Meier and Sattler, 2009).

20.6 Other applications of industrial solar chemistry

20.6.1 Closed-loop energy storage systems

The utilization of the solar potential via thermochemical processes can be applied to closed-loop energy storage systems for the storage and transportation of solar energy, as discussed in Chapter 11. The idea of closed-loop energy storage was first suggested in the 1970s and it involved gas phase reactions in endothermic and exothermic reactors with associated counterflow heat exchangers. In this area of solar thermochemistry, the solar methane reforming (Abbas and Wan Daud, 2010b) and the ammonia solar dissociation reaction systems have received much attention (Dunn *et al.*, 2012).

20.6.2 Waste processing

Besides solar fuels that can replace fossil fuels in various applications, concentrated solar energy may also be used directly to satisfy thermal or power needs of various processes. For instance, solar energy could be incorporated in the sector of waste treatment that comprises another modern-day management problem that deals with hazardous compounds. After basic processing, such products are usually disposed of in sites with limited storage capacity. Due to this space limitation, technologies that recycle hazardous materials and convert them into valuable products have been developed. The recycling technologies used require thermal processes with high energy demand and thus use huge amounts of fossil fuels. Incorporation of solar energy in such processes would play a significant role both economically and from an environmental point of view (Steinfeld and Meier, 2004).

An attractive way to treat toxic chemical wastes (including large varieties of industrial products, pharmaceuticals, and everyday chemicals) and avoid the production of toxic products during their combustion (Tributsch, 1989), would be to first pyrolyze them in closed reactors and then treat them under suitable conditions (temperature and pressure) with hydrogen. The final products of this process would be similar to upgraded products retrieved from natural gas and mineral oil (Tributsch, 1989). This process would have even higher worth if the hydrogen used were derived from solar energy and water. A similar process, that requires high temperatures and solar hydrogen as a reducing agent, could be applied for the recycling of oxidized metals (e.g., Fe_2O_3, Al_2O_3, CuO or PbO).

By-products that may derive from these processes, such as soot and amorphous carbon, could be used in other applications, for example the tire and color industries. Besides the significant environmental benefits, such applications also have high economic benefits that are more considerable

for industries, since they produce valuable by-products and eliminate the high cost of the disposal of their chemical wastes (Tributsch, 1989).

20.6.3 Reduction of carbon dioxide emissions

Synergy with carbon capture and storage

The various endothermic reactions that have been discussed that potentially convert hydrocarbons to H_2 and CO_2 are also those that are proposed for potential CO_2 emission-free processes. In this scenario, some of the fossil fuel itself is oxidized to provide the heat input for the reactions. CO_2 is then scrubbed from the product gas for sequestration. The challenge in CO_2 emissions is currently focused on finding storage sites capable of hosting quantities reaching annually 25 billion tons ('Basic Research Needs for Solar Energy Utilization', 2005). Such sinks, which could be geological formations, the ocean, saline aquifers, terrestrial ecosystems, etc., in order to be effective should provide extremely low leakage rates, since only 1% leakage rate could result in reversing any sequestration effort in a period of only 100 years (Muradov and Veziroglu, 2008), Even by using the safest, long-term CO_2 storage option, predictions concerning both security issues and investment costs cannot be defined precisely (Knight, 2010; IEA, 2009). In theory, storages sites are more than enough to satisfy global requirements for CO_2 storage, but in practice it is estimated that a very small proportion of those sites could be utilized (IEA, 2009; Van Noorden, 2010).

Whilst such technologies can be considered as future commercial competitors of CST, there is the potential of combining solar-driven reactions with carbon capture technologies to produce the end products. In this scenario, the solar input will significantly reduce the amount of CO_2 per unit of H_2 that must be separated and stored.

Reduction of carbon dioxide emissions from the metallurgical industry

Another sector that consumes a lot of electricity and heat and thus is also responsible for a large share of anthropogenic greenhouse gas emissions is the metallurgical industry. It was estimated (in Steinfeld and Meier, 2004) that by replacing the non-renewable energy in the technology used for processing of aluminum (which requires very high temperatures ~2200°C) by energy deriving from solar irradiation, the CO_2 emissions produced would be reduced by ~90%. In that sense, solar energy either directly (by solar furnaces) or indirectly (through the production of solar fuels) could be applied to multiple industrial processes that demand high amounts of energy (usually electricity), high process temperatures or a combination of both.

20.7 Conclusions

The high power density, ease of transportation and storage, and many years of development of internal combustion engine technologies have put hydrocarbon fuels at a privileged position in our energy mix. While for many years we have been accustomed to consider hydrocarbon fuels as a primary energy source, we must today adopt a different point of view, in order to mitigate the environmental, political and other consequences of today's fossil hydrocarbon-based economy: reducing our dependence on fossil hydrocarbon fuels is necessary. However, this should not prevent hydrocarbons from being used as a preferred energy carrier.

In order to invest in a sustainable future, the alternative energy sources explored should be not only environmentally friendly but also capable of meeting the continuously growing world energy demand. The most promising candidate is solar energy, which can be employed in various applications and can be exploited either directly as a heat source in several processes or indirectly through energy carriers.

The direct use of solar energy, though, comes with several limitations (e.g., solar energy is not always available, should be consumed in a narrow area from its production point, etc.) that could be easily overcome when storing it as an 'energy carrier' such as hydrogen or a hydrocarbon. In order to maximize the 'eco-friendly' nature of solar energy, the hydrogen should be derived from carbonaceous-free or at least renewable carbonaceous sources (such as water or bio-fuels). However, in order to progress an orderly transition, there is a strong argument for combining solar thermal processing with fossil fuel feedstocks or biomass to produce hybrid solar fuels.

Finally, solar energy could be exploited in hydrocarbon production processes. In these processes, CO_2 emissions are captured at the point of generation and are treated as a valuable feedstock that reacts with hydrogen and is recombined back to solar liquid fuels. In this way both the issues of the high cost of implementing the new and appropriate infrastructure to utilize an alternative energy carrier (i.e. pure hydrogen) into an almost fully fossil fuel dependent world and CO_2 storage, can be overcome simultaneously, ensuring clean and cost-effective energy sufficiency in a carbon-neutral future.

20.8 Acknowledgements

We are grateful to Dr Giles Flamant of CNRS-PROMES, for his valuable contributions to the present work, and in particular for the part concerning the SOLHYCARB solar reactor. Our work in the area of solar chemistry and reactors has been supported by the European Commission through

projects HYDROSOL, HYDROSOL II, HYDROSOL-3D, SOLHYCARB, SOLREF and HYCYCLES.

20.9 References

Abanades S., Flamant G. (2006a) 'Solar Hydrogen Production from the Thermal Splitting of Methane in a High Temperature Solar Chemical Reactor', *Solar Energy*, 80 (10), 1321–1332.

Abanades S., Flamant G. (2006b) 'Thermochemical Hydrogen Production from a Two-Step Solar-Driven Water-Splitting Cycle Based on Cerium Oxides', *Solar Energy*, 80 (12), 1611–1623.

Abanades S., Flamant G. (2008) 'Hydrogen Production from Solar Thermal Dissociation of Methane in a High-Temperature Fluid-Wall Chemical Reactor', *Chemical Engineering and Processing: Process Intensification,* 47 (3), 490–498.

Abanades S., Charvin P., Flamant G., Neveu P. (2006) 'Screening of Water-Splitting Thermochemical Cycles Potentially Attractive for Hydrogen Production by Concentrated Solar Energy', *Energy*, 31 (14), 2805–2822.

Abanades S., Charvin P., Lemont F., Flamant G. (2008) 'Novel Two-Step SnO_2/SnO Water-Splitting Cycle for Solar Thermochemical Production of Hydrogen', *International Journal of Hydrogen Energy*, 33 (21), 6021–6030.

Abbas H.F., Wan Daud W.M.A. (2010a) 'Hydrogen Production by Thermocatalytic Decomposition of Methane Using a Fixed Bed Activated Carbon in a Pilot Scale Unit: Apparent Kinetic, Deactivation and Diffusional Limitation Studies', *International Journal of Hydrogen Energy*, 35 (22), 12268–12276.

Abbas H.F., Wan Daud W.M.A. (2010b) 'Hydrogen Production by Methane Decomposition: A Review', *International Journal of Hydrogen Energy*, 35 (3), 1160–1190.

Abraham B.M., Shhreiner F. (1974) 'General Principles Underlying Chemical Cycles Which Thermally Decompose Water into the Elements', *Industrial and Engineering Chemistry Fundamentals*, 13 (4), 305–310.

Agrafiotis C., Roeb M., Konstandopoulos A.G., Nalbandian L., Zaspalis V.T., Sattler C., Stobbe P., Steele A.M. (2005) 'Solar Water Splitting for Hydrogen Production with Monolithic Reactors', *Solar Energy*, 79 (4), 409–421.

Agrafiotis C., Lorentzou S., Pagkoura C., Kostoglou M., Konstandopoulos A.G. (2006a) 'Advanced Monolithic Reactors For Hydrogen Generation From Solar Water Splitting', *Proceedings of SolarPACES*, 13th International Symposium on Concentrated Solar Power and Chemical Energy Technologies, June 20–23, Seville, Spain.

Agrafiotis C., Pagkoura C., Lorentzou S., Hoguet J.C., Konstandopoulos A.G. (2006b) 'Material Technologies Developments for Solar Hydrogen', *Proceedings of the 16th World Hydrogen Energy Conference*, June 13–16, Lyon, France.

Agrafiotis C.C., Mavroidis I., Konstandopoulos A.G., Hoffschmidt B., Stobbe P., Romero M., Fernandez-Quero V. (2007a) 'Evaluation of Porous Silicon Carbide Monolithic Honeycombs as Volumetric Receivers/Collectors of Concentrated Solar Radiation', *Journal of Solar Energy Materials and Solar Cells*, 91, 474–488.

Agrafiotis C., Lorentzou S., Pagkoura C., Konstandopoulos A.G., Roeb M., Neises M., Rietbrock P.M., Säck J.P., Sattler C., Stobbe P., Steele A.M. (2007b) 'The HYDROSOL Process: Solar-Aided Thermo-Chemical Production of Hydrogen

from Water with Innovative Honeycomb Reactors', *2nd International Workshop on Hydrogen* (IWH2), October 27–29, Ghardaïa, Algeria.

Amin A.M., Croiset E., Epling W. (2011) 'Review of Methane Catalytic Cracking for Hydrogen Production', *International Journal of Hydrogen Energy*, 36 (4), 2904–2935.

Anikeev V.I., Parmon V.N., Kirillov V.A., Zamaraev K.I. (1990) 'Theoretical and Experimental Studies of Solar Catalytic Power Plants Based on Reversible Reactions with Participation of Methane and Synthesis Gas', *International Journal of Hydrogen Energy*, 15 (4), 275–286.

Avdeeva L.B., Reshetenko T.V., Ismagilov Z.R., Likholobov V.A. (2002) 'Iron-Containing Catalysts of Methane Decomposition: Accumulation of Filamentous Carbon', *Applied Catalysis A: General*, 228 (1–2), 53–63.

Balat M., Balat M., Elif Kırtay E., Balat H. (2009) 'Main Routes for the Thermo-Conversion of Biomass into Fuels and Chemicals. Part 2: Gasification Systems', *Energy Conversion and Management*, 50 (12), 3158–3168.

Barbooti M.M., Al-Ani R.R. (1984) 'The Copper-Chlorine Thermochemical Cycle of Water Splitting for Hydrogen Production', *Thermochimica Acta*, 78 (1–3), 275–284.

'Basic Research Needs for Solar Energy Utilization' (2005) *Report on the Basic Energy Sciences Workshop on Solar Energy Utilization*, April 18–21, 2005, Publication: Renée M. Nault, Argonne National Laboratory.

Bilgen E., Galindo J. (1981) 'High Temperature Solar Reactors for Hydrogen Production', *International Journal of Hydrogen Energy*, 6 (2), 139–152.

Bilgen E., Ducarroir M., Foex M., Sebieude F., Trombe F. (1977) 'Use of Solar Energy for Direct and Two-Step Water Decomposition Cycles', *International Journal of Hydrogen Energy*, 2, 251–257.

Böhmer M., Langnickel U., Sanchez M. (1991) 'Solar Steam Reforming of Methane', *Solar Energy Materials*, 24, 441–448.

Boltzmann L. (1886) 'Der zweite Hauptsatz der mechanischen Wärmetheorie', *Almanach der kaiserlichen Akademie der Wissenschaften*, 36, 225–259.

Carty R.H., Mazumder M.M., Schreider J.D., Panborn J.B. (1981) 'Thermochemical Hydrogen Production', GRI-80/0023, *Gas Research Institute for the Institute of Gas Technology*, 1–4*,* Chicago, IL.

Dahl J.K., Buechler K.J., Finley R., Stanislaus T., Weimer A.W, Lewandowski A., Bingham C., Smeets A., Schneider A. (2004) 'Rapid Solar-Thermal Dissociation of Natural Gas in an Aerosol Flow Reactor', *Energy*, 29 (5–6), 715–725.

Diver R.B., Miller J.E., Allendorf M.D. (2008) 'Solar Thermochemical Water-Splitting Ferrite-Cycle Heat Engines', *Journal of Solar Energy Engineering*, 130 (4), 041001-1–041001-8.

Dunn R., Lovegrove K., Burgess G. (2012) 'A Review of Ammonia-based Thermochemical Energy Storage for Concentrating Solar Power', *IEEE Journal*, 100 (2), 391–400.

Ehrensberger K., Frei A., Kuhn P., Oswald H.R., Hug P. (1995) 'Comparative Experimental Investigations of the Water-Splitting Reaction with Iron Oxide $Fe_{1-y}O$ and Iron Manganese Oxides $(Fe_{1-x}Mn_x)_{1-y}O$', *Solid State Ionics*, 78 (1–2), 151–160.

Ehrensberger K., Kuhn P., Shklover V., Oswald H. (1996) 'Temporary Phase Segregation Processes During the Oxidation of $(Fe_{0.7}Mn_{0.3})_{0.99}O$ in N_2-H_2O Atmosphere', *Solid State Ionics*, 90 (1–4), 75–81.

Figueiredo J.L., Órfão J.J.M., Cunha A.F. (2010) 'Hydrogen Production via Methane Decomposition on Raney-Type Catalysts', *International Journal of Hydrogen Energy*, 35 (18), 9795–9800.

Flamant G., Hernandez D., Bonet C., Traverse J.P. (1980) 'Experimental Aspects of the Thermochemical Conversion of Solar Energy: Decarbonation of $CaCO_3$', *Solar Energy*, 24, 385–395.

Francis T.M., Lichty P.R., Weimer A.W. (2010) 'Manganese Oxide Dissociation Kinetics for the Mn_2O_3 Thermochemical Water-Splitting Cycle. Part 1: Experimental', *Chemical Engineering Science*, 65 (12), 3709–3717.

Funk H., Diaz H., Liang X., Carney C.S., Weimer A.W., Li P. (2008) 'Hydrogen Generation by Hydrolysis of Zinc Powder Aerosol', *International Journal of Hydrogen Energy*, 33 (4), 1127–1134.

Funk J.E., Reinstorm R.M. (1966) 'Industrial and Engineering Chemistry Process Design and Development', *Industrial and Engineering Chemistry Process Design and Development*, 5 (3), 336–342.

Gaudernack B., Lynum S. (1998) 'Hydrogen from Natural Gas without Release of CO_2 to the Atmosphere', *International Journal of Hydrogen Energy*, 23 (12), 1087–1093.

Gokon N., Hasegawa T., Takahashi S., Kodama T. (2008a) 'Thermochemical Two-Step Water-Splitting for Hydrogen Production Using Fe-YSZ Particles and a Ceramic Foam Device', *Energy*, 33 (9), 1407–1416.

Gokon N., Takahashi S., Yamamoto H., Kodama T. (2008b) 'Thermochemical Two-Step Water-Splitting Reactor with Internally Circulating Fluidized Bed for Thermal Reduction of Ferrite Particles', *International Journal of Hydrogen Energy*, 33 (9), 2189–2199.

Gregg D.W., Aiman W.R, Otsuki H.H., Thorsness C.B. (1980) 'Solar Coal Gasification', *Solar Energy*, 24 (3), 313–321.

Graves C., Ebbesen S.D., Mogensen M., Lackner K.S. (2011) 'Sustainable Hydrocarbon Fuels by Recycling CO_2 and H_2O with Renewable or Nuclear Energy', *Renewable and Sustainable Energy Reviews*, 15 (1), 1–23.

Hall C.C., Hsensel V. (1945) 'The Fischer-Tropsch Plant of Ruhrchemie A.G.', Fuels and Lubricants (http://www.fischer-tropsch.org/primary_documents/gvt_reports/CIOSC/cios_30_69/cios_30_69_toc.htm).

Haueter P., Moeller S., Palumbo R., Steinfeld A. (1999) 'The Production of Zinc by Thermal Dissociation of Zinc, Oxide-Solar Chemical Reactor Design', *Solar Energy*, 67 (1–3), 161–167.

Hirsch D., Steinfeld A. (2004) 'Solar Hydrogen Production by Thermal Decomposition of Natural Gas Using a Vortex-Flow Reactor', *International Journal of Hydrogen Energy*, 29 (1), 47–55.

Holladay J.D., Hu J., King D.L., Wang Y. (2009) 'An Overview of Hydrogen Production Technologies', *Catalysis Today*, 139, 244–260.

IEA (2009) 'Carbon Capture and Storage', *Technology Roadmap*, International Energy Agency.

IEA (2010) 'Concentrating Solar Power', Technology Roadmaps, Paris, France (http://www.iea.org/papers/2010/csp_roadmap.pdf).

IEA (2011a) 'International Energy Outlook 2011', US Energy Information Administration (http://www.eia.gov/forecasts/ieo/more_highlights.cfm#world).

IEA (2011b) 'Annual Energy Outlook 2011–with Projections to 2035', US Energy Information Administration.

Inoue M., Hasegawa N., Uehara R., Gokon N., Kaneko H., Tamaura Y. (2004) 'Solar Hydrogen Generation with $H_2O/ZnO/MnFe_2O_4$ System', *Solar Energy*, 76 (1–3), 309–315.

Ishihara H., Kaneko H., Hasegawa N., Tamaura Y. (2008) 'Two-Step Water-Splitting at 1273–1623 K Using Yttria-Stabilized Zirconia-Iron Oxide Solid Solution via Co-Precipitation and Solid-State Reaction', *Energy*, 33 (12), 1788–1793.

Kaneko H., Gokon N., Hasegawa N., Tamaura Y. (2005) 'Solar Thermochemical Process for Hydrogen Production Using Ferrites', *Energy*, 30 (11–12), 2171–2178.

Kaneko H., Yokoyama T., Fuse A., Ishihara H., Hasegawa N., Tamaura Y. (2006a) 'Synthesis of New Ferrite, Al-Cu Ferrite, and its Oxygen Deficiency for Solar H_2 Generation from H_2O', *International Journal of Hydrogen Energy*, 31 (15), 2256–2265.

Kaneko H., Miura T., Ishihara H., Yokoyama T., Chen M., Tamaura Y. (2006b) 'Solar Rotary Reactor for Continuous H_2 Production Using Two-Step Water Splitting Process', WHEC 16, June 13–16, Lyon, France.

Kaneko H., Miura T., Fuse A., Ishihara H., Taku S., Fukuzumi H., Naganuma Y., Tamaura Y. (2007) 'Rotary-Type Solar Reactor for Solar Hydrogen Production with Two-Step Water Splitting Process', *Energy and Fuels*, 21 (4), 2287–2293.

Kang K.S., Kim C.H., Cho W.C., Bae K.K., Kim S.H., Park C.S. (2009) 'Novel Two-Step Thermochemical Cycle for Hydrogen Production from Water Using Germanium Oxide: KIER 4 Thermochemical Cycle', *International Journal of Hydrogen Energy*, 34 (10), 4283–4290.

Knight H. (2010) 'The Next Best Thing to Oil', *New Scientist*, 2274.

Kodama T. (2003) 'High-Temperature Solar Chemistry for Converting Solar Heat to Chemical Fuels', *Progress in Energy and Combustion Science*, 29 (6), 567–597.

Kodama T., Gokon N. (2007) 'Thermochemical Cycles for High-Temperature Solar Hydrogen Production', *Chemical Reviews*, 107 (10), 4048–4077.

Kodama T., Kondoh Y., Yamamoto R., Andou H., Satou N. (2005) 'Thermochemical Hydrogen Production by a Redox System of ZrO_2-Supported Co(II)-Ferrite', *Solar Energy*, 78 (5), 623–631.

Kodama T., Gokon N., Yamamoto R. (2008) 'Thermochemical Two-Step Water Splitting by ZrO_2-Supported $Ni_xFe_{3-x}O_4$ for Solar Hydrogen Production', *Solar Energy*, 82 (1), 73–79.

Kogan M., Kogan A. (2003a) 'Production of Hydrogen and Carbon by Solar Thermal Methane Splitting. I. The Unseeded Reactor', *International Journal of Hydrogen Energy*, 28 (11), 1187–1198.

Kogan M., Kogan A. (2003b) 'Production of Hydrogen and Carbon by Solar Thermal Methane Splitting. II. Room Temperature Simulation Tests of Seeded Solar Reactor', *International Journal of Hydrogen Energy*, 29 (12), 1227–1236.

Kogan M., Kogan A., Barak S. (2005) 'Production of Hydrogen and Carbon by Solar Thermal Methane Splitting. III. Fluidization, Entrainment and Seeding Particles into a Volumetric Solar Receiver', *International Journal of Hydrogen Energy*, 30, 35–43.

Konstandopoulos A.G., Lorentzou S. (2010) 'Novel Monolithic Reactors for Solar Thermochemical Water Splitting', in *On Solar Hydrogen and Nanotechnology* (Vayssieres L., ed.), John Wiley & Sons, Singapore.

Konstandopoulos A.G., Papaioannou E., Zarvalis, D., Skopa, S., Baltzopoulou P., Kladopoulou E., Kostoglou M., Lorentzou S. (2005) 'Catalytic Filter Systems with Direct and Indirect Soot Oxidation Activity', SAE Technical Paper No. 2005-01-0670, SAE SP, 1942, *Diesel Exhaust Emission Control*, 167–182. Also in SAE Trans. 114 (*J. Fuels & Lubricants*), 243–258.

Lédé J. (1999) 'Solar Thermochemical Conversion of Biomass', *Solar Energy*, 65 (1), 3–13.

Lichty P., Perkins C., Woodruff B., Bingham C., Weimer A. (2010) 'Rapid High Temperature Solar Thermal Biomass Gasification in a Prototype Cavity Reactor', *Journal of Solar Energy Engineering*, 132 (1), 011012 (7 pages).

Lundberg M. (1993) 'Model Calculations on Some Feasible Two-Step Water Splitting Processes', *International Journal of Hydrogen Energy*, 18 (5), 369–376.

Martín M., Gallardo V., González Pardo A., Gonzalez-Aguilar J., Romero M., Iranzo A., Salva A., Tapia E. (2011) 'Thermal and Optical Analysis of a 100 kW_{th} Multi-Tubular Reactor for Hydrogen Production Based on a Two-Step Thermochemical Cycle Integrated in a Solar Tower', *International Conference on Hydrogen Production ICH2P-11*, Paper No. 315SOL, June 19–22, Thessaloniki, Greece.

Masel R.I. (2001) *Chemical Kinetics and Catalysis*, Wiley-Interscience, New York.

Matsunami J., Yoshida S., Oku Y., Yokota O., Tamaura Y., Kitamura M. (2000) 'Coal Gasification with CO_2 in Molten Salt for Solar Thermal/Chemical Energy Conversion', *Solar*, 25 (1), 71–79.

McQuillan B.W., Brown L.C., Besenbruch G.E., Tolman R., Cramer T., Russ B.E. (2005) 'High Efficiency Generation of Hydrogen Fuels Using Solar Thermochemical Splitting of Water', Report GA-A24972, General Atomics, San Diego, CA.

Meier A., Sattler C. (2009) 'Solar Fuels from Concentrated Sunlight', *IEA Solar-PACES Implementing Agreement*, SolarPaces, August 2009.

Melchior T., Perkins C., Lichty P., Weimer A.W., Steinfeld A. (2009) 'Solar-Driven Biochar Gasification in a Particle-Flow Reactor', *Chemical Engineering and Processing*, 48 (8), 1279–1287.

Möller S. (2005) 'SOLREF – Solar Steam Reforming, Solar-SMR', Technology Platform Operation Review Days, December 8–9, Brussels, Belgium.

Möller S., Palumbo R. (2001a) 'Solar Thermal Decomposition Kinetics of ZnO in the Temperature Range 1950–2400 K', *Chemical Engineering Science*, 56 (15), 4505–4515.

Möller S., Palumbo R. (2001b) 'The Development of a Solar Chemical Reactor for the Direct Thermal Dissociation of Zinc Oxide', *ASME – Journal of Solar Energy Engineering*, 123 (2), 83–90.

Muradov N.Z., Veziroglu N.T. (2008) 'Green Path from Fossil-based to Hydrogen Economy: An Overview of Carbon-Neutral Technologies', *International Journal of Hydrogen Energy*, 33 (23), 6804–6839.

Nakamura T. (1977) 'Hydrogen Production from Water Utilizing Solar Heat at High Temperatures', *Solar Energy*, 19 (5), 467–475.

Njobeni S. (2011) 'PetroSA Technology Ready for Next Stage', Business Day – News Worth Knowing, May 10 (http://www.businessday.co.za/articles/Content.aspx?id=142267).

Norman J.H., Besenbruch G.E., Brown L.C., O'Keefe D.R., Allen C.L. (1982) 'Thermochemical Water-Splitting Cycle, Bench Scale Investigations, and Process

Engineering', Final report for the period February 1977 through December 1981, General Atomics Corp., La Jolla, CA.
Opdal O.A. (2006) Project Report, by Department of Energy & Process Engineering, Faculty of Engineering Science and Technology, Norwegian University of Science and Technology.
Perkins C., Weimer A.W. (2004) 'Likely Near-Term Solar-Thermal Water Splitting Technologies', *International Journal of Hydrogen Energy*, 29 (15), 1587–1599.
Perkins C., Lichty P.R., Weimer A.W. (2008) 'Thermal ZnO Dissociation in a Rapid Aerosol Reactor as Part of a Solar Hydrogen Production Cycle', *International Journal of Hydrogen Energy*, 33 (2), 499–510.
Perry R.H. (2008) *Perry's Chemical Engineers' Handbook*, 8th edn (Green D.W., ed.), McGraw-Hill.
Pregger T., Graf D., Krewitt W., Sattler C., Roeb M., Möller S. (2009) 'Prospects of Solar Thermal Hydrogen Production Processes', *International Journal of Hydrogen Energy*, 34 (10), 4256–4267.
Richter C., Blanco J., Heller P., Mehos M., Meier A., Meyer R., Weiss W. (eds) (2008) 'Solar Power and Chemical Energy Systems', *SolaPACES Annual Report 2008*, International Energy Agency.
Rochlin L., Purchase R., Ryan M. (eds) (2011) 'Liquid Sunshine', *Solar Australia*, November (2), pp. 24–26.
Rodat S., Abanades S., Flamant G. (2010a) 'Experimental Evaluation of Indirect Heating Tubular Reactors for Solar Methane Pyrolysis', *International Journal of Chemical Reactor Engineering*, 8, Art. No. 25.
Rodat S., Abanades S., Sans J.L., Flamant G. (2010b) 'A Pilot-Scale Solar Reactor for the Production of Hydrogen and Carbon Black from Methane Splitting', *International Journal of Hydrogen Energy*, 35 (15), 7748–7758.
Rodat S., Abanades S., Flamant G. (2011) 'Co-Production of Hydrogen and Carbon Black from Solar Thermal Methane Splitting in a Tubular Reactor Prototype', *Solar Energy*, 85 (4), 645–652.
Roeb M., Monnerie N., Schmitz M., Sattler C., Konstandopoulos A.G., Agrafiotis C., Zaspalis V.T., Nalbandian L., Steele A.M., Stobbe P. (2006a) 'Thermo-Chemical Production of Hydrogen from Water by Metal Oxides Fixed on Ceramic Substrates', *Proceedings of the 16th World Hydrogen Energy Conference*, June 13–16, Lyon, France.
Roeb M., Sattler C., Klüser R., Monnerie N., de Oliveira L., Konstandopoulos A.G., Agrafiotis C., Zaspalis V.T., Nalbandian L. (2006b) 'Solar Hydrogen Production by a Two-Step Cycle Based on Mixed Iron Oxides', *Journal of Solar Energy Engineering – Transactions of the ASME*, 128 (2), 125–133.
Roeb M., Neises M., Säck J.P., Rietbrock P., Monnerie N., Dersch J., Schmitz M., Sattler C. (2009) 'Operational Strategy of a Two-Step Thermochemical Process for Solar Hydrogen Production', *International Journal of Hydrogen Energy*, 34 (10), 4537–4545.
Roeb M., Säck J.P., Rietbrock P., Prahl C., Schreiber H., Neises M., Graf D., Ebert M., Reinalter W., Meyer-Grünefeldt M., Sattler C., Lopez A., Vidal A., Elsberg A., Stobbe P., Jones D., Steele A., Lorentzou S., Pagkoura C., Zygogianni A., Agrafiotis C., Konstandopoulos A.G. (2011) 'Test Operation of a 100 kW Pilot Plant for Solar Hydrogen Production from Water on a Solar Tower', *Solar Energy*, 85 (4), 634–644.

Sasol (2011) 'Sasol Facts 2011 – Your Blueprint to the World of Sasol' (http://www.sasol.com/sasol_internet/downloads/11029_Sasol_Facts_2011_1309786765289.pdf).

Sibieude F., Ducarroir M., Tofighi A., Ambriz J. (1982) 'High-Temperature Experiments with a Solar Furnace: the Decomposition of Fe_3O_4, Mn_3O_4, CdO', *International Journal of Hydrogen Energy*, 7 (1), 79–88.

Stein W., Edwards J., Hinkley J., Sattler C. (2009), 'Solar Thermal Steam Reforming'. In *Encyclopedia of Electrochemical Power Sources*, J. Garche, Editor-in-Chief Elsevier, Amsterdam, pp. 300–312.

Steinfeld A. (2002) 'Solar Hydrogen Production via a Two-Step Water-Splitting Thermochemical Cycle Based on Zn/ZnO Redox Reactions', *International Journal of Hydrogen Energy*, 27 (6), 611–619.

Steinfeld A. (2005) 'Solar Thermo-Chemical Production of Hydrogen – A Review', *Solar Energy*, 78 (5), 603–615.

Steinfeld A., Meier A. (2004) 'Solar Fuels and Materials', *Encyclopedia of Energy*, 5, 623–637.

Steinfeld A., Weimer A.W. (2010) 'Thermochemical Production of Fuels with Concentrated Solar Energy', *Optics Express*, 18 (9), A100–A111.

Steinfeld A., Kuhn P., Reller A., Palumbo R., Murray J., Tamaura Y. (1998a) 'Solar-Processed Metals as Clean Energy Carriers and Water-Splitters', *International Journal of Hydrogen Energy*, 23 (9), 767–774.

Steinfeld A., Brack M., Meier A., Weidenkaff A., Wuillemin D. (1998b) 'Solar Chemical Reactor for Co-Production of Zinc and Synthesis Gas', *Energy*, 23 (10), 803–814.

Sundrop Fuels Inc. (2009) 'Converting the Sun's Energy into Clean, Affordable Fuels', Press Release (http://www.sundropfuels.com/fact.pdf).

Takahashi Y., Aoki H., Kaneko H., Hasegawa N., Suzuki A., Tamaura Y. (2004) 'Oxygen-Gas-Releasing Reaction of Zn Ferrite by Xe Lamp Beam Irradiation in Air at 1800 K', *Solid State Ionics*, 172 (1–4), 89–91.

Tamaura Y., Steinfeld A., Kuhn P., Ehrensberger K. (1995) 'Production of Solar Hydrogen by a Novel, 2-Step, Water-Splitting Thermochemical Cycle', *Energy*, 20 (4), 325–330.

Tamaura Y., Kojima M., Sano T., Ueda Y., Hasegawa N., Tsuji M. (1998) 'Thermodynamic Evaluation of Water Splitting by a Cation-Excessive (Ni, Mn) Ferrite', *International Journal of Hydrogen Energy*, 23 (12), 1185–1191.

Tamaura Y., Uehara R., Hasegawa N., Kaneko H., Aoki H. (2004) 'Study on Solid-State Chemistry of the $ZnO/Fe_3O_4/H_2O$ System for H_2 Production at 973–1073 K', *Solid State Ionics*, 172 (1–4), 121–124.

Tofighi A. (1982) 'Contribution à l'étude de la Decomposition des Oxydes de fer au Foyer d'un Four Solaire', Ph.D. Thesis, L'Institut National Polytechnique de Toulouse, France.

Tributsch H. (1989) 'Feasibility of Toxic Chemical Waste Processing in Large Scale Solar Installations', *Solar Energy*, 43 (3), 139–143.

Trombe F., Gion L., Royere C., Robert J.F. (1973) 'First Results Obtained with the 1000 kW Solar Furnace', *Solar Energy*, 15, 63–66.

Trommer D., Hirsch D., Steinfeld A. (2004) 'Kinetic Investigation of the Thermal Decomposition of CH_4 by Direct Irradiation of a Vortex-Flow Laden with Carbon Particles', *International Journal of Hydrogen Energy*, 29 (6), 627–633.

Van Noorden R. (2010) 'Carbon Sequestration: Buried Trouble', *Nature*, 463, 871–873.

Weimer A.W., Dahl J., Buechler K., Lewandowski A., Pitts R., Bingham C., Glatzmaier G.C. (2001) 'Thermal Dissociation of Methane Using a Solar Coupled Aerosol Flow Reactor', NREL/CP-570-30535, *Proceedings of the 2001 DOE Hydrogen Program Review*.

World Nuclear Association, Hore-Lacy I. (2009) 'Hydrogen Production from Nuclear Power'. In: *Encyclopedia of Earth*, Cleveland C.J. (ed.), Environmental Information Coalition, National Council for Science and the Environment, Washington, DC.

Wyss J., Martinek J., Kerins M., Dahl J.K., Weimer A., Lewandowski A., Bingham C. (2007) 'Rapid Solar-Thermal Decarbonization of Methane in a Fluid-Wall Aerosol Flow Reactor – Fundamentals and Application', *International Journal of Chemical Reactor Engineering*, 5 (1).

Zeman F.S., Keith D.W. (2008) 'Carbon Neutral Hydrocarbons', *Philosophical Transactions of the Royal Society A*, 366, 3901–3918.

Zhang T., Amiridis M.D. (1998) 'Hydrogen Production via the Direct Cracking of Methane over Silica-Supported Nickel Catalysts', *Applied Catalysis A: General*, 167 (2), 161–172.

Index